

**THE APPLICATION OF NEURAL
NETWORKS TO NON-DESTRUCTIVE
TESTING TECHNIQUES**

James Nicholas Watson BSc (Hons) MSc GradInstP

**A thesis submitted to Napier University,
in partial fulfilment of the requirements for the
Degree of Doctor of Philosophy**

**School of the Built Environment
Napier University
Edinburgh, U.K.**

2001

This copy of the thesis has been supplied on condition that anyone who consults it is understood to recognise that the copyright rests with its author. No quotation from the thesis and no information derived from it may be published without the prior written consent of the author or the University (as may be appropriate).

Abstract

The low strain test method has become the prevalent method for integrity testing of cast *in situ* foundation piles. The automated interpretation of the sonic echo traces resulting from this test would prove beneficial to industry through the standardisation of the test method procedure and a reduction in the time spent analysing results. Therefore, in this research the generalisation and feature extraction strengths of artificial neural networks have been exploited to aid test trace interpretation.

This study involved the identification of three multilayer networks considered most suitable for the heteroassociative function approximation task described above. Multilayer Perceptron (MLP) networks, Radial Basis Neural Networks (RBNN) and Wavelet Basis Neural Networks (WBNN) have all been trained using numerically generated data and their performances compared to identify the optimum network type. While each network presented similar strengths and weaknesses in fault diagnosis, statistical analysis suggested that the MLP network was marginally more successful in quantifying changes in cross-sections along the pile length. Field data from three test sites have confirmed that the network can identify, locate and quantify significant ($\pm 13\%$) changes in diameter along the pile length (within known test method limitations). The network has also diagnosed changes in diameter at the pile head. This task is notoriously difficult using conventional techniques and has been facilitated through the development of a novel pre-processing technique: the wavelet *mobility scalogram*.

Declaration

This thesis is submitted to Napier University for the Degree of Doctor of Philosophy. The work described in this thesis was carried out under the supervision of Dr Charles Fairfield, Dr Chuen Wan and Professor Alan Sibbald. The work was undertaken in The School of the Built Environment (formerly The Department of Civil and Transportation Engineering), Napier University, Edinburgh.

In accordance with the Regulations of Napier University governing the requirements for the Degree of Doctor of Philosophy, the candidate submits that the work presented in this thesis is original unless otherwise referenced within the text.

The following papers published in journals or conference proceedings were derived from the work in this thesis. Selected papers published prior to this thesis being prepared are included in Appendix 2. Full permission from the relevant publisher or copyright holder has been obtained.

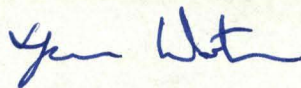
- (1) Watson J N, Fairfield C A, Sibbald A, and Wan C L, Neural Networks for Piled Foundation Integrity Assessment, Proc. 6th Int. Conf. Structural Faults and Repair, London (1995) pp83-91.
Commendation for Conference Award from Editorial Board.
- (2) Watson J N, Fairfield C A, Wan C L, and Sibbald A, The Use of Artificial Neural Networks in Pile Integrity Testing, Developments in Neural Networks and Evolutionary Computing for Civil and Structural Engineering, Ed. Topping B H V, Civil-Comp Press (1995) pp7-14.
- (3) Addison P S, Sibbald A and Watson J N, Wavelet Transform: A Mathematical Microscope with Civil Engineering Applications, Insight, Vol.39, No.7 (1997) pp493-497.
- (4) Addison P S and Watson J N, Wavelet Analysis for Low Strain Integrity Testing of Foundation Piles, Proc. 5th Int. Conf. Inspection, Appraisal, Repairs and Maintenance of Buildings and Structures, Singapore (1997) pp15-16.

- (5) Watson J N, Addison P S and Sibbald A, Non-Destructive Testing of Foundation Piles using the Wavelet Transform, Proc. 12th Am. Soc. Civ. Eng., Eng. Mech. Division Conf., La Jolla, California, USA (1998) (Distributed on CD-ROM).
- (6) Addison P S, Watson J N and Sibbald A, Wavelet Filtering of Low Strain Integrity Test Data, Proc. 37th Annual Brit. Conf. NDT, Newcastle (1998) pp15-17.
- (7) Addison P S, Watson J N and Murray K B, Wavelet Transform Applications: Testing, Turbulence and Tachycardia, Wavelets: The Key to Intermittent Information, The Royal Society, London, Feb.24-25, (1999). (*Poster Presentation*)
- (8) Addison P S and Watson J N, Wavelet Transforms: Structural Testing and Tachycardia, SET for BRITAIN, Reception for Young Researchers at the House of Commons, London, 15 March, (1999). (*Poster Presentation*)
- (9) Watson J N, Addison P S and Sibbald A, The De-Noising of Sonic Echo Test Data Through Wavelet Transform Reconstruction, J. of Shock and Vibration, Vol. 6 (1999) pp267-272.
- (10) Addison P S, Watson J N and Sibbald A, The Practicalities of using Wavelet Transforms in the Non-Destructive Testing of Piles, Proc. 13th Am. Soc. Civ. Eng., Eng. Mech. Division Conf., Baltimore, Maryland, USA (1999) (Distributed on CD-ROM).
- (11) Watson J N, Addison P S, and Sibbald, Temporal Filtering of NDT Data using Wavelet Transforms, Proc. 14th Am. Soc. Civ. Eng., Eng. Mech. Division Conf., Austin, Texas, USA (2000) (Distributed on CD-ROM).

Other Publications by the author:

- (12) Jotischky H, Kennedy R, Morgan N and Watson J, Information Technology at the Paint Research Association (PRA), J. Oil and Colour Chemists Assoc., Vol. 75, No. 2 (1992) pp74-76.
- (13) J N Watson, Temporal Difference Learning in Neural Networks, MSc Thesis, Queen Mary and Westfield College, University of London (1993).

- (14) Addison P S and Watson J N, The Wavelet Transform as a Tool for the Analysis of Surface Roughness, SiF News, Paint Research Association, No.9 (1997) pp5-7.
- (15) Watson J N, Addison P S, Clegg G R, Holzer M, Sterz F and Robertson C E, Evaluation of Arrhythmic ECG Signals using a Novel Wavelet Transform Method, Resuscitation, Vol. 19, No. 5 (2000) pp121-127.
- (16) Clegg G R, Addison P S, Watson J N, Holzer M, Sterz F R and Robertson C E, Hidden Structure Revealed in Ventricular Fibrillation Using a Wavelet Decomposition Based Analysis, J. of Accident and Emergency Medicine, No. 17 (2000) p59 (abstract).
Winner of the EMRs Scholarship Prize for Best Piece of Original Research at the Annual Scientific Meeting of the Faculty of Accident and Emergency Medicine (1999)
- (17) Addison P S, Watson J N, Clegg G R, Holzer M, Sterz F and Robertson C E, Evaluating Arrhythmias in ECG Signals using Wavelet Transforms, IEEE Engineering in Medicine and Biology, Vol. 19, No. 5 (2000) pp104-109.
- (18) Addison P S, Murray K B, Watson J N, Wavelet Transform Analysis of Open Channel Wake Flows, Am. Soc. Civ. Eng. J. Eng. Mech. (In print: January 2001).
- (19) Addison P S, Watson J N, Clegg G R, Steen P A and Robertson C E, Co-ordinated Atrial Activity During Ventricular Fibrillation made Visible in Surface ECG Using Wavelet Decomposition, Trans. IEEE Engineering in Medicine and Biology (*Accepted for publication*).



James Nicholas Watson, BSc (Hons) MSc GradInstP

Acknowledgement

The author expresses his gratitude for the assistance and encouragement of his supervisors Dr Charles Fairfield, Dr Chuen Wan and Professor Alan Sibbald. Their recommendations and constructive discussions have been very much appreciated by the author. He also thanks the School of the Built Environment, Napier University for making the facilities available for this work and all the students and staff who have made his stay both enjoyable and memorable.

The author acknowledges the support of the Engineering and Physical Sciences Research Council (EPSRC) who supported this work through research studentship number 93315803.

The author is indebted to the twenty companies that replied to his industry survey for their help. Too many to mention here, a list of these companies can be found in Appendix I. Particular thanks are due to Simon French and Dick Stain of Testconsult Ltd, and Stephen Kemp of Technotrade Ltd who gave up their time to answer questions, demonstrate software, participate in meetings and provide test data for analysis. Mike Kightley and Richard Nicholson of Testal Ltd are also particularly thanked for organising site access, validating the author's data acquisition system, and demonstrating the equipment commercially available for pile testing.

The author thanks Dr Paul Addison, colleague and friend, for introducing him to the delights of Wavelet Analysis and who consequently had to endure two research projects and three years of pile testing (EPSRC Grant Refs GR/L27947 and GR/L96202).

Finally, the author thanks his family, Joan and Katy Watson for their continued support during the production of this thesis and Christine for making it worthwhile. This thesis is dedicated to the memory of the author's late father, Kenneth Watson, whose passionate wish, to see its completion, was sadly denied.

CONTENTS

Abstract	i
Declaration	ii
Acknowledgement	v
Contents	vi
List of Figures	xi
List of Tables	xviii
Notation	xx
CHAPTER 1 Introduction	1
1.1 Research Overview	1
1.2 Piled Foundation Testing	2
1.3 Artificial Neural Networks	3
1.4 Key Research Objectives	4
1.5 Thesis Structure	5
CHAPTER 2 Piled Foundations: Associated Defects and Their Detection	7
2.1 Foundations	7
2.2 Piled Foundations	8
2.2.1 Pile Types	8
2.2.1.1 Large Displacement Piles	8
2.2.1.2 Small Displacement Piles	10
2.2.1.3 Non Displacement Piles	10
2.2.1.4 Micro Piles	12
2.3 Faults Associated with Cast <i>in situ</i> Piles	12
2.4 Piled Foundation Load Testing	16
2.4.1 Static Load Testing	16
2.4.2 Dynamic Load Testing	17
2.4.3 Statnamic® Testing	19
2.4.4 The Application of Neural Computing to Load Testing	20
2.5 Integrity Testing	21
2.5.1 Direct Integrity Test Methods	22
2.5.2 Indirect Integrity Test Methods	23
2.5.2.1 Internal Techniques	23
2.5.2.2 External Techniques	25
2.5.2.3 Remote Techniques	27
2.5.2.4 Experimental Techniques	28
2.6 Industry Survey	29
2.7 Low Strain Integrity Testing	30
2.7.1 Pile Excitation and Response Detection	30
2.7.2 Pulse Propagation	32

2.7.2.1	Pulse Generation	32
2.7.2.2	Reflections from the Pile Toe	33
2.7.2.3	Partial Reflections from Changes in Pile Properties	35
2.7.3	Limitations of Low Strain Integrity Test Methods	37
2.7.4	Effects of Soils on Installed Piles	40
2.7.5	Sonic Echo Response Interpretation	42
2.7.6	Transient Dynamic Response Interpretation	43
2.7.7	Automated Interpretation of Low Strain Test Results	46
2.8	Summary and Conclusions	49

CHAPTER 3 Artificial Neural Networks for Signal Processing and Fault Detection 65

3.1	Application Identification	65
3.2	AI Strategies for System Modelling and Classification	66
3.2.1	Syntactic Processing and Tree Search Algorithms	67
3.2.2	Probabilistic Classifiers	69
3.2.3	Nonmonotonic and Fuzzy Logic	71
3.2.4	Learning Networks	72
3.2.4.1	The Biological Inspiration for Neurocomputing	72
3.2.4.2	Artificial Neural Networks : A Definition	73
3.3	Artificial Neural System Components	74
3.3.1	Processing Units	74
3.3.2	Activation State	75
3.3.3	Output Function	75
3.3.4	Pattern of Connectivity	75
3.3.5	Rule of Propagation	76
3.3.6	Activation Rule	76
3.3.7	Learning Algorithm	77
3.3.8	External Environment	78
3.4	ANNs: Their Application to Signal Processing and Structural Testing	78
3.4.1	Unsupervised Learning	78
3.4.2	Supervised Learning	81
3.4.3	Heteroassociative Vector Mapping and Function Approximation	83
3.4.4	Multilayer Neural Networks	85
3.4.4.1	Multilayer Perceptron (MLP)	87
3.4.4.2	Radial Basis Neural Networks (RBNN)	97
3.4.4.3	Wavelet Basis Neural Networks (WBNN)	99
3.5	Learning Systems' Functional Equivalence	102
3.6	Application Development Methodology	106
3.6.1	Application Identification and Feasibility	107
3.6.2	System Development	108
3.6.3	Deliverable System Validation	108
3.7	Summary and Conclusions	108

CHAPTER 4	Feasibility Study	121
4.1	One Dimensional Modelling	122
4.1.1	Wave Tracing	122
4.1.2	Composite Systems	123
4.2	Finite Element Analysis (FEA)	125
4.2.1	Model Element Type	129
4.2.2	Element Aspect Ratio	132
4.2.3	Loading and Boundary Conditions	134
4.2.3.1	Impact Pulse Shape	134
4.2.3.2	Combined Nodal Loading	136
4.2.3.3	Boundary Conditions	137
4.2.4	Material Assignments	138
4.2.4.1	Concrete Properties	138
4.2.4.2	Soil Properties	143
4.2.4.3	Material Damping	145
4.2.5	Dynamic Control and Convergence Criteria	152
4.2.6	Model Validation Using Field Test Data	155
4.2.6.1	Site Investigation Data	156
4.2.6.2	FEA Model	157
4.2.6.3	Results Comparison	158
4.3	Remarks Concerning FEA Modelling	160
4.4	Technical Feasibility	161
4.5	Fault Identification in an Uninstalled Pile	161
4.5.1	Problem Domain Definition	161
4.5.2	Data Presentation	161
4.5.3	Network Output	162
4.5.4	Learning and Test Sets	162
4.5.5	Learning Parameters	162
4.5.6	Network Structure	164
4.5.7	System Repeatability	165
4.5.8	Network Results	165
4.5.9	Noise Utilisation	166
4.6	Summary and Conclusions	167
CHAPTER 5	Hardware and Software Development	203
5.1	System Flexibility	203
5.2	Data Acquisition Equipment	204
5.2.1	New Equipment Overview	205
5.2.2	Impact Testing Equipment	205
5.2.3	AD Converter and Junction Box	205
5.2.4	Acquisition Software	208
5.2.4.1	Main Program Loop	209
5.2.4.2	Data Collection	210

	5.2.4.3	Appending Data to File Records	212
	5.2.4.4	Saving Current File Record	212
5.3		Neural Network Software Development	213
	5.3.1	Multilayer Perceptron	213
	5.3.1.1	Network Structure	214
	5.3.1.2	Network Initialisation	215
	5.3.1.3	Algorithm Implementation	215
	5.3.1.4	Software Validation	216
	5.3.2	Radial Basis Networks	218
	5.3.2.1	Network Structure	219
	5.3.2.2	Network Initialisation	219
	5.3.2.3	Algorithm Implementation	222
	5.3.2.4	Software Validation	223
	5.3.3	Wavelet Basis Neural Networks	225
	5.3.3.1	Network Structure	226
	5.3.3.2	Network Initialisation	227
	5.3.3.3	Algorithm Implementation	229
	5.3.3.4	Software Validation	229
5.4		Summary and Conclusions	231

CHAPTER 6 Application Development 250

6.1		Introduction	250
6.2		Network Pre-Processing	251
	6.2.1	Time Based Methods	252
	6.2.1.1	Cross and Auto Correlation	252
	6.2.1.2	Enhanced Time History	253
	6.2.2	Frequency Based Methods	254
	6.2.2.1	Spectral Analysis	254
	6.2.2.2	The Mobility Spectrum	255
	6.2.3	Wavelet Methods	256
	6.2.3.1	The Continuous Wavelet Transform	256
	6.2.3.2	The Mobility Scalogram and 'Modmax'	258
		Temporal Filtering	
	6.2.3.3	The Discrete Wavelet Transform	260
	6.2.4	Relative Performances of Pre-Processing Methodologies	261
6.3		Post-Processing	264
6.4		Training Set Dependency	267
6.5		Multilayer Perceptron Networks	268
	6.5.1	Parametric Investigation	268
	6.5.2	The Use of Uncorrelated Noise	270
	6.5.3	Network Sensitivity and Selectivity	270
6.6		Radial Basis Neural Networks	272
	6.6.1	Parametric Investigation	273
	6.6.2	Network Sensitivity and Selectivity	274
6.7		Wavelet Basis Neural Networks	275

6.7.1	Parametric Investigation	275
6.7.2	Network Sensitivity and Selectivity	276
6.8	Comparison of Network Performances	277
6.9	Summary and Conclusions	279
 CHAPTER 7 System Field Testing		 321
7.1	Introduction	321
7.2	Kirkintilloch Site	322
	7.2.1 Hardware Validation	322
	7.2.2 Installed Driven Pile	324
7.3	Blyth Site	325
	7.3.1 Test Site Results	326
	7.3.1.1 Piles with Necking	326
	7.3.1.2 Piles with Cracking	328
	7.3.1.3 Piles with Occluded Voids	328
	7.3.1.4 Pile with a Soft Toe	329
	7.3.1.5 Piles with Bulbing	329
	7.3.1.6 Pile with Weakened Concrete	331
	7.3.1.7 Defect Free Pile	332
	7.3.2 General Points	332
7.4	Bothkennar Site	334
	7.4.1 Test Results	336
	7.4.2 Effects of Exposed Pile Section	337
7.5	Summary and Conclusions	338
 CHAPTER 8 Conclusions		 367
8.1	Key Objective Achievements	368
8.2	Conclusions Specific To Modelling	369
8.3	Conclusions Specific To System Development	370
8.4	Conclusions Specific To Field Testing	372
 CHAPTER 9 Recommendations for Future Research		 374
9.1	Introduction	374
9.2	Pile Response Modelling	374
9.3	Hardware	375
9.4	Signal Pre-Processing	376
9.5	Neural Systems	377
 Appendix 1	 Industry Questionnaire	
Appendix 2	Published Papers	

List of Figures

CHAPTER 1

There are no figures associated with Chapter 1

CHAPTER 2

Figure 2.1	The forces acting on an axially loaded pile in equilibrium	55
Figure 2.2	A summary of piling techniques	55
Figure 2.3	Stages of construction of a percussion bored pile	56
Figure 2.4	Stages of construction of a rotary bored pile	56
Figure 2.5	Stages of construction of a CFA bored pile	56
Figure 2.6	The formation of pile necking	57
Figure 2.7	Plates illustrating losses in section caused by groundwater and uplift	57
Figure 2.8	The method of cross hole sonic coring.	58
Figure 2.9	A typical (TDR) frequency response curve for a cylindrical pile.	58
Figure 2.10	The method of parallel seismic testing	59
Figure 2.11	The low strain testing of a cast in situ pile	59
Figure 2.12	Stress wave propagation in a free-free and fixed-free beam	60
Figure 2.13	Time and frequency responses at the head of a free-free and fixed-free beam	60
Figure 2.14	Conditions under which reflections occur within a foundation pile	61
Figure 2.15	Signal attenuation with respect to pile diameter and soil types	61
Figure 2.16	Theoretical response of a sonic echo test	62
Figure 2.17	Mobility response curve of an installed cylindrical pile	62
Figure 2.18	Mobility response curve of a damaged cylindrical pile	63
Figure 2.19	Modelled frequency response of a damaged pile using SIMINTEG	63
Figure 2.20	An example of a impedance profile as generated by IMPRO	64

CHAPTER 3

Figure 3.1	Simplified representation of two interconnected neurons	116
Figure 3.2	Examples of popular network topologies	116
Figure 3.3	The basic components of a PDP system	117
Figure 3.4	Examples of popularly employed unit activation functions	117
Figure 3.5	The external environment and its relationship to the ANN	118
Figure 3.6	A generic model for multi layered neural systems	119
Figure 3.7	Component stages of ANN application development	120

CHAPTER 4

Figure 4.1	An electrical analogue of an installed pile	172
Figure 4.2	A lumped mass model of a pile soil system	172
Figure 4.3	FEA pile head responses for quadrilateral and triangular elements	173
Figure 4.4	Principle stresses and mesh during pulse propagation	173
Figure 4.5	Gauss point stresses about the pile toe	174
Figure 4.6	Nodal velocity response during pulse propagation	175
Figure 4.7	Reflection coefficient dependency on element aspect ratio	175
Figure 4.8	Hammer impact spectral and temporal responses	176
Figure 4.9	Half-sine and Gaussian input pulse approximations	176
Figure 4.10	Power spectra for Half-sine and Gaussian approximations	176
Figure 4.11	Experimental and FEA model dimensions for uninstalled piles	177
Figure 4.12	Experimental and FEA modelled pile head response of a defect free, uninstalled pile	178
Figure 4.13	Experimental and FEA modelled pile head response of an uninstalled pile with necking	179
Figure 4.14	Experimental and FEA modelled pile head response of an uninstalled pile with bulbing	179
Figure 4.15	Experimental and FEA modelled pile head response of a second defect free, uninstalled pile	180
Figure 4.16	Experimental and FEA model dimensions for damped pile	180
Figure 4.17	Experimental pile head response of a gravel damped pile	181
Figure 4.18	FEA pile head response of a gravel damped pile	181
Figure 4.19	FEA response of a gravel damped pile, without tie supports	181
Figure 4.20	Experimental pile head response of a sand damped pile	182
Figure 4.21	FEA pile head response of a sand damped pile	182
Figure 4.22	FEA response of a sand damped pile, without tie supports	182
Figure 4.23	Signal attenuation of FEA trace with respect to wave theory	183
Figure 4.24	Attenuation dependency on time step value and mesh density	184
Figure 4.25	Time step dependency for implicit and explicit integration methods	185
Figure 4.26	Explicit dynamic control results for an uninstalled pile	185
Figure 4.27	Finite element mesh for an installed pile	186
Figure 4.28	Field test results for a defect free pile	187
Figure 4.29	FEA results for a defect free pile	187
Figure 4.30	Field test mobility curve for a defect free pile	188
Figure 4.31	FEA mobility curve for a defect free pile	188
Figure 4.32	Field test results for a pile with necking	189
Figure 4.33	FEA results for a pile with necking	189
Figure 4.34	Field test mobility curve for a pile with necking	190
Figure 4.35	FEA mobility curve for a pile with necking	190
Figure 4.36	Field test results for a pile with two necks	191
Figure 4.37	FEA results for a pile with two necks	191
Figure 4.38	Field test mobility curve for a pile with two necks	192
Figure 4.39	FEA mobility curve for a pile with two necks	192

Figure 4.40	Field test results for a pile with bulbing	193
Figure 4.41	FEA results for a pile with bulbing	193
Figure 4.42	Field test mobility curve for a pile with bulbing	194
Figure 4.43	FEA mobility curve for a pile with bulbing	194
Figure 4.44	Field test results for a pile with two bulbs	195
Figure 4.45	FEA results for a pile with two bulbs	195
Figure 4.46	Field test mobility curve for a pile with two bulbs	196
Figure 4.47	FEA mobility curve for a pile with two bulbs	196
Figure 4.48	Network performance with respect to learning parameters	197
Figure 4.49	Early weight changes with respect to learning parameters	197
Figure 4.50	Network convergence with respect to layer topology	198
Figure 4.51	Network performance dependency on number of hidden layers	198
Figure 4.52	Network performance dependency on units per hidden layers	198
Figure 4.53	System repeatability experiments	199
Figure 4.54	The effects of noise on system performance	199
Figure 4.55	Network performance with respect to defect position and length	200
Figure 4.56	Network response for a defect free pile	200
Figure 4.57	Samples of system responses from the network's test set	201
Figure 4.58	System response to experimental data	202

CHAPTER 5

Figure 5.1	Previously employed data acquisition hardware (schematic)	234
Figure 5.2	Previously employed data acquisition hardware (plates)	235
Figure 5.3	Previously employed data acquisition hardware (labelled plate)	235
Figure 5.4	Purpose developed data acquisition hardware (schematic)	236
Figure 5.5	Purpose developed data acquisition hardware (plate)	237
Figure 5.6	Signal conditioning unit and instrumented hammers	237
Figure 5.7	Junction box circuit diagram	238
Figure 5.8	Junction box with lid removed (plate)	238
Figure 5.9	A window capture of the data acquisition software	239
Figure 5.10	Flow diagram of data acquisition software main program loop	240
Figure 5.11	Flow diagram of data acquisition module	241
Figure 5.12	Flow diagram of data appending module	242
Figure 5.13	Network convergence curves for the XOR problem with respect to hidden unit number	243
Figure 5.14	Network convergence curves for the XOR problem with respect to learning parameters	243
Figure 5.15	A window capture of the ANN BP simulator in operation	244
Figure 5.16	A window capture of the Kohonen simulator in operation	244
Figure 5.17	Results illustrating the performance of the Kohonen simulator	245
Figure 5.18	Results illustrating the initialisation procedure of an RBNN	246
Figure 5.19	The convergence curve of an RBNN with 100 hidden units	247
Figure 5.20	A performance comparison between networks that did and did not undergo initialisation	247
Figure 5.21	An example of a 2-D Mexican hat wavelet	248

Figure 5.22	The convergence curve of an WBNN with 100 hidden units	248
Figure 5.23	A performance comparison between WBNNs pre and post BP training	249
Figure 5.24	Thumbnail histograms illustrating network parameter distributions pre and post BP training	249

CHAPTER 6

Figure 6.1	A block diagram of the final system processes	284
Figure 6.2	An input force trace from the Blyth test site	285
Figure 6.3	Field traces of a defect free pile and a pile with necking (Piles 1 and 2)	285
Figure 6.4	Field traces of a CFA 250mm diameter pile (Pile 3)	286
Figure 6.5	Field traces of a CFA 300mm diameter pile (Pile 4)	286
Figure 6.6	The mobility curve and reflectogram of a defect free pile	287
Figure 6.7	The reflectograms of Piles 2, 3 and 4	288
Figure 6.8	The complex Mexican hat and its spectrum	289
Figure 6.9	The mobility scalogram of Pile 1	289
Figure 6.10	The 'modmax' scalogram and reconstructed trace of Pile 1	290
Figure 6.11	The wavelet based reflectograms of Piles 2, 3 and 4	291
Figure 6.12	Wavelet shapes and spectra of the Daubechies d2, d4 and d8 orthonormal wavelets	292
Figure 6.13	The decimated, dyadic grid of the discrete wavelet transform frame	292
Figure 6.14	The discrete wavelet transform and reconstruction of Pile 4	293
Figure 6.15	The discrete wavelet transform filtered trace of Pile 3	294
Figure 6.16	The convergence curves of networks presented with mobility curve data	294
Figure 6.17	Examples of ANN reconstruction from mobility curve data	295
Figure 6.18	The convergence curves of networks presented with wavelet encoded data	296
Figure 6.19	Hinton-like diagrams illustrating the input weights of the Fourier and wavelet networks	296
Figure 6.20	Examples of ANN reconstruction from wavelet encoded data	297
Figure 6.21	Comparison of input encoding methods	298
Figure 6.22	Comparison of output encoding methods	299
Figure 6.23	Convergence curve shapes with respect to training set size	300
Figure 6.24	Network mean pattern errors with respect to training set size	300
Figure 6.25	Training set convergence curves with respect to set population	301
Figure 6.26	Test set convergence curves with respect to set population	301
Figure 6.27	MLP performance with respect to learning parameters	302
Figure 6.28	Convergence curve shapes with respect to learning parameters	302
Figure 6.29	MLP performance with respect to architecture topology	303
Figure 6.30	An example of overtraining in a 160 unit MLP network	303
Figure 6.31	Mean pattern error with respect to injected uncorrelated noise	304
Figure 6.32	Examples of field test results with and without noise added	304

Figure 6.33	Errors in calculated pile profile with respect to fault position	305
Figure 6.34	Errors in calculated change in radius at a fault with respect to that fault's position	305
Figure 6.35	Errors in calculated change in radius at a fault with respect to that fault's axial length	306
Figure 6.36	Errors in calculated change in radius at a fault with respect to that fault's change in radius	306
Figure 6.37	Examples of network performance for piles with small defects	307
Figure 6.38	Examples of network performance for piles with large, single defects	307
Figure 6.39	Examples of network performance for piles with defects near the pile toe	308
Figure 6.40	Examples of network performance for piles with multiple faults	308
Figure 6.41	RBNN performance with respect to learning parameters	309
Figure 6.42	RBNN performance with respect to architecture topology	310
Figure 6.43	Errors in calculated change in radius at a fault with respect to that fault's position	311
Figure 6.44	Errors in calculated change in radius at a fault with respect to that fault's axial length	311
Figure 6.45	Errors in calculated change in radius at a fault with respect to that fault's change in radius	312
Figure 6.46	Examples of network performance for piles with small defects	312
Figure 6.47	Examples of network performance for piles with large, single defects	313
Figure 6.48	Examples of network performance for piles with defects at the pile head	313
Figure 6.49	Examples of network performance for piles with no defects	314
Figure 6.50	Examples of network performance for piles with multiple defects	314
Figure 6.51	WBNN performance with respect to learning parameters	315
Figure 6.52	WBNN performance with respect to architecture topology	315
Figure 6.53	Errors in calculated change in radius at a fault with respect to that fault's position	316
Figure 6.54	Errors in calculated change in radius at a fault with respect to that fault's axial length	316
Figure 6.55	Errors in calculated change in radius at a fault with respect to that fault's change in radius	317
Figure 6.56	Examples of network performance for piles with small defects	317
Figure 6.57	Examples of network performance for piles with large, single defects	318
Figure 6.58	Examples of network performance for piles with defects at the pile head	318
Figure 6.59	Examples of network performance for piles with no defects	319
Figure 6.60	Examples of network performance for piles with multiple defects	319

Figure 6.61	The effects on network performance of a reduction in the number of hidden units	320
Figure 6.62	Relative network performance for estimation of arbitrary pile profiles with respect to axial location	320

CHAPTER 7

Figure 7.1	The geographical locations of the three test sites used	341
Figure 7.2	Testing of uninstalled piles (plate)	342
Figure 7.3	The 3 uninstalled piles tested (plate)	342
Figure 7.4	A recorded impact trace and spectrum	343
Figure 7.5	The pile head response of a defect free pre-cast pile	343
Figure 7.6	The pile head response of a pile with bulbing	344
Figure 7.7	The pile head response of a pile with necking	344
Figure 7.8	The field test data and FEA modelled trace of an installed pre-cast pile	345
Figure 7.9	The ANN calculated profile for an installed pre-cast pile	345
Figure 7.10	A plan view of the Blyth test site	346
Figure 7.11	The calculated pile profile error for the Blyth data with respect to axial location	347
Figure 7.12	ANN test results for Pile 1	348
Figure 7.13	ANN test results for Pile 2	348
Figure 7.14	ANN test results for Pile 3	349
Figure 7.15	ANN test results for Pile 5	349
Figure 7.16	ANN test results for Pile 7	350
Figure 7.17	ANN test results for Pile 8	350
Figure 7.18	ANN test results for Pile 9	351
Figure 7.19	ANN test results for Pile 10	351
Figure 7.20	ANN test results for Pile 11	352
Figure 7.21	ANN test results for Pile 12	352
Figure 7.22	ANN test results for Pile 13	353
Figure 7.23	ANN test results for Pile 14	353
Figure 7.24	ANN test results for Pile 17	354
Figure 7.25	ANN test results for Pile 18	354
Figure 7.26	ANN test results for Pile 19	355
Figure 7.27	ANN test results for Pile 24	355
Figure 7.28	The effects of artificially reducing soil damping	356
Figure 7.29	The drop in computed pile radius over the first 2.5m	356
Figure 7.30	The plan for the Bothkennar test site	357
Figure 7.31	The Liverpool University test area at Bothkennar	358
Figure 7.32	The soil constituents and bulk density at Bothkennar	359
Figure 7.33	The soil shear modulus at Bothkennar	359
Figure 7.34	Sleeve dimensions of the test piles at Bothkennar	360
Figure 7.35	Pile head preparation (plate)	360
Figure 7.36	Computed and target profiles for test pile T02	361
Figure 7.37	Computed and target profiles for test pile T03	361

Figure 7.38	Computed and target profiles for test pile T07	362
Figure 7.39	Computed and target profiles for test pile T09	362
Figure 7.40	Computed and target profiles for test pile T10	363
Figure 7.41	Computed and target profiles for test pile T11	363
Figure 7.42	Computed and target profiles for test pile T12	364
Figure 7.43	De-noised field data for pile T09 with FEA equivalents	364
Figure 7.44	The excavation of pile A01 (plates)	365
Figure 7.45	The effects of pile head excavation on calculated pile diameter	366

CHAPTER 8

There are no figures associated with Chapter 8

CHAPTER 9

There are no figures associated with Chapter 9

APPENDIX 1

There are no figures associated with Appendix 1

APPENDIX 2

There are no figures associated with Appendix 2

List of Tables

CHAPTER 1

There are no tables associated with Chapter 1

CHAPTER 2

Table 2.1	Pile Defects: Causes and Occurrence	15
Table 2.2	Pile Integrity Test Methods Summary	21

CHAPTER 3

Table 3.1	Business Plan Components Pertinent to a Non-Commercial Research Project	106
-----------	---	-----

CHAPTER 4

Table 4.1	A Comparison of FEA and Theoretical Coefficients of Reflection	133
Table 4.2	Theoretical, Experimental and FEA Modelled Stress Wave Velocities	141
Table 4.3	Quantified Partial Reflections from Discontinuities: Experimental, FEA modelled and Theoretical	142
Table 4.4	Given Values of Poisson's Ratio	144
Table 4.5	Internal Damping in Soils	145
Table 4.6	Concrete Pile Material Properties	148
Table 4.7	Material Properties for Modelled Soils	149
Table 4.8	Pulse Propagation Velocities	149
Table 4.9	Measured Soil Properties with Depth	157
Table 4.10	Material Assignments for FEA model	158
Table 4.11	FEA Modelled and Field Test Trace Comparison	159
Table 4.12	Dynamic Pile Head Stiffnesses	160

CHAPTER 5

Table 5.1	The Cell Structure For a Pile Record	208
Table 5.2	The Data Structure of an MLP Network	214
Table 5.3	The Truth Table for the XOR Logic Gate	217
Table 5.4	A Comparison of Experimental and Published Results for the XOR Problem	217
Table 5.5	Sample Outputs from Networks that: (a) Solved the Problem, and (b) are in a Local Minimum	218

CHAPTER 6

Table 6.1	Pattern Errors in Calculated Pile Radii	266
Table 6.2	Learning Rate Equivalence	269
Table 6.3	Optimum Mean Pattern Errors for the Three Network Types	280

CHAPTER 7

Table 7.1	Results from Uninstalled Piles at Kirkintilloch	323
Table 7.2	Material Properties Employed for Kirkintilloch Site Modelling	324
Table 7.3	Summary of the Bothkennar Piles Included in this Study	334
Table 7.4	Material Properties Employed for Bothkennar Site Modelling	335
Table 7.5	A Comparison of Field Test Results and Design Pile Dimensions	336

CHAPTER 8

There are no tables associated with Chapter 8

CHAPTER 9

There are no tables associated with Chapter 9

APPENDIX 1

There are no tables associated with Appendix 1

APPENDIX 2

There are no tables associated with Appendix 2

Notation

Unless otherwise stated in the text, the symbols used in this document are listed below. Roman characters are given first followed by Greek characters. Acronyms are given after the list of symbols. The units used in this thesis are SI, or derived, units where possible.

Roman characters

A	Cross sectional area (m^2)
a_0	Rayleigh mass damping coefficient
a_1	Rayleigh stiffness damping coefficient
A_B	Attenuation parameter
a_i	The activation value of unit i
a_s	FEA structural accelerations
\underline{B}_s	FEA strain displacement matrix
c	Stress wave group velocity (ms^{-1})
\underline{C}	Centres matrix for an ANN with radial activation functions
\underline{C}_d	FEA damping matrix
c_{ji}	Scalar centre associated with the connection from unit i to j
c_p	Dashpot damping parameter
c_s	Surface wave velocity (ms^{-1})
d	Pile diameter (m)
D_n	ANN activation function distance measure with metric n
\underline{D}_s	FEA matrix of elastic constants
E	Elastic (Young's) Modulus (Nm^{-2})
e	Error associated with white (uncorrelated) noise
E_e	Euclidean pattern error
E_t	Total electrical circuit voltage
f	Frequency (Hz)
F	Force (N)
$F(z)$	Activation function of ANN unit

$\underline{F}^{[e]}$	Total external force applied to FEA element
$\underline{F}_b^{[e]}$	FEA Force vector due to element body loads
$\underline{F}_s^{[e]}$	FEA Force vector due to element surface tractors
$\underline{F}_c^{[e]}$	FEA Force vector due to element applied concentrated loads
$f^{[e]}$	Force per unit volume
f_{cu}	Concrete cube strength (Nmm ⁻²)
G	Shear modulus (GNm ⁻²)
g_k	Gain function for temporal signal enhancement
$H_n^{F(z)}$	ANN functional descriptor with activation function F and metric n
I_t	Total electrical circuit current
j_c	Case soil damping parameter
$\underline{K}^{[e]}$	FEA stiffness matrix
L	Axial length (m)
\underline{M}	FEA mass matrix
\underline{N}_s	Matrix of FEA interpolation functions
P(x)	Impedance Profile
P(z)	Probability Distribution Function
P_{bu}	Ultimate base resistance (N)
P_{su}	Ultimate shaft resistance (N)
P_u	Ultimate load capacity (N)
\mathfrak{R}^d	d dimensional Real vector space
R(t)	Reflectogram
$R_{d(max)}$	Maximum dynamic component of driving resistance
R_i	FEA concentrated load
R_{max}	Maximum measured driving resistance
R_s	Resistance of Mobilised Soil
$R_{s(max)}$	Maximum static component of driving resistance
r	Pile radius (m)
r_t	Input pulse rise time (s)
t	Time (s)
$t^{[e]}$	Surface tractors (force/unit area)

u	Displacement (m)
$v_{h(max)}$	Maximum pile head velocity response (ms^{-1})
v_s	FEA structural velocities
W	Weight (N)
\underline{W}	ANN weight matrix
$W_{a,b}$	Wavelet coefficient for scale and translation values a and b
w_{ji}	Scalar weight value from unit i to j
x	Axial position (m)
\underline{x}	Vector input to ANN
x_i	Scalar input to ANN unit i
\underline{Y}	Target (required) output vector of ANN
\hat{Y}	Vector output of ANN
y_i	Target (required) output of ANN unit i
\hat{y}_i	ANN output of unit i
Z	Soil Impedance

Greek characters

α	ANN learning rate parameter
β	Shear wave velocity
γ_s	FEA element structural strain
δ_c	Oscillatory decrement of decay
$\delta_j(p)$	Error associated with unit j for pattern p
δ_s	FEA element structural displacement vector
\underline{d}^{el}	Nodal displacement vector for element e
ε	Axial strain
η_d	d dimensional vector for the parameterisation of a continuous function
θ	ANN activation function threshold value
λ	Momentum parameter for MLP network training
λ_l	Load transfer parameter for pile driving
μ	Viscous parameter for visco-elastic soil modelling

$\mu_{A_{ij}}(x_i)$	Membership function describing the membership value of input variable x_i for fuzzy set A_{ij}
ν	Material Poisson's ratio
ξ	Material damping ratio
π	Numerical constant Pi (3.14159...)
ρ	Material density (in the case of soils: bulk density)
σ_i	Receptive field parameter for a radial activation function
σ_s	FEA element structural stress
τ_{\max}	Highest radial frequency of a system's dynamic load
ψ	'Mother' wavelet function
ω	Radial frequency

Acronyms

ADC	Analogue to Digital Converter
AI	Artificial Intelligence
ANN	Artificial Neural Network
API	Application Program Interface
BASIC	Beginners' All-purpose Symbolic Instruction Code
BNC	Bayonet Neill-Concelman
BP	Back Propagation
CAPWAP	Case Pile Wave Analysis Package
CEBTP	Centre Expérimental de Recherches et d'Etudes du Bâtiment et des Travaux Publics
CFA	Continuous Flight Auger
CIRIA	Construction Industry Research and Information Association
CRP	Constant Rate of Penetration
CWT	Continuous Wavelet Transform
DFT	Discrete Fourier Transform
DMA	Direct Memory Access
DoE	Department of the Environment
DTI	Department of Trade and Industry

DWT	Discrete Wavelet Transform
EPSRC	Engineering and Physical Sciences Research Council (UK)
FEA	Finite Element Analysis
FFT	Fast Fourier Transform
FIFO	First In First Out (microelectronic buffer)
FRF	Frequency Response Function
ICE	Institution of Civil Engineers
ID3	Iterative Dichotomiser 3
IEEE	Institute of Electrical and Electronics Engineers
KBES	Knowledge Based Expert System
ML	Maintained Load
MLP	Multilayer Perceptron
p.d.f.	Probability Distribution Function
PCMCIA	Personal Computer Memory Card International Association
PDP	Parallel Distributed Processing
RBNN	Radial Basis Neural Network
SE	Sonic Echo
TDR	Transient Dynamic Response
TNO	Nederlandse Organisatie voor Toegepast-Natuurwetenschappelijk Onderzoek (Netherlands Organisation for Applied Scientific Research)
WBNN	Wavelet Basis Neural Network

1. Introduction

1.1 RESEARCH OVERVIEW

The low strain test method, as described below in Section 1.2, has become the prevalent method for integrity testing of cast *in situ* foundation piles. The automated interpretation of the sonic echo traces resulting from this test would prove beneficial to industry through: the standardisation of the test method procedure and a reduction in the time spent analysing results. The research presented here pertains to the use of artificial neural networks for the fulfilment of the primary requisites of this test method:

- i) The identification of a test trace atypical of that which is expected. (Primary Goal)
- ii) To deduce from this trace a profile characteristic of the pile under investigation.

This study, therefore, involved the identification of three multilayer networks considered most suitable for the heteroassociative function approximation task described above. Multilayer Perceptron (MLP) networks, Radial Basis Neural Networks (RBNN) and Wavelet Basis Neural Networks (WBNN) have all been trained using numerically generated data and their performances compared to identify the optimum network type. While each network presented similar strengths and weaknesses in fault diagnosis, statistical analysis suggested that the MLP network was marginally more successful in quantifying changes in cross-sections along the pile length. Field data from three test sites have confirmed that the network can identify, locate and quantify significant ($\pm 13\%$) changes in diameter along the pile length (within known test method limitations). The network has also diagnosed

changes in diameter at the pile head. This task is notoriously difficult using conventional techniques and has been facilitated through the development of a novel pre-processing technique: the wavelet *mobility scalogram*.

1.2 PILED FOUNDATION TESTING

The practice of filling a hollow shaft with stone to support a superstructure has been performed for centuries in the form of 'well foundations'. Today, using modern installation techniques, large diameter, bored, cast *in situ* piles can have diameters of up to five metres and reach depths of over sixty metres^{1,1}. These *non-displacement* piles produce lower installation vibration and can be of larger diameters than other pile types. However, they are susceptible to potentially catastrophic changes in pile cross-section occurring during the installation process, namely *necking* and *bulbing*^{1,2}.

Load testing is the only way to ensure an installed pile is capable of fulfilling its design criteria, but this method is both time consuming and expensive. More recently the development of digital electronics has led to integrity test methods which, in conjunction with conventional load testing, have become a practical means for the rapid checking of pile groups. The most common of these integrity tests are the sonic echo and transient shock methods. Both these methods are examples of impact testing where the pile head response to an instrumented hammer blow is measured using a calibrated accelerometer.

Although quick and inexpensive these sonic tests have their limitations. The low stress impact of a hand held hammer leads to problems with signal attenuation in long piles or those with high aspect ratios. Faults at the pile head and small discontinuities are also difficult to detect due to signal superposition and high pulse to fault length ratios. This was highlighted by the 1992 'Stresswave Conference' Competition and the subsequent correspondence concerning it in *Ground Engineering*^{1,3,1,4,1,5}. Here, commercially available test equipment achieved an average score of only 40% in the detection of faults in a set of specially constructed

piles. This having been said, discussions between the author and a number of representatives of the larger test houses confirms that, in general, their clients' requirement of an integrity test method is the ability to identify anomalous responses with an indication of the primary reason for the aberration. The results from a integrity test should never be considered definitive. Either the pile under investigation is further scrutinised using more sophisticated techniques or, if it is more cost effective, a new pile is constructed adjacent to it.

There is, therefore, an advantage in automating the work carried out by the test analysts so standardising this highly subjective task. In a survey of companies that carry out these tests the author found that every respondent declared an interest in automating this procedure and stated they would employ a new method if it was shown to aid fault detection. The results of this industry survey can be found in Chapter 2.

1.3 ARTIFICIAL NEURAL NETWORKS

An artificial neural network (ANN) is a biologically inspired, adaptive data processing tool. It learns through training and is capable of generalisation which makes it ideal for finding practical solutions to problems in frustrated systems (problems with no unique, ideal solution).

The analysis of a spectrum or time trace from a sonic test is essentially a pattern recognition task. A time space vector representing the pile head response must be mapped to a spatial domain describing the pile profile. It is, therefore, proposed to exploit the generalisation and feature extraction strengths of a neural network to aid test trace interpretation.

As this project is particularly driven by industry requirements the overall project plan is based on the business plan development described by Hecht-Neilson^{1,6}. Aspects specific to the product marketing, however, are beyond the scope of this research project and, therefore, not addressed here. The technical feasibility and

system development plan for this research will broadly followed the recommendations of the UK's Department of Trade and Industry ^{1,7}. This publication has been specifically produced as a guide for application development with respect to neural systems.

1.4 KEY RESEARCH OBJECTIVES

Below is a list of key objectives that were considered essential for the successful completion of this research project:

- i) To review the methods currently employed in the integrity testing of cast *in situ* foundation piles and to investigate neural network architecture and applications concerned with signal processing and fault detection.
- ii) To develop a numerical model for the simulation of a pile head's response to a hammer blow. This generated data will be used in the supervised learning of neural systems and must be validated through field test data.
- iii) To conduct a feasibility study. By limiting the problem domain it must be shown that a neural system can be trained to acquire the necessary mapping such that the primary research objectives can be fulfilled (see Section 1.1).
- iv) To investigate the effect of pre-processing on system performance. This should include novel wavelet transforms as well as conventional Fourier techniques.
- v) To establish an optimum network architecture and training method for a more flexible, practical system from the limited problem domain of the feasibility study.
- vi) To evaluate the system in the field. This will necessitate the development of suitable data acquisition equipment.

1.5 THESIS STRUCTURE

Chapter 2 : Piled Foundations: Associated Defects and Their Detection

This chapter presents a review of current piling practice, the faults associated with cast *in situ* piles and the methods used for their detection. Also included are the results of an industry questionnaire identifying the most popular of the described techniques.

Chapter 3 : Artificial Neural Networks for Signal Processing and Fault Detection

The theory of neural methods and their alternatives are reviewed. Their strengths and applicability with particular reference to fault detection are described. The system development plan defining the structure of subsequently reported experimentation is also given.

Chapter 4 : Feasibility Study

In this chapter a full feasibility study into the accessibility of suitable training data and the ability of a network to diagnose faults in a very restricted problem domain is given. Finite element models developed by the author and employed for trace generation are also validated through comparison with 1-D theory and published laboratory and field test results.

Chapter 5 : Hardware and Software Development

Here the hardware and software developed for data acquisition are described. The neural network simulators developed for this investigation are also described and their ability to learn specific functional mappings is measured to confirm their performance.

Chapter 6 : Application Development

A full parametric investigation of the Multilayer Perceptron, Radial Basis and Wavelet Basis neural networks is reported. This includes aspects of pre- and post-processing, and the pattern dependency of the resultant networks. An error analysis of network performance is also given and used in the selection of the final network used for field test evaluation.

Chapter 7 : Field Test Evaluation

The selected network described in Chapter 6 is evaluated in field trials. Results from three test sites are presented, namely: Stent Piling Ltd's site near Kirkintilloch, and the EPSRC's test sites at Blyth and Bothkennar.

Chapter 8 : Conclusions

This Chapter draws together the conclusions of the preceding chapters and provides summary conclusions of the research as a whole.

Chapter 9 : Recommendations for Future Research

Here suggestions for the logical continuation and development of the work described in this thesis are given.

REFERENCES

- (1.1) Cementation Piling and Foundations Ltd, Trade Literature (1994).
- (1.2) Sliwinski Z J, and Fleming W G K, The Integrity and Performance of Bored Piles, Piling and Ground Treatment, Thomas Telford Ltd (1984) pp 211-223.
- (1.3) van Weele B, Integrity Test was not Questionable, Ground Engineering, Vol. 26, No.3 (1993) pp 14-15.
- (1.4) Stain R, Competition was not Applicable, Ground Engineering, Vol. 26, No. 3 (1993) p 15.
- (1.5) Turner M J, Integrity Test Usefulness is not the Issue, Ability is, Ground Engineering, Vol. 26, No. 6 (1993) pp 27-28.
- (1.6) Hecht-Nielsen R, Business Plan Development, in Neurocomputing, Addison-Wesley (1991), pp358-406.
- (1.7) DTI, Neural Computing Learning Solutions: Best Practice Guidelines for Developing Neural Computing Applications, Department of Trade and Industry (UK) (1994).

2. Piled Foundations: Associated Defects and Their Detection

2.1 FOUNDATIONS

The Code of Practice for Foundations^{2.1}, BS8004, defines a foundation as:

'...that part of the structure designed and constructed to be in direct contact with, and transmitting loads to, the ground.'

These can be divided into two classes: shallow foundations (strip, pad and raft) and deep foundations (cofferdams, caissons, piles and deep basements). The foundation choice is made with reference to the superstructure specification and the site investigation data, see BS5930: Code of Practice for Site Investigations^{2.2}.

Shallow foundations are generally considered to be those with a depth of less than 3m below the finished ground level. They are especially suited for structures where hard rocks, e.g. limestone, sandstone, slates and shales, occur near ground level. They may also be used on soft shales, mudstone, sound chalk and compacted sands or gravel although in all these cases settlement must be considered. Generally shallow foundations are not suitable for soft clays, silts or organic soils.

Where there are no shallow strata strong enough to support the building, using the methods described above, a deeper foundation must be used. Deep foundations are not often required when rock is found near ground level except when only very small deformations are permissible, or the rock is shattered or heavily weathered. In the case of soft clays, silts, organic soils, made ground and fill, deep foundations are nearly always employed to reach a stronger bearing strata beneath the comparatively weak top layer(s). In Britain these deep foundations more usually take the form of piled foundations^{2.3}.

2.2 PILED FOUNDATIONS

Piles support a superstructure by transferring load to a lower stratum of rock or through the skin friction formed at the pile/soil interface. Using the symbols prescribed by Poulos and Davis^{2,4} the ultimate load capacity of a single pile, P_u can be described by Equation 2-1 below. Here P_{su} is the ultimate shaft resistance, P_{bu} is the ultimate base resistance and W is the weight of the pile as indicated in Figure 2.1.

$$P_u = P_{su} + P_b - W \quad (2.1)$$

Piles that support predominantly through base resistance are known as end-bearing while those that support through shaft resistance are known as skin friction piles.

2.2.1 Pile Types

The basic pile types can be divided into two sections: displacement and non-displacement. In displacement piling the surrounding soil moves as the pile is inserted. In non-displacement piling the soil is removed and the resultant void is filled to form the foundation. The displacement category can be subdivided into small and large displacement types as shown in Figure 2.2.

This research is concerned with the integrity testing of cast *in situ* concrete piles. Its findings may, however, also be pertinent to some driven types. The review below therefore covers all pile types with special reference to the bored cast *in situ* class. Although the majority of faults associated with these piles are produced after installation^{2,5}, these are predominantly at the pile head and can be detected by visual inspection. This project is mainly concerned with faults that occur during installation and so, for cast *in situ* piles, the construction process is also described.

2.2.1.1 Large Displacement Piles

Displacement piles are usually driven by a hammer; of either diesel or drop type. The diesel hammer is more flexible as leaders, guides for the falling hammer, are not required, but in soft soil, with low driving resistance, cylinder compression may be reduced so lowering its effectiveness. Two methods less often employed are: hydraulic jacking, which is confined to use with smaller micropiles, and the

vibratory method, which is used in cohesionless soils where fluid like properties are induced, so reducing skin friction.

Timber piles, although still extensively used in Scandinavia, are now uncommon in the U.K. as the limiting factor in their design is often the size and availability of the wood. More usually used are the **Precast concrete piles** that come in square or hexagonal sections of 150-500mm. They are constructed from rolled steel and fine grade concrete. Single piles are normally 5-15m long, but piles of over 100m have been installed through joining pile sections by bayonet or socket and locking pins. For **prestressed concrete piles** the increase in construction complexity is compensated for by a smaller cross section being needed for an equivalent bearing capacity. The growth in tensile strength means there is also less risk of cracks appearing during driving. Concrete displacement piles are usually used where their relative ease of installation is an advantage, such as wharves and jetties, and in soft soils where the intrinsic process of compaction is an advantage.

Driven Cast in Place piles are constructed using forming tubes that are either made from steel or concrete and may be removable or permanent. Those piles with a removable steel forming tube are driven with a conical toe of precast concrete or a steel plate for softer ground. They are typically of 200-600mm diameter and are driven by drop or diesel hammers. Once the founding level is reached a reinforcement cage is inserted and the concrete is added as the shell is removed. Problems associated with these piles include disruption of surrounding piles during driving and heave from soil consolidation. All driven cast in place piles have the advantages of being easily trimmed to the required length and the relatively straightforward way the base can be enlarged. However, they all suffer in that driving can damage adjacent piles and the limitation in depths that can be reached (20-30m).

Due to the driven cast in place installation process being so similar to that of bored cast in place piles their faults are typically of the same type. These are described fully in Section 2.3, Faults Associated with Cast *in situ* Piles. This parity, therefore, suggests that any analysis method developed during this research will also be relevant to the testing of the driven types of pile.

2.2.1.2 Small Displacement Piles

These piles are all similar in that they present a lower cross sectional area and so produce a smaller displacement and less soil compaction when driven.

Screw Piles are used in soft clays and silts of considerable depth where penetration to a stiffer layer is impractical. They are made of cast iron, steel or reinforced concrete with a screw at the bottom providing a larger bearing area at depth. **Steel 'X', 'H' and 'I' Section Piles** are used mainly in hard driving conditions. They can punch through thinner hard strata to thicker supporting strata up to 40m beneath.

Open Ended Piles overcome some of the flexing encountered by the slender piles above through their increased section, however problems arise when plugs form inside the hollow pile. This increases displacement and lead to heave in dense pile groups. It is often necessary, therefore, to bore out the inside of the piles as they are driven. Their relative ease of installation and the higher impact and lateral, bending loads means these piles are often used for marine applications.

2.2.1.3 Non Displacement Piles

In non-displacement piles a void is created through rotary or percussion boring and the hole is filled with concrete and reinforcement. Commonly piles with a diameter greater than 600mm are known as large diameter bored piles, otherwise the piles differ mainly through their method of construction. These types of pile have the advantages of being low in installation vibration and can be of relatively large dimensions. However, they are susceptible to necking and bulbing, and enlarged ends (underreams) cannot be formed in cohesionless soils. It is these types of pile that, because they are constructed underground, need the improved remote testing that this research aims to provide.

Small diameter percussion bored piles have diameters between 300-600mm and can be bored in an environment with confined headroom using a tripod and winch, see Figure 2.3. The winch is driven by a diesel or compressed air engine which repeatedly drops a cutter into the borehole. In cohesive soils the cutter is an open cylinder which, after a number of cycles, is brought to the surface and emptied. Stiffer clays often require the cutter to be weighted and water added to aid progress. In granular soils a heavy shell with a one way valve at its bottom is used with a temporary steel casing. In all of the above scenarios boulders and cobbles are broken

using an 'I' section chisel. A reinforcement cage may then be placed before the concrete is added as the casing is withdrawn. Using this method depths of up to 30m are achievable with piles that can support loads approaching 1500kN.

Rotary bored piles are used for the majority of large diameter cast *in situ* piles. In the UK this usually takes the form of a crane mounted auger, see Figure 2.4. A short flight auger is sufficient for clay soil, but for weak rock or cobbles a heavy duty auger or drilling bucket is necessary.

Two methods are employed for supporting the boreholes of large diameter piles. In loose soil, normally found at the surface, a metal casing is inserted either by drop hammer or vibratory methods. The foot of the casing is kept just ahead of the cutting edge of the auger to prevent soil collapsing into the borehole. These casings are taken up to 25m down into a cohesive stratum beyond which the boring can continue without the risk of collapse. For deep boreholes the use of temporary casing is expensive and time consuming so a bentonite suspension is often used to support the walls. Here the level of bentonite is kept at least 1.5m above the water table to provide enough pressure to support the walls.

The reinforcement caging, which usually takes the form of a rolled steel spiral with longitudinal support, is lifted, with spacers, into the borehole after which the concrete can be simply poured in using a hopper tube. As the concrete is poured the casing is slowly retrieved, its lower edge always remaining slightly below the concrete level. When concreting under water or through a bentonite suspension it must be added through a tremie pipe.

These piles have diameters ranging from 400mm-5m and can reach depths of more than 60m. The larger piles take working loads of approaching 30,000kN; a load far in excess of any driven pile.

One additional advantage of rotary bored piles is the ability to underream the pile when in dry, cohesive soil. Here a special tool is dropped down the borehole and enlarges the base to up to 8m diameter so improving its end-bearing capacity. The additional complexity of this task means it is only really practical when boring is difficult and the additional work is preferable to boring a larger diameter pile.

Continuous flight auger (CFA) piles are produced with diameters ranging from 300-1200mm. They cause minimum vibration and are quickly installed as no casing

is involved. They also negate the need for a tremie pipe when piling takes place beneath the water table. However, they can only be used in sands, gravels and clays since boring is continuous and consequently no drilling or chiselling can take place.

The CFA is screwed into the ground to the depth required; up to 30m. Then, as the auger is removed, concrete is injected through its the hollow stem to the void formed beneath. After the auger is removed reinforcement caging can be added, see Figure 2.5. Grout intruded piles are smaller diameter piles where the concrete has been replaced by grout. CFA piles support working loads of up to 5000kN and can be used to form contiguous, interlocking piled walls.

2.2.1.4 Micro piles

Micro piles are piles of a diameter less than 250mm. They are commonly used for underpinning or to support light superstructures on weak soil, but can also be used for anchoring buoyant structures or vibration sensitive machinery and for soil reinforcement. Their smaller size allows installation techniques which facilitate piling and reinforcement in enclosed spaces.

When driven the piles are usually steel tubes either pneumatically jacked or hammer driven into the soil. They are then filled with grout yielding a design load of up to 350kN. Cast *in situ* piles are typically formed as the Pali Radice Piles of Fondedile Foundations Limited^{2.6}. These use a rotary drill with cutting edges to form a hole through any existing foundation into the ground beneath. Grout is then pumped into it via a tremie pipe before a reinforcement cage is inserted.

2.3 FAULTS ASSOCIATED WITH CAST IN SITU PILES

Piled foundations are usually employed when ground conditions are too poor to allow the practical or economic use of shallow, spread foundations^{2.7}. As a natural consequence of this many of the faults associated with piling are concerned with the surrounding soil's lack of cohesion or saturation. A full review of these problems was published by the Construction Industry Research and Information Group (CIRIA) in 1977 and reprinted, with amendments, in 1985 (Report PG2, Thorburn and Thorburn)^{2.8}. This report suggested that the direct causes of pile defects can be categorised under the seven headings below.

- i) **Overbreak.** Almost exclusively found in water bearing strata overbreak was found to be '*responsible for a significant proportion of all the defects which have been observed and recorded*'. During the boring process soil cavities around the borehole may be formed, if a temporary steel casing is employed in the pile construction then they will remain there until it is removed. At this point the concrete may flow into the cavity causing an increase in pile cross section. This in itself is not a major problem, but this increase in cross section is often accompanied by a, potentially dangerous, loss in cross section further up the pile (necking), Figure 2.6. Even if the concrete is of a low workability and does not immediately flow into the cavity, by mixing with the groundwater eventually it is likely to slump resulting in a loss of cross section. Even in dry conditions if the concrete is of a high enough workability air in surrounding soil can be replaced leading to the formation of bulbs and necks.
- ii) **Debris in the pile bore.** In both large and small diameter cast *in situ* piles evidence was presented where natural debris or site rubbish in the borehole caused a loss of base resistance.
- iii) **Extraction of temporary casing.** As well as being an effect of overbreak (i) necking can also be a feature at the pile head. While the casing is being removed there is friction between its internal wall and the concrete shaft which results in uplift. This vertical force, when combined with the naturally occurring lateral forces exerted by the surrounding soil, means that towards the pile top (at 3.5m in the quoted case), where there is only a small head of concrete, necking may occur. See Figure 2.7 for an example of such a fault.
- iv) **Soil displacement - driven cast in place piles.** The temporary casing sometimes used in pile construction may, on occasions, be driven. Especially in cohesive strata, such as clay, this will lead to lateral and vertical displacement of surrounding soil which can have detrimental consequences for adjacent piles in a densely populated group.
- v) **Unsuitable steel reinforcement.** If the steel reinforcement is too closely separated and a low slump concrete is used then there is a risk that the concrete will not be able to penetrate the cage. This will result in a loss in pile cross section and leave the cage open to groundwater attack.

vi) **Unsuitable mix design.** These faults are usually associated with low slump concrete where lack of workability causes discontinuities in the pile shaft. However, it is also pointed out that high water content mixes can result in an unacceptable amount of bleeding from the exposed concrete surface at the head of the pile.

vii) **Incorrect concrete placing and compaction.** When the temporary casing is lifted beyond the concrete level debris may fall into the shaft which, if concreting is then continued, can lead to discontinuities in the pile. Also collected groundwater in the borehole can cause leaching of the cement at the pile base leading to a drop in concrete integrity. This section of the report concludes with the statement that the compaction of concrete in piling can cause difficulties in casing extraction and that no defects were reported when self compaction of concrete was relied upon.

The report continues by commenting on problems related to groundwater attack where it states that when fast flowing groundwater is encountered leaching of the cement may occur. However it should be noted that no evidence for the chemical attacking of cast in place concrete piles was revealed.

The report also summarises the indirect causes of pile defects (e.g. inadequate site supervision) which is beyond the scope of this project.

It should also be noted that faults linked with the extraction of temporary casing and poor concrete mix are common with driven cast *in situ* piles, as reported by Healy and Weltman in the CIRIA publication *Survey of problems associated with the installation of displacement piles* (PG8)^{2.10}. Hence many of the integrity test procedures reported in Section 2.4, below, are relevant to both bored and driven cast *in situ* piles.

Sliwinski and Fleming^{2.11} provide additional insight into the effects of water in the borehole. They describe how, as grout is washed from the mix, the poured cement separates until all the water is absorbed. The remaining cement above will then have a different consistency. This stratification, with bleed water beneath, can lead to discontinuities. If a contractor attempts to rectify this by adding low workability concrete to absorb the water then the problem can be worsened with the concrete 'hanging up' so producing an occluded void.

Fleming also provides a summary of report PG4 along with the results of a four year survey into the causes and regularity of defects, Table 2.1 below^{2.5}. This survey revealed that 1.78% of all piles examined showed some kind of problem.

Table 2.1 Defect causes and their occurrence (After Fleming^{2.5}).

Problem Cause†	%
Soil contamination in top 2m	9.3
Contamination in range 2 to 7 m	5.0
Poor or wrong quality concrete	2.6
Voids adjacent to pile shaft causing loss of concrete	0.8
Damage caused by trimming or excavation after pile installation	82.1
Unknown	0.2

† In addition 50 piles (of 28,204) were shown to have cracks which were clearly due to tensile stress in the section resulting from heave or movement of the ground following excavation.

Ellway^{2.12} reported 4% of 4,400 small diameter (<600mm diameter) cast *in situ* piles had 'significant structural faults'. He attributed a third of these failures to post-installation events. A further third to weak concrete at the head - top 2m - of the pile, and the final third to changes in section or concrete contamination below a 2m depth.

The most striking of these results are the very high percentage of physical damage caused after installation. However, most of these faults occur at the pile head and can be identified through visual inspection which means they will not have a particularly large influence on this project.

Both Ellway and Fleming's results were obtained through the sonic integrity test methods. These methods are notoriously difficult to interpret, with different subterranean events causing similar test results; a change in acoustic impedance can be caused by either a change in section or concrete density, and changes in soil properties can also produce misleading results (see Section 2.7, below). Assumptions must therefore be made e.g. homogeneity of concrete mix, accuracy of site investigation data *etc.* These assumptions along with subjective nature of the interpretation and the possibility of different installation methods and pile types within the tested populations can explain the differences in the details within the

surveys. Despite these differences the main conclusions to be drawn from these pieces of work are the same.

- i) The percentage of faulty piles produced during the installation process is very small - between 1.5 and 5 percent.
- ii) Debris, soil cavities and poor concrete mix are the three main causes of pile defect during construction. These produce a loss in pile stiffness often caused by a reduction in its cross section.
- iii) Any defects formed are more likely to be found towards the head of the pile. This is shown in both Ellway and Fleming's work where the results correlate extremely well.

In Fleming's survey there is a higher degree of faults caused by soil contamination compared to those due to voids adjacent to the pile shaft. This contradicts the CIRIA report. However, this may be explained by the fact that Fleming based his work solely on the techniques and working practice of one firm, Cementation Piling and Foundations Ltd., while the CIRIA report related to nineteen different contractors and eight building consultants. It is therefore suggested that Fleming's results may be contractor dependant and that the CIRIA report should be considered a truer reflection of the general case.

Turner^{2,13} has attempted to categorise these faults into four types:

- Type A) Changes to the intended shape of the pile body itself.*
- Type B) Total rupture of the pile in the form of a transverse crack or break across the body of the pile.*
- Type C) Changes in the internal properties of the pile.*
- Type D) Features that affect the interaction of the pile with its environment and, consequently, its ability to transfer the design load into the surrounding soil or rock.*

He also presents a nomenclature for pile features and defects which the author will attempt to adhere to in an effort to support the standardisation and increase clarity.

2.4 PILED FOUNDATION LOAD TESTING

2.4.1. Static Load Testing

According to BS8004, Code of Practice for Foundations, a load test is made '*...for the purpose of finding the settlement to be expected at the estimated working load,*

or some multiple thereof, determining the ultimate bearing capacity, or checking the structural soundness of a pile.'^{2.1}.

Two types of static load testing can be carried out on a foundation pile; constant rate of penetration (CRP) or maintained load (ML).

In the CRP test the pile is jacked into the ground at a constant rate (~0.8mm/min), through continuously altering the applied load, until the point of failure. Failure is described as the point at which either the pile continues to be displaced without an increase in the applied load or when the pile displacement for a load increment is greater than one tenth of the diameter of the pile base. From the load versus settlement graph taken during this test the plastic working settlement of the pile as well as the ultimate bearing capacity can be calculated. However, the CRP test is not designed as a method for the derivation of pile settlement and it is suggested that a composite test of ML testing followed by a CRP test should be employed^{2.14}. Tomlison states that the lack of information on elastic settlement and the high loads used in this form of testing make it best suited for research purposes where fundamental pile behaviour, e.g. ultimate bearing capacity, is being studied^{2.15}.

For the ML test a proof load is applied to the pile at regulated increments whilst measuring its settlement. Ideally this proof load should be held for 24 hours before it is removed, again at intervals. From this test it can be inferred whether the pile will support its maximum working load without too high a degree of settlement. In most cases this knowledge is all that is required of any pile test and so it is this method that is more often employed.

2.4.2. Dynamic Load Testing

Here the pile head's velocity response to a measured high strain impact is recorded and analysed. Not to be confused with high strain integrity testing this method attempts to extrapolate the pile's static behaviour from its response to a dynamically applied load. More specifically the test can be used to evaluate pile capacity, soil resistance distribution, immediate settlement characteristics, hammer transfer energy (efficiency), and pile stresses during driving^{2.13}. It is usually practised on driven piles as an impact hammer will already be available on site while for bored piles extra, heavy, equipment is needed to carry out the test (Rausche *et al.*^{2.16}).

Initial attempts to deduce static load capacity from soil conditions and pile head response were carried out by Case Western Reserve University in the mid 1970's. They assumed the total driving resistance has static and dynamic components. They further presumed:

$$R_{\max} = R_{s(\max)} + R_{D(\max)} \quad (2.2)$$

where R_{\max} is the maximum, measured driving resistance $R_{S(\max)}$ is the maximum static component and $R_{D(\max)}$ the maximum dynamic component. Gobel *et al.*^{2.17} then demonstrated that:

$$R_{S(\max)} = R_{\max} - j_c \left[\frac{2EA}{c} \cdot v_{h(\max)} - R_{\max} \right] \quad (2.3)$$

where E = concrete's Young's Modulus

A = the pile cross sectional area

c = the stress wave velocity within the concrete

$v_{h(\max)}$ = maximum pile head velocity at impact

and j_c = a soil damping constant, known as the Case damping constant

Static tests on a number of piles in a group can be used to calculate j_c while E , A and c are known. If, then, $v_{h(\max)}$ and R_{\max} are measured for further piles within the group their static load capacity can also be found.

Corté and Bustamante^{2.18} have compared static loading and Case methods at various test sites and made a number of conclusions. The most relevant to this research is that protruding reinforcing bars in bored cast *in situ* piles make dynamic testing particularly difficult. It is also noted that these type of methods are based on the assumption that the resistance forces are constant during the test. In fact, upward travelling stress waves from the lower part of the pile can reduce soil resistance towards the head. Consequently this method cannot be used without static test calibration to as a means to finding the bearing capacity of piles. In reality, therefore, this method is not generally used as a predictive method, but is more usually employed to check and control the driving of piles.

For predictive testing of a soil's resistive forces numerical methods are more usually employed. These involve modelling the pile system with a hybrid version of Smith's lumped mass-and-spring model^{2.19} and computing the expected response for various values of the pile/soil system. When the computed and experimental values for a

given pile match the soil parameters are presumed to have been found and the bearing capacity can be deduced without the need of an empirical damping factor.

Research on this technique began in 1964 at Case Western Reserve University the result of which was the response simulator, CAPWAP (Case Pile Wave Analysis Package). Today there are a number of other response simulators to choose from e.g. TNOWAVE from the Central National Council for Applied Scientific Research (TNO) in Holland^{2.13} and SIMINTEG from the Centre Experimental de Recherches et des Travaux Publics (CEBTP) in France^{2.13}. The speed and results, in general, from this test are favourably reported by Mure *et al.*^{2.20}, who also describes the test procedure in more detail. Dynamic testing is quicker than the static load test where each individual test may take over twenty four hours. Typically ten piles a day may be tested using the dynamic method. However, it has also been pointed out that damping forces used in the computer modelling do not account for all transient phenomena in the real case (e.g. curing, primary consolidation, concrete homogeneity, constant pile section etc.) and that consequently large discrepancies can exist in the bearing capacity predictions for static and dynamically tested piles^{2.18}.

2.4.3 STATNAMIC[®] Testing

Introduced in 1989 by Berminghammer Foundation Equipment and TNO Building and Construction Research this method, it is claimed, combines the static load displacement behaviour of static load testing with the speed of dynamic testing^{2.21}.

A cylinder is bolted on to the pile head and a reaction mass is placed over it. Solid fuel propellant is then ignited inside the cylinder and high pressure gasses accelerate the reaction mass. Then opposing reaction to this gently forces down on the pile with the weight of the reaction mass equal to about 5% of the applied load. The pile top force and displacement is measured using load cells and a laser system. Data is recorded by TNO's Foundation Pile Diagnostic System (FPDS); a 486-PC based system with a 50kHz sampling rate. Mobilised capacity and static load displacement behaviour can then be presented immediately on site.

It is suggested that the comparatively low release and application of forces leads to the elimination of tensile stresses so compressing the pile and soil as a single unit. This should lead to a truer reflection of the static, load displacement behaviour of the pile than that of dynamic tests where high accelerations leads to stress wave

propagation through the pile. Thus the Statnamic system provides a direct measurement of the pile-soil behaviour.

This new method was first discussed in detail at the First International Statnamic Seminar in Vancouver, 1995. Here Inamura *et al.*^{2,22} reported that, for large cast *in situ* piles, statnamic tests gave a reliable characterisation of static load settlement except for settlement in the elastic region.

2.4.4. The Application of Neural Computing to Load Testing

Static load testing is a direct measurement method used to ensure foundation piles fulfil their design criteria. It is unlikely that any contractor or engineer would deem it either necessary or judicious to employ a nondeterministic analysis method based on a neural system for the interpretation of load settlement curves. However, the statistical probability of a faulty pile being present in the randomly selected sample of piles to be load tested is small^{2,5}. Current research is therefore centred on complementary test methods to identify potentially faulty piles for the static load test set, thus reducing the amount of built-in over design necessary in the pile group.

This research should therefore aspire to use a neural system to improve the analysis of these complementary tests' results.

Statnamic testing does not have the facility for the rapid testing of large pile groups. It is being marketed as a better quality assurance test than dynamic testing while being quicker than load testing. Being a new development; training data for this system would be limited, and with so few testhouses currently offering the service the need of a neural system for interpretation is questionable. This is especially true when one considers the results processing time to test time ratio. Typically only three 600 ton tests can be carried out per rig per day and so a need for the rapid, automated processing of large result sets is unlikely.

The Case method is discounted as being a rarely used theory based test used in driven rather than the cast *in situ* piling. This leaves the CAPWAP-like methods most likely benefit from an automated interpretation method to render the iterative wave-matching procedure redundant. However, as previously mentioned, this method of testing is rarely used on cast *in situ* piles. This is because of the availability of alternative test methods which have been specifically developed to augment the static load test procedure rather than replace it. These integrity test

methods, as described below, typically allow the testing of tens of piles per day and would therefore more likely benefit from the development of a reliable, automated system for the interpretation of their results.

2.5 INTEGRITY TESTING

The term integrity testing is generally taken as to comprise of those test methods used to investigate the soundness of a foundation pile and more specifically to evaluate the 'integrity' of the material used in its construction^{2,23}. One of the first full reviews of pile integrity test techniques was the CIRIA/DoE report PG4 of 1977^{2,24}. Here Weltman discusses the usefulness of integrity testing in the selection of piles to be load tested and proclaims the necessity of the tests to have '*...reliable, readily interpreted results.*'

As described above, the need for a rapid, reliable method of testing to complement the load test has lead to the rapid development and use of a number of these techniques. The remainder of this section will discuss the evolution of the integrity test methods, their relative merits and their popularity within the Civil Engineering Community.

The Integrity Test methods can be broadly divided into direct and indirect techniques as described in Table 2.2, below. Direct methods involve the visual or mechanical examination of a pile or the direct measurement of an engineering characteristic. Indirect techniques involve the measurement of a pile attribute, which may not be directly related to a structural performance, but from which its integrity can be inferred.

Table 2.2 Pile Integrity Test Methods.

REVIEW	Direct Testing	Indirect Testing
1977 (Weltman)	Excavation Drilling Integral Compression Test	Acoustic (Sonic Coring) Radiometric Seismic (Pulse Echo) Dynamic (Vibration) CCTV Electrical (experimental)

1985 (Fleming <i>et al.</i>)	Excavation Drilling Stress (Dynamic load test)	Acoustic (Sonic Coring) Radiometric Seismic (Pulse Echo) Dynamic (Vibration) CCTV Electrical
1988 [†] (ICE Specification for Piling)	—	Acoustic (Sonic Echo and Transient Dynamic Response) Vibration Sonic Coring
1995 (Turner)	Excavation / Extraction Load Testing Dynamic Load Testing Integral Compression Test Drilling	Sonic Coring Radiometric CCTV Calliper Logging Water or Air Test Low Strain Impact Tests Horizontal Vibration High Strain Impact Test Electrical Ultrasonic Parallel Seismic

Described as the most widely used integrity tests in the UK i.e. not a full review.

2.5.1 Direct Integrity Test Methods

The **extraction** and **excavation** techniques are essentially visual inspection methods where the pile is exposed, either fully or partially, to reveal the presence of any defects. Both these methods require heavy plant and are time consuming to execute. They are therefore exclusively used in the surveying of known defects near the pile head. These methods have the additional disadvantage of reducing the bearing capacity of friction piles and causing disruption to adjacent work.

In the 1996 CIRIA report^{2,13}, which supersedes the previously mentioned RG7, Turner also classifies **load testing** as a direct means of integrity assessment. These techniques all suffer from the problems outlined in Section 2.4 and will not be further discussed here. However the time and expense involved in these processes need to be reiterated and their failure to test large pile groups in their entirety restated.

Exploratory Drilling or Boring of a pile is primarily used to investigate the extent of a known defect. It is time consuming and expensive for deeper faults, but is the most frequent way of directly investigating internal features within a pile^{2,13}.

All these direct methods, by their nature, require little in the way of post-processing. However, they are not suited for the rapid checking of a large group of piles because of the additional time and expense involved in their implementation. Rather, they are more usually used to investigate the integrity of piles with known or strongly suspected anomalies.

2.5.2 Indirect Integrity Test Methods

Indirect techniques provide information on a pile's integrity from tests not directly related to its structural performance. These methods have been subdivided by Turner into classes of internal, external, and remote techniques. The major test methods for each class are described below along with a number of experimental techniques.

2.5.2.1 Internal Techniques

These procedures are used to investigate a pile's internal construction and features through the examination of boreholes or pre-installed access ducts. The most common of these techniques is **sonic logging**; either cross-hole or single hole.

Cross-hole sonic logging (also known as sonic coring) is a method for checking the homogeneity and integrity of mass concrete foundations such as cast *in situ* piles and diaphragm walls. Two probes, a transmitter and receiver, are lowered down a pair of water filled ducts, see Figure 2.8. They are then raised, in parallel, at around 20cm/s while the transmitter emits 10 sonic pulses per second^{2,25,2.13}. The signal at the receiver is recorded and translated into a graphical profile, see below right. Anomalous regions become clearly visible and may then be further investigated at a higher resolution.

This method suffers from the necessity that the piles to be tested must be pre-selected. There is also the risk that the inclusion of the steel or plastic ducts may lead to the creation of additional defects and poor bonding between them and the concrete can yield an anomalous response. However, it has become popular for the checking of long, large-diameter, cast *in situ* piles because of the lack of depth limitations and the relative speed of the test.

For single-hole sonic logging a transceiver is used: a single vertical probe housing both the transmitter and receiver separated by an acoustic isolator. A longer transit time for emitted pulses over a region of the pile indicates the inhomogeneity of the immediately surrounding concrete. This will either be due to a drop in propagation velocity or a longer path length taken by the emitted pulse. The depth of penetration of this test is dependent upon the equipment employed, but Turner^{2,13} quotes published data that suggests the maximum depth is 100mm from the duct wall. This means that only a small volume of pile is sampled from a single hole, because of this the cross-hole method is almost exclusively employed.

Radiometric methods of pile testing follow in the same vein as sonic coring methods, except radiation energy is used instead of acoustic. **Backscatter** techniques like single-hole sonic logging uses a single duct or borehole. Two main methods are employed:

- i) Gamma ray techniques: where a count of backscattered radiation is an indication of the density of the surrounding material.
- ii) Neutron scattering: where the count of 'slowed' neutrons indicates the degree of water content within the surrounding material. This in turn indicates changes in material properties.

In **cross-hole transmission techniques** the number of gamma particles received at a detector, having travelled across a known distance of material, is indicative of the material density. Neither of these methods are in regular use in the UK due to the need for radioactive isotopes. Gamma radiography is, however, offered as a service by, amongst others, Testconsult Ltd, although prospective clients are warned it is '*Very expensive, and requires massive shielding and safety precautions...*'^{2,26}.

Other internal techniques include the use of fibre optic video endoscopes^{2,26} for the inspection of boreholes or ducts within the pile. This method, as reported by Turner, can make feature detection more difficult than one might expect and is not a practical method for the testing of large pile groups, but rather a means for investigating suspected defects.

2.5.2.2 External Techniques

External techniques involve methods of evaluation that tests the pile's integrity without entering its interior. They include vibration testing, low and high strain integrity testing, and ultrasonic velocity tests.

Vibration testing was introduced by the Centre Expérimental de Recherches et d'Études du Bâtiment et des Travaux Publics (CEBTP) in the late 1960's. It was presented as a method for the testing of whole pile groups in conjunction with conventional load tests. The method is explained in great detail in the 1974 paper 'From theory to field experience with the non-destructive vibration testing of piles' by Davis and Dunn^{2,27}.

In this technique an electrodynamic vibrator is attached to the upper face of the pile head. This is driven by a sine wave generator to excite the pile at frequencies ranging from 1 to 1000 Hz. The amplitude of vibration is dynamically altered through a feedback system such that the force applied to the pile is consistent for all frequencies. A velocity transducer mounted on the pile head is used to monitor the vertical velocity response to this excitation.

From Δf in the response curve, see figure 2.9, one can either assume concrete integrity and so deduce the pile length or assume the pile is of design length and so infer concrete density. The apparent stiffness of the pile head can also be deduced from the gradient of the line between point M and the origin. Large pile features can be detected through changes in the response shape^{2,13,2,27}.

This method of testing requires a high degree of pile preparation: the head must be ground to a smooth horizontal finish, steel plates are attached and epoxy resins applied. This along with the test itself is comparatively time consuming and therefore expensive when compared to the sonic tests described below. However, there is no improvement on the results obtained by the Transient Dynamic Response method through this additional cost and so this method has become largely redundant in the UK, see Section 2.6: Industry Survey, below.

Low strain methods are generally split into three distinct classes^{2,12,2,13,2,28}: pulse echo, sonic echo (SE), and transient dynamic response (TDR). All involve the axial excitation of the pile through striking it with an instrumented hammer, and a measurement of the pile head response, usually by a calibrated accelerometer.

The stress wave front generated by the hammer impact travels down the pile's length undergoing partial reflections from features and changes in its surrounding soil. The pile's response to this excitation is, therefore, representative of its structural characteristics and environment. However, because of signal noise and attenuation, the subjective nature of interpretation and assumptions made during the test (e.g. one-dimensional wave propagation, concrete homogeneity etc.) no inferences on pile serviceability can be made. Rather the tests are used to detect piles with anomalous responses and give a suggestion as to the reason of these anomalies. These piles can then be further tested using direct measurement techniques if required.

For the sonic echo time domain test the pile head's velocity response is usually investigated. This is because the act of integrating the longitudinal acceleration trace intrinsically smoothes some of the high frequency components generated through surface waves induced on the pile head's upper face. It also has the additional benefit of illustrating the phase of the reflected signal - information used to infer whether a signal reflection is from an increase or decrease in pile section. The TDR method is the Fourier Transform of the velocity response - usually divided by the spectrum of the input pulse to produce the mobility curve. The sonic echo and transient dynamic response methods are described in more detail in Section 2.7.

The pulse echo method investigates the 'ringdown' -the drum-like vibration of the pile head's top face- of the acceleration response of the hammer impact. For a straight, defect free pile producing no echoes apart from those from the pile base the response should be an exponentially decaying sinusoid. If unexpected features within the pile or changes in pile/soil interaction are pronounced enough to produce additional echoes then these will result in irregularities within the trace envelope. Because it is this trace envelope that is investigated in this technique the phase information is lost - the envelope amplitude is proportional to vibrational energy at the pile head which is not a vector quantity. For this reason and the fact that the SE test allows for greater signal processing (signal averaging, noise filtering, auto-correlation *etc.*) the pulse echo test has been largely superseded by the SE and TDR tests and is no longer in commercial use.

High strain integrity testing is based upon the same principle as low strain testing. That is: the axial response to a hammer blow is characteristic of the pile's shape and environment. However, in this case a heavier drop hammer falling onto the

cushioned pile head is used instead of a hand held hammer. Sensors at the pile head measure the impact force and velocity response.

The development of this method was a natural evolution from the dynamic load testing techniques discussed in Section 2.4.2. However, these methods were employed primarily to investigate pile/soil interaction where the cushioned blow, with its low frequency components, was advantageous. For integrity testing the relatively long rise time of the input pulse means a loss in resolution in the processed results and therefore an inability to distinguish smaller defects. The obvious benefit of this method is the increased pile length that can be tested because of the additional energy transferred at impact.

This method was originally developed for driven piles where the pile driving rig could be utilised. For cast in place piles the additional plant, pile preparation, time and money involved in this test means that it not used for the checking of pile groups.

In **ultrasonic velocity tests** the exposed part of a concrete pile can be tested for homogeneity and quality. The velocity of an ultrasonic pulse, measured between a transmitter and receiver positioned across the pile shaft, is dependent upon the density and elastic properties of the concrete. Variations in the concrete's homogeneity or features within the pile (e.g. voids, honeycombing) will result in changes in this velocity. Because this technique can only be used on exposed sections of the pile it is generally used in investigation work where a defect is suspected at the pile head. It is not used as a means of testing the integrity of installed piles.

2.5.2.3 Remote Techniques

Remote techniques are used when the pile itself cannot be accessed - usually because the superstructure has already been erected above the pile head.

The only reported method of remote testing is parallel seismic testing as described by Williams and Stain^{2.29}, see Figure 2.10. Here, by measuring the transit times of a hammer induced stress wave at various pile depths it is possible to calculate the extent of continuous concrete.

This technique is only practised when access to the pile head is no longer possible, on piles less than 10m long, and in unchanging ground conditions. It is therefore rarely used and is unlikely to benefit from any neural post processing.

2.5.2.4 Experimental Techniques

During the 1970s a number of **electrical techniques** were introduced as methods to check the integrity of piles. All used the reinforcement bars as one electrode and measured the electromagnetic potential at a second. This measured potential is defined by the electronic resistance of the concrete and soil, and of the pile shape. There were four main methods presented:

- i) resistance to earth
- ii) self potential
- iii) resistivity testing
- iv) induced polarisation

Of these it is the resistance to earth method that has undergone most research. Here a potential is applied between the pile reinforcement and a return electrode installed in the ground some distance from the pile. The potentials at intermediate positions between the these two electrodes are then measured and the graph of potential with respect to electrode spacing is plotted. This method is a comparison technique which needs to check a number of piles in similar ground conditions from which an expected response can be derived. Faulty piles will cause the graph produced to be distorted from this anticipated result; the form of distortion indicating the type of defect detected. These methods can only be used to check lengths of pile that include reinforcement. The success of acoustic techniques led to the demise of research into electrical methods in the early 1980's and none have been implemented commercially.

Both CIRIA reports^{2,13,24} also describe the **Integral Compression Test**. In this technique steel tendons are cast into the toe of the pile. After the concrete has cured they are stressed and the head movement is used to infer the pile's structural integrity. The method was suggested by Moon in 1972^{2,30} for large bored piles, but because of the complexity of its execution and the fact it gives no information on pile-soil interaction it is not used commercially.

2.6 INDUSTRY SURVEY

In his 1996 CIRIA publication^{2.13} Turner reported that by far the most widely used integrity test methods were the low strain methods - particularly on small diameter piles. While the sonic logging techniques are increasingly being used for large diameter piles where the lack of depth limitations becomes a necessity. This is corroborated by the Institution of Civil Engineers (ICE) publication *Specification for Piling*^{2.14} where three methods of integrity testing are discussed: low strain, sonic logging, and vibrational.

The author has made a survey of the availability and cost of these three integrity test methods. From the forty different companies that purport to perform pile integrity tests and were included in the New Civil Engineer Foundations Supplements 1993 and 1995^{2.31,2.32}, twenty replied to the questionnaire found in Appendix I. A list of the responding companies is also included in this appendix.

A number of these replies (four) reported that although the service was offered by the company it was sub-contracted to a third party who had already received a questionnaire.

Low strain, acoustic techniques, i.e. sonic echo (SE) or transient dynamic response (TDR), were carried out by all the respondents and on average it cost £8 per pile to carry out the test. The TDR method was, on average, about £2 per pile more expensive due to the extra post processing involved.

The vibrational method cost about £17 per pile and only 7% of the companies practised it with no-one considering it more accurate than the TDR test. One respondent suggested it was '*no longer a practical test*' while another reported that, to his knowledge, only two companies offered this service (including his) and that his testhouse had not used this method for a number of years.

Sonic coring was available from 25% of the respondents. The cost of this test was difficult to gauge because it has to be structurally designed into the pile which adds expense. Costs increased as a function of pile length and the number of ducts per pile. Most firms quoted for the day rather than per pile (£400-£1000). On further discussion with a number of the respondents it has become apparent that a line has been drawn between large and small diameter piles. The majority of pile contractors and test houses carry out the low strain tests due to the simplicity of the test, the

relative cheapness of the equipment involved and the fact there is a larger market for this service. Sonic logging is generally carried out by the larger specialist test houses and those companies that construct larger diameter, deeper cast *in situ* piles for which the test method is more usually used. Problems reported with this test include difficulties in detecting foreign bodies within the pile and drawing up the transmitter and receiver at a constant, parallel rate.

In conclusion it can be seen that since the publishing of Thorburn and Thorburn's 1977 CIRIA report^{2,8} the evolution of digital hardware and mathematical tools has led to the low strain integrity tests dominating the field. This is due to the test being relatively inexpensive and rapidly executable while producing a success rate comparable with the other test methods discussed. The sonic coring method is more sparingly used because of the relative size of the markets involved; more small diameter piles are produced than large. An analyst using the impact acoustic method is more likely to have a large number of results to interpret at the end of a days testing due to the relative speeds of the test and the increased likelihood of the piles being situated as part of a large group. It therefore follows that this method would most benefit from a reliable form of automated post processing. Also the high complexity of the problem domain leads to the subjective nature of its interpretation which appears to suggest it would profit from the use of a neural, post processing system. For these reasons the low strain integrity tests have been chosen as the methods employed in this project. In the next section these techniques are described in more detail and the current methods for their automated interpretation are discussed.

2.7 LOW STRAIN INTEGRITY TESTING

2.7.1 Pile Excitation and Response Detection

For low strain integrity testing the pile is struck by a small 3lb (1.36 kg) hand-held instrumented hammer, see Figure 2.11 (a). The hammer has an integrated-circuit piezoelectric force sensor enclosed in the striking end of its head. This produces an electrical signal proportional to the shape distortion of the piezoelectric crystal which in turn is proportional to the impact force. The hammer can therefore be used to trigger the data capture equipment when a threshold voltage is exceeded.

With a dual channel AD converter the input force and pile head response can then be measured with respect to time. A typical data capture system (TNO's Foundation

Pile Diagnostic System) allows for 14 bit resolution at a sampling rate of 50kHz. It is not disclosed whether the dual channels are multiplexed to a single AD converter which would effectively half the sampling rate. However even if this is the case the sampling rate would be enough to allow for over ten fold oversampling for TDR tests (up to 2kHz) and is at least an order of magnitude less than the typical rise time of the input pulse (~0.5ms for a plastic tipped hammer).

The rise time of the input pulse, and therefore its frequency components, can be altered through the choice of hammer tip. The striking end of the hammer can have tips of a differing hardness screwed on to it, typically: rubber, plastic, aluminium or steel. Harder materials will give a faster rise time and therefore a broader frequency range.

Higher frequencies allow greater resolution in the recorded response, but these components' energy dissipate quicker so leading to a faster attenuation of the signal. A compromise is generally met through the use of a plastic tipped hammer which covers ranges approaching 2kHz. If a defect is suspected at the pile head then an aluminium tip is then used as the greater resolution becomes a necessity while the increased attenuation is less of an influencing factor.

Some test houses do specify the need for ground or bush hammered areas of the pile head to improve hammer/pile and sensor/pile contact^{2.33,2.34}, see figure 2.11 (b). Most guides, however, simply require that the pile be trimmed to sound concrete and reinforcement bars bent or cut so leaving a relatively flat, accessible surface^{2.13,2.35,2.36,2.37}. The head must also be free from surface water and pile cap reinforcing steel.

The pile head response to the hammer impact is more usually measured using a calibrated accelerometer^{2.33,2.34,2.35,2.36}, although geophones (velociometers) may be used^{2.38}.

The active component of an accelerometer is a piezoelectric element that links its base with a free seismic mass. This element acts as a spring in that the inertia of the mass causes a shape distortion as the base is accelerated. The change in shape causes a measurable charge to be produced across the element which, because the mass is constant, is proportional to the seismic mass' acceleration. Since the seismic mass accelerates with the same magnitude and phase as the base, the measured charge is proportional to the acceleration of the surface onto which the base is

mounted^{2,39}. This is true over the linear frequency range of the accelerometer which, for accelerometers chosen for pile testing, will typically have lower and upper frequency limits of 0.1Hz and 5kHz respectively (Brüel & Kjær Type 4370 Delta Shear[®] Accelerometer).

A PCB[®] Impulse Force Hammer will typically produce an output of the order $0.2 \text{ mV/N}^{2,40}$ while the above mentioned accelerometer produces $10 (\pm 2\%) \text{ mV/ms}^{-2,41}$. Due to the small currents created by these transducers signal conditioning units must be employed. The purpose of these units is to convert the high impedance output of the piezoelectric device into a low impedance signal suitable for direct input to the analysing equipment. They may also amplify the signal to match the input sensitivity of the analysing equipment, integrate the signal, or filter the signal of unwanted components.

Although there are a plethora of vibrational amplifiers on the market - Brüel & Kjær offer a range of more than five products^{2,39} - most commercially available pile testing equipment is supplied with purpose built pre-amplifiers for the hammer and accelerometer. These allow the tester to move freely within the pile group carrying simply the pre-amplifiers, hammer and accelerometer connected to the stationary data capture and analytical instrumentation through a long roll of, low impedance, coaxial cable

2.7.2 Pulse Propagation

2.7.2.1 Pulse Generation

The point excitation of a body can cause the generation of a number of structural distortions. Longitudinal and surface waves are produced along with flexural and torsional deformations. In the case of a cylindrical body, such as a pile, struck centrally at its head torsional and flexural motion can be largely ignored: torsional because the pile is struck perpendicular to the top surface and flexural because it is hit centrally so the loading is not eccentric.

Surface, or Raleigh, waves are produced through Poisson's ratio effects. Oliver^{2,42} describes how when a rod like structure is struck, although most energy is transferred to a longitudinal wave packet, some is dissipated at the head through end resonance. As the pile is struck the centre is depressed causing the edge to move up and in. The centre then moves back through its start position and begins to bulge up

while the edge moves down and out. This resonance continues, to a decreasing degree, causing a ring-down effect as sympathetic longitudinal waves are produced. An approximate calculation of the frequency of oscillation of this resonance can be made if shear stresses are ignored. For a pile of diameter, d , and surface wave velocity, c_s , the frequency produced can be estimated from:

$$f = \frac{c_s}{d} \quad (2.4)$$

This estimation was found to correspond well with experimental results obtained by Steinbach and Vey^{2.43}. Chan^{2.44} has calculated a typical value for c_s for a concrete foundation pile assuming values of Young's modulus, $E=38.4 \text{ kN/mm}^2$, density, $\rho=2400 \text{ kg/m}^3$, and Poisson's ratio $\nu=0.24$. This gives a value of $c_s=2331 \text{ m/s}$. For piles of less than 1m diameter the resonance frequency will be above 2kHz and outside the range of the examined bandwidth for plastic tipped hammer impacts. Their effects can therefore be eradicated to a greater extent through low pass filtering. For testing using aluminium tipped hammers or on piles of more than 1m diameter these effects, as well as other random noise effects, are reduced through time averaging multiple responses recorded with the accelerometer at different positions on the pile's top surface.

The estimation of pile shape and density therefore revolves around the consideration of the longitudinal stress wave (p-wave) pulse with a displacement, u , described by Equation 2.5, below. In all cases below it is presumed the ratio between the pile diameter and principal wavelength component of the generated pulse is small i.e. it is presumed that the pulse is non-dispersive and propagates in a direction perpendicular to the pile's top surface.

$$u = f(x - ct) \quad (2.5)$$

where f is a function describing the pulse shape, x is a position along the axis of pulse propagation, t is the time and c is the pulse velocity.

2.7.2.2 Reflections from the Pile Toe

Consider an incident wave with particle displacement described by Equation 2.6, below.

$$u = f_i(x-ct) \quad (2.6)$$

Where u is displacement, x the position along the beam, c the stress wave velocity, t the time and f_i describes the pulse shape. When this reaches the end of a rod like structure of length L a reflected wave is produced:

$$f_r(x+ct) \quad (2.7)$$

The particle displacement and velocity, respectively, at the pile toe ($x=L$) is therefore:

$$u = f_i(L-ct) + f_r(L+ct) \quad (2.8)$$

which is the general solution to the one dimensional wave equation for a uniform rod or beam.

From Hooke's Law we obtain the equation below:

$$F = -EA\varepsilon = -EA \frac{\delta u}{\delta x} \quad (2.9)$$

Where F is the force acting on a particle within the rod, E is the material's Young's modulus, A is the cross sectional area of the rod and ε is longitudinal strain. So from 2.8 and 2.9 we obtain

$$F = -EA \frac{df_i}{d(x-ct)} - EA \frac{df_r}{d(x+ct)} \quad (2.10)$$

or

$$F = F_i + F_r \quad (2.11)$$

Where indices i and r represent incident and reflected portions of the pulse (from the pile toe). The particle velocity can then be written as

$$v = v_i + v_r \quad (2.12)$$

where v_i and v_r are the particle velocities associated with the force waves F_i and F_r and are connected through the equalities:

$$v_i = + \frac{F_i}{A \cdot c \cdot \rho} \quad (2.13)$$

$$v_r = -\frac{F_r}{A.c.\rho} \quad (2.14)$$

where, again, A is the cross sectional area of the pile, c is the wave propagation velocity and ρ the pile material density.

For a beam with a **fixed end** the particles' velocity and displacement must disappear and so:

$$v_i = -v_r \quad (2.15)$$

and from 2.13, 2.14 and 2.15:

$$\frac{F_i}{A.c.\rho} = -\frac{(-F_r)}{A.c.\rho} = \frac{F_r}{A.c.\rho} \quad (2.16)$$

so from 2.11:

$$F = 2F_i \quad (2.17)$$

Hence, the force at a fixed end will be twice that of the original excitation force and because F_i equals F_r (2.16) a compressive wave will be reflected as a compressive wave and tensile wave reflected as a tensile wave - though the particle velocity is opposite (2.15). For example, see Figure 2.12.

For a reflection from a **free end** the stress at the toe must disappear. So from 2.11 :

$$F_i = -F_r \quad (2.18)$$

And so from 2-12, 2-13 and 2-14:

$$v = \frac{2F_i}{A.c.\rho} \quad (2.19)$$

So the reflected pulse at a free end of a beam has a particle velocity double that of the particle velocity of the wave propagating through that beam and that pulse will have the opposite phase as the incident wave (2.18). That is a compressive wave will be reflected as a tensile wave and vice versa. A diagrammatic representation of these formulae are shown in Figure 2.12.

The recorded pile head responses of these theoretical beams would appear as Figure 2.13. Where $\Delta t = 2L/c$ and $\Delta f = 1/\Delta t$; L being the length of the beam in question.

In practice an installed pile will have neither of these perfect responses, but will have a base support of intermediate stiffness, as reported in field tests carried out by Davis and Dunn^{2.27}. The interpretation of these responses are discussed in Sections 2.7.3 for Sonic Echo traces and 2.7.3 for frequency spectra.

2.7.2.3 Partial Reflections from Changes in Pile Properties

As well as reflections from the pile toe partial, and total, reflections can be produced from features within the pile profile. Namely changes in the pile cross sectional area and changes in its material characteristics. To understand this equation 2-6, describing the stress wave's propagation, must be reconsidered.

By finding the derivatives of u , particle displacement, with respect to x , beam position, and t , time, it can be shown that the stress at a point, σ , is described by Equation 2.20.

$$\sigma = -\rho c \frac{\partial u}{\partial t} \quad (2.20)$$

So the ratio between the stress and velocity at any point is ρc . When multiplied by the sectional area of the object in question this ratio is known as the characteristic impedance of the material and can be used to calculate the proportion of a pulse reflected when a boundary between two different materials or changes in cross sectional area are encountered. At an interface two conditions must hold:

- 1) The forces on each side of the interface are equal : $(\sigma_i + \sigma_r).A_1 = \sigma_t.A_2$
- 2) The particle velocities must be continuous : $v_i - v_r = v_t$

Thus Equations 2.21 are derived.

$$r = \frac{z_2 - z_1}{z_2 + z_1} \quad t = \frac{2z_1}{z_2 + z_1} \quad (2.21) \text{ a, b}$$

where r and t are coefficients of reflection and transmission respectively. The proof of this can be found in many undergraduate textbooks e.g. Burton^{2.45}.

As summarised in Figure 2.14, the characteristic impedance of the pile, z , is directly related to its cross sectional area. However the density and wave velocity are linked to the concrete strength logarithmically which must, therefore, change considerably to produce a significant reflection^{2.13}. This method is consequently more sensitive to changes in section and is less able to determine the material characteristics of the pile.

Although it would appear, at first glance, that the pile profile can be inferred from any recorded trace this method has many practical limitations. The reflected pulse's amplitude is a function of the concrete impedance and soil or environmental changes. This means assumptions must be made, usually concerning the homogeneity of the concrete mix, and soil properties must be known. Also attenuation produced by the surrounding soil may restrict the returning pulses to an undetectable amplitude. These along with other restraints on this method's accuracy are discussed in more detail below, Sections 2.7.3 and 2.7.4.

2.7.3 Limitations of Low Strain Integrity Test Methods

Although there are many papers and documentation relating to the limitations of the low strain integrity test method there still appears to be some debate over the precise extent of these restraints. This is most clearly illustrated in the communications and papers published in the journal *Ground Engineering* over the period November 1992 to November 1995. These were initiated by a competition run in conjunction with the 4th International Stresswave conference^{2.46}. Here ten piles were cast with predesigned faults before being lowered into driven steel casings which were then backfilled to recreate *in situ* soil conditions. The twelve participating companies were subsequently asked to match ten cross section profiles with the ten test traces obtained from the installed piles.

The results were initially considered disappointing with the average score being only four out of ten and the winning score only seven^{2.46}. In a response Stain^{2.47} highlighted some of the weaknesses of the competition design. Of most relevance to this research is the proposed heuristic that the normal useful depth of stress wave penetration is around thirty pile diameters; a heuristic corroborated by test results collated by Turner^{2.13} and Braque^{2.38}. This is however dependent upon soil conditions, see Section 2.7.4 below. Although van Weele^{2.48} in a reply to Stain's criticisms points out that, because the toe reflection is clearly visible in the test

traces, this aspect ratio can be exceeded in soft soils he does concur that the position and extent of defects are of primary importance when considering the applicability of the test.

Turner^{2.49} in his contribution to the debate pointed out the ambiguities of similar traces being produced by different pile profiles. In particular he points out the significance of the axial length of a fault when interpreting a test result. It has been shown in Sections 2.7.2.3 how a reflected wave's amplitude is dependant upon the change in the pile's material impedance. In practice, however, a fault such as a bulb, neck or crack involves a return to the pile's design section. This means a tensile reflection will be followed by a compressive one or vice versa. If these reflections' sources are close with respect to the rise time of the input pulse then the superposition of the two will lead to a small, sometimes negligible, response at the pile head. Furthermore, even if the two reduced reflections are detectable it is difficult to infer, with confidence, whether they have been caused by a fault of large change in section, but small axial length, or a smaller reduction in section extending over a longer portion of the pile. However, in practice most faults occur within two metres of the pile head allowing the use of an input pulse with a faster rise time. This is particularly true of cracks which are more usually generated at the pile head, where lateral support is smaller, by plant machinery or during pile cropping. It is, nevertheless, generally agreed that faults of the order of 10mm or less which do not extend over the entire section of the pile are undetectable at any point along the pile length. While complete severance of the pile section will lead almost inevitably to total reflection so making investigation of the pile beneath that point untenable^{2.12}.

Ellway^{2.12} states that low strain testing cannot determine the axial extent of anomalies citing the example: a hairline crack across the entire extent of the pile section gives the same trace as a meter long void. This example, however, can be considered a special case as total reflection is involved. No anomalies below an event causing total reflection can be detected and so to use this as a corollary for a hypothesis specifically concerning the detection of axial information would seem unsound.

Both van Weele^{2.48} and Turner^{2.49} are less harsh in their views on the inference of fault length. A pulse generated by a hand held hammer with a plastic tip typically has a rise time of 0.5ms and a velocity of 3000-4000ms⁻¹. This leads to an effective pulse length of the order 3-4m. The superposition of the reflected waves from two boundaries therefore produces more ambiguous trace as the gap between these

boundaries becomes less. As a general guide van Weele suggests that defects with an axial length of less than 0.8-1.0m cannot be uniquely determined while smaller faults of the order of 10mm, even those producing a greater than 50% loss in section, will be undetectable.

The smallest detectable ratio of impedance change at a reflecting boundary is about 1:0.8 for an decrease in pile properties or 1:1.2 for an increase; this is the equivalent of a 10% change in pile diameter or a 15Nmm^{-2} change in concrete strength^{2,12}. The reflected pulses become increasingly pronounced as the ratios widen until, when the ratios exceed 1:0.25 (or 1:4), total reflection occurs.

It should be noted at this point that, because reflection is a function of change in impedance, pile properties that change gradually with depth may be undetectable. This is true if the magnitude of any individual reflection is outside the sensitivity range of the equipment used and is a recognised limitation of this test method.

The position of a defect also has an effect on its detectability. Faults towards the head of the pile may be difficult to detect for two reasons:

- 1) The impact is a point load yet the theory used in trace interpretation requires a planar wave perpendicular to the pile head surface. Within two or three pile diameters of the pile head, therefore, the wavefront's curvature is of such an extent that it cannot be considered negligible.
- 2) For a plastic tipped, handheld hammer the stress wave wavelength is of the order 4m and so changes in impedance in the top 2m of the pile will produce an echo at the pile head while it is still under load. If of a sufficiently low magnitude this reflection will be hidden by the continued impact. The best one can hope for is a significant distortion of the early part of the recorded trace to indicate a possible defect.

As previously stated (2.7.1) the use of an aluminium or steel tipped hammer will produce a pulse with higher frequency components allowing better resolution at the pile head. Also visual inspection of the area may be possible for the very top portion of the pile. Chan^{2,44} reported that for the same extent of defect smaller values of dynamic stiffness are obtained if the fault is near the pile head. As a value for the dynamic stiffness can be deduced from the mobility curve of the pile (see Section 2.7.6, below) this graph can be used to infer impedance changes at the pile head^{2,38}.

Although these actions may help in their discovery, defects at the pile head are still intensely difficult to detect.

The pile's acoustic length - the calculated length of the pile - can only be found if a reflection from the toe is detected. For the calculation the stress wave's propagation velocity must be assumed ($3000-4000\text{ms}^{-1}$) which means the length can only be found to $\pm 10\%$ accuracy^{2.13}. This means faults near, or at, the pile toe cannot be identified reliably. A reflection from the pile toe will only occur if there is a significant difference in impedance with that of the material beneath it. The toe may also be undetectable if a strong acoustic boundary above it prevents the propagation of the stress wave to lower portions of the pile or if the signal attenuation is such that the wave energy dissipates before returning to the pile head, see Section 2.7.6 below.

The other limitations on this method are largely based on the hardware involved in data acquisition. These are summarised in Section 2.7.1 above.

2.7.4 Effects of Soils on Installed Piles

The installation of a pile into a soil medium bears two consequences: signal attenuation and possible partial reflection.

Signal attenuation occurs through partial transmission of the signal beyond the pile base and soil resistance along the pile shaft. Laboratory studies showing the effects of damping from soils have been published by Ding *et al.*^{2.50} and Armstrong^{2.51}. Both conclude that the environment of the installed pile must be considered for test results to be relevant. The other conclusions of Ding *et al.* should only be considered true for the reported experiments. Due to the limitations described above it cannot be true in the general case that:

'By applying the theory of wave propagation and the pile top response curve, the type, degree, location of the damage of the fault pile can be obtained and its results are in accord with the preset situations.[sic.]' or that: 'The support soil of the pile can be judged.'

As previously stated, the signal reflection at the pile base is dependant upon the difference between the pile impedance and the impedance of the material impedance beneath its toe (see Section 2.7.3, above). As reported by Wong^{2.52}, if while an incident wave travels down a rod it meets an external soil resistance, scattering of

the wave occurs. This soil resistance will be a function of the shear stress on the pile wall due to adhesion and skin friction. In turn the magnitude of this shear stress is dependant upon the shear strain and strain rate of the soil. Poskitt^{2.52} describes the shear stress in terms of a visco-elastic formula whereby the stress is defined as the sum of viscous and elastic components, equation 2.22 below.

$$\tau = \lambda_l \cdot u + \mu \cdot \frac{\delta u}{\delta t} \quad (2.22)$$

where τ = shear stress λ_l = load transfer parameter
 u = pile displacement μ = viscous parameter

The first term is the elastic term which, because of the low strains involved in this form of testing, is considered to be linear. The second term considers the viscous nature of soil with the forces produced dependant upon strain rate (in this case the pile wall velocity).

Although sound in its derivation the above formula with, its esoteric soil parameters, does not lend itself readily to the application of trace analysis. Briard's^{2.38} formula (2.23), on the other hand, produces an attenuation factor that has been successfully used for analysis in the frequency domain^{2.27} and by Paquet for the modelling of pile-soil interaction²⁻³⁸.

$$A_B = \frac{1}{r} \cdot \frac{\rho'}{\rho} \cdot \frac{\beta'}{c} \text{ in Neper m}^{-1} \quad (2.23)$$

where A_B = attenuation parameter β' = shear stress wave velocity in soil (ms^{-1})
 ρ' = soil density (kg.m^{-3}) ρ = concrete density (kg.m^{-3})
 r = pile radius (m) c = propagation velocity in concrete (ms^{-1})

The above formulae was validated by Paquet through data describing pile-soil interaction collated by CEBTP in conjunction with its European partners^{2.38}. He also produced a diagram summarising the test's empirical depth of penetration from this database, see Figure 2.15.

As well as attenuation when a boundary between soil strata is reached there is also the possibility of the partial reflection of the propagating wave. A change from stiff to a weak soil has the same effect as a decrease in section. While a change from a weak to a stiffer layer will act as an increase in section^{2.13}. Wong^{2.52} states that if the

mobilised soil resistance is R_s , the magnitude of the reflected wave can be predicted from wave propagation theory as Equation 2.24 :

$$v_r = -\frac{R_s}{(2Z)} \quad (2.24)$$

Where Z is the acoustic impedance of the pile.

It should be noted here that changes in soil stiffness are often the cause of changes in pile section. As the soil changes from a soft layer to a stiffer, deeper layer so the pile diameter may change from an oversized dimension to its designed section. Thus the reflected pulse's amplitude would be representative of the change in section and change in soil characteristics. Site investigation data, specifically cone penetration data and bored samples, must therefore be rigorously examined before an attempt is made to interpret test results.

2.7.5 Sonic Echo Response Interpretation

Most of the previous sections have described the factors influencing the velocity response, recorded in the time domain, during low strain integrity testing. It has been shown how the integrated accelerometer trace is characteristic of the pile's shape, construction and environment, see Figure 2.6. This data can, however, be enhanced to facilitate its interpretation.

The most basic of signal accentuation is its amplification with respect to time. This is usually increased exponentially to counteract the effects of soil attenuation and increase the magnitude of reflections from lower parts of the pile.

The signal to noise ratio can then be reduced by irradiating some of the random noise through the use of multiple signal averaging and auto correlation techniques^{2.12,2.43}. Low pass filtering can also be used to reduce unwanted high frequency components, however it is suggested that this should not be carried out using hardware networks as these produce undesirable phase changes in the lower frequency range during impact testing^{2.39}.

More recently testhouses have introduced the concept of the reflectogram^{2.35,2.38}. Here the deconvolution of the signal with respect to the input pulse is carried out to find the impulse response function of the pile. This is the time based equivalent of

the pile mobility spectra - see Section 2.7.6, below. The trace is compared with the expected response of a nominal pile of infinite length with the same design section and construction in the same ground conditions. By amplifying the resultant trace as a function of the prevailing soil conditions a reflectogram is produced from which an impedance log can be deduced.

The impedance log is essentially a graph of pile impedance against depth and its automated construction is discussed in Section 2.7.7 below. For best results it is suggested that the impedance profile, sonic echo response and frequency response (see Section 2.7.6) are all referenced when drawing conclusions on the integrity of a foundation pile^{2.13,2.35,2.44}.

2.7.6 Transient Dynamic Response Interpretation

An alternative way of presenting the information held in the time trace is to transform the data from the temporal to frequency domain. This transformation is more usually effected through Cooley and Tukey's Fast Fourier Transform (FFT) Algorithm^{2.54}. Although it has a faster execution time than other signal decomposition methods it suffers from the same limitations as all Discrete Fourier Transform (DFT) techniques, namely: leakage, aliasing and picket fence effects^{2.55}. However, with ten fold oversampling and low pass filtering reducing the effects of aliasing, the inherent limitations of the physical test method restrict the influence of these processing errors to a negligible degree.

The frequency spectrum of the recorded velocity trace is dependant upon the shape of the input pulse. When an instrumented hammer is used, however, the spectrum of the pulse can also be calculated. This can then be divided into the response spectrum to produce the mobility spectrum of the pile. The mobility curve is input pulse independent and characterises the pile shape, construction and environment. It is the equivalent of the pile's impulse response function in the time domain.

The theory behind the interpretation of mobility spectra stem from work carried out by Davis and Dunn^{2.27} on the steady state response of a foundation pile to vibrational excitation. For an undamped undamaged pile of constant section and material content the theoretical mobility curves were shown in Figure 2.13. However, when the pile is embedded in soil its movements are damped and its base fixity is neither completely fixed nor free, giving a response as Figure 2.17.

For Figure 2.17 the frequencies at which resonance occurs are equally spaced at intervals:

$$\Delta f = \frac{c}{2L} \quad (2.25)$$

where c is the wave propagation velocity and L is the length of the pile. The mean value of the mechanical admittance, N_A , is the inverse of the mechanical impedance of the pile and is given as:

$$N_A = \frac{1}{\rho c A} \quad (2.26)$$

Where ρ and A are the density and cross sectional area of the pile respectively.

The values P and Q provide a measure of the damping effects of the soil such that:

$$P = N_A \coth(A_B L) \quad (2.27)$$

$$Q = N_A \tanh(A_B L) \quad (2.28)$$

when A_B is Briard's damping factor, as introduced in Section 2.7.4 Equation 2.25. So from equations 2.27 and 2.28 we have:

$$N_A = \sqrt{PQ} \quad (2.29)$$

and so $\coth(A_B L) = \sqrt{PQ}$ (2.30)

From Δf , assuming c , the acoustic length of the pile can be calculated from 2.25. The apparent mass of the pile can be determined from Equation 2.31, below:

$$M = LA\rho = \frac{1}{2\Delta f N} \quad (2.31)$$

For low frequency excitation the consequences of inertia become less significant and the pile-soil unit is assumed to act as a single, rigid body. This gives the linear region OM in Figure 2.17. The inverse of the slope of this straight line is a measurement of the apparent dynamic stiffness at the pile head. This is particularly useful for indicating abnormalities at the head of the pile; a difficult task when attempted using the time domain velocity response (see Section 2.7.5).

The position and degree of a simple defect can also be found from its spectrum. Consider the mobility curve of a pile with a neck as in Figure 2.19.

Having assumed $\rho=2400 \text{ kg.m}^{-3}$, and $c=4000 \text{ ms}^{-1}$ the two lengths associated with the two resonant frequency intervals within the spectrum can be calculated (2.32):

$$L_H = \frac{c}{2\Delta f} = \frac{4000}{2 \times 980} = 2\text{m} \qquad L = \frac{4000}{2 \times 200} = 10\text{m} \qquad (2.32)$$

And these are in turn associated with two areas of cross section, namely:

$$A_{\max} = \frac{1}{N_A \rho c} = 0.65 \text{ m}^2 \qquad (2.33)$$

$$A_{\min} = 0.36 \text{ m}^2$$

Thus the pile profile has been inferred from the mobility curve. In practice, the mobility curve is more usually further complicated by the exposure of the pile head, changes in soil conditions, and the heterogeneity of the pile's concrete. However, Davis and Dunn have presented four examples of the use of mobility spectra investigation for pile testing. Effectively they compare the measured pile stiffness and peak separation with the expected values to find those with atypical responses for further investigation. The pile admittance was used to infer concrete quality.

This process of interpretation was developed for steady state vibration testing where there was no time trace to investigate. Today, with impact testing, the TDR method is a means of presenting the same data in a different format. Indeed, with the complex part of the spectra being disregarded, as appears invariably to happen, it is impossible to reconstruct the temporal trace from the mobility curve. It can therefore be reasonably argued that there is an inherent loss of information involved in the transfer of data from the time to the frequency domain.

As a method of presenting data to the human analyst, however, this method has a number of advantages. The fact that the FFT gives a time averaged summary of the frequency components means that many of the characteristics of the chart are directly related to the pile characteristics. This is true for such things as material admittance, pile head stiffness and acoustic length. This and its usefulness in indicating defects in the upper portion of the pile has left the method in wide spread use today. More often in conjunction with its time based partner the sonic echo test.

2.7.7 Automated Interpretation of Low Strain Test Results

BS8004 specifies that an integrity test '*...should be undertaken by persons experienced in the methods and capable of interpreting the results*'^{2.1}. This means for each set of tests an expert analysis should be on site. Indeed some companies employ two people to carry out each test: a technician to acquire the data and an analyst to interpret it^{2.35}.

Conventionally the interpretation of complex returning pulses from low strain integrity tests have used the same wave matching techniques as described in Section 3.2.2: Dynamic Load Testing. Here the head velocity of a reference pile, known to be sound, is used to estimate soil and concrete parameters which can then be used to calculate the expected responses for different pile shapes using the lumped mass model. If a pile is then tested and produces an atypical trace a series of responses can be generated until the simulated results match the experimental one. At this point the user has found an estimate of the suspect pile's profile. This process is explained in more detail by Middenthrop and Reiding^{2.56} with special reference to the TNOWAVE signal simulator. CEBTP practise this technique in the frequency domain using their SIMINTEG software to model the piles' responses, see Figure 2.19.

The cost incurred through having an analyst on site, and the time taken when using an iterative process to analyse the test results, has encouraged a great deal of research into the simplification of trace explication.

Although some attempts have been made to improve the method of information presentation to the human investigator, such as Chan's use of the cepstrum and liftering techniques^{2.28,2.44}, most research has been in the automatic interpretation of the time domain data.

By considering the pile length as a number of discrete elastic columns of uniform length and interpreting the returned trace as a summation of reflections from these sections it should be possible to obtain an estimate of the pile profile if the concrete's physical properties are assumed constant.

This method has been adopted, with some degree of success, by Kido *et al.*^{2.57} at Tohoko University in Japan. However, their model was only tested on uninstalled

test piles containing a single defect which results in the system being impractical for field use. As stated earlier the environment into which the pile is cast will have a considerable effect on its impulse response and so ground conditions cannot be assumed to be negligible.

More practical systems, which take into account ground conditions, have been developed by TNO^{2.58} and CEBTP^{2.38}.

The TNO method involves using data from a sound pile to form a 'shaft friction model' of the soil/pile interaction, much like the wave matching technique. The impulse response function of the pile, the inverse Fourier transform^{2.54,2.55} of the pile mobility, is first calculated. As in the other cases the method continues with the assumption that pulse propagation acts as a one dimensional wave in an elastic medium. Friction elements model the surrounding soil as viscous dampers, with parameters derived from a sound pile's trace. These elements are considered to be located around those of the discretised pile length. The pile profile can then be calculated through a step-by-step wave evaluation taking into account all the wave paths that could contribute to a certain reflection, including the friction elements. This method has proved effective in finding faults in computer modelled piles, but the tests effectiveness is very much dependant upon the 'quality' of the signal trace to be interpreted. It is assumed that 'quality' in this case equates to the complexity of the trace as caused by changing ground conditions or multiple reflections. A simpler trace with few salient peaks, each of a comparatively large amplitude, will be easier for the system to interpret.

The CEBTP method considers the impulse response of the damaged pile with reference to that of the expected response for an infinitely long sound pile in the same soil conditions. Unlike the TNO method this 'expected response' is computer generated using the SIMINTEG software. Attenuation caused by prevailing soil conditions is then corrected for using Briard's formula. This produces the reflectogram described in Section 2.7.5 in which all soil influences have been eliminated. The impedance profile, $P(x)$, can then be reconstructed from the corrected reflectogram, $R(t)$, through the following summations:

$$S(t) = \int R(t) dt \quad (2.34)$$

$$P(t) = P(x/c) = \frac{1 - S(t)}{1 + S(t)} \quad (2.35)$$

Where $P(t)$ corresponds to the ratio of impedances between that at position $t.c$ (time \times velocity) and the expected impedance. Figure 2.20 shows the impedance log of a pile with a bulb as derived from the mobility curve to its left. The curved nature of the defect and toe is caused by the lack of high frequency components in the reflectogram. SIMINTEG generates the response in the frequency domain and the test results will range up to only about 2kHz. Thus the reflectogram, which is generated through the reverse FFT of these curves, will not contain any sharp discontinuities as these necessarily contain mainly high frequency components.

The IMPRO tool is reportedly under-utilised by clients^{2.26} possibly showing a natural reservation on the part of the market to move to a deterministic method for the automated interpretation of test traces. The fact that the impedance profile can be reconstructed from the corrected reflectogram is indisputable although it would be advantageous if the minutes taken to generate it could be reduced to seconds. However, the correction for soil effects using SIMINTEG produces limitations on the method. The software can cope with a maximum of nine soil strata, enough for most practical applications, but the matching of suitable parameters for the modelling of the nominal reference pile is not a negligible task. The worked example in the text of the paper is for the profile of computer generated pile and so the nominal reference pile can be modelled with identical, perfect, soil parameter values. Failure to get this high degree of accuracy in practice will produce additional components in the reflectogram and so, therefore, in the impedance profile. There is also a divergence of the reconstructed trace from the required trace even in this idealised example due to multiple reflections between impedance, and soil, boundaries. Using a site mean trace as the reference trace, as the TNO method uses, could reduce these problems although this would result in the reflection from the toe being lost. Hence the use of an infinitely long nominal pile for reference.

There is also a second technique discussed in the Paquet^{2.38} paper. This is an iterative method whereby the pile and its surrounding soil are discretised into individual strata. Consecutive impedance values are then calculated from preceding values starting with the boundary conditions at the head of the pile which are known. This method, however, suffers from two reported drawbacks:

- 1) It is very time consuming, because of its iterative nature.
- 2) Poorly chosen soil parameters may lead to negative values of impedance.

This method is not therefore generally used except in conjunction with the first method for validation.

Finally a completely different approach was employed by Comerford *et al.*^{2.59} where a knowledge based system is used to interpret the response signal. Here the signal is divided into a series of straight lines of differing length and slope. This descriptive series can then be considered as a sentence which can be parsed to reveal its meaning. The parsing method used was the definite clause grammar (DCG) system embedded in the PROLOG theorem prover, a description of which can be found in Bratko^{2.60}. The rules and heuristics are defined by the programmer and the trace is interpreted by fitting it to one of the series of templates described by them. This method is reported to have an 80% success rate in predicting the serviceability of 150 test piles. However, no field tests are reported and the effects of the pile environment are not considered. It should also be noted that by representing the test data in such a way there is an inherent loss of resolution. Moreover the methods weaknesses are the same as any natural language parser, namely that traces cannot be considered *context free* and, therefore, has a very large grammar. Other problems associated with this application and the methodology it employs are described in Section 3.2.

The use of neural networks for the interpretation of pile test data is limited. One example of neural networks as an alternative for the pile driving formula has been found. For the interpretation of low strain integrity tests one neural based expert system has been found. All of these academic systems are limited in their problem domain and untested in the field. They are discussed more fully in the following chapter: Artificial Neural Networks for Signal Processing and Fault Detection.

2.8 SUMMARY AND CONCLUSIONS

The load bearing capacity and settlement characteristics of a cast *in situ* pile can only be satisfactorily deduced from static load tests.

Load testing of entire pile groups is impractical. Integrity testing is therefore employed to find piles with atypical acoustic characteristics which can then be load tested or investigated further. This enables all piles with suspected abnormalities to be included in the test set so limiting the over design necessary in the pile group.

The most widely used integrity test for small diameter cast *in situ* piles, in the UK, is the low strain integrity test.

Conventional interpretation of these tests' results requires the iterative process of wave matching which can involve a great deal of time and, therefore, expense.

Recently developed deterministic methods for the automated reconstruction of the pile profile from test results suffer from the high degree of processing necessary in the wave trace methods and the accuracy needed in soil modelling.

This thesis will continue with an investigation into the use of Artificial Neural Networks for trace interpretation. Being an adaptive processing tool it is possible this method will learn, through example, the salient features necessary for the accurate interpretation of the sonic echo trace.

REFERENCES

- (2.1) British Standards Institution, BS 8004, Code of Practice for Foundations, (1986).
- (2.2) British Standards Institution, BS 5930, Code of Practice for Site Investigation, (1981).
- (2.3) Tomlinson M J, and Palmer D J, Are Piles Necessary and What Determines Choice?, in Piles and Foundations, Ed. Young F E, Thomas Telford Ltd (1981) pp111-120.
- (2.4) Poulos H G, and Davis E H, Pile Foundation Analysis and Design, John Wiley and Sons (1980).
- (2.5) Fleming W G K, Faults in Cast in Place Piles and their Detection, Proc. of 2nd Int. Conf. on Structural Faults and Repair (1985) pp301-310.
- (2.6) Fondedile Foundations Ltd., Specification for the Design and Construction of Pali Radice Piles, Trade Literature, (1995).
- (2.7) Terzaghi K, and Peck R B, Pile Foundations, Soil Mechanics in Engineering Practice, Second Edition, John Wiley & Sons (1967) pp525-555.
- (2.8) Thorburn S, and Thorburn J Q, Review of Problems Associated with the Construction of Cast-in-place Concrete Piles, Construction Industry Research and Information Association, Report PG2 (1977).
- (2.9) Fleming W G K, Weltman A J, Randolph M F, and Elson W K, Integrity Testing, Piling Engineering, JohnWiley and Sons (1986).

- (2.10) Healy P R, and Weltman A J, Survey of the Problems Associated with the Installation of Displacement Piles, Construction Industry Research and Information Association, Report PG8 (1980).
- (2.11) Sliwinski Z J, and Fleming W G K, The Integrity and Performance of Bored Piles, Piling and Ground Treatment, Thomas Telford Ltd (1984) pp211-223.
- (2.12) Ellway K, Practical Guidance on the Use of Integrity Tests for the Quality Control of Cast-in-Situ Piles, Ground Engineering, Vol. 20, No. 7 (1987) pp8-13.
- (2.13) Turner M J, The Role of Integrity and Other Non-Destructive Testing in the Evaluation of Piled Foundations, Construction Industry Research and Information Association, Report R144, (1996).
- (2.14) The Institution of Civil Engineers, Specification for Piling: Contract Documentation and Measurement, Thomas Telford Ltd (1988).
- (2.15) Tomlinson, M J, Foundation Design and Construction, 6th Edition, Longman Scientific and Technical, (1995).
- (2.16) Rausche F, Garland E, and Hussein M, Pile Integrity by High and Low Strain Impacts, Proc. of 3rd Int. Conf. on the Application of Stress Wave Theory to Piles (1988) pp44-55.
- (2.17) Corté J-F, and Bustamante M, Experimental Evaluation of the Determination of Pile Bearing Capacity from Dynamic Tests, Proc. of 2nd Int. Conf. on the Application of Stress Wave Theory on Piles (1984) pp17-24.
- (2.18) Goble G G, Likins G E, and Rauche F, Bearing Capacity of Piles from Dynamic Measurements, Final Report, Department of Civil Engineering, Case Western Reserve University (1975).
- (2.19) Smith E A L, Pile-Driving Analysis by the Wave Equation, Journal of the Soil Mechanics and Foundations Division, American Society of Civil Engineers, Vol. 86, Pt SM4 (1960) pp35-61.
- (2.20) Mure J N, Knightley M L, Gravare C-J, and Hermansson I, CAPWAP-an Economical and Comprehensive Alternative to Traditional Methods of Load Testing Piles, Piling and Ground Treatment, Thomas Telford Ltd (1984) pp225-232.
- (2.21) Bretinghamhammer Ltd, Statnamic Load Test, World Wide Webb Internet Address: <http://netaccess.on.ca/hammer/stat.html>, (1996).
- (2.22) Inamura T, Moni Y, Matsuki Y, and Tanikawa M, Statnamic Load Testing on a Large Cast-in-Situ Concrete Pile, 1st Int. Statnamic Seminar, Canada, (1995).

- (2.23) Turner M J, The Use of Integrity Testing in Evaluating Foundation Piles, Proc. of 2nd Int. Conf. on Foundations and Tunnels, Vol.1 (1989) pp307-316.
- (2.24) Weltman A J, Integrity Testing of Piles: a Review, Construction Industry Research and Information Association, Report PG4 (1977).
- (2.25) Testconsult Ltd., Worldwide Testing and Inspection Services: Pile Testing, Sonic Coring, Trade Literature (1995).
- (2.26) Testconsult Ltd., IMPRO- a new tool, Testconsult CEBTP Newsletter, Winter (1992) p4.
- (2.27) Davis A G, and Dunn C S, From Theory to Field Experience with the Non-Destructive Vibration Testing of Piles, Proc. Inst. Civ. Engrs, Part 2, 57, December (1974) pp571-593.
- (2.28) Chan H-F C, Heywood C, Forde M C, and Batchelor A J, Developments in Transient Shock Pile Testing, Proc. of Int. Conf. on Foundations and Tunnels (1987) pp245-261
- (2.29) Williams H T, and Stain R T, Pile Integrity Testing - Horses for Courses, Proc. Int. Conf. on Foundations and Tunnels, Engineering Technics Press (1987) pp184-191.
- (2.30) Moon M R, A Test Method for the Structural Integrity of Bored Piles, Civ. Eng. and Publ. Wks. Rev., May, (1972) pp476-480.
- (2.31) Foundations Supplement, New Civil Engineer, Thomas Telford Ltd., December, (1993).
- (2.32) Foundations Listing, New Civil Engineer, Emap Business, December (1995) pp47-56.
- (2.33) Testconsult Ltd., Worldwide Testing and Inspection Services: Pile Testing, Trade Literature, (1996).
- (2.34) TESTAL, Pile Integrity Testing, Trade Literature, Testing and Analysis Ltd, (1995).
- (2.35) N.D. Technology, Pile Integrity Testing Using the Diagnostic Pile Analyser, Trade Literature, (1996).
- (2.36) England M, A Guide to Low Strain Integrity Testing, Cementation Piling and Foundation Ltd, (1995).
- (2.37) The Institution of Civil Engineers, Specification for Piling, Thomas Telford Ltd, (1988).
- (2.38) Paquet J, Pile Integrity Testing - the CEBTP Impedance Profile, Proc. Conf. Institution of Civil Engineers, In: Piling Europe, London (1992).
- (2.39) Anon, Sound and Vibration Product Catalogue, Brüel & Kjær (1993).

- (2.40) PCB Piezotronics, Calibration Certificate, Impulse Force Hammer Type 086B20, Serial No. 3689 (1989).
- (2.41) Brüel & Kjær, Calibration Chart for Accelerometer Type 4370, Serial No. 1426071 (1988).
- (2.42) Oliver J, Elastic Wave Dispersion in a Cylindrical Rod by Wide Band Short Duration Pulse Technique, J.A.S.A., Vol. 29 (1957) pp189-194.
- (2.43) Steinbach, J, and Vey E, Caisson Evaluation by the Stress Wave Propagation Method, J. Geotechnical Engineering Division, A.S.C.E., Vol. 101, GT4 (1975) pp361-378.
- (2.44) Chan H-F C, Non-Destructive Testing of Concrete Piles using the Sonic Echo and Transient Shock Methods, PhD Thesis, University of Edinburgh, (1987).
- (2.45) Burton R B, Reflection from a Discontinuity, Vibration and Impact, Addison-Wesley (1958) pp226-229.
- (2.46) Wheeler P, Stresswave Competition, Ground Engineering, Vol.25, No. 9 (1992) pp25-26.
- (2.47) Stain R T, Test's Integrity is Questionable, Ground Engineering, Vol. 26, No. 1 (1993) p7.
- (2.48) van Weele B, Integrity Test was not Questionable, Ground Engineering, Vol. 26, No.3 (1993) pp 14-15.
- (2.49) Turner M J, Integrity Test Usefulness is not the Issue, Ability is, Ground Engineering, Vol. 26, No. 6 (1993) pp27-28.
- (2.50) Ding J H, Xu F Z, Liu Y B, and Huo L Y, The Experimental Study on Transient Method Used in the Non-Destructive Quality Checking and Measuring of the Pile Foundation, Proc. Int. Conf. on Struct. Dynamics, Vibration, Noise and Control (1995) pp990-995.
- (2.51) Armstrong D, Integrity Testing of Structures Using Modal Testing, PhD Thesis, Napier University, Edinburgh, (1995).
- (2.52) Wong K Y, Small Strain Sonic Pile Tests the Need for Caution, Ground Engineering, Vol. 25, No. 11, (1995).
- (2.53) Poskitt T J, A Question of Integrity, Ground Engineering, Vol. 24, No. 11, (1994).
- (2.54) Cooley J W, and Tukey J W, An Algorithm for the Machine Calculation of Complex Fourier Series, in Digital Signal Processing, Eds Rabiner L R, and Rader C M, IEEE Press (1972) pp223-227.
- (2.55) Bergland G D, A Guided Tour of the Fast Fourier Transform, in Digital Signal Processing, Eds Rabiner L R, and Rader C M, IEEE Press (1972) pp228-239.

- (2.56) Middendorp P, and Reiding F J, Determination of Discontinuities in Piles by TNO Integrity Testing and Signal Matching Techniques, Proc. of 3rd Int. Conf. on the Application of Stress Wave Theory to Piles (1988) pp33-43.
- (2.57) Kido K, *et al.*, Shape Estimation of Foundation Concrete Piles by Analysing Reactions of Pile Head to Hammer Pulse, Proc. of 3rd Int. Conf. on the Application of Stress Wave Theory on Piles (1988) pp107-114.
- (2.58) van Staalduin P C, Bielefeld M W, and Middendorp P, A Direct Prediction Technique for Discontinuities in Piles, Proc. of 2nd Int. Conf. on Foundations and Tunnels, Vol.1 (1989) pp303-306.
- (2.59) Comerford J B, Blockley D I, and Davis J P, A Knowledge Based System to Interpret Results from Pulse-Echo Pile Integrity Tests, Proc. of Institution of Civil Engineers, Vol. 90, Pt 1 (1991) pp189-204.
- (2.60) Bratko I, PROLOG Programming for Artificial Intelligence, Second Edition, Addison-Wesley, (1991).

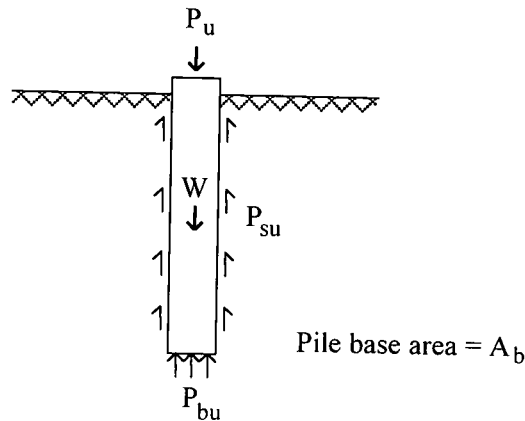


Figure 2.1 The forces acting on an axially loaded pile in equilibrium.

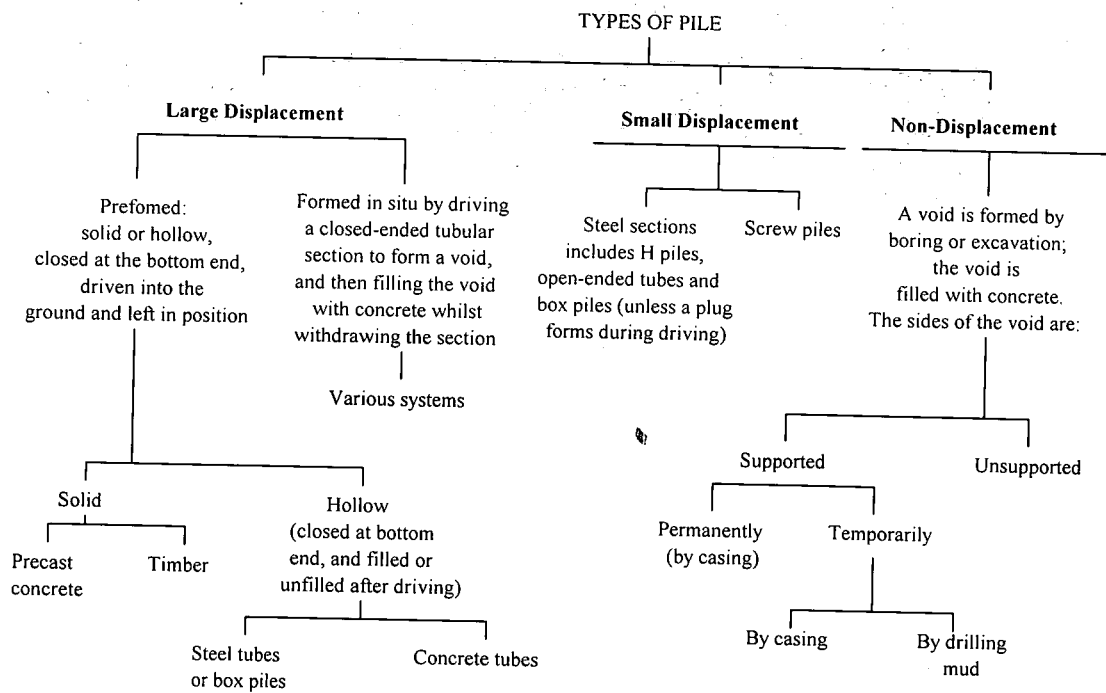


Figure 2.2 Summary of various piling techniques (After BS8004^{2.1}).

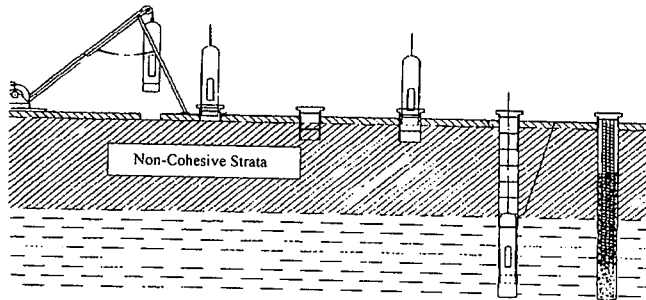


Figure 2.3 Stages of construction of a percussion bored pile, courtesy of Cementation, Piling and Foundations Ltd.

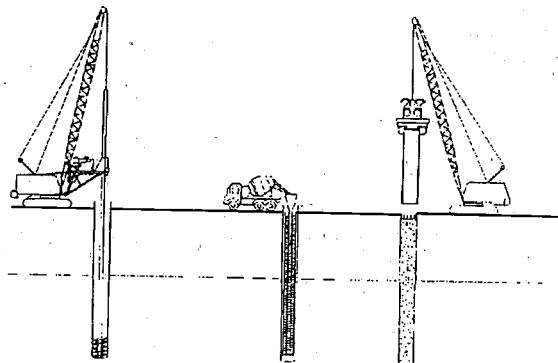


Figure 2.4 Stages of construction of a rotary bored pile, courtesy of Cementation, Piling and Foundations Ltd.

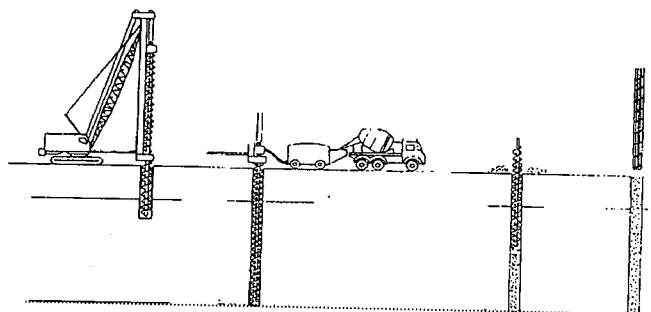


Figure 2.5 Stages of construction of a CFA bored pile, courtesy of Cementation, Piling and Foundations Ltd.

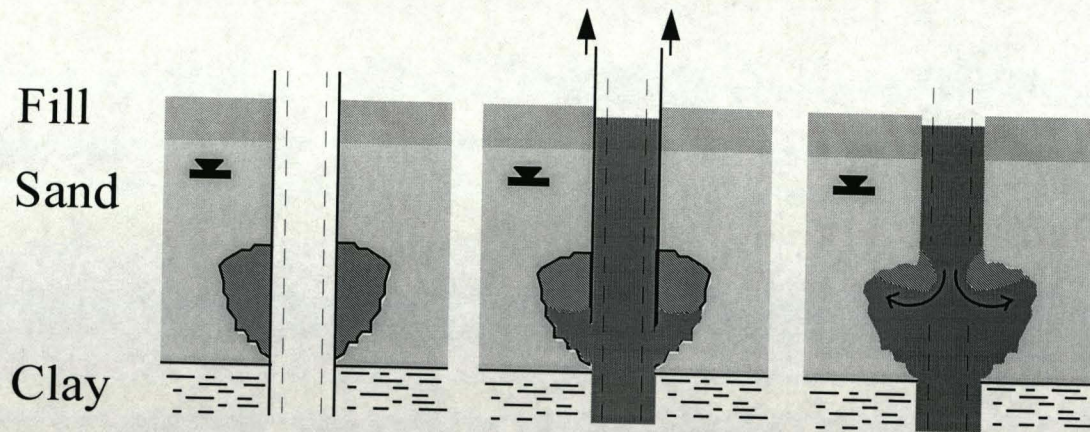


Figure 2.6 The formation and effect of cavities during casing extraction.

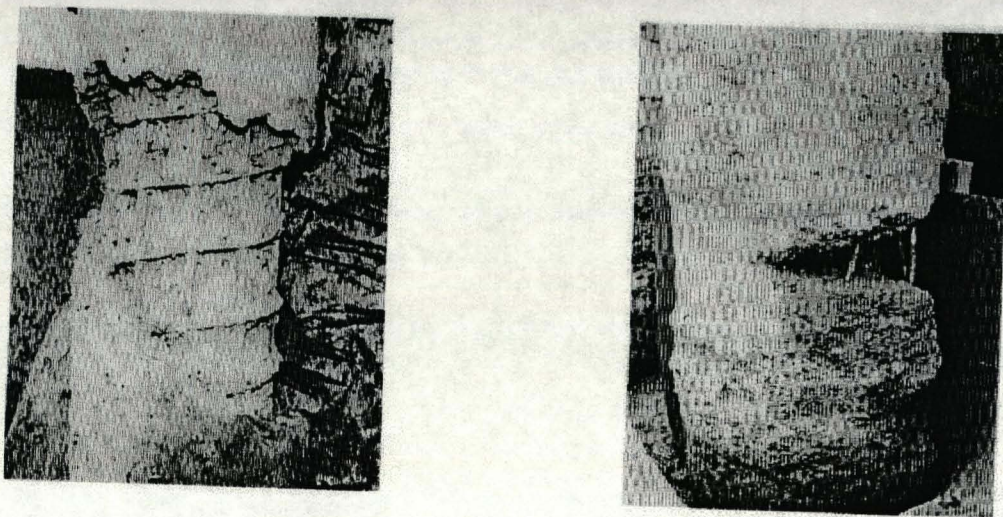


Figure 2.7 Loss in section caused by groundwater (left) and uplift during casing extraction (right) (after Fleming *et al.*^{2.9})

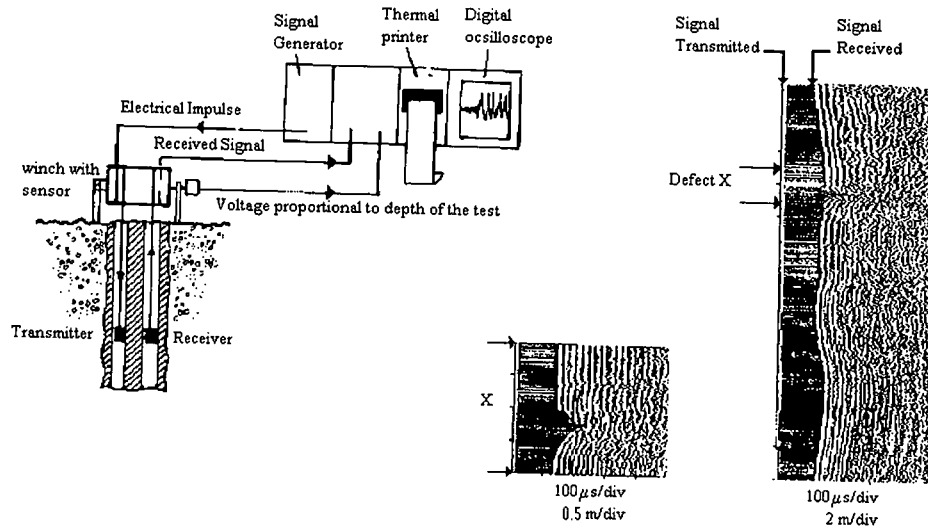


Figure 2.8 Cross-hole sonic coring: method (left) and results plot (right). (Courtesy of Testconsult Ltd).

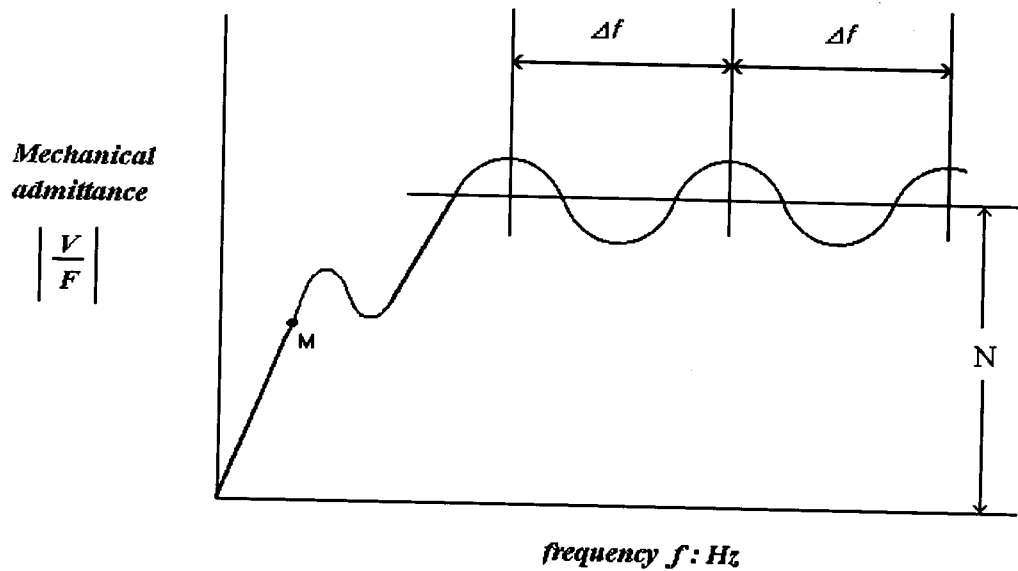


Figure 2.9 A typical frequency response curve for a cylindrical pile.

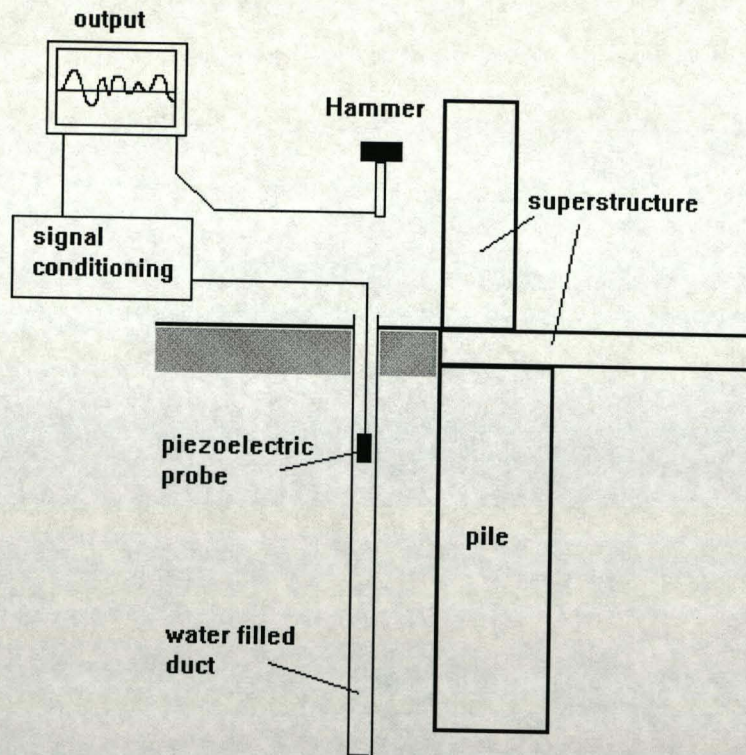


Figure 2.10 Parallel Seismic Testing for the remote testing of foundation piles.

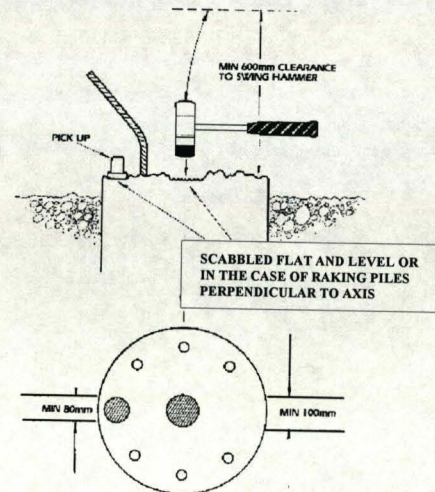
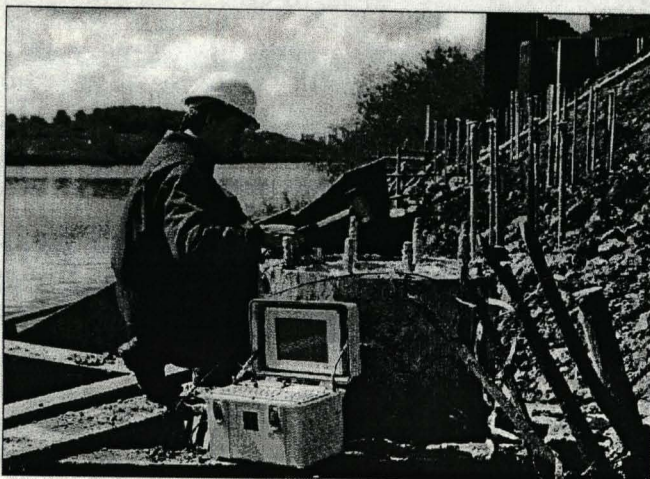


Figure 2.11 The low strain integrity testing of a cast *in situ* pile (a) and an example of pile preparation (b) - Both courtesy of Testconsult Ltd.

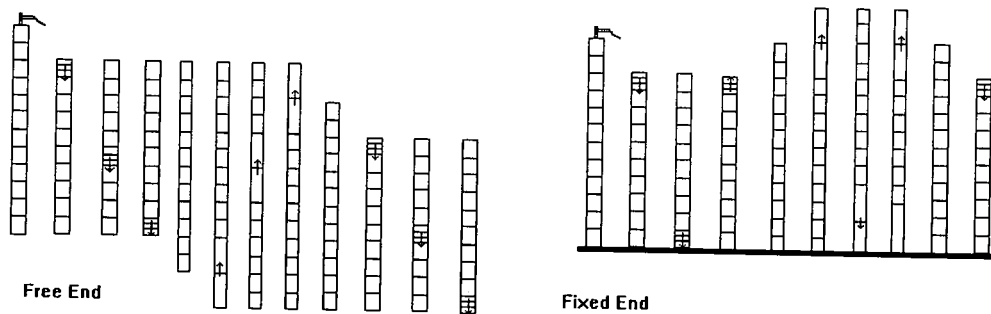


Figure 2.12 Stress wave propagation through a free-free and fixed free beam.

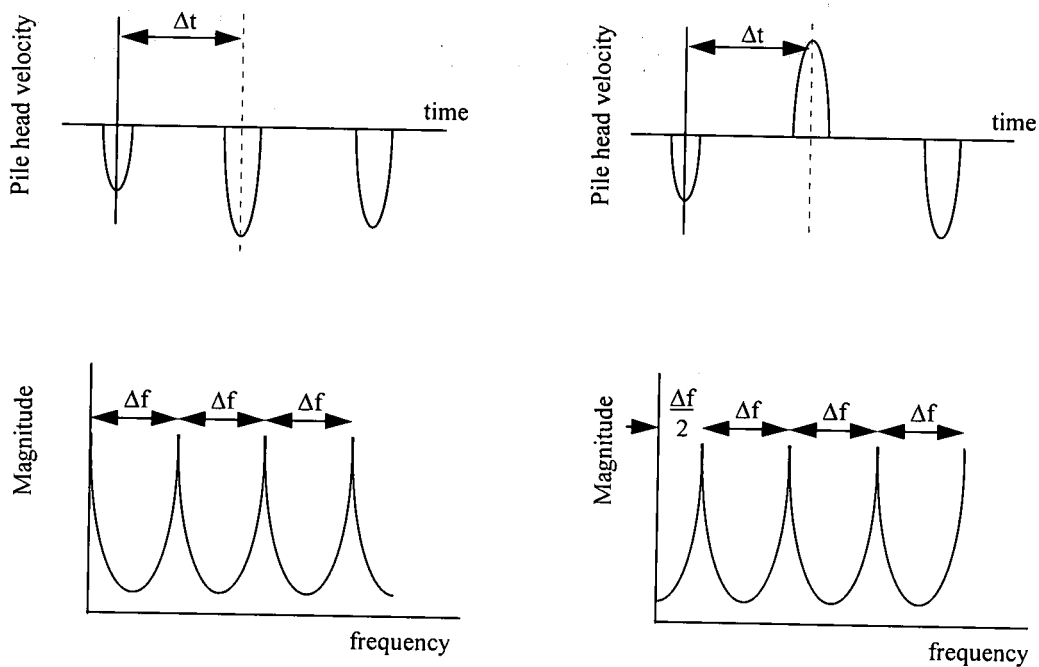
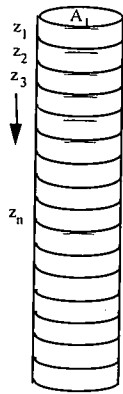


Figure 2.13 Theoretical time and frequency responses for a free-free and fixed-free beam.



Consider the segmented pile left

$$z_n = A_n \cdot \rho_n \cdot c$$

where z_n = material characteristic impedance
 ρ_n = element density
 c = stress wave propagation velocity
 A_n = element area

For a stress wave travelling in a downward direction partial or total reflection occurs when: $z_{n+1} \neq z_n$

Figure 2.14 Conditions under which reflections from within a foundation pile may occur.

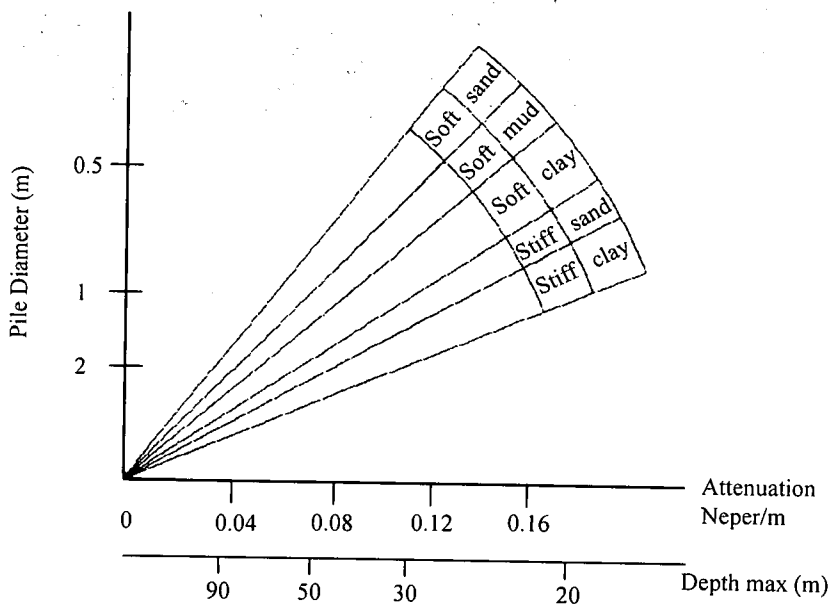


Figure 2.15 Attenuation as a function of diameter and soil type (After Paquet^{2.38}).

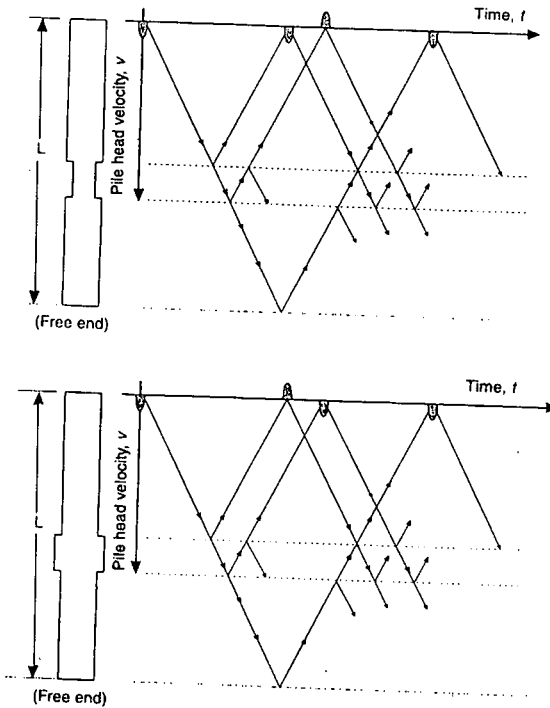


Figure 2.16 The theoretical responses for time based (sonic echo) tests (After Turner^{2.13}).

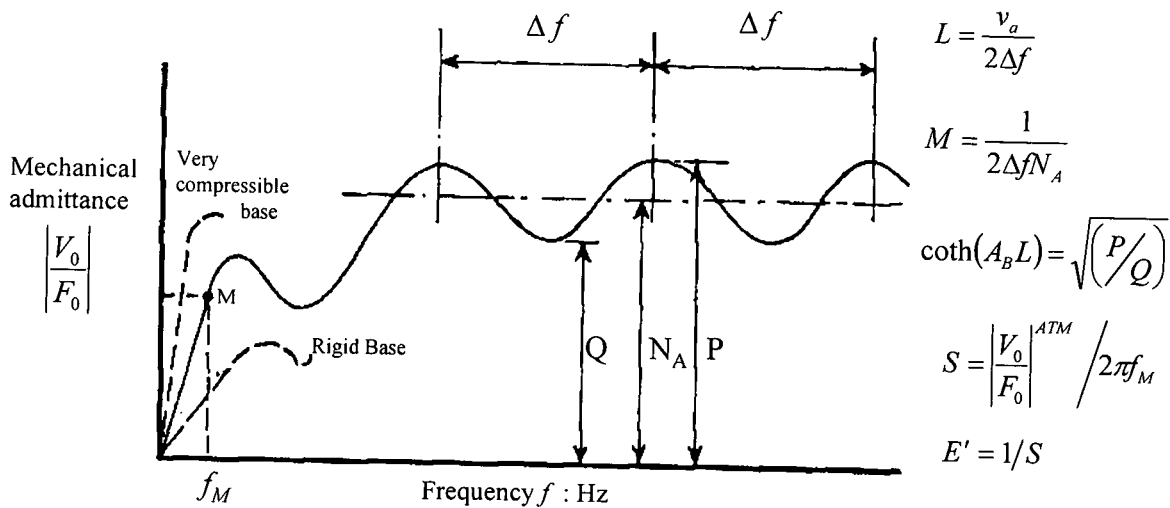


Figure 2.17 The response curve of an installed cylindrical pile (After Davis and Dunn^{2.27}).

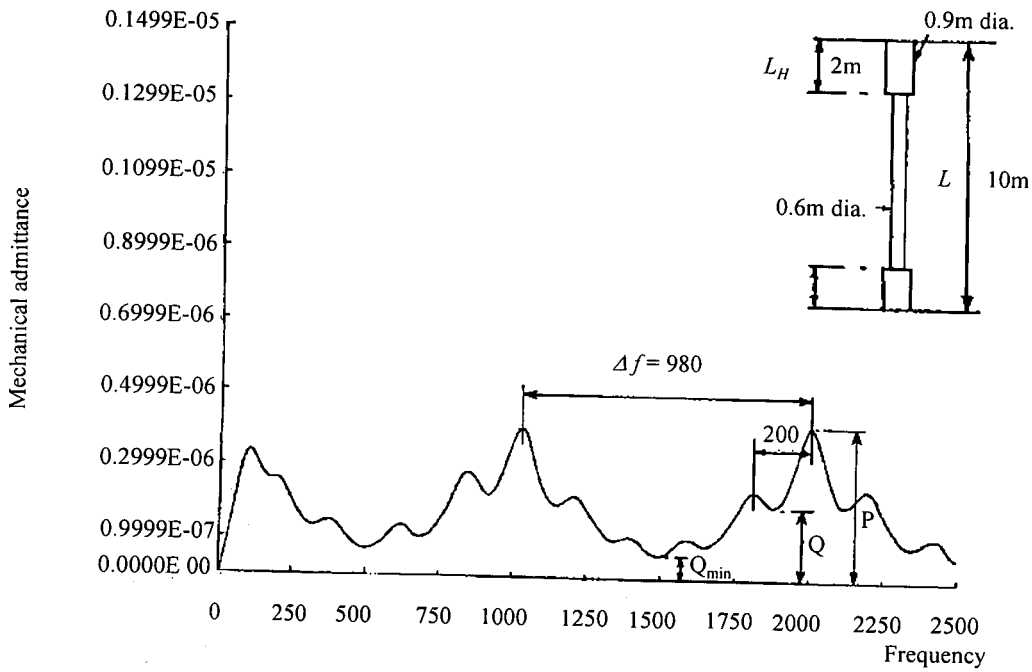


Figure 2.19 The response curve of a damaged pile (After Davis and Dunn^{2,28}).

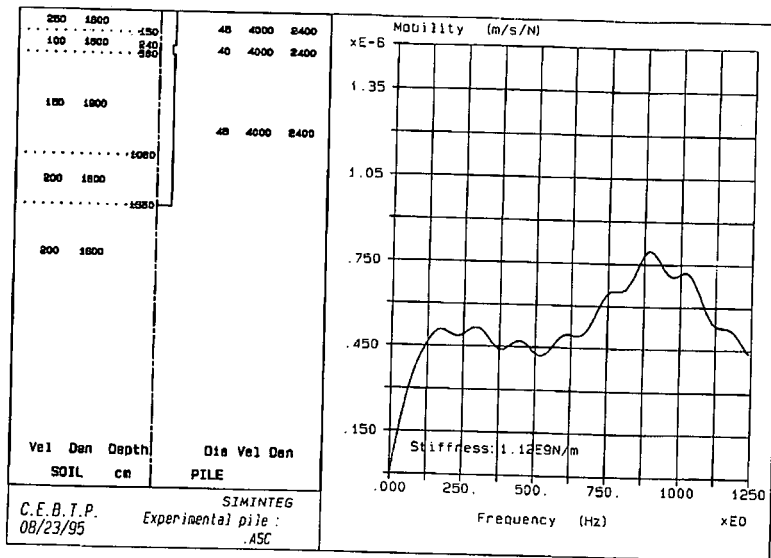


Figure 2.19 A SIMINTEG modelled frequency response for a pile with necking in varying soil conditions (Courtesy of Testconsult Ltd)

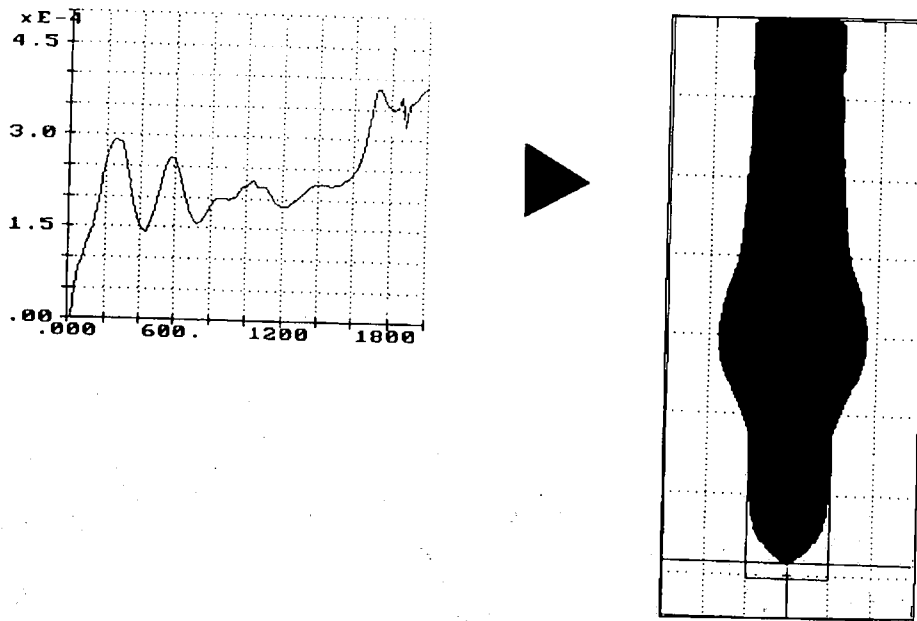


Figure 2.20 An impedance log (right) obtained from the mobility curve (left) using IMPRO; CEBTP's automatic Impedance Log generator^{2,25}.

3. Artificial Neural Networks for Signal Processing and Fault Detection

3.1 APPLICATION IDENTIFICATION

The problem domain with respect to this application has been described fully in the previous chapter. Essentially the system requirement is summarised as the automated interpretation of sonic test data to produce an output characterising a pile's integrity.

The systems input parameters may therefore comprise:

- i. Sonic echo test trace.
- ii. Site investigation data.
- iii. Test data from other piles in the pile group under investigation.
- iv. A simulated, expected, response of the pile under investigation.

The parameters that may be used by the devised system are limited to the above by the test method employed: the impact response test. They are the parameters currently used in the human, expert, interpretation of sonic echo tests. It is likely that any combination of these available inputs will be pre-processed to reduce the dimension of the input space of the system and highlight its salient components.

The ideal output of any test system will be compromised by the limitations of its applied methodology. As described in Section 2.7.3, it is not possible to derive an arbitrarily precise topological profile of an installed pile using an indirect testing technique such as the sonic echo test. Instead, the goals of any neural system produced should be the same as those in the expert human interpretation and contemporary automated techniques. That is:

- i. The identification of a trace atypical of its expected result. (Primary Goal)

- ii. The production of an impedance profile characteristic of the pile/soil system. (Secondary Goal)

Clearly the primary goal is a necessity for the system to be of any use at all. However, the realisation of the secondary goal will, as a natural consequence, result in the accomplishment of the primary. Given the existence of the deterministic wave tracing methods described in Chapter 2 it is likely that the usefulness of any system produced will be quantified by its effectiveness in fulfilling Goal ii. Further to discussions with industry representatives¹ it is recognised that the absolute completion of goal two is not a necessity for the development of a useful system. The test limitations are well known within industry and an automated system capable of identifying an atypical trace and 'suggesting' the primary fault associated with the trace features would be a significant advance on present test protocols.

The application of Artificial Neural Networks (ANN's) to pile integrity testing in this project will take an empirical approach as recommended by the Department of Trade and Industry's (DTI) published guidelines^{3.1} and Hecht-Neilson's book *Neurocomputing*^{3.2}- Section 3.5. This will follow a discussion of neural system components, Section 3.3, and a review of artificial neural network solutions to signal processing and NDT problems, Section 3.4.

3.2 ARTIFICIAL INTELLIGENCE (AI) STRATEGIES FOR SYSTEM MODELLING AND CLASSIFICATION

Given the application description in Section 3.1, above, the problem becomes a task in pattern recognition and function approximation. A mapping must be made from the input pattern space representing the observables in the field tests to an output vector characterising the system goals. This mapping will involve stages of:

- i. Feature extraction: this stage involves the encoding of the raw data to a form suitable for processing.
- ii. Feature selection: the reduction of the input space to those parameters salient to the problem solution.
- iii. Classification: the heteroassociative mapping of these features to the required system output.

¹ R. Stain & S. French (Testconsult Ltd), M. Kightly (TESTAL Ltd), and S. Kemp (Technotrade Ltd)

This breakdown, suggested by Schalkoff^{3.3}, should be considered a guide for the sensible labelling of the various stages of pattern recognition tasks; it is not definitive. For methods based on Bayesian statistics stages (i) and (ii) may be carried out by the data acquisition mechanism^{3.4}. While for syntactic pattern recognition systems part (i) will be the preprocessing of the raw data into symbolic primitives and parts (ii) and (iii) will be defined by a rule base grammar, as described by Gonzalez and Thomason^{3.5}. For neural networks, preprocessing may include part(i), parts (i) and (ii), or neither if the raw data is presented directly.

Rajagopalan and Kalyanasundaram^{3.6} identify non-destructive testing and evaluation as a prime candidate for AI applications due to the high degree of knowledge uncertainty associated with it. According to their definitions, the non-deterministic nature of sonic echo trace interrogation would make such an application a 'Level II' AI system. That is, a 'true' Artificial Intelligence system capable of interpretation through learning. Although they imply the generalisation and interpolation strengths of neural networks through the recognition of their ability to find acceptable solutions to frustrated classification problems (systems with no single ideal solution) no specific mention of networks as universal approximators is given. No comparison with other classification methods, other than fuzzy logic, is provided. The remainder of this section will review some of these techniques with emphasis on signal interpretation.

The primary uncertainty intrinsic to this problem is caused by absent information. This leads to difficulty in modelling the system algebraically in a deterministic fashion. Whether a neural network, when used as a universal function approximator, is truly a system exhibiting artificial intelligence is a matter for philosophical debate. Certainly assumptions and generalisations are made during the computation process and it must induce an abstract rule base through training. The author does not intend to enter this debate, but states, while acknowledging other researchers' reservations, that for the purposes of this work a neural network is classed as an artificial intelligence system.

3.2.1 Syntactic Processing and tree search algorithms

In syntactic processing the data to be interpreted is encapsulated in symbolic form. This is particularly useful for systems where the interconnections of features describe important information i.e. the context in which a feature is found is important to its interpretation. In pattern recognition tasks the signal to be processed

is described by a series of simple shapes or 'primitives'. The primitive set can be considered a lexicon of the knowledge system and the rules that govern any subsequent processing, almost exclusively of the form 'if...then...else', its grammar.

This approach was applied to pile integrity testing by, Commerford *et al.*^{2.59}, as described in Section 2.7.7. Here the primitives are straight lines of measured incline and length that approximate the pulse echo trace from a pile head. The fact that straight lines are used means there is immediate loss in trace resolution and hence information content. Indeed the selection of primitive types is of primary importance. Rengaswamy and Vekatasubramanian^{3.11} note the necessity of a priori knowledge of the signal under investigation and propose a neural network system for the selection of an optimal primitive set. The context grammar is also defined 'by hand', that is it is programmed rather than generated through a process of automated induction. This suggests either the system under investigation is deterministic or the defined grammar is unsound. It is known that this system is non-deterministic because of the uncertainty outlined in Chapter 2 and described by Rajagopalan and Kalyanasundaram^{3.6}. It must therefore be concluded that, as the piles' soil environment is not considered and no field tests applied, this system would not be effective in its primary purpose: to interpret sonic echo test data for *in situ* piled foundations.

It is suggested that the above method could be improved upon through the more appropriate selection of primitives and the automated inference of the grammar rules - grammatical inference can be made through a variety of algorithms, as described by Schalkoff^{3.12}. However, given that the intrinsic goal of the application, as already stated, is the mapping of one vector space to another, intuitively it would appear unlikely that any system produced would be comparable in its effectiveness with a methodology specifically developed for such a task. Syntactic processing is more usually employed in the type of knowledge based expert system (KBES) described by Yeh *et al.*^{3.13} where it is used in the diagnosis of damage during the driving of pre-stressed concrete piles.

Here 15 bounded *symptom attributes* are symbolically encoded for use by the KBES. For example the predicate 'hammer' may take the argument 1 if a smaller hammer is used, 2 for a medium weight or 3 for a heavy hammer. It is reported that these 15 attributes and the rule base are defined in the PROLOG based system which suggests a 'closed world' first-order predicate calculus (based) unification strategy is then applied to instantiate the 12 unbound variables describing the *causes* of these

symptoms e.g. the 'hammer_heavy' predicate may become true so indicating the hammer energy is too high.

The rule base, or grammar, in this example is inferred through the 'ID3 inductive learning algorithm' (Iterative Dichotomiser 3^{3.14}). The method reports superior results to the 'expert interview' method of rule base inference - the 'hand made' method used by Commerford, but does not report its strength as compared to a human expert. A lack of flexibility in the knowledge representation is reported in that the careful selection of attributes and training data is of great importance, but no mention is made of the lack of flexibility in the system output. One might expect 'concrete honeycombing' and 'poor strength concrete' to give similar symptoms, but the system as presented can only select one as its diagnosed cause.

This lack of flexibility is due to ID3 classifying inputs in terms of discrete finite memberships. Thus there is no handling of uncertainty. ID3 first produces a postulated decision tree using a subset of the training examples and then refines it through exceptions in the remainder of this data set. This implied determinism means the system is highly dependant on the selection of training data and symptom attributes. It also means, as with most deterministic systems, it does not perform well with noisy data.

The difficulty in deriving a suitable lexicon of primitives and the lack of uncertainty handling makes this methodology an unlikely choice for the interrogation of potentially highly complex temporal traces. All the remaining methodologies include intrinsic strategies for the management of uncertainty and nondeterminism.

3.2.2 Probabilistic Classifiers

One way of handling uncertainty is to consider the problem in terms of probability density functions (p.d.f.s). Probability based, decision rules for the classification of a d dimensioned pattern, \underline{x} , into a class, ω_i , are derived through the conversion of an a priori class probability, $P(\omega_i)$, into an a posteriori probability $P(\omega_i | \underline{x})$ using Bayes theorem, Equation 3.1. Where \underline{x} is the input vector to the system.

$$P(\omega_i | \underline{x}) = \frac{[p(\underline{x} | \omega_i)P(\omega_i)]}{p(\underline{x})} \quad (3.1)$$

This leads to the partitioning of the measurement space, \mathfrak{R}^d , through, so called, decision boundaries.

For parametric estimation the p.d.f. of the class-conditional distribution function, $P(\underline{x}|\omega_i)$, is assumed (e.g. Gaussian or Uniform). The parameters describing this p.d.f. may be assumed as in the Maximum Likelihood^{3.7} case or derived as in Bayesian Estimators^{3.8}. The values assigned to these parameters are converged upon through training. Observed measurements belonging known classes are used with regression techniques to minimise a cost function associated with system performance.

When the underlying class-conditional p.d.f. is unknown a nonparametric approach must be taken to describe its shape. Models for the p.d.f. are again estimated through learning and various approaches have been successfully applied e.g. histogram^{3.9} (bin counting), Parzen^{3.8, 3.9} (kernel fitting) and k^{th} -NN^{3.8, 3.9} (nearest neighbour) methods.

Bayesian probabilistic models have been used extensively for classification tasks, especially in the field of biological signal processing^{3.10}. However for heteroassociative, continuous, modelling, as described in Section 3.1, a number of problems arise.

The dimensionality of the system is large. That is, dimensions of the input observations and required output (pile/soil descriptor), even with encoding, will be large. The number of observations (the size of the training set) with respect to the solution search space will, therefore, be a sparse representation of the system to be modelled. This means even if the training data represents a smaller localised area of the input space it can be reasonably expected that the p.d.f.s of the classification regions will be poorly defined. This problem is accentuated through the realisation that no a priori knowledge of the class-conditional p.d.f.s can be assumed and so a nonparametric approach would have to be taken.

Secondly the system required is not essentially a classifier, but a black box model to map an observed temporal measure to a spatial description of the pile/soil system. That is, the interpretation of the signal must go further than the division of \mathcal{R}^d into a number of decision regions. \mathcal{R}^d must be continuously mapped to a second hyperspace the dimensions of which describe the pile/soil system. Also, the system to be modelled is neither a probabilistic nor stochastic process. It might be presented in a pseudo probabilistic form, e.g. class ω_i representing the probability of a fault at location i given a trace \underline{x} , but these classes would not be mutually exclusive and a

quantitative estimate of the degree of defect would involve secondary processing of a complexity comparable to the original problem.

For heteroassociative vector mapping other methodologies, with rigorous mathematical proofs regarding their suitability to such universal function approximation tasks, are described below.

3.2.3 Nonmonotonic and Fuzzy Logic

Non monotonic reasoning is an extension of predicate calculus that can be summarised as a system of beliefs. Often referred to as *possible world* models, it allows rules of the form:

IF *there is a feature at time t* **THEN** *there is possibly a defect at location l.*

Essentially conventional propositional calculus is augmented, in the case of modal logic^{3.15}, with two new operators. These describe a proposition as being 'possibly true' or 'necessarily true'. This feature allows a system's beliefs to change as evidence (knowledge) is acquired and discarded. However, for the problem described above the knowledge is static: it is the sonic echo trace and pile environment details. This method for handling uncertainty is more usually employed in knowledge representation systems involving autonomous agents where environmental variables change with time and so, therefore, must the agent's beliefs.

Instead of introducing an operator allowing the predicate to take on a tentative truth assignment that can be retracted later, as in non-monotonic reasoning, another method allows the predicate to be assigned a numerical 'truth value'. That is a value, say, between 0 (false) and 1 (true) which is ascribed according to the evidence supporting the predicate. A predicate can thus be described by its corresponding *degree* of membership to a given set^{3.16}. The ability to map a predicate into many, sometimes contradictory, decision regions allows a blurring of the decision boundaries and leads to, so called, *fuzzy* sets. The logic that governs the inference from these sets is therefore known as *fuzzy logic* and made up of *fuzzy rules*.

Processing within a fuzzy system can be summarised as three stages:

- i. Fuzzification : the act of defining the degree membership of an input variable x_i to each available fuzzy set, A_{ji} , through a membership function $\mu_{A_{ij}}(x_i)$. These

membership functions are often symmetric about a centre and monotonic on each side of this centre (e.g. Gaussian, triangular, or exponential).

- ii. Fuzzy Inference: the fuzzy rule base can be written in linguistic form,

R^j : **IF** (X is A_j) **THEN** (Y is B_j)

Where X and Y are input and activation vectors respectively and A_j and B_j are fuzzy sets associated with rule j . These rules can then be combined through a variety of inference regimes^{3.17} to produce an activation value, y_j , which is also associated to a series of fuzzy sets with varying degrees of membership.

- iii. Defuzzification: when all the rules in the fuzzy system are evaluated the activation values, Y, are combined to assign a truth value to the output predicates. This usually involves the normalisation of the activation values, Y, which can then be used as evidence (weighted according to their individual membership values) for a given output, z_k , e.g. centre-of-gravity defuzzification^{3.17}.

Clearly the assignment of degrees of truth to handle uncertainty adds a flexibility not found in predicate calculus or classical propositional logic. However, the addition of these terms requires the complexity of the inference method and rule base to increase to facilitate it. A great deal of recent research has therefore focused on the use of neural networks to offset some of this additional computation. Originally fuzzy concepts were incorporated into more conventional multilayer perceptron networks^{3.18} (MLP - see Section 3.4.3.1). More recently unification proofs have shown the equivalence, given certain restrictions, of fuzzy systems and radial basis networks^{3.19,3.20,3.21} (RBNN's). Given this functional equivalence and the need for more than the classification strengths offered by fuzzy systems the neural networks computational efficiency and function approximation through learning would seem more appropriate for the task described.

3.2.4 Learning Networks

3.2.4.1 The Biological Inspiration For Neurocomputing

The human brain is a collection of about 10^{11} nerve cells (neurons) each connected to around 10^4 others. There are two main types of neuron: the *interneuron*, that is a

localised processing neuron with input and output connections of a limited range (~100 μm), and the *output cells* that connect the regions of the brain. Although the physiology of the brain is complex and not fully understood superficially the workings appear relatively clear. Each neuron has a collection of nerve fibres, dendrites, and an axon which branches into strands and sub-strands. These strands are connected to the dendrites of other neurons, or direct to their cell body, through a chemical junction known as a synapse – Figure 3.1.

At an instant in time the neuron accepts many inputs and combines them to attain a level of activation - being a chemical process the method of combination may be a complex, but is often modelled as a simple summation. If the level of activation reaches a threshold limit then the neuron 'fires' and transmits through its axon to other connected neurons. As each branch of the axon transmits across a synaptic junction it is this junction that determines the potential transfer to the receiving dendrite. Each dendrite can receive an input from many synapses and can be inhibited or excited by the connection. Hence the computational dynamics of the working brain is extremely complex.

In practise, the massive parallelism of the brain's processing method is clearly more efficient for certain tasks than conventional, serial, techniques: a small child is better able to distinguish complex shapes or understand language than any computer yet produced. As the brain became better understood and modular electronic devices became more widely available so, therefore, attempts to mimic its processing method began.

3.2.4.2 Artificial Neural Networks: A Definition

As a formal answer to answer the question: '*what is a neural network?*' the author quotes Hecht-Nielson from his celebrated book *Neurocomputing*^{3,22}. This definition gives greatest flexibility in the choice of activation function, pattern of connectivity and learning paradigm without compromising the basic premise of neural networks: their intrinsic parallelism through localised processing.

Definition (After Hecht-Nielson) - *A Neural Network is a parallel, distributed processing structure consisting of processing elements (which can possess a local memory and carry out localized information processing operations) interconnected via unidirectional signal channels called connections. Each processing element has a single output connection that branches ('fans out') into as many collateral connections as desired; each carries the same signal - the processing element output signal. The processing element output signal can be of any type desired. The information processing that goes on within each processing element can be defined arbitrarily with the restriction that it must be completely local; that is, it must depend only on the current values of the input signals arriving at the processing element and via impinging connections and on values stored in the processing element's local memory.*

An Artificial Neural Network (ANN) is, therefore, a biologically inspired, adaptive data processing tool. It learns through training and may be capable of generalisation, interpolation and extrapolation. Like its biological inspiration its performance also degrades gracefully with respect to system damage. These ANN's are examples of *Parallel Distributed Processing* so called because the output of the system is dependent upon the 'state' and structure of the entire network, i.e. distributed, and any processing is therefore intrinsically parallel. The main components of an ANN are now described below.

3.3 ARTIFICIAL NEURAL SYSTEM COMPONENTS

3.3.1 Processing Units

The basic building block of any ANN is the processing element. This is often referred to as a neuron through the analogy with biological systems, but to emphasise the large discrepancies between the biological neuron and its simpler, fabricated equivalent it is more usually labelled a *unit*. An artificial neural system is made up of a number of interconnected units each taking a series of inputs and combining them in a predefined manor to form an output. A unit may be described

as an *input unit* if it takes an input from the external environment, an *output unit* if it presents its output to the external environment or a *hidden unit* if it is limited to having connections only with other units.

3.3.2 Activation State

For a system of N units the state of the network, at a time, t , is represented by an N dimensional vector, $\mathbf{a}(t)$. Each element of the vector describes the activation value for a single unit. Hence the activation of a unit, u_i , can be written as $a_i(t)$ where $i \in \text{Integer Numbers with } 1 \leq i \leq N$. It is the pattern of activation over all the units that describes what the system is representing at a moment in time. Activation values may be discrete or continuous: if continuous they may be bounded or unbounded, if discrete they may be binary or from a non-binary discrete set.

3.3.3 Output Function

Each unit, u_i , has an associated output which is transmitted to neighbouring units or the external environment. This output is a function of the current state of activation of that unit such that

$$o_i(t) = f_i(a_i(t)) \quad (3.2)$$

where o_i is the output of unit i and f_i is its output function. Often the output function is the identity function and so the unit output is equal to its activation. However it may equally be a threshold like function to more closely model the biological case or stochastic. Here the output is determined, non-deterministically, from a probability distribution function which, in turn, is dependent upon the unit's activation.

3.3.4 Pattern of Connectivity

Units are connected together through weighted channels. These weights are usually held in matrix form and describe the system's pattern of connectivity. Often it is assumed each connection to a unit simply provides an additive contribution to its net

input. The weight value between two units, from u_i to u_j , is labelled w_{ji} and is held in matrix $\underline{\mathbf{W}}$. The absolute value of w_{ji} defines the strength of the connection while its sign signifies whether the connection is excitatory or inhibitory. In the general case, however, different types of channel may be treated separately and the pattern of connectivity becomes a collection of matrices. For example, the inhibitory and excitatory connections may be separated; each could then be processed independently by the receiving unit. The system would then need two weight matrices to describe its pattern of connectivity. It is, therefore, the pattern of connectivity that describe the networks topographical architecture, see Figure 3.2.

3.3.5 Rule of Propagation

The rule of propagation is the method by which the output vector, $\underline{\mathbf{o}}(t)$, describing the output of all the units is combined with the pattern of connectivity to produce a unit's net input. As mentioned above there may be a number of patterns of connectivity and therefore there will be the same number of net inputs to a given unit. For a unit u_i and pattern j the net input may be labelled net_{ij} , for a system with just one pattern of connectivity this is reduced to net_i . The more complex the patterns of connectivity, in general, the more complex the rule of propagation. All the systems considered in this research – and the vast majority in other research – have just one pattern of connectivity and therefore one rule of propagation: the vector product of the output vector and the weight matrix, as given in Equation 3.3 below.

$$\underline{\mathbf{net}}(t) = \underline{\mathbf{W}} \underline{\mathbf{o}}(t) \quad (3.3)$$

3.3.6 Activation Rule

The activation rule is the method by which a unit's activation is combined with its net inputs to produce a subsequent activation value. This takes the form of a function, \mathbf{F} , such that for a system with m patterns of connectivity the new state of activation is given by:

$$\mathbf{a}(t+1) = \mathbf{F}(\mathbf{a}(t), \mathbf{net}(t)_1, \mathbf{net}(t)_2, \dots, \mathbf{net}(t)_m) \quad (3.4)$$

So for a system with a single pattern of connectivity the coupling between two units is described in Figure 3.3 (c.f. Figure 3.1).

The most common types of activation function are those of the type:

$$a_i(t+1) = \mathbf{F}(\mathbf{net}_i(t)) = \mathbf{F}(\sum \omega_{ij} o_j(t)) \quad (3.5)$$

and of those the most commonly employed are the Heaviside and linear threshold functions and continuously differentiable, monotonic, functions such as the sigmoid function, as illustrated in Figure 3.4.

3.3.7 Learning Algorithm

As shown above, unlike conventional techniques where complex instructions are executed in a serial fashion, in a neural network a number of simple processing units interact together in parallel to process data. It is the complexity of this interaction that enables convoluted problems to be solved. To hand pick the channel weights of these connections would necessitate the complete understanding of the problem to be solved which would imply a conventional, deterministic method would be better suited to the task. The strength of ANN's is that they do not require programming. The weight matrix evolves during a training period and learns how to perform the requisite task.

It is often convenient to think of an ANN, therefore, as two coupled dynamic systems: one that *given* the problem *alters* the weights in an attempt achieve a suitable activation state and another that *given* the weights *alters* its activation state in an attempt to solve the problem. The various training paradigms and their associated network architectures will be discussed in detail in Section 3.4 along with their application to signal processing and structural testing.

3.3.8 External Environment

Any neural system must exist within the context of an external environment. This environment is defined by Rumelhart *et al.*^{3.60} as the '*time-varying stochastic function over the space of input patterns*'. In making this definition, therefore, the external environment is described from the ANN's perspective and includes everything outwith the neural network, as illustrated in Figure 3.5. Clearly, therefore, this external environment must accurately model the problem domain. That is, the pre-processed raw data, which will form this pattern space, must contain the necessary information for the network to fulfil its required task. The considered utilisation of preprocessing techniques can greatly improve network performance and so the selection of encoding strategies plays a significant part of the systems overall development, see Section 3.5, below.

3.4 ANN's: THEIR APPLICATION TO SIGNAL PROCESSING AND STRUCTURAL TESTING

Artificial Neural Network Systems can be broadly categorised into two classes: those trained using supervised and unsupervised learning. For supervised learning the training data is made up of input and output pairs. The availability of this target data, the required output for a given input, allows the network, potentially, to learn arbitrary vector mapping - assuming the training data is representative of the mapping required. For systems where the required output is unknown unsupervised training can be used to cluster the training data into statistically similar classes. Some of the more commonly used examples of these paradigms are now described with special emphasis on their application to structural testing.

3.4.1 Unsupervised Learning

Also known as self-organising networks, these ANN's have no defined output associated with their training. Instead the network must induce patterns and

categories within the input data for coding to output. Hertz *et al.*^{3.40} have listed the generic applications of such a network as:

- i. **Familiarity or Principle component analysis.** Where the output of a network indicates the similarity between the currently presented input and those upon which it has been trained.
- ii. **Clustering or Prototyping.** Here the network may group the input patterns into statistically similar categories. In the latter case the output could be a standard archetype of the input's class.
- iii. **Encoding.** From consideration of the applications above it becomes apparent that if the output space is smaller than the input space a such a network could be utilised as a method for data encoding .
- iv. **Feature mapping.** Given a fixed, unary, output array an input pattern could be, effectively, 'demultiplexed' onto this array providing a topographical map of the input, i.e. statistically similar inputs would excite geometrically close outputs.

As it appears the latter two applications are natural extensions of the first two the remainder of this section will review first the *feature extraction* and then the *categorisation* properties of the more popular self-organising networks.

For feature extraction networks a Hebbian based learning paradigm^{3.30} is often employed. Here weights are altered during training as a function of the activation of the two units they connect. In *plain Hebbian learning* this means :

$$\Delta w_{ij} = \alpha a_j a_i \quad (3.6)$$

where α is a scaling constant known as the learning rate and is give a value between 0 and 1. As described in section 3.3.2, above, a is the activation for units i and j . In such a network the patterns presented most often during training will produce the largest output. However, without a constraint on Δw , it can be shown^{3.40} that $\underline{\mathbf{W}}$ will increase continuously and will not converge on a stable state thus training never terminates.

By modifying the Hebbian rule for a single layer feedforward network with a single linear output unit Oja^{3.26} forced the weight matrix, $|w|$, to approach 1 without the need of an explicit renormalisation step. Convergence is not guaranteed for this learning rule only the existence of a stable state solution where this solution is the first principle component of the input data. The first principle component is defined as the direction, in terms of input vector dimensions, of maximum variance within the input space with respect to the training set. That is, a principle component axis is derived that best 'spreads' the input data set.

Oja^{3.45} and Sanger^{3.46} both extended this paradigm for a feedforward single layer network with N output units to find the N principle components of a data set. The second principle component being the direction of maximum variance perpendicular to the first in the weight space. The third being the direction of maximum variance perpendicular to the first two - and so on. In fact, in general, the k^{th} principle component direction is the direction of the eigenvector associated with the k^{th} largest eigenvalue of the covariance matrix of the input data and if this data has zero mean it can be shown^{3.40} that for Sanger's rule the weight vectors become exactly the first N principle component directions.

The second generic application of self organising networks, *categorisation*, involves the clustering of inputs with statistically similar properties into *classes*. Often referred to as *unsupervised competitive learning*, the output units compete on a 'winner takes all' basis such that only the most successful is active for a given input pattern. This method is often employed for data encoding. For example a large input pattern can be mapped to a unary output code to be used as a parameter in an artificial intelligence system or as a method for data compression.

A simple single layer system used for such tasks is the Kohonen^{3.23} network. Statistically this network provides a method for vector quantisation. For a system where an N dimensional input is to be categorised into M classes the network architecture consists of N input units and M linear output units with a single weight channel going from each input to each output. The output units compete on a

'winner takes all' basis - the winner being the unit with the N-dimensional weight vector closest to the presented input pattern. During training^{3.12} the weights of the winning unit for a given pattern are increased to reinforce its association. However, the weights of units that are geometrically (topologically) close to the winning unit are also increased, but to a lesser degree, according to their distance away from it. Hence, geometrically close output units become descriptors of statistically similar classes. A number of refinements to this simplified version of the learning methodology are required to reduce convergence to local minima in the weight space and redundancy in the output^{3.24}, but categorisation using this scheme has proved successful in many areas^{3.25} such as motor control^{3.26} and speech recognition^{3.27}.

The problem domain for this application describes the mapping of an input space encapsulating the integrity test data to an output vector indicative of the pile's structure and environment. This continuous mapping cannot be applied directly using the above techniques. If the required application solution was the classification of the input data into pass/fail groups then the clustering methods above could be utilised, however, this would still require expert interpretation of the failed traces to fulfil client requirements. Nevertheless the methods above could be employed for the automated parameterisation of the integrity test data for input to a further, interpretation, module. Their application to this task is discussed in relation to radial basis neural networks (RBNN) and counterpropagation networks in Sections 3.4.4.2 and 3.4.2 respectively, below.

3.4.2 Supervised Learning

When the target output for a given input is known then the network is trained to model the association between the given input and output patterns. For this reason supervised training can be further subdivided into autoassociative and heteroassociative tasks.

In autoassociative networks the system is required to reproduce its input pattern as its output. Although, this may at first appear a trivial task such networks are characterised by their complex activation dynamics. This is caused by their, often

near, fully connective topology. The philosophy behind these networks is that the dynamic system's structure can be altered through training such that its stable states correspond to the required patterns. As a consequence of this, subsequent to training, when an incomplete or noisy pattern is presented to the network the system's activation state will converge, in time (iterations in the discrete case), to the state of the training pattern that most closely resembles it.

The patterns upon which the network has been trained effectively become 'stored' within its pattern of connectivity and the system's memory becomes *content addressable*. An example of a network capable of this *nearest neighbour approximation* is the Hopfield network^{3.39}. In its discrete form the Hopfield network is an autoassociative, nearest neighbour, pattern encoder that learns binary (or bipolar) spatial patterns using Hebbian learning. It is a fully connected system, that is all units are connected to all other units, with the exception of self connection. This system has been researched and applied in many fields including image processing, speech processing and pattern classification. The reader is referred to Simpson^{3.41} for a list of over thirty references to such work. For fault diagnosis Barrios and Lemus^{3.28} have applied such autoassociative networks, including the Hopfield network, to the identification of faults in semiconductor manufacture. After production, a silicon wafer may contain a number of faulty chips. The geometric distribution of these faulty chips may contain a clue as to the manufacturing fault causing them. The neural systems are, therefore, trained using archetypal chip patterns of known classes of fault. When a wafer is then presented, post training, the network converges on this archetype allowing the identification of the fault process - with a reported success rate of over seventy five percent in the prototype system.

Autoassociative networks have been used extensively for the processing of noisy or incomplete data when a known number of limited states are required as described above. They would, however, be of little use for classifying a sonic echo trace where:

- i. the size of the input space would necessitate a prohibitive number of network units. For a Hopfield network the maximum patterns that can be stored are of the order $N/\log(N)$ where N is the number of units^{3.42}.
- ii. the above system is discrete and linear - to employ the continuous, nonlinear (second order) version of the Hopfield network would produce a highly unstable system of extremely complex dynamics.
- iii. the concept of an archetypal training pattern from the sonic echo traces is absurd as it is a continuous nonlinear system being analysed.

Heteroassociative nearest neighbour classification can be achieved using layered networks such as the counter propagation network of Hecht-Nielsen^{3.47}. Here the input patterns are categorised by a Kohonen network of the type described above. The output from this network is then fed as an input to a layer of Grossberg instar/outstar^{3.48} units which decode it into the required output values. It effectively, therefore, acts as a look up table. However, it has the ability to handle uncertainty because the Kohonen layer forces the input of the outstar to be of a type it has been trained on. In fact, the resultant output of the network is the output of the training pattern that most resembles the presented pattern. A similar network has been applied by Travers^{3.49} in identifying, through nearest neighbour classification, the sound of a reinforcing wire snapping in a prestressed concrete pipe.

The problem with nearest neighbour classification, as described above, is that because it acts as a content addressable memory no generalisation, interpolation or extrapolation occurs. The relationship between the input and output spaces are not learned - the patterns are. As a consequence of this, its successful application to the analysis of the continuous and large input space of this problem domain would appear unlikely. Research efforts are instead focussed on the heteroassociative function approximation networks described below.

3.4.3 Heteroassociative Vector Mapping and Function Approximation

Function approximation through neural computation is essentially an exercise in nonlinear black box modelling. With no assumptions being made about the physical

system being modelled the black box structure must be based on families of models that have proved successful for similar systems in the past^{3.50}.

For function approximation the networks most often employed can be subclassed into feedforward (those without feedback) and recurrent networks (those containing feedback), see Figure 3.2.

For feedforward networks the lack of feedback ensures the stability of the activation state for any presented input. For function approximation tasks by far the most researched type of network used is the multilayer family. The topology of such networks is summarised in Figure 3.2. Here each element of the input pattern vector is fed through weighted channels to each unit in the layer above until the final layer, the output layer, presents its output to the external environment; that is, there is maximal, feedforward, inter-layer connection, but zero intra-layer connection. There are existence proofs, for certain members of this family of networks, that demonstrate that any continuous function can be modelled given enough hidden units^{3.51,3.52}. However, excitement about the consequences of these proofs must be tempered by the realisation that they do not consider the problem of deriving the pattern of connectivity through learning, i.e. the practicality of finding this system, and the ambiguity of the phrase '*given enough hidden units*'. The application of such networks are described in more detail in Section 3.4.4, below.

Recurrent networks are more usually used for continuous temporal pattern prediction tasks where the current state of the network is dependent upon the past states as well as the current input values i.e. non-Markovian systems. The network presented in Figure 3.2 is a *partially recurrent network* in that only its output is fed back to the system input to providing a *context*^{3.38} for future outputs. By definition, however, recurrent networks allow for arbitrary unit connections^{3.38}. The complex dynamics of such networks have restricted its use to problems of signal prediction and control e.g. [3.53, 3.54] where a continuous, unbounded temporal signal is to be analysed or predicted. Methods for minimising this complexity through the use of many smaller modular recurrent systems with time delay features such as the Pipeline Recurrent Neural Network (PRNN)^{3.55} have been introduced, but recent research by Mandie

and Chambers^{3.56} suggests further insight into the system dynamics for this network type is still required.

For the application under investigation the network input can be considered bounded. The length of the recorded trace and environmental parameters is finite and there is no need to process the data 'on the fly'. Even without parameterisation of the recorded trace the vector holding its time sampled values is limited in size by the physical range of pile lengths that can be tested. For this reason the research described herein concentrates on multilayer feedforward networks of the type described below.

3.4.4 Multilayer Neural Networks

For function approximation of static systems, i.e. those with no feedback, it is assumed we have a relation described by Equation 3.7, below.

$$\underline{y} = f(\underline{x}) + e \quad (3.7)$$

Where \underline{y} can be considered the system output, \underline{x} the input and f is some a nonlinear function belonging to a given function space (e.g. continuous, integrable). Independent of \underline{x} the system is also assumed to contain a component of white noise, e . The problem then becomes: the estimation of a function, \hat{f} , that is a nonparametric approximation of f given the training data of input/output pairs. In other words

$$\hat{\underline{y}} = \hat{f}(\underline{x}) \quad (3.8)$$

where $\hat{\underline{y}}$ is an approximation for the output given \underline{x} . For the sake of practicality the function \hat{f} is parameterised, hence it is an approximation, by a finite dimension parameter vector η_d following the nomenclature of Sjöberg *et al.*^{3.50}. This parameter vector then becomes a descriptor of the network topology, activation function, pattern of connectivity *etc.* and 3.8 can be rewritten

$$\hat{y} = \hat{f}(\underline{x}, \eta_d) \quad (3.9)$$

For multilayer systems with a single hidden layer and a linear output layer we have

$$\hat{f}(\underline{x}, \eta_d) = \sum_k w_k g_k(\underline{x}) \quad (3.10)$$

where g_k are known as the basis functions^{3.50} and the parameterised function, \hat{f} , becomes a function expansion. For nonlinear black box models a single, parameterised, 'mother basis' function is used and so

$$g_k(\underline{x}) = F(\underline{x}, b, a) \quad (3.11)$$

where, for example, a and b may be the centre and width parameters when F is a radial function. For functions of a ridge construction such as the sigmoid F takes a single parameter, b , often described as the function's temperature. This single layer model is illustrated in Figure 3.6(a).

For multilayer systems, however, the output from the first layer can be fed into a second layer, whose output can, in turn be fed to a third, and so on - Figure 3.6(b). The question of how many layers to use in practical applications is more usually answered empirically through a comparison of system performance in a parametric study. Theoretical proofs exist, as mentioned above for sigmoid units, that a single layer of units can approximate a given, continuous function, arbitrarily well. However, Kůrková^{3.51} extends Kolmogorov's theorem to two hidden layers and provides an estimate for the number of hidden units necessary. One advantage in employing multiple layers of units is the potential reduction in the dimensions of the solution space of the network which, in turn, reduces the number of training patterns necessary to describe it. Morgan *et al.*^{3.57} have shown how a linear superposition of sigmoid functions, a ridge function, can more accurately approximate 3-dimensional peak functions through use of a second hidden layer so indicating the potential usefulness of systems with multiple hidden layers.

The task of finding a suitable nonlinear black box model now reduces to the subtasks:

- i. Select the training set that accurately describes the function to be approximated in the areas of interest.
- ii. Select the mother basis function - the activation function in neural network parlance.
- iii. Determine the number of units to be used and their topology - the network architecture.
- iv. Determine the basis parameters of the activation function - a and b in the examples above.
- v. Determine the system weights to output - vector w of Equation 3.10.

Task one is assumed and addressed, exhaustively, in Chapter 4 - Feasibility Study.

For task two, historically, two functional basis have become prevalent for function approximation using neural networks: the sigmoid function and the radial basis function. Each will be described below with special reference to their respective uses in signal processing and non-destructive testing. A third, more recently developed network, the wavelet network is also described. As tasks three, four and five are dependent upon the chosen activation function, methodologies for their completion are also described, separately, in the sections below.

3.4.4.1 Multilayer Perceptron (MLP)

The term 'perceptron' was originally used to describe units with *linear* activation functions^{3.31}. Indeed it is the title of Minsky and Papert's^{3.37} book describing the limitations of systems made up of such units. However, it has since become recognised terminology for systems made up of units with continuously differentiable monotonic ridge activation functions (e.g. tanh, sigmoid) and so the author uses the phrase 'multilayer perceptron' in this context, with reservations.

During learning in these networks changes in the weight matrix, $\underline{\mathbf{W}}$, are made with respect to the effectiveness of the network performance. The most common forms of supervised learning are: *error-correction learning*, *reinforcement learning* and *stochastic learning*.

Reinforcement learning and stochastic learning are more usually employed when there is no exact target data available, but less detailed information on the system performance is, e.g. in the extreme case simply whether the output is correct or not. Because the system's feedback is limited to a scalar value rather than a target vector no error gradient information is available and so a degree of randomness is necessary to enable a search of the weight space until an acceptable solution is found. This is usually achieved through the use of stochastic units e.g. Williams^{3,43} or stochastic weight training e.g. *simulated annealing* described by Hinton and Sejnowski^{3,34}. For systems where the required output is known (e.g. the pile profile) error-correction learning is almost exclusively applied.

In error-correction learning the weights between units are adjusted in proportion to the difference between required and computed values of each unit in the output layer. The general equation for such a learning rule is therefore given as:

$$\Delta\omega_{ji} = \alpha(y_j - \hat{y}_j)a_i \quad (3.12)$$

Where $\Delta\omega_{ji}$ is the change in weight value from unit u_i to unit u_j , a_i is the activation of unit u_i and $(y_j - \hat{y}_j)$ is the difference between the target and measured output of unit u_j . α is a scaling constant known as the learning rate and is give a value between 0 and 1.

Original work carried out by McCulloch and Pitts^{3,31}, Widrow and Hoff^{3,32}, and Rosenblatt^{3,31} used linear activation units and were therefore limited to a single layer systems because of the so called *credit assignment problem*. Specifically this meant it was not possible to calculate the contribution to the system error of a unit in a

hidden layer. Hence its associated error could not be used in Equation 3.12. Minsky and Papert^{3.37} proved how the limitation of the single layer systems, in turn, meant that the system suffered from the *linear separability constraint*. That is, the networks could only solve problems that were linearly separable in the solution space.

Rumelhart, Hinton and Williams' *back propagation algorithm*^{3.35} (BP) extended Widrow's δ -learning rule, Equation 3.12, to the general case. The BP algorithm works for layered networks with continuously differentiable, monotonic activation functions such as the sigmoid function of Figure 3.4. This allows, the error associated with a given output to be affiliated with weights at lower levels in the system so offering a solution to the credit assignment problem. It is this form of network that has been used in the majority of heteroassociative problems in the last ten years.

In BP learning an attempt is made to minimise the error in the output of the system for the data in the training set. This is done by changing the weights in proportion to the effect this alteration will have on the pattern error, (3.13)

$$\Delta w_{ij} = -\alpha \frac{\partial E}{\partial w_{ij}} \quad (3.13)$$

again α is the *learning rate* and takes a value between zero and one. Its optimum value is usually found through a parametric study - too low and the weights take a long time to converge and are more susceptible to local minima convergence^{3.58}, too high and the system units may suffer from premature saturation^{3.59}. The pattern error, E , is usually taken as the Euclidean error, (3.14).

$$E = \frac{1}{2} \sum_j (y_j - \hat{y}_j)^2 \quad (3.14)$$

where y_j is the target output and \hat{y}_j is the observed output estimate for unit j .

Equation (3.13) can be rewritten using the chain rule as Equation (3.15), below.

$$\frac{\partial E}{\partial w_{ij}} = \frac{\partial E}{\partial \hat{y}_i} \cdot \frac{\partial \hat{y}_i}{\partial net_i} \cdot \frac{\partial net_i}{\partial w_{ij}} \quad (3.15)$$

Using a summation definition of net_i , see Section 3.3.5: rule of propagation, from Equations (3.13), (3.14) and (3.15) the weight update rule for a pattern, p becomes

$$\Delta w_{ji}(p) = \alpha \delta_j(p) O_i(p) \quad (3.16)$$

where O_j is the output from the unit feeding into the weight and δ is the error associated with the unit in the layer above. For output units this error is the output error of the unit scaled by the differential of the activation function, F' , the second component of (3.15), as shown in equation (3.17)

$$\delta_j(p) = F'(net_j(p))(y_j(p) - \hat{y}_j(p)) \quad (3.17)$$

However, for hidden units there is no target or required outputs so the errors from the layer above are fed back through the weights to give the unit an error value consistent with its contribution to the pattern error. This means a hidden unit's error is described by Equation (3.18), below.

$$\delta_j(p) = F'(net_j(p)) \sum_k \delta_k(p) w_{kj} \quad (3.18)$$

Where the k units are those in the layer immediately above unit j . So a learning algorithm has now been described which, as the training set is repeatedly cycled through, changes the weights in such a way as to minimise the system error. However, it should be noted that there is no guarantee of convergence to an optimum weight matrix using this method. The weight space through which the network evolves to its final state is full of ravines and basins of stable states from which the network cannot *descend* to the optimum solution; these are the so called *local minima*, which are to be avoided so the network can evolve to its *global minimum*.

The problem of local minima can be reduced through the appropriate selection of starting values for $\underline{\mathbf{W}}$ ^{3.58} or the introduction of a momentum term to Equation 3.13 thus

$$\Delta w_{ij}(t) = -\alpha \frac{\partial E}{\partial w_{ij}} + \lambda \Delta w_{ij}(t-1) \quad (3.19)$$

The weight update rule now becomes also a function of past updates and has the effect of accelerating long term trends in the training data. This makes the weight update less sensitive to noise in the test set and can help pull the weights out of local minima. Again, values range between zero and one and are usually found through parametric studies, but a value approaching 0.9 is often quoted^{3.42}.

The function approximation abilities of the multilayer network have been used in a diversity of applications. In the field of signal processing much research has been done in the areas of sonar and radar decoding, a survey of which has been carried out by Roth^{3.61}, and in natural language processing such as the well documented NETtalk system of Sejnowski and Rosenberg^{3.62}.

In the field of damage location Worden *et al.*^{3.63} have used multilayer ANN'S to detect failures of members in large frame structures using strain gauge information. Wu *et al.*^{3.64} have attempted to perform similar tasks by training an ANN to decode the spectral response of a structure to a geological tremor. In both these examples the networks have been trained to identify the failure of simple frame structures using experimental and finite element generated data. The extension of these laboratory models to the 'real world' would involve the accurate mathematical modelling of large scale heavily damped structures under dynamic, environmental loading. These issues are not addressed. However, as an academic exercise, Worden *et al.* draw some conclusions pertinent to this research. Specifically: (i) faults in an experimental model can be identified using a neural network trained on finite element generated data and (ii) the network must be trained to identify noise corrupted data i.e. networks trained using finite element results can become too sensitive and so lose effectiveness when presented with noisy data from the 'real world'.

In the area of sonic echo testing the work of Pratt and Sansalone^{3.65}, and Begum and Chamberlain^{3.66} have suggested that a void in a concrete slab can be located using a normalised spectrum of its impact response. Both methods use finite element modelling to provide the training data for a, back-propagation trained, multilayer neural network with one hidden layer of units with sigmoid activation functions. Begum and Chamberlain give a limited description of the topology of the network and system performance. Pratt and Sansalone give the network topology as 150 input units, 30 hidden units and 11 output units. In both cases the output units provide a single unit indicating the likelihood of a flaw, given the presented data, and the remaining units show the approximate depth of that flaw. For Pratt and Sansalone this is given as an array of probabilities of a flaw at 10% , 20%, 30%, *etc.* of the slab's design thickness. For Begum and Chamberlain the output is effectively the same, except they label the outputs as the probability of a flaw at *normalised depth ranges*. In both cases the propagation velocity of the stress wave is assumed so allowing the depth associated with a frequency to be calculated from Equation 3.20, below (c.f. Equation 2.25).

$$d^{(q)} = \frac{c_p}{2 \cdot f^{(q)}} \quad (3.20)$$

Where c_p is the stress wave propagation velocity and $f^{(q)}$ is the frequency in the response spectrum associated with the depth, $d^{(q)}$. The spectral amplitudes are then presented to the network as a function of associated depth divided by the design depth, hence normalised spectra, rather than frequency.

Of primary concern in evaluating both these papers is the size of the weight space, and so the systems solution space, with respect to the number of training patterns being used to describe it. While the exact topology of and Begum and Chamberlain's network is not provided, given its description, it can reasonably be assumed to be of the order of Pratt and Sansalone's. That is, 150 input units and 30 hidden units. Even if the input units' value was bound between zero and one with a zero point one resolution the bounded region \mathfrak{R}^{150} , the input space, would take 10^{150} observations,

or training patterns, to describe completely. Begum and Chamberlain describe their number of training patterns as 'limited' while Pratt and Sansalone report two hundred patterns being used - the description of the pattern space is, therefore, necessarily sparse. The networks described have an enormous capacity for pattern learning and great care must be taken to ensure they do not overtrain; that is, they learn the input-output relationship for each pattern '*parrot fashion*' rather than learning the general rules governing the mapping from the input to the output space. Essentially the network then becomes a content addressable memory, as described above. Usually, the method used to ensure overtraining, or overfitting as it is sometimes referred to, has not taken place is to withhold a proportion of the training data and use it as a test set. The system performance can then be quantitatively evaluated through previously unseen data.

Using this method Begum and Chamberlain report the average success of the network at detecting flaws of a given depth. These results suggest the network has been successful in finding a fault's position through function approximation of the systems impulse response. However, no indication of the variance of these means are given and so the network's effectiveness for a given pattern cannot be fully evaluated.

Pratt and Sansalone do not use this method as they report it as being unreliable. However, no alternative method has been suggested, instead the authors appear to allow the training patterns to be altered to ensure the networks effectiveness in fault-finding. While this allows the extraction of patterns that cannot be defined due to test method limitations - the example of faults near the slabs' top surface when a hammer producing a pulse with too long a rise time is quoted - this is in no way a measure of the networks effectiveness. Instead it would appear to be an empirical method for evaluating the test method's effectiveness - the networks' effectiveness being assumed. It is also apparent from the quoted results that the probability of a fault being present is inferred by the network from the presence, or otherwise, of a reflection from the expected position of the slab base (c.f. Figure 9 in their paper^{3.65}). This network would clearly not be robust enough to detect faults in systems where the base reflection cannot be predicted with any degree of accuracy. For example the

reflection from a pile toe where accuracy of the order of 10% can be achieved at best.

A reduction in the input space of such a neural network can be achieved through presenting the fundamental modes of vibration from an impact test rather than the entire spectrum. Kirkegaard and Rytter have successfully used this encoding method in an attempt to locate and quantify cracking^{3.67} in a small steel member. However, the extension of these laboratory systems to industrially useful applications involves the careful identification of the task expected of the neural network and collation of training data representative of the system to be modelled both in terms of quality and quantity.

In the sphere of geotechnical engineering Goh has shown the applicability of neural systems in modelling nonlinear relationships^{3.68}. Specifically two examples were provided: the prediction of ultimate bearing capacity of a square footing in sand and the ultimate shear strength of a deep reinforced concrete beam. Both were unremarkable in that the network was trained using data known to give good approximations to laboratory tests using derived mathematical formulae. However, as a feasibility study the work illustrates the ability of a feedforward multilayer network to model these known nonlinear relationships using function approximation.

Chan *et al.*^{3.69} have attempted to use a multilayer network with one hidden layer to predict the static bearing capacity of a driven pile from parameters measurable during pile driving. The required output of the system is the static bearing capacity derived using the CASE and CAPWAP methods described in Section 2.4.2, but using just three input parameters as used by the simplified Hiley formula, namely: the measured driving energy transferred to the pile, the pile set, and the elastic compression of the pile and soil. The hope was that using these three measurable parameters a neural network could infer an approximation of the ultimate bearing capacity as accurately as the CASE and CAPWAP method without the explicit use of their esoteric damping parameters.

Unfortunately these researchers only had sixty eight data sets with which to test and train the network. Inevitably overtraining of the system is reported and, as the data sets are taken from only two sites, conclusions on the method applicability in general are impossible. However, even when training is stopped as the test data error begins to increase, i.e. when overfitting starts, the test set give a lower mean pattern error than the training set. It would at first appear that the network 'knows' more than it has been taught. But from a comparison of the network results with the CAPWAP/CASE calculated results it becomes apparent that there are a number of results with very large ($\geq 20\%$) errors. While there are only two of these spurious results in the test set there are eight in the training set - hence the larger mean pattern error in the training set. In fact, the simplified Hiley formula produces an equally large error for many of these same input patterns and so it becomes apparent that this is an example of a network where there is inadequate information to allow it to learn the required mapping. The presented parameters fail to encapsulate the data necessary for the network to statistically model the physical system and so make an accurate function approximation. This research, therefore, illustrates the importance of the sensible selection of network input parameters. If the input space is too large with respect to the training set size overtraining occurs. However, if it is truncated to the extent that its information content is compromised the problem may become intractable and the network will not be able to learn the necessary mapping.

Finally, in the only example found of the application of neural networks to integrity testing of foundation piles Yeh *et al.*^{3.70} have augmented the system described in Section 3.2.1 to include neural processing. Again the KBES is to derive the reason for a faulty prestressed pile installation from a set of symptoms. This time, however, eighteen symptom predicates - for example 'cracking occurred one side of the pile' - are given a value one (true), minus one (false) or zero (don't know) and are used as eighteen inputs in a multilayer feedforward network with a single hidden layer, also with eighteen units, but with a sigmoid activation function. There are twelve linear output units one for each of the previously described causal predicates - e.g. 'driving in very hard rock or soil'. The network is, therefore, taught to identify the reason for the failure of the pile driving attempt using 120 training and tested using 120 test patterns. Given the large number of units and therefore weight space it would appear

surprising at first that the issue of overtraining is not addressed, however on inspection of the test and training data it becomes apparent that the decision boundaries being derived are remarkably consistent and so interpolation and generalisation is not required of the network. The network is not being asked to handle the uncertainty in the input data. Instead when a network has input values that are unknown (i.e. given the value zero) their effect on the output is exhaustively tested by iteratively testing all those inputs with values of minus one and one, so ensuring the derived cause does not change. This methodology does not, it appears, consider the combinative effect of the unknowns and it would seem to negate the whole point of using neural networks for handling uncertainty. Given the reasonable consistency of the problem space decision regions and the low number of input predicates and output classes it is reasonable to suggest that a fuzzy logic approach would be better at handling uncertainty in the input data rather than the repeated use of a multilayer network. If a neural network is to be used there are many architectures more suitable to such a task. For classification the Hopfield and Counterpropagation networks described in Section 3.4.2 have been applied successfully to a number of similar problems. They would negate the need for repetitive use of a network with static dynamics by converging on the best fit, nearest neighbour, solution.

A number of practical issues pertaining to this paper also need to be address.

- i. It is not true in the general case that $F' = O(1-O)$ where F' is the differential of the activation function and O is the output of a unit with activation function F , as suggested in equation (4). This is only true of the sigmoid activation function used in this case where

$$\frac{\partial O}{\partial net} = \frac{\partial}{\partial net} \frac{1}{1 + \exp^{-net}} = \frac{1}{1 + \exp^{-net}} \left(1 - \frac{1}{1 + \exp^{-net}} \right) = O(1-O) \quad (3.21)$$

- ii. Strictly, it is not true that '*...learning results are not affected by initial network weights...*'. The reason initial weights are given small values is to

prevent the net input to a hidden unit being high at the start of training so forcing an output from that unit's *saturated region*. This would result in a very small gain term ($O(1-O)$ for sigmoid units) and greatly inhibit learning. Effectively, premature saturation would be induced at the start of training. The reason initial weights should be random is because the feedforward networks cannot *break symmetry*; that is, if all the weights are the same, the same error will be back propagated to each hidden unit and the weight update for each channel leading to a given unit in the layer above will change by the same amount - hence these weight values will always remain the same. Consequently the selection of suitable values for the initial weights is considered of great importance when designing a network - see Wessels and Barnard^{3.58}: '*Avoiding False Local Minima by Proper Initialization of Connections*'.

Given the evidence of the MLP's track record in a multitude of problems involving to temporal signal processing and, indeed, structural analysis it reasonable to predict that its function approximation strengths may be utilised for the interpretation of sonic echo test traces. However, it is recognised that multilayer networks with alternative, radial, activation functions may be better suited to the task. Two such systems are described, below.

3.4.4.2 Radial Basis Neural Networks (RBNN)

Instead of a function asymptotic to its maximum and minimum values as its input tends to $\pm\infty$, such as the sigmoid and tanh functions used above, Moody and Darken^{3.71} suggested localised function as an activation function. Specifically they used a normalised Gaussian activation function of the form described by Equation 3.22 for the hidden units.

$$F_i(\underline{x}) = \frac{\exp\left(-(\underline{x} - \underline{c}_i)^2 / 2\sigma_i^2\right)}{\sum_k \exp\left(-(\underline{x} - \underline{c}_k)^2 / 2\sigma_k^2\right)} \quad (3.22)$$

Where \underline{x} is the input vector, and unit i gives a maximum response as the input vector approaches the centre of the activation function \underline{c} . The variance of the Gaussian, σ ,

describes the receptive field of the unit activation^{3.42} and is often referred to as its width.

These radial basis neural networks (RBNN), as they are known, take less time to train than MLP networks and are better at modelling nonlinearities due to the compact nature of their activation function^{3.1}. Girosi and Poggio^{3.52} have also provided a proof suggesting Gaussian functions of radial argument can be used to approximate, arbitrarily well, continuous functions. They further state that, because this proof is derived from regularisation theory, this approximation can be considered a *best approximation* and unique. As this is not something that can be claimed by MLP networks with sigmoid activation functions, they conclude, RBNNs should be more suited to function approximation tasks. Essentially this means that for a given RBNN there exists a unique set of parameters (centres, widths *etc.*) that best approximate the function being modelled - this cannot be said to be true of the MLP.

Although empirical evidence^{3.42,3.57} also suggests that an arbitrary function can be approximated using one hidden layer in RBNNs rather than the two required in MLPs there are a number of practical difficulties in implementing such a network.

The first is a consequence of the localised nature of the activation function: the number of hidden units required for a given task expands exponentially with respect to the number of input units. This means such networks are not well suited to larger applications^{3.1}.

There is also the difficulty of selecting the centres and widths of the basis functions. The centre values are more usually derived using conventional, unsupervised, learning methods such as Kohonen's vector quantisation method^{3.42}. The widths can then be ascribed values proportional to the density of other centres in that region. As with all unsupervised learning there is the consequential problem of knowing when learning is complete and whether the weights accurately describe the p.d.f. of the input space. However, once these values have been ascribed the weights from the hidden layer to the output layer can be found reasonably easily: either through a pseudo inverse method, if the output units are linear^{3.1}, or through conventional gradient descent methods^{3.42}, as described above.

Given that it is transient features within the sonic echo trace that correspond to finite changes in acoustic impedance along the pile length it is possible that the localised

nature of the radial basis activation function will improve system performance when compared to MLP networks. However, such a network will require a high degree of encoding to reduce the dimensions of the input space. This will potentially lead to a reduction in the information content of the presented pattern. As the relative effectiveness of RBNNs and MLP networks cannot be predicted through theory both must be compared empirically. This can be achieved through the direct contrasting of relative system performances - as reflected in the (UK's) Department of Trade and Industry's case study examples^{3.1}.

3.4.4.3 Wavelet Basis Neural Networks (WBNN)

In the previous sections two multilayer networks and their associated activation functions have been introduced. The sigmoid unit, where the pattern space is regionalised by the superposition of series of hyperplanes, and the radial basis unit where the same pattern space can be divided using hyperellipsoids. It has been pointed out that, although empirically successful, the theory for MLP's does not suggest how many hidden units to use and the initialisation procedure of small, random weights leads to slow early learning and the possibility of converging on non-optimum local minima. This is overcome, to some extent, when radial basis units are used. Here, the centres of the Gaussian functions are determined through vector quantisation methods. Still though the functions' widths are determined on an *ad hoc* basis - usually through looking at the training points' density around these centres. A more effective solution may be to employ a functional basis that has been better described theoretically so providing a better understanding of the working of the neural network. Such a basis is found in wavelet theory and its application to neural networks was suggested, independently, by a number of researchers [e.g. 3.72, 3.73].

The wavelet transform, as it is presently known, was first introduced by Grossmann and Morlet in the early 1980's^{3.74,3.75}. For an one dimensional signal, the continuous wavelet transform takes the form of the two dimensional unfolding of the signal into a time-scale half plane where the wavelet coefficient, $W_{a,b}$, represent the inner product of the signal with an *analysing wavelet*, ψ , at location 'b' and dilation 'a'. This function is said to be a wavelet if it satisfies *the admissibility condition*:

$$\int_b^{\infty} \frac{|\hat{\Psi}(\omega)|^2}{\omega} d\omega = \int_{-\infty}^0 \frac{|\hat{\Psi}(\omega)|^2}{|\omega|} d\omega = C_{\psi} < +\infty \quad \text{if } a \in \mathfrak{R}^+ \quad (3.22)$$

In practice this condition implies that the mean component of the wavelet is zero. A formalisation of conditions of wavelet legitimacy can be found in Grossmann *et al*^{3.76}. The function is normalised so that the energies of wavelets of differing dilations are conserved. Hence the dilation of $\psi(x)$ by 'a' and translation of 'b' is defined as :

$$\psi_{a,b}(x) = \frac{1}{\sqrt{a}} \psi\left(\frac{x-b}{a}\right) \quad (3.23)$$

And the wavelet transform coefficient $W_{a,b}$ as:

$$W_{a,b} = \frac{1}{\sqrt{a}} \int_{-\infty}^{+\infty} f(x) \bar{\psi}_{a,b}(x) dx \quad \text{where } \bar{\quad} \text{denotes complex conjugate} \quad (3.24)$$

It can be shown^{3.77} that the signal can then be recovered from:

$$f(x) = \frac{1}{C_{\psi}} \int_b^{+\infty} \int_{-\infty}^{+\infty} W_{a,b} \psi_{a,b}(x) db \frac{da}{a^2} \quad (3.25)$$

From 3.25 it then becomes apparent that any continuous function can be recovered from the reconstruction of a series of wavelet functions, and in its discretised form from Equation (3.25) and be rewritten in the form of an approximation network:

$$f(x) = \sum_{i=1}^N w_i \psi(a_i(x-b_i)) \quad \omega_i, a_i, b_i \in \mathfrak{R} \quad (3.26)$$

where $\psi(\cdot)$ is the mother wavelet function, a_i are the dilation parameters, b_i are the translation parameters and w_i are linear weights. The dual indices have been replaced

by a single one for simplification and N is the number of wavelets used for the approximation (c.f. Equation 3.11). The accuracy with which the function, f , can be approximated is, therefore, be dependent upon the number of wavelet units, N , and the ability to find the parameters ω_i , a_i and b_i .

Equation 3.26 is a one dimensional wavelet network. To generalise it to the multidimensional case, that is, to form a network capable of approximating functions in $L^2(\mathcal{R}^n)$ where n is the dimension of the input space, a direct product form of the network was introduced^{3.72}. However, because the nonlinear computation in each unit, for this network, is directly proportional to the dimension n the number of such operations are much larger than in the sigmoid equivalent. Zhang^{3.78} then suggested the extension of 3.26 using radial wavelets thus

$$f(x) = \sum_{i=1}^N \omega_i \psi(\text{diag}(a_i)(x - b_i)) + c^T x + \theta \quad (3.27)$$

where θ is a bias term and c^T is parameter added to capture more easily the linear characteristics of the system being modelled. In practice, however, this ‘cascade’ term, known as the direct linear combination parameter, is often ignored^{3.79,3.80,3.81}.

As well as having the advantage of an activation function compact in both spatial and spectral domains using radial wavelet networks allows an estimate of vectors a_i and b_i to be made and the number of wavelet necessary for a given approximation^{3.79}. Thus the network can be initialised in a non-random fashion.

Essentially this initialisation takes the form of three steps^{3.78}.

- i. Search the input training patterns to find the truncated subset of \mathcal{R} applicable to the approximation i.e. the values of \underline{x} are, presumably, bound and so there is no need to search all of \mathcal{R} for values of a and b .

- ii. Reduce this subset by excluding wavelets with support not containing any data points in the training data - these will not contribute to the approximation of function, f .
- iii. Obtain an near optimum subset of N wavelets from the remaining superset to approximate the function f .

The third of these initialisation processes is a constructive, iterative, method known as stepwise selection by orthogonalisation. Essentially, firstly, the wavelet best approximating the function f is selected. Next the wavelet best approximating it in conjunction with the first is selected. Then the one best approximating f with the first two, and so on until N wavelets have been selected. An orthogonalisation step between each choice ensures a wavelet is not picked when its ability to discriminate is already encapsulated by a previously selected wavelet. It is possible to stop this iterative process when an error threshold is reached so the number of hidden units N is found automatically. These parameters can then be fine tuned using conventional gradient descent methods - see Section 3.5, below.

Although the study of wavelet networks is in its infancy they have been successfully applied to problems in nonlinear time series prediction^{3.81} and control^{3.80}. The author has shown, in previously published work, how filtering sonic echo traces in the wavelet domain has improved signal clarity when compared to conventional Fourier techniques^{3.82,3.83}. It is reasonable, therefore, to suppose that using wavelet methods to identify regularity in the pattern space might improve network performance.

3.5 Learning Systems' Functional Equivalence

The uncertainty handling abilities of MLP networks have been used for the inference of fuzzy set membership values since the early 1990's [e.g. 3.20]. However, Jang and Sun^{3.84,3.85} showed that, given certain strict conditions, there is an equivalence between Radial Basis Neural Networks and Fuzzy inference systems with Gaussian membership functions. Zhang^{3.79} has pointed out that radial wavelet networks can be considered a Radial Basis Neural Network and Morgan *et al.*^{3.57} have shown

experimentally how an MPL network with two hidden layers of sigmoid functions can 'mimic' a Radial Basis Function Neural Network.

Given this evidence of system equivalence Sjöberg *et al.*^{3.50} produced a comprehensive overview of black box modelling describing the generic methodology of function approximation using multi-variable basis functions. The choice of basis function (e.g. sigmoid, radial, wavelet *etc.*) was considered and various regression techniques described. The functional equivalence insinuated by this paper is explicitly stated through the introduction of a unification algorithm by Reyneri^{3.21} who describes all networks in terms of weighted radial basis functions (WRBF's) as well as the usual network topology, see Equation 3.28 below.

$$\hat{Y} = H_n^{F(z)}(\underline{X}, \underline{C}, \underline{W}, \underline{\theta}) \quad (3.28)$$

Where \hat{Y} is the system output vector and is a function of:

\underline{X} : the input vector

\underline{C} : a centre matrix e.g. centres for RBNNs, locations for WBNNs

\underline{W} : a weight matrix e.g. weights for sigmoid units, dilation for WBNN's

$\underline{\theta}$: an optional bias vector (as used in MLP's)

and

$F(z)$: the activation function of the units

The value n is the units' *metric* and is used to describe the network's rule of propagation i.e. how the units' inputs are combined to produce an output - see Equation 3.29, below.

$$\hat{y}_j = \begin{cases} F\left(\sum_i \omega_{ji} \cdot (x_i - c_{ji}) + \theta_j\right) & \text{for } n = 0 \\ F\left(\sqrt[n]{\sum_i \omega_{ji} \cdot D_n(x_i - c_{ji})} + \theta_j\right) & \text{for } n \neq 0 \end{cases} \quad (3.29)$$

where the distance function, D_n , is given by

$$D_n(x_i - c_{ji}) = \begin{cases} (x_i - c_{ji}) & \text{for } n = 0 \\ |x_i - c_{ji}|^n & \text{for } n \neq 0 \end{cases} \quad (3.30)$$

One can see immediately how a function described as Equation 3.31, below, is the equivalent of a MLP network with a single hidden layer. Here there are no centres to consider, i.e. $\underline{C}=0$, and the unit metric, n , is zero. Hence F^1 is the sigmoid function of the hidden layer and F^2 is the linear output function with \underline{W} and $\underline{\theta}$ representing the weights and biases to the hidden and output layers.

$$\hat{\underline{Y}} = H_0^{F^2(z)} \left(H_0^{F^1(z)} \left(\underline{X}, \underline{0}, \underline{W}^1, \underline{\theta}^1 \right), \underline{0}, \underline{W}^2, \underline{\theta}^2 \right) \quad (3.31)$$

Similarly, radial basis function networks and radial wavelet networks, called *wavelons* in this paper, can be described using this model.

The advantage of considering the different networks in this generic way is the added functionality it allows. Unlike conventional MLP's this model allows each hidden unit to take a bias for each input (by allowing a centre matrix \underline{C}) instead of single unit bias θ . This has the reported effect of accelerated learning and reducing the probability of getting stuck in local minima. When considering this claim it should be noted that, through simple linear algebra, any combination of these multiple biases can be shown to be the equivalent of a single bias. This is because, for the MLP, the activation function involves a simple summation of the weighted inputs. By assigning a weight matrix to radial basis functions a this paper also provides a method for automatically converging on near optimal values for the width of the Gaussian function. This learning paradigm takes the form of a gradient descent method and parameter changes are given as Equations 3.32-3.34, below.

$$\Delta \omega_{ji} = -\alpha_{\omega} \cdot \delta_j \cdot F'(z_j) \cdot \left[\frac{z_i}{n(z_i)^n} \right] \cdot [D_n(x_i - c_{ji})] \quad (3.32)$$

$$\Delta\theta_i = -\alpha_\theta \cdot \delta_j \cdot F'(z_j) \cdot \left[\frac{z_i}{n(z_i)^n} \right] \quad (3.33)$$

$$\Delta c_{ji} = -\alpha_{c\omega} \cdot \delta_j \cdot F'(z_j) \cdot \left[\frac{z_i}{n(z_i)^n} \right] \cdot \omega_{ji} \cdot \left[n \cdot D_{n-1}(x_i - c_{ji}) \cdot \text{sgn}(x_i - c_{ji}) \right] \quad (3.34)$$

where the parameters α are the appropriate learning coefficients and z_j is the argument of the activation function, F . As with the back propagation algorithm of MLP learning δ is the unit error and is defined as:

$$\delta_j = \frac{\partial E}{\partial y^j} = (\hat{y}_j - y_j) \quad (3.35)$$

for output units, j , c.f. BP learning, above.

$$\delta_j = \sum_i \delta_i \cdot F'(z_i) \cdot \left[\frac{z_i}{n(z_i)^n} \right] \cdot \omega_{ij} \cdot \left[n \cdot D_{n-1}(x_j - c_{ij}) \cdot \text{sgn}(x_j - c_{ij}) \right] \quad (3.36)$$

for hidden units, j , where units i are in the layer above.

For the special case $n=0$ the terms inside the square brackets disappear and one can see how, for MLP learning, the above equations resolve to the standard back propagation (BP) algorithm of Equations 3.13-3.18. This training paradigm also gives a method for training radial wavelet networks following the initialisation described in Section 3.4.4.3.

While it is recognised that this learning methodology may give superior results to conventional training methods for Radial Basis Neural Networks it is considered prudent to employ the methods described in Section 3.4.4.2 as well as this more novel approach in an attempt to find the optimal network for the given application. Due to the publication of the methodology being so recent, no empirical comparisons of the two approaches have yet been published.

3.6 APPLICATION DEVELOPMENT METHODOLOGY

The methodology framework for the research carried out in this project is based on that recommended for commercial neurocomputing projects by Robert Hecht-Nielsen in his book '*Neurocomputing*'^{3.2}. His project plan subdivisions are summarised in Table 3.1, below. Beside each task is an evaluation of its applicability to non-commercial research projects and, for those that are relevant, the section of this thesis where it is discussed.

The project definitions and goals are determined at the start of this chapter. However, these have only been stated after a rigorous description of the problem domain: that is, sonic echo integrity testing of cast *in situ* foundation piles. This description has taken the form of a market analysis in that , as well as a review of current test methods, industry has been contacted directly in order to ascertain the most useful direction any research should take, see Chapter 2: Industry Survey.

Table 3.1 The eleven aspects of a business plan pertinent to a commercial research venture (after Hecht-Nielsen^{3.2}) and their applicability to a non-commercial research project.

Business Plan Development Subsection (Hecht-Nielsen)	Applicability to non commercial research
Project Definition	✓ Section 3.1
Goals	✓ Section 3.1
Technical Feasibility	✓ Chapter 4
Market Analysis	✓ Research to be industrially relevant (Chapter 2)
Development Plan	✓ Chapter 3 (particularly 3.6)
Marketing and Sales Plan	✗ No Sales
Production Plan	✗ Prototype only
Organisation and personnel	✗ No other personnel
Schedule	✓ Gantt chart of predicted time scales
Budget	✗ Grant funded
Financing and Ownership	✗ EPSRC Grant Funded

The technical feasibility and system development plan for this research has broadly followed the recommendations of the UK's Department of Trade and Industries '*best practice guidelines for developing neural computing applications*'^{3.1}.

Effectively the three subsections of application development that are described below, and summarised in Figure 3.7, are the next four chapters of this thesis: Feasibility study, Hardware and Software Development, Application Development, and Field Testing.

3.6.1 Application Identification and Feasibility

The factors indicating the potential advantage of a neural computing application over other, conventional, computing technologies are given as^{3.1}:

- i. the application deals with poor or incomplete data
- ii. the application requires integration of different types of data - e.g. site investigation (environmental) data and sensor signals
- iii. it is difficult to specify a mathematical model that accurately describes the system
- iv. the application needs to be adaptive - i.e. the necessity of learning during operation

Given that the project definition stated in Section 3.1 fulfils the first three of these 'positive pointers' it is reasonable to suggest that a suitable system for neural computation has been identified.

The feasibility of the application is proved in Chapter 4. Here the two primary necessities for feasibility confirmation are addressed:

- i. The technical feasibility of the application. This is suggested through the identification of faults in a simple, uninstalled, concrete pile.
- ii. The availability, range, practicality and cost of data collection. It is shown that installed pile sonic echo traces can be accurately modelled using finite element analysis methods.

3.6.2 System Development

The system development of the neural application takes a cyclic empirical approach, summarised in Figure 3.7. A number of pre-processing methods are evaluated and an optimal feedforward network found by direct comparison of those described above. Chief considerations during system development are^{3.1}:

- i. pre- and post-processing methodology (input/output encoding)
- ii. selection of neural network architecture
- iii. optimisation of neural network size and complexity
- iv. optimisation of training algorithm (cost function, momentum parameters *etc*)

A number of system prototypes are, therefore, applied to the problem: MLP, RBNN, and WBNN. Each is optimised for system performance and compared to identify the superior system architecture.

3.6.3 Deliverable System Validation

System validation is achieved by three means:

- i. The ability of the network to successfully interpret mathematically generated data known to fall outwith the data upon which it has been trained. Thus the interpolation and extrapolation strengths of the network can be quantitatively evaluated.
- ii. The ability of the network to successfully interpret 'real data' from field tests (the EPSRC test sites at Blyth and Bothkennar). Thus the generalisation and uncertainty handling strengths of the network can be quantitatively evaluated.

3.7 SUMMARY AND CONCLUSIONS

Sonic Echo Integrity Test data from cast *in situ* foundation piles are a suitable candidate for processing by neural networks because: they contains noisy and uncertain data, it is difficult to model the system mathematically, and the system is required to integrate different types of data i.e. temporal (the trace), spatial (the environment) and, possibly, linguistic (the pile type).

Artificial neural networks can be broadly divided into two classes: those taught by supervised and unsupervised paradigms. For systems with a known or required

output supervised methods are more usually employed. In this problem, the generation of training data through numerical modelling will provide both the pile head responses and the required network outputs.

Of the supervised methods by far the most widely researched network topology is the multilayer feedforward type. For static mapping of a continuous input space to output space, i.e. function approximation tasks, these networks have proved particularly successful.

The activation functions employed in multilayer feedforward networks are often of a monotonic, continuous, ridge-like construction. However, theoretical evidence suggests that radial constructs such as the Gaussian or wavelet types give better function approximation results at a cost of network size.

The optimum network type is usually found through empirical measures.

Multilayer feedforward networks have been successfully applied to fault diagnosis tasks in the field of concrete testing and in geotechnical investigation.

A number of networks applied to structural testing tasks have been trained using mathematically modelled data and give good results when tested on 'real', field data.

This thesis will continue with an investigation into the technical feasibility of applying artificial neural networks to the automated interpretation of sonic echo test data using feedforward network architectures.

REFERENCES

- (3.1) DTI, Neural Computing Learning Solutions: Best Practice Guidelines for Developing Neural Computing Applications, Department of Trade and Industry (UK) (1994).
- (3.2) Hecht-Nielsen R, Business Plan Development, in Neurocomputing, Addison-Wesley (1991), pp358-406.
- (3.3) Schalkoff R, Pattern Recognition Overview, in Pattern Recognition: Statistical, Structural and Neural Approaches, John Wiley & Sons (1992), pp2-15.
- (3.4) Devijver P A and Kittier J, Introduction, in Pattern Recognition : A

- Statistical Approach, Prentice/Hall International (1982), pp1-21.
- (3.5) Gonzalez R C and Thomason M G, Syntactic Pattern Recognition : An Introduction, Addison-Wesley (1982).
 - (3.6) Rajagopalan C and Kalyanasundaram P, The role of artificial intelligence in non-destructive testing and evaluation, Insight, Vol. 38, No. 2, pp118-123.
 - (3.7) Sivia D S, Parameter Estimation II, in Data Analysis a Bayesian Tutorial, Oxford Science Publications (1996), pp37-80.
 - (3.8) Schalkoff R, Supervised Learning (Training) Using Parametric and Nonparametric Approaches, in Pattern Recognition: Statistical, Structural and Neural Approaches, John Wiley & Sons (1992), pp58-83.
 - (3.9) Devijver P A and Kittier J, Probability Density Function Estimation, in Pattern Recognition : A Statistical Approach, Prentice/Hall International (1982), pp422-432.
 - (3.10) Ciaccio E J, Dunn S M, and Akay M, Biosignal Pattern Recognition and Interpretation Systems, IEEE EMB Magazine, Vol. 13, No. 1 (1994), pp129-135.
 - (3.11) Rengaswamy R and Vekatasubramanian, A syntactic pattern recognition approach for process monitoring and fault diagnosis, Engineering Applications of Artificial Intelligence, Vol. 8, No. 2, pp35-51.
 - (3.12) Gonzalez R C and Thomason M G, Grammatical Inference, in Syntactic Pattern Recognition : An Introduction, Addison-Wesley (1982), pp216-270.
 - (3.13) Yeh Y-C, Kuo Y-H and Hsu D S, Building KBES for diagnosing PC Pile with inductive learning, J. Comp. In Civil Engng, Vol. 6, No. 2 (1992), pp200-219.
 - (3.14) Quinlan J R, Learning efficient classification procedures and their application to chess games, in Machine Learning: an Artificial Intelligence Approach, Ed Quinlan J R, Addison-Wesely (1983), pp157-173.
 - (3.15) Hughes G E and Cresswell M J, An Introduction to Modal Logic, Universal Paperback (1968).
 - (3.16) Zadeh L A, Fuzzy Sets, Information and Control, Vol. 8 (1965) pp338-353.
 - (3.17) Wang L, Adaptive Fuzzy Systems and Control, Englewood Cliffs, NJ:Prentice-Hall (1994).
 - (3.18) Pal S K and Mitra S, Multilayer Perceptron, Fuzzy Sets and Classification, IEEE Trans. on Neural Networks, Vol. 3, No. 5 (1992)

- pp 683-697.
- (3.19) Jang J-S and Sun C-T, Functional Equivalence Between Radial Basis Function Networks and Fuzzy Inference Systems, IEEE Trans. on Neural Networks, Vol. 4, No. 1 (1993) pp 156-159.
 - (3.20) Jang J-S and Sun C-T, Response to Discussion on : Functional Equivalence Between Radial Basis Function Networks and Fuzzy Inference Systems, IEEE Trans. on Neural Networks, Vol. 9, No. 6 (1998) pp 1531-1532.
 - (3.21) Reyneri L M, Unification of Neural and Wavelet Networks and Fuzzy Systems, IEEE Trans. on Neural Networks, Vol. 10, No. 4 (1999) pp801-814.
 - (3.22) Hecht-Nielsen R, Introduction: what is Neurocomputing?, in Neurocomputing, Addison-Wesley (1991), pp1-20.
 - (3.23) Kohonen T, Self-Organised Formation of Topologically Correct Feature Maps, Biological Cybernetics, 43 (1982) pp59-69.
 - (3.24) Desieno D, Adding a Conscience to Competitive Learning, Proc. Int. Conf. On Neural Networks, I, IEEE Press (1988) pp117-124 .
 - (3.25) Ritter H and Schulten K, Kohonen's Self-Organising Maps: Exploring their Computational Capabilities, , IEEE Int. Conf. on Neural Networks , Vol I (1988) pp109-116.
 - (3.26) Graf D H and LaLonde R W, A Neural Controller for Collision-Free Movement of General Robotic Manipulators, IEEE Int. Conf. on Neural Networks , Vol I (1988) pp77-84.
 - (3.27) Kohonen T, Mäkisara K and Saramäki, Phonetic Maps - Insightful Representation of Phonetic Features for Speech Recognition, Proc. 7th Int. Conf. On Pattern Recognition, New York: IEEE (1984) pp182-185.
 - (3.28) Barrios L J and Lemus L, Associative Neural Networks for Fault Diagnosis in Semiconductor Manufacture, Tasks and Methods in Applied Artificial Intelligence, Proc. 11th Int. Conf. On Industrial and Engineering Applications of Artificial Intelligence and Expert Systems, Springer (1998) pp582-592.
 - (3.29) McCulloch W S and Pitts W, A Logical Calculus for the Ideas Immanent in Nervous Activity, Bulletin of Mathematical Biophysics, No. 5 (1943) pp115-133.
 - (3.30) Hebb D O, The Organisation of Behaviour New York: Wiley (1949).
 - (3.31) Rosenblatt F, Principles of Neurodynamics, New York: Spartan (1962).
 - (3.32) Widrow B and Hoff M E, Adaptive Switching Circuits, WESCON Convention Record: Part 4 (1960) pp96-104.

- (3.33) Rumelhart D E, McClelland J L and The PDP Research Group, Parallel Distributed Processing, Volume 1: Foundations, MIT Press, (1986)
- (3.34) Hinton G E and Sejnowski T J, Learning and Relearning in Boltzmann Machines, in Parallel Distributed Processing, Volume 1: Foundations, Eds Rumelhart D E, McClelland J L and The PDP Research Group, MIT Press, (1986) pp282-317.
- (3.35) Rumelhart D E, Hinton G E and Williams R J, Learning Internal Representations by Error Propagation, in Parallel Distributed Processing, Volume 1: Foundations, Eds Rumelhart D E, McClelland J L and The PDP Research Group, MIT Press, (1986) pp318-362.
- (3.36) Kurková V, Kolmogorov's Theorem and Multilayer Networks, Neural Networks, Vol. 5, (1992) pp501-506.
- (3.37) Minsky M L and Papert S A, Perceptrons, Expanded Edition, MIT Press (1988) [*First edition Cambridge: MIT Press (1970)*].
- (3.38) Hertz J, Krough A, and Palmer R G, Recurrent Networks, Introduction to the Theory of Neural Computing, Addison Wesley, (1991) pp163-196.
- (3.39) Hopfield J J, Neural Networks and Physical Systems with Emergent Collective Computational Abilities, Proc. Of the National Academy of Sciences, USA 79 (1982) pp2554-2558.
- (3.40) Hertz J, Krough A, and Palmer R G, Optimisation Problems in Image Processing, Introduction to the Theory of Neural Computing, Addison Wesley, (1991) pp81-87.
- (3.41) Simpson P K, Artificial Neural Systems, Pergamon Press, (1990).
- (3.42) Hertz J, Krough A, and Hertz, Introduction to the Theory of Neural Computing, Addison Wesley, (1991).
- (3.43) Williams R, Reinforcement Learning Connectionist Systems, Northeastern University, College of Computer Science Technical Report, NU-CCS-87-3, (1987).
- (3.44) Oja E, A Simplified Model as a Principle Component Analyzer, J. Math. Biology, Vol. 15 (1982), pp267-273.
- (3.45) Oja E, Neural Networks, Principle Components and Subspaces, Int. J. of Neural Systems, Vol. 1 (1989) pp61-68.
- (3.46) Sanger T D, Optimised Unsupervised Learning in a Single-Layer Linear Feedforward Neural Network, Neural Networks, Vol. 2 (1989) pp423-428.
- (3.47) Hecht-Nielsen R, Counterpropagation Networks, Applied Optics, Vol. 26 (1987) pp4979-4984.

- (3.48) Grossberg S, Embedding Fields: A Theory of Learning with Physiological Implications, *J. Math. Psychology*, Vol. 6 (1969) pp209-239.
- (3.49) Travers F A, Acoustic Monitoring of Prestressed Concrete Pipe, *Proc. 6th Int. Conf. Structural Faults and Repair*, Vol. 3 (1995) pp111-123.
- (3.50) Sjöberg J, Zhang Q, Ljung L, Beneviste A, Deylon b, Gloennec P-Y, Hjalmarasson H and Juditsky A, Nonlinear Black-Box Modelling in System Identification: a Unified Overview, *Automatica*, Vol. 31 (1995).
- (3.51) Kůrková V, Kolmogorov's Theorem and Multilayer Neural Networks, *Neural Networks*, Vol.5 (1992) pp501-506.
- (3.52) Girosi F and Poggio T, Networks and the Best Approximation Property, MIT AI Memo No. 1164 (1989).
- (3.53) Aussem A and Murtagh F, Combining Neural Network Forecasts on Wavelet-transformed Time Series, *Connection Science*, Vol. 9, No.1 (1997) pp113-121.
- (3.54) Kirkegaard P H, Modelling of Non-linear Structures using Recurrent Neural Networks, *Developments in Neural Networks and Evolutionary Computing for Civil and Structural Engineering*, Civil-Comp Press (1995) pp51-58.
- (3.55) Haykin S and Li L, Non-linear Adaptive Prediction of Nonstationary Signals, *IEEE Trans. on Signal Processing*, Vol. 43 (1995) pp526-535.
- (3.56) Mandie D P and Chambers J A, Towards an Optimal PRNN-Based Non-linear Predictor, *IEEE Trans. on Neural Networks*, Vol. 10, No. 6 (1999).
- (3.57) Morgan P, Curry B and Beynon M, Comparing Neural Network Approximations for Different Functional Forms, *Expert Systems*, Vol. 16, No. 2 (1999) pp60-71.
- (3.58) Wessels L F A and Barnard E, Avoiding False Local Minima by Proper Initialization of Connections, *IEEE Trans. on Neural Networks*, Vol.3, No. 6 (1992) pp899-905.
- (3.59) Lee Y, Oh S-H and Kim M W, An Analysis of Premature Saturation in Back Propagation Learning, *Neural Networks*, Vol. 6 (1993) pp719-728.
- (3.60) Rumelhart D E, Hinton G E and McClelland J L, A General Framework for Parallel Distributed Processing, in *Parallel Distributed Processing, Volume 1: Foundations*, Eds Rumelhart D E, McClelland J L and The PDP Research Group, MIT Press, (1986) pp45-76.
- (3.61) Roth M W, Survey of Neural Network Technology for Automated

- Target Recognition, IEEE Transactions on Neural Networks, Vol. 1, No. 1 (1990).
- (3.62) Sejnowski T J and Rosenberg C R, Parallel Networks that Learn to Pronounce English Text, Complex Systems, No. 1 (1987) pp145-168.
- (3.63) Worden K, Ball A D and Tomlinson G R, Fault Location in a Framework Structure using Neural Networks, Smart Materials & Structures, No. 2, (1993) pp189-200.
- (3.64) Wu X, Ghaboussi J and Garrett Jr J H, Use of neural networks in detection of structural damage, Computers and Structures, Vol. 42, No. 4 (1992) pp649-659.
- (3.65) Pratt D and Sansalone M, The use of a Neural Network for Automating Impact Signal Interpretation, Proc. of the Rev. Progress Quantitative Nondestructive Evaluation, Vol. 10 (1991) Plenum Publishing Corp.
- (3.66) Begum R and Chamberlain D, Integrity Testing of Concrete Surfaces using Neural Networks, Proc. Int. Symposium Non-Destructive Testing in Civil Engng (NDT-CE) (1995) pp1339-1346.
- (3.67) Kirkegaard P H and Rytter A, The use of Neural Networks for Damage Detection and Location in a Steel Member, Neural Networks and Combinational Optimisation in Civil and Structural Engineering, Civil-Comp Press (1993) pp1-10.
- (3.68) Goh A T, Some Civil Engineering Applications of Neural Networks, Proc. Instn Civ. Engrs Structs and Bldgs, Vol. 104 (1994) pp463-469.
- (3.69) Chan W T, Chow Y K and Liu L F, Neural Network: An Alternative to Pile Driving Formulas, Computers and Geotechnics, Vol. 17 (1995) pp135-156.
- (3.70) Yeh Y-C, Kuo Y-H and Hsu D-S, Building KBES for Diagnosing PC Pile with Artificial Neural Network, J. of Computing in Civil Engineering, Vol. 7, No.1 (1993) pp71-93.
- (3.71) Moody J and Darken C, Fast Learning Networks for Locally-Tuned Processing Units, Neural Computation, Vol. 1, No. 2 (1989) pp281-284.
- (3.72) Zhang Q and Benevise A, Wavelet Networks, IEEE Trans. on Neural Networks, Vol. 3, No. 1 (1992) pp889-898.
- (3.73) Boubez T I, Receptive Field Partitioning for Wavelet Networks, in Artificial Neural Networks for Speech and Vision, Ed. Mammone R J, Chapman and Hall (1994) pp79-96.
- (3.74) Goupillaud P, Grossmann A, and Morlet J, Cycle-Octave and Related Transforms in Seismic Signal Analysis, Geoexploration, Vol. 23 (1984) pp85-102.

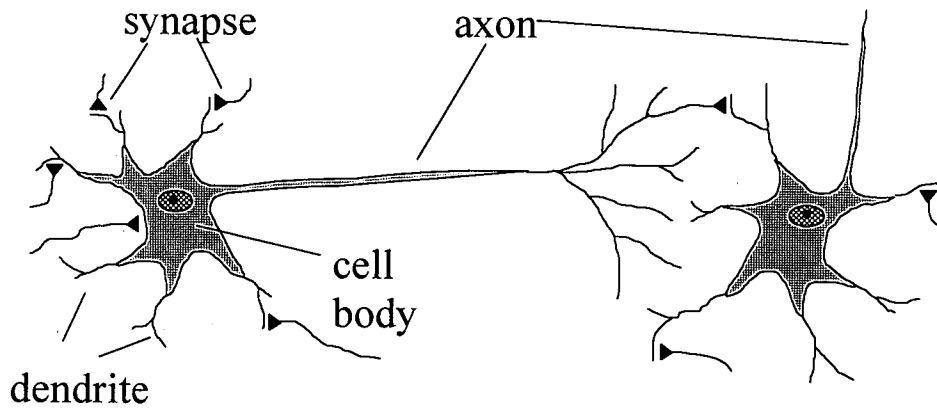


Figure 3.1 Simplified representation of two connected neurons.

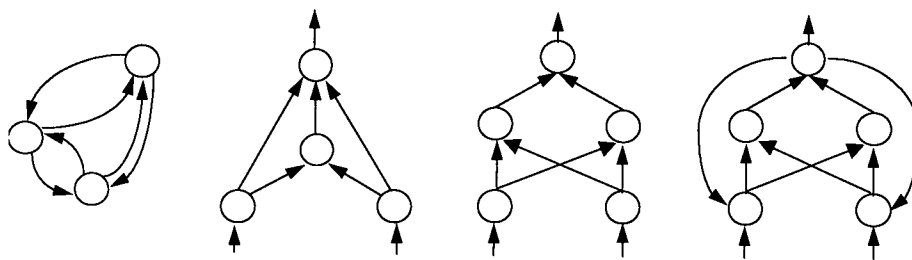


Figure 3.2 Examples of some of the more popular network architectures. From left to right: a fully connected network, a feed-forward network, a feedforward multilayer network and a multilayer network with feedback (Recurrent network).

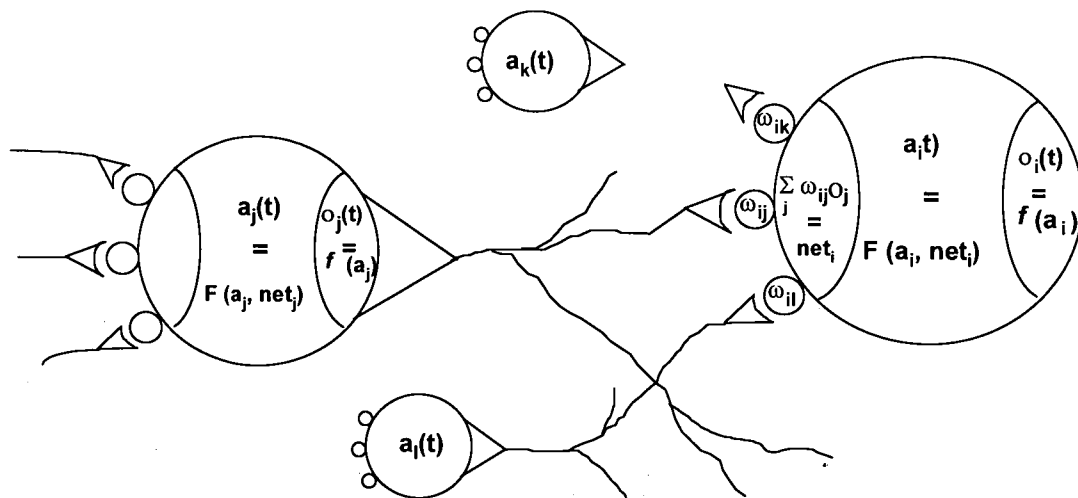


Figure 3.3 The basic components of a PDP system (after Rumelhart *et al*^{3.33}).

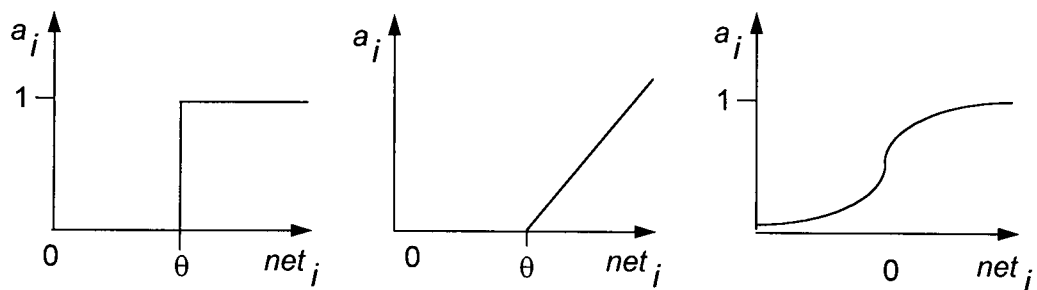


Figure 3.4 The Heaviside, Linear Threshold and Sigmoid activation functions. Where θ is a pre-defined threshold value.

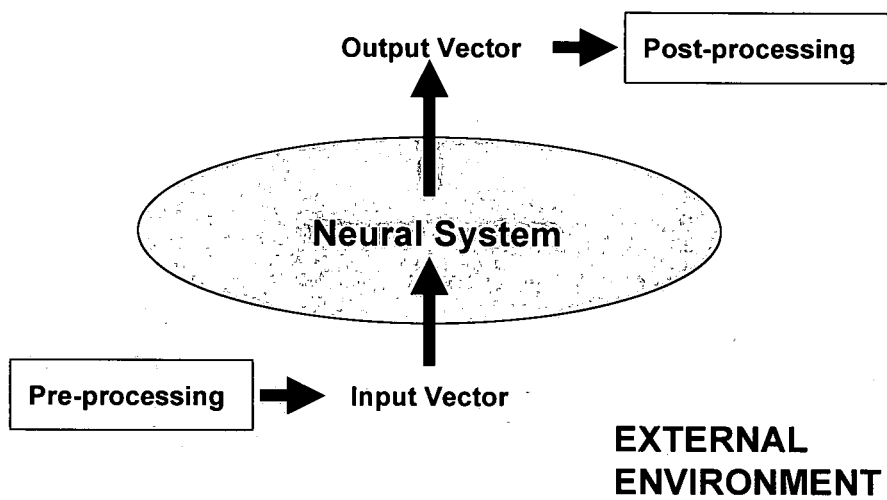


Figure 3.5 The external environment and its relationship with the neural network.

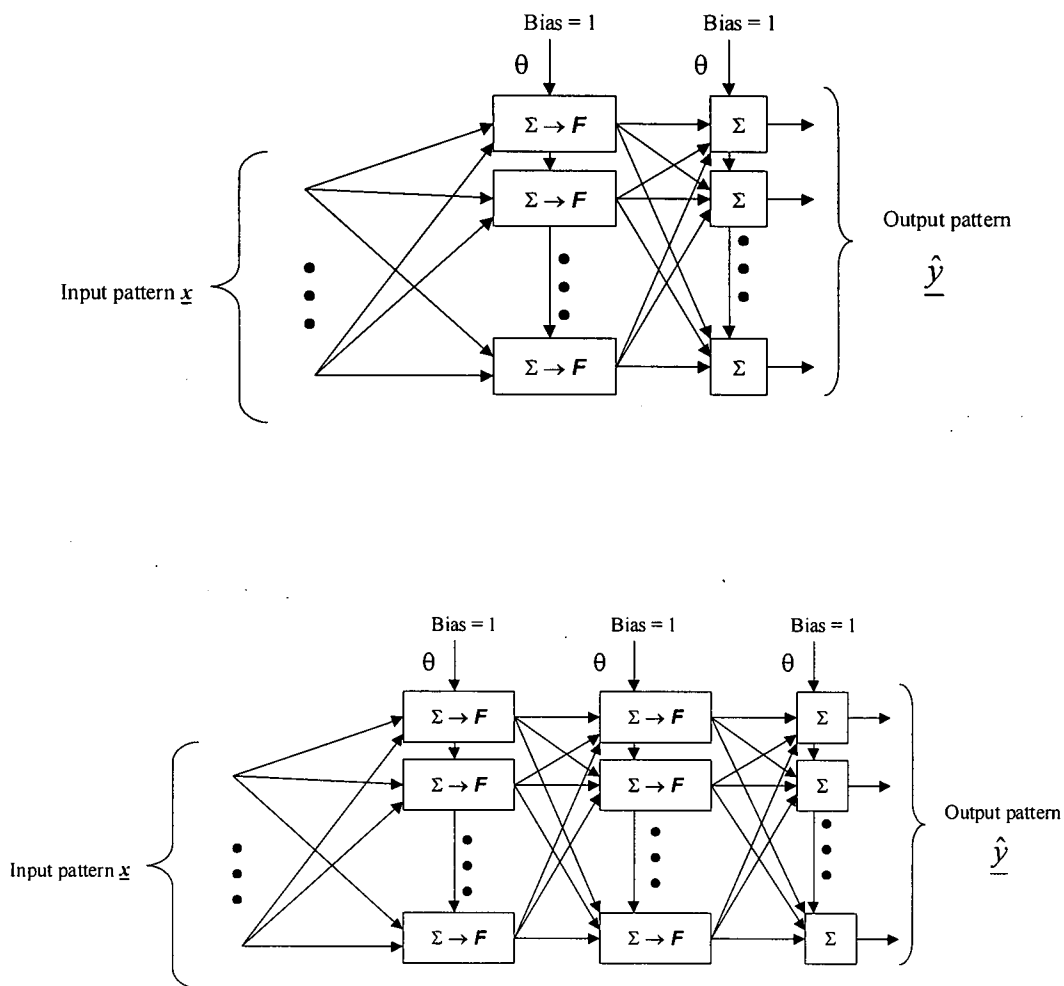


Figure 3.6 showing the generic model for (a, top) a single and (b, bottom) two layer network. The bias term, as in Figure 3.4, provides a threshold value for the activation function, F .

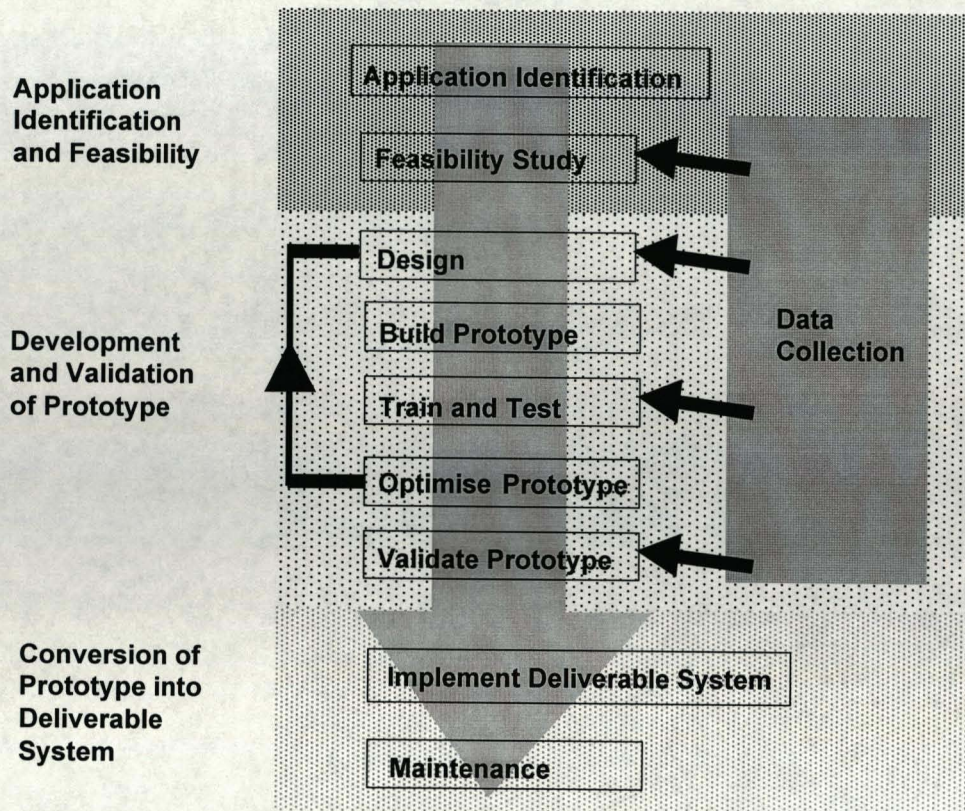


Figure 3.7 Stages of neural network application development (After DTI [UK]^{3.1}).

4. Feasibility Study

As discussed in the previous chapter, of paramount importance when deciding whether a problem is suitable for the application of neural networks is: (1) the availability of representative data for network training and (2) the technical feasibility of finding an acceptable solution using a network approach. This chapter is, therefore, broadly divided into two parts.

The direct use of field test data for network training is impossible. Even if enough data could be obtained from industrial collaborators the lack of a generic test protocol leads some test houses not to record the impact force traces and often no documentation of soil conditions are kept. This coupled with the fact that the true impedance profile of the pile-soil system can only be estimated through expert interpretation means neither the input nor output vectors for network training can be known with any degree of confidence. The first half of this chapter, therefore, describes alternative means of pile test modelling and presents a method for the generation of test traces through finite element analysis. The method is validated through comparison with contemporary theory, published laboratory tests, and industry supplied field test data.

The appropriateness of neural network utilisation for the interpretation of pile integrity test data has already been discussed in Chapter 3. The second part of this chapter provides empirical evidence for the applicability of such an approach. That is, it provides a technical feasibility study by considering uninstalled concrete beams and a simple, multi-layered network's ability to identify, quantify and locate faults within them. Specifically this section considers the ability of a network to identify the type (neck or bulb) of defect in a beam of fixed length and change in radius. It is also required to detect the axial length of this fault and its position.

The chapter concludes with a summary of the findings of the study and presents the case for development of the system for the interpretation of installed foundation piles.

4.1 ONE DIMENSIONAL MODELLING

4.1.1 Wave Tracing

The pile head response to an impact force may be estimated through the convolution of the system's impulse response and the shape of the impact force. Effectively this is the opposite process of that described in Section 2.7.7 where a pile's impedance profile is generated by stratifying the pile along its axial length and calculating the necessary changes in impedance to create the received pile head response. In this case, however, the impedance profile is known and its impulse response is calculated through consideration of a singularity (Dirac function) as it propagates through the strata. As the pulse reaches a change in mechanical impedance it splits into two: one transmitted component and one reflected; the coefficients of reflection and transmission being described by Equations (2.21 a and b). A recursive processes of pulse splitting and following may then be used to estimate the pile head response to the given input. Attenuation of particle velocities due to prevailing soil conditions may be included by utilising Briard's formula (2.23).

Chan^{4.1} reports good correlation between experimental results and those calculated through such a method, 'Simulation By The Method of Convolution', for an uninstalled circular beam. However, he reports that the computational power necessary to follow multiple wave fronts in piles containing many changes in mechanical impedance becomes prohibitively large. While computing power has improved considerably in the last ten years it is also noted that such a method cannot estimate the observed reflections caused by changes in the surrounding soil stiffness without modifying the effective mechanical impedance of the pile. Such a modification would involve the estimation of the soil mobilised by the propagating

pulse which in turn requires a knowledge of stress dissipation with respect to radial distance from the pile-soil interface.

The lack of theory for the necessary alterations in effective mechanical impedance and the inefficient nature of its computation, therefore, prohibits this method from being suitable for the task of generating the many and varied traces necessary for neural network training.

4.1.2 Composite Systems

A more computationally efficient method for the generation of a pile head's response can be derived by the decimation of the system under investigation into component parts. The pile may be modelled using an electrical analogy, such as that described by Davis and Dunn^{4.2} and illustrated in Figure 4.1. By representing the force at the pile head, F , as the total circuit current, I_t , and the velocity of the pile head, v , as the applied circuit voltage, E_t , then the mechanical impedance of the system, $|F/v|$, can be found from the electrical admittance of the circuit model, $|I_t/E_t|$. Referring to Figure 4.1, capacitance represents the pile mass per unit length, while pile and soil stiffness are represented by coil inductance. The signal attenuation, i.e. soil damping, is modelled using resistors.

The circuit parameters are presented in terms of the pile's cross sectional area, the concrete stiffness, Poisson's ratio, density, and the soil's shear modulus and the shear wave velocity. These are derived from the previously discussed theories proposed by Paquet^{4.3} and Briard^{4.4}. The methodology was developed in the 1970s to simulate the frequency response of a pile during vibration testing. Consequently its usefulness in generating the temporal response of the pile head to an impact excitation is limited.

With the widespread availability of increasingly powerful computers, today, installed piles are more commonly modelled as mechanical, Winkler type, systems^{4.1,4.5,4.6,4.7} such as that illustrated in Figure 4.2. These models consider the pile as a number of rigid masses connected together by a series of springs and dashpots and interfacing with the soil through further springs and dashpots. In practice the dashpots between

the pile's lumped masses, c_p in Figure 4.2, are often ignored as the soil damping term dominates the overall system damping. These models are more conducive to the stepwise time iterations necessary for the temporal modelling of impact testing. Such modelling has its origins in the need to predict a pile's response to large dynamic strains; typically during pile driving^{4,8} or when designed to carry a dynamic load^{4,5,4,7}. They have, nevertheless, also been used for the modelling of small strain integrity test data^{4,1,4,6} with some degree of success.

However, these models produce an idealised one dimensional approximation of the required pile head response. For the higher strain problems for which the model is designed trace features such as pile head ringdown, lateral reflections and refraction, can be considered negligible, but in low strain testing the lack of these features make it unrepresentative of the system being modelled. Also implicit to such models is the assumption that the shear waves emanating from the pile-soil interface propagate only horizontally and so radial soil displacements are ignored. Often the spring and dashpot parameters are derived assuming elastic layer of infinite extent, -the soil - containing a rigid inclusion of unit thickness: a unit length of pile^{4,5,4,6}. Hence, the front of the propagating stress wave is restricted to being purely planar in nature. The model can be further compromised by assumptions necessary for the derivation of the spring and damping parameters at the pile base where the toe is often be modelled as a circular footing on an elastic half space^{4,6}.

Intuitively, a more suitable model would also appear to involve lateral decimation of the pile-soil system as well as the longitudinal decimation described above. This would allow the soil to be modelled, like the pile, in terms of lumped masses. Thus, the necessary degrees of freedom would be introduced to provide for radial propagation of stresses within the pile and in the surrounding soil. This negates the need to derive abstract spring and dashpot parameters. Such a method is the finite element method. Liao and Rosset^{4,6} have conducted a comparison between a one dimensional lumped mass spring and dashpot model, of the type described above, and an axisymmetric, 2-D continuum, finite element model (see Section 4.2, below) for low strain integrity testing. They confirm that the finite element results more closely resemble those found in practice. Indeed of the other two examples of spring

and dashpot models referenced above, Markis and Gazetas^{4,7} use finite element analysis to derive their values for stiffness and damping parameters, while Michaelides *et al.*^{4,5} use finite element results as one of the methods for validating their method of parameter derivation.

The improved results attainable through the finite element method come at the cost of computational time and complexity. However, for neural network training, the need for training set data to represent accurately that of the problem domain is of primary importance and so, given that this increased computer time is not prohibitively large, such a compromise is considered justified.

4.2 FINITE ELEMENT ANALYSIS (FEA)

This form of analysis originated from advances in aeronautical structural analysis in the early 1960's. The basic hypothesis upon which the method is based is that a large continuum can be modelled analytically by subdivision into smaller 'finite elements'. These finite elements are connected such that each element boundary is topologically compatible with its neighbours while also satisfying the complete structure's defined boundary conditions. A complex structural response to loading may then be estimated through the combination of responses from its much simpler component parts. A more detailed description of the finer points of the finite element method may be found elsewhere^{4,9,4,10,4,11}, but for the sake of completeness a brief précis of the subject fundamentals is now presented.

The size and shape of the, previously mentioned, constituent elements of the structural model are described in terms of nodal co-ordinates. For the finite element displacement method, the structural displacements, δ_s , are assumed to have unknown values only at these nodal points. The variation within the nodes being described through interpolation functions, thus:

$$\delta_s = \underline{N}_s \underline{\delta}^{[e]} \quad (4.1)$$

Here $\underline{\delta}^{[e]}$ is the vector of nodal displacements and \underline{N}_s is a matrix of the set of interpolation functions, also known as the 'shape function matrix'. The strains within an element may hence be related to displacements by Equation 4.2, below.

$$\gamma_s = \underline{B}_s \underline{\delta}^{[e]} \quad (4.2)$$

Where \underline{B}_s is the strain-displacement matrix, more usually composed of derivatives of the shape functions. From 4.2, for linear elasticity, the stresses within an element can be derived through use of a matrix of elastic constants, \underline{D}_s , as Equation 4.3, below.

$$\sigma_s = \underline{D}_s \gamma_s \quad (4.3)$$

Where σ_s is the stress and γ_s the, previously derived, strain.

The governing equations for static equilibrium are derived from the principle of virtual work^{4,12}. Here, the potential energy of the system is minimised and it is assumed that for any small displacement imposed on the body the total internal work must equal the total external work for equilibrium to be maintained. Which leads to the virtual work equation for an element of

$$\underline{K}^{[e]} \underline{\delta}^{[e]} = \underline{F}^{[e]} \quad (4.4)$$

where

$$\underline{K}^{[e]} = \int_e (\underline{B}_s^T \underline{D}_s \underline{B}_s) \partial V \quad (4.5)$$

is known as the stiffness matrix and

$$\underline{F}^{[e]} = \underline{F}_b^{[e]} + \underline{F}_s^{[e]} + \underline{F}_c^{[e]} \quad (4.6)$$

is known as the element force vector containing components

$$\underline{F}_b^{[e]} = \int_{\underline{V}_e} \underline{N}^T \underline{f}^{[e]} \partial V \quad (4.7)$$

where \underline{F}_b is the force vector due to element body loads, \underline{f} , with units force per unit volume and

$$\underline{F}_s^{[e]} = \int_{\underline{S}_e} \underline{N}^T \underline{t}^{[e]} \partial S \quad (4.8)$$

is the force vector due to element surface tractions, \underline{t} , with units force per unit area and

$$\underline{F}_c^{[e]} = \sum_i \underline{R}_i \quad (4.9)$$

is the total applied concentrated loads to the element where subscript i denotes the point of contact.

Rearranging equation 4.4, the displacement $\delta^{[e]}$ can be derived, with respect to given structural boundary conditions, thus

$$\{\delta\} = [K^{-1}]\{F\} \quad (4.10)$$

where $\{\cdot\}$ denotes a vector over all nodes and K^{-1} is the inverse stiffness matrix. Hence, nodal stresses and strains can be derived as

$$\{\gamma\} = [B]\{\delta\} \quad (4.11)$$

and $\{\sigma\} = [D]\{\gamma\} \quad (4.12)$

Although the equations above (4.2-4.12) may be applied to structures with static or slowly changing load levels, for systems with more rapidly changing load conditions, such as the impact testing of piled foundations, inertial and damping forces must be integrated into the equilibrium equations. In such cases it is assumed that

accelerations and velocities can be approximated by the same interpolation functions as displacement and so velocity, v_s , can be described by

$$v_s = \dot{\delta} = \underline{\underline{N}}_s \dot{\delta}^{[e]} \quad (4.13)$$

and acceleration, a_s , by

$$a_s = \ddot{\delta} = \underline{\underline{N}}_s \ddot{\delta}^{[e]} \quad (4.14)$$

The body force described by equation 4.7 then becomes

$$\underline{\underline{F}}_b^{[e]} = \int_e \underline{\underline{N}}_s^T [f^{[e]} - \rho^{[e]} \underline{\underline{N}}_s \ddot{\delta}^{[e]} - c^{[e]} \underline{\underline{N}}_s \dot{\delta}^{[e]}] \partial V \quad (4.15)$$

where ρ is the material density and c is the material damping constant which is reflective of the well known, Newtonian, dynamic equilibrium equation

$$\underline{\underline{M}} \ddot{\delta} + \underline{\underline{C}}_d \dot{\delta} + \underline{\underline{K}} \delta = \underline{\underline{F}}(t) \quad (4.16)$$

where $\underline{\underline{M}}$ is the mass matrix and $\underline{\underline{C}}_d$ the damping matrix.

Clearly the solutions to the equations of equilibrium for a system are unlikely to be solvable analytically and so iterative procedures are utilised that converge upon acceptable approximations of these solutions e.g. the Newton-Raphson iteration^{4.12}. The selection of the solution search procedure, its parameter values and the convergence criteria applied will, therefore, have an effect on the final solution.

This section will continue with an explanation of the modelling procedure for installed foundation piles as used in this project. Parametric studies for the selection of mesh (nodal/element) density are presented and the selection of material parameters justified. The section concludes with a validation of the model through

comparison with previously published experimental work and industry supplied data from sonic echo tests of installed foundation piles.

4.2.1 Model Element Type

Historically when modelling an installed pile foundation two dimensional methods are applied. Here, the symmetry of the pile soil system is exploited to reduce the computational complexity of the solution space. Clearly, for such an assumption to be made the loading conditions must also be presumed to be symmetric, a presumption which is justified in the case of small strain integrity testing. In three dimensions, when soil is modelled as an annulus of elastic material surrounding the pile, the size of the system becomes prohibitively large for modelling the many variations of pile shape and soil type necessary in this application. Typically, although the system size increases with r^2 , where r is (approximately) the radius of the soil annulus, the computational time increases by a far greater margin as the model size necessitates more 'page swapping' with the computer work station's hard disk drive. That is, the required system memory for the FEA model becomes far larger than the physical memory of the computer and so 'virtual memory' from slower, peripheral, devices needs to be employed.

For two dimensional modelling two types of elements have been employed in published research. The previously mentioned work by Liao and Rosset employed quadrilateral axisymmetric elements^{4.6,4.13} while Wong and Topping used plane strain quadrilateral elements^{4.14}. When using plain strain elements of constant geometry to model the pile soil system, unlike the axisymmetric case, there is no intrinsic geometric damping associated with an increased lateral distance from the pile centre. In applying this method the author has also found the signal attenuation to be lower than that predicted by Briard's formula. It is suggested that this is due to the effective increase of the pile's cross-sectional area to perimeter ratio and so, in this study, axisymmetric elements have been used. These produce a logarithmic decrement of decay of the signal very much of the order predicted by theory. For an empirical validation of this statement, see Section 2.6.2.

As in previous work, the pile-soil system has been modelled as a 2-D continuum with material properties assumed to be linear elastic with elements of the isoparametric type. Such assumptions have been shown to be justified for the case of small strain testing - see Section 4.2.4. However, results obtained using quadrilateral elements produce a ringdown effect in the reflected pulse echo. This ringdown is not, as might be expected, resonance at the pile head from the initial hammer impact, but from resonance at the pile toe. An example is given in Figure 4.3(a). Here the pile modelled is of 11.4m length with a 0.4m diameter installed in stiff over stiff/very stiff clay. The reader is referred to Section 4.2.6.3 for a full discussion of the material parameters used in this model and Figure 4.28 for the expected result from field testing. Although this effect is in keeping with the published results of Liao and Rosset^{4,6} it is unrepresentative of all the experimental and field results collated by the author. It is noted here that Liao and Rosset make no comparisons of their work with either experimental or field test results^{4,6,4.13}. Indeed, it is hard to imagine how the pulse echo technique could have ever been successfully applied if such results were representative of field test data. The ringing is caused by the material stiffness differential between pile toe and the soil base. Effectively, when no structural damping is included in the model, as in previous work^{4,14}, an end resonance is produced with an amplitude proportional to the materials' respective stiffness. In the example given the pile's Young's modulus is about two orders of magnitude larger than that of the surrounding soil ($3 \times 10^{10} \text{ Nm}^{-2}$ and $5 \times 10^8 \text{ Nm}^{-2}$ respectively). It has been found that this effect can be diminished by two means: the use of triangular elements and the inclusion of material damping.

Figure 4.3 (b) shows the trace obtained using identical material properties and node positions, but with triangular rather than quadrilateral elements. As can be seen the high amplitude resonance has been replaced by a lower amplitude, lower frequency resonance. Figure 4.4 (a) shows the resultant stress distribution within part of the pile-soil system as the stress wave reaches the pile toe while 4.4 (b) shows the distribution just after reflection for the triangular element case (again, the reader is referred to a later diagram, Figure 4.27, to see the dimensions of the entire mesh shown to scale). On both illustrations the deformed mesh is superimposed with a magnification factor of fifteen thousand to aid clarity.

As expected, in both cases the majority of the system's constituent stresses are constrained within the pile member as it, effectively, acts as a wave guide. However, noticeable in the quadrilateral case is the stress build up immediately beneath the pile toe. Here, the planar nature of the stress wave in conjunction with the regular quadrilateral shape of the elements appears to produce a punching stress beneath the pile toe. It is also noticeable in the highlighted regions A, B, A' and B', that the mesh deformation is smoother across the triangular elements when compared the quadrilateral ones

Figure 4.5 shows the principal stresses about the pile toe for the constituent elements' Gauss points - the grey area is the pile toe. Outwardly pointing arrows indicate compressive forces, inwardly pointing tensile; the length of the arrow tail indicates the stress magnitude. Both mesh types illustrated show the system state at 3.5 milliseconds when the stress at the pile toe is at a maximum - as indicated by the high compression values perpendicular to the direction of propagation of the wavefront. It is clear from the quadrilateral mesh that the elements directly under the pile toe resonate with successive compressive then tensile layers. The fact that the stresses remain localised beneath the pile toe is further illustrated in the legend associated with Figure 4.4 (a). Here the minimum stress is found at node 1275 - the node at the bottom right corner of the mesh. The stress magnitude of 10^{-21} Nm⁻² indicates negligible effects at this point. For the triangular elements, however, although the soil elements directly under the pile toe are, as expected, in compression, no such localised resonance has occurred. Instead, the minimum stress at node 1275 is very much larger (0.4 Nm⁻²) - although still negligible with respect to the stresses inside the pile body. This indicates that the localised resonance has been replaced by a lower amplitude, lower frequency system resonance which, although still undesirable, is preferable as it can be effectively negated through including soil damping in the model.

The values and method of modelling soil damping is discussed below in Section 4.2.4 - 'Material Assignments'. For the purposes of this section, however, it is sufficient to remark that the values used are completely consistent with given

empirical results and very small: typically the damping ratio is less than 5%. The reader is directed to Figures 4.28 and 4.29, part of the system validation section, for an illustration of how the inclusion of damping eliminates the resonance found in Figure 4.3 (b) and gives a good approximation of field test results.

4.2.2 Element Aspect Ratio

Ill-conditioned elements can have a detrimental effect on a finite element model's effectiveness. The primary cause of ill-conditioning in continuum modelling is the inclusion of elements with large aspect ratios (the ratio of longest to shortest element side length) and so for triangular elements a well conditioned shape will be close to an equilateral triangle. For the pile-soil complex under investigation, however, the aspect ratio of the system itself is large. In modelling it, therefore, the processing time can be greatly reduced by 'stretching' the elements along its longest dimension so enlarging their aspect ratio. Hence, it is necessary to undertake a parametric study to identify the optimum aspect ratio of the constituent elements.

For the purposes of this parametric study an infinitely long, uninstalled, circular member is considered. The member has an increase in section at a point along its axial length. From Equations 2.21 (a) and (b) it is possible to predict the amplitude of the reflected stress wave from this change in section using one dimensional wave theory. Although, it should be noted here that the planar nature of the propagating wavefront is assumed. It is, however, also known from theory that for such a one dimensional model, particle velocity is linked to stress through Equation 4.17.

$$\sigma = -\rho c \frac{du}{dt} \quad (4.17)$$

Where σ is the stress, ρ is the material density, c the group velocity and the differential represents particle velocity. With the material properties being constant before and after the change in section, therefore, the ratios of reflected and transmitted stresses at this boundary also hold for the particle velocities. Hence, with no damping in the system, by considering the axial (y-component) velocity trace of

an element node above the section change with respect to time, the peak and trough in the trace can be used to compare the actual coefficient of reflection with theory. Such a trace is illustrated in figure 4.6 by way of example. The coefficient of reflection for this case is calculated as 0.91 for a theoretical value of 0.92. The node selected for investigation, as in all the experiments, was that which was half way between the pile head and the change in section.

The finite element system being used is the LUSAS finite element system^{4,12} for which the maximum recommended element aspect ratio is 7:1. Radial dimensions of the pile were selected, as Table 4.1, to produce theoretical coefficients of reflection varying between about 0.2 and 0.9. The longitudinal dimensions of the elements were altered for each experiment set to produce a further set of results for elements with aspect ratios varying between two and six.

Table 4.1 A Comparison FEA and Theoretical Coefficients of Reflection

Initial Pile Radius r_0 (m)	Initial Sectional Area A_0 (m ²)	Increased Pile Radius r_1 (m)	Increased Sectional Area A_1 (m ²)	Theoretical Coefficient of Reflection (R)
0.05	0.008	0.25	0.196	0.92
0.05	0.008	0.15	0.071	0.80
0.10	0.031	0.15	0.071	0.61
0.10	0.031	0.2	0.126	0.39
0.20	0.126	0.25	0.196	0.22

The results from all these experiments are plotted on the graph in Figure 4.7. The graph plots the ratio of the modelled reflection coefficient to the expected value against the aspect ratio of the elements used. The plot clearly indicates a deterioration of the models' effectiveness as the aspect ratio increases, with all results starting within 5% of the expected values. The degradation accelerates as the aspect ratio increases beyond four with the larger coefficients of reflection being modelled generally better than the smaller ones. It should be noted that the number of lateral divisions of the pile remained constant for each experiment, five as in [4.6],

and so this effect may be caused by the coarser lateral decimation of piles with larger radii. However, its inconsistency suggests that it is more likely to be due to numerical round-off errors becoming more significant for the cases where smaller reflections occur.

For this study, therefore, the aspect ratio of the models' constituent elements is limited to values of less than four. In fact, to add a margin of safety and to allow for better longitudinal resolution when modelling axial faults the longest dimensions of the elements used are always reduced such that an aspect ratio of three is never exceeded. For further validation of this working heuristic the model of the structurally sound sprung supported pile used in Section 4.2.3 is repeated with a double density mesh. As shown in Figure 4.12, there is no discernible change in the generated pile head response when using twice as many elements to model the pile.

4.2.3 Loading and Boundary Conditions

4.2.3.1 Impact Pulse Shape

Convention dictates that the impulse excitation produced by a hammer blow be modelled as a half-sine shape^{4.1,4.6,4.15}. However, on inspection of impact traces, such as those presented by Sibbald^{4.16}, it is evident that this approximation does not strictly confer with experimental traces - see Figure 4.8 (a) and (b). As can be seen in this example, there is a leading and trailing tail-off associated with the impact. This feature is consistent and observable in other published examples^{4.1,4.17}.

For an impulse with a 0.5ms rise time, as is typical for impact testing using a short sledge hammer with a medium softness plastic tip, the pulse may be modelled as a Gaussian, as shown in Figure 4.9. Here the equation of impact, $g(t)$, is described by

$$g(t) = \exp\left(\frac{-(t-t_o)^2}{r_i^2/2}\right) \quad (4.18)$$

where t_o is the time of maximum force and r_t is the given rise time of the pulse. Comparing this to the standard equation for a Gaussian, as in Equation 3.22, the standard deviation can be described as the rise time of the pulse divided by two. Hence, in excess of 95% of the work done by the impact occurs within the ascribed rise and fall time of the pulse with the remainder providing the tails more in keeping with experimental results.

While this alteration does not produce any marked change in the velocity response of the pile head in time it does alter the frequency based mobility curve. The flatter power spectrum associated with the half sine impact shown in Figure 4.10 (a) shows an accelerated decay as its first turning point is reached at around 1500Hz. The size of the lobes following this minimum are of a far higher order than that of the experimental results for pulses of a similar rise time: namely those of the medium and soft hardness, plastic tipped, hammer. The number of these lobes is also very much less than that of the experimental results and more in keeping with the harder tipped, shorter duration, impacts. For the Gaussian shaped pulse, however, the number and magnitude of the lobes above the first minimum are more like experimental results while the position of this minimum is still around the required value ($\approx 1750\text{Hz}$). Further to this, the rate of decay of the power spectrum's magnitude better reflects that of the experimental data.

Although it is known^{4.1} that the coherence of impulse functions of this duration reduces for frequencies above 1250Hz, this suggested limit is often exceeded. The author has found examples, from industry, of mobility curves extending beyond 2000Hz - although no values above 1700Hz were considered in any integrity calculations^{4.18}, see, for example, Figure 4.46. The unnaturally large nature of these lobes when modelling using the half-sine input distorts the mobility curve to a degree that it becomes unrepresentative of such *in situ* measurements. The accelerated decay of the half-sine spectrum around its first minimum also produces a more rapid rise in the mobility spectra about this point, as reflected in the published work of Liao and Rosset^{4.6}. For this study, therefore, the shape of the impact pulse is modelled as a Gaussian, as described above. For an example of a mathematically generated

mobility curve using such an impulse function and its associated field test curve the reader is referred to Figures 4.30 and 4.31.

4.2.3.2 Combined Nodal Loading

As discussed in Chapter 2, in practice, noise produced through pile head oscillations is more usually reduced through ensemble averaging of a number of velocity responses measured at different positions on the pile head. For axisymmetric modelling, however, this method becomes impossible as the loading is assumed to be symmetric about the system's centreline. If an off centre point load is applied to the pile head it is swept through 2π radians to produce an annular force in three dimensions thus the impact must be limited to a position at centre of the pile head's top surface. Nevertheless, here, as this model is of a linear elastic type, the effect is mimicked by applying a patch load across the entire pile head so reducing the effect of pile head oscillation. The measured response at a given position on the pile head can then be considered the superposition of the responses, at that position, for all possible impact points - the recorded pile head response being the superposition of all these impacts.

Again, since the model is linear elastic and isotropic, the absolute magnitude of the applied pulse is of little significance for the temporal response at the pile head. A higher maximum force simply results in a higher magnitude of response - the normalised shape of responses are identical. However, for mobility curve analysis the impact force magnitude becomes important for the calculation of dynamic stiffness - the gradient reciprocal of the linear region of the graph as the frequency tends to zero. If the central load values applied on the pile's top surface are the same for each node the total applied load can be calculated from

$$F_{total} = 2\pi.n.F_{nodal} \quad (4.19)$$

where n is the number of nodes to which the force is applied, F_{nodal} is the force applied to each node and the 2π factor reflects the sweeping of the one radian segment described in the two dimensional model about its centre line.

For the sake of completeness the value of maximum force applied in this study is given as 5000 newtons per node, this value is of the order of that used in the other quoted studies. This loading methodology provides favourable results when compared to *in situ* traces in both time and frequency domains and gives good correlation for calculated values of dynamic stiffness - see Section 4.2.6, 'Model Validation Using Field Test Data'.

4.2.3.3 Boundary Conditions

For axisymmetric analysis using the LUSAS finite element software no rigid body translation of the model is recorded as node positions are described in terms of a local co-ordinate system rather than globally. However, the axisymmetric method allows the nodes along the centreline of the model lateral movement, i.e. movement in the x direction perpendicular to the stress wave's direction of propagation. Rigid restraints in this dimension have, therefore, been added to prevent this.

The size of the soil annulus surrounding the pile body is calculated with respect to the theoretical stress and shear wave velocities of that soil. The equations governing these velocities are given as

$$c = \sqrt{\frac{E(1-\nu)}{\rho(1+\nu)(1-2\nu)}} \quad (4.20)$$

$$\beta = \sqrt{\frac{E}{2\rho(1+\nu)}} \quad (4.21)$$

where c and β are longitudinal stress and shear wave velocities respectively. E is the soil's Young's modulus, ρ its density and ν its Poisson's ratio.

By way of example, the systems modelled for the validation of this methodology have a top soil with values of: $E=2.6 \times 10^8 \text{ Nm}^{-2}$, $\rho=2125 \text{ kgm}^{-3}$ and $\nu=0.4$. The piles under consideration are all under 12m in length and so, assuming the stress wave propagation velocity in concrete is more than 3000ms^{-1} , the time traces considered are no longer than 10 ms duration. For this case, therefore, the pile annulus must be greater than 1.05m ($= \beta \times 0.01/2$) to ensure any shear waves reflected from the soil boundary do not interfere with those reflected from the pile toe. In fact, to add a margin of safety, the soil annulus in this case is set as 2m. It should also be noted here that any reflected waves have little or no effect on the response at the pile head as they are strongly attenuated by the soil damping. Thus, as can be seen in Section 4.2.6, no observable aberrations are found when comparing mathematically generated time traces with field test data. Nodes along the soil boundary are given rigid supports in both x and y dimensions, as illustrated in Figure 4.27.

4.2.4 Material Assignments

The materials used in this study are assumed to have linear elastic, isotropic characteristics. The model is described in terms of a two dimensional continuum. The material properties are, therefore, described in terms of their Young's modulus, density and Poisson's ratio. A small degree of material damping is also included in the model. In the following sub-sections these assumptions are justified and methods for the derivation of their values are discussed.

4.2.4.1 Concrete Properties

The stress-strain relationship of concrete is non-linear. However, this non-linearity is caused by microcracking at its constituent cement paste-aggregate interfaces^{4.19}. For smaller strains, therefore, this dependence converges to a linear relationship as little or no cracking occurs. It is also noted that for rapidly applied loads ($<0.01 \text{ s}$) the recorded strains become smaller and the curvature of the stress-strain graph becomes greatly reduced^{4.20}. Thus, this dynamic modulus approximates to the concrete's, low

strain, initial tangent modulus; although, in practice, the dynamic modulus is usually marginally greater than that of the static case. For very low strain, dynamic loading, therefore, the elasticity of concrete can be assumed to linear. The value of the concrete's elastic modulus may be derived from stress wave propagation velocities using Equation 4.20 or through 4.22 where Poisson's ratio effects have been ignored.

$$c \approx \sqrt{\frac{E}{\rho}} \quad (4.22)$$

Clearly, the concrete density can be inferred from the design mix or measured from concrete samples. However, the Poisson's ratio is more difficult to establish. It may be derived from the resonant frequency of a concrete sample of length, L , from Equation 4.23, below.

$$\left(\frac{c}{2nL}\right)^2 = \frac{1-\nu}{(1+\nu)(1-2\nu)} \quad (4.23)$$

Where, as before, c and ν are pulse velocity and Poisson's ratio respectively and n is the resonant frequency under investigation in hertz^{4.20}. Typical values of Poisson's ratio for concrete are given as 0.15-0.25 for low strain measurements^{4.21}, but for dynamic measurements this range narrows to 0.20-0.24^{4.20}. For pile testing empirical evidence shows the value of Poisson's ratio has negligible effect on the pile head response^{4.22}. In this study, therefore, as in others^{4.1,4.6,4.14,4.22} a value has been assumed at 0.22, the middle of the aforementioned range.

These methods for the derivation of concrete material properties have been used to model experimental results for uninstalled concrete beams published by Chan^{4.1}. Figure 4.11 shows the design of the three beams under investigation and the finite element meshes used to model them. Beam 1 was defect free, beam 2 had a neck at three metres and beam 3 had a bulb at the pile toe. The concrete density is given as 2360kgm⁻³ and its cube strength, f_{cu} , as 25Nmm⁻².

Equation 4.20 is derived using the theoretical propagation of stress waves in an unbounded elastic medium. For pulse propagation in a rod like structure, when lateral strains are considered, theory suggests that Poisson's ratio effects diminish as the pulse wavelength increases with respect to the rod diameter^{4,23}. This is true to a limiting case where the ratios of these measures is infinite when the propagation velocity tends to Equation 4.22. For this study, a pulse with a measured duration of 1ms and a measured propagation velocity of around 3500ms^{-1} will have a pulse width at least an order of magnitude larger than the pile diameter. When estimating material parameters from experimental velocity measurements, therefore, Equation 4.22 is used.

The concrete's Young's modulus is, therefore, estimated from the measured pulse propagation velocity (3450ms^{-1}) as 28.1 GPa. As discussed earlier, the Poisson's ratio is assumed as 0.22.

The experimental velocity trace for the defect free beam is shown in Figure 4.12 with the finite elements results in Figure 4.13, beneath. During the experimental procedure the beam was suspended by ties from a crane. This has resulted in internal reflections at the support positions and a secondary peaking during the trace that gradually becomes more pronounced with time. By mimicking these ties through the inclusion of sprung supports at 1m and 4.5m in the finite element model similar results can be obtained. The trace is not identical with the experimental case because the exact positions of the ties were not given and the axisymmetric nature of the finite element model necessitates the supports circumnavigating the entire pile circumference. However, the introduction of the second peak and its gradual increase in magnitude with respect to the reflections from the pile toe is evident.

A second plot is presented of the results when double the number of elements are used to ensure the effect is independent of mesh density. The third plot on this graph shows the resultant trace when no spring supports are used.

Theoretical velocity values are compared to experimental and finite element generated values in Table 4.2. The results correlate well with experimental and finite

element values falling within 0.4% of one another. It is also noticeable that the finite element result is within 0.4% of the theoretical value where Poisson's ratio effects are ignored. This supports Wong's claim^{4.22} that Poisson's ratio values have negligible effect on the pile head response when generated through the finite element method.

Table 4.2 A Comparison of Theoretical, FEA and Experimental Stress Wave Velocities

	Propagation Velocity (ms ⁻¹)
Theoretical (without Poisson's ratio)	3450
Theoretical (with Poisson's ratio)	3686
Experimental (after Chan ^{4.1})	3450
Finite Element	3437

The finite element generated traces for the beams containing a neck and bulb are shown in Figures 4.13 and 4.14 respectively along with the experimental pile head response.

In both cases direct, numerical comparisons of the reflected peak magnitudes with the input pulse magnitude are inappropriate as the magnitude of the input pulse is dependent upon the position of measurement. However, the ratio of peak magnitudes for the first two reflections can give an indication of modelling effectiveness as here the propagating wavefront can be considered planar. These can be compared to theory by considering the path of an impulse through the beams. In the case of the beam with necking the first returning echo would have undergone one reflection while the second, from the increase in section at the bottom of the neck, one transmission followed by a reflection and a further transmission. For the beam with bulbing, the first echo has undergone one boundary reflection while the second has undergone a transmission, a total reflection at a free end and a further transmission.

The ratios of absolute magnitude for the first two reflections for each of these beams along with the measured pulse velocities are summarised in Table 4.3. Also presented are the calculated values from one dimensional wave theory.

For the beam with necking the finite element trace has an error of 13% when compared to theory. The measured experimental value has a larger error of 20%. This is because of the slightly longer rise time of the input pulse for the experimental case where superpositioning of the two reflections has a more pronounced effect on the results. This effect is even more noticeable in the case of the beam with bulbing where closer proximity of the origins of the returned echos has resulted in differences of 50% with theory. This superpositioning is also reflected in the apparent increase in pulse group velocity. If, however, the shape of the impulses are assumed to be Gaussian with a rise time of 0.5ms and a temporal separation calculated from the theoretical pulse propagation velocity (3450 ms^{-1}) the superpositioning can be accounted for and the new expected ratios given as: 1.7 and 0.3 for the beams with necking and bulbing respectively. Both finite element and experimental measures are equal to the calculated values for the pile with bulbing and the experimental ratio is within 6% of that calculated for the pile with necking .

Table 4.3 Quantified Partial Reflections from Discontinuities:

Experimental, FEA and Theoretical

		Experimental	FEA	Theory (Dirac)	Theory (Gaussian)
Pile with Neck (Figure 4.14)	Magnitude ratio of first two reflections	1.8	1.7	1.5	1.7
	Calculated pulse velocity (ms^{-1})	3628	3529	3450	3450
Pile with Bulb (Figure 4.15)	Magnitude ratio of first two reflections	0.3	0.3	0.6	0.3
	Calculated pulse velocity (ms^{-1})	3550	3623	3450	3450

These results illustrate the problems associated with small scale testing where multiple internal reflections occur due to support conditions. Nevertheless, the finite element model has been shown to produce results that are consistent with both published experimental work and one dimensional wave theory.

4.2.4.2 Soil Properties

As in the case of concrete the stress-strain relationship in soils is a non-linear relationship with soil stiffness increasing with increasing deviator stresses in typical laboratory (triaxial) testing^{4.24}. Stress history, saturation, particle size and shape, strain rate, time (consolidation effects), and voids ratio can all contribute to this non-linearity. However, at very small strains the shear modulus reaches a nearly constant limiting value, G_0 . Viggiani and Atkinson^{4.25} quote this elastic region as being for strains of less than 0.01% for low plasticity soils and 0.001% for plastic clays - well above the strains associated with low strain integrity testing. Importantly, it is also noted that at these strains volumetric and shear deformations are almost fully recoverable so justifying the continuum modelling of the pile soil interface.

De Magistris *et al.*^{4.26} have investigated the very low strain quasi-elastic properties of dynamically loaded geomaterials through triaxial testing using a highly controllable servo motor. Their experiments for undrained cyclic testing of silty sand illustrate the effective stiffening of soils at high strain rates (7 seconds/cycle [$\approx 0.14\text{Hz}$] at 0.00075% strain) with the stress-strain response becoming more linear accompanied by a decrease in energy dissipation and, therefore, damping. This is reflected by an apparent increase in the initial Young's modulus for higher strain rates and lower damping ratios.

The elastic properties of *in situ* soils may be estimated from site investigation data: typically cone penetration measurements and seismic shear wave velocities. Then the Young's modulus, E , can be derived from the measured shear modulus, G , by Equation 4.24 and soil densities can be estimated from 4.25 or measured from core samples.

$$G = \frac{E}{2(1+\nu)} \quad (4.24)$$

$$G = \rho\beta^2 \quad (4.25)$$

However, for the data used in this study no values of Poisson's ratio, ν , are given. These must therefore be assumed as empirical measures taken from literature, see Table 4.4 below.

The range of some of these values can produce values of E that may vary by up to 7% from the actual value. Nevertheless, the large errors associated with the methods of *in situ* measurement and the small effect the Poisson's ratio has on overall system response supports this approximation as acceptable.

Table 4.4 Given values of Poisson's Ratio

Source	Soil Type	Poisson's Ratio Range
After Winterkorn and Fang ^{4.27}	Clay, Saturated	0.50
	Clay, with sand and silt	0.30-0.42
	Clay, unsaturated	0.35-0.40
	Loess	0.44
	Sandy soil	0.15-0.25
	Sand	0.30-0.35
After Das ^{4.28}	Loose Sand	0.20-0.40
	Medium Dense Sand	0.25-0.40
	Dense Sand	0.30-0.45
	Silty Sand	0.20-0.40
	Sand and Gravel	0.15-0.35

While it is appreciated that the above estimates and assumptions will lead to inaccuracies in the model it should also be recognised that there are intrinsic errors associated with sampling and testing techniques, and variations in soil properties through site variability, inhomogeneity, and anisotropy.

4.2.4.3 Material Damping

Signal attenuation in the propagating stress wave during low strain pile integrity testing is predominantly caused by the transmission of energy across the pile periphery into the surrounding soil. As such, it is primarily a function of the pile and soil's relative stiffness and density, and the pile's circumference. However, an intrinsic material property of the soil and concrete is damping. For small strains and high strain rates the effect of this damping is small^{4.26} and is invariably ignored^{4.1,4.2,4.4,4.5,4.7,4.13,4.15}. However, its inclusion can, numerically, compensate for the resonance caused by the perfectly elastic system modelled in finite element analysis. The collated, empirical, values of the damping ratios for dynamically tested soils are given in Table 4.5.

Table 4.5 Internal Damping in Soils (After Whitman and Richart^{4.29})

Soil Type	Damping Ratio (%)
Dry Sand and Gravel	3-7
Dry and Saturated Sand	1-3
Dry Sand	3
Dry and Saturated Sands and Gravel	5-6
Clay	2-5
Silty Sand	3-10
Dry Sand	1-3

Factors influencing the values shown in Table 4.5 include shear strain amplitude, shear strain rate, axial strain rate and confining pressures. However, more recent measures by Abbiss^{4.30} indicate that for low strain field measures ($\sigma < 10^{-3}$ %) the damping is asymptotic to values of this order (<10%) and consistent for the test method used to obtain them (hysteretic, impulse or resonance). This characteristic is, further, found^{4.5} to be independent of soil plasticity (plastic index) for very low strains ($\sigma < 10^{-3}$ %). These findings correlate well with the laboratory tests of De Magistris *et al.*^{4.26} who indicated that, for increasing strain rates the values for the

initial damping ratios of Metramo silty sand are asymptotic to a value of around 1% for the range of tested confinement pressures. With the damping values being so small the signal attenuation in a pile test is dominated by material differences between the pile and soil, hence ignoring internal damping is justified. However, including it in this study provides a degree of numerical damping thus improving system results while remaining consistent with theory.

The damping in soils is generally considered hysteretic in nature due to the energy dissipated within the system through inter-particle friction. In such cases the damping is considered a retarding force proportional to particle displacement and in phase with particle velocity. However, soil is more usually modelled as a, simpler, visco-elastic medium where the degree of damping is proportional to the particle velocity^{4,27}. These systems are generally rationalised through considering a single degree of freedom sprung, rigid mass with dashpot damping as more complex multiple degree of freedom systems can be described in terms of the linear superposition of such systems. After an impulse excitation the system is left in free vibration. Subsequent changes in the amplitude of vibration are then described by the system's decrement of decay, δ_c , where

$$\delta_c = \frac{1}{n} \ln \left(\frac{z_x}{z_{x+n}} \right) \quad (4.26)$$

n is the number of cycles of vibration that have occurred between measurements z_x and z_{x+n} . This decay constant is linked to the damping ratio, ξ , through Equation 4.27, below.

$$\delta_c = \frac{2\pi\xi}{\sqrt{1-\xi^2}} \quad (4.27)$$

Structural damping is, however, usually found to be frequency dependent in that the damping effects for a given frequency of excitation will be lessened as that frequency approaches the resonant frequency of the undamped structure. In the finite element system used in this study this dependency is modelled through proportional (or

Rayleigh) damping. Here, the arbitrary assumption is made that the system damping is a linear combination of the mass and stiffness matrices. As the damping distribution for a given structure is rarely known in great detail this assumption is considered a reasonable approximation as long as: (1) the system damping is not greater than an order of 10% above critical damping and (2) damping is not constrained to a small region of the structure^{4.12}. As neither of these limitations are surpassed by the system under investigation (the damping is small and contained within a large continuous region of the model) it is considered a justifiable approximation to the true case.

For Rayleigh damping, therefore, the damping matrix of Equation 4.16 becomes:

$$C = a_0M + a_1K \quad (4.28)$$

Where a_0 and a_1 are known as Rayleigh damping coefficients. It can be shown that from Equation 4.28 the following relationship holds^{4.31}

$$\xi_i = \frac{a_0}{2\omega_i} + \frac{a_1\omega_i}{2} \quad (4.29)$$

For two known damping ratios for two, usually modal, frequencies the Rayleigh damping coefficients can be evaluated from the resulting simultaneous equations.

An investigation on the effect of soil damping on stress wave amplitude in a pile soil system has been carried out by Armstrong at Napier University^{4.17}. Here a 4m pile was tested undamped and damped by sand and then gravel. For the undamped case, as with Chan^{4.1}, the pile was slung under a crane by flexible ties. As illustrated in Figure 4.15, this, again, resulted secondary reflections caused by the support conditions. The material properties for the experimental and finite element piles are given in Table 4.6. The damping ratio for reinforced concrete is given^{4.32} as 0.15-1.0%. If it is assumed that the frequency dependence of this damping rises from 0%

at zero hertz to 1% at around 800Hz, where the input component frequencies reduce rapidly, values of a_0 (0.0) and a_1 (4.24×10^{-6}) can be derived from Equation 4.29.

Table 4.6 Pile Concrete Material Properties

Property	Experimental (after Armstrong ^{4.17})	Finite Element
Young's Modulus (Nm^{-2})	1.297×10^{10}	1.297×10^{10}
Density (kgm^{-3})	2360	2360
Poisson's Ratio	-	0.22

The results of the finite element experiment are shown graphically in Figure 4.15. The propagation velocity from the finite element trace of 2330ms^{-1} is within 1.5% of the measured experimental value (2300ms^{-1}) and within 0.7% of the theoretical value using Equation 4.22 (2344ms^{-1}).

For the sand and gravel damped cases the pile was housed in a wooden box, filled with uncompacted soil and held in place by three support ties, as illustrated in Figure 4.16. Also in this figure is the finite element model. Unfortunately, modelling the square box using an axisymmetric model is impossible and so, to reduce the prominent boundary reflections that result from this imposed symmetry, but are not present in the small scale tests, the size of the soil annulus is increased to 1250mm from the design size of 350mm.

The experimental results for the gravel and sand damped pile are shown in Figures 4.17 and 4.20 respectively. Only the material density for the damped experiments has been given and so other physical properties are estimated from literature^{4.27} as summarised Table 4.7. Again, the frequency dependence of the damping coefficient is assumed to rise from zero to the stated value at around 800Hz, beyond which it rises rapidly. This provides a value consistent with theory for the frequencies of interest and a higher value for the much larger frequencies generated by the modelling process - so called 'numerical damping'.

Table 4.7 Material Properties for modelled soils

	Gravel	Sand
Density (kgm^{-3})	1600	1470
Young's modulus (Nm^{-3}) ^{4.28}	7.0×10^7	1.7×10^7
Damping Ratio, ξ (%)	10%	4%
Damping Coefficients (a_0, a_1)	0, 4.0×10^{-5}	0, 1.6×10^{-5}
Poisson's ratio ^{4.28}	0.3	0.25

It is noticeable that both traces have a large trough following the initial impact, and subsequent reflections. This trough, it has been found, is apparent when the support ties are included in the model, as illustrated in Figures 4.18 and 4.21. Again, because of the imposed symmetry of the system and the difficulty in finding an exact spring constant for these ties, as the traces continue the modelled results diverge from the experimental case. However, from the initial impact to the first toe reflection, before multiple internal reflections have occurred, this trough is evident and is consistent with the experimental results in that it is more pronounced in the case of the gravel damped pile where the stiffness at the pile head is effectively increased by the denser stiffer material.

Figures 4.19 and 4.22 illustrate the finite element generated traces for the gravel and sand damped piles where the support ties have been excluded. Direct numerical comparison with the experimental results is inappropriate because of the different support conditions and errors inherent in the estimation of soil properties. However, the drop in propagation velocity reported by Armstrong^{4.17} in the damped experimental case is also found in the finite element trace, as summarised in Table 4.8.

Table 4.8 Pulse Propagation Velocities

	Experimental group velocity (after Armstrong ^{4.17}) (ms^{-1})	Finite Element group velocity (ms^{-1})
Undamped Pile	2300	2330
Sand Damped	2050	2202
Gravel Damped	1950	2162

The attenuation of the propagating stress wave can, however, be compared with theory. Reaffirming Briard's formula as Equation 4.30, below, the attenuated velocity magnitude, having travelled a distance, L , is given by Equation 4.31.

$$A = \frac{1}{r} \frac{\rho_{soil}}{\rho_{pile}} \frac{\beta}{c} \quad (4.30)$$

$$v(t) = v_0 e^{-LA} \quad (4.31)$$

where v_0 is the initial velocity and, as before, r is the pile radius, ρ the density, β the soil's shear wave velocity and c the pulse propagation velocity within the pile.

Clearly then, these equations can be rewritten in terms of time to give:

$$v(t) = v_0 e^{-t \frac{\rho_{soil} \beta}{\rho_{pile} r}} \quad (4.32)$$

Hence, if it is assumed that the maximum nodal velocity within the pile model at any one time is representative of that at the stress wave peak the attenuation of this value with time can be compared with theory. This assumption is considered sound for the defect free piles under investigation here as there are no partial reflections apart from at the pile toe.

Such traces are shown for the gravel and soil models described above in Figures 4.23 (a) and (b). For these experiments the gravel stiffness was increased to $14.7 \times 10^7 \text{ Nm}^{-2}$ in order to provide a better differential between the soils for comparison. A number of conclusions can be drawn directly from these graphs. First the addition of concrete damping has increased signal attenuation. This added damping has a less pronounced effect in the case of the gravel damped pile where attenuation due to the soil stiffness is larger and, therefore, dominates. It can also be noted that the addition of soil material damping does not discernibly change the degree of attenuation for the values used. Figure 4.23 (a) shows that the attenuation in the case of the gravel damped pile, when concrete damping is ignored, correlates well with that of the 1-D

theoretical values. This is to be expected as the theory does not consider material damping effects. The fact that the soil damping has reduced spurious reflections from the 'box' boundary is also evident from the later section of the traces. These reflections have been caused by the increase in stiffness of the gravel modelled. Thus a larger proportion of stresses are transferred across the pile periphery into the soil and the soil's shear wave propagation velocity is increased such that reflections from the system boundary become apparent in the recorded trace.

However, for the sand damped pile of Figure 4.23 (b) the attenuation is appreciably less than that of theory. The fact that theory correlates well with traces where concrete damping has been included is serendipitous and not expected (concrete damping is not included in the quoted 1-D theory). The cause of this aberration is identified in the parametric studies shown in Figure 4.24.

The model used for the results in Figure 4.24 is a 0.8m diameter, 11.7m pile in a lower stiffness soil ($E = 5 \times 10^7 \text{ Nm}^{-2}$) with density 1800 kgm^{-3} . The pile's material properties are given as $E = 3.5 \times 10^{10} \text{ Nm}^{-2}$ and density 2400 kgm^{-3} . The increased dimensions of this model indicate that the effects are independent of pile geometry and give a longer trace for analysis, uninterrupted by reflections at the pile's head and toe. Figure 4.24 (a) verifies that the effect is independent of the time step used in the analysis. It is evident that for all the step sizes analysed the difference in particle velocities is less than 10% and any difference does not increase with time.

However, when the lateral resolution, i.e. the mesh density across the piles-soil section, is changed the resultant traces' correlation with theory also changes. As the mesh becomes more dense and the lateral distance between nodes becomes less - the value dx in Figure 4.24 (b) - so the model fits better with theory. It is, therefore, hypothesised that for lower stiffness soils the nodal displacements, and therefore strains, at the pile periphery are larger and so require a denser mesh to model them accurately. The surrounding soil's deformation is effectively 'undersampled' by the nodes in coarse meshes. While the stiffness and mass matrices are linearly proportional for all mesh densities the deformation geometry results in higher proportional strains being found nearer the pile soil-interface. Thus this geometric

non-linearity can only be modelled if the node density is sufficient to model the curvature of the soil displacement. If the mesh is too coarse the strain is effectively calculated over a larger distance and reduced such that its effects are diminished.

This would account for higher stiffness soils, such as the gravel damped pile modelled above and the *in situ* piles described below, fitting well with theory as here the lower soil displacements result in lower strains. Thus there will be less curvature in the soil with respect to distance from the pile periphery and so a coarser mesh than that used in lower stiffness soils will suffice. It would also explain the change in propagation velocity observed for coarser meshes in Figure 4.24 (b). As the nodal distances increase so the recorded strains within the soil decreases and any retarding force will be lessened.

For the *in situ* piles in this study the recorded shear modulus of the surrounding soils are all larger than the uncompacted gravel of the above experiments. Hence, the model mesh density used above is justified. However, if modelling, for example, micro-piles in a loose granular soil this effect should be considered when choosing a suitable mesh topology.

4.2.5 Dynamic Control and Convergence Criteria

The equations of dynamic equilibrium summarised in Equation 4.16 may be used to reproduce the time history response of a structure to a forcing function through step by step integration. This direct integration method utilises two basic concepts^{4.12}:

- i. The dynamic equilibrium equations are satisfied at discrete time points, Δt apart, within the solution interval.
- ii. The change in displacement, velocity and acceleration during these time intervals are postulated. These postulates being definitive of the direct integration scheme applied.

The set of direct integration schema may be subclassed into explicit and implicit methods. Both estimate the unknown displacement, velocity and acceleration at a

time $t+\Delta t$ from the known conditions at t . For explicit dynamics the subsequent system state is resolved from consideration of the equilibrium conditions in its current state. For the implicit case the state at $t+\Delta t$ is obtained by considering the equilibrium at time $t+\Delta t$.

The finite element software used in this study is the LusasTM finite element system^{4,12}. For this case the explicit method offered is the central difference integration scheme while the implicit method is the Hilber-Hughes-Taylor scheme^{4,12}.

For the explicit method displacements for the subsequent time step are estimated from current nodal velocities. This being the case the method is only conditionally stable, that is small time steps must be used to ensure system stability. The critical time step value, which must not be surpassed to ensure stability is given as:

$$\Delta t_{cr} = \frac{2}{\omega_{max}} \quad (4.33)$$

where ω_{max} is the maximum modal resonance of the system under investigation.

For implicit dynamics the equilibrium at time $t+\Delta t$ is calculated from the solution of the equilibrium equation at time step $t+\Delta t$. Thus the solution is necessarily stable and larger time steps can be implemented. However, this comes at the computational cost of inverting the stiffness matrix for each time step. Hence a compromise must be met between speed of solution and stability of results.

For the explicit case the system is limited to being modelled by equally sided elements. As such, for the sake of comparison, Figure 4.25 shows the results from an uninstalled beam made up of square elements. The maximum frequency of oscillation is assumed to be that of the pile head resonance. This can be estimated from the calculated Rayleigh wave velocity and pile diameter from Equation 2.4. If it is assumed that the Rayleigh surface wave is only slightly less than the calculated

shear wave velocity then $\omega_{max} \approx 48\text{kHz}$ and so $\Delta t_{cr} \approx 4.2 \times 10^{-5}$. However, for propagating stress waves the critical time step may also be estimated from

$$\Delta t_{cr} \leq \frac{s}{c} \quad (4.34)$$

where s is the shortest internodal length and c is the pulse propagation velocity. From this the critical time step is estimated as 7.5×10^{-6} seconds. It is this value, the smaller of the two estimates, that is, therefore, chosen as the critical time step length.

For the implicit dynamic method it is suggested^{4,12} that the employed time step should be smaller than that associated with the highest frequency of the system's dynamic load, τ_{max} . That is

$$\omega_{max} = 4\tau_{max} \Rightarrow \Delta t = \frac{0.5}{\omega_{max}} \quad (4.35)$$

For the applied Gaussian pulse, in this case, it can be seen that the power spectrum has low values above 750Hz and so the maximum recommended Δt is calculated as 2.6×10^{-5} seconds.

Referring to Figure 4.25, therefore, it is apparent that the implicit case gives expected results for Δt values even above this recommended value. For the explicit case, however, a resonance has occurred for time steps nearly an order of magnitude lower than the calculated critical time step value. The frequency of oscillation is larger for the shorter time step which supports the view that this is a numerical aberration and is probably caused by internodal resonance rather than structural resonance.

When applied to a larger model of a soil damped pile the results shown in Figure 4.26 are obtained. These results also show a high degree of oscillation, however, the geometric damping provided by the increased system size and inclusion of the soil along with the larger nodal distances has resulted in these oscillations reducing with

time. At 2413Hz, they are also of the order of the expected pile head oscillations calculated by Equation 2.4 as about 3kHz. The response is in marked contrast with the required response shown in Figure 4.28 and that produced by the implicit method shown in Figure 4.29. Here, the pile head ringdown is far less pronounced and the size of the reflection from the pile toe far smaller. It is, however, typical of the published results of Liao and Roesset^{4,6,4.13} who have used the explicit method to generate their results. It is, therefore, suggested that the larger oscillations and increased magnitude of reflection is a result of the stiffness matrix not being inverted and 'overshoot' of the estimated nodal displacements. To improve results the time step would have to be further reduced from those shown in Figures 4.25 and 4.26.

The necessity of a far smaller time step and a finer mesh obligated by the use of square elements means the time saved through using the explicit method is minimal when compared to the necessarily stable implicit integration method. For this study, therefore, the implicit, Hilber-Hughes-Taylor, method has been employed with a time step of 5×10^{-5} seconds.

The results shown have all been obtained through keeping the system default convergence criteria. All these time steps converged on a stable solution within three iterations and no improvement in performance was found by tightening the criterion. Convergence is, therefore, defined by that recommended by Lusas Ltd^{4.12}. Specifically, the Euclidean incremental displacement norm must drop to less than 1%. That is the norm of the iterative nodal displacements as a percentage of the norm of the displacements for that time step must fall to less than 1%. Effectively, this is a measure of how much the structure has moved during the current iteration. Thus, as a solution is converged upon, the value reduces with each iteration until the convergence criterion has been met.

4.2.6 Model Validation Using Field Test Data

This field data was collected as part of the EPSRC (then SERC) investigation into pile testing at the Blyth test site. It has been kindly supplied by Testconsult Ltd, UK^{4.33} along with all the laboratory material test results. It is almost uniquely suited

to the validation of the FEA model described above as a number of designed faults have been deliberately included in the installed piles for research purposes. The data has been collected using the CEBTP dual channel TD-1 data acquisition equipment and a small sledge, instrumented, hammer, as described in Chapter 2. All field test results are presented as an ensemble average of those collected for the named pile to reduce ringdown effects.

The 40m × 35m site contains twenty five installed concrete piles of various lengths and 0.75m diameter. The piles are uncapped and are 5m apart enabling pile grouping effects to be ignored. Five piles have been chosen for verification purposes. Each has a design length of around 11.5m and design faults given as:

- i. Sound Pile
- ii. Single 0.6m length neck at 3.45m
- iii. Two necks, each of 0.6m length at positions: 2.4m and 6.9m
- iv. Single bulb of 2.5m length at 4m
- v. Two bulbs, each of 2.4m length at positions: 1.55m and 5.6m

All design dimensions are included in Figures 4.28,4.32,4.36,4.40, and 4.44 next to the recorded field trace for that pile.

4.2.6.1 Site Investigation Data

The dynamic modulus for the pile concrete was derived from ultrasonic pulse velocity measurements on cube samples using Poisson's ratio values obtained from cylinder resonant frequencies. For the four samples tested the measured dynamic modulus is given as $3.25 \times 10^{10} \pm 8\%$. Poisson's ratio and density values are not given. The soil environment is described as stiff over very stiff clay with a thin peat layer at the surface. The water table is measured at 10m depth and shear modulus and shear wave velocities given in Table 4.9.

Table 4.9 Measured Soil Properties with Depth

Depth (m)	Description	Shear Modulus (MNm ⁻²)	Shear Wave Velocity (ms ⁻²)
0.0-0.2	Peat	-	145
0.2-1.5	Stiff Clay	67	175
1.5-3.0	Stiff Clay	89	200
3.0-4.0	Stiff Clay	119	230
4.0-	Stiff / Very Stiff Clay	235	320

4.2.6.2 FEA Model

One example of the various meshes used for this model is shown in Figure 4.27. This is for the defect free pile with axisymmetric triangular elements as before. The lateral dimension of these elements (dx) is 0.1m with an aspect ratio of 1:3 which, as discussed above, is a suitable mesh density for the soil stiffness of Table 4.9.

The node and element positions remain the same for all models with only the elements' material assignments changing for the different piles. The system model is, therefore, limited to a resolution of 0.3m in the axial dimension and 0.1m in the lateral one. Thus these models are not exact reflections of the in situ case, but rather close representations. These inaccuracies, however, only represent about 3% of the pile length and 6% of the pile radius.

The soil is modelled as two strata with a Poisson's ratio assumed as that of unsaturated clay given in Table 4.4, that is 0.4. Thus, the Young's modulus and density of the soil can be derived from Equations 4.24 and 4.25 respectively. The density of the concrete is calculated from the measured pulse velocity in the field test results and the given dynamic Young's modulus. The Poisson's ratio of the concrete is assumed as 0.22. The damping ratio of the soil is taken as 5%, see Table 4.6. As the soil damping dominates to such an extent in these tests concrete material damping is ignored. The numerical assignments for the materials in these models are summarised in Table 4.10, below.

Table 4.10 Material Assignments for FEA model

	Concrete	Soil ₁ (depth: 0-4m)	Soil ₂ (depth: 4-15m)
Young's Modulus (MNm ⁻²)	3.25	250	650
Poisson's Ratio	0.22	0.4	0.4
Density (kgm ⁻³)	2420	2250	2295
Damping Ratio (%)	0	5	5

4.2.6.3 Results Comparison

The traces for the field test data and finite element generated data can be found in Figures 4.28-4.47. A summary of these results is presented in Table 4.11, below.

Table 4.11 FEA and Field Test Trace Comparison

	Feature	Feature Depth (m) for $c = 3500-4000\text{ms}^{-1}$		
		Design	Field Test	FEA model
Sound Pile	Toe	11.3	10.9-12.5	10.8-12.3
Pile with neck	Neck Onset	3.45	3.4-3.9	3.2-3.6
	Neck End	4.06	Not observed	3.9-4.4
	Toe	11.8	Not observed	Not observed
Pile with two necks	1 st Neck Onset	2.39	2.4-2.8	2.3-2.6
	1 st Neck End	3.00	3.3-3.7	3.0-3.4
	2 nd Neck Onset	6.87	Not observed	Not observed
	2 nd Neck End	7.48	Not observed	Not observed
	Toe	11.3	Not observed	Not observed
Pile with bulb	Bulb Onset	4.00	4.6-5.3	4.0-4.6
	Bulb End	6.50	6.4-7.3	5.6-6.4
	Toe	11.0	Not observed	Not observed
Pile with two bulbs	1 st Bulb Onset	1.55	3.1-3.5	1.9-2.2
	1 st Bulb End	3.85	4.9-5.6	3.3-3.8
	2 nd Bulb Onset	5.65	Not observed	Not observed
	2 nd Bulb End	8.05	Not observed	Not observed
	Toe	11.3	Not observed	Not observed

Immediately noticeable is the fact that the large defects have shielded any features below them from being detected. This is consistent for both finite element and field test data. It is also to be expected given that the change in radius for bulbing (doubling r) and changes in radius for necking (halving r) result in coefficients of reflection of 0.6 and 0.4 respectively. Thus after any given fault - of two changes in section - only about a third at most of the propagating stress wave will be transmitted beneath it. This coupled with the higher degree of attenuation at greater soil depths prevent any indication of pile structure beneath the first fault.

Variability in concrete material properties means the propagation velocity can only be estimated as being between 3500-4000ms⁻¹. For the defect free pile the design length of the pile falls within the acoustic lengths estimated for from these velocities.

For piles with necking (Figures 4.32, 4.33, 4.36, 4.37) both the decrease and increase in radial section have been detected although the position of this increase appears to be estimated deeper than its design depth. This is due to the superpositioning of the two reflected pulses as discussed in Section 4.2.4.1.

This is also true for the piles with bulbs where it is noticeable that the gradual increase in section does not appreciably change the pulse shape in the finite element trace. However, in the field test traces the ramped increase in section over a 1.3m length has caused a smaller reflection than might be expected from a stepped increase. Note that the reflected pulse from the decrease in section in Figure 4.40 is larger than the earlier echo even though it has a smaller incident amplitude due to previous reflections and attenuation. The necessarily discrete nature of the finite element method, therefore, appears to model discrete changes more accurately than smoother more gradual changes.

The mobility curves for field test and finite element data are presented in Figures 4.30, 4.34, 4.38 and 4.42, and 4.31, 4.35, 4.39 and 4.43 respectively. The dynamic stiffness estimates from these graphs are presented in Table 4.12, below.

The absolute values are all slightly higher in the finite element cases than those of the in-situ tests. This may be due to the simplification of the soil stratification for modelling purposes or, more likely, the fact that the radius of the piles in the field, 0.375m, was rounded to 0.4m for the purposes of the FEA model.

Table 4.12 Dynamic Pile Head Stiffness

Pile	In-Situ Testing (MNmm ⁻¹)	FEA Model (MNmm ⁻¹)
1	1.7	2.4
2	2.1	2.7
3	1.8	2.1
4	2.3	2.5
5	2.6	2.8

In both cases the pile stiffness of those with necks are less than those with bulbs. As expected the lowest value for the faulty piles is for that with two necks and the highest for that with two bulbs. It is noticeable, however, that the pile head stiffness is higher, in both finite element and field test data, for the pile with one neck (pile 2) than for the defect free pile.

4.3 REMARKS CONCERNING FEA MODELLING

The finite element model described above has been shown to produce reflection coefficients and attenuation consistent with 1-D theory. This being the case it may be argued that the simpler 1-D methods may be employed to generate the necessary time traces for neural network training. However, as is apparent from the field test data ringdown is still prevalent after filtering through ensemble averaging. This feature is also observable in the finite element data, but not for 1-D simulation. It would not, therefore, be sensible to train a neural network without this correlated noise included as spurious results would likely be produced. Given the necessity for neural network training data to be representative of that which it will be expected to interpret in the field the FEA method is consequently the method of choice for training data simulation.

4.4 TECHNICAL FEASIBILITY

The appropriateness of neural network utilisation for the interpretation of pile integrity test data has been discussed in Chapter 3. The ability of a multilayered feedforward network to 'peak pick' in NDT spectra is known and well documented - Sections 3.4.4.1-3.4.4.3. The second part of this chapter provides empirical evidence for the ability of such networks to cope with the superpositioning of reflections in the time domain in order that the length of any fault can be established. That is, it provides a technical feasibility study by considering uninstalled concrete piles and a multi-layered network's ability to identify, quantify and locate faults within them. The successful completion of this task was considered adequate evidence that the problem domain could be extended to include installed foundation piles of an arbitrary profile.

4.5 FAULT IDENTIFICATION IN AN UNINSTALLED PILE

4.5.1 Problem Domain Definition

The problem domain was limited to uninstalled piles of 5.5m length and 0.75m radius. Specifically this section considers the ability of a network to identify the type (neck or bulb) of defect in a pile of fixed length and change in radius. It was also required to detect the axial length of this fault and its position.

4.5.2 Data Presentation

By visual inspection of the generated time traces it was apparent that a defect's position and type was most recognisable from the start of the trace, before the signal becomes too complex through the superposition of reflected waves - see for example Figures 4.12 and 4.13. It was the first 7.5ms of the generated traces that were, therefore, discretised and presented to the network as its input data. This allowed two reflections from the pile base to be included in each input pattern. Experiments using

25, 50 and 100 linear input units were tried with 50 units giving best results. It is this configuration that was, therefore, adopted.

4.5.3 Network Output

The network's output was designed to be representative of the pile radius at various points along its axial length. As the problem domain was limited to a 5.5m pile with only one degree of defect the output was chosen to be 22 units with outputs ranging from 1 to -1. Each unit represented a 0.25m length of the pile and its outputs corresponded to the likelihood of that length being a neck (-1), a bulb (1) or being sound (0). A sensible choice for the output units' activation function is, therefore, the hyperbolic tangent function with its output range of -1 to +1.

4.5.4 Learning and Test Sets

By choosing to consider the pile in 0.25m sections there were 552 (276x2) combinations of defect length and position within the pile (although some of these give identical results - a defect length of zero gives the same trace wherever it is positioned). Two traces were removed from this set leaving 550 patterns (the cases where the defect ran the entire length of the pile, i.e. a sound pile of a different diameter). From this set 100 randomly chosen patterns were withdrawn. This test set was later used to evaluate the network, while the remaining 450 patterns, the training set were used to teach it.

4.5.5 Learning Parameters

As described in Chapter 3, the learning rate defines the size of step the network takes as it converges on its final solution. If the step is too large the network may not have the resolution to evolve to a suitable state whereas if it is too small the convergence may become unacceptably slow. While Rumelhart, McClelland *et al.*^{4.34} suggest a learning rate of 0.25 or less, Neural Ware Inc.^{4.35} the manufacturers of the software simulator used in this preliminary research suggest a value of around 0.9. However, these values appear to have been chosen with the sigmoid activation

function in mind rather than the tanh function employed in this study. Preliminary testing indicated that initial weight changes using such values were too large. This resulted in the units being forced to give outputs from their saturated region so leading to a very poor system performance.

Two methods may be employed to counteract this problem. First the learning rate can be lowered to reduce the magnitude of the weight changes. Second the net input to the unit can be scaled, using the temperature parameter described in Chapter 3, so flattening the activation function. This will enlarge its linear region and reduce a unit's output for a given input.

A full parametric study of these changes effect on network learning is shown in Figures 4.48 and 4.49. Here the network effectiveness was measured by averaging the mean squared output error over all the patterns in the test set. The mean squared output error being described by Equation 4.36, below.

$$E = \frac{1}{N} \sum_j^N (\hat{y}_j - y_j)^2 \quad (4.36)$$

where N is the number of output units, \hat{y}_j the target output for the unit j and y_j the observed output.

This study shows the 'ravine' of suitable values that may be chosen and how they strongly correlate with the initial weight changes of a typical hidden unit. If the values are both large the weight change is too large and the network learns badly. If both values are too small then the weight change is very small and the network doesn't learn at all (for the smallest values the weight update is zero to 5 decimal places).

This experiment was repeated with networks of one, two and three hidden layers and it was found that the more hidden layers there are the more the network was affected by the choice of learning parameter. This is due to early learning in multilayer

networks being slowed by the gain term in the weight update rule ($\tanh'[\text{net}_i]$). This, in turn, reduces the weight changes for the lower layers of the system which are reduced even further when the net input is scaled. Values were chosen that produced good results for up to three hidden layers and encouraged a reasonable rate of convergence to the system's state of optimum performance. The scale selected for this study was, therefore, 0.1 and the learning rate 0.25, as illustrated in Figure 4.50. As can be seen these are classic plots of network learning. The systems containing more layers took longer to train, but converged to a slightly better solution. One epoch is one cycle through the training set and the three layer system converged to its optimum value after around 400 epochs.

4.5.6 Network Structure

In selecting the network architecture the developer is forced to compromise between system performance and speed of training. As seen above, the more layers present in a system, the more epochs the network takes to train. Also because of the increase in the number of weights each epoch takes up more CPU time. Training then becomes a time consuming process. It is also true that simply making the network bigger does not necessarily increase its performance. As described in Chapter 3 overtraining occurs when the network capacity is too large for the task it has been set to learn. The network overfits the training data and learns it 'parrot fashion' rather than learning the general rules needed to effect the mapping. This leads to poor results when the network is assessed using the test data. Conversely bottlenecking occurs when there are not enough units in a hidden layer for the network to make an adequate *internal representation* of the presented data resulting in a loss of performance.

A full study of the relative performances of different system architectures are shown in Figures 4.51 and 4.52. These graphs show the optimum results obtained by the network. However, it should be noted that some of the larger systems did go on to overtrain.

This parametric study of the network architecture revealed that the most suitable networks were either a one layer network with twenty units or a two layer one with ten units in each layer. In the networks with more units the increase in system performance was small compared with the increase in training time. One point of note is that the network's performance did not appreciably improve when more than two layers are used. This concurs with Kolmogorov's theorem which states that any continuous function can be approximated using one hidden layer and any non-continuous function can be approximated with two^{4.36}.

The final network selected for analysis was, therefore, a three layer network with an input layer of fifty linear units, one hidden layer of 20 non-linear, tanh, units and an output layer of 22 non-linear, tanh, units. This was trained using the back propagation algorithm with a learning rate of 0.25 and a temperature factor of 0.1 scaling the units' net input.

4.5.7 System Repeatability

The system's consistency was ensured by repeating the experiment a further four times. Each network had a different training set and different starting weights (small and random as suggested by Rumelhart, *et al.*^{4.34}). The results presented in Figure 4.53 verify that this network's performance was independent of training set and starting weights.

4.5.8 Network Results

One of the benefits of repeating the experiment four times was that a map of the network's fault finding abilities could be made in the knowledge that the results are not training set dependent. Figure 4.55 is such a map with the lighter areas indicating larger errors. This clearly illustrates how the network found difficulties in detecting smaller defects (areas to the left side of the graph), defects at the pile head (areas towards the bottom of the graph) and defects at the pile toe (the diagonal line where defect position and defect length equal five and a half). This is what one might expect from visual inspection of the time traces and is strong evidence that the

network learned the rules governing the interpretation of these traces.

Figures 4.56 and 4.57 show, graphically, examples of the system's output for some of the test set. In Figure 4.56 the output for the sound pile can be seen. The top trace shows the required output for the time trace presented while beneath this is the actual response of the network. For the sound pile, therefore, a constant value of zero is wanted as neither necking (-1) nor bulbing (+1) is present. This format is followed for Figure 4.57, although the labelling has been removed for the sake of clarity.

In Figure 4.57 a set of outputs representative of test set are shown. These support the earlier assertions made about the network's strengths and weaknesses. Small necks are hardly detectable and necking at the pile head leads to spurious outputs for the length below the defect.

The apparent ability of the network to detect bulbing more efficiently than necking may, in fact, be due to the change in cross sectional area being greater for the bulbing examples than for the necking ones. Hence no conclusions can be drawn from this observation.

The problem of detecting the smallest defects (0.25m) may be explained by the sampling rate of the trace presented to the network. In the time between samples (0.15ms) a stress wave travelling at 3500ms^{-1} will cover about half a meter. The temporal resolution of the pile response may, therefore, be too coarse to be transformed to such a high spatial resolution. Increasing the sampling rate of the time trace, however, will necessitate an increase in the number of input units. This leads to an increase in size of the weight space and so to the problem of overtraining. Suitable pre-processing offers a potential solution to this dilemma and is discussed, with reference to system development, in Chapter 6.

4.5.9 Noise Utilisation

One of the advantages of using artificial neural networks is their ability to overcome the problem of noise in the test set. This is shown in Figure 4.54 where one can see

that the networks performance gradually decreases as the maximum amplitude of the noise is increased.

This noise was uniformly distributed over a defined bandwidth and was injected into the net inputs of all the network's units. The average absolute value for the net input to a hidden unit was about five, therefore a noise value of one corresponds to around 20% noise in the unit's input. The networks effectiveness diminished slowly, with no catastrophic failure. This characteristic of ANNs is known as *graceful degradation* and is considered a major advantage in the use of this processing method.

The injection of noise, however, can also have a positive effect. When used sparingly it can force the network to generalise on only the most salient points in the training set. Twenty percent noise was added to our system at the start of training dropping exponentially to zero as the end of training approached (1500 epochs). This led to a trained system which gave reasonable values for experimental traces published by Chan^{4.1}, even though the error for the finite element training data was higher (Figure 4.58).

The poor response for the necking trace is probably due to the low frequency term present in the experimental data, but missing in the finite element data. However, the system has undeniably differentiated between the faulty piles and the sound one and has made a reasonable attempt to identify the defects present.

4.6 SUMMARY AND CONCLUSIONS

Representative training data is recognised as a prerequisite for successful neural network learning.

Network training using collated field test data is impossible due to uncertainty inherent in both input and output data sets.

The finite element method is a method of generating time traces which include features associated with pile head ringdown and radial shear wave propagation within the soil.

The presented model has measured particle velocity attenuation consistent with that of one dimensional wave theory. The mesh density required for this correlation to hold is dependent on the stiffness of the soil being modelled. Lateral nodal distances of 0.1m were found to be acceptable for soil stiffness greater than $2 \times 10^8 \text{ Nm}^{-2}$ while for soils of $2 \times 10^7 \text{ Nm}^{-2}$ this distance needed to be halved.

The proportion of the incident pulse that is reflected and transmitted across a change in pile section is consistent with one dimensional wave theory. For FEA elements with an aspect ratio of less than 4 the numerically modelled results are consistently within 5% of those calculated through 1-D theory.

Results for the finite element model are consistently larger (around 10%) than *in situ* field test results due to the difference in design radius. Calculated fault depths are consistent with theory and correspond well with field test data. For all 5 piles considered the design pile length is within the range calculated from the resultant trace and the limiting propagation velocities: 3500ms^{-1} and 4000ms^{-1} .

Finite element generated traces for uninstalled concrete beams have been used to train a multi-layered network with hyperbolic tangent activation units using the back propagation algorithm.

The network has successfully identified the position and axial length of faults with these piles with a degree of effectiveness consistent with the known limitations of the test method. That is, smaller faults and faults at the pile head and toe are more difficult to detect.

This network has identified faults in experimental data when the finite element training data has had white noise (20% of the average input unit value) added to it.

These results support the hypothesis that a neural network trained using finite element trained data may provide a tool for the automated interpretation of sonic echo, integrity test traces.

This thesis will continue with a summary of the hardware and software necessary for the development and utilisation of such a system.

REFERENCES

- (4.1) Chan, H-F C, Non-Destructive Testing of Concrete Piles using the Sonic Echo and Transient Shock Methods, PhD Thesis, University of Edinburgh, 1987
- (4.2) Davis, A G , and Dunn, C S , From Theory to Field Experience with the Non-Destructive Vibration Testing of Piles, Proc. Inst. Civ. Engrs, Part 2, 57, December 1974, pp 571-593.
- (4.3) Paquet, J, Pile Integrity Testing - the CEBTP Impedance Profile, Proc. Conf. Institution of Civil Engineers, In: Piling Europe, London, 1992.
- (4.4) Briard M, Controle des Pieux par la Methodes des Vibrations, Annls Inst. Tech. Batim., 21st Year, No. 270 (1970) pp105-107.
- (4.5) Michaelides O, Gazetas G, Bouckovalas G, and Chrysikou E, Approximate Non-Linear Dynamic Axial Response of Piles, Géotechnique, Vol. 48, No. 1 (1997) pp33-53.
- (4.6) Liao S T, and Roesset J M, Dynamic Response of Intact Piles to Impulse Loads, Int. J. for Numerical and Analytical Methods in Geomechanics, Vol. 21 (1997) pp255-277.
- (4.7) Makris N, and Gazetas G, Displacement Phase Differences in Harmonically Oscillating Pile, Géotechnique, Vol. 43, No. 3 (1993), pp135-150.
- (4.8) Smith E A L, Pile Driving Analysis by the Wave Equation, J.S.M.F.D, A.S.C.E., Vol. 86, SM4 (1960) pp35-61.
- (4.9) Chandrupalta T R, and Belegundu A D, Introduction to Finite Elements in Engineering, Prentice-Hall, Englewood Cliffs , New Jersey (1991).
- (4.10) Desai C S, Finite Element Procedure, Prentice-Hall, Englewood Cliffs ,

- New Jersey (1979).
- (4.11) Bathe K -J, Finite Element Procedure, Prentice-Hall, Englewood Cliffs , New Jersey (1996).
 - (4.12) FEA Ltd, LUSAS Theory Manual I, Finite Element Analysis Ltd, Kingston Upon Thames, UK.
 - (4.13) Liao S T, and Roesset J M, Identification of Defects in Piles Through Impact Testing, Int. J. for Numerical and Analytical Methods in Geomechanics, Vol. 21 (1997) pp277-291.
 - (4.14) Wong F L and Topping B H V, Finite Element Studies for Non-Destructive Vibration Testing, Computers and Structures, Vol. 31, No. 3 (1988) pp653-669.
 - (4.15) Topping B H V and Wong F L, Finite Element Modelling of The Sonic Method of Testing Masonry Structures, Computers and Structures, Vol. 41, No. 1 (1991) pp109-136.
 - (4.16) Sibbald A, Impact hammer Testing of Masonry Sewers, PhD Thesis, University of Edinburgh (1987).
 - (4.17) Armstrong D M, Integrity Assessment of Structures Using Modal Testing, PhD Thesis, Napier University, Edinburgh (1994).
 - (4.18) Blyth SERC Project, Testconsult Ltd, (c1990).
 - (4.19) Nevill A M, Elasticity, Shrinkage, and Creep, in Properties of Concrete, 3rd Edition, Longman Scientific and Technical (1993) p359.
 - (4.20) Neville A M and Brooks J J, Elasticity and Creep, in Concrete Technology, John Wiley and Sons (1993) p209.
 - (4.21) Khalaf F M, Hendry A W and Fairbairn D R, Mechanical Properties of Materials used in Concrete Blockwork Construction, Magazine of Concrete Research, Vol. 44, No. 158 (1992) pp1-14.
 - (4.22) Wong F L, Investigations into Non-Destructive Methods of Structural Testing Using Finite Element Analysis, PhD Thesis, University of Edinburgh (1987).
 - (4.23) Kolsky, Stress Waves in Solids, Oxford University Press (1953)
 - (4.24) Keedwell M J, Rheology and Soil Mechanics, Elsevier Applied Science Publishers (1984)
 - (4.25) Viggiani G and Atkinson J H, Géotechnique, 45, No. 2 (1995) pp249-265
 - (4.26) De Magistris F S, Koseki J, Amaya M, Hamaya S, sato T, and Tatsuoka F, A Triaxial Testing system to Evaluate Stress-Strain Behaviour of Soils for Wide Range of Strain and Stress Rate, Geotechnical Testing Journal, Vol. 22, No.1 (1999) pp44-60

- (4.27) Winterkorn H F and Fang H-Y, Foundation Engineering Handbook, Van Nostrand Rienhold (1975)
- (4.28) Das B M, Advanced Soil Mechanics, 2nd Edition, Taylor and Francis (1997).
- (4.29) Whitman R V and Richart F E Jr, Design Procedures for dynamically loaded foundations, J. Soil Mech. And Found. Div. Proc., ASCE 93, No. SM6 (1967) pp169-193
- (4.30) Abbiss C P, The Effects of Damping on the Interpretation of Geophysical Measurements, Géotechnique, Vol. 36, No. 4 (1986) pp563-580.
- (4.31) Ali-Ahmed H, Non-Destructive Testing of Arch Bridges, PhD Thesis, Napier University, Edinburgh (1998)
- (4.32) Smith J W, Vibration of Structures, Applications in Civil Engineering Design, Chapman and Hall (1988)
- (4.33) Testconsult Ltd., Blyth SERC Project, Project Report, Testconsult Ltd., Warrington, UK (c1990)
- (4.34) Rumelhart D E, McClelland J L and The PDP Research Group, Parallel Distributed Processing, Volume 1: Foundations, MIT Press, (1986)
- (4.35) Neuralworks Professional II, User Manual, Neural Ware Inc., (1988)
- (4.36) Kůrková V, 'Kolmogorov's Theorem and Multilayer Neural Networks', Neural Networks, Vol.5 (1992) pp501-506.

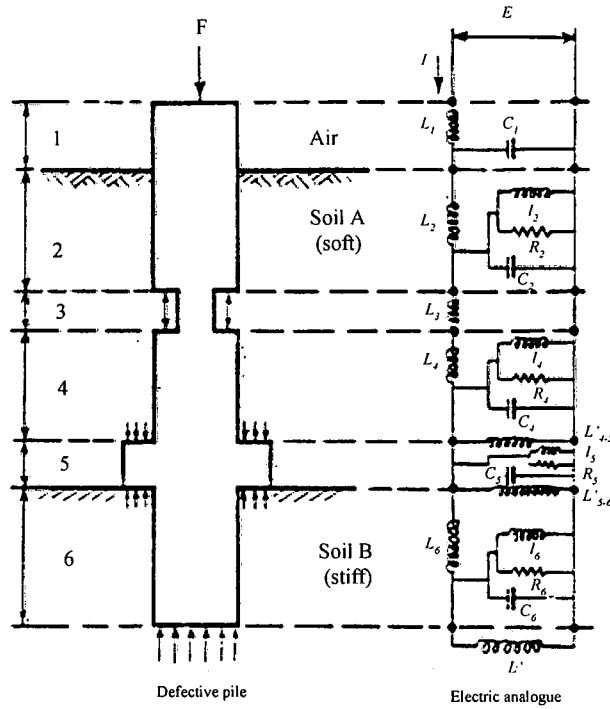


Figure 4.1 Electrical analogue of an installed piled foundation (after Davis and Dunn^{4.2})

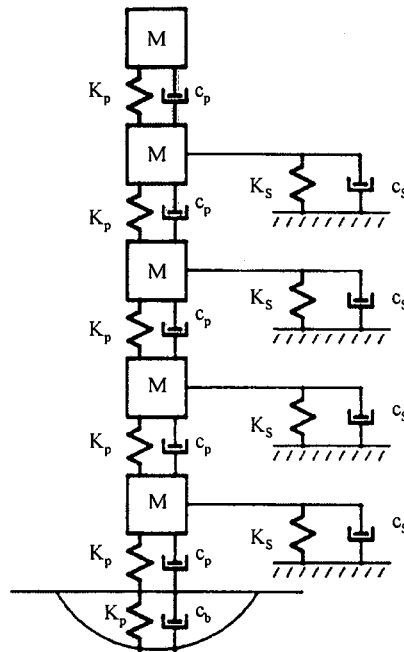


Figure 4.2 Lumped mass model of a pile-soil system (after Chan^{4.1})

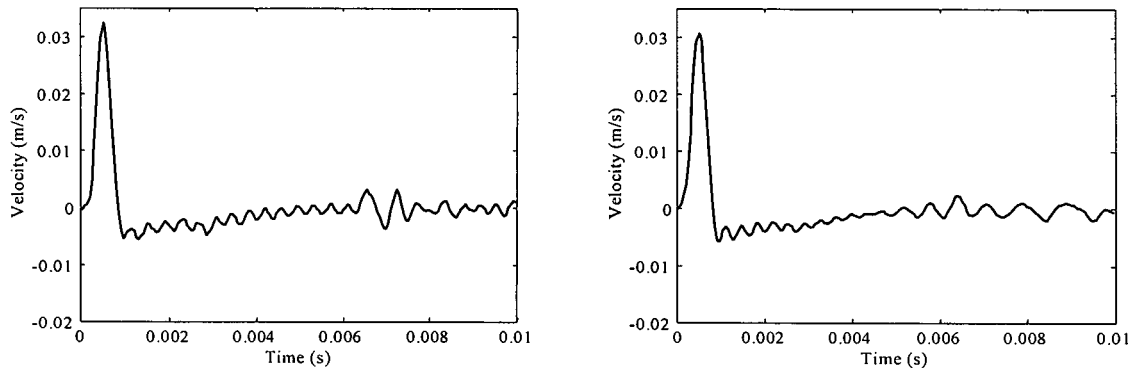


Figure 4.3 Velocity response from a model containing (a), left, quadrilateral elements and (b), right, triangular elements

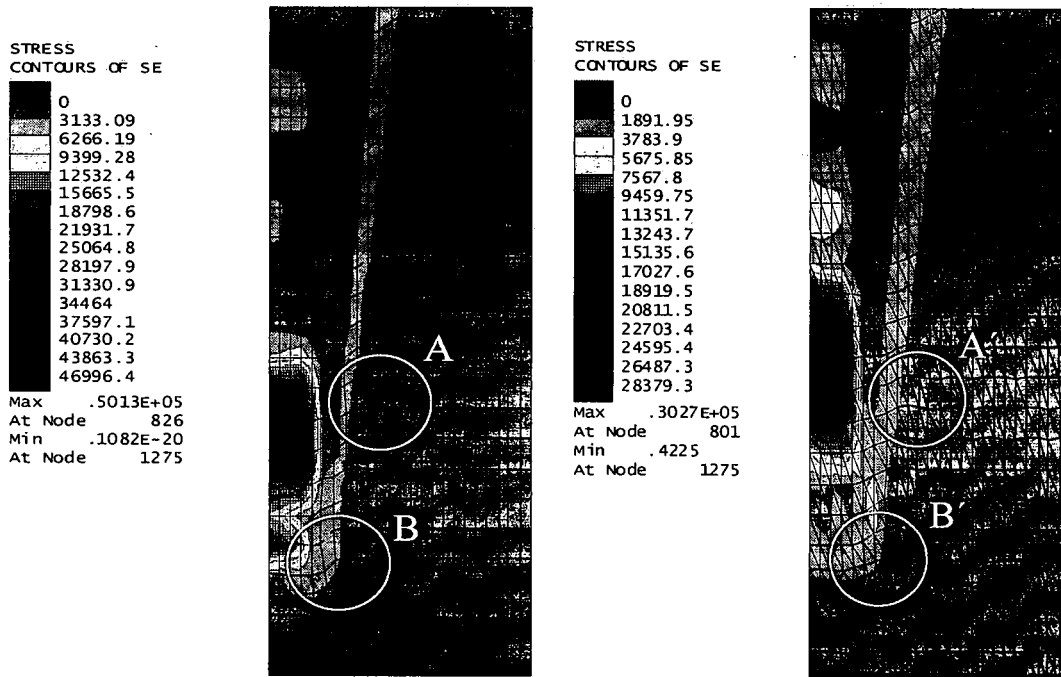


Figure 4.4 Contour plots of principal stresses with deformed mesh superimposed for (a), left, quadrilateral elements and (b), right, triangular elements

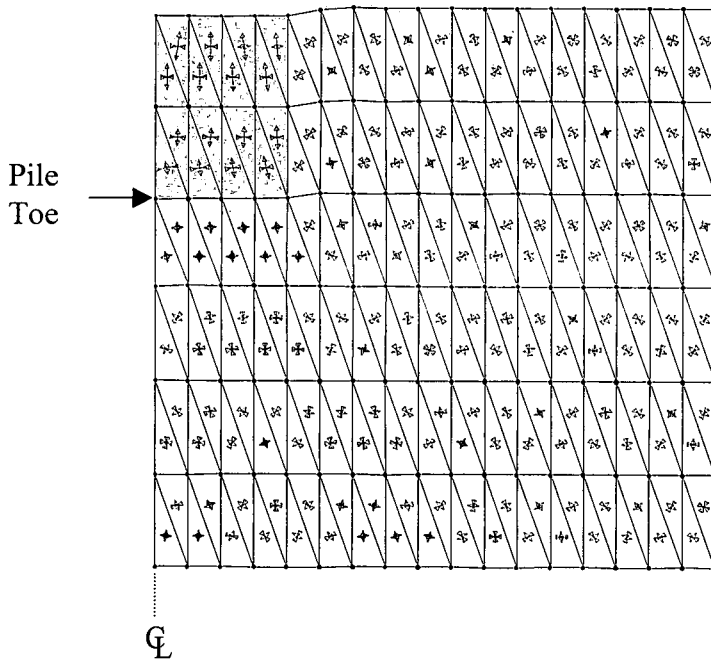
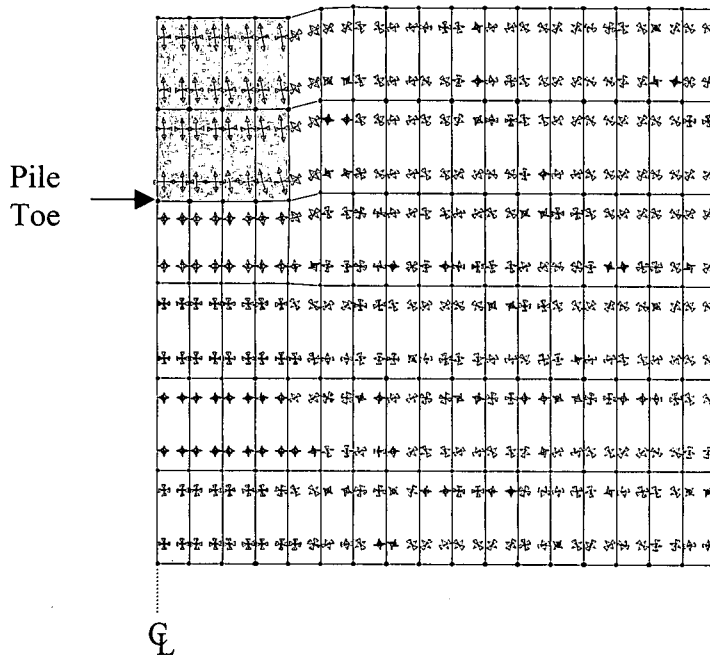


Figure 4.5 Gauss point stresses with deformed mesh superimposed about the pile toe for (a), top, quadrilateral elements and (b), bottom, triangular elements

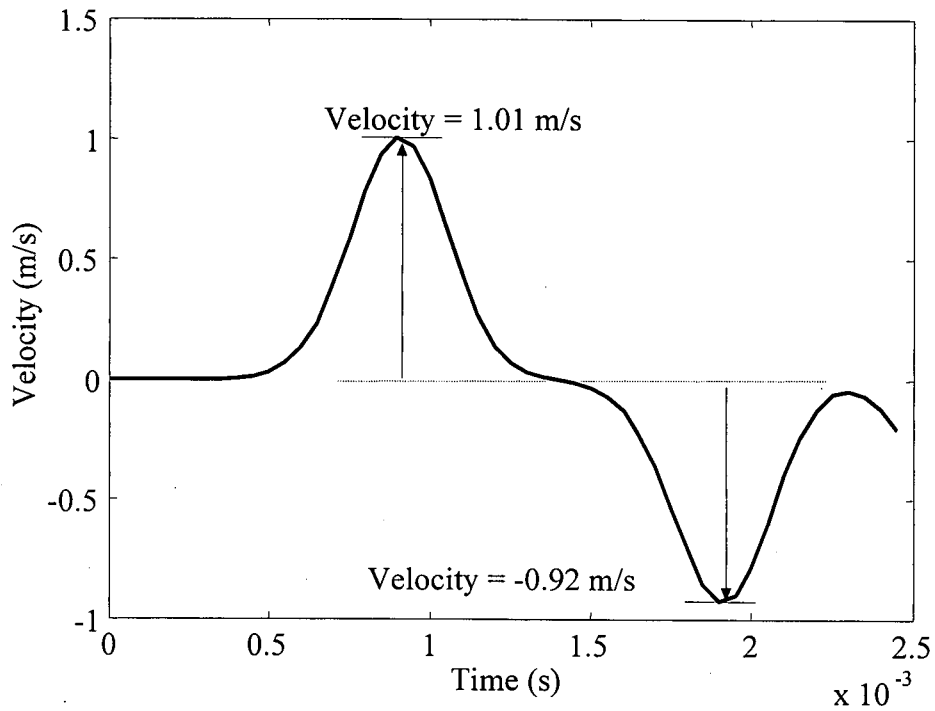


Figure 4.6 Nodal velocity response due to propagating stress wave with reflection

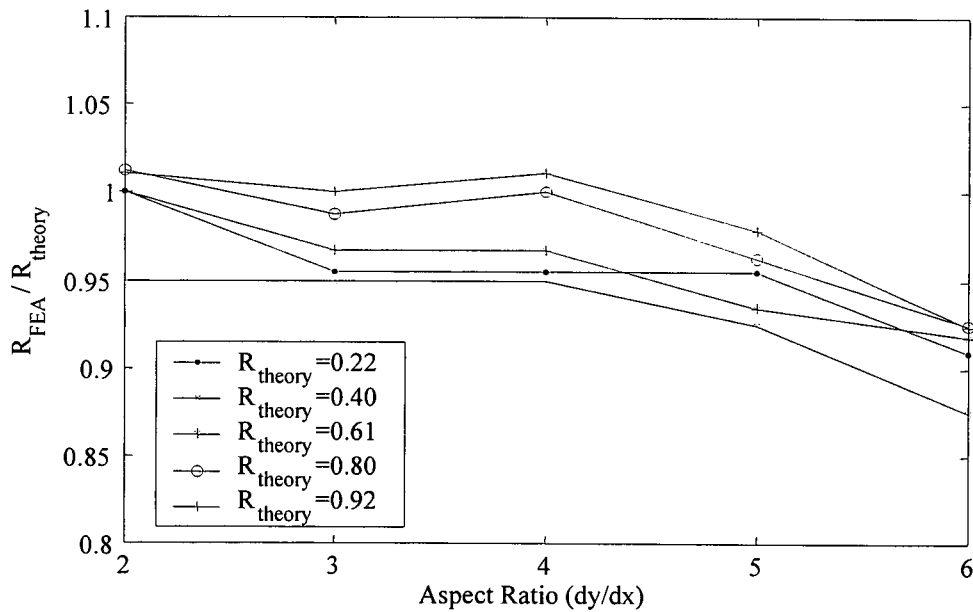


Figure 4.7 Reflection coefficient dependency on element aspect ratio

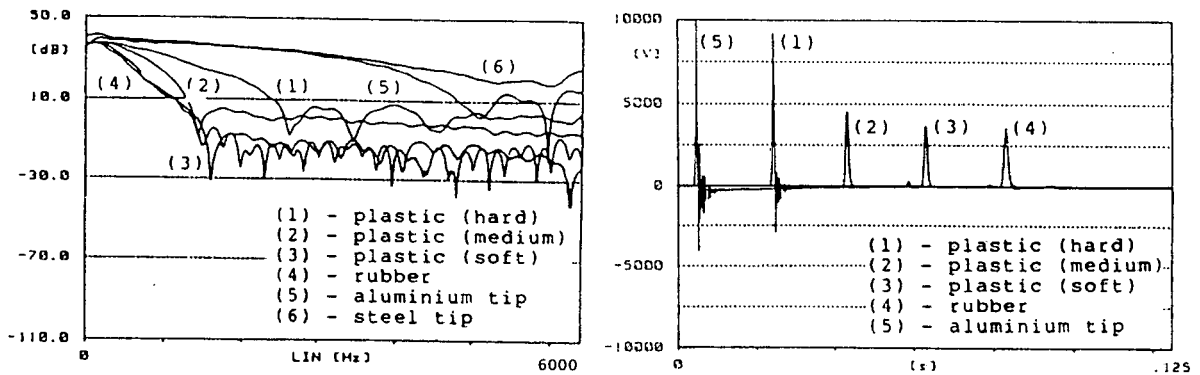


Figure 4.8 Small sledge hammer (a), left, spectral responses and (b), right, time traces (after Sibbald^{4.16})

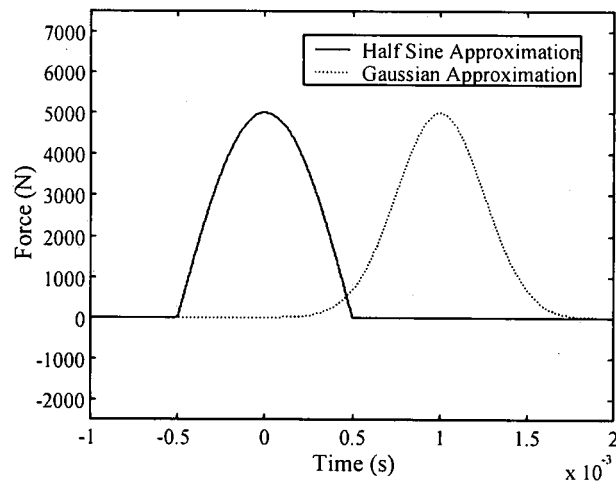


Figure 4.9 Half sine and Gaussian input pulse approximations

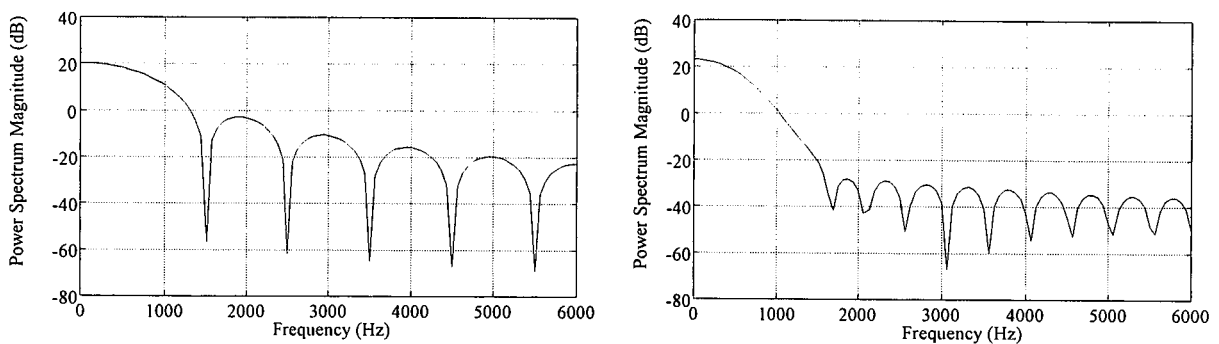


Figure 4.10 Power spectra for (a), left, half sine pulse and (b), right, Gaussian pulse

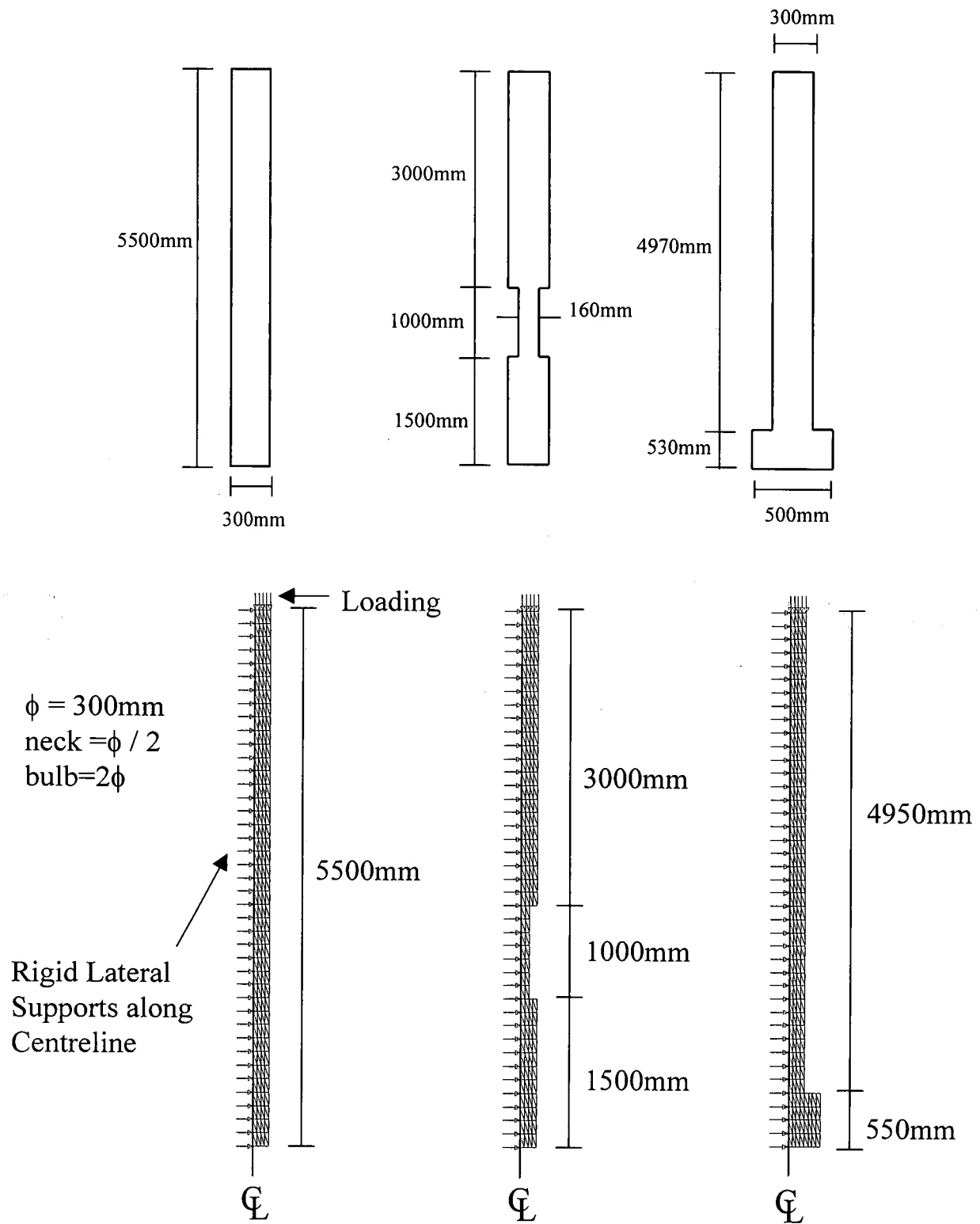


Figure 4.11 Experimental models (after Chan^{4.1}), top, and finite element models, bottom

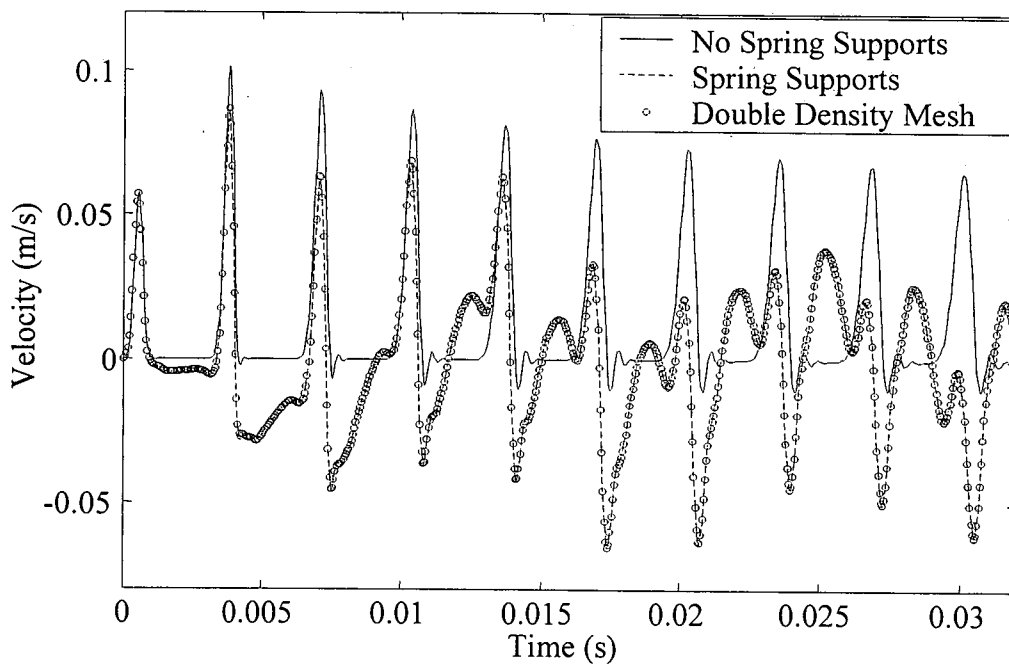
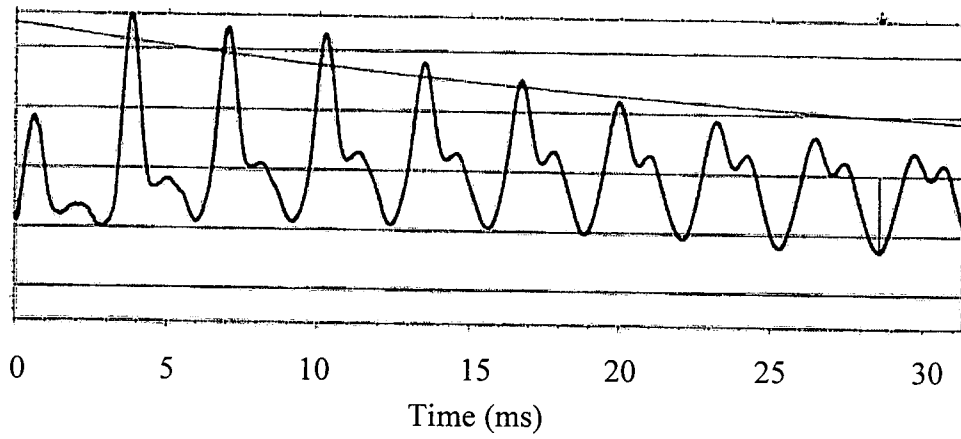


Figure 4.12 The velocity response of an uninstalled, defect free, pile (after Chan^{4.1}), top, and its modelled Finite Element results, beneath.

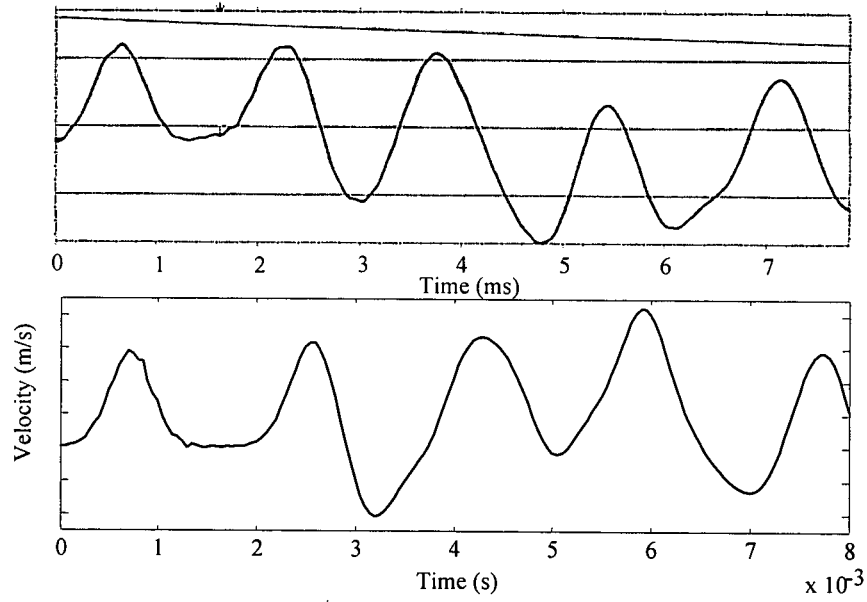


Figure 4.13 Velocity response of an uninstalled pile with necking (a), top, experimental (after Chan^{4.1}) and (b), bottom, finite element generated

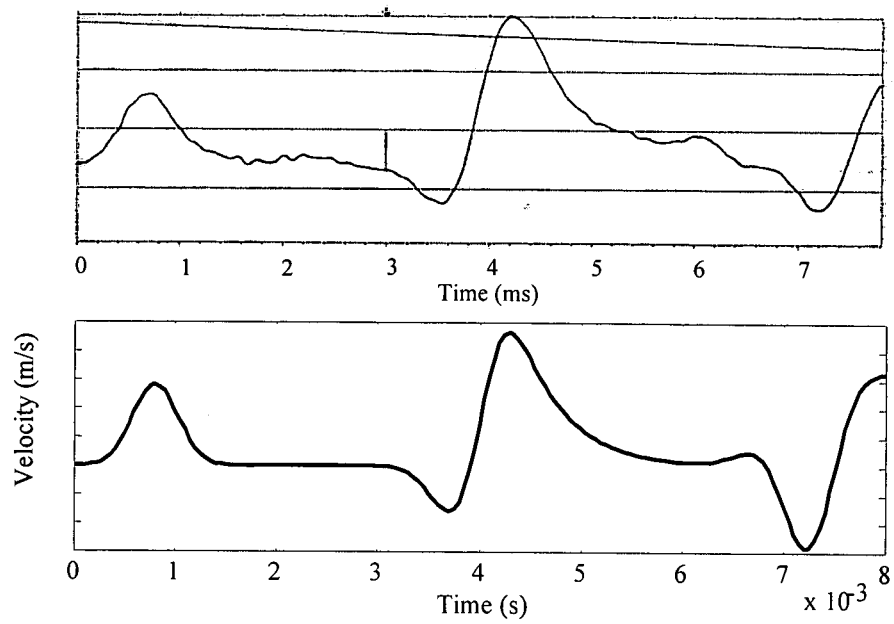


Figure 4.14 Velocity response of an uninstalled pile with bulbing (a), top, experimental (after Chan^{4.1}) and (b), bottom, finite element generated

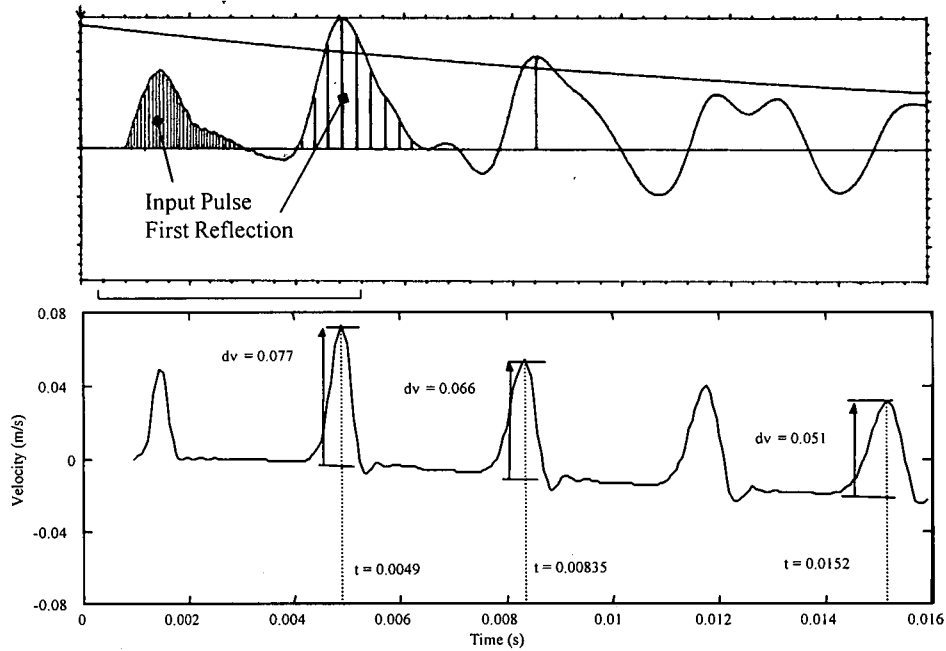


Figure 4.15 Velocity response of an uninstalled, defect free, pile (after Armstrong^{4.17})

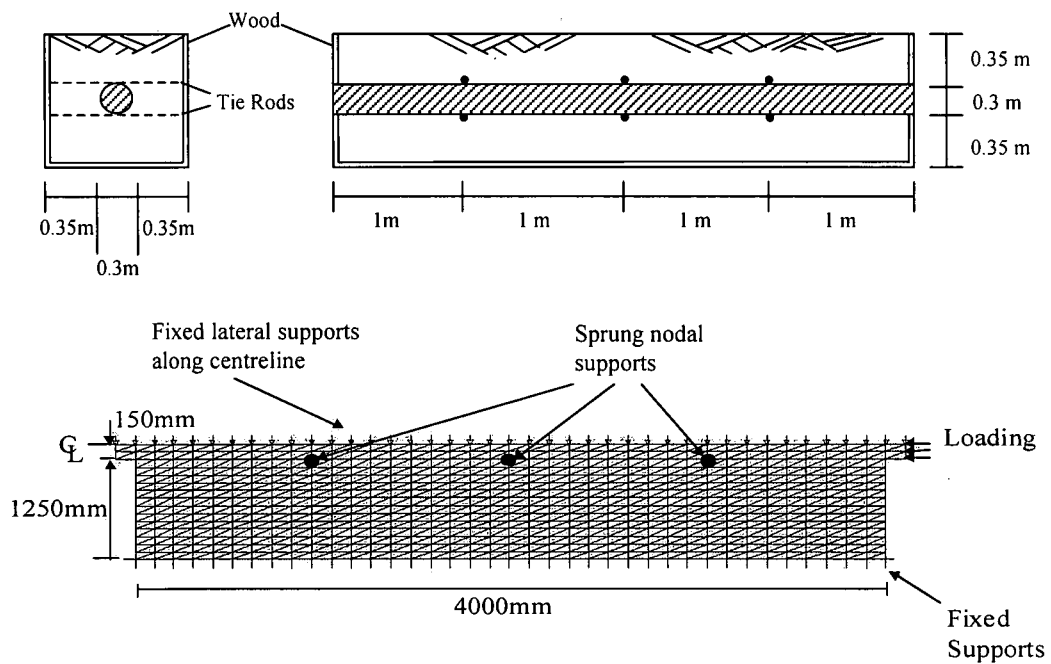


Figure 4.16 Experimental setup for small scale testing of installed foundation piles (after Armstrong^{4.17}), top, and finite element model, bottom.

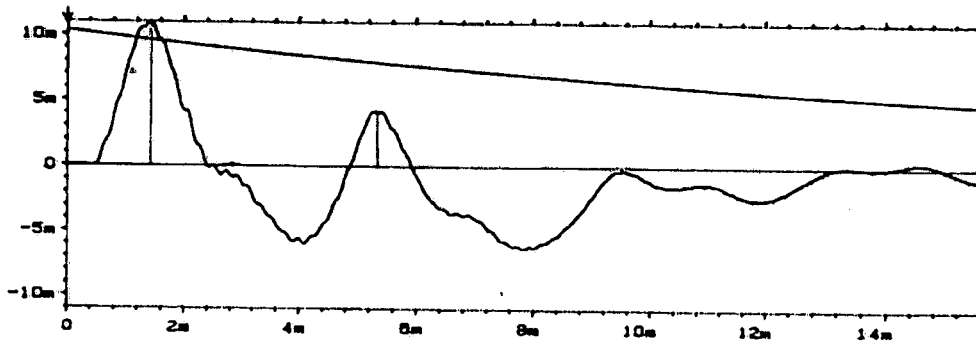


Figure 4.17 Experimental pile head velocity response for a gravel damped pile (after Armstrong^{4.17})

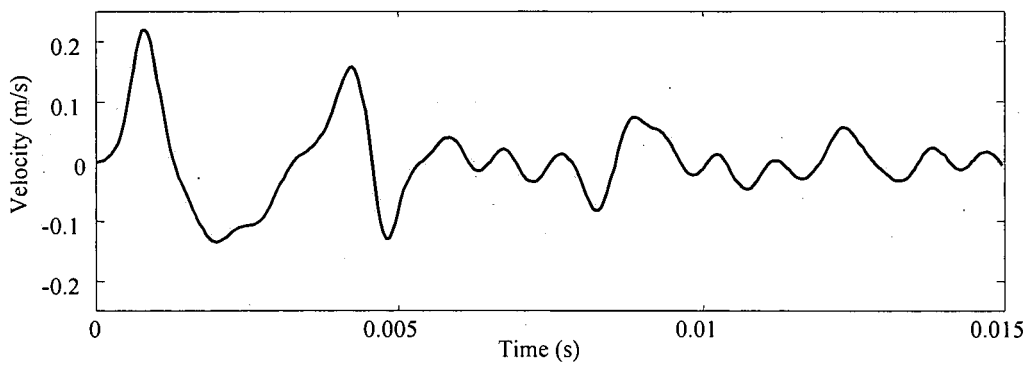


Figure 4.18 Finite element generated response with support ties

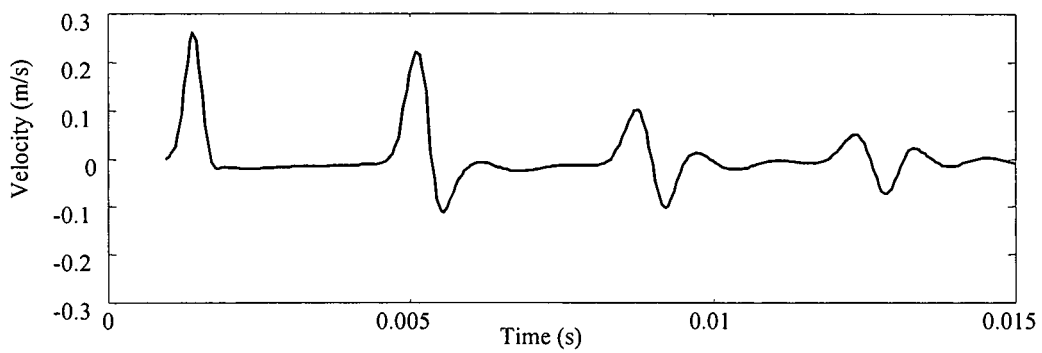


Figure 4.19 Finite element generated response without support ties

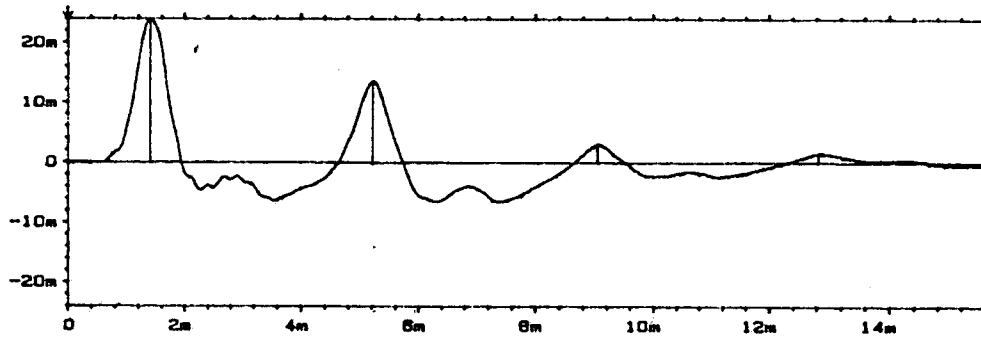


Figure 4.20 Experimental pile head velocity response for a sand damped pile (after Armstrong^{4,17})

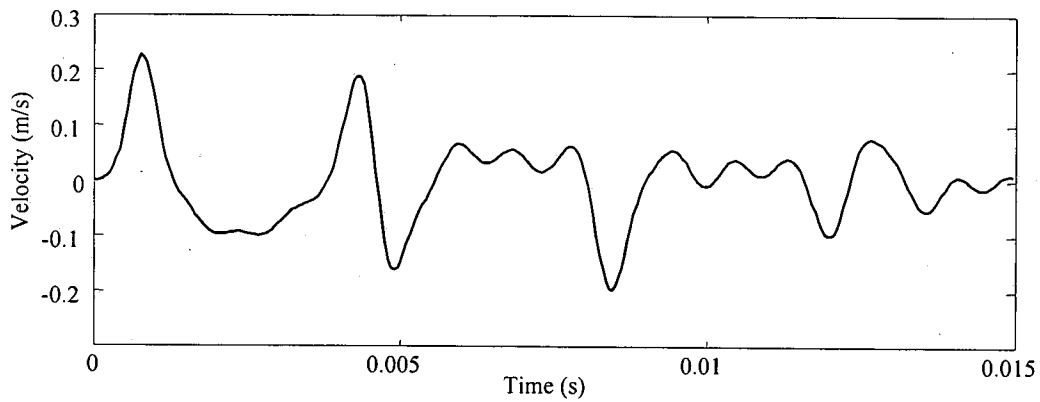


Figure 4.21 Finite element generated response with support ties

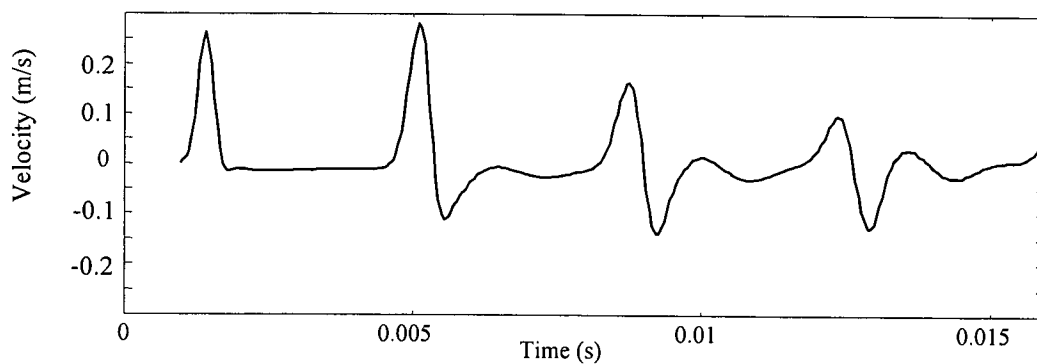


Figure 4.22 Finite element generated response without support ties

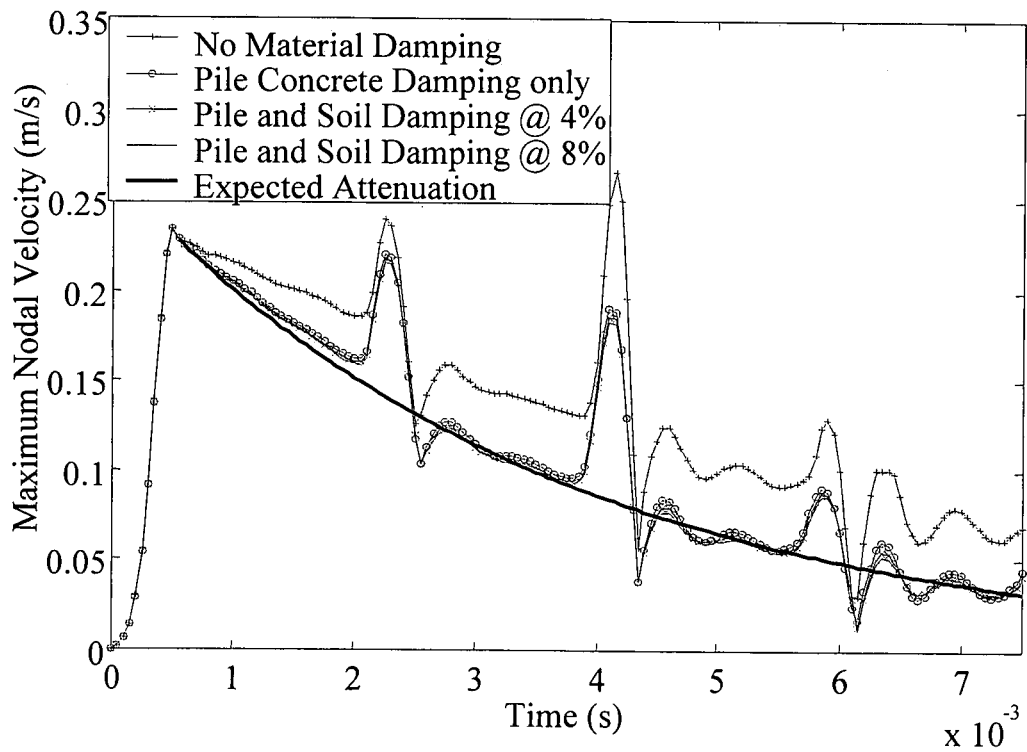
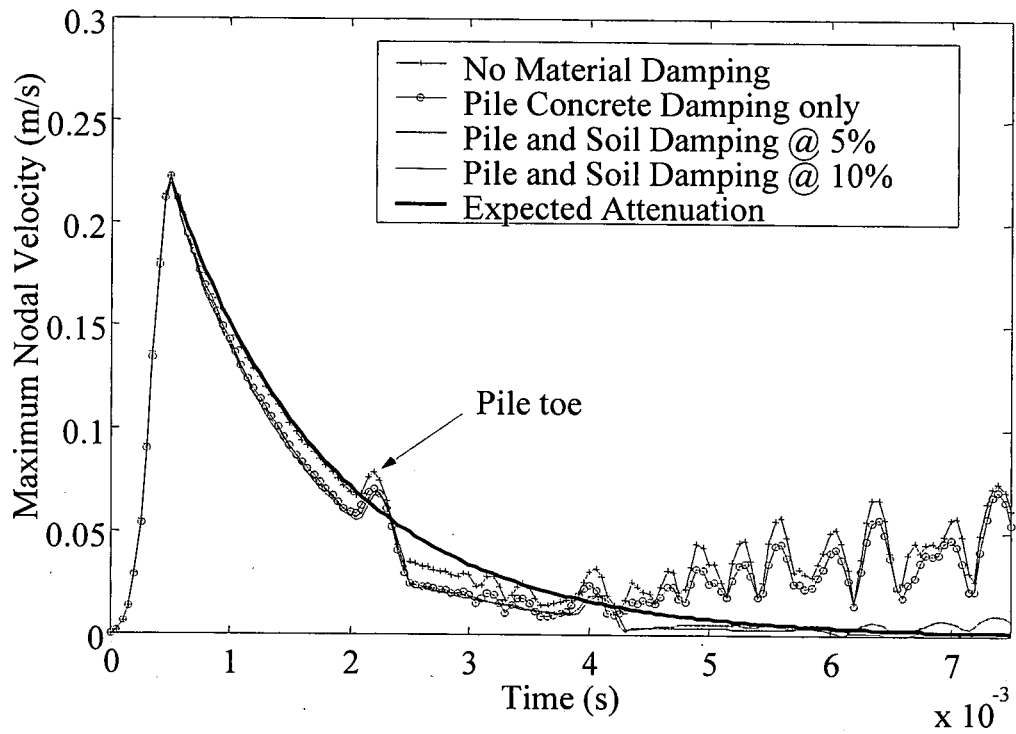


Figure 4.23 Nodal response envelope with predicted response from Briard damping equations for (a), top, gravel and (b), beneath, sand

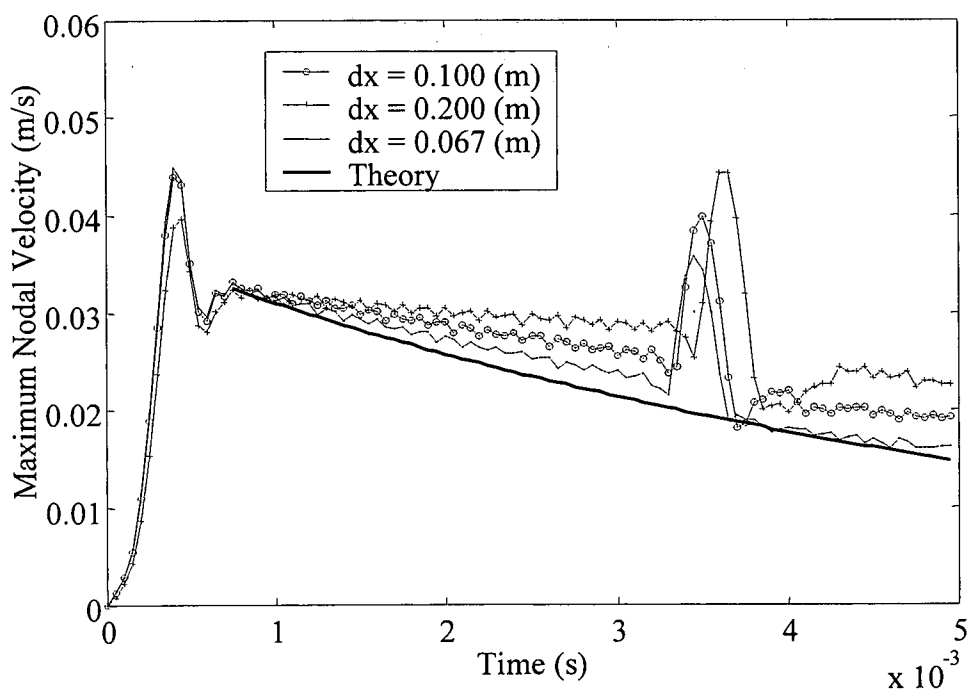
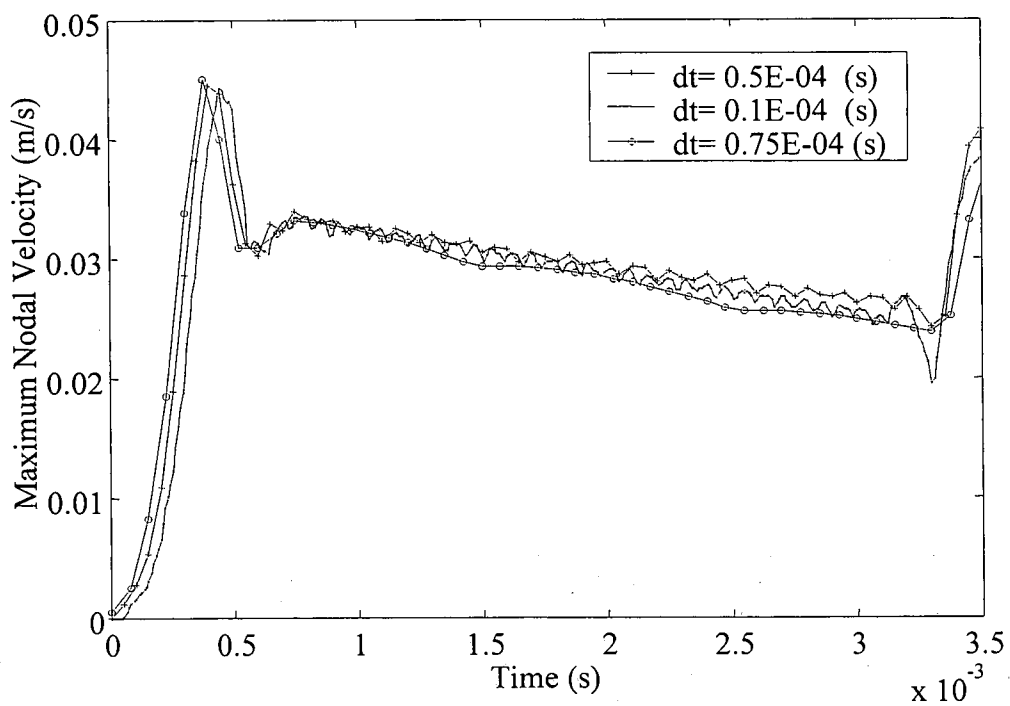


Figure 4.24 Attenuation dependency upon (a), top, time step value, dt , and (b), beneath, lateral element dimension i.e. element widths, dx , across the pile-soil section

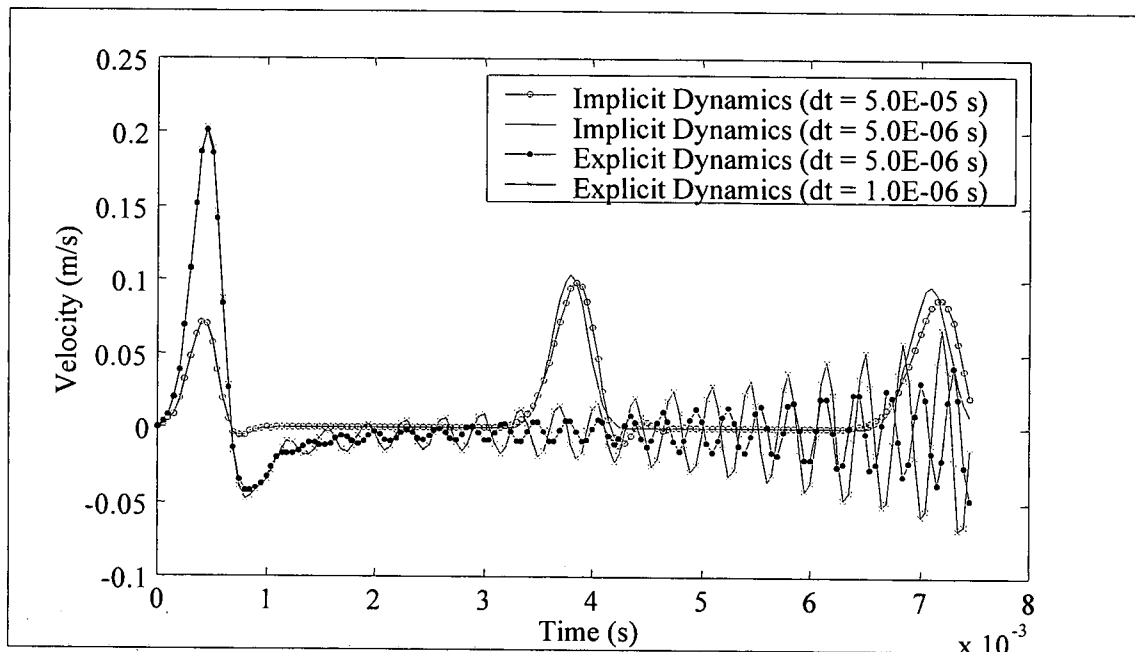


Figure 4.25 Parametric study of time step dependency for an uninstalled pile using explicit and implicit methods

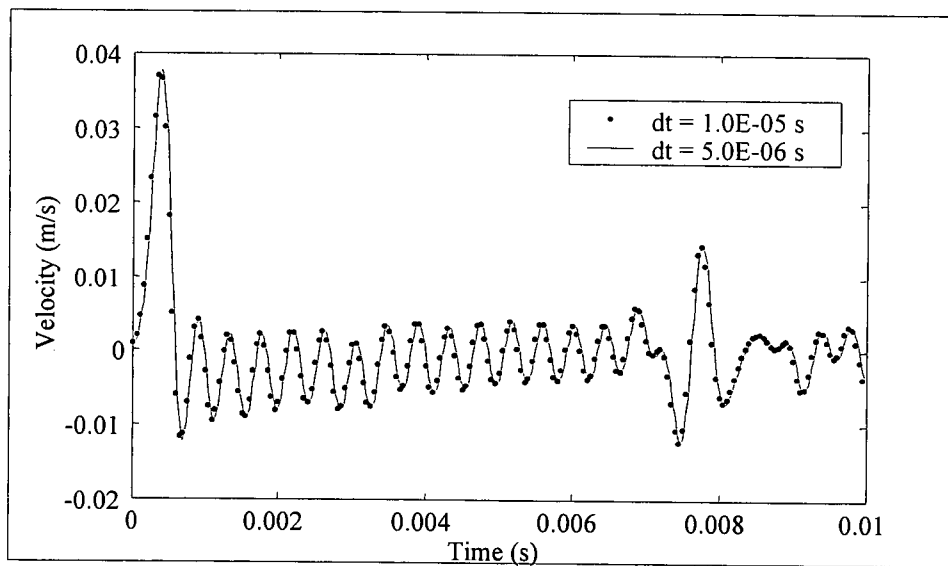


Figure 4.26 Explicit dynamic control method for an installed pile.

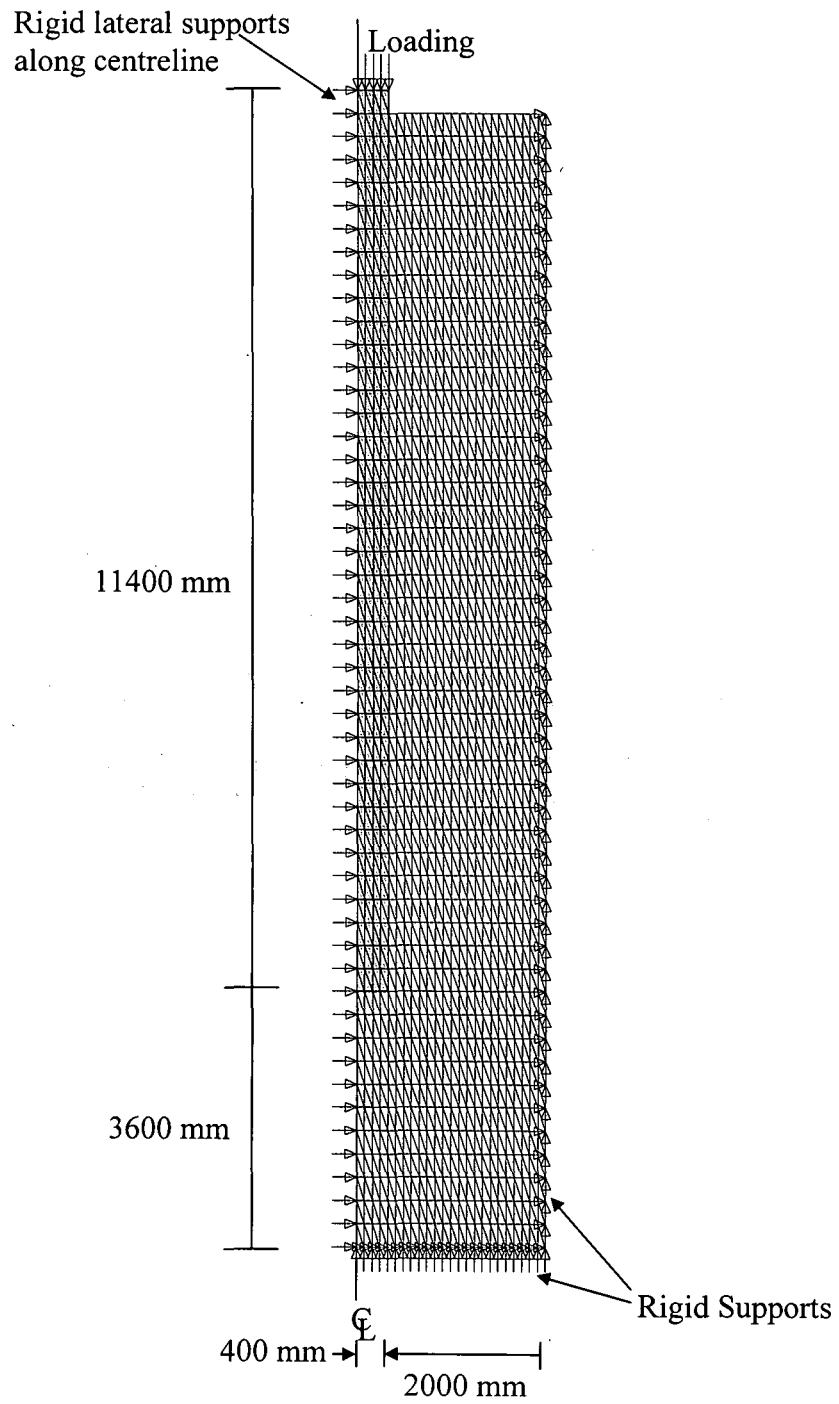


Figure 4.27 Finite element model for an installed foundation pile.

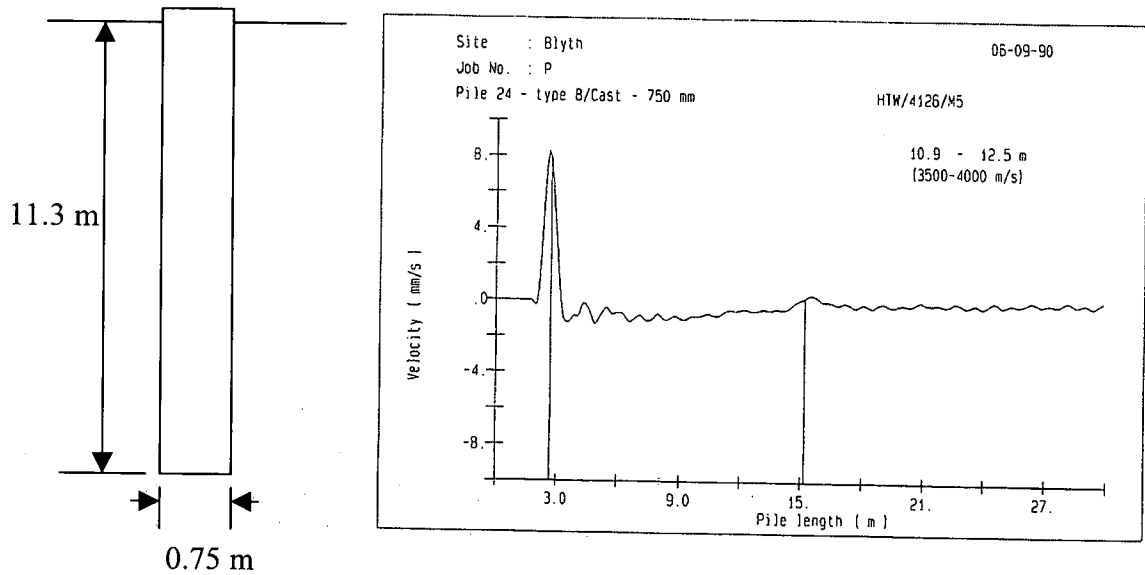


Figure 4.28 Field test results for a defect free pile (courtesy Testconsult Ltd)

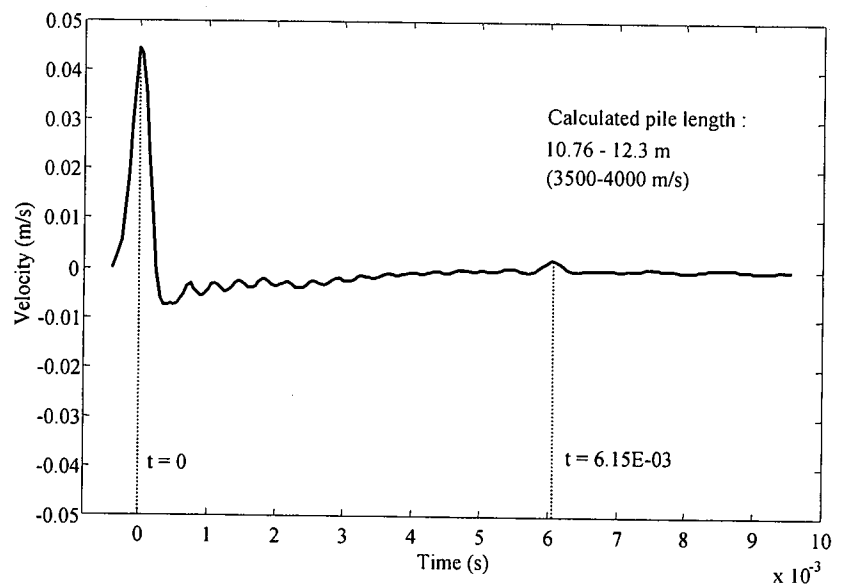


Figure 4.29 Finite element generated response for pile of Figure 4.28

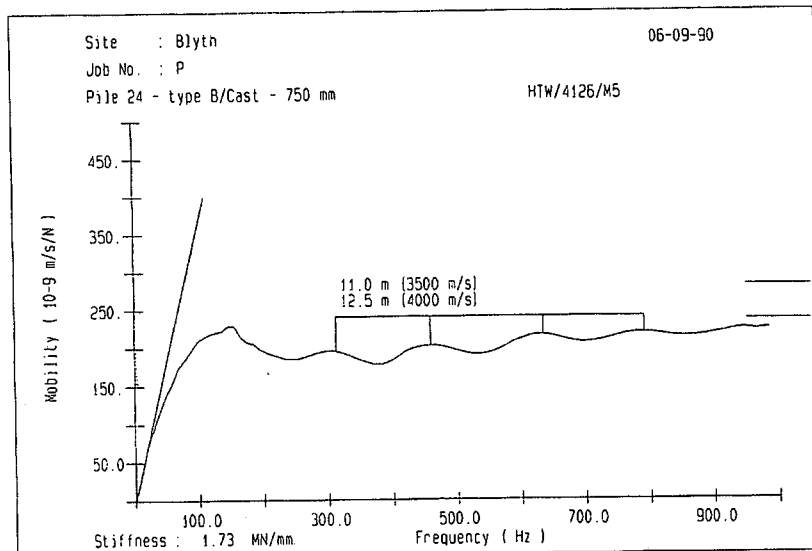


Figure 4.30 Field test mobility curve for pile of Figure 4.28

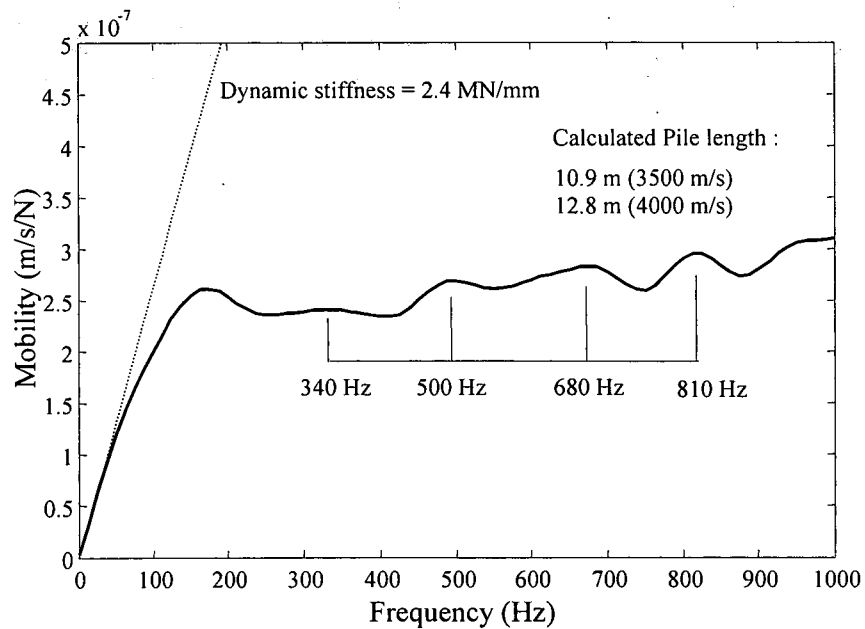


Figure 4.31 Mobility curve for finite element generated trace of Figure 4.29

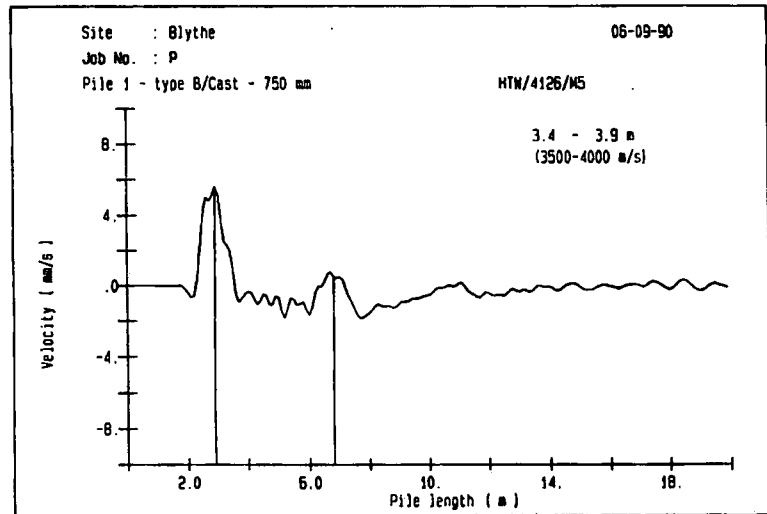
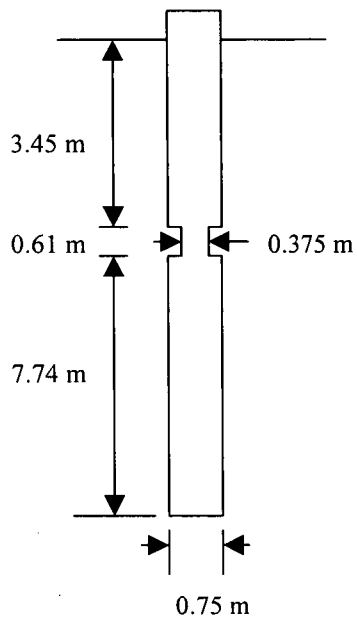


Figure 4.32 Field test results for a pile with necking (courtesy Testconsult Ltd)

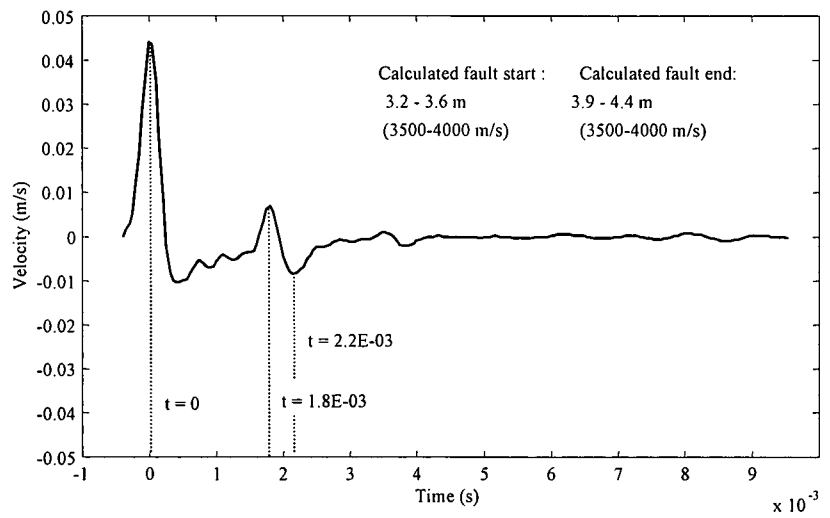


Figure 4.33 Finite element generated response for pile of Figure 4.32

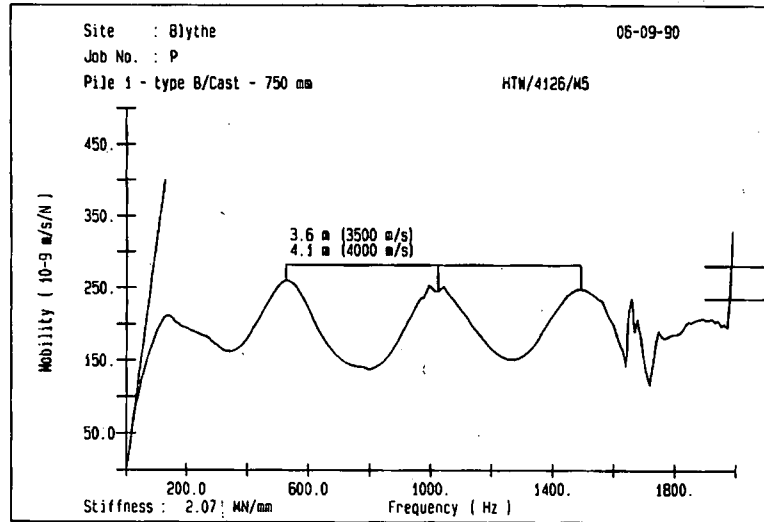


Figure 4.34 Field test mobility curve for pile of Figure 4.32

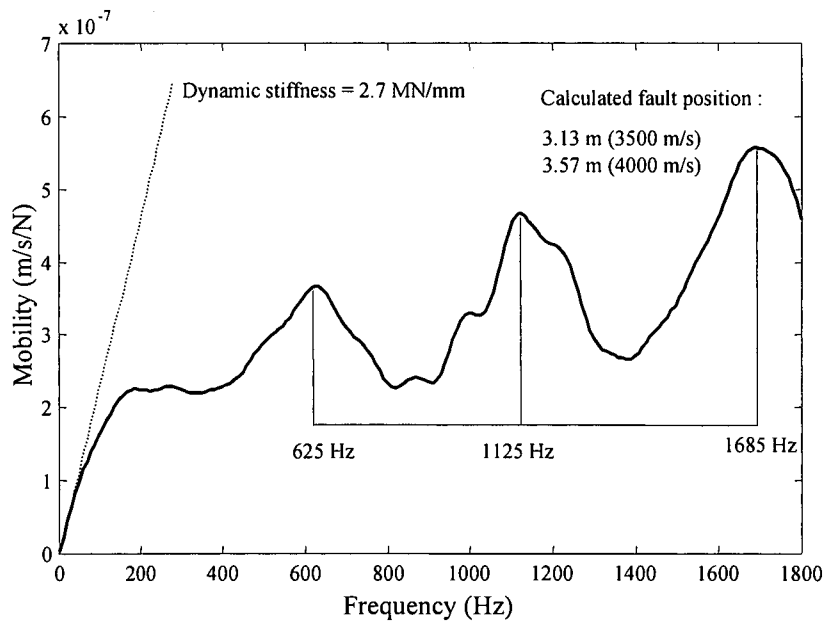


Figure 4.35 Mobility curve for finite element generated trace of Figure 4.33

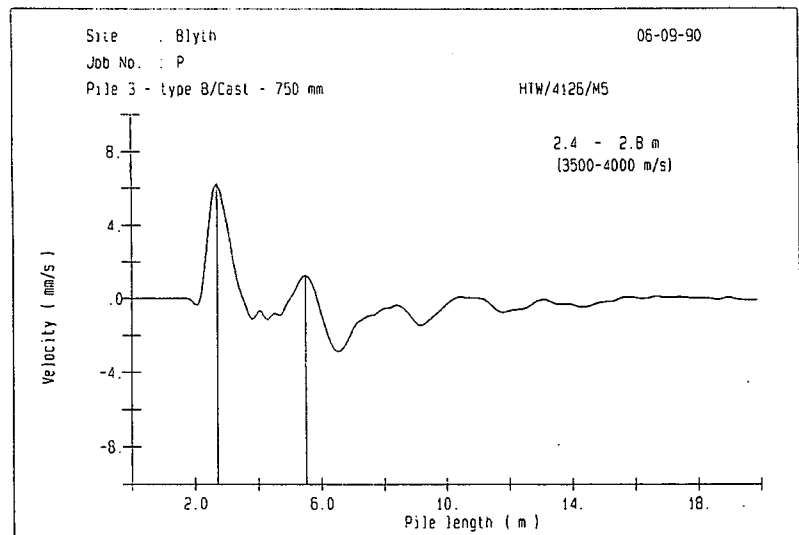
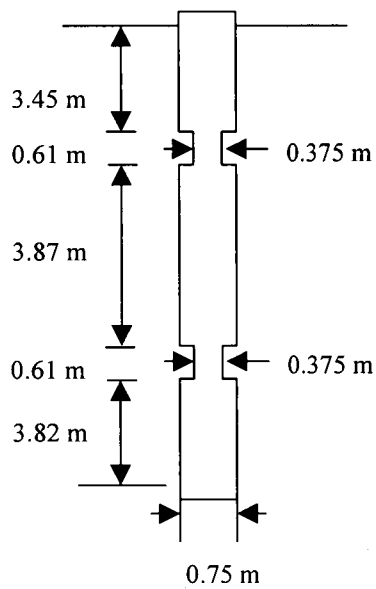


Figure 4.36 Field test results for a pile with two necks (courtesy Testconsult Ltd)

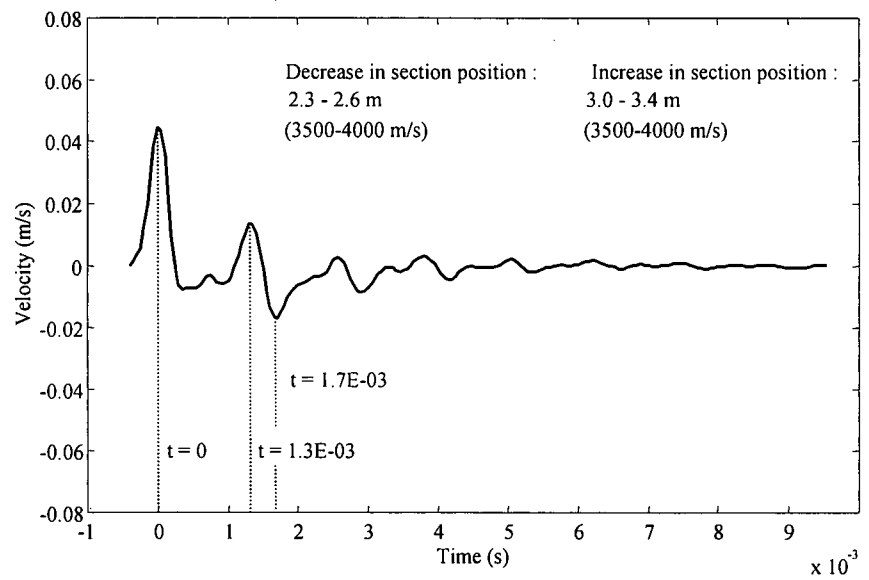


Figure 4.37 Finite element generated response for pile of Figure 4.36

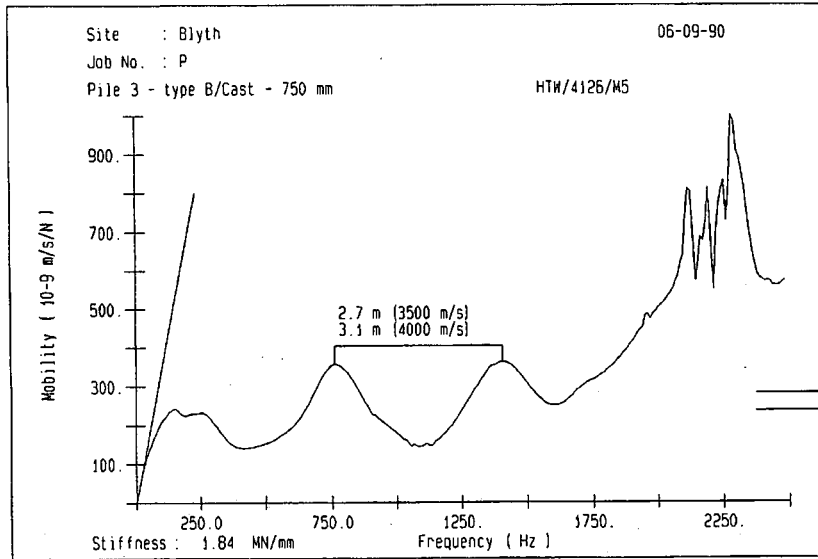


Figure 4.38 Field test mobility curve for pile of Figure 4.36

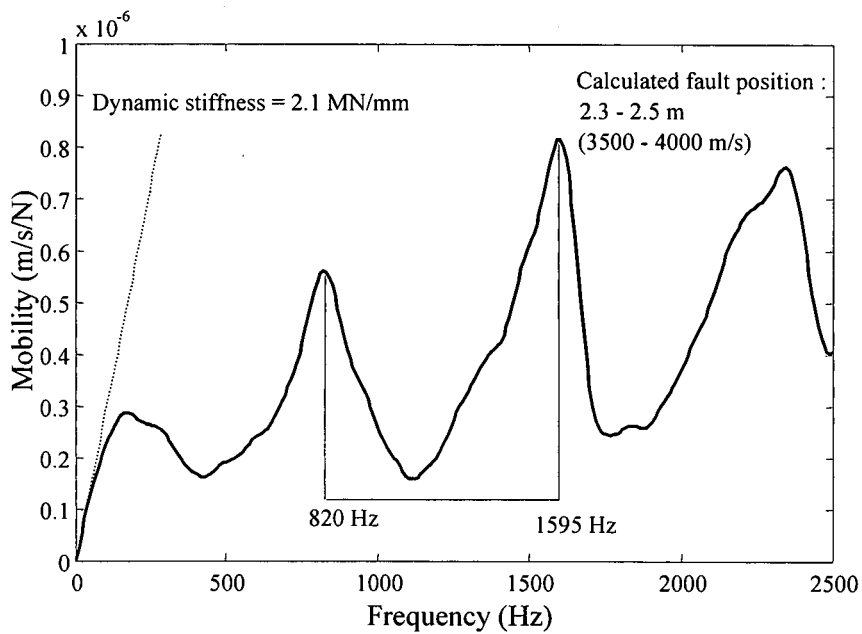


Figure 4.39 Mobility curve for finite element generated trace of Figure 4.37

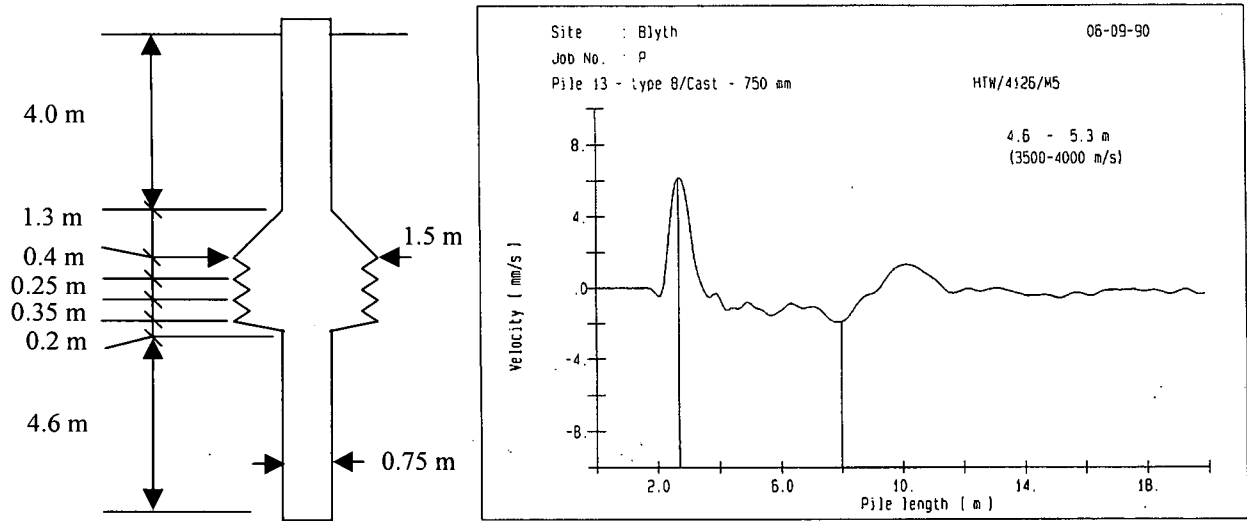


Figure 4.40 Field test results for a pile with bulbing (courtesy Testconsult Ltd)

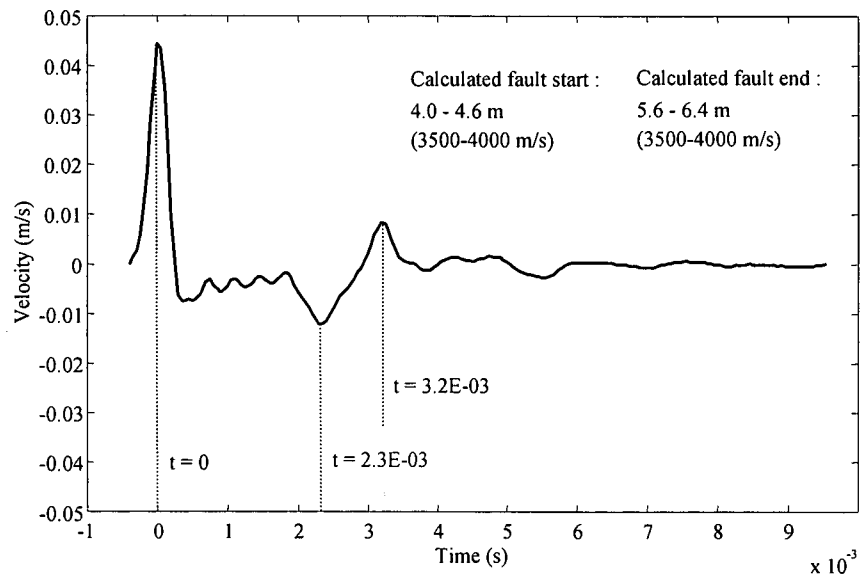


Figure 4.41 Finite element generated response for pile of Figure 4.40

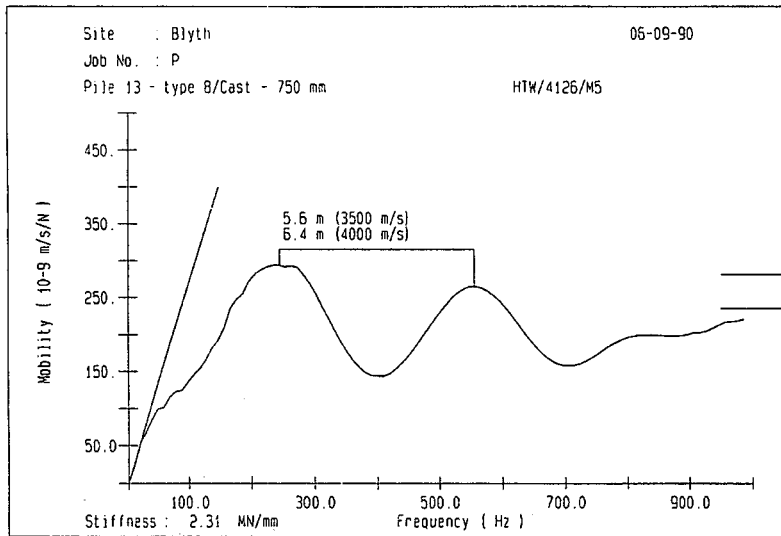


Figure 4.42 Field test mobility curve for pile of Figure 4.40

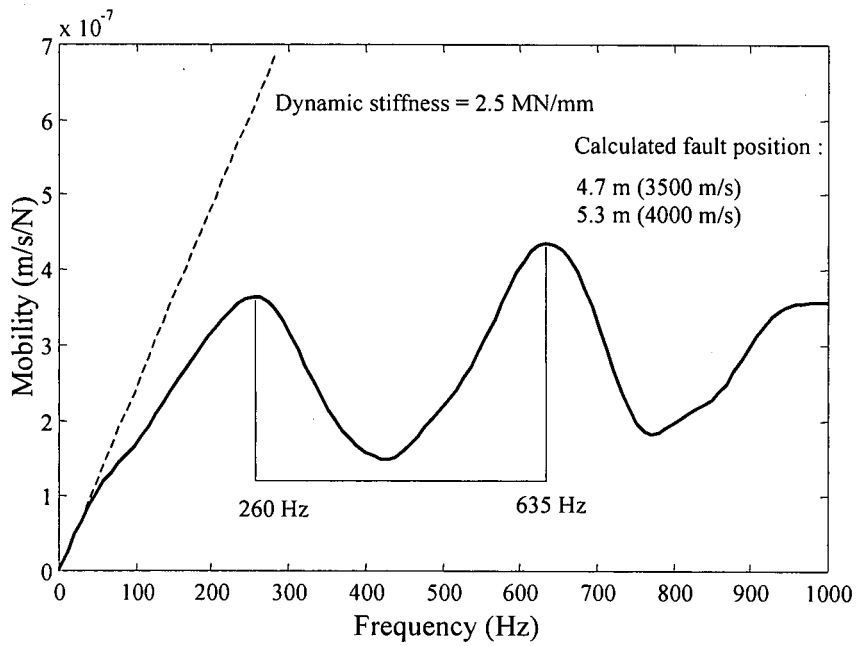


Figure 4.43 Mobility curve for finite element generated trace of Figure 4.41

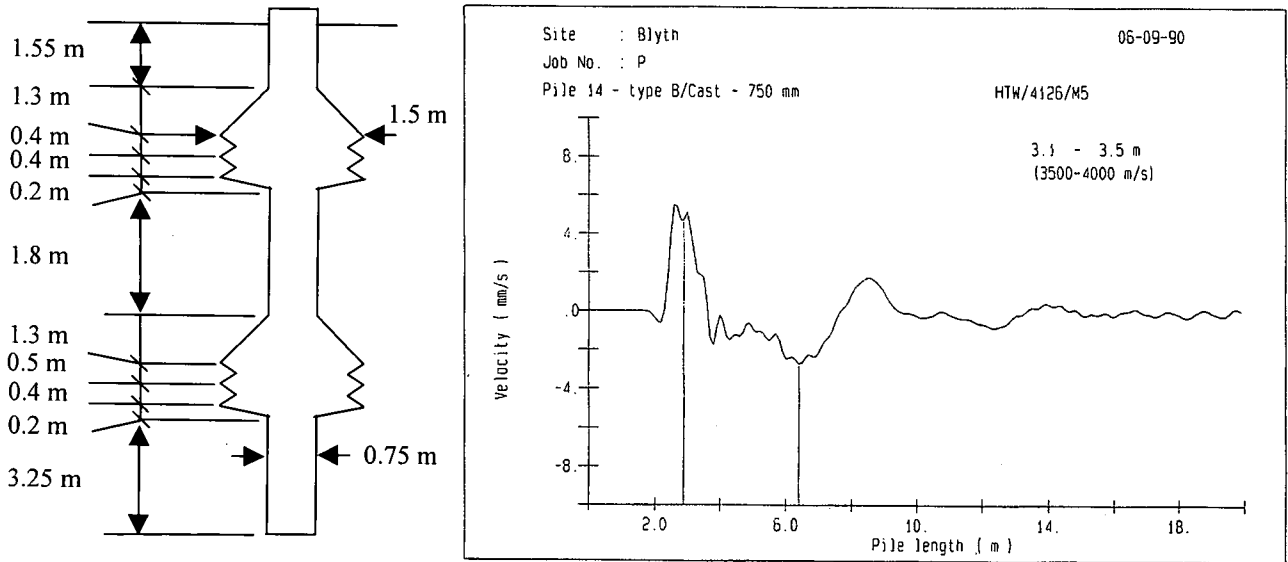


Figure 4.44 Field test results for a pile with two bulbs (courtesy Testconsult Ltd)

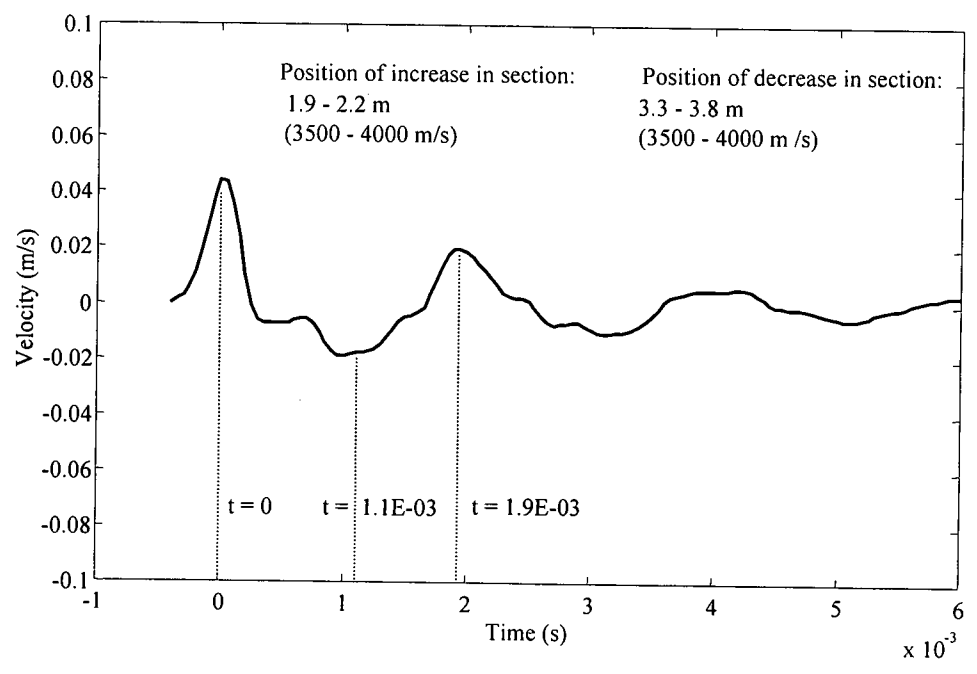


Figure 4.45 Finite element generated response for pile of Figure 4.44

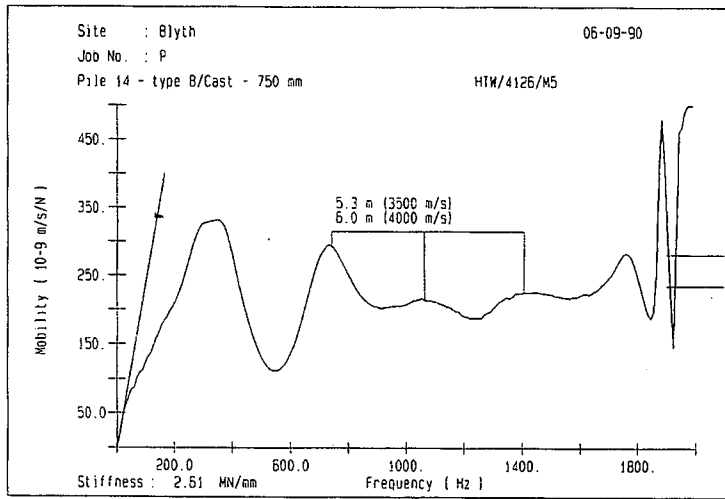


Figure 4.46 Field test mobility curve for pile of Figure 4.44

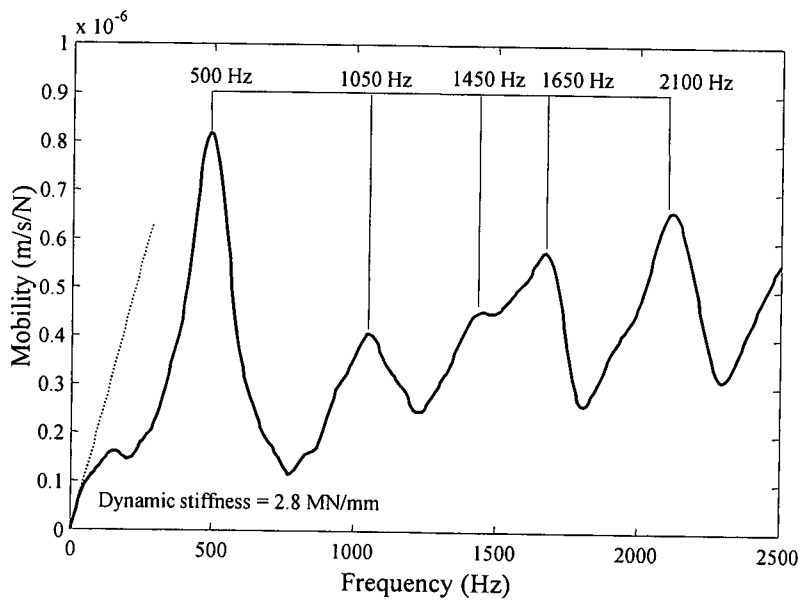


Figure 4.47 Mobility curve for finite element generated trace of Figure 4.45

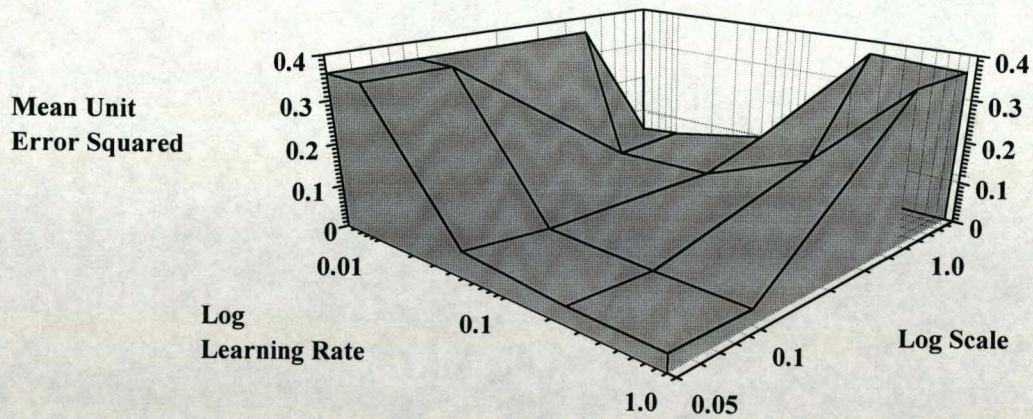


Figure 4.48 Network effectiveness with respect to learning parameters

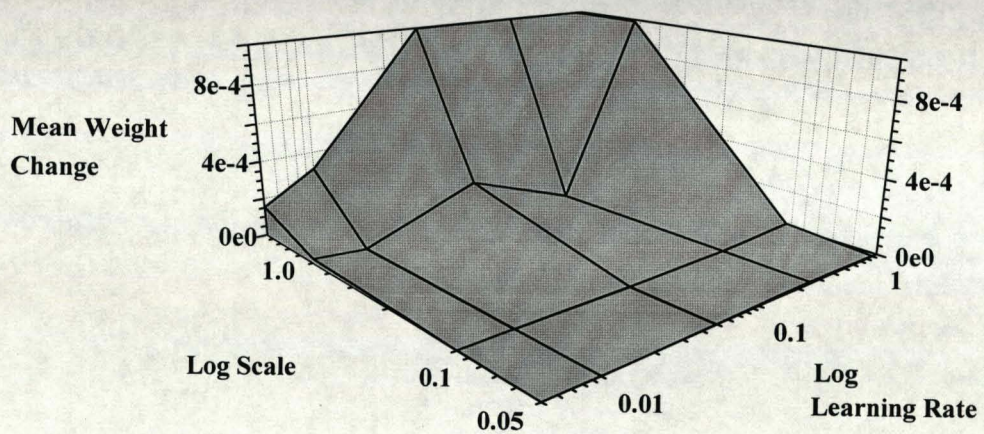


Figure 4.49 Early weight changes with respect to learning parameters

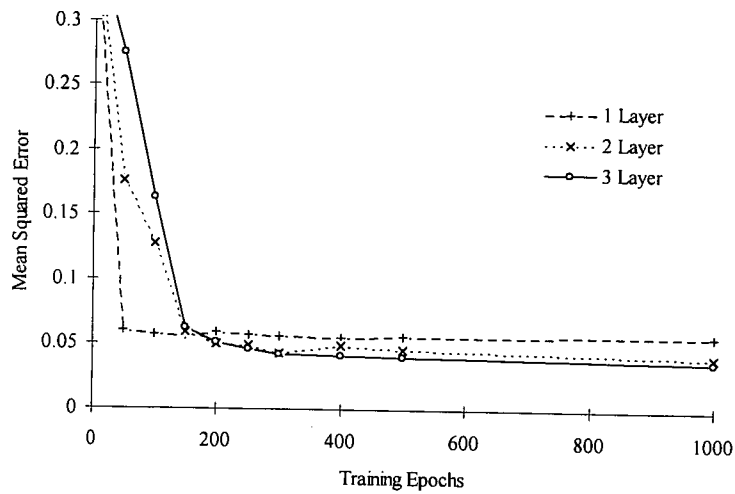


Figure 4.50 Network error convergence with respect to layer topology ($T=0.1, \alpha=0.25$)

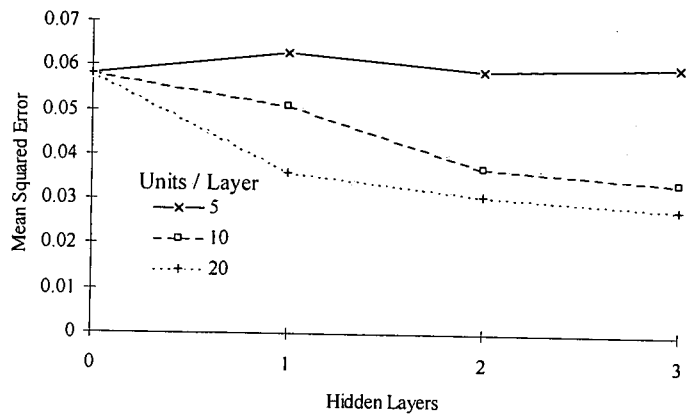


Figure 4.51 Optimal performance dependency on the number of hidden layers

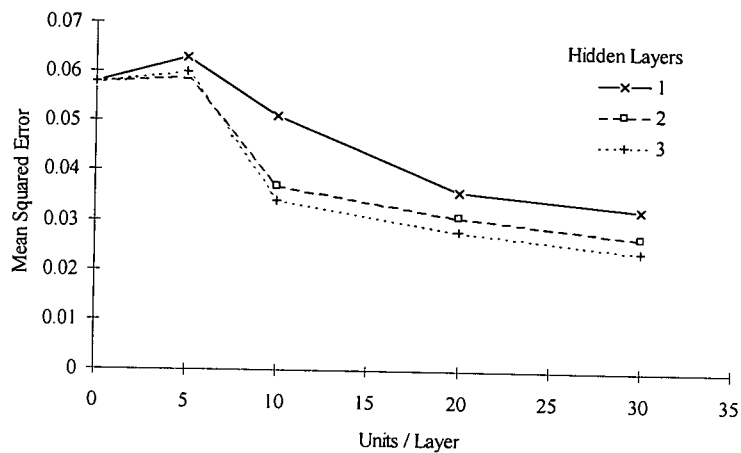


Figure 4.52 Optimal performance dependency on units per hidden layer

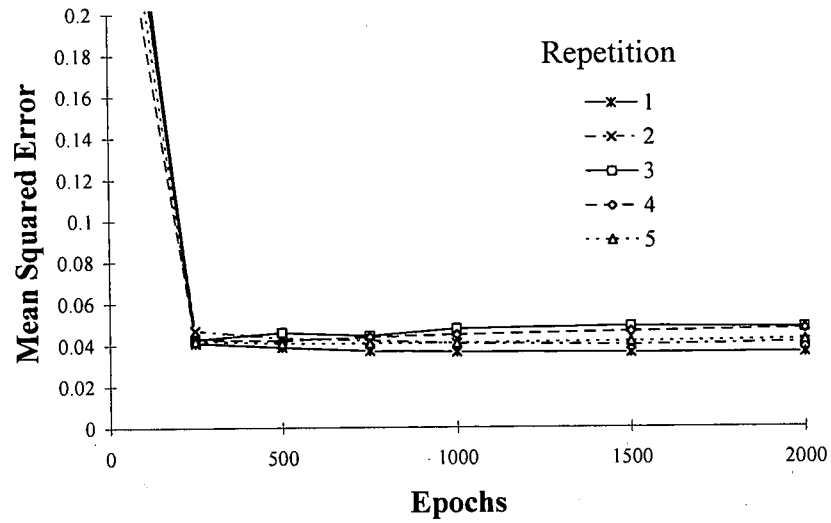


Figure 4.53 System repeatability

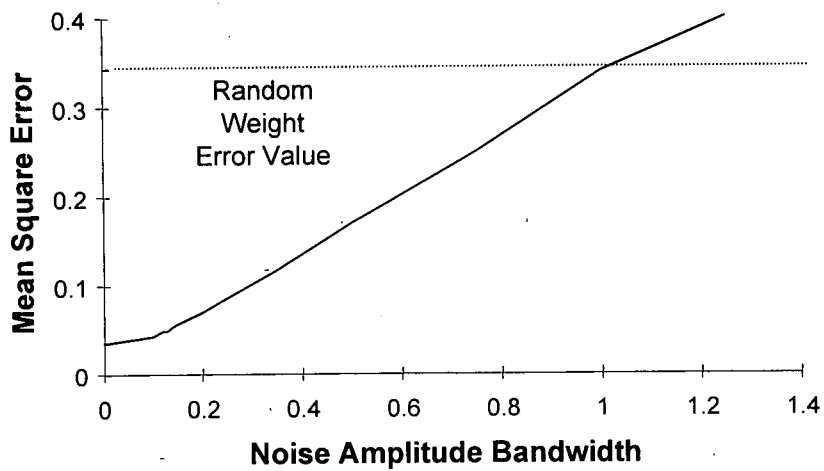


Figure 4.54 The effect of noise on the system performance

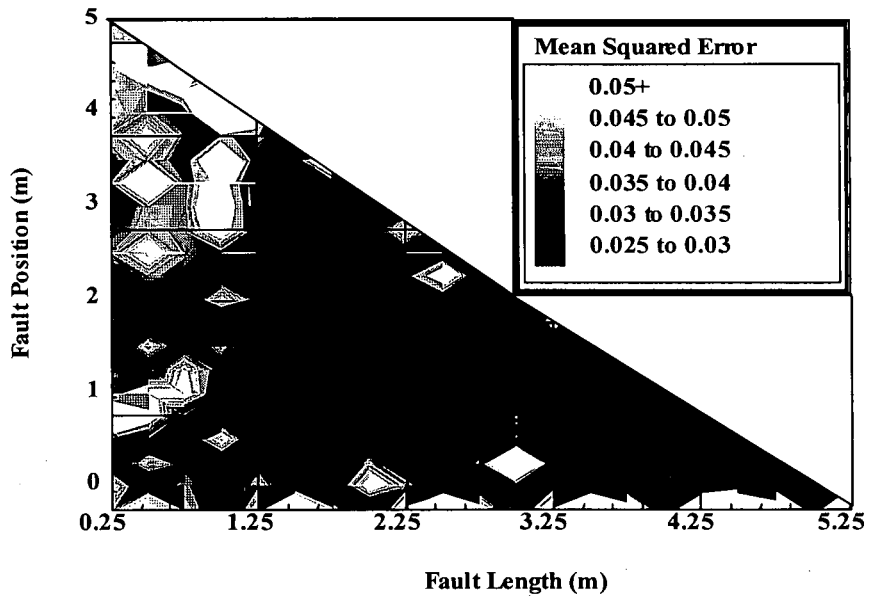


Figure 4.55 Network effectiveness with respect to defect position and length

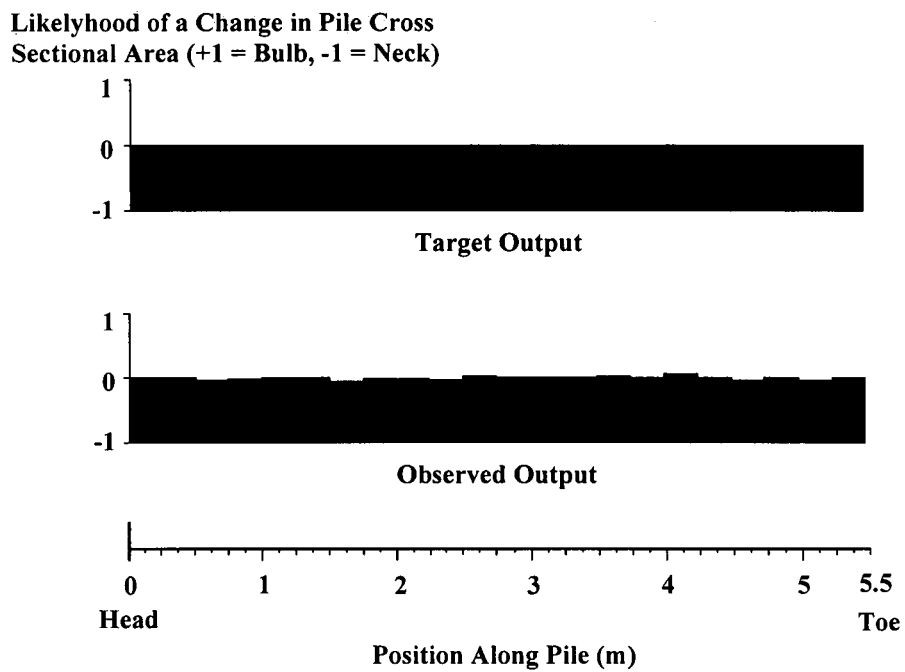


Figure 4.56 The required and observed network output for a sound pile

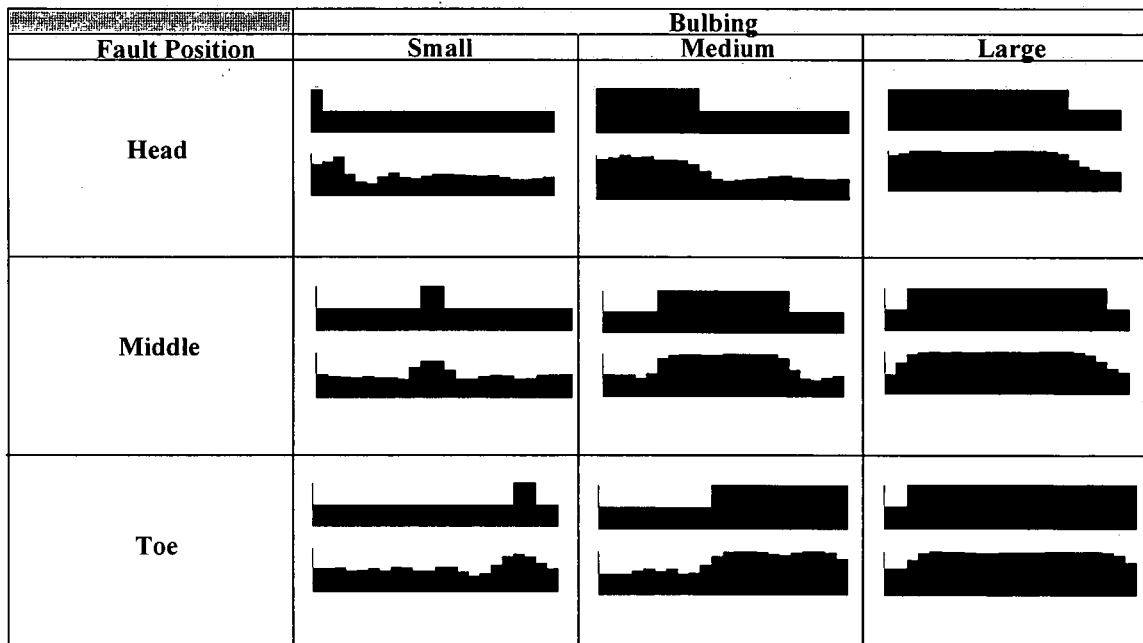
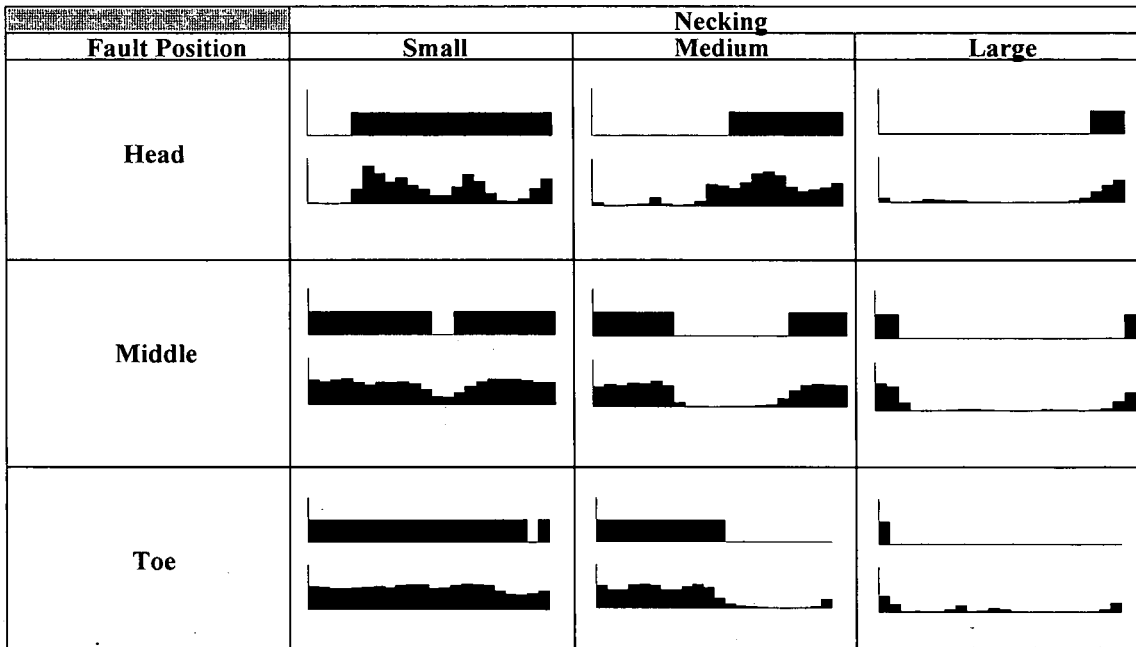


Figure 4.57 Samples of system responses from the network's test set

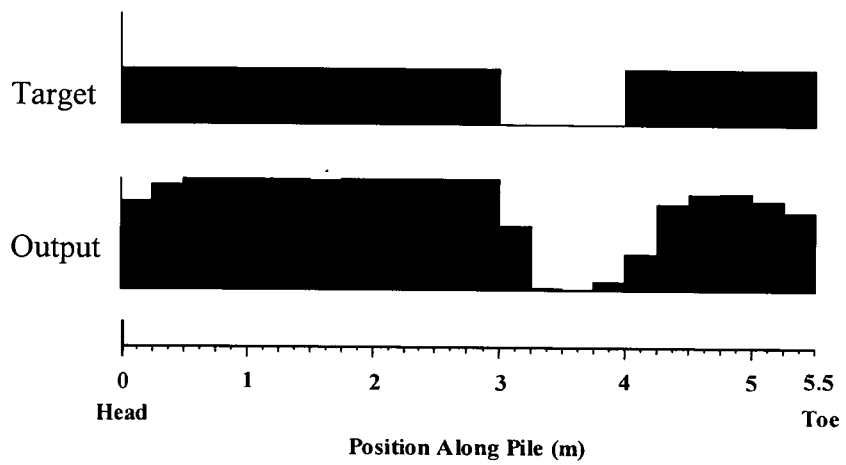
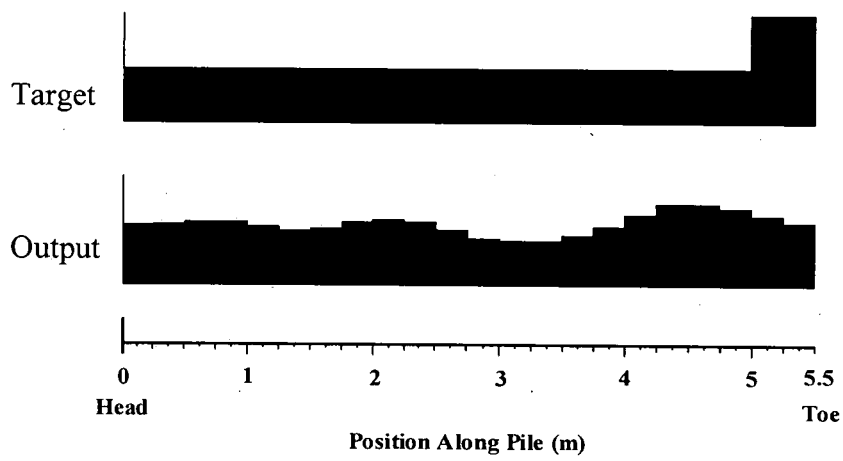
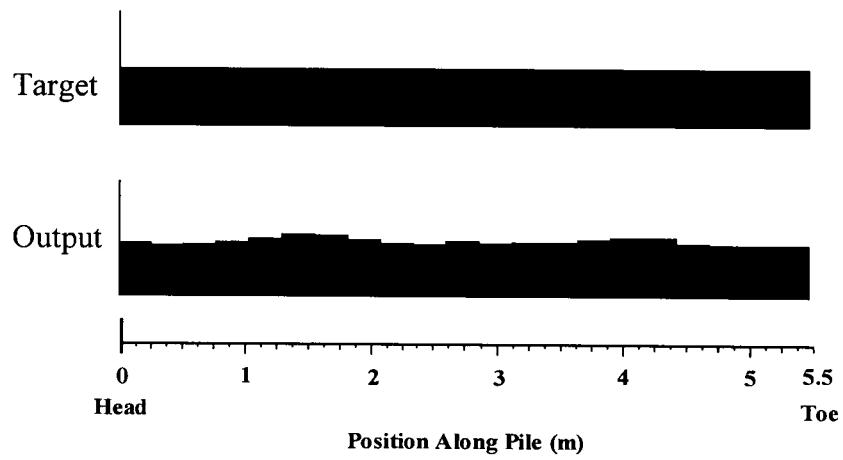


Figure 4.58 System response to experimental data

5. Hardware and Software Development

5.1 SYSTEM FLEXIBILITY

In deciding the best route to take during the research and development of a system such as this a compromise must be made between simplicity and flexibility. There are a multitude of neural network simulators for the PC which are simple to use and have been optimised for maximum speed of computation. One such system, NeuralWorks Professional II^{5.1}, has been used for the feasibility study in the previous chapter. However, in using such software the developer is restricted to the networks and training algorithms it supports. For systems utilising the novel gradient descent algorithms described in Chapter 3, or those based on wavelet networks no such third party software, as yet, exists.

The temptation of the developer may then be to program the system from scratch. The author has experience of programming low level neural network simulators in Pascal^{5.2}. The time consuming process of altering and recompiling low level code is not conducive to the overall speed of system development. It is also extremely difficult for other people to interpret and often necessitates the porting of data to other third party software, e.g. spreadsheets, for data presentation and analysis.

Matlab[®] is a technical computing environment that provides the user with a graphical interface, memory management, and a high level programming language not unlike Fortran or BASIC^{5.3}. It has been developed specifically for mathematical programming and is optimised for matrix manipulation and linear algebra of the type used in Neural Network simulation. It also has a number of useful predefined

functions for data manipulation, such as fast Fourier transforms and matrix pseudo inverse generators. It also provides data presentation procedures including both 2-D and 3-D graph plotting.

Importantly for this application, it also provides a facility for linking with C++ programs through an Application Program Interface (API). In particular, it allows such low level programs to be linked with the API to provide a Dynamic Linked Library which can then be called as though it were a Matlab command. Hence, it facilitates the combining of low level hardware programs, such as those necessary to access data acquisition equipment, with a system entirely developed and run within the Matlab environment.

This environment is, therefore, seen as a compromise between speed of software execution and speed of system development. With the speed of execution not being of primary importance during the development stages the added flexibility provided when compared with specialist neural network simulators makes it ideal for a study such as this. The software described in Sections 5.2.3 and 5.3 has, therefore, been developed within the Matlab environment.

5.2 DATA ACQUISITION EQUIPMENT

During the last fifteen years a great deal of research has been carried out at Napier University and the University of Edinburgh in the field of impact testing of large engineering structures. These projects include the testing of piled foundations^{5.4}, masonry sewers^{5.5}, and masonry arch bridges^{5.6,5.7}. Common to all this research is the equipment used for data acquisition.

The main components of this testing equipment are illustrated in Figure 5.1. Essentially the sensing devices and signal conditioning units are the same as those used for commercial testing, as described in chapter two. Specifically, a Brüel & Kjær accelerometer and Piezotronics 3 kg small sledge instrumented hammer are used with signal conditioning applied through their specified charge amplifiers.

However, unlike in the commercial case, the readings from these units are fed to a dual channel spectrum analyser, a Brüel & Kjær model 2034. Here, the test data can be sampled at up to 64kHz per channel and have various windows - exponential, flat-topped, Hanning, Kaiser-Bessel *etc.* - applied before being analysed, e.g.: auto- or cross-correlation, auto- or cross-spectra, cepstrum, coherence, or impulse response functions. The results from this analysis are then either printed on a HP7475 plotter or transferred to a portable 'lunchbox' computer through an IEEE 488 interface.

All the processing carried out in hardware using the dual channel analyser can now be carried out using functions contained in the Matlab signal processing 'toolbox' and, with the increase in computer power over the last decade, can be calculated with no discernible slowing of the speed of computation. As shown in Figures 5.2 and 5.3 the equipment is bulky and so not very mobile. The requirement of a power generator and the size of the dual channel analyser along with its stand necessitates a transit type van for transportation and slows the rate at which piles may be tested on site considerably. It is also noted that, with analysis now being carried out on a portable computer, the dual channel analyser's role is reduced to that of an analogue to digital converter (ADC). More compact, specialist, devices exist for this task which can greatly improve the portability of the equipment and negate the need for a power generator. A new, more compact, data acquisition system has, therefore, been developed for this study.

5.2.1 New Equipment Overview

The impact testing equipment, that is the sensors and hammers, used in this study are the same as those used in the old system and described in Section 5.2.2. However, as shown in Figure 5.3, the output of the sensor signal conditioning units are now fed into a junction box which is connected to a ADC card in a laptop computer. These connections and hardware specifications are discussed in Section 5.2.3. As can be seen from the photographs in Figure 5.4, the equipment's overall size is reduced so improving portability and facilitating hardware protection during inclement weather conditions. The use of this new equipment, has however, necessitated the

development of new software to control it. This software is described in Section 5.2.4.

5.2.2 Impact Testing Equipment

The sensors used in this study are the same as those used in the previously mentioned research and by industry. Specifically, the hammers used are the Piezotronics (PCB) 'hand sledge' (3 lb - 1.36 Kg head) and 'sledge' (12 lb - 5.44 Kg head) instrumented hammer types: 086B20 and 086B50. These hammers are shown in the photograph of Figure 5.6 and are supplied with interchangeable tips of: rubber, soft plastic, hard plastic and aluminium.

The hammers and accelerometers used are 'modally tuned', i.e. the accelerometer has a spectral sensitivity range that includes the frequency components of the impact excitation produced by the hammer. The accelerometer used in this study is the Piezotronics type 353B33 which has a spectral sensitivity of 1-4000Hz and is, therefore, suitable for use with both these hammers as well as the 1 lb, 0.45 Kg, 'heavyweight' hammer (type 086C05) which is also shown in Figure 5.6.

Both hammers and accelerometer are supplied with the same signal conditioning unit: the PCB 480E09. This is a battery powered charge amplifier that provides a linear gain of 1, 10 or 100 to a maximum value of ± 4.5 volts. The 480E09 unit supersedes the 480D06 that has been used successfully as part of the preceding test equipment for a number of years. It is shown in Figure 5.6.

5.2.3 AD Converter and Junction Box

The choice of analogue to digital converter is primarily dependent upon the required signal sampling rate and voltage step resolution (i.e. 8, 12 or 16 bit). Most commercial testing companies employ purpose built hardware for pile testing. Technotrade, however, use hardware developed 'in-house' with a system similar to that used for this study. Following consultations with a company representative a suitable converter was selected as the PCM-DAS16D/16. This PCMCIA type II card

fits directly into the expansion slot of a laptop computer. It allows two channels to be sampled simultaneously at 50kHz and is a 16 bit converter giving a voltage step resolution of 0.000305 Volts at ± 10 volts full scale deflection. This is the best resolution currently available for converters of this type and the sampling rate allows ten fold over-sampling of the frequencies of interest.

This card has a number of other important features that should be noted at this point: a 256 sample First In First Out (FIFO) buffer is comparatively large for ADCs of this type and ensures no data is lost when transfer requests are made to the computer's CPU. The card's software driver supports the fast direct memory access (DMA) transfer of data and background collection of data into a circular buffer. This means a trigger mechanism can be programmed in software as previously acquired data can be checked while subsequent data is being collected. This card also contains an on board amplifier, that can be programmed through software. This avoids the need for additional external devices and allows data ranges of $\pm 10\text{v}$, $\pm 5\text{v}$, $\pm 2.5\text{v}$, and $\pm 1.25\text{v}$ to be collected without the having to manually alter hardware settings.

The signal conditioning units and computer are both battery operated and, as such, have electrically isolated earths. This means no isolation barrier is necessary and so the screened output of the signal conditioning unit can be connected directly to the differential input of the AD converter. However, the system's noise immunity can be reduced by earthing the low input of the channel through a $10\text{k}\Omega$ resistor^{5,8}, as shown in the circuit diagram of Figure 5.7.

The card is supplied with a screw-in terminal board and connecting cable. The board has been housed in a junction box along with the 'pull-down' resistors and BNC sockets for connecting the coaxial cables from the signal conditioning units. This junction box along with the ADC card is shown in Figure 5.8 - the box lid has been removed to reveal the screw-in terminal board.

5.2.4 Acquisition Software

To improve its ease of use the software for data collection has been designed so that all relevant parameter control and data views are available from a single user window. It has been developed using Matlab's Graphical User Interface (GUI) layout tool which facilitates the inclusion of pull-down menus and push button controls so reducing the user input errors associated with scripted commands.

The results set from a tested pile, which may be made up of a number of traces, is saved in a single file. Individual traces are of a Matlab *structure* data type and the collection of traces saved as a *cell array*. The advantage of using cell arrays rather than matrices for storing multiple results is the flexibility it allows. The size of the array need not be pre-defined and length of the components within the array need not be the same. Hence, one pile record may hold three sets of traces while another five and likewise, within a pile record, one trace vector might hold 1024 values while another, sampled at a different rate, 2048. Matlab's structure type is essentially the equivalent of a record in lower level programming with a hierarchical format allowing a number of fields to be associated with a single variable.

An example of a cell from an pile record array, 'piledat', is shown in Table 5.1. In this case the cell is the first in the array; as signified by the one inside the braces. The mnemonic following the period defines the structure's field name.

Table 5.1 The cell structure for a pile record

Field	Contents
piledat{1}.for	Vector of force trace
piledat{1}.vel	Vector of velocity trace
piledat{1}.rate	Scalar of sample rate
piledat{1}.gain	Scalar of ADC gain
piledat{1}.H_gain	Scalar of hammer pre-amplifier gain
piledat{1}.A_gain	Scalar of accelerometer pre-amplifier gain
piledat{1}.comments	User's text comments

There are only two scripted inputs the user can enter and these are optional. Edit boxes allow comments to be associated with a collected trace and the name of the data file to be altered. A default file name is, however, assigned as each pile is tested to free the user from having to continually enter new names and ensure old data is not overwritten. The name is generated from the current date - the number of days after 1st January 2000 - and the number of files already saved on that day.

As can be seen in Figure 5.9 the resultant application displays the input force and velocity traces of the data measured immediately previously and the ensemble average of the velocity data collected for the pile under test. All the graphs are scaled automatically using Matlab's 2-D *plot* function. Apart from having the facility for changing the programmable AD converter values and pre-amplifier settings, through the pull-down menus at the bottom right of the window, the user basically has three control options, each being initiated by a button push and described, in turn, below.

5.2.4.1 Main Program Loop

The program is initiated through a call from Matlab's command window. The main program loop is described by the flow diagram of Figure 5.10. The variables, including the pile's file name, are initialised with their default values and an empty figure is presented. The system then waits for a user input. The default values are given as: sample rate of 50kHz per channel, sample size of 1024, ADC gain range of ± 10 v, hammer gain of x1, and accelerometer gain of x10. These default values may be changed before testing commences by editing the program text file. If the value selected in one of the pull down menus is changed then the associated variable for the subsequent data collection is also, automatically, changed. If the exit button is pressed the program terminates and control returns to the Matlab command window. If any of the other buttons are pressed control passes to the code associated with that button, as described below, before returning to the main program loop. Control returns to a point labelled by the off-screen link '1' in Figure 5.10.

5.2.4.2 Data Collection

The AD converter is controlled through software drivers containing a low level command set that can be accessed from a number of programming languages including Visual Basic and Visual C/C++. Following consultation with the board suppliers (Talisman Electronics, UK) it has been confirmed that no direct support for Matlab exists and consequently this, so called, 'Universal Library'^{5.9} has to be ported to Matlab through a lower level interface. As mentioned above Matlab supports the integration of Visual C++ programs when linked with its Application Program Interface^{5.10}. Hence, for this application much of the data collection module has been written in Microsoft Visual C++ before being compiled into a Matlab linked Dynamic Link Library which can then be called from within Matlab as if it were a normal, scripted, command file.

Most of the relevant technical information necessary for programming this application can be found in the documentation supplied with Matlab^{5.10} and the ADC^{5.9}. However, one important piece of information discovered by the author, but not explicitly documented in the literature, should be noted. The Universal Library function that reserves the memory into which the collected data is passed, `cbWinBufAlloc`, appears to execute `GlobalAlloc` with the `MEM_FIXED` flag set. This means the returned memory handle is, in fact, a physical memory location. Although this somewhat esoteric piece of information will be superfluous for most readers it provides a route out of a potential compatibility hazard in that both Matlab and the Universal Library routines like to have control over the allocation of memory. Any reader tempted to reproduce this work will, therefore, be pleased to realise that because `cbWinBufAlloc` returns a physical memory address the information from the AD converter can be accessed *as if* Matlab had allocated the memory for it without the need to rectify conflicting memory handles. This having been said the author does not intend to go into the peculiarities and technicalities of low level programming, but rather directs the reader to Figure 5.11 where an overview diagram of the work can be found.

Referring to Figure 5.11, all the components inside the dotted rectangle are written in the C++ module. As can be seen, when called the parameters passed define the required sample rate, gain and number of samples. The board is then initialised using the Universal Libraries' 'cbDeclareRevision' command and dynamic memory assigned, as described above. The AD converter is then prompted to start data collection.

The options chosen for collection require the converter to continuously place its data into the memory reserved for it looping back to the start of this buffer when it reaches the end. This is done in background mode so that the computers central processing unit (CPU) can continue executing code while it is being carried out. The transfer is carried out using the direct memory access (DMA) block mode. This moves the data in blocks of 256 samples and is the quickest transfer method.

By continuously collecting data and checking its maximum level a software trigger is has been produced. Using a circular buffer ensures the length of the time spent waiting for an event is not restricted to system memory. In fact, the only restriction is the type of the sample counter with respect to the required sample rate. The sample counter is of type *long*, a 32 bit integer, which means at 100kHz sampling rate the maximum effective time the trigger can wait for an event before looping back on itself is six hours. It is felt unlikely that for this application a user would take this long to strike a pile head. The trigger time-out value has, therefore, been set at ten seconds after which if no event is detected an error message appears in the Matlab command window and control returns to the main program loop.

An event is defined here as the detection of a 10% change in the average reading over 64 samples in the hammer input channel. If an event is recorded a number of further samples are collected. This number is dependent upon the number of samples requested and the number of pre-trigger samples required. For this application 1024 samples per channel are more usually taken 128 of which contain the pre-trigger data.

Background data collection is then stopped. The data collected in memory has samples from the two channels interleaved. They are, therefore, sorted before being passed back to the Matlab calling program as return parameters. These returned vectors are raw sixteen bit integers which are translated to engineering units through a second Matlab program. This program has, however, been written in the 'normal' scripted format as this makes it easier to alter should alternative hardware be employed. At this stage the integers are translated to volts from the AD converter and pre-amplifier gains stored with the traces. These are then changed to force in newtons or acceleration in ms^{-2} according to the calibration certificates of the instrumented hammer and accelerometer used. The acceleration curve is then integrated numerically to produce a velocity trace. These velocity and force traces are then presented in the appropriate charts in the user window, as shown in Figure 5.9.

5.2.4.3 Appending Data to Pile Records

Having viewed the new data collected in the force and velocity plots the user can then decide to append it to the record of the pile under test. In this case the 'Add trace' button is pressed. This adds a new cell containing the data into the current results array and updates the ensemble average plot in the top right corner of the window. If the traces in the record are of different lengths or sample rates they are linearly interpolated before the averaging takes place. Note, this interpolation is purely for viewing purposes; the raw data remains unchanged in its collected form. Results can only be added to a pile record once after a collection is made to avoid problems associated with the accidental 'double clicking' of this button. This process is summarised in the flow diagram of Figure 5.12.

5.2.4.4 Saving Current Pile Record

By pressing the 'Next Pile >>' button the data held in the current pile record is stored under the defined file name. The plots within the window are then cleared, a new file name generated, and the current pile record is emptied ready for new traces to be collected. The other user options, including the text comments, remain the same as it is assumed the next pile tested will require similar values. Control is then

returned to the main program loop. As this is a relatively short, simple process it is also described in the flow diagram of figure 5.10. If there is no data yet collected this button is disabled to guard against accidental 'double clicking' leading to empty files being stored.

5.3 NEURAL NETWORK SOFTWARE DEVELOPMENT

The new hardware having been described, this chapter continues by focussing on the Matlab routines written for the neural network simulators.

As stated in Chapter 3, three layered network types are investigated with respect to this application: the multi-layered perceptron (MLP), the radial basis neural network (RBNN) and the wavelet basis neural network (WBNN). Each network's software is described below along with a simple validation experiment to confirm it performs as expected.

In all these cases the testing and training data sets are held in structured variables containing two fields: *input* and *output*. Each field contains a single matrix. The number of rows in these matrices, which is the same in both cases, correspond to the number of patterns in the set. The number columns in the input and output matrices respectively describes the number of input and output units in the network. These values, therefore, need not be defined explicitly.

5.3.1 Multi-Layered Perceptron

The procedures for training a multi-layer perceptron network are based on the algorithms described in Chapter 3, specifically Equations 3.13-3.19. The network may have an unlimited number of layers and an unlimited number of units in each layer. Each layer may be made up of either sigmoid, hyperbolic tangent, or linear activation functions. Different layers are permitted to have different activation functions and the hidden and input layers have a bias unit appended to them automatically.

5.3.1.1 Network Structure

To accommodate the variability in the number and size of hidden layers permitted for each network Matlab's cell array is, again, employed. As in the data acquisition case a structured type is used to hold all the network information; thus each network can be accessed, passed as a parameter, saved *etc.* as a single variable.

An example of such a variable, *net*, with all its associated fields can be found in Table 5.2, below. The learning, momentum and scaling parameters are as described in Chapter 3. In this case the network has an input layer of 15 units (16 with bias), a single hidden layer containing 10 units (11 with bias) and 5 output units. The weight matrices cell array, therefore, holds two matrices: one 10x16 describing the weights from the input to hidden layer, and one 5x11 describing those from the hidden to the output layer. The activation function for each layer is described by a text string in a cell array. Note that although there are three layers only two activation functions are given. This is because the input layer is assumed to be linear. The network in Table 5.2, therefore, has a hidden layer with sigmoid activation functions and a linear output layer. The *epoch* field simply records the number of epochs on which the network has been trained.

Table 5.2 An example of the data structure of an MLP network

Field	Contents	Example value
net.alpha	Learning rate	0.25
net.lambda	Momentum term	0.9
net.T	Scaling Parameter (Temperature)	1.0
net.epochs	Epoch count	0
net.w	Cell array of weight matrices (one per layer)	{[10x16 double] [5x11 double]}
net.act	Cell array of Unit activation type	{'sig' 'lin'}

5.3.1.2 Network Initialisation

The number and size of the fields associated with each network makes initialisation in Matlab's command window time consuming and complex. A command file, *Mlp_init*, has therefore been developed to automate this procedure. This text file, containing all the instructions necessary to produce a network structure, is edited and run. Its return value is a initialised network that can then be trained as required. The network's initial weights are small and random^{5.11} and, for any weight, ω_{ji} , its value is given as $|\omega_{ji}| < 1$. These values can, however, easily be scaled as required for a given application.

5.3.1.3 Algorithm Implementation

The task of network training has been modularised through the production of a suite of smaller simpler routines. These are given as:

- i. *train_network* : the routine called from the Matlab command window that takes as its parameters the network to be trained, the training and test set, the method of training (epoch or pattern), and the interval length between network 'saves'. This is the only routine called directly by the user. It randomises the presentation order of the patterns in the training set and may be edited to add noise to the input patterns using Matlab's built-in *rand* command.
- ii. *train_pattern* : is called by *train_network*. It takes as its arguments a single input-output training pattern pair and the network being trained. It returns a cell array of the same dimensions of the weight matrices holding the weight changes associated with that pattern.
- iii. *getoutputs* : is called by *train_pattern*. It returns a cell array of unit outputs for each layer, including bias units, but not including the input layer which is the same as the input pattern. These are calculated from the network parameters and input pattern under investigation.
- iv. *dout* : is also called by *train_pattern* and it returns the differential gain term, δ in Equations 3.13-3.19, used in the weight update calculations. It takes as its

arguments the output values calculated by *get_outputs* and the cell array defining the activation function of the hidden and output layers, *net.act*.

- v. *act* : is the final program of the suit. From the net input of a unit calculated in *get_outputs* and that unit's scaling parameter, *net.T*, it returns the units output with respect to its defined activation function.

By modularising network training in such a way subroutines such as *getoutputs* become available to other routines written to evaluate the effectiveness of the trained network.

During network learning the training and test set mean pattern error is evaluated as described by Equation 4.36. This convergence curve is presented as a graph, as illustrated in Figure 5.15, so allowing the effects of the weight changes to be observed as training progresses.

5.3.1.4 Software Validation

The software was tested by reproducing some of the published work of the Parallel Distributed Processing Research Group at MIT^{5,11}. Specifically, the work involves a network with a single hidden layer being used to solve the classic exclusive OR (XOR) problem. The input-output mapping to be produced is summarised in the truth table of Table 5.3. This problem cannot be solved using a layered network without at least one hidden layer containing at least two units. For an adequate solution to be derived, therefore, the back propagation learning algorithm must be successfully applied. Like the original work all hidden and output units have a sigmoid activation function. Since a specific non-linear mapping is required and the training set is so small there is no test set associated with this problem. Instead, as in the original work, the system is said to have converged on an adequate solution when the mean pattern error has dropped below a value of 0.01.

5.3 The truth table for the XOR gate

Input		Output
1	2	
0	0	0
0	1	1
1	0	1
1	1	0

As in the published case results have been obtained for changes in the number of hidden units (Figure 5.13) and learning rate (Figure 5.14). The momentum term is set at 0.9. The experimental results from this study are summarised along with the published results in Table 5.4, below. The associated errors for the experimental results have been calculated using the median quartile method of those experiments that converge.

Table 5.4 Comparison of experimental and published results for the XOR problem

Learning Rate	Number of Hidden Units	Epoch of convergence (experimental)	Epoch of convergence (published ^{5,11})
0.25	2	260±37	245
0.25	32	125±6	120
0.1	2	600±42	450
0.75	2	100±17	68

As can be seen from the results of Table 5.4 the convergence epoch for the experimental results are all of the order of those from previously published work. The experimental results took slightly longer to converge, but this is explained by the doctoring of the training set by the MIT group. In their experiments they recognised that a output values of one and zero can never be obtained by a sigmoid unit as this activation function is asymptotic to these values. The required outputs for their experiments are, therefore, 0.1 and 0.9 rather than 0 and 1. Consequently their networks take marginally less time to converge.

Interestingly some of the experimental networks get caught in the local minima described by previous researchers. When the network outputs are investigated they give exactly the results expected with the outputs for inputs {1 1} and {1 0} being 0.5. These are shown in Table 5.5 where the solved problem is that of Figure 5.13(a) 'run 1' and the local minimum case is that network with the convergence curve of 'run 3'. In fact, in the published case, these input patterns are {1 1} and {0 1}, but given the intrinsic system symmetry caused by the arbitrary labelling of hidden units this local minimum is essentially the same.

Table 5.5 Outputs for :

(a) a solved problem		(b) one caught in a local minimum	
Inputs	Output	Inputs	Output
0 0	0.0441	0 0	0.0377
0 1	0.9605	0 1	0.9554
1 0	0.9605	1 0	0.4993
1 1	0.0418	1 1	0.5047

As expected any failure to converge is most prevalent in systems with less hidden units - those with less escape routes in the system weight space. Network learning is inhibited when the learning rate is high because the weight matrix cannot resolve to the optimum solution. It is also inhibited when the learning rate is low because weight updates are small. The optimum rate is, as expected, an interim value; in this case 0.25. The software has, therefore, successfully resolved a non-linear mapping to a degree consistent with previously published results and can be used in this study with confidence.

5.3.2 Radial Basis Networks

The radial basis networks investigated in this study are limited to those with a single hidden layer. As reported in Chapter 3, current research suggests that a single layer is all that is required to approximate an arbitrary function. Unlike the multi-layered perceptron case there is no standard test to confirm the software's capability. However, Morgan^{5.12} *et al.* have successfully used graphical means to show an activation function's ability to approximate a given mapping. In this study, therefore,

the network's effectiveness will be illustrated by training it to approximate a two dimensional function the output of which can then be presented in graphical form.

5.3.2.1 Network Structure

The network structure for the Radial Basis Neural Network (RBNN) case is identical to that described for the Multi-Layered Perceptron case with a few exceptions. Firstly, there is no need for the cell array describing the input and output units activation function as these are now limited to being a Gaussian for the hidden layer and a linear summation for the output. Next, as well as the weight matrices cell array there is a centres cell array. This holds the required centre values for each hidden unit; the c_{ji} values of Equations 3.29 to 3.34. Finally, as also shown in these equations, more than one learning rate is required. Consequently, for this study, there are three learning rates: one for the centre value updates, and two for each weight matrix updates.

5.3.2.2 Network Initialisation

As described in Section 3.4.4.2, an RBNN may be created through use of a Kohonen network to find appropriate Gaussian centres. The receptive fields of the unit's activation can then be estimated from the density of other centres in that region and the output weights from pseudo inverse methods. In this study, however, this method is used to initialise the network. The network parameters are then fine tuned using the gradient descent algorithm described in Equations 3.29 to 3.34. It is shown later, in Section 5.3.2.4, that combining these methodologies gave improved network performance when compared to using either one individually.

The centres of the hidden units are, therefore, found using a Kohonen network similar to that described by Hertz *et al.*^{5.13}. The neighbourhood function is defined by a Gaussian and the learning rate is dynamic. As the vector quantisation proceeds the user is presented with a window of the type shown in Figure 5.16. This provides information on the current learning rate value, the width of the neighbourhood function and the distribution of winning patterns associated with a given hidden unit.

The latter of these plots gives a good indication of the progress of the quantisation of the pattern space. As learning nears completion the distribution amongst all the units should be approximately even.

The Kohonen network architecture is simply a two layer system with an input and output layer. The number of units in the output layer is defined by the number of hidden units required by the RBNN network. The interconnecting weights between these layers will later describe the Gaussian centres of the RBNN. They are initially given small random values and then updated during training according to the weight update rule of Equation 5.1.

$$\Delta\omega_{ji} = \alpha\Lambda(j, j^*)(x_i - \omega_{ji}) \quad (5.1)$$

As before, α is the learning rate, but here it is reduced as training progresses and the network converges on a solution. The parameter j^* indicates the winning output unit, that is the unit that has associated weights closest to the input pattern presented. The measurement of closeness is the Euclidean distance between the input pattern and the units' weights. The subtraction term drags the weight vector belonging to the winning unit, ω_j , towards that of the input pattern. The previously mentioned neighbourhood function, Λ , has the value 1 for the weights fanning into the winning unit and then drops for the other units as their topographical distance increases with respect to the winning one. The width of this neighbourhood function decreases during training. In early training it is large to prevent any one unit dominating, i.e. always being the winner, while in later training it is smaller to give better network resolving power. Hence, over time, the network divides the input pattern space equally with respect to the geometry of the hidden units.

This process is illustrated by the plots of Figure 5.17. Here, fifty units are used to describe an 'L' shaped pattern space made up of Cartesian co-ordinate pairs. As training progresses gradually the pattern space is covered by the line describing the weights of the fifty output units. This illustration is similar to that given by Hertz *et al.*^{5.12} and is presented as evidence of the effectiveness of the network software.

For the RBNN network, therefore, the hidden unit centres are simply the weights converged upon by the Kohonen network. However, there is no hard and fast rule in defining the initial values for the widths of these functions (the σ of Equation 3.22). In this study a method based on the k^{th} nearest neighbour non-parametric paradigm is used. As indicated later in the software validation section (Section 5.3.2.4) this approach gives acceptable results as an initial estimate. Intuitively it also appears sensible given that the number of salient neighbouring patterns can be estimated as the number of patterns in the training set divided by the number of hidden units in the RBNN. Thus, the standard deviation of the Gaussian functions is set as that of the Euclidean distance to the k^{th} nearest neighbour where k is the number of patterns divided by the number of hidden units.

Finally the weights for the multi-layered network must be calculated. The weights to the hidden units are derived from the widths of the Gaussian function. As described above the activation function for the units in the hidden layer are as described in Equation 3.22, however, to be used in conjunction with the gradient descent algorithm described in Equations 3.29-3.34 the σ of Equation 3.22 must be translated into equivalent weights for the initialised network.

Consequently the activation of Equation 3.22, loses its normalising denominator and becomes

$$F_j(\underline{x}) = \exp \left(- \frac{\left(\sqrt{\sum_i \omega_{ji} (x_i - c_{ji})^2} \right)^2}{2} \right) \quad (5.2)$$

By simple comparison with Equation 3.22, remembering the denominator has been dropped, it becomes apparent that:

$$\forall_i : \omega_{ji} = \omega_j = \frac{1}{\sigma_j^2} \quad (5.3)$$

where σ_j is the standard deviation associated with hidden unit j and ω_{ji} is the weight from input unit i to hidden unit j .

The output values from each hidden unit, for each input pattern, can now be calculated and the weights matrix, W , to the linear output units derived as:

$$W = (H^T Y)^T \quad (5.4)$$

Where H^T signifies the pseudo inverse of the matrix holding the hidden units' output for each input pattern and Y is the matrix of required, or target, outputs. The superscript 'T' signifies the matrix transpose. This process is greatly simplified by the Matlab command *pinv* which returns the pseudo inverse matrix of that which is passed to it.

Hence, a network of a form compatible with the novel gradient descent algorithm described by Equations 3.29-3.34 has been derived using conventional vector quantisation techniques.

5.3.2.3 Algorithm Implementation

The network is initialised using the technique described above by a function, *rbnn_init*, which, in turn, calls the function *kohonen* to derive the Gaussian centres and widths. The back propagation procedure is described by Equations 3.29-3.34. It is noted at this point that the metric for radial basis activation functions 2 and the function itself, $F(z)$ in the aforementioned equations, described by Equation 5.5, below.

$$F(z) = e^{\left(-\frac{z^2}{2}\right)} \quad (5.5)$$

As in the MLP case, the problem has been modularised into a series of smaller functions. These are given as:

- i. rbnn_bp*: as in the MLP case this routine is called from the Matlab command window and takes as its parameters the network to be trained, the training and test set, the method of training (epoch or pattern), and the interval length between network 'saves'. This is the only routine called directly by the user. It randomises the presentation order of the patterns in the training set and may be edited to add noise to the input patterns using Matlab's built-in *rand* command.
- ii. rbnn_trainpat*: is called by *rbnn_bp*. It takes as its arguments a single input-output training pattern pair and the network being trained. It returns a cell array of the same dimensions of the weight matrices holding the weight changes associated with that pattern and a second cell array holding the changes to the activation function centres.
- iii. rbnn_getoutputs*: is called by *rbnn_trainpat*. It takes as its parameters the network being trained and the current input pattern. It returns two cell arrays holding the units' outputs and their output function differentials: $F'(z)$, of Equations 3.32-3.34.

These routines can be seen to be similar to those for MLP training except that: (1) because the activation types are set, there is no need for the *act* function and (2) the hidden unit output and output differential is calculated by, and returned from, a single function. This is because the differential is no longer a simple function of the unit output, as is the case for linear, sigmoid and hyperbolic tangent activation functions. It is, therefore, quicker and more convenient to calculate its value along with that of the units' output as intermediate terms are shared by both calculations.

5.3.2.4 Software Validation

As previously stated the software's effectiveness has been validated by training it to approximate an arbitrary function with two inputs and a single output. This can then be presented graphically to confirm that the software works as required. The 2-D function used is shown in Figure 5.18. It consists of a Gaussian, a spike and a plateau

on a 51x51 grid so providing 2601 training patterns. Also shown in Figure 5.18 are the results from three initialised networks containing 10, 100 and 400 units respectively. As expected, as the number of hidden units increase so did the network's resolution of the pattern space. Hence, its ability to model the function was also improved.

The graph of Figure 5.19 illustrates the reduction in the recorded mean pattern error when the back propagation procedure is applied. Here, the network containing 100 hidden units has been trained for a total of 100 epochs. The mean pattern error decreases from 15 to around 4; a reduction of over 70%. The procedure's effectiveness is even more apparent when the network's function approximation after back propagation training, as shown in Figure 5.20, is compared to that of the pre-trained network in Figure 5.18. The network has modelled the discontinuities associated with the spike and plateau more ably than the initialised network with four times the number of units. The error associated with the regions containing the Gaussian, spike and plateau reduce by 85%, 27% and 25% respectively. Not surprisingly, given the shape of the activation function, it is the Gaussian that has benefited most from the BP training. However, it is clear that the approximation of all the features within the function have been significantly improved through the application of BP training.

Also shown in Figure 5.20 is a network that has been trained purely using the back propagation approach i.e. its initial weights and centres were given small random values as in the MLP case. For this network, also containing 100 hidden units, the mean pattern error never drops below 25 during 100 training epochs. These results suggest that the network has become stuck in a local minimum. Although the central Gaussian is very well modelled the centres cannot 'break away' to model the other features of the function. Thus the importance of suitable network initialisation is illustrated and the effectiveness of back propagation training subsequent to this initialisation shown.

5.3.3 Wavelet Basis Neural Networks (WBNNs)

The wavelet networks described by Zhang^{5.14} and introduced in chapter 3 are similar in construction to the RBNNs described in the previous section. The network topology is identical with a single hidden layer and a summation output layer made up of linear units. The difference between the two is in the activation function employed in this hidden layer.

The Wavelet Transform (WT) was introduced in the early 1980s^{5.15,5.16} as a signal processing technique that overcomes one of the inherent problems of conventional Fourier techniques, namely the retention of temporal information. It provides a method for the decomposition of non-stationary signals such that scale characteristics and feature location can be highlighted simultaneously through the unfolding of a one dimensional signal into two dimensions. A consequential property of the wavelet transform, therefore, is its ability to characterise localised regularity within the function under investigation^{5.17}. As described in Section 3.4.4.3, it is these properties the author is attempting to utilise in producing a wavelet network.

The activation function is described as a wavelet if it adheres to three primary conditions:

- i. It must have finite energy.
- ii. If $g(\omega)$ is the Fourier Transform of the wavelet, $g(t)$, then the *admissibility condition* must hold i.e. the functions mean should be zero. Hence:

$$C_g = \int_0^{\infty} \frac{|\hat{g}(\omega)|^2}{\omega} d\omega < \infty \quad \text{when the dilation parameter, } a \in +\mathcal{R} \quad (5.6)$$

- iii. For complex wavelet functions the Fourier transform should be real and vanish for $\omega \leq 0$.

In this study the wavelet employed is the Mexican Hat wavelet. Of the real wavelet types used in signal processing this Gaussian derivative is the most often employed because it has good support in both time and frequency domains. The wavelet with optimal time-frequency support is the Morlet wavelet. This, however, is a complex wavelet and, as such, introduces inherent difficulties in calculating error contributions and activation derivatives for wavelet networks. The Mexican Hat wavelet is, also, the wavelet type used by Zhang in his example of a wavelet network application and is, therefore, the only wavelet for which there is a precedent for use in this type of wavelet network. The Mexican Hat wavelet has been shown by the author to have favourable properties for use in the de-noising of sonic echo traces from pile integrity testing^{5,18}. The definition for the Mexican Hat wavelet, as used in this study, is given in equation 5.7, below.

$$\psi(x) = \left(1 - \|x\|^2\right) e^{-\frac{\|x\|^2}{2}} \quad (5.7)$$

where

$$\|x\|^2 = x^T x \quad (5.8)$$

and

$$\psi_{a,b}(x) = \frac{1}{a^{d/2}} \psi\left(\frac{x-b}{a}\right) \quad \text{where } x, b \in \mathfrak{R}^d \quad (5.9)$$

Equation 5.9 encapsulates the wavelet function that has undergone translation b and dilation a . An example of the Mexican Hat wavelet for $d=2$, with $b=\{0,0\}$ and $a=7$ is shown in Figure 5.21.

5.3.3.1 Network Structure

The network data structure for the wavelet networks is identical to that described for the RBNNs in Section 5.3.2.1. In this case, however, the centres and widths of the

radial basis units become the translation and dilation parameters of the wavelet functions respectively.

5.3.3.2 Network Initialisation

With reference to the initialisation procedure described in Chapter 3: Zhang^{5.14} states that the calculation of the total wavelet basis set, that is the intersect of the entire wavelet bases and those whose support covers at least one data point in the training set, is 'not very sensitive' to the input pattern dimension. While it is true that interrogating the training data to find the basis (i.e. dilation and translation parameters) of interest will reduce the search space considerably the size of the input dimension will clearly have an effect on the size of the resultant basis set. Due to the input to the radial wavelet being a scaled Euclidean distance measure, as the dimensionality of the input vector increases so will the number of permutations of 'b', the translation vector, which fall within the support of a given dilation value.

Even for the compact example used to illustrate the radial basis network where the data has no inherent sparsity the number of frames in the final set from which an initial network is to be drawn, L , is in excess of 300,000 bases. In this case five translation positions for each input dimension at each dilation level are considered.

Although a value of 300,000 does not seem large in itself the modified Gram-Schmidt algorithm described by Zhang^{5.14} for the selection of the network's chosen wavelet regressors involves the use of three $L \times N$ matrices, where N is the number of patterns in the training set. These matrices are accumulator matrices and so must be held in memory rather than calculated at each iteration within the algorithm. Further to this each basis in the set must be considered at each iteration. The modified Gram-Schmidt algorithm as described here is also only pertinent to problems where the network output, \hat{y} , is a scalar. That is, while the input vector, $x \in \mathfrak{R}^d$, the output, $\hat{y} \in \mathfrak{R}$. For the method to be extended to vector outputs the network must be modularised and the initialisation process repeated for each output unit.

These factors combined suggest that even for the simple example used in the radial basis case this method for network initialisation is prohibitively complex (in the computational sense) for the applications under investigation. This is particularly true when one considers that this is an initialisation procedure and further computation is necessary subsequent to its completion.

For this application, therefore, an initialisation process is presented that is similar to that used in the Radial Basis case. That is, a Kohonen network is used to describe the input space in terms of wavelet translation parameters - the centres in the RBNN case. Noting that the radial Mexican Hat wavelet has a Gaussian envelope, the distribution of the Euclidean distance measures from these centres for each training pattern is then used to estimate a suitable dilation parameter - much in the same way the standard deviation values are estimated for the RBNNs.

For the Mexican hat wavelet described above the standard deviation of the main lobe, as visible in Figure 5.21, is approximately $\sqrt{2}$ times smaller than that of the equivalent radial basis function. That is, for the activation function values around the k nearest neighbours of the wavelet translation parameters to be similar to those around the centres of the equivalent radial basis function the dilation parameter must be $\sqrt{2}$ times larger than the standard deviations calculated for the radial basis case. Once this scaling has been applied the weights of the network can be derived in exactly the same way as for the RBNN case. The weights to the hidden units being calculated from the wavelet dilation parameters as, c.f. Equation 5.3,

$$\forall_i : \omega_{ji} = \omega_j = \frac{1}{a_j^2} \quad (5.10)$$

With the hidden unit parameters having been defined the weights to the output units are then derived using the pseudo inverse method described in Section 5.3.2.2. Hence, a network of a form compatible with the gradient descent algorithm described by Equations 3.29-3.34 has been derived using vector quantisation techniques rather than the prohibitively complex Gram-Schmidt algorithm described by Zhang.

5.3.3.3 Algorithm Implementation

The initialisation and back propagation training of wavelet networks is essentially identical to that of radial basis networks. The network is initialised using a function *wbnn_init*, as described above. The network is then trained using a suite of functions: *wbnn_bp*, *wbnn_trainpat*, and *wbnn_getoutpus*. The arguments passed and structure of these routines are identical to their radial basis equivalents described in Section 5.3.2.3. The coding of the functions are, however, obviously different in that the activation function and its derivative now takes the form of a Mexican Hat wavelet rather than the Radial Basis function. With reference to Equations 3.19-3.34, the metric of the radial wavelet, like the radial basis function, 2.

5.3.3.4 Software Validation

As in the RBNN case the software's effectiveness has been validated by training it to approximate the function of Figure 5.18. After initialisation the resultant WBNN function approximation for a 100 unit network is presented in Figure 2.23. As can be seen from the start of the convergence curve of Figure 5.22 this initial approximation has a mean pattern error of the order of that of the equivalent RBNN network (≈ 15), shown in Figure 5.19. Subsequent to back propagation training the error drops from 13 to 5; a reduction in excess of 60%. The resultant, trained network, is also presented in Figure 5.23. As in the RBNN case the function approximation of all features within the trace has improved. For the regions containing the Gaussian, spike and plateau the approximation error has reduced by 43%, 24% and 16% respectively.

Of note in the convergence curve of Figure 5.22 is the large spike at around 55 epochs. This type of feature has been noted in a number of back propagation curves for both radial basis and wavelet networks. It is suggested that this is a consequence of altering two function parameters during each network update. Although individually the effects of changing the weights and centres may reduce the pattern error as required there is no guarantee that altering both simultaneously will produce

such a reduction. In every case in which this feature is observed, however, the error is reduced to its previous, lower, level within a few subsequent epochs.

From the initialised network output of Figure 5.23 one can see that the flat regions of the surface do contain more ripples than in the radial basis case. This is due to the undulations in the activation function. Each negative lobe in the Mexican hat function must be cancelled by adjacent units. In the RBNN case this is not the case as the activation function is always positive. The consequence of the negative side lobes is also observable in the back propagation trained network of Figure 5.23 where a small trough of negative values can be seen around the spike and plateau features. This effect should not be taken as an indication that the RBNN is more effective for function approximation tasks in the general case, but rather that for this simple function, which is made up of only positive features and with no inherent regularity, the RBNN is better suited. For the general case it is easy to imagine a function that would be more readily modelled using the wavelet network - at a trivial level, for example, that of Figure 5.21.

Finally, shown in Figure 5.24, is a series of histograms indicating the distribution of input and output weights, and hidden unit translations (wavelet centres). Immediately obvious from the third column is the fact that the centres have remained within the limits of the training pattern space (-25 to +25) and no spurious values have resulted from back propagation training. It is also apparent that the input layer weights now contain a number of larger weights and so some hidden unit wavelet functions contain lower dilation parameters (Equation 5.10). Thus, it is apparent that the wavelet network has correctly modelled the surface features, specifically the spike, through the migration of the function centres and contraction of the wavelet dilation parameters during learning. This is presented as further evidence that the network training has progressed as required and that the software can be used with confidence.

5.4 SUMMARY AND CONCLUSIONS

Commercially available data acquisition equipment is light and robust, but inflexible in its usage and prohibitively expensive for research purposes.

Equipment previously employed by the University for data acquisition is bulky and complex in its usage. It is neither conducive to the rapid checking of pile groups nor the 'on-line' analysis of collected data of the type required in this study.

A new data collection system has been developed for this study. For each component there exists a precedent of its use for data collection within the pile testing industry.

Purpose written software has been developed to control this hardware through a graphical user interface and port the collected data directly to Matlab™ for subsequent analysis.

A suite of programs have been written for the initialisation and training of Multi-layered Perceptron (MLP) networks, Radial Basis Neural Networks (RBNN) and Wavelet Basis Neural Networks (WBNN).

For RBNN's, training through vector quantisation initialisation followed by back propagation learning has indicated improved results over those using either one of these methods independently.

A new method for initialising WBNNs has been presented based on the vector quantisation method used for RBNNs. This is computationally quicker and less memory intensive than the suggested modified Gram-Schmidt algorithm. No claims are made about relative performances of the two methods.

Validation of the network simulator software has been presented. For the MLP case previously published results have been satisfactorily reproduced. For the RBNN and WBNN networks an arbitrary function containing a spike, a Gaussian and a plateau has been approximated with results consistent with those that are expected. That is,

network performance improved as the number of hidden units was increased and improved further subsequent to back propagation training.

REFERENCES

- (5.1) Neuralworks Professional II, User Manual, Neural Ware Inc., (1988)
- (5.2) Watson J N, Temporal Difference Learning in Neural Networks, MSc Thesis, Queen Mary and Westfield College, University of London, (1993)
- (5.3) Using Matlab[®], Revision 5.3, The MathWorks, Inc., USA (1999)
- (5.4) Chan, H-F C, Non-Destructive Testing of Concrete Piles using the Sonic Echo and Transient Shock Methods, PhD Thesis, University of Edinburgh, (1987)
- (5.5) Sibbald A, Impact Hammer Testing of Masonry Sewers, PhD Thesis, University of Edinburgh (1987)
- (5.6) Armstrong D M, Integrity Assessment of Structures Using Modal Testing, PhD Thesis, Napier University, Edinburgh (1994)
- (5.7) Ali-Ahmed H, Non-Destructive Testing of Arch Bridges, PhD Thesis, Napier University, Edinburgh (1998)
- (5.8) Computer Boards Inc., PCM-DAS16D/16, User Manual, Revision 3, (1999)
- (5.9) Computer Boards Inc., Universal Library, Function Reference, Revision 5, (1998)
- (5.10) Matlab Application Programming Interface Guide, Version 5, The MathWorks, Inc., USA (1998)
- (5.11) Rumelhart D E, Hinton G E and Williams R J, 'Learning Internal Representations by Error Propagation', in Parallel Distributed Processing, Volume 1: Foundations, Eds Rumelhart D E, McClelland J L and The PDP Research Group, MIT Press, (1986) pp318-362
- (5.12) Morgan P, Curry B and Beynon M, 'Comparing Neural Network Approximations for Different Functional Forms', Expert Systems, Vol.

- 16, No. 2 (1999) pp60-71
- (5.13) Hertz J, Krough A, and Palmer R G, Introduction to the Theory of Neural Computing, Addison Wesley, (1991) p239
- (5.14) Zhang Q, 'Using Wavelet Network in Nonparametric Estimation', IEEE Trans. on Neural Networks, Vol. 8, No. 2 (1997) pp227-236
- (5.15) Goupillaud P, Grossmann A and Morlet J, Cycle-Octave and Related Transforms in Seismic Signal Analysis, Geoexploration, Vol. 23 (1984), pp85-102
- (5.16) Grossmann A and Morlet J, Decomposition of Hardy Functions into Square Integrable Wavelets of Constant Shape, SIAM J. Math. Anal. Vol. 15, No. 4 (1984), pp723-36
- (5.17) Mallat S and Hwang W L, Singularity Detection and Processing with Wavelets, IEEE Trans. Info. Theory, Vol. 38, No. 2 (1992), 617-643
- (5.18) Watson J N, Addison P S and Sibbald A, 'The De-Noising of Sonic Echo Test Data through Wavelet Transform Reconstruction', The Journal of Shock and Vibration, *In Print* (2000).

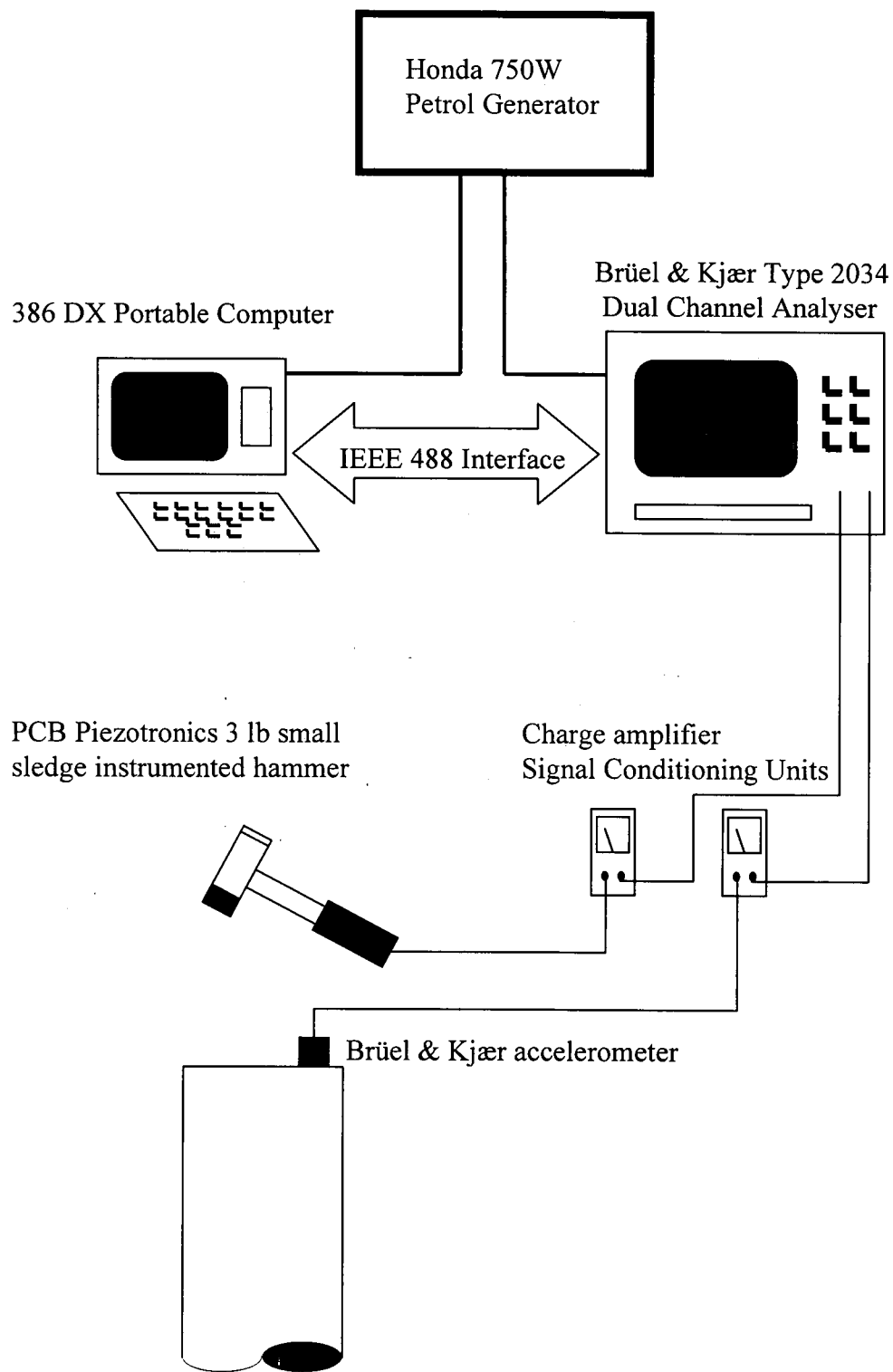


Figure 5.1 A schematic of the impact testing equipment previously used for NDT research by Edinburgh and Napier Universities .

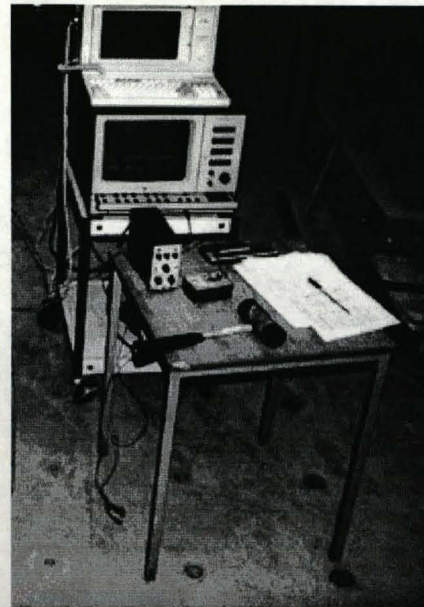


Figure 5.2 The Honda generator (left) and testing equipment (right) described in the schematic of Figure 5.1

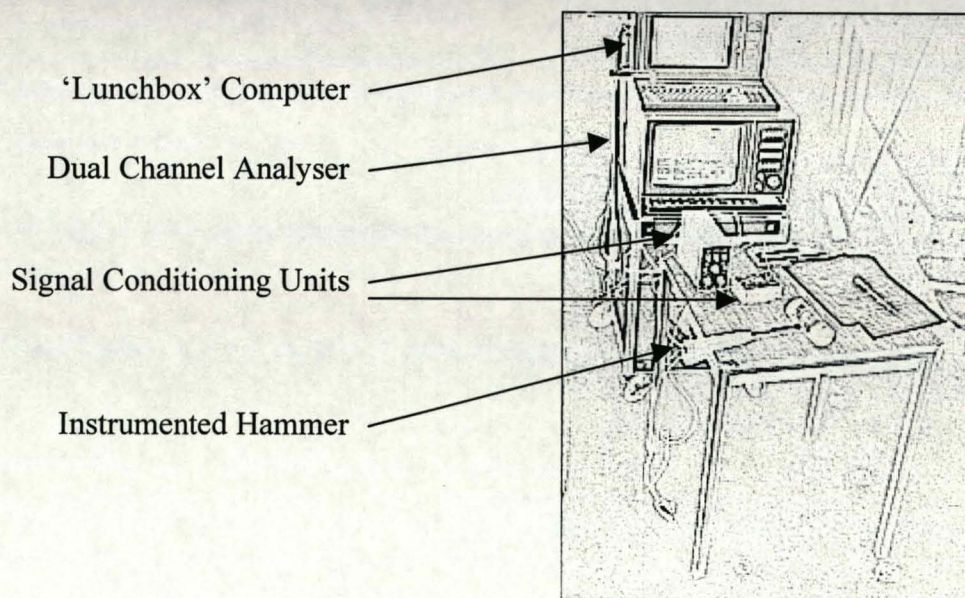


Figure 5.3 An edge diagram of the testing equipment of Figure 5.2 with labelled components.

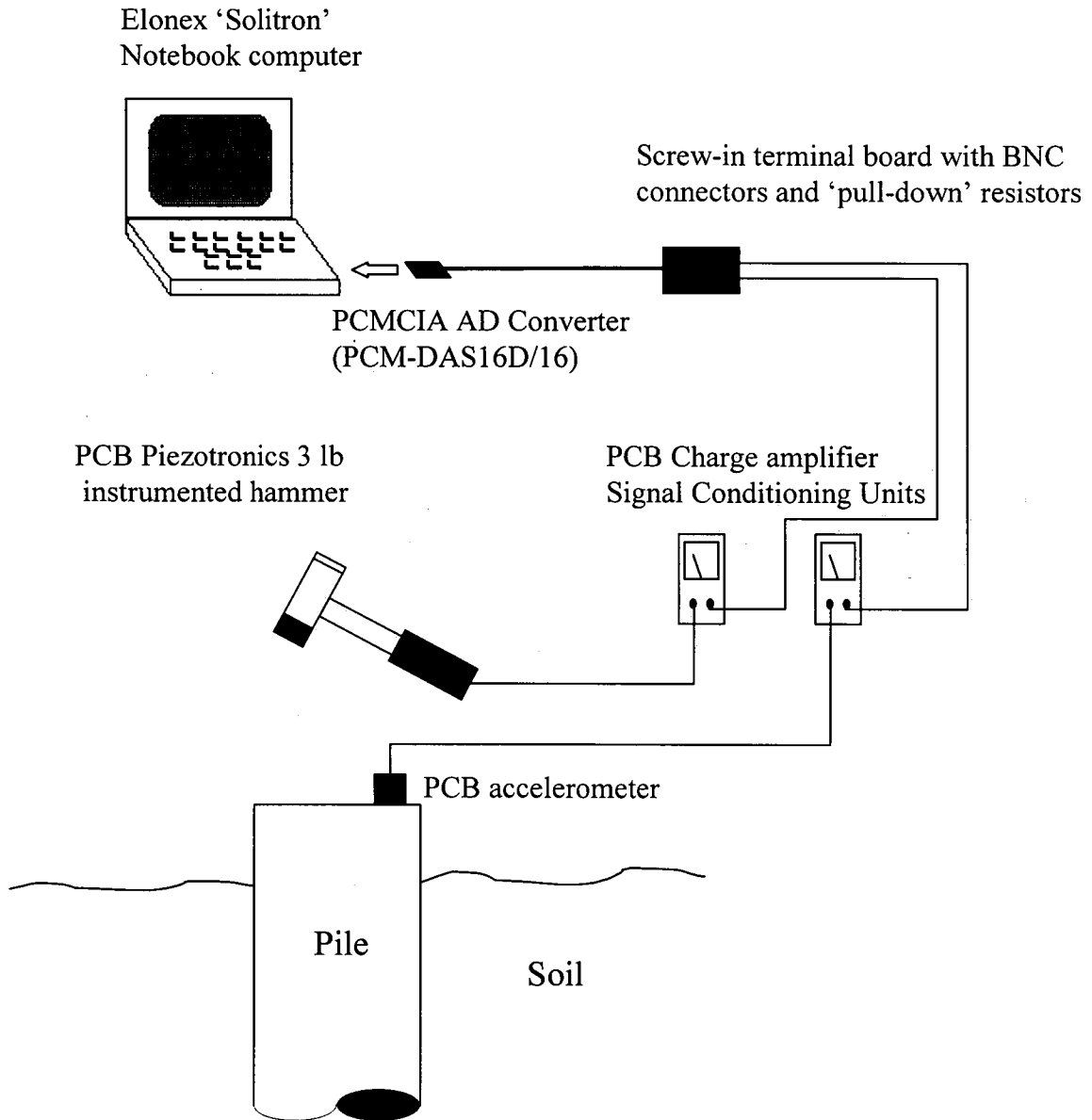


Figure 5.4 A schematic of the equipment developed for the collection of data presented in this study



Figure 5.5 The equipment used for data collection in this study, as described in the schematic of Figure 5.4



Figure 5.6 The PCB signal conditioning unit type 480E09 (left) and, from top to bottom, 12 lb 'sledge', 3 lb 'hand sledge', and 1lb 'heavyweight' hammers (right)

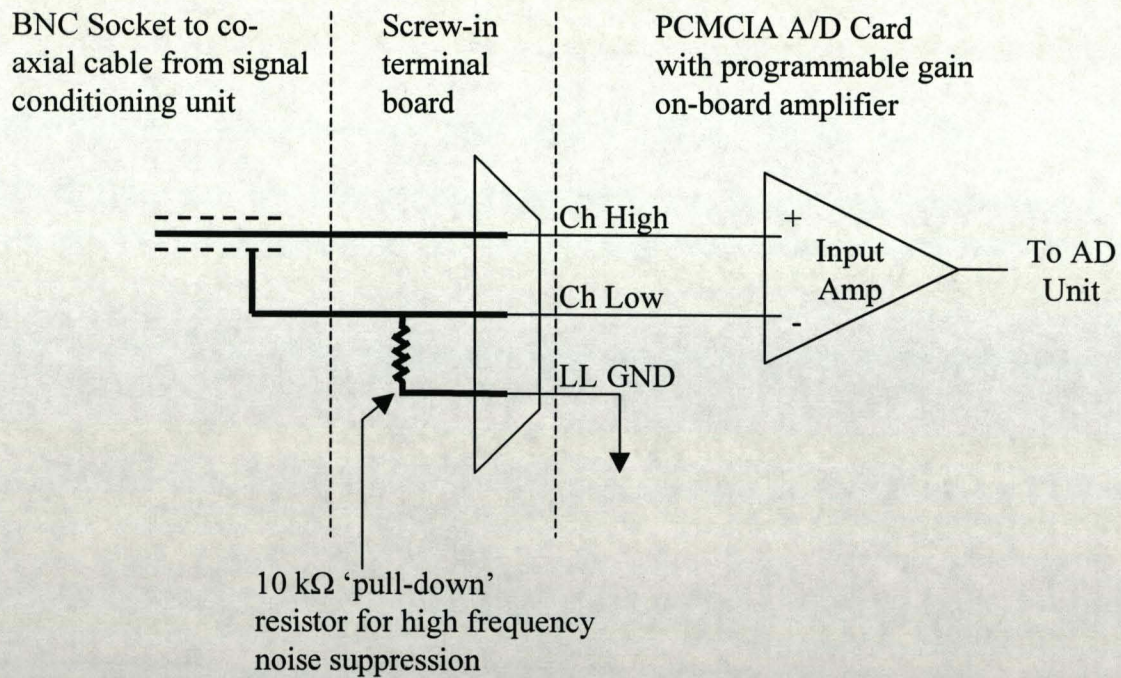


Figure 5.7 A circuit diagram for a single channel in the junction box of Figure 5.4. The co-axial cable from the signal conditioning units is mapped to the differential inputs of the ADC through a screw-in terminal board

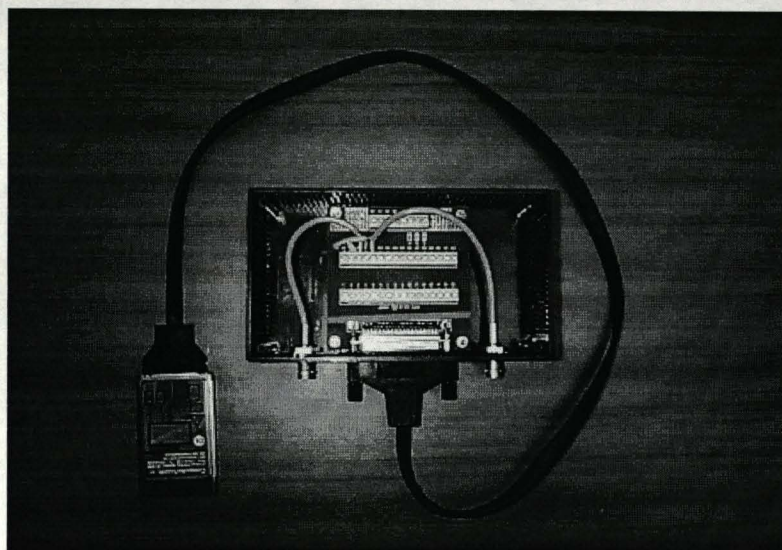


Figure 5.8 The junction box with lid removed showing the screw in terminal board (centre) and the PCMCIA AD converter card which fits directly into the laptop PC (left)

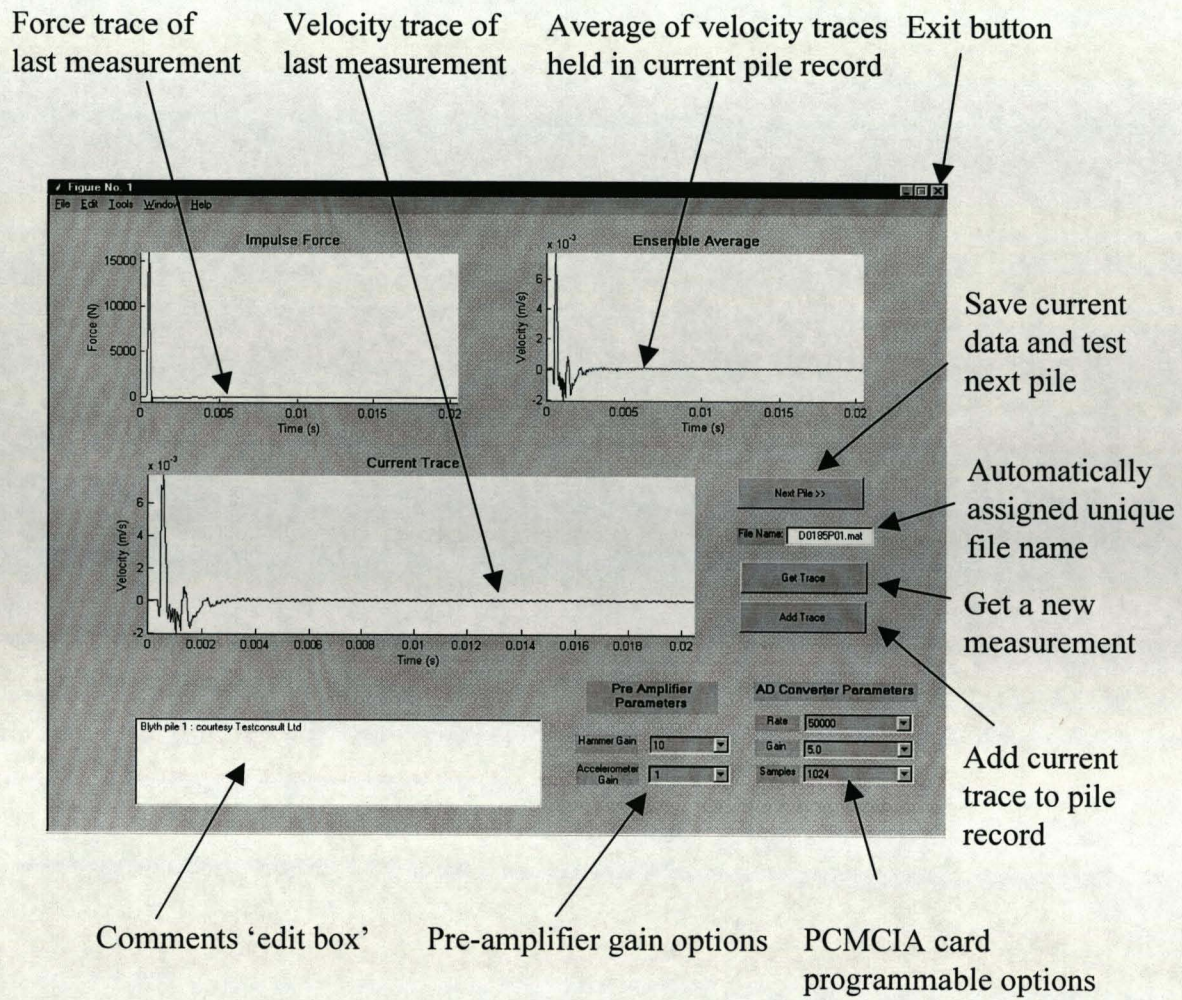


Figure 5.9 A window capture from the data acquisition software with component labelling.

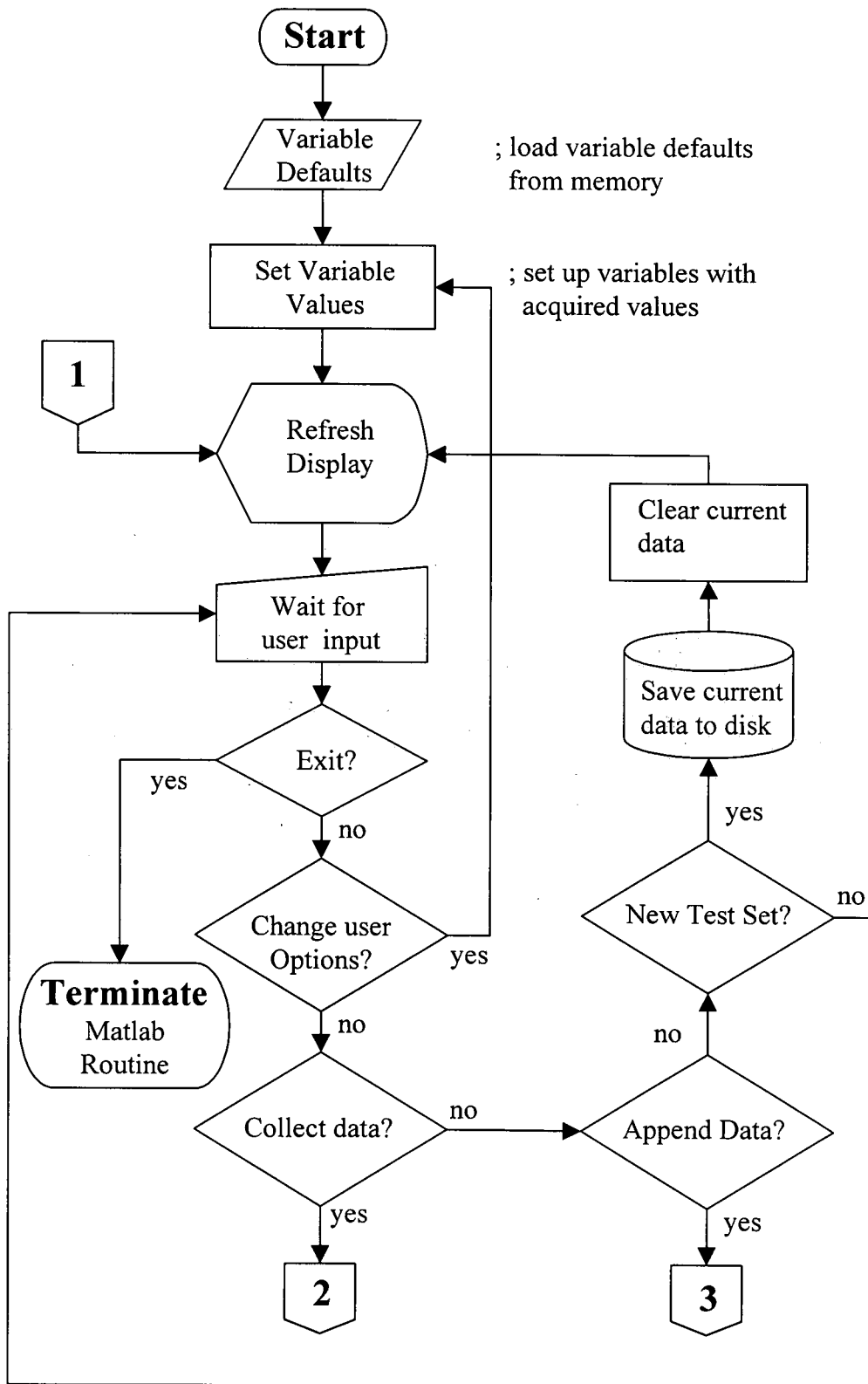


Figure 5.10 A flow diagram of the main program loop for the data collection software. Off-screen links '2' and '3' are described in subsequent Figures 5.11 and 5.12

Collect data, parameters passed include:
sample rate, number of samples and gain

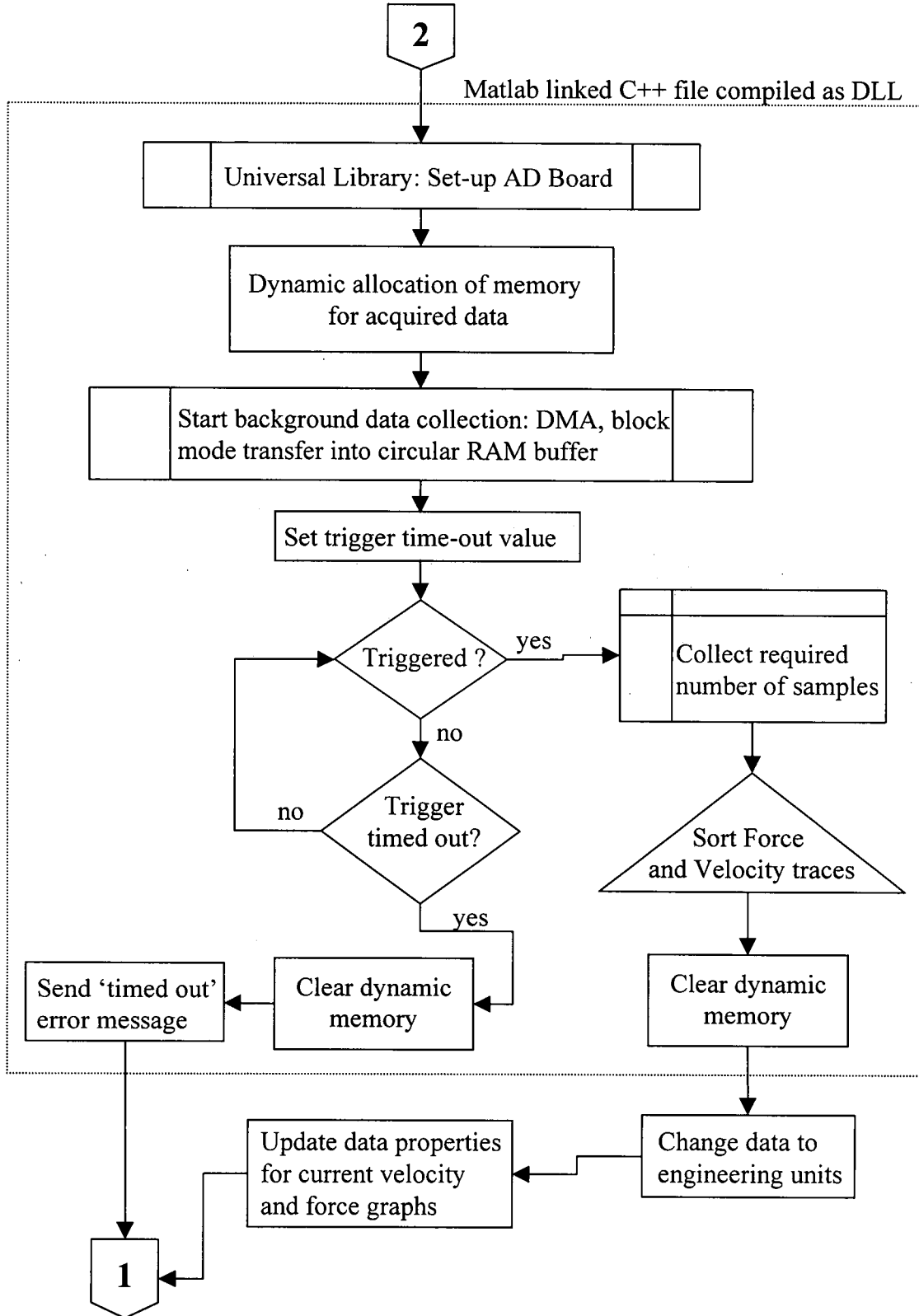


Figure 5.11 A flow diagram of the data acquisition module of the data collection software. Off-screen links '1' and '2' are links to the main program loop of Figure 5.10

Append data to pile array record

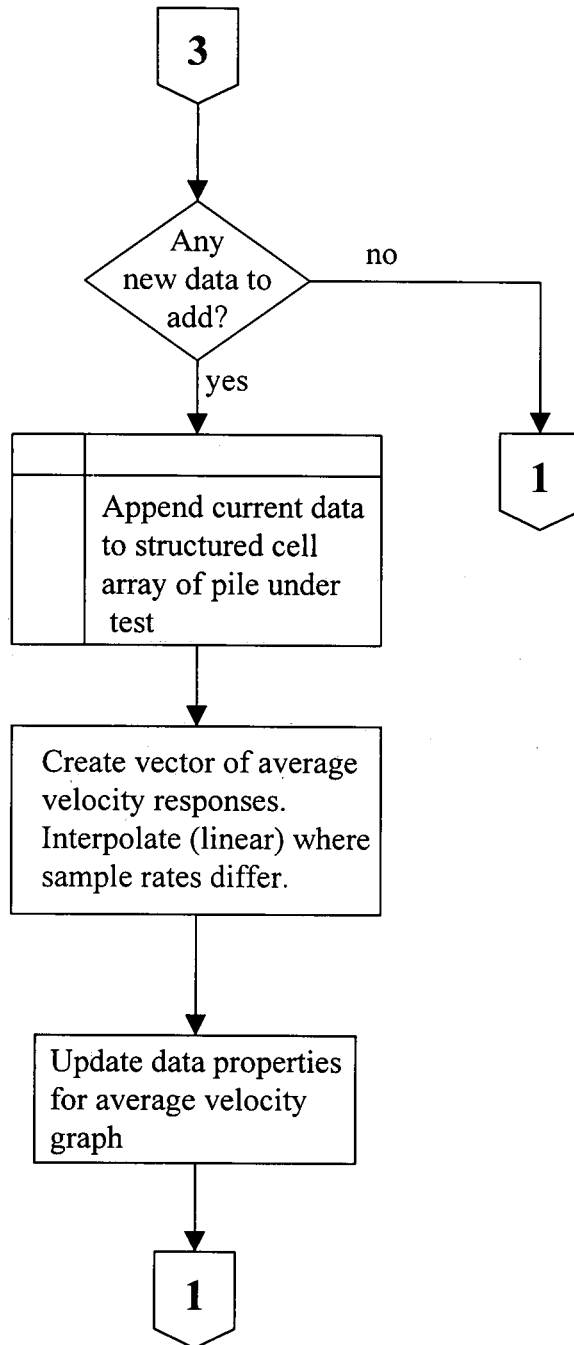
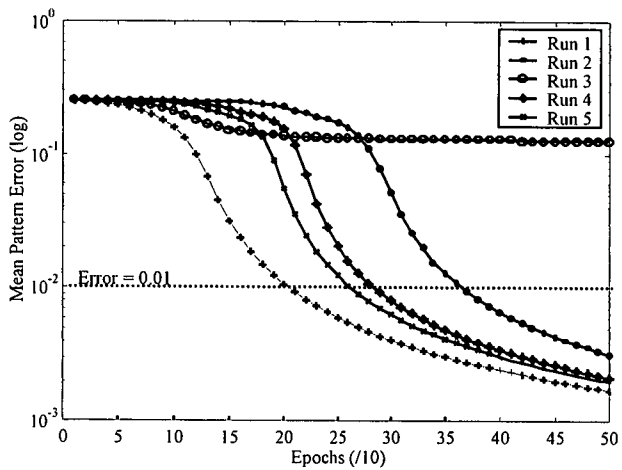
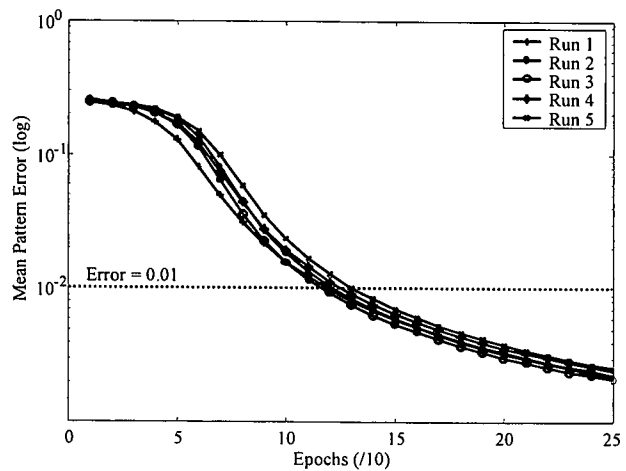


Figure 5.12 A flow diagram for the data appending module in the data acquisition software. Here, the previously collected data is appended to the current pile record. Off-screen links '1' and '3' are links to the main program loop of Figure 5.10

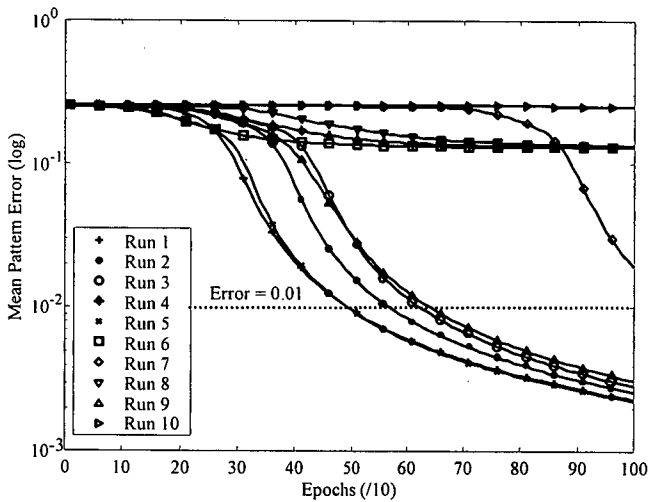


(a) 2 Hidden units ; $\lambda=0.9$; $\alpha=0.25$

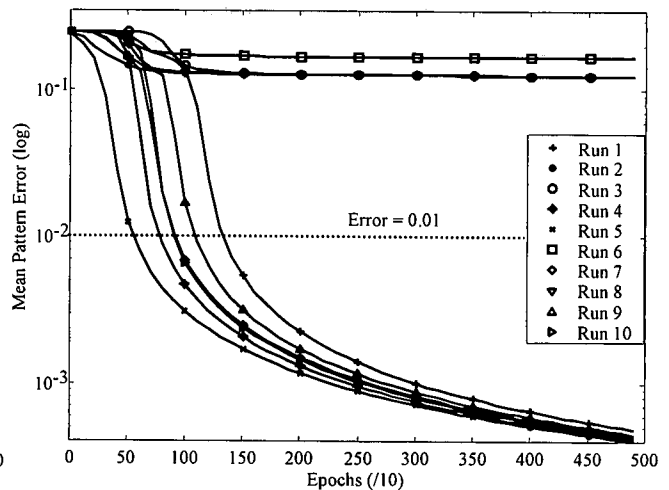


(b) 32 Hidden units ; $\lambda=0.9$; $\alpha=0.25$

Figure 5.13 Graphs illustrating the convergence curves for the classic XOR problem. The feedforward networks with sigmoid activation functions have 2 (left) and 32 (right) hidden units. Each has a learning rate, α , of 0.25 and a momentum value, λ , of 0.9



(a) 2 Hidden units ; $\lambda=0.9$; $\alpha=0.1$



(b) 2 Hidden units ; $\lambda=0.9$; $\alpha=0.75$

Figure 5.14 Further graphs illustrating the convergence curves for the XOR problem. As in figure 5.13, these results are for feedforward networks with sigmoid activation functions, however here both have 2 hidden units and learning rates of 0.1 (left) and 0.75 (right).

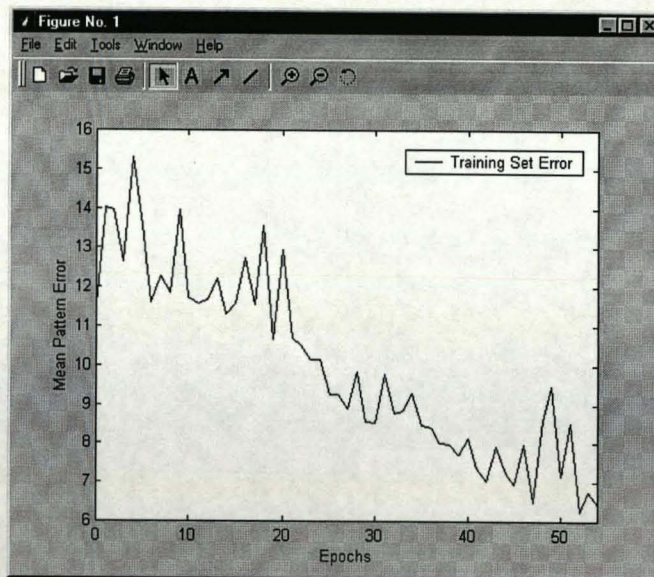


Figure 5.15 A window capture illustrating the convergence curve presented to the user during network training. In this case no test set is defined and so only the training error curve is shown. The same window is presented during MLP, RBNN, and WBNN back propagation training

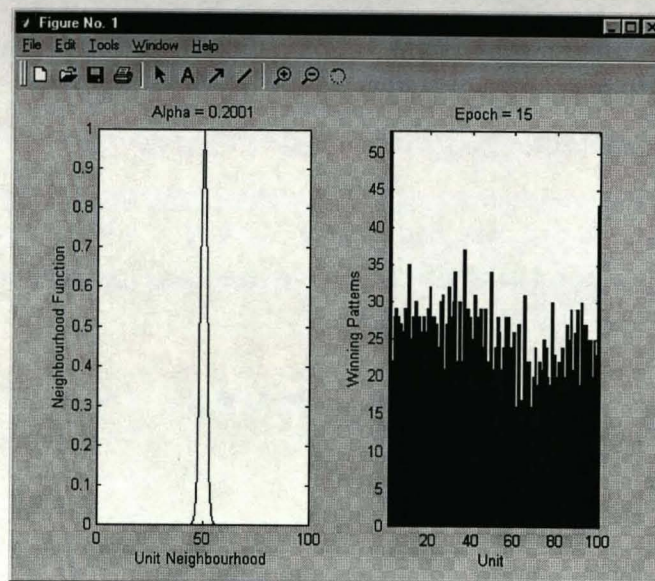
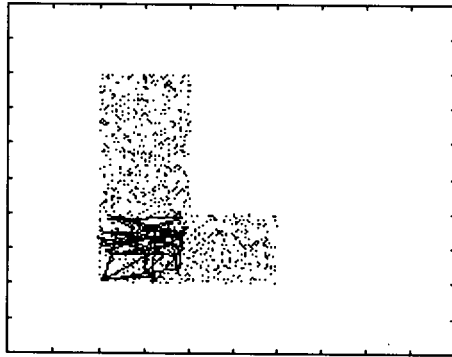
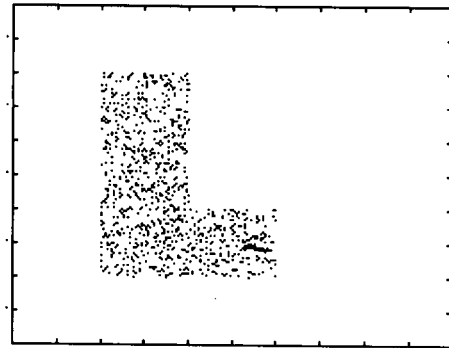


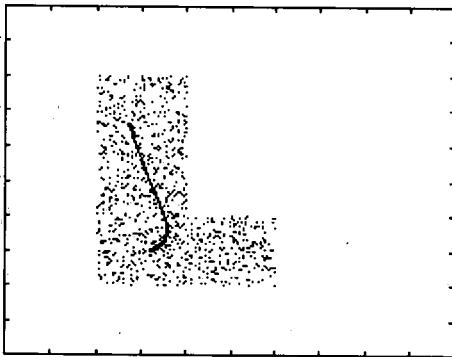
Figure 5.16 A window capture illustrating the data presented to the user during Kohonen network training. Here, the left hand graph indicates the extent of the neighbourhood function while the right hand graph shows the number of patterns associated with each winning unit. The learning rate for the current iteration and the epoch number are also presented at the top of the window



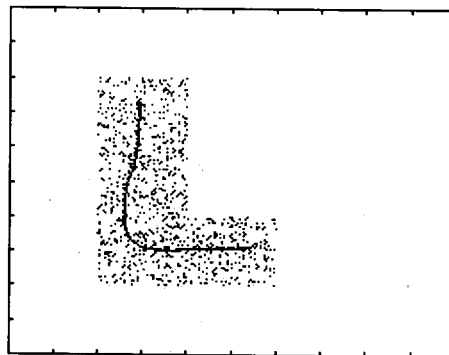
Epochs = 0



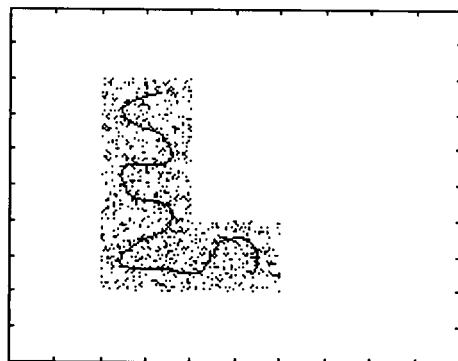
Epochs = 1



Epochs = 5



Epochs = 20



Epochs = 100

For this experiment:

50 units (describing pattern space)

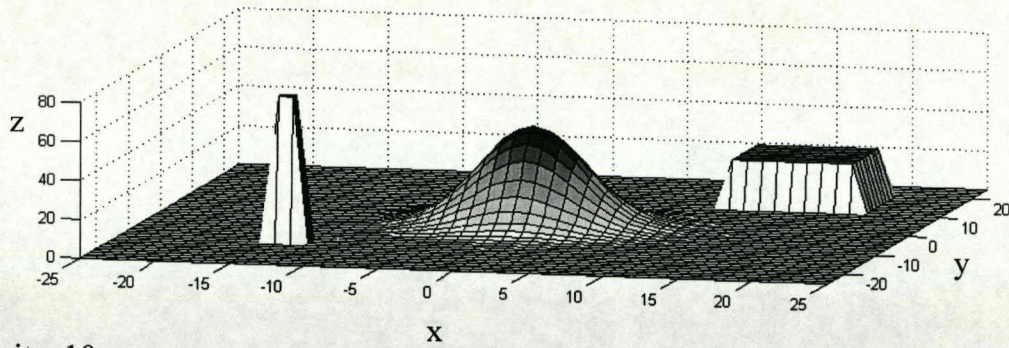
1000 training patterns (defining pattern space)

Learning rate, $\alpha \propto (1 - t / t_{\max})$

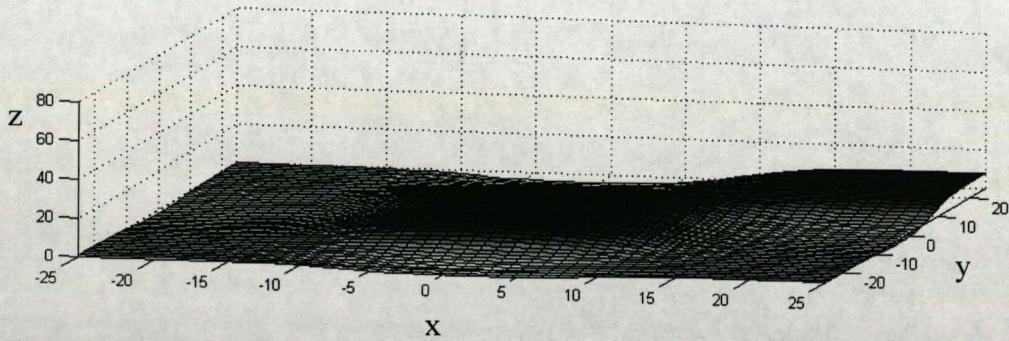
Standard deviation of Gaussian
neighbourhood function,
 $\sigma \propto \exp(-t / t_{\max})$

Figure 5.17 The utility of the Kohonen network developed for use in this study. A set of 1000 Cartesian co-ordinate pairs make up an 'L' shaped pattern space of constant density. As training progresses the weights of the fifty unit Kohonen network, shown here as a line, converge on a solution such that each unit's weights has an equal number of nearest neighbours in the pattern space. (c.f. Hertz *et al.*^{5.12})

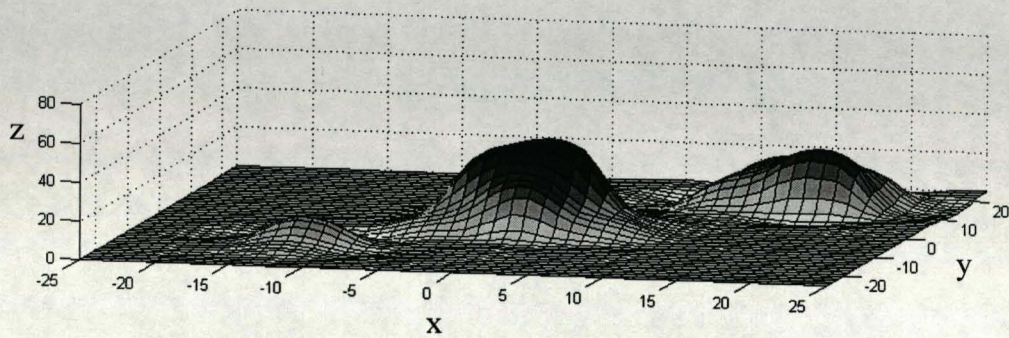
Training data



Units=10



Units=100



Units=400

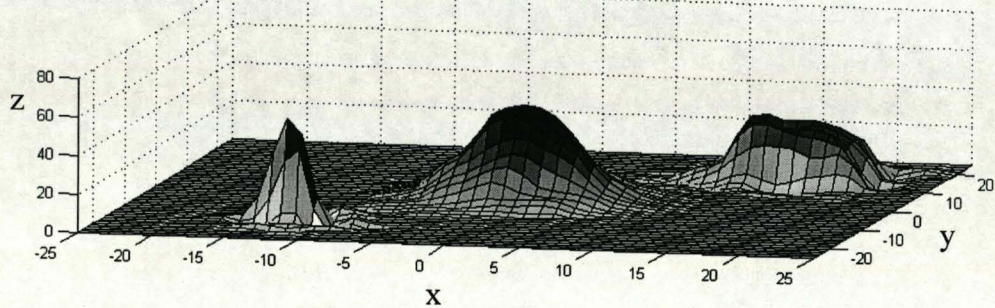


Figure 5.18 The results of the initialisation procedure of a number of Radial Basis Neural Networks. Top is the training set describing an arbitrary 2-D function made up of a Gaussian, a spike and a plateau. Beneath is the networks' approximation of this function following initialisation. From the second plot down the networks contain 10, 100 and 400 hidden units respectively

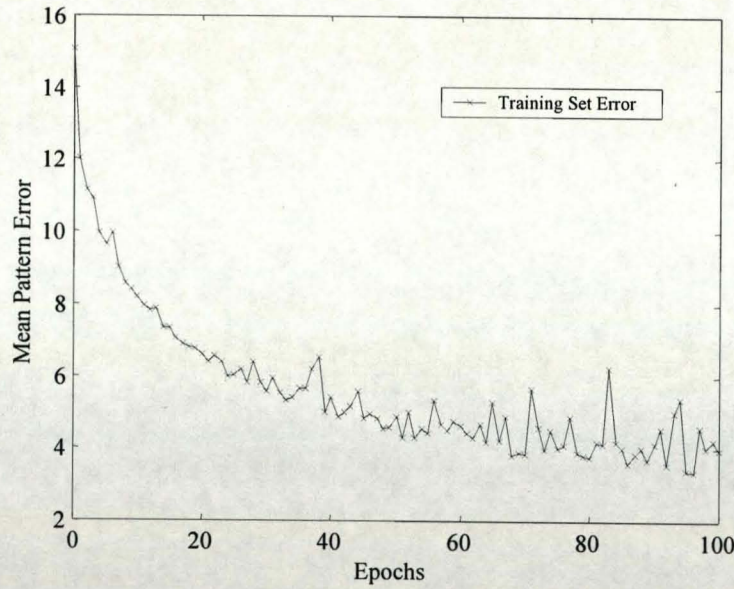
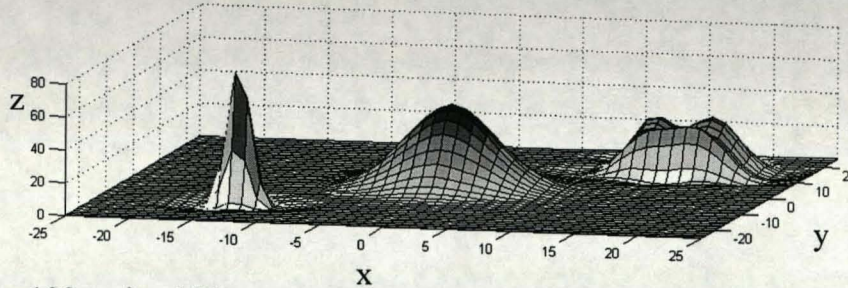


Figure 5.19 The convergence curve of the Radial Basis Network with 100 hidden units of Figure 5.18 using back propagation learning post initialisation. The learning rates for hidden weight changes, output weight changes and Gaussian centre changes, are given as $\alpha_w(\text{hidden})=0.00001$, $\alpha_w(\text{output})=0.05$, and $\alpha_c=0.0005$ respectively

Epochs=100, units=100



Epochs=100, units=100

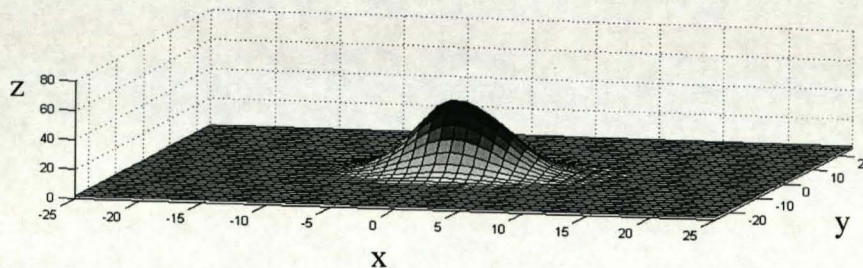


Figure 5.20 The network approximation of the function shown in Figure 5.18 after back propagation training. Top, after initialisation and, bottom, without initialisation (i.e. the network starts with small random weights and centres). Note, for the network that is not initialised the mean pattern error never drops below 25 and the network appears to be caught in a local minimum about the central Gaussian.

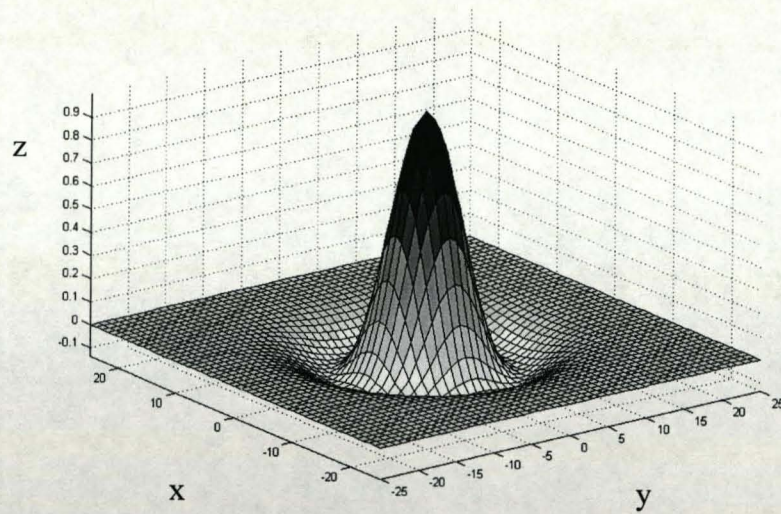


Figure 5.21 The 2-D Mexican hat wavelet centred on $(x=0, y=0)$ with a dilation parameter value, $a = 7$

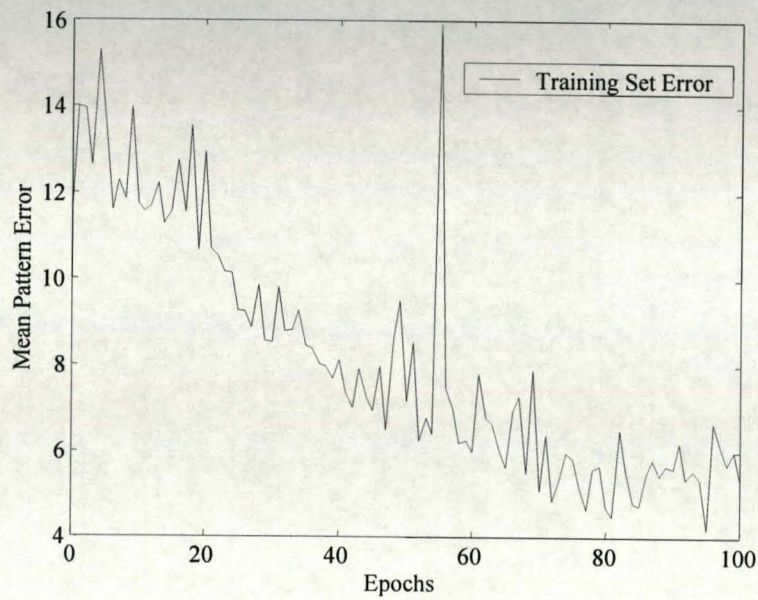
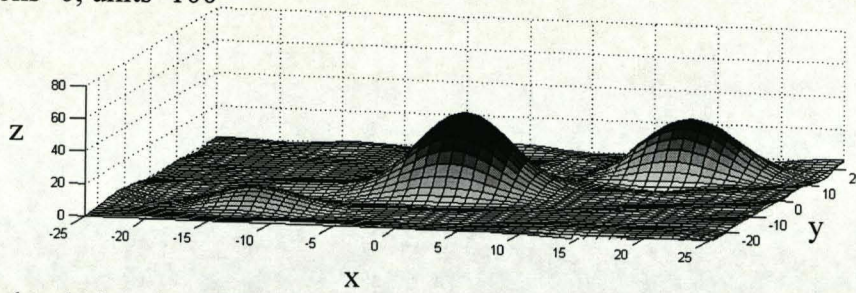


Figure 5.22 The convergence curve of the Wavelet Basis Neural Network with 100 hidden units using back propagation learning post initialisation. The learning rates for hidden weight changes, output weight changes and wavelet centre changes, are given as $\alpha_w(\text{hidden})=0.000001$, $\alpha_w(\text{output})=0.1$, and $\alpha_c=0.0005$ respectively

Epochs=0, units=100



Epochs=100, units=100

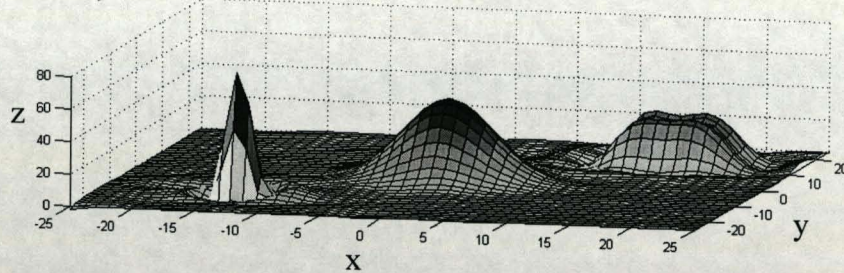


Figure 5.23 A 100 unit wavelet network's approximation of the function presented in figure 5.18 post initialisation (top) and after subsequent back propagation learning (bottom). Learning parameters and the convergence curve are given in figure 5.22

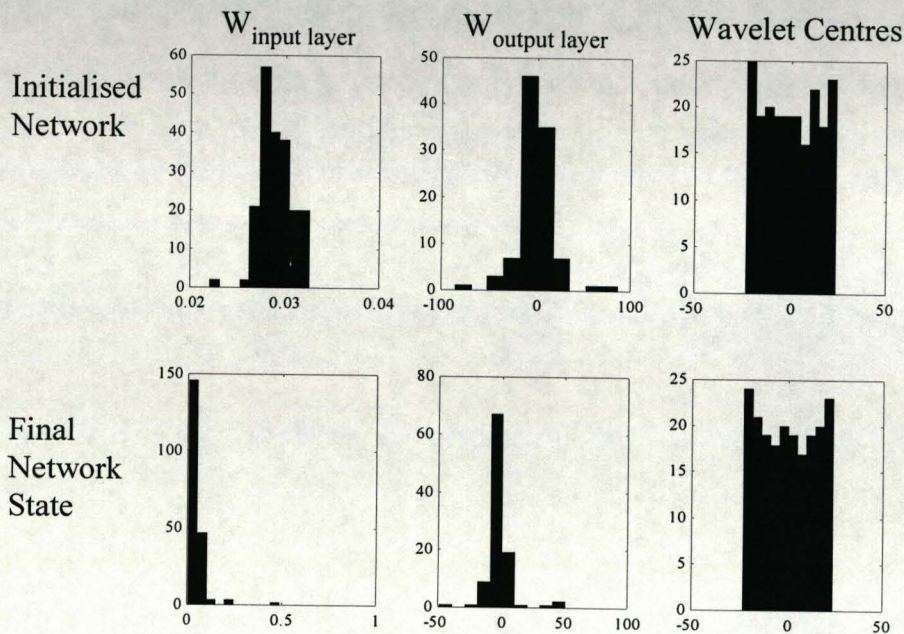


Figure 5.24 Some thumbnail histograms indicating changes in the network's weight and centre values pre (top) and post (bottom) back propagation training. Of note is the continued restriction of centre values to the pattern space limits of -25 to +25 while the distribution within these limits has changed

6. Application Development

6.1 INTRODUCTION

In this Chapter the findings of the preliminary investigations of Chapter 4 are extended and applied to installed foundation piles of varying lengths and with varying degrees of defect. An optimum architecture and learning paradigm is found for each of the networks chosen in Chapter 3 as suitable candidates for this task, i.e.: multilayer perceptron (MLP), radial basis (RBNN) and wavelet basis neural networks (WBNN). The relative performance of each network type is then considered before the most successful is chosen for use on field test data. Various pre- and post-processing methodologies are considered and compared with respect to resultant network performance. The final system chosen incorporates novel wavelet transform de-noising techniques, dynamic signal enhancement and Fourier encoding of the sonic echo time trace which is then interpreted by a MLP neural network - as described by Figure 6.1. The results of the field test validation of the selected network are presented in Chapter 7.

The site data selected for this investigation comes from the Blyth test site and the problem domain, therefore, is restricted to piles of the type found there. Specifically this means the training data is restricted to piles of length 9m to 13m with a diameter of 0.8m. The Blyth site data and finite element methodology for trace generation is described fully in Chapter 4.

Clearly the ultimate goal of presenting an accurate pile profile for any arbitrarily shaped pile is unachievable. As discussed in Chapter 2 larger faults at the head of

the pile will mask faults towards the pile toe. Also, a change in radius of 100% will give close to 100% reflection thus any further increase in section will have no effect on the resultant sonic echo trace. A pragmatic approach must, therefore, be taken in selecting the data included in the training and test sets. Training the networks on truly random pile profiles will not only lead to greater uncertainty in the problem domain, but render the problem intractable. Hence, a pseudo-random data set has been used in the training of the networks. The maximum changes in section along the pile length are restricted to 75% increase or decrease in radius. The position of the first change in section is also restricted such that the training set pattern distribution is not biased towards diagnosing faults at the pile head. Further to this, pre-processing of the network target data occurs before training to minimise the degree to which the network is required to make impossible diagnoses. This process is described fully in Section 6.3.

This chapter continues with a discussion of the data pre-processing methods and network output before continuing with an investigation into the training set dependency of system performance. A full parametric investigation into the three network types is then reported followed by a discussion of their relative strengths.

6.2 NETWORK PRE-PROCESSING

The importance of pre-processing in relation to a neural network's final performance is well documented. Menéndez *et al.*^{6.1} have shown that the pre-processing of sonar signals has a direct relation to not only on a network's rate of learning, but also its resultant competence. A number of pre-processing methodologies have therefore been considered for both the de-noising and encoding of the pile traces for use in this study.

The traces used in this investigation are shown in Figures 6.2-6.5. Figure 6.2 is a typical input force excitation as described in Chapter 4. Figure 6.3 shows the velocity response obtained from two of the piles at the Blyth test site under investigation and will subsequently be referred to as Pile 1 and Pile 2. Pile 1 is a defect free pile while Pile 2 is a pile with a 50% loss in radius at 3.6 metres. Figures

6.4 and 6.5 are velocimeter traces kindly provided by Technotrade Ltd. They are uncalibrated and have no associated force trace provided. However, they are included in this study as they represent the worst case of ringdown (pile head resonance) the author has yet found. Essentially it is suggested that if the selected methodology can successfully de-noise these traces, it will be able to de-noise the vast majority of presented field results. These piles have quoted diameters of 250mm and 300mm, and design lengths of 5m and between 5 and 9m respectively. They will subsequently be referred to as Piles 3 and 4.

6.2.1 Time Based Methods

6.2.1.1. Cross and Auto Correlation

When attempting to analyse time series histories of the type found in impact testing the conventional methodology for estimating time delays to reflection echoes involves the cross correlation of the input pulse with the recorded velocity response or the auto correlation of the velocity response^{6.2,6.3}. The auto-correlation function gives a measure of the degree to which a signal, $a(t)$, is similar to a displaced version of itself, $a(t + \tau)$, as a function of the time displacement. Mathematically this function is written as:

$$R_{aa}(\tau) = \lim_{T \rightarrow \infty} \int_0^T a(t) a(t + \tau) dt \quad (6.1)$$

While the cross correlation of two signals gives of the degree to which a signal, $a(t)$, is similar to a second signal, $b(t)$, as a function of the time displacement between them. Mathematically this function is written as:

$$R_{ab}(\tau) = \lim_{T \rightarrow \infty} \int_0^T a(t) b(t + \tau) dt \quad (6.2)$$

The most common application of these methodologies are the determination of time delays, the identification of transmission paths and the detection of signals buried in

extraneous noise. The main weakness of these methods is their inability to cope with non-stationary time series as, by definition, they are measuring the correlation of signals with a temporal displacement. The signals under analysis in this study were non-stationary. Traces typically contain base-line drift (Figure 6.3), exponentially decaying ringdown (Figures 6.4 and 6.5), and frequency dependant signal attenuation (hence the use of hammer tips of different hardness). These methods of analysis when applied to pile integrity testing have therefore been restricted to academic exercises and are not generally used by industry as a practical method for de-noising traces. A more suitable method for temporal de-noising and feature extraction, the wavelet transform, has been identified and developed by the author in Section 6.2.3.

6.2.1.2 Enhanced Time History

As applied by industry, there are three standard steps applied to minimise the signal to noise ratio for time series analysis of sonic echo test traces. All have been discussed in Chapter 2. The first is the reduction of white noise in the trace through ensemble averaging of a number of recorded tests. The second reduces correlated noise, specifically ringdown, through the low pass filtering of the trace (typically at 1500-2000 Hz). Finally a dynamic gain may be applied, more usually an exponentially increasing gain, to compensate for the attenuation of features found later in the trace.

Typically, however, Fourier filtered traces will still contain some elements of ringdown which when accentuated through a dynamic gain can dominate the resultant trace. A field engineer can easily alter the gain parameters to optimise the trace for visual inspection using standard analysis software; Pile Dynamics' PIT software, for example, allows this to be done in just three keystrokes. However, a more robust methodology is required for the automated de-noising of the trace. While uncorrelated noise is often used to improve network learning correlated noise is highly detrimental to a neural network's ability to generalise during training and hence to its eventual quality of performance.

6.2.2 Frequency Based Methods

6.2.2.1 Spectral Analysis

A frequency spectrum is derived from a time signal through the application of a Fourier transform, more usually using software and the Fast Fourier Transform algorithm. The Fourier transform of an ensemble averaged set of traces is known as the auto-spectrum while the transform of a single trace the instantaneous spectrum. The spectrum of a cross-correlation function is described as the cross-spectrum. All these methods are used in the field of modal analysis, a technique widely employed in non-destructive testing, where frequency response to an input excitation is used to determine a structure's integrity.

Neural network analysis has been used extensively in peak picking and spectral analysis as described in Chapter 3. The encoding of a long temporal trace into a few pertinent frequency coefficients is a favoured way of reducing the size of the input space of the neural network. Kirkegaard and Rytter^{6.4} have encoded modal data from the impact testing of a steel bar to teach a neural network to diagnose the position and extent of cracking within it. Specifically they present their network with the scaled change in frequency in the first five fundamental modes of vibration from that of a sound bar.

The author has reproduced^{6.5} these results for uninstalled concrete piles (see Appendix 2). The input to the network consisted of 17 linear units. These are presented with data showing the change in frequency response between the pile being tested and the expected response for that pile if it were sound. More specifically, it has as its inputs, for each of the lowest five modes:

- i) The change in mode frequency between equivalent modes from the sound and suspect pile.
- ii) The change in magnitude for equivalent modes in the normalised instantaneous spectrum.

- iii) The difference in phase between equivalent modes for the sound and suspect pile.

Two further units present the network with the design length and cross-section of the tested pile. This is because a single network is required to test piles of different dimensions and so the faults are found with respect to the tested piles' dimensions.

The output of the network consisted of 50 linear units each representing 0.2m sections. This covers up to a maximum pile length of 10m. This output array has been called the difference profile as it is trained to report the change in the tested pile's profile from the expected profile. For example a sound pile has all zero outputs as its profile does not deviate from the expected, while a pile with necking will have zeros everywhere apart from those units corresponding to the position of the neck. The activation of these outputs will be representative of the change from the expected pile radius at this point.

A system was developed, through parametric analysis, containing 30 hidden units with sigmoid activation functions. It is able to detect bulbing and necking in finite element generated velocity response spectra. The network performance is consistent with known test method limitations and is pile length independent. While providing further empirical evidence that neural systems are robust enough to handle piles of varying length and with varying degrees of defect its limitations make it inapplicable to installed foundation piles. The training data is restricted to piles with a single fault and because all the data is finite element generated the input excitation is completely consistent across all patterns. For real heavily damped systems such as installed piles automated peak picking becomes a problem in itself and the measured response is highly input dependent.

6.2.2.2 The Mobility Spectrum

Of more relevance to pile testing is the mobility, or mechanical admittance, spectra described in Chapter 2. Specifically this can be described as the Frequency Response Function (FRF) of the system with respect to velocity, that is:

$$H(\omega) = \frac{V(\omega)}{F(\omega)} \quad (6.3)$$

Often in modal analysis the direct calculation of Equation 6.3 is inappropriate due to the presence of noise. However, in pile analysis the spectrum above 1500 Hz is rarely considered and the coherence of the spectrum below this value is high enough for the direct calculation of $H(\omega)$ from Equation 6.3.

Its time domain equivalent, the impulse response function, is often referred to as the reflectogram in literature. It is the basis for the wave tracing techniques described in Chapter 2 because, like its frequency domain equivalent, its shape is approximately input magnitude independent. Considering the spectral make-up of the input pulse (Figures 4.8 and 4.10) it is apparent that the limiting frequency of the resultant reflectogram is defined by the point at which this spectrum reaches its first minimum. Otherwise, with its value being so relatively small, this frequency will dominate the resultant reflectogram. For the example reflectograms shown in Figures 6.6 and 6.7, therefore, the Fourier cut-off frequency is given as 1000 Hz.

6.2.3 Wavelet Methods

As described in Section 3.4.4.3: the Wavelet Transform (WT) was introduced in the early 1980's^{6,6.6.7} as a new signal processing technique that overcomes one of the inherent problems of conventional Fourier techniques, namely the retention of temporal information. It provides a method for the decomposition of non-stationary signals such that scale characteristics and feature location can be highlighted simultaneously through the unfolding of a one dimensional signal into two dimensions.

6.2.3.1 The Continuous Wavelet Transform

The continuous wavelet transform was introduced in Section 3.4.4.3 and described by Equations 3.22-3.25. Essentially, instead of decomposing the signal under

investigation into a series of continuous sinusoids, as in the case of Fourier analysis, the trace is described by a basis set of discrete functions of finite temporal and frequency support. This *unfolding* of the signal into two dimensions, dilation and translation, provides a decoupling of frequency components within the trace whilst retaining a degree of temporal information.

Mallat and Hwang^{6.8} and, Grossmann and Morlet^{6.7}, four of the pioneers of modern wavelet analysis, have co-authored papers reporting the WT's usefulness in detecting singularities and discontinuities in traces when compared to Fourier based methods. Related research in vibration analysis has recently been published by Staszewski^{6.9,6.10,6.11} and Newland^{6.12}.

A multitude of wavelets, which satisfy the constraints described in Chapter 3, are available to the researcher. Each has different mathematical properties which render it more suitable for given applications. Staszewski employs the Morlet wavelet for detection of system non-linearity through the identification of damping and stiffness parameters for multi-degree-of-freedom systems^{6.9,6.11} during transient testing. The Morlet wavelet has good support in both frequency and time domains which allows the decoupling of the system's various modes of vibration with respect to time. This makes it very effective for this application.

Newland^{6.12} applies his own wavelet, the harmonic wavelet, to the analysis of bending wave propagation within a struck mild steel beam. This wavelet is similar in shape, and therefore properties, to the Morlet wavelet except that, being defined in the Fourier domain, it can be forced to be orthogonal for each dilation scale. Again this demonstrates the wavelet's ability to separate the spectral components of the propagating pulse. This is important in an application such as this as the group velocity of bending waves within a beam is frequency dependent and so, with multiple reflections also occurring, the time domain response record becomes too complex for direct interpretation.

For a problems involving large scale heavily damped systems such as sonic pile testing, in practice, there are rarely multiple longitudinal reflections and the

frequency dependence of group velocities is negligible. Thus, as long as feature types can be differentiated through scale, the temporal isolation of these trace features is of a greater importance than the decoupling of their frequency components. For the investigation detailed herein, therefore, the Mexican hat wavelet, has been used. The author, along with his colleagues, has published a number of papers describing the merits^{6.13,6.14,6.15} and practicalities^{6.15} of wavelet analysis of foundation piles using this wavelet. When compared to those wavelets mentioned above, although compactness in the frequency domain is compromised, this wavelet has far better temporal support. This leads to improved signal reconstruction properties after filtering. For this research the complex version of this wavelet is employed. This has a Gaussian envelope and so the modulus plot does not include the side lobes associated with the real version - the real part of the complex wavelet shown in Figure 6.8.

Figure 6.9 shows the application of the continuous wavelet transform to the velocity response trace of Pile 1. The wavelet domain data is presented in the form of a scalogram (the lower plot of Figure 6.9). This filled contour plot has the translation, b , value along the horizontal axis and the dilation, a , value along the vertical axis. By convention the vertical axis is a minus log scale so that smaller a values, i.e. smaller wavelet widths, are at the top of the graph. This leads to discontinuities in the one-dimensional trace effectively being pointed to by the two dimensional scalogram. Also apparent in this plot is the decomposition abilities of the wavelet transform. The higher frequency ringdown is found towards the top of the scalogram while the echo from the pile toe, with its lower frequency components can be seen throughout all scales (dilations).

6.2.3.2 The Mobility Scalogram and 'ModMax' Temporal Filtering

In this section a new concept in wavelet analysis is presented. As previously described the notion of wavelet analysis can be summarised as the convolution of an analytical function of multiple dilations with the signal under investigation. As such the calculation of the wavelet coefficients for a given scale can be more efficiently calculated in the frequency domain where the wavelet function becomes, effectively,

a band pass filter. Hence, for a given scale, or wavelet dilation, the coefficients can be obtained from the inverse Fourier Transform of the product of the signal spectrum with the wavelet spectrum at that dilation, thus:

$$W(a,b) = \frac{\sqrt{a}}{2\pi} \int_{-\infty}^{+\infty} V(\omega) \psi^*(a\omega) e^{i\omega b} d\omega \quad (6.4)$$

where a is the wavelet dilation value, ψ the wavelet function spectrum and the superscript '*' represents the complex conjugate. As in Equation 6.3, $V(\omega)$ is the Fourier Transform of the velocity response. However, noting the equality of Equation 6.3 it becomes apparent that the spectrum of the velocity signal in Equation 6.4 can be replaced with that of the mobility curve, $H(\omega)$ in Equation 6.3. The scalogram then becomes, effectively, the wavelet transform of the reflectogram and so becomes input magnitude, and shape, independent. This scalogram has, therefore, been labelled the *mobility scalogram*.

Further to this, temporal de-noising can be applied through the implementation of the, so called, 'modmax' or *modulus maxima* technique^{6,17}. Here, the energy in the scalogram is redistributed to its maximal modulus turning points with respect to each scale. A plot of the type shown in Figure 6.10 is then produced. By following these contours from lower dilation (frequency) scales up to the high frequency scales a method is produced for differentiating the high frequency components caused by ringdown and those of the reflected echoes and input pulse, i.e. those components with associated lower frequency terms. The use of this technique also drastically reduces the number of non-zero terms in the presented scalogram. Consequently this method is considered useful for the encoding of trace information. The reconstructed traces of the wavelet filtered signals for Piles 1 to 4 are shown in Figures 6.10 and 6.11. These reconstructions have been generated using only the ten largest coefficients from the filtered modulus maxima scalogram. As can be seen while the amplitude of the trace features are of the order of those of the reflectograms of Figures 6.6 and 6.7 their shapes better represent those of the original traces. This is due to the retention of salient high frequency components while the high frequency noise has been eradicated. The suggestion that wavelet filtering is more efficient

than Fourier filtering has been shown theoretically by Donohoe^{6.18}. The author and his colleagues have shown further examples of the applicability and usefulness of modulus maxima filtering in pile integrity testing in their publications^{6.19} reproduced in Appendix 2.

6.2.3.3 The Discrete Wavelet Transform

The implementation of the wavelet transform for discrete signals can be performed by the discrete wavelet transform (DWT). The DWT allows for the decomposition of the signal into a basis set described by a dyadic decimated frame. The first wavelet dilation has the wavelet centred and covering the entire signal. At each subsequent level the dilation is halved (hence dyadic) so smaller features within the signal are resolved. As the dilation is halved so the translation step is halved (hence decimated) so avoiding overlap in the locations analysed thus avoiding redundancy in the transform set, as illustrated in Figure 6.13. The number of required operations for the DWT are, therefore, less than those needed for the continuous case so reducing computation time and the number of resultant coefficients.

In this investigation the Daubechies wavelets of orders 4, 6, 8, 12, 16 and 20 were considered^{6.15,6.20}. Examples of some of these wavelets' shapes and frequency make-up are shown in Figure 6.12. This wavelet system has been chosen because it is orthonormal and complete. This allows for the regeneration of the original signal from the decomposed data and, due to its orthonormality, it lends itself to the discrete wavelet transform. The resultant scalogram from the decomposition of Pile 3's test trace using the Discrete Wavelet transform and the D(8) wavelet is shown in Figure 6.14. The lack of redundancy in the wavelet space results in a good quality reconstruction of the original signal using only 64 of the original 1024 coefficients. For this reason the DWT is being used for an increasing number of data compression applications. However, the loose frequency support as indicated in the plots of Figure 6.12 and the lack of shift invariance in the decimated frame means there is a frequency leakage across scales. This means spurious high frequency terms are found even in reconstructed traces that have been truncated at lower dilation levels. For example, Figure 6.15 shows how, when truncated at level 5, the reconstructed

traces of Pile 3 contain aspects of ringdown rendering it inappropriate for the de-noising of the trace.

6.2.4 Relative Performances of Pre-processing Methodologies

Initially a comparison between mobility curve and wavelet mobility scalogram encoding of the sonic echo test data is considered. To establish the ability of a network to decode the presented data, i.e. the ability of a network to produce an internal representation of the pattern space, the network is required to reproduce the reconstructed reflectogram. By training this mapping rather than that of pile profile all uncertainty in the required task is eliminated. The network is learning a deterministic inverse transform and results of the learning process are purely a function of the input encoding.

The mobility curve data is presented to 64 input units: 32 for the real parts of the pattern and 32 for the imaginary parts. For a signal sampling rate of 50 kHz with 1024 samples in the acquired trace, this corresponds to the spectral components up to 1500Hz. For the encoded wavelet scalogram data the largest 16 components of the filtered modulus maxima plot are presented. Each component being described by four integers, one each for: scale (a parameter), translation (b parameter), real component and imaginary component. Hence, both networks have identical input dimensions. The required output trace is subsampled to 64 points to reduce the dimensions of the weight space and so the likelihood of overtraining.

In both cases the networks employed were simple multi-layer perceptron networks with linear output units and sigmoid hidden units. The optimum network performance for the mobility curve inputs are presented for network architectures of 60 hidden units within one and two hidden layers in Figure 6.16. The mean pattern error, as described in Chapter 4, descends below a value of 0.02 for both networks. This is a performance reflected by the sample outputs presented in Figure 6.17.

For the encoded wavelet data, however, as shown in Figure 6.18, the mean pattern error never reaches a value less than 0.05, even when 3 layer systems are employed.

By looking at the Hinton-like diagrams of Figure 6.19 it becomes apparent that, for the wavelet encoded network, the weights from one of the hidden units, unit 42 dominates. This was particularly true for those weights leading to the start of the trace where the dominant input pulse occurs. This was not the case for the mobility curve network where, although the weights to the output units representing the start of the trace were also higher, they were well distributed across all the hidden units in the network.

These results would suggest that learning has been inhibited by the additional data encoding in the wavelet case. Further to this the introduction of a temporal component to the presented data lead to a biasing of the network performance. Specifically, with higher wavelet coefficient inputs being directly associated with higher output values the network has minimised the pattern errors in the training set by modelling the input pulse very well, as indicated by the sample traces of Figure 6.20. Consequently features later in the trace have been neglected to the detriment of network performance. This was not true in the mobility curve case where, because data describing the reflectogram trace was distributed across all the input units, no hidden units dominated during training.

These results would clearly indicate that, in preference, the network input should be a continuous description of a vector space so reducing the decoding required of the network. However, the de-noising abilities of the wavelet transform may be used in conjunction with the signal enhancement techniques of Section 6.2.1.2 to improve network performance. A series of further experiments have, therefore, been performed.

By producing a reflectogram through use of the mobility scalogram, as described above, dynamic gain can be applied to the de-noised trace without amplifying the frequencies associated with low pass Fourier filtering. In this study the signal lengths are all 1024 samples long with the expected reflection from the pile toe found approximately half way along the trace. The dynamic gain therefore takes the form of a Hanning-like function where the start and end of the trace have a gain of one while the maximum gain of ten is found at the centre of the trace. The Hanning

function is often used in signal processing as a windowing function^{6.3}. Specifically it is used to minimise the effects of any discontinuity between the start and ends of a trace as the Fast Fourier Transform assumes a periodic signal. It is, therefore, a function naturally suited for this role although, in this case, it has been altered by scaling it by 4.5 and then adding 1 to fulfil the function description above. Thus it is described by Equation 6.5, below.

$$g_k = 1 + 4.5 \left(1 - \cos \left(2\pi \frac{k}{n+1} \right) \right), \quad k = 1, \dots, n \quad (6.5)$$

where g_k is the gain value and n the total number of samples in the trace. The enhanced reflectogram is then encoded to the Fourier domain in order to reduce the dimension of the input space and so the chance of overtraining. This *enhanced* mobility curve is compared directly with the original mobility curve patterns in Figure 6.21. The third trace in these graphs is for an input of a logarithmic version of this enhanced curve. It is proposed that by taking the logarithm of the enhanced mobility curve, as in the decibel scale, smaller changes in the curve will become resolvable allowing a more accurate diagnosis of the pile integrity to be made. Given the success of the mobility curve at reproducing the reflectogram, the output for this network is required to produce the radial axial profile (cross-section) along the pile length in an array of 50 units, each corresponding to a 0.3m length.

As indicated by the graphs in Figure 6.21 the enhanced mobility data improved network performance. This improvement was reflected both in the training and test set convergence curves. The logarithmically scaled data had a smoother curve that converged quicker, although the eventual test set error was similar to that of the enhanced mobility data. It is suggested that this faster, smoother convergence is due to the smoothing of the pattern space resulting from the logarithmic scaling. That is, the closer proximity of the input patterns means less of the weight space is searched for a suitable solution.

In subsequent experiments, therefore, the pre-processing and input encoding of the sonic echo data starts with the production of a de-noised reflectogram using wavelet

techniques. This signal then has a dynamic gain applied to it to before being transformed to the Fourier domain. The 32 resultant coefficients spanning up to 1500 Hz are then separated into their real and imaginary parts. The logarithm of the magnitude of these components (plus one to avoid polarity changes) is taken and the subsequent 64 component array used as the input pattern.

6.3 POST-PROCESSING

As mentioned in the introduction to this chapter, the uncertainty associated with this problem, if unrestricted, leads to an intractable problem description. If the propagating stress wave is attenuated to an excessive degree, either through damping or reflections, no further diagnosis of the pile's integrity can be made. However, this does not mean a useful tool cannot be produced using this technique. Indeed the limitations of low strain test methods are well known by industry and documented in Chapter 2. The difference between an 85% and a 100% loss in section may not be resolvable, but the fact either is detected with respect to the design section will provide a useful quality assurance tool. In reality, low strain test methods are never used in isolation. Rather they are used to identify anomalous results in large pile groups which may then be investigated further using more sophisticated, and therefore expensive, techniques.

The use of Finite Element Analysis to generate the training data has the additional advantage that an estimate of those features that might be diagnosed can be made. In the same way that the propagating stress wave can be followed to validate the FEA model with respect to theory, as in Chapter 4, so its attenuation at a position along the pile can be quantified. Any feature found after the pulse has attenuated below a pre-set level can be ignored in training and the network thus absolved from the requirement of making impossible diagnoses. For all experiments, therefore, when the amplitude of the propagating stress wave drops below 10% of its original magnitude during its initial propagation down the pile no further diagnosis of changes in section are required of the network. In selecting 10% it is recognised that any returning pulse will undergo further attenuation on its path back to the pile head and, therefore the network is expected to be able to resolve a return pulse 2%

(remembering the doubling of velocity at a free end of a bar) of its original amplitude. These values have been calibrated by observations of field test results - specifically the knowledge that a returned pulse from an 11.7m defect free pile (Pile 1) can be seen.

For the experimentation described the change in radial section at any one point is also restricted to 100% of the design radius. That is, a total loss in section is allowed and a doubling of the pile radius is allowed. For the piles considered in this study any more than a 100% increase in radius would result in less than 20% transmission of particle energy through the change in section and as such very little information from below the fault would be resolved.

The design radius of the piles under investigation is 0.4m and so the output of the network never exceeds 0.8. The output units used in subsequent experimentation involving multi-layered perceptron networks are therefore hyperbolic tangent or sigmoid units depending on whether the required output varies between 0 and 1 or -1 and 1.

The possible network architectures for this problem may be categorised into two sub-groups. The network may be modularised such that a collection of networks are developed each producing an output for an individual section of pile length. However, in this study a single network presents the user with an array representative of the pile profile. This is because for the WBNN and RBNN networks the initialisation process will provide identical networks whether the output units are considered individually or collectively. Subsequent training would, therefore, be unlikely to produce significantly different network performances.

With regard to output resolution: each output unit represents the pile profile for a 0.3m length, this being the resolution of the finite element model. An array of 50 units, therefore, provides a profile estimate up to a maximum of 15m i.e. the toe should be observable for all piles within the problem specification.

Four different methods of output array values, from which the pile's radial profile can be calculated, have been considered:

- i) The pile radius at the output units' specified position.
- ii) The pile radius squared (\propto area) at the output units' specified position.
- iii) Changes in radius squared. As reflection amplitudes are primarily caused by changes in area it is sensible to hypothesise that a relationship would be more easily found by requiring the network to output an array of these changes in cross-sectional area.
- iv) A difference array. An array of differences in radius from that expected for an infinitely long pile of the same design radius in the same soil conditions .

The results of these experiments are shown in Figure 6.22. The network used in these experiments is a MLP network with two hidden units each containing 50 units. Although these results confirm that monotonic learning is achieved in all cases, the mean pattern error cannot be compared directly as an indication of relative network performance. Clearly, for example, the output array for the change in area case will be mostly zeros and so the network output may be completely wrong in producing all zeros for all patterns and yet still give a small mean pattern error. In order that like be compared with like, therefore, the errors for the calculated radius profile in each case, for all patterns, are given in Table 6.1. The variance in the pattern errors are also provided in this table. Although it is recognised that the mean pattern error distribution is not a normal distribution this measure does give an indication of the relative network selectivity.

Table 6.1 Pattern Errors in Calculated Profile Radii

Array Type	Minimum Mean Pattern Error	Variance of n error measures: $x_{1..n}$ defined by : $\frac{n\sum x^2 - (\sum x)^2}{n(n-1)}$
Profile Radius	0.67	0.20
Profile Area	0.80	0.19
Area Change	0.93	0.25
Difference Array	0.64	0.17

The first observation to be made from these results is the relatively large error associated with the network that has attempted to diagnose changes in cross-sectional area along the pile length - literally changes in radius squared. This is due to the errors in the subsequently calculated radius profile being cumulative. For example if an erroneous change in section were diagnosed at the pile head that error will be carried through the calculated pile radius for the remainder of the profile.

The results for the networks presenting the pile radius and difference array profiles had almost identical results. However, the difference array provides results that are both superior in the mean pattern error and the consistency of these calculations. It is hypothesised that this is due to the network's output being naturally centred on the most sensitive region of the hyperbolic tangent activation function. That is, in general the output for a sound pile will be zero up to the pile toe. This is also the part of the activation function with the greatest gradient and furthest away from its saturated regions. The network is, therefore, intrinsically more able to resolve deviations from this norm. It is the difference array that is, therefore, adopted as the network output for subsequent experimentation.

6.4 Training Set Dependency

For the study completed herein a total of 500 test traces have been generated by Finite Element Analysis. This corresponds to about five weeks of solid computer time on a Pentium™, 166MHz machine. Although increasing the number of patterns generated may improve subsequent performance the additional time necessary to produce such an increased set was deemed inappropriate for a proof of principle study such as this. As shown in diagrams 6.23 and 6.24 for a MLP network containing two hidden layers each of fifty units overtraining is prevented when the training set used contains in excess of four hundred traces. At this point the test set error reduces significantly: by over 15%. Subsequent increases in the size of the training set result in a far smaller decrease in error. Consequently in the experimentation presented in this thesis the five hundred patterns have been split such that a training set of 450 patterns is used with a test set of 50 patterns.

The implications of having a relatively small test set are illustrated in Figures 6.25 and 6.26. Statistical aberrations can result from the test set sample not being representative of the overall pattern set. For this reason all comparative studies have been made using the same training and test set. Additionally all error analysis has been made from concatenated results from a series of experiments. Each network is trained ten times; each time with a different set of fifty test patterns. Significantly, the overall network strengths and weaknesses observed for each test set are the same. This would appear to confirm that these differences are representative of the distribution of the test set rather than diverging network performances.

6.5 MULTILAYER PERCEPTRON NETWORKS

In all the experiments described in Section 6.5 the units' activation function used is the hyperbolic tangent function. Following the experimentation outlined in Section 4.5.6, the temperature parameter (the scaling value of the net unit input) has a set value of 10. This is consistent with a network initialisation where initial weights are set to random values between -1 and 1 such that premature saturation of the network is inhibited.

6.5.1 Parametric Investigation

The learning parameters for which optimum values must be derived are the learning rate and momentum term, as described in Chapter 3. These values are derived from a parametric study, but cannot be considered independent variables. This is because the application of a momentum term increases the *effective* learning rate for constant trends in the training data such that:

$$\alpha_{eff} = \frac{\alpha}{(1 - \lambda)} \quad (6.6)$$

This being the case the graph of Figure 6.27 contains four plots. One each for momentum, λ , values of 0, 0.3, 0.6 and 0.9. The plots illustrate how, in all cases, an optimum value for the learning rate, α , is reached. As shown in Figure 6.28 for rates below this learning is prohibitively slow while for higher values the convergence curves are less smooth. This is a result of the larger size of the weight updates leading to the network being unable to converge on a suitable solution in the weight space. For this reason the parameter values selected are those that produce the lowest error, with the lowest learning rate. Hence, they are selected as a learning rate of 0.1 and a momentum of 0.9. Interestingly the relationship of Equation 6.6 does appear to hold for this training set, as illustrated in Table 6.2. This would confirm the presence of statistically consistent trends within the data from which the network is able to form a function approximation. If this were not the case, and the network learned as a content addressable memory, the momentum term would have little effect and the system with the lower learning rate would learn too slowly to converge on an optimal solution within the epochs completed.

Table 6.2 Learning Rate Equivalence

α_{eff}	Learning rate (α)	Momentum (λ)	Training Set Error	Learning Rate (α)	Momentum (λ)	Training Set Error
0.25	0.25	0	0.16	0.025	0.9	0.15
0.1	0.1	0	0.25	0.01	0.9	0.25
0.025	0.025	0	0.45	0.0025	0.9	0.45
0.01	0.01	0	0.54	0.001	0.9	0.54

With respect to the number of units and layers employed i.e. the topology of the network: the results from a parametric study carried out using the learning parameters chosen above is presented in Figure 6.29. It appears that networks containing only five units per layer have a reduced pattern error, but on inspection of the network outputs it is apparent that the network simply differentiates between piles of which the toe is visible and those that it cannot. No diagnosis of faults along the pile length are made.

It is apparent that the errors for networks containing more than one layer are consistently lower than those containing just one. However, the addition of a third hidden layer does not appear to significantly improve network performance - which, as stated in Chapter 3 is in accordance with Kolmogorov's theorem. Overtraining occurs in all networks when the number of units per layer is greater than one hundred - as illustrated in Figure 6.30. Given that the networks' mean pattern error does not improve significantly above forty hidden units and the need to ensure overtraining does not occur the network selected for performance analysis is that with two hidden layers each containing forty units.

6.5.2 The Use of Uncorrelated Noise

As confirmed in the feasibility study of Chapter 4 the inclusion of uncorrelated white noise in the system input can assist in the prevention of overtraining. This improves generalisation so improving the results for field test data. In this case the noise is measured as a percentage of the maximum absolute input value in the pattern set.

The graph of mean pattern error with respect to this noise is shown in Figure 6.31 and is consistent with the findings of Chapter 4 shown in Figure 4.54. However, in this case no observable improvement is found by including noise as illustrated by the examples of Figure 6.32. It is suggested that this is because the model being employed in this study better represents the field data being tested and the pre-processing employed minimises small temporal characteristics of the mathematically modelled data that encourages overtraining.

6.5.3 Network Selectivity and Sensitivity

During the parametric studies presented above the mean pattern error, a Euclidean cost function as defined in Equation 3.14, has been presented as a measure of the network's ability to carry out its required task. Using a pattern error to quantify network efficiency is however inappropriate because faults of smaller axial lengths may be completely missed yet still have a relatively small associated error.

Alternatively, a measure can be carried out on each unit individually to produce a measure of the networks' abilities with respect to a fault's position or severity. For example, Figure 6.33 provides a plot of the mean unit error with respect to that unit's position along the pile. However, this does not take into account any *a priori* knowledge of the test method employed and the fact that of primary importance is the diagnosis of the first significant fault in the pile: information on subsequent faults is useful, but not essential as low strain integrity testing is primarily an exercise in identifying anomalous responses. Specifically it is known that faults underlying other faults are more difficult to detect and so to present the data as in Figure 6.33 can be misleading. For all the error analysis presented in this and subsequent sections, therefore, only piles containing a single fault are considered. 'Single fault' meaning a single neck, bulb, loss in section or gain in section. The measure of the network's ability is then summarised as the error in diagnosis of the change in section at the centre of this fault.

The graph of Figure 6.34 shows the mean unit error for faults with respect to its position along the pile length. The error bars are obtained through the median quartile method, their large size being indicative of the fact that the variables upon which these graphs are taken are not independent i.e. there is an error distribution associated with each error value. As expected, faults towards the toe are larger, but faults of shorter axial length at that position will have a comparatively much larger value than the average, hence the large upward error bar. An example of the network's diagnosing abilities deteriorating with respect to position is shown in Figure 6.39. However, the network has been able to diagnose faults at the pile head from the frequency information, for example see Figure 6.40. This ability is not possible using conventional techniques because of the difficulty in resolving reflections from close to the pile head. The ability to diagnose the presence of a fault from dynamic stiffness measures in the frequency domain has, however, been predicted by Chan^{6.21}.

Figure 6.35 shows how faults with a small axial length are more difficult to diagnose with respect to the average. This is as expected by theory: as shown in Chapter 4 the superpositioning of reflections from two spatially close changes in section causes the

return echoes to be very much smaller than those that may be expected. Examples of the network output for smaller changes compared to larger changes are shown in Figures 6.37 and 6.38. Also apparent from Figure 6.35 is the increase in error associated with fault lengths over 5.5m. It is suggested this is due to the fact that, by definition these faults will have their centre further down the pile length and so, as previously mentioned, the larger error may be expected.

With respect to the degree of defect, that is the amount by which the fault's radius deviates from the design radius: the results shown in Figure 6.36 are inconclusive. They appear to indicate that larger errors were more difficult to detect. However, a number of factors should be considered when analysing these results. The first is of primary importance. The larger errors are small in comparison with the required change in section. For example an error of 0.008 corresponds to an error in calculated radius of 9mm for a 200mm change in section. It is also true that a larger error for larger losses in section is acceptable as long as the percentage error allows that change to be identified. A possible reason for the degradation of performance for larger changes in section is the shape of the activation function of the output units. As previously mentioned the hyperbolic tangent function has its most sensitive area, that where its gradient is highest, for output values nearer zero. However, the same shape that makes it ideal for resolving smaller errors means it is least sensitive as the outputs near its asymptote values of -1 and 1; i.e. higher magnitude outputs. While the required outputs of this network never exceed 0.3 it would explain the reduction in performance for larger magnitude faults.

Further examples showing the network's success in resolving piles containing multiple faults are given in Figure 6.40.

6.6 RADIAL BASIS NEURAL NETWORKS

For the parametric investigation involving Radial Basis Neural Networks identical training and test sets are applied as those in the MLP case. The initialisation and subsequent back-propagation training of the networks are as described in Chapter 5 and so the network output is composed of linear activation units.

6.6.1 Parametric Investigation

For the investigation carried out in this study three learning parameters were derived. As described in Chapter 3, for radial functions two learning rates are required: one for the weight updates and one for the hidden unit centres. Preliminary investigations by the author, as well as providing 'ball park' values around which the study reported below was based, found that faster learning can be achieved when the two layers of weights have different learning rates applied to them. It is hypothesised that this is due to activation functions of the hidden and output units being different. Effectively the output of a hidden unit is very much more sensitive to a change in its fan-in weights compared to that of a linear output unit. It is, therefore, reasonable to find that the optimum values for the learning rate differ for the two levels.

The results of this parametric study are shown in Figure 6.41. For each experiment while one parameter is varied the others remain static as either: $\alpha_c=5\times 10^{-4}$, $\alpha_{wi}=1\times 10^{-6}$, or $\alpha_{wo}=1\times 10^{-2}$. Where α_c is the learning rate for activation centres, α_{wi} is the learning rate for weights from the network inputs, and α_{wo} is the learning rate for weights to the network outputs. These values were estimated from the initial investigation on a 50 hidden unit network.

The results indicate that overall network performance was not particularly dependent upon α_{wi} although there was an optimum value at around 10^{-3} . This value was a compromise between the gradient and smoothness of the convergence curve. For higher values the curve became very noisy and very little learning occurs while for much lower values the convergence curve decayed very slowly. This effect was also found for both other learning rates where raising the value increased the spiking in the convergence curve; decreasing the value decreased rate of convergence. The selected values of the learning parameters are, therefore, given as: $\alpha_c=5\times 10^{-2}$, $\alpha_{wi}=1\times 10^{-3}$, and $\alpha_{wo}=1\times 10^{-2}$.

Using the parameters selected above this experiment has been repeated for systems with various numbers of hidden units. The results of this study are presented in Figure 6.42. In these results an optimum network is clearly found to contain around 35 units. Overtraining was evident in all systems containing over 80 units.

6.6.2 Network Selectivity and Sensitivity

The initial observation of the error analysis of Figures 6.43-6.45 is the marked similarity of the results to those of the two layer MLP results of Figures 6.34-6.37. The general trends of higher errors for faults further down the pile and those with particularly large or small axial lengths are the same (see also the examples in Figures 6.46 and 6.47). This would appear to confirm the equivalence of the two network types as outlined in Chapter 3. However, in all cases, although the graph shapes for the errors are similar the values for the MLP case are consistently smaller, as are the error bars associated with these value. It is also noticeable that the graph of errors with respect to fault length is less consistent in this trend i.e. the resultant plot is far 'spikier' even though it is presented with a larger scale.

It is hypothesised that this is due to the enclosed nature of the hidden unit activation functions making the training more pattern set dependent. Specifically, by regionalising the input space with respect to pattern density, and then to produce an output that is, essentially, independent of all patterns of any (Euclidean) distance away from that which is presented the output will become highly sensitive to the statistics of the pattern set. This can be thought of as an addendum to the so called '*curse of dimensionality*' mentioned in Chapter 3. That is, as the dimension of the input space increases, so the number of hidden units in the input space must increase to accurately regionalise it. However, as a consequence of this the number of patterns in the training set must also increase to better describe the pattern population density of the problem domain. Although the statistics of the pattern set are clearly of great importance to the MLP networks it is apparent that, for this case, the monotonic activation functions make this network's performance less dependent thereon.

One advantage of the localised nature of the radial basis activation function is the apparent ability of the network to isolate spatial regions of the pile more effectively than the MLP case. Empirical evidence for this is found in the Figures 6.46-6.49 where the toe of the pile is better defined than the more rounded toes of Figures 6.37-6.39. This effect is also discussed in Section 6.8, below.

6.7 WAVELET BASIS NEURAL NETWORK

As in the RBNN case, for the parametric investigation involving Wavelet Basis Neural Networks identical training and test sets are applied as previously described. The initialisation and subsequent training of the networks were all as described in Chapter 5, and the output composed of linear activation units. The error analysis is carried out using ten repetitions of the chosen network with a different test set each time. This allowed all of the pattern set to be included in the evaluation of network performance.

6.7.1 Parametric Investigation

As with the RBNN network the optimum values for three learning rates are derived from a series of experiments. Again, the presented results have been preceded by a preliminary parametric study to provide a 'ball-park' estimate of the salient regions over which the final investigation should take place. For the results presented in Figure 6.51 while one parameter is varied the others remain static as either: $\alpha_c=5 \times 10^{-2}$, $\alpha_{wi}=1 \times 10^{-4}$, or $\alpha_{wo}=1 \times 10^{-2}$. Where α_c is the learning rate for activation centres, α_{wi} is the learning rate for weights from the network inputs, and α_{wo} is the learning rate for weights to the network outputs. These values were estimated from the initial investigation on a 50 hidden unit network.

The graphs for the function centres and weights to outputs are similar to those of the RBNN network both in form and results. That is an optimum value is found below which learning is slow while higher values result in noisier convergence. The network performance, however, does appear to be far more dependent upon the value of the learning rate of the weights to the hidden layer (c.f. Figure 6.41). For

the higher level values of this parameter the convergence curve is extremely noisy to the point that no learning occurs at all. Remembering that the weights being updated in this layer are effectively the square root of the dilation parameter of the activation wavelet function, it is apparent that the change in polarity of the Mexican Hat function employed in this network makes it particularly susceptible to larger changes in this value. In the RBNN's as a weight in this layer decreases so the output of a given unit for a given pattern will become, monotonically, smaller. For the WBNN's, however, the output may change polarity before again increasing to an asymptotic value of zero as shown in Figure 5.21. If the changes in weight value for this layer, therefore, is large the repercussions for the output of the system may be extreme, hence the necessity in keeping weight changes for this level small. The selected values of the learning parameters are, therefore, given as: $\alpha_c=1 \times 10^{-2}$, $\alpha_{wi}=1 \times 10^{-6}$, and $\alpha_{w0}=1 \times 10^{-3}$.

Using these parameter values this network has been repeated for systems with various numbers of hidden units. The results of this study are presented in Figure 6.52. In these results a optimum network is found to contain around 50 units. Unlike the results of the RBNN shown in Figure 6.42 for the WBNN case the effects of overtraining are very much less pronounced. The mean test pattern error for systems with 100 hidden units still decreases with training, but the convergence curve is a lot noisier than those containing a smaller number of units. As the mean pattern error presented is the mean of the last 25 epochs this is reflected in the larger recorded values. Convergence in the smaller networks is also to a lower level than that found in the equivalent RBNN networks. It is presumed that the increased number of units required to produce equivalent network performance in the WBNN case is simply due the difference in shape of the activation function with respect to that which is being approximated.

6.7.2 Network Selectivity and Sensitivity

The graphs of Figures 6.53-6.55 shows, again, how faults with smaller axial length and those near the pile toe have higher measured errors - see also for examples Figures 6.56-6.60. The error values and bars are larger than those measured for the

MLP networks for equivalent faults, but approximately the same as the RBNN case. However, it is noticeable that the shapes of graphs 6.54 and 6.55 better approximate to the shapes of the MLP than the RBNN network. In fact, the error graph with respect to fault length (Figure 6.54) is considerably smoother even than that of the MLP case (Figure 6.35). It is hypothesised that this is due to the shape of the activation function employed. That is, it is known, for both RBNN's and WBNN's, that geometrically close hidden units will have similar activation values for similar, in the Euclidean sense, inputs. Referring to Chapter 5, it is also known that during the initialisation process the nearest k neighbours are required to produce outputs approaching the activation function maximum, where k is the number of patterns in the training set divided by the number of hidden units. As a consequence of the support of the Mexican Hat function being larger than that of the Radial Gaussian function, therefore, the resultant output of a given output unit will be dependant upon a proportionally greater number of hidden units in the WBNN case. It may also be that this more distributed contribution from the hidden layer to an output layer value is the reason that overtraining is less apparent in the WBNN's case. If an output is less 'hidden unit dependant' then, by implication, it is less pattern space dependant.

6.8 COMPARISON OF NETWORK PERFORMANCES

In all the networks studied the initial change in radius caused by a fault has been consistently identified in form, i.e. neck or bulb, and position *unless* it has been missed completely. Only faults where a change in section of 0.1m or less has occurred over an axial length of less than 0.6m have changes been missed completely. This is on the borderline of test method limitations where, as discussed in Chapter 2, current evidence suggests faults with an axial length of less than 1m cannot be reliably diagnosed and those of less than 10cm cannot be detected unless it involves close to a complete loss in section. However, there is plenty of misdiagnosis of second or third changes in section. This is predominantly due to:

- i) Faults beneath the first fault are hidden to a degree.

- ii) Traces of piles containing multiple faults are less well described in the training set than those containing a single fault. That is, as more changes in radius occurs over the length of the pile so the possible permutations of these changes increases exponentially. The pattern space of these multiple faults is, therefore, less precisely described by the training set.

However, as the principal task of the network is to find anomalous traces, the ability to correctly identify either the first or dominant fault within the pile would still make it a useful tool.

As indicated in Figure 6.61 the more hidden units in the network, the more able the system is to model sharper discontinuities within the pile profile. However, the use of more hidden units results in a better resolution of the input space and, hence, an improved description of that space is required i.e. more patterns are required in the pattern set.

This is particularly apparent in the RBNNs and WBNNs where input space undergoes vector quantisation during the initialisation procedure without reference to the required output. The MLP network appears to work better in this respect were it gives a consistently lower error when identifying a single fault along a pile length.

Better pattern errors observed during training of the networks containing radial activation functions can be seen to be due to these networks being better at identifying whether the pile toe is visible or not i.e. the localised activation function appears better able to model localised regions of the pile profile. This is graphically illustrated in Figure 6.62 in a comparison of unit errors for all patterns in the pattern set (not just those containing a single fault) and for all three chosen networks.

As can be seen in this figure the increase in the MLP pattern error is caused entirely by the larger error associated with the profile after the pile toe. For arbitrary pile profiles less than 9m from the pile head all networks produce similar errors. Since the MLP is clearly superior in identifying profiles containing a single fault, is more consistent in its selectivity and comparable with the other networks in diagnosing

arbitrary pile profiles it has been selected as the network of choice for evaluation using field test data.

6.9 SUMMARY AND CONCLUSIONS

A new concept in sonic echo data processing has been described: *the mobility scalogram*. De-noising using this method produces an input excitation independent trace better representative of the original signal than Fourier filtered equivalent.

Parametric studies suggest that presenting the data as a continuous vector representation of the resultant trace gives superior error measures to those when the trace is further encoded into its predominant features. The de-noised and enhanced time history is, therefore, transformed into the Fourier domain to reduce the size of the input space before being used as the network input in its entirety. Specifically the network input consists of 64 scalar values. One for each of the imaginary and real components of the 32 discrete frequencies up to a 1500Hz limit. Faster learning rates have been achieved by presenting these scalars in a logarithmic form.

Following a parametric study the output chosen for the network consists of a 50 unit array. Each unit presents the change in radius over a 0.3m unit length to that which is expected from an infinitely long pile of the same design radius in the same environment.

For the five hundred patterns available for this study optimum pattern errors in an MLP network containing one hidden layer of 50 units was seen to drop by over 15% when over 400 patterns were included in the training set. Subsequent increases in the size of the training set did not provide equivalent increases in network performance. Consequently, in this study, the training set consisted of 450 patterns while the test set held 50. For error analysis of network performance, therefore, experiments were repeated 10 times, each time with a different test set.

For the MLP network with hyperbolic tangent hidden and output units the optimum learning rate was found to be 0.1 and momentum 0.9. While adding a second hidden layer of units did consistently improve network performance with respect to the number of units per layer, adding a third did not. The topology of the selected network, therefore, consisted of two hidden layers each of 40 hidden units.

For both radial systems, improved results were obtained when two different learning rates were applied to the two weight layers.

Optimum mean pattern errors were obtained for the Radial basis networks of thirty five hidden units with learning parameters: $\alpha_c=5 \times 10^{-2}$, $\alpha_{wi}=1 \times 10^{-3}$, and $\alpha_{wo}=1 \times 10^{-2}$. Optimum mean pattern errors were obtained for the Wavelet basis networks of fifty hidden units with learning parameters: $\alpha_c=1 \times 10^{-2}$, $\alpha_{wi}=1 \times 10^{-6}$, and $\alpha_{wo}=1 \times 10^{-3}$.

The best pattern error for the three network types are shown in Table 6.3, below.

Table 6.3, Optimum Mean Pattern Error for the Three Network Types

Network Type	Optimum Mean Pattern Error
MLP	0.506
RBNN	0.486
WBNN	0.462

Although the results would appear to indicate improved performances for the radial activation functions these results are biased by their better isolation of the regions beneath the pile toe. This would indicate that radial activation functions are better for isolating local changes due to their enclosed decision regions.

For all the network types described, their ability to identify a fault decreased with the depth of that fault. The spatial length of the input pulse applied was 3.5m ($3500\text{ms}^{-1} \times 1 \times 10^{-3}\text{s}$). In all cases the neural networks could identify changes in section within 1.75m of the pile head.

The MLP network was superior in identifying profiles containing a single fault, is more consistent in its selectivity and comparable with the other networks in diagnosing arbitrary pile profiles. As it is the dominant, or first, fault identification that is of primary importance in pile integrity testing it is the MLP that has, therefore, been selected as the network of choice for evaluation using field test data.

REFERENCES

- (6.1) Menéndez C, Ordieres J B and Ortega F, Importance of Information Pre-Processing in Improvement of Neural Network Results, *Expert Systems*, Vol. 13, No. 2 (1996) pp95-103.
- (6.2) Newland D E, Correlation, in *An Introduction to Random Vibrations, Spectral and Wavelet Analysis*, Third Edition, Longman Scientific and Technical (1993) pp21-32.
- (6.3) Broch J T, Cross-Correlation and Cross-Spectral Density Measurements, in *Mechanical Vibration and Shock Measurement*, Brüel & Kjær, (1973) pp246-255.
- (6.4) Kirkegaard P H and Rytter A, The use of Neural Networks for Damage Detection and Location in a Steel Member, *Neural Networks and Combinational Optimisation in Civil and Structural Engineering*, Civil-Comp Press (1993) pp1-10.
- (6.5) Watson J N, Fairfield C A, Wan C L, and Sibbald A, The Use of Artificial Neural Networks in Pile Integrity Testing, *Developments in Neural Networks and Evolutionary Computing for Civil and Structural Engineering*, Ed. Topping B H V, Civil-Comp Press (1995) pp7-14.
- (6.6) Goupillaud P, Grossmann A and Morlet J, Cycle-Octave and Related Transforms in Seismic Signal Analysis, *Geoprospection*, Vol. 23 (1984), pp85-102.
- (6.7) Grossmann A and Morlet J, Decomposition of Hardy Functions into Square Integrable Wavelets of Constant Shape, *SIAM J. Math. Anal.* Vol. 15, No. 4 (1984) pp723-36.
- (6.8) Mallat S and Hwang W L, Singularity Detection and Processing with

- Wavelets, IEEE Trans. Info. Theory, Vol. 38, No. 2 (1992) pp617-643.
- (6.9) Staszewski W J, Identification of Damping in MDOF Systems using Time-Scale Decomposition, J. Sound and Vibration, Vol. 203, No. 2 (1997) pp283-305.
- (6.10) Staszewski W J, Wavelet Based Compression and Feature Selection for Vibration Analysis, J. Sound and Vibration, Vol. 211, No. 5 (1998) pp735-760.
- (6.11) Staszewski W J, Identification of Non-linear Systems using Multi-scale Ridges and Skeletons of the Wavelet Transform, J. Sound and Vibration, Vol. 214, No. 4 (1998) pp639-658.
- (6.12) Newland D E, Ridge and Phase Identification in the Frequency Analysis of Transient Signals by Harmonic Wavelets, J. Vibration and Acoustics, Vol. 121, No. 2 (1999) pp149-155.
- (6.13) Addison P S, Sibbald A and Watson J N, Wavelet Transform: A Mathematical Microscope with Civil Engineering Applications, Insight, Vol.39, No.7 (1997) pp493-497.
- (6.14) Watson J N, Addison P S and Sibbald A, Non-Destructive Testing of Foundation Piles using the Wavelet Transform, Proceedings of the 12th ASCE Eng. Mech. Conference, la Jolla, California, USA, 17-20 May (1998) (on CD-ROM).
- (6.15) Watson J N, Addison P S and Sibbald A, The De-Noising of Sonic Echo Test Data Through Wavelet Transform Reconstruction, Journal of Shock and Vibration, Vol. 6 (1999) pp267-272.
- (6.16) Addison P S, Watson J N and Sibbald A, The Practicalities of using Wavelet Transforms in the Non-Destructive Testing of Piles, 13th ASCE Eng. Mech. Division Conference, Baltimore, MD, USA, June 13-16 (1999) (on CD-ROM).
- (6.17) Lu J, Weaver J B, Healy D M Jr, and Xu Y, Noise Reduction with Multiscale Edge Representation and Perceptual Criteria, Proc of IEEE-SP Int. Symposium on Time-Frequency and Time-Scale Analysis, Victoria, BC, October (1992).
- (6.18) Donohoe D L, and Johnstone I M, Ideal Spatial Adaptation of via

- Wavelet Shrinkage, *Biometrika*, Vol. 81, (1994) pp425-455.
- (6.19) Watson J N, Addison P S and Sibbald A, Temporal Filtering of NDT Data using Wavelet Transforms, 14th ASCE Eng. Mech. Division Conference, USA, June (2000) (on CD-ROM).
- (6.20) Addison P S and Watson J N, Wavelet Analysis for Low Strain Integrity Testing of Foundation Piles, Proc. 5th Int. Conf. on Inspection, Appraisal, Repairs and Maintenance of Buildings and Structures, Singapore, May (1997) pp15-16.
- (6.21) Chan, H-F C, Non-Destructive Testing of Concrete Piles using the Sonic Echo and Transient Shock Methods, PhD Thesis, University of Edinburgh, (1987)

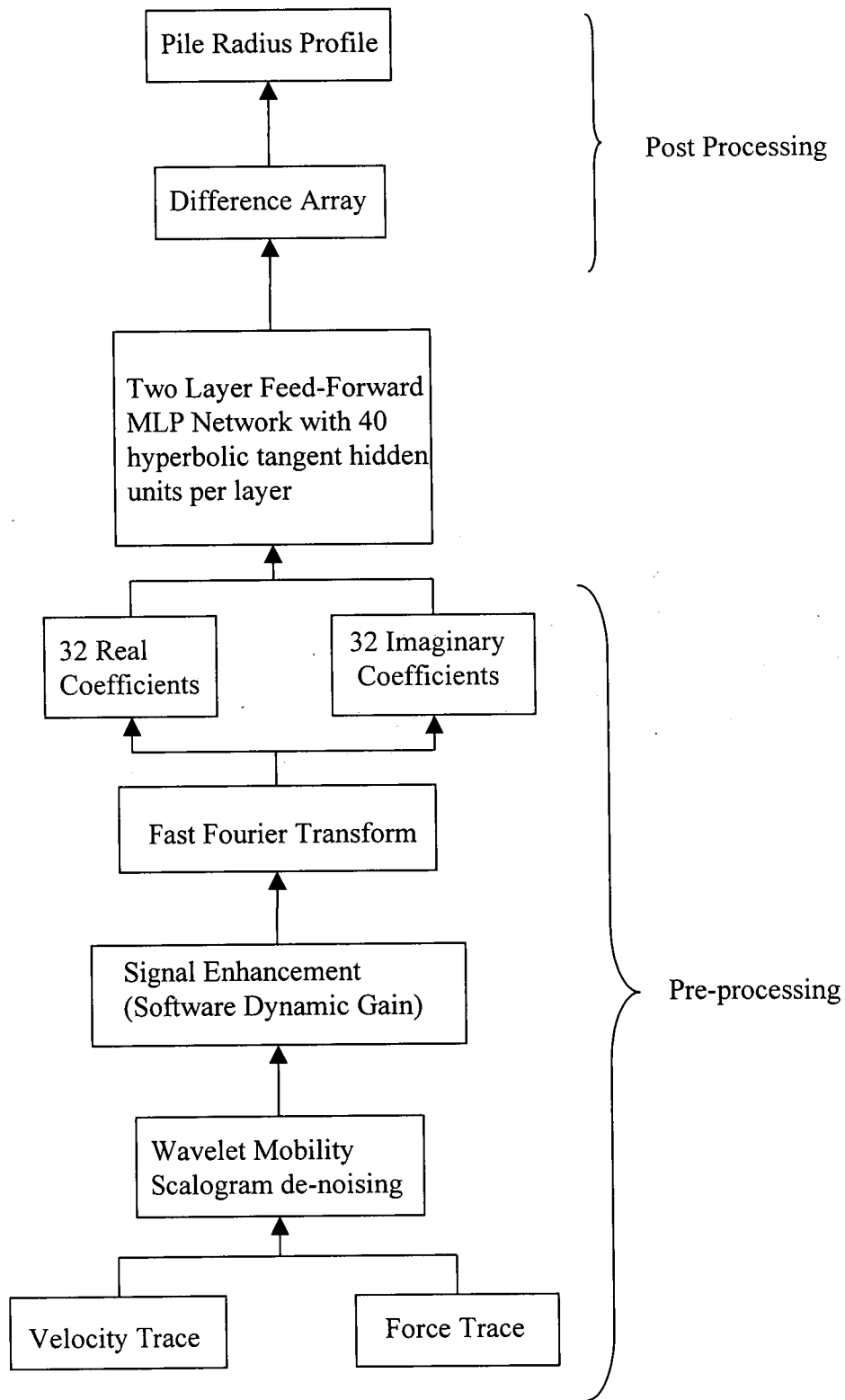


Figure 6.1 A block diagram of the final system processes for the interpretation of low strain integrity test traces.

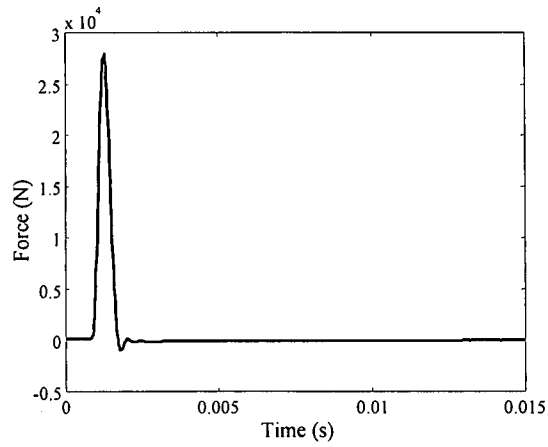


Figure 6.2 A force excitation trace obtained when striking a pile head. This example is the force trace associated with Figure 6.3, below, where a 3 lb hand held sledge hammer with a hard plastic tip has been used. Courtesy Testconsult Ltd.

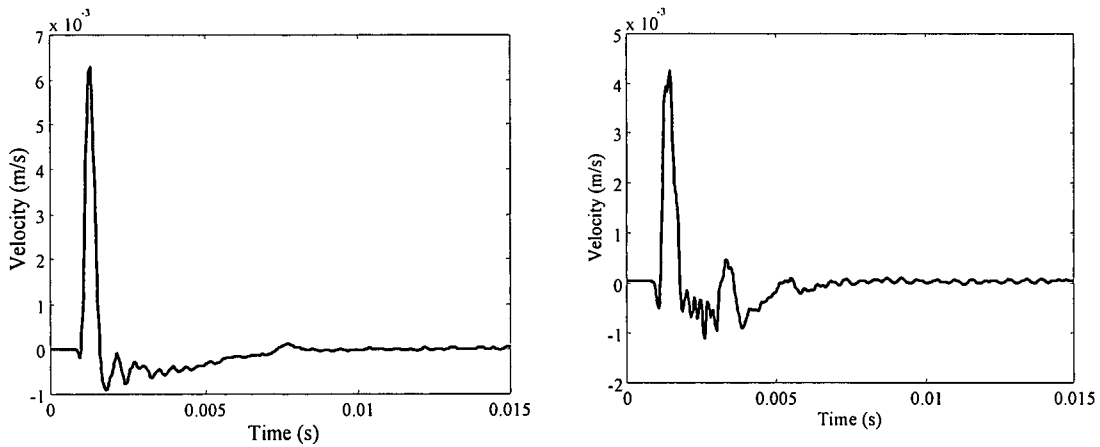


Figure 6.3 Showing the velocity trace from: (a) a sound pile, left, and (b) a pile with necking at 3.45m. Both piles have a diameter of 750mm and a design length of 11.3m. Courtesy Testconsult Ltd.

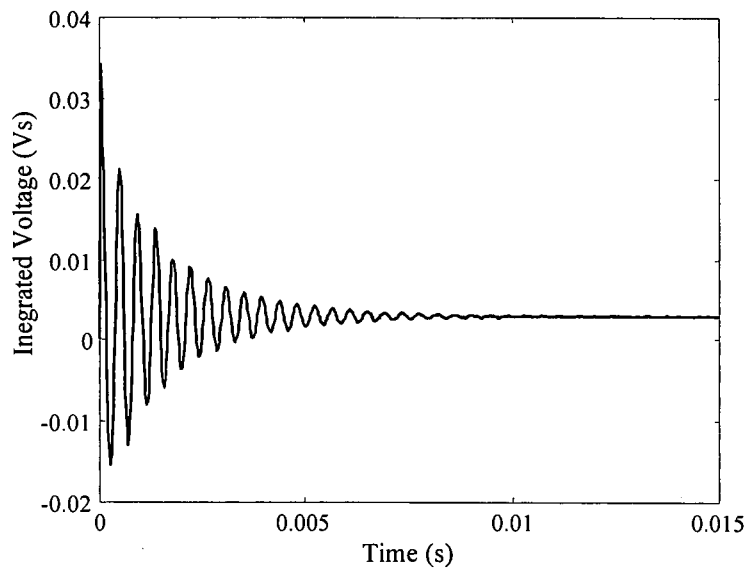


Figure 6.4 A sonic echo trace for a continuous flight augered pile with 250mm diameter and 5m design length. The data is presented as integrated voltage as no calibration data was supplied. Data courtesy of Technotrade Ltd.

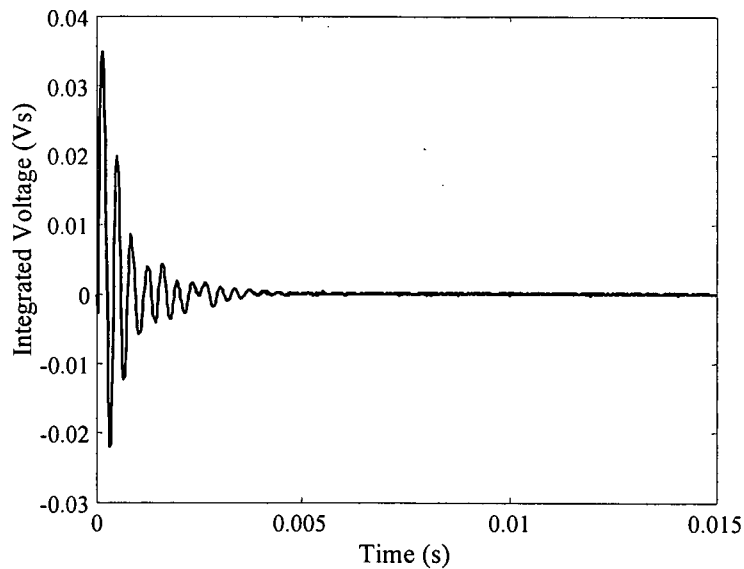


Figure 6.5 A sonic echo trace for a bored cast in situ pile with 300mm diameter and a design length of between 5 and 9m. The data is presented as integrated voltage as no calibration data was supplied. Data courtesy of Technotrade Ltd.

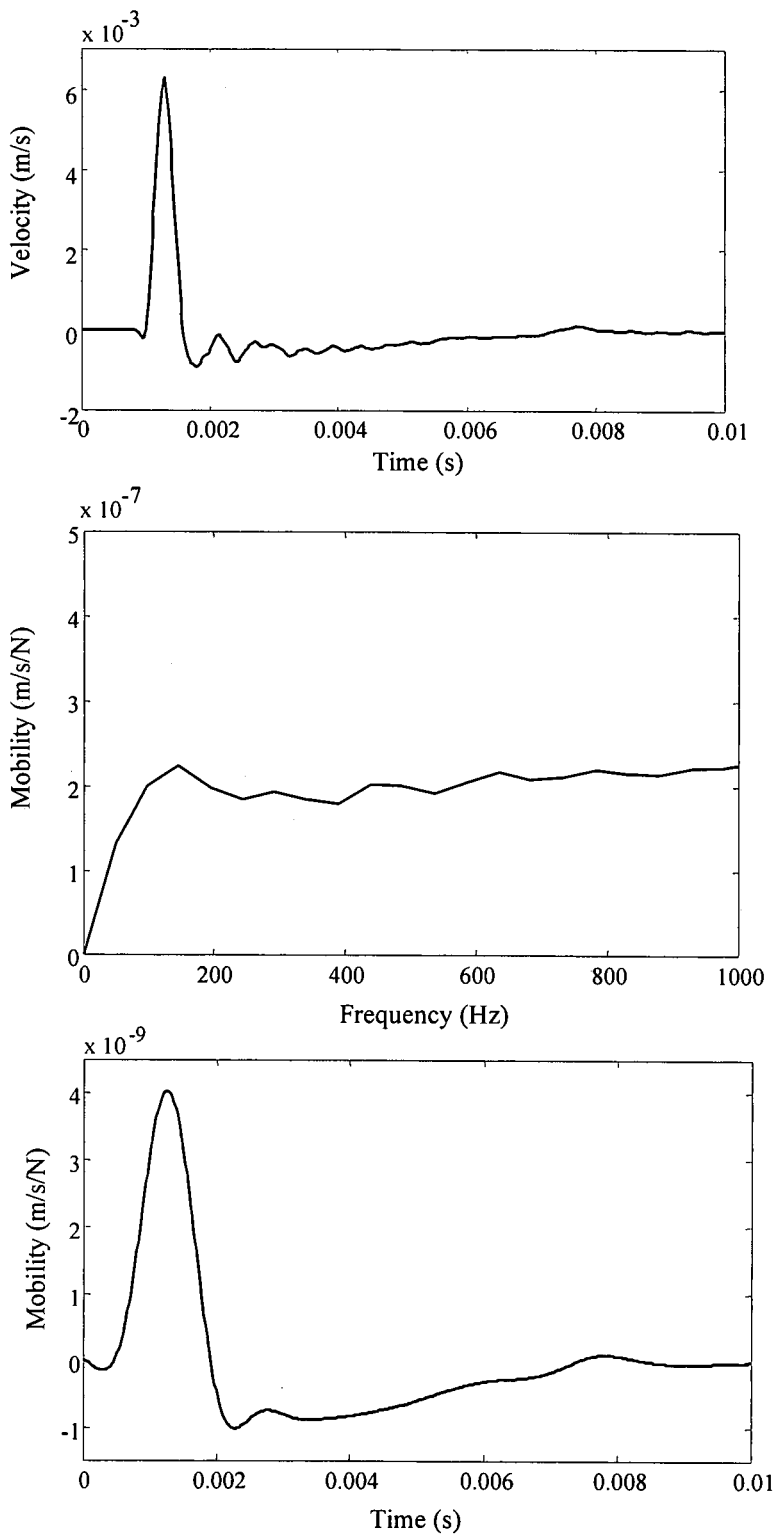


Figure 6.6 The velocity trace for pile 1, top, its mobility curve beneath, and the reconstructed reflectogram, bottom. The mobility curve has been truncated at 1000 Hz, hence the smoother nature of the reflectogram

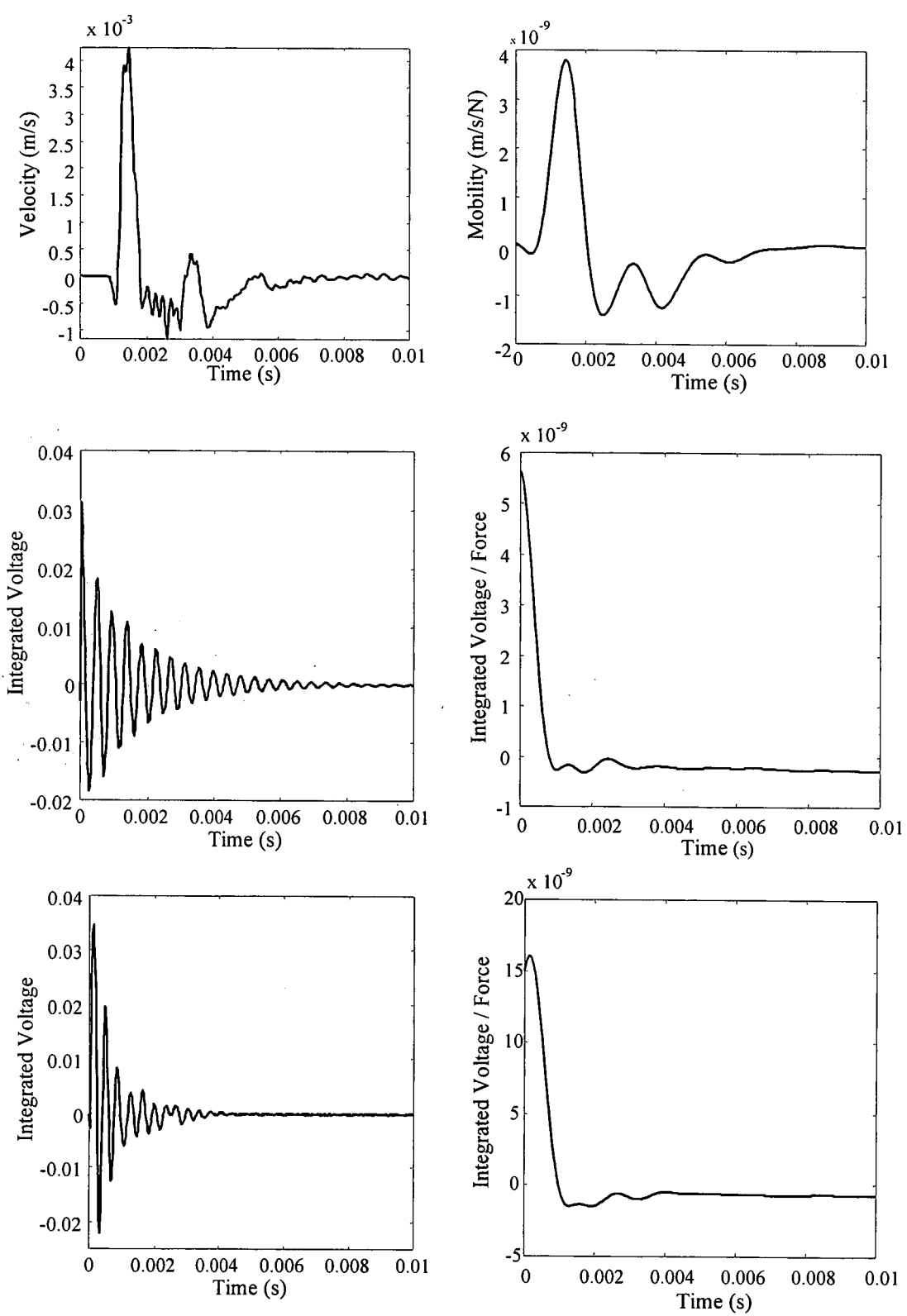


Figure 6.7 The original traces (left) and reconstructed traces (right) for piles 2, 3, and 4. Again, the mobility curve has been truncated at 1000Hz.

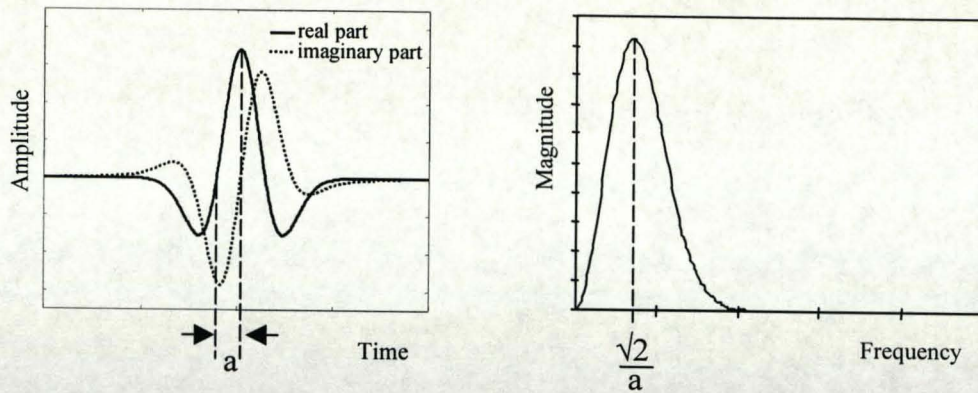


Figure 6.8 The complex Mexican hat wavelet (left) and its associated frequency spectrum (right). The wavelet has no negative frequency components and has support in the time and frequency domains linked through the dilation parameter 'a'.

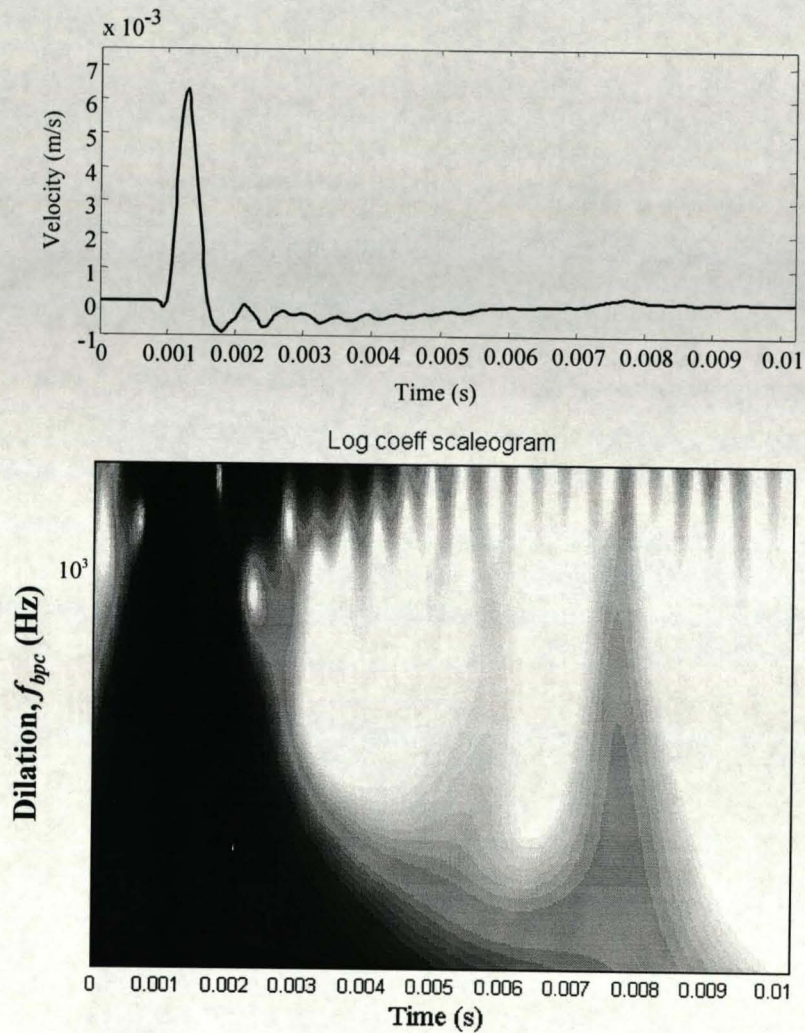


Figure 6.9 The trace for pile 1 with its associated Mobility Scalogram. Note the darkened area at around time=75ms indicating the pile toe.

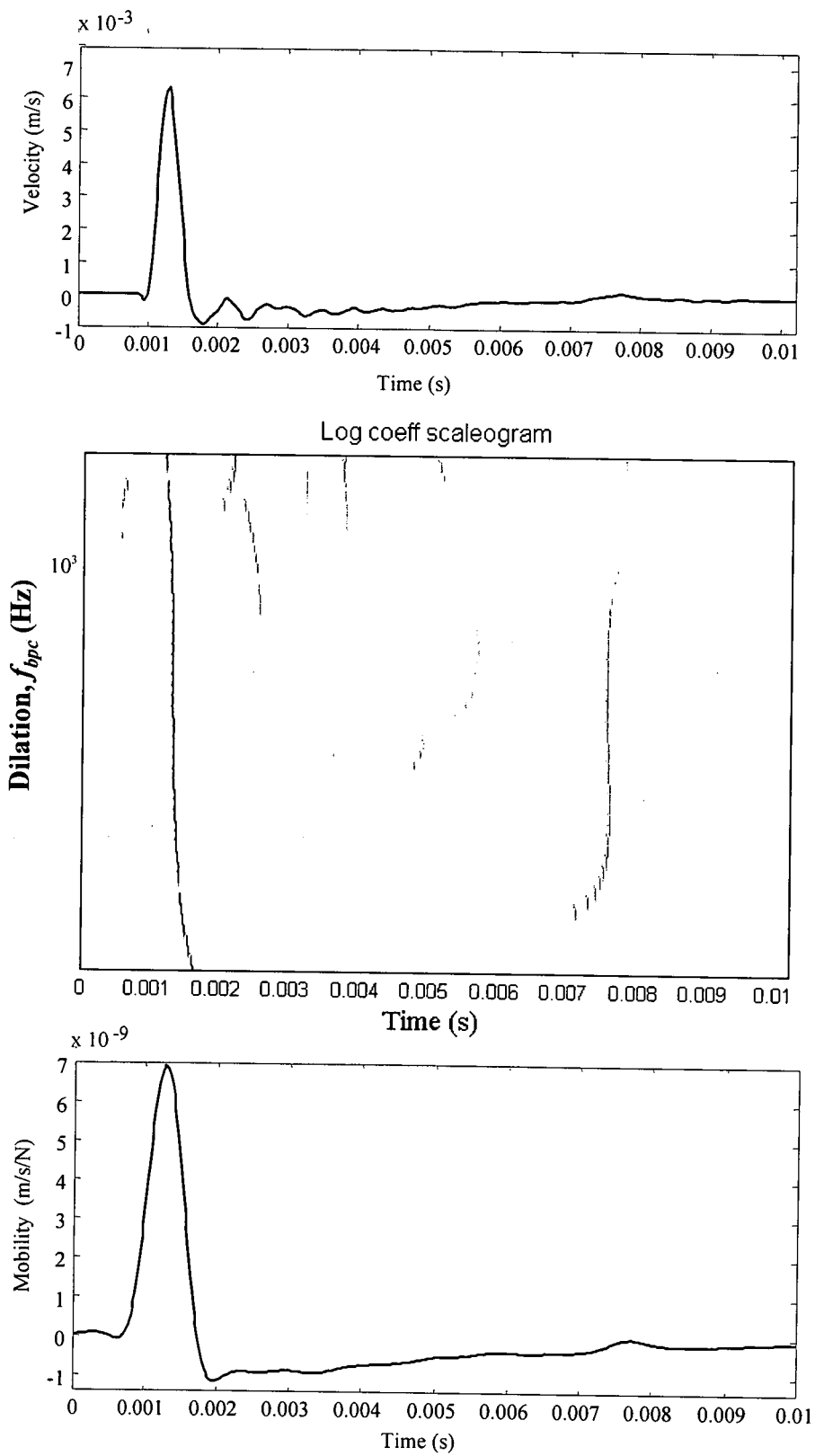


Figure 6.10 The original trace for pile 1, its associated modulus maxima scalogram, and the reconstructed trace using the largest 10 coefficients from the scalogram

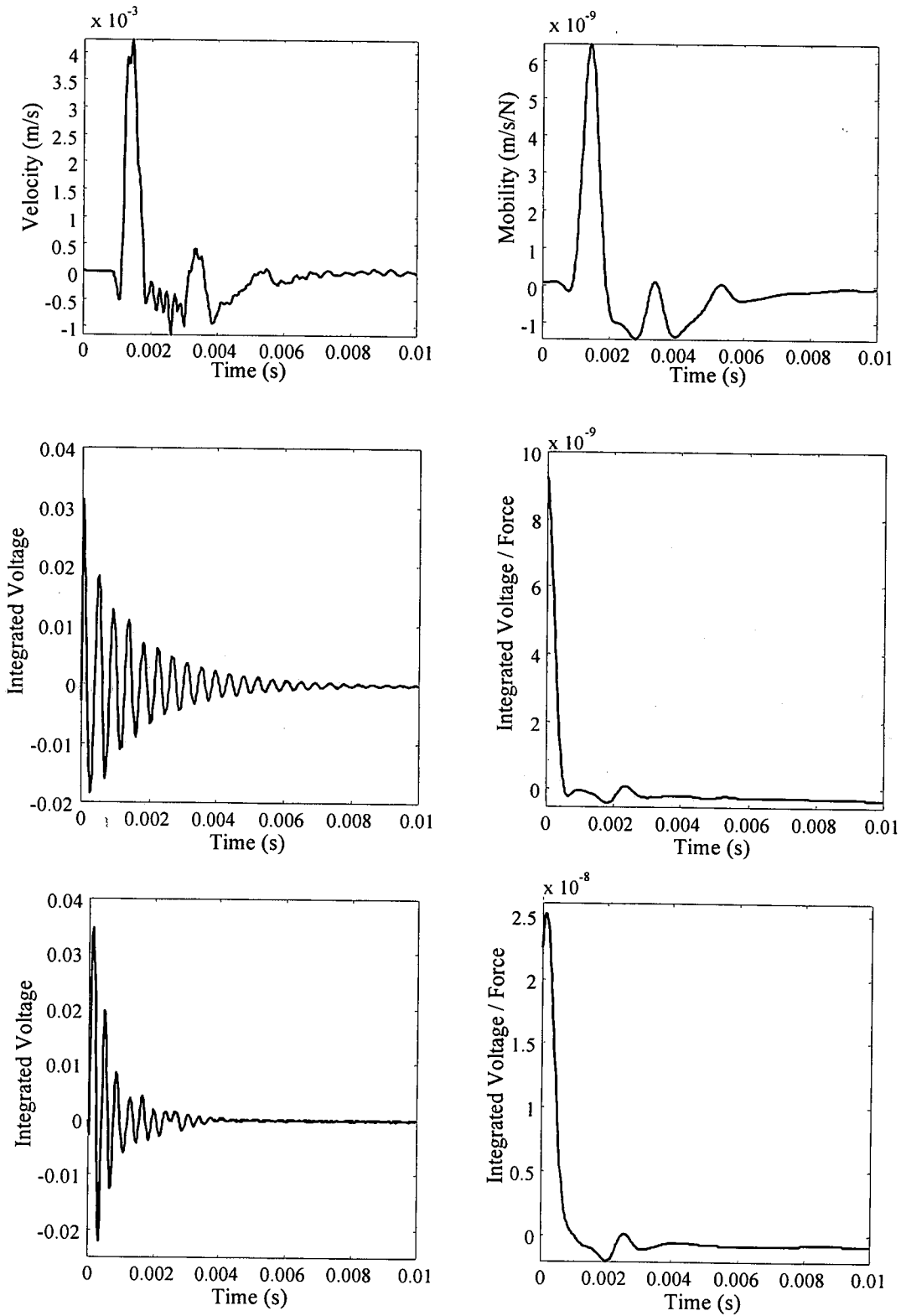


Figure 6.11 The original traces (left) and reconstructed traces (right) for piles 2, 3, and 4. Note the similarity in amplitude and shape of the reconstructed trace with the reflectograms of Figures 6.6 and 6.7.

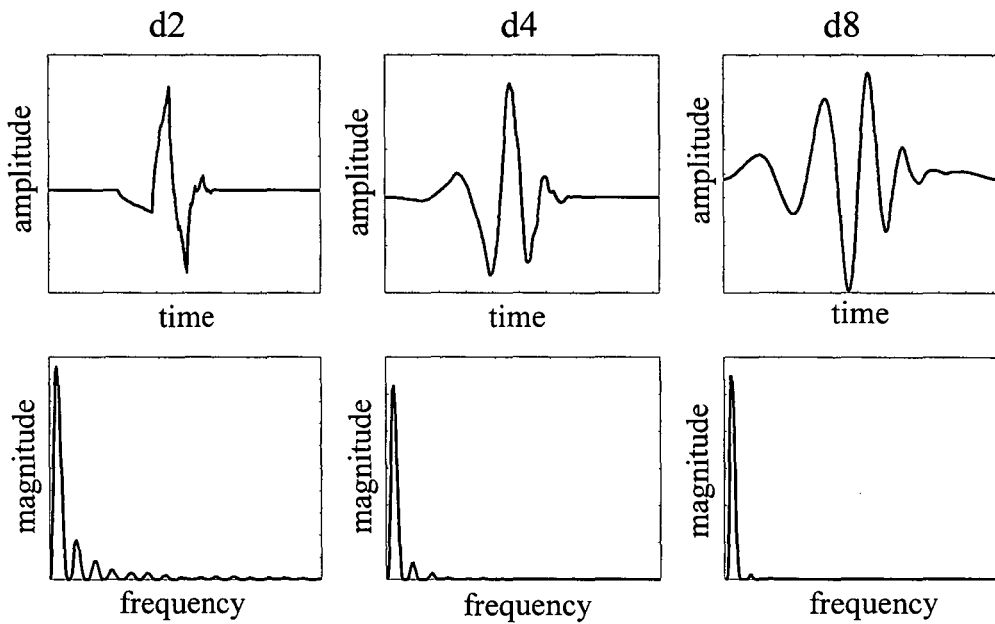


Figure 6.12 The esoteric shapes of Daubechies' d2, d4 and d8 orthonormal wavelets. The number corresponds to the number of filter coefficients. As this increases so does the regularity of the wavelet shape and the compactness of its frequency support, but at a cost to its temporal support. Being a digital filtering technique the data is presented with arbitrary units.

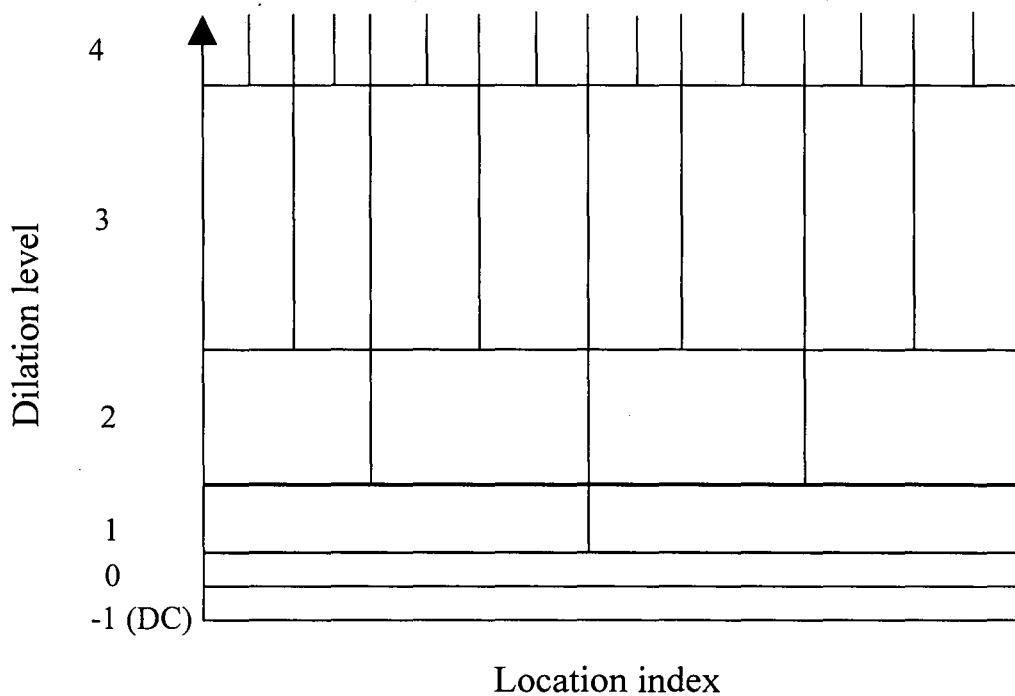


Figure 6.13 A diagrammatic representation of the Heisenberg boxes indicating the frequency (dilation) and time (location) resolutions for an orthonormal, complete wavelet set i.e. the wavelet frame takes the form of a decimated, dyadic grid.

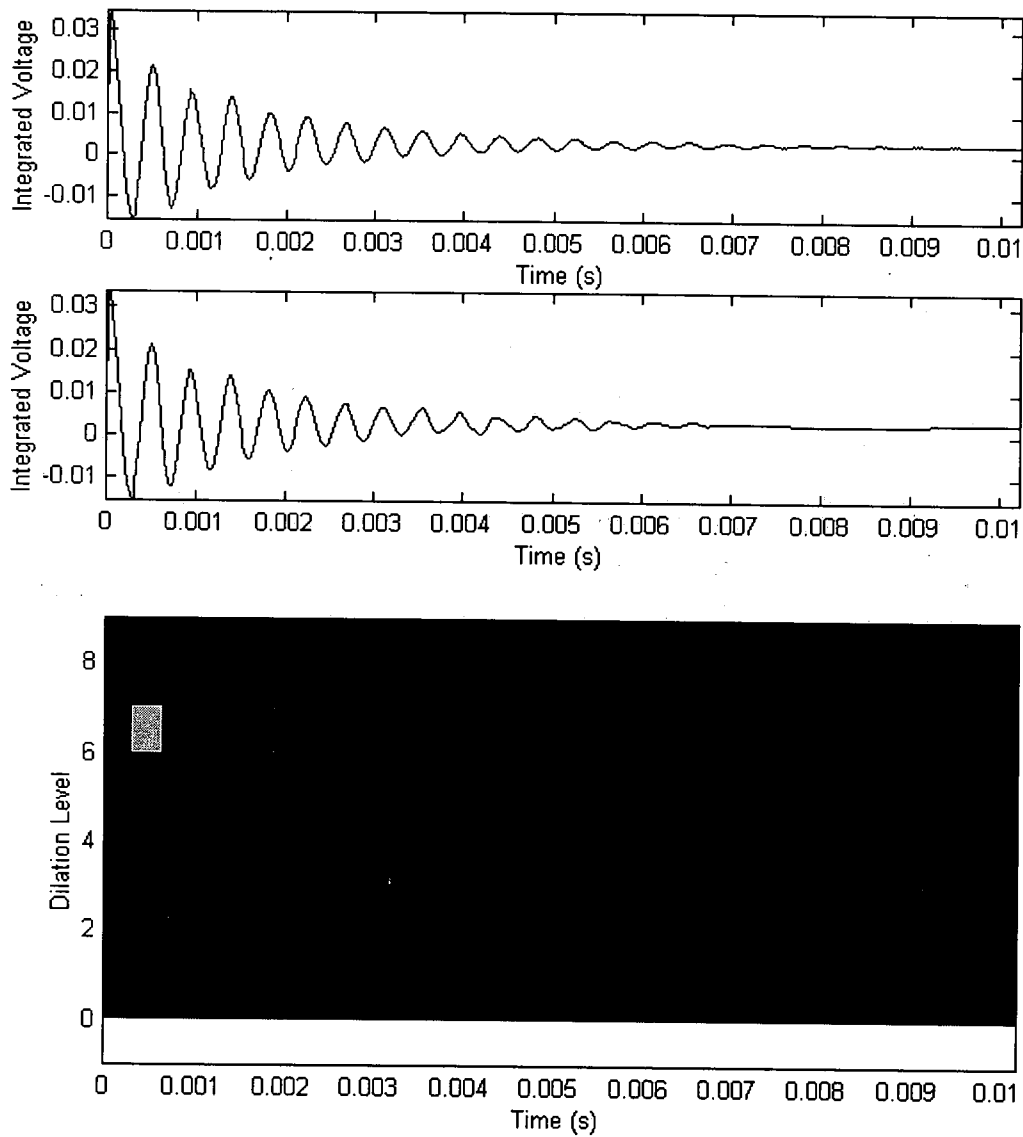


Figure 6.14 Showing the original trace for pile 3, top, and, below this, its reconstruction from the highest 64 coefficients (of 1024) from its associated scalogram, bottom. Note that in this case, the reconstruction retains high frequency components. Hence this methodology is employed in an increasing number of data compression applications.

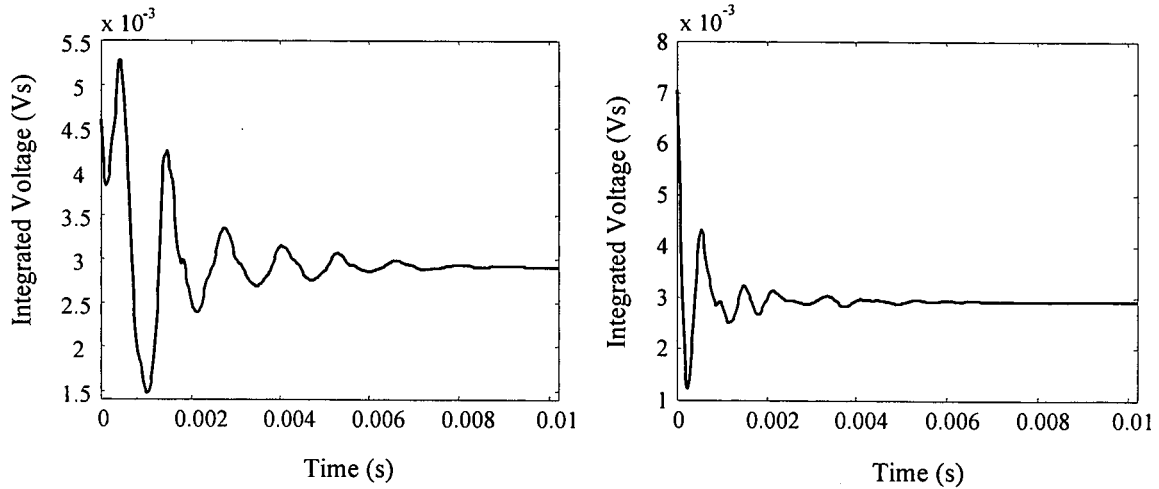


Figure 6.15 Showing how, even when the wavelet frame is truncated at level 5, the frequency component make-up of the wavelets and the decimated construct of the frame is not conducive to the effective parameterisation of the sonic echo trace of pile 3. The traces presented are reconstructed from the largest 32 coefficients of the original trace decomposition using the Daubechies d4 wavelet (left) and the d8 wavelet (right).

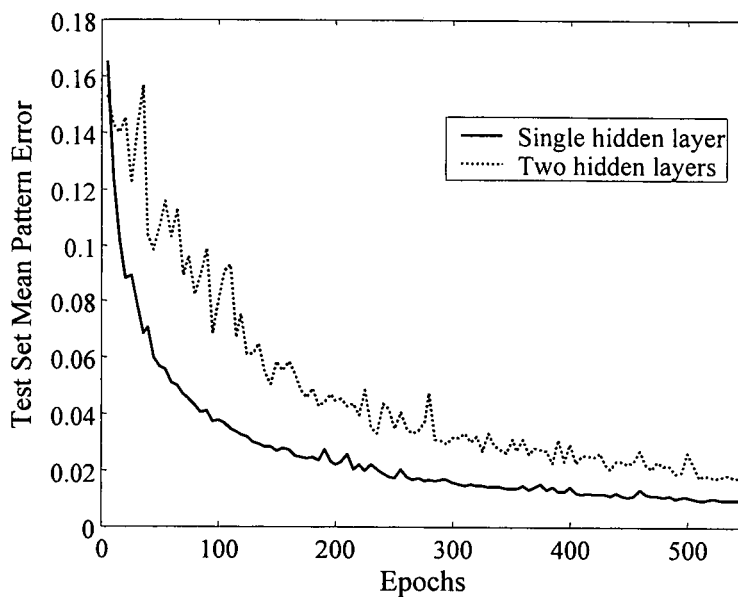


Figure 6.16 The convergence curves from a single layer MLP network of 60 hidden units and a two hidden layer system each layer also of 60 units. The network hidden units have sigmoid activation functions and the learning rate is given as 0.1. This network has successfully learned to reconstruct the original trace reflectogram from the presented mobility curve (see Figure 6.17 for examples).

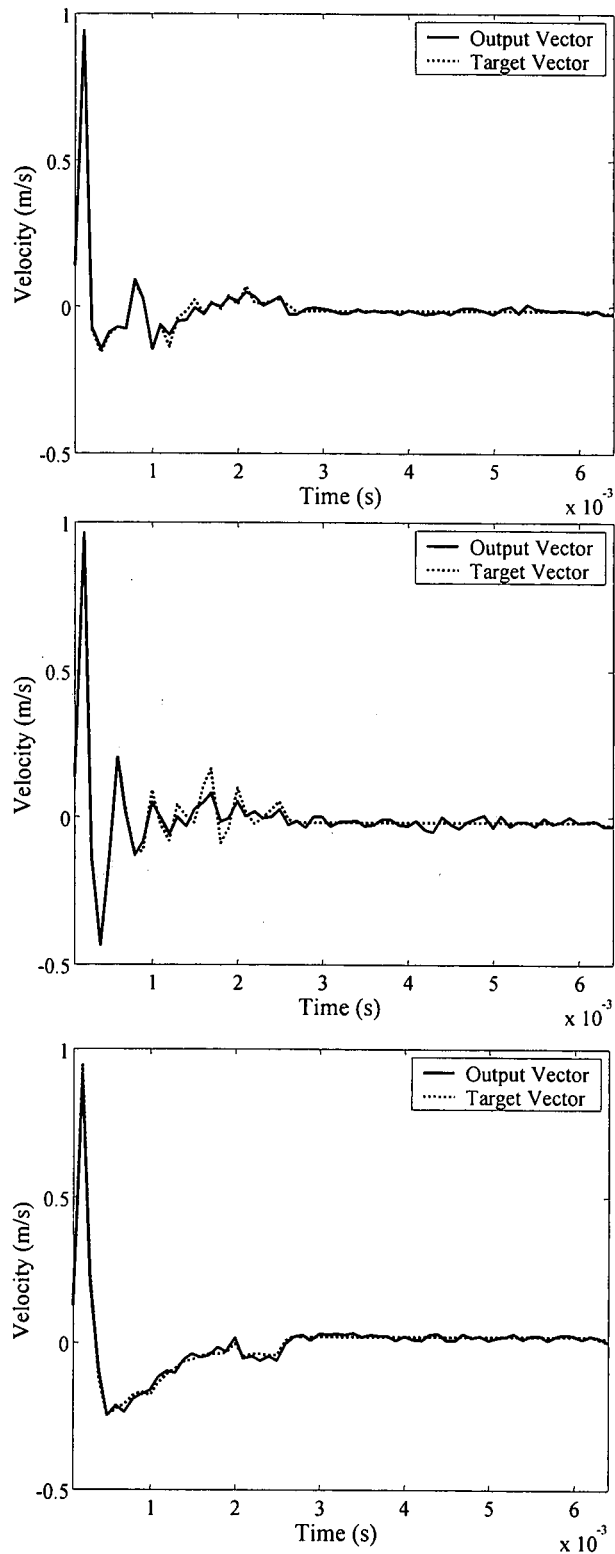


Figure 6.17 Three arbitrarily chosen examples of the outputs for the single layer network of Figure 6.16. The ability of the network to reconstruct features within the original reflectogram is found to be frequency dependent. Lower amplitude, higher frequency, components are less accurately modelled.

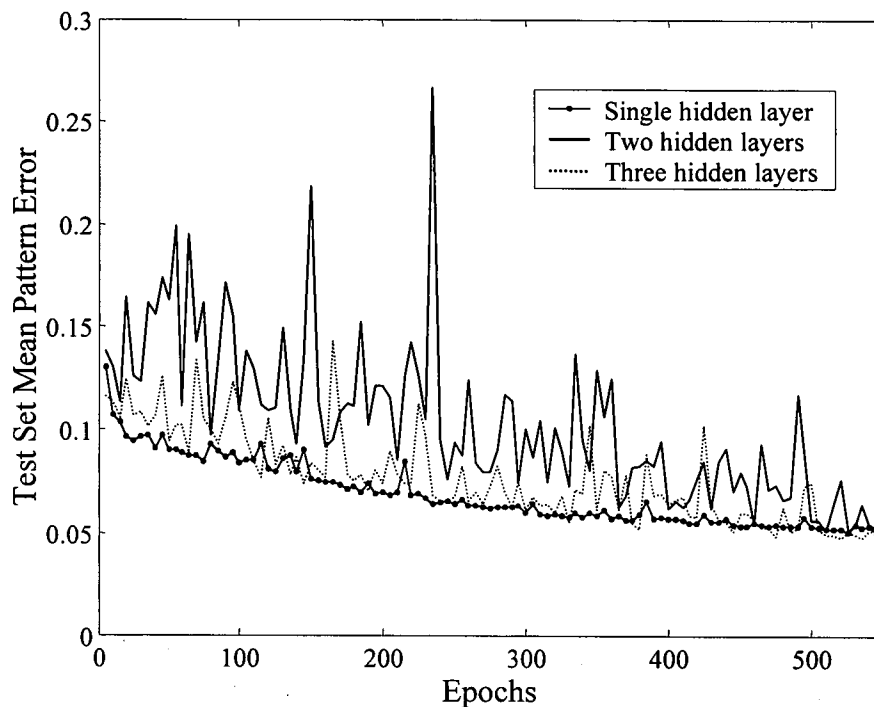


Figure 6.18 The convergence curves from a layered MLP network of 60 hidden units in each layer. The network hidden units have sigmoid activation functions and the learning rate is given as 0.1. The network is less effective at reconstructing the original trace reflectogram using the wavelet coefficient data than when using the Mobility curve data, as in Figure 6.16.

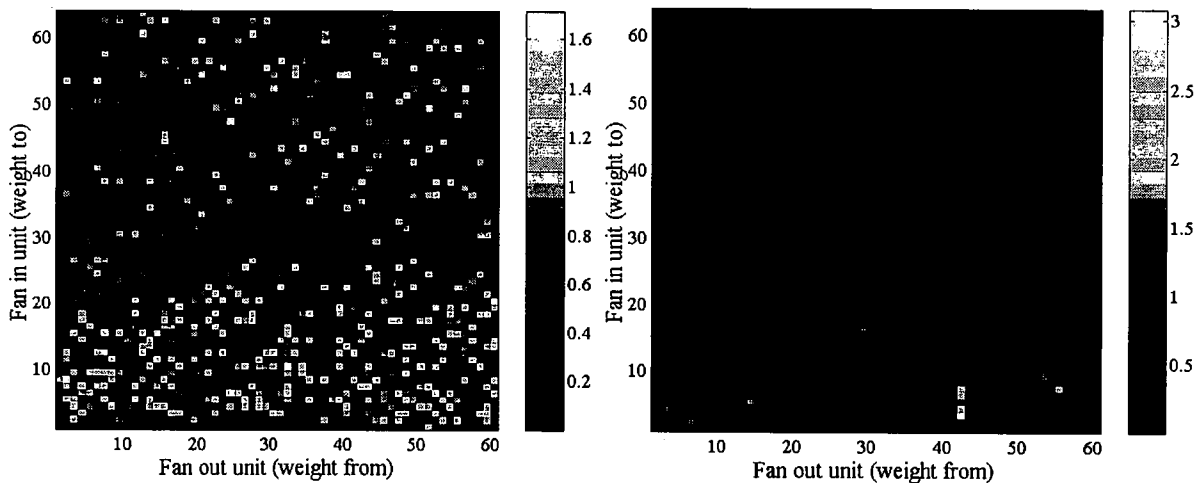


Figure 6.19 Shows the weight matrix from the hidden to output units for the networks using mobility curve data (left) and wavelet data (right). Both are the single hidden layer networks. The weights leading to the left hand part of the reconstructed trace (containing the high amplitude input pulse) are towards the bottom of the graphs and generally have larger amplitudes. Although they are well distributed across all the units in the left hand graph for the wavelet coefficient case one hidden unit, unit 42, dominates.

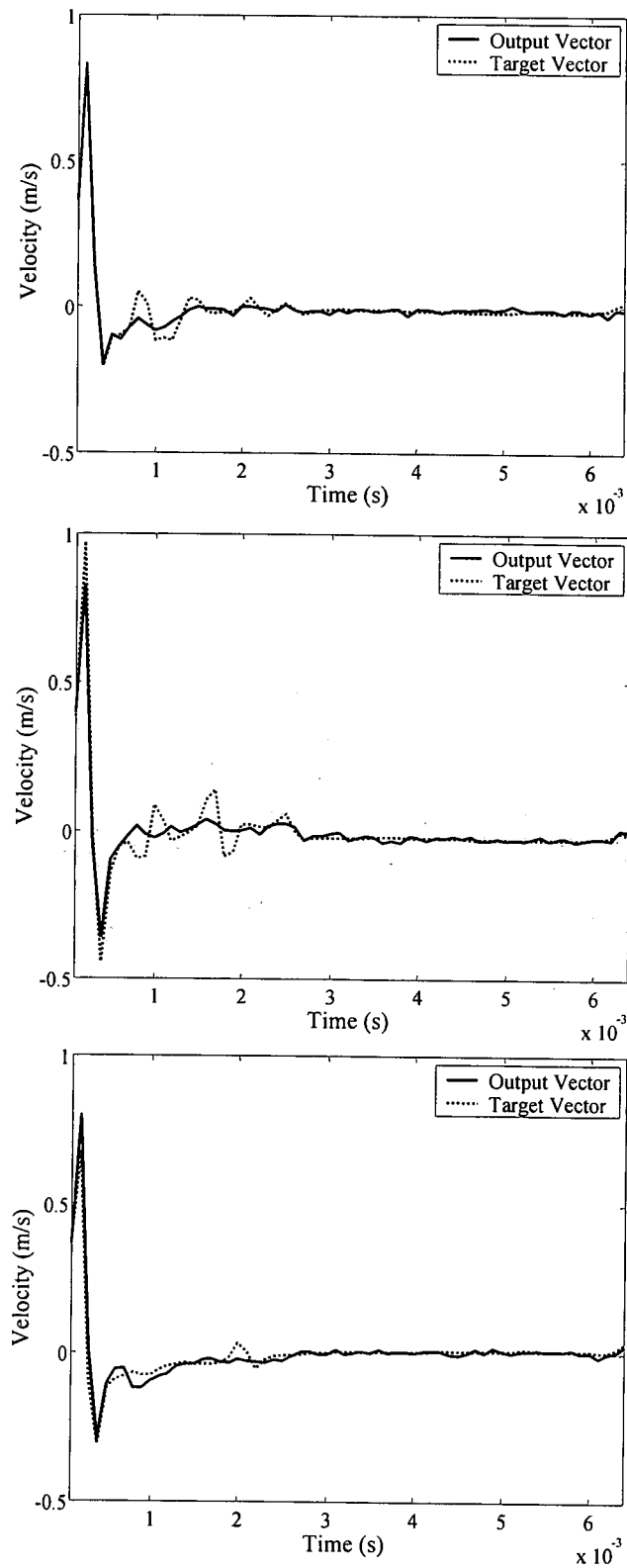


Figure 6.20 Shows examples of the single layered wavelet pre-processed network of Figure 6.18. As suggested by the single, dominating, hidden unit of Figure 6.19 the network has reduced the pattern errors by fitting the high amplitude input pulse well. However, especially obvious in the bottom plot, where a returned echo is completely missed, it is apparent that this is at a cost to features later in the trace.

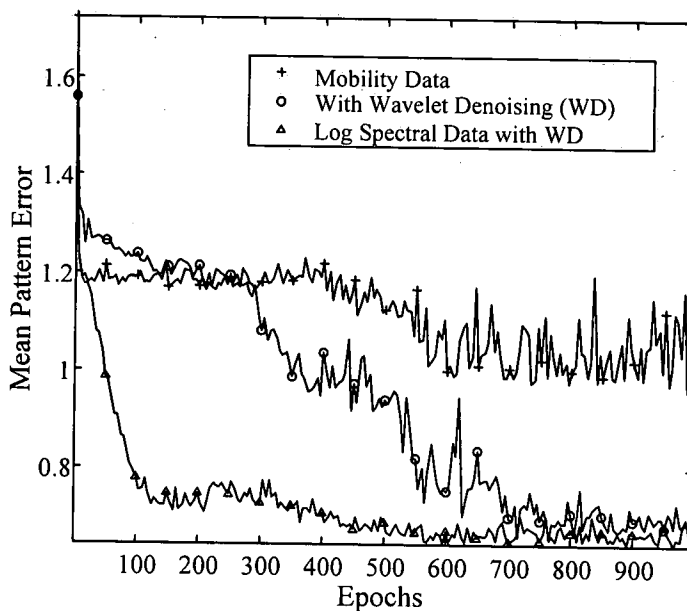
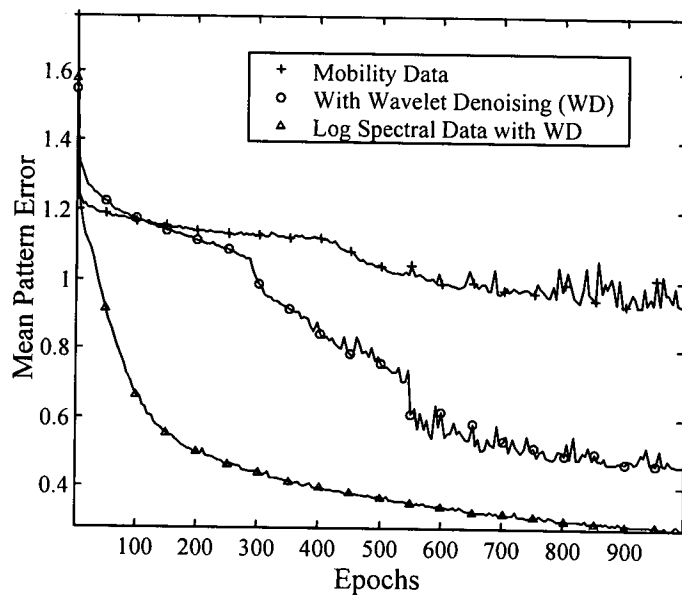


Figure 6.21 Showing network effectiveness with respect to the input encoding and pre-processing. Top, is the training set convergence curve and below the test set curve. Of particular note is the increase in learning rate and network effectiveness for those networks with Wavelet denoising.

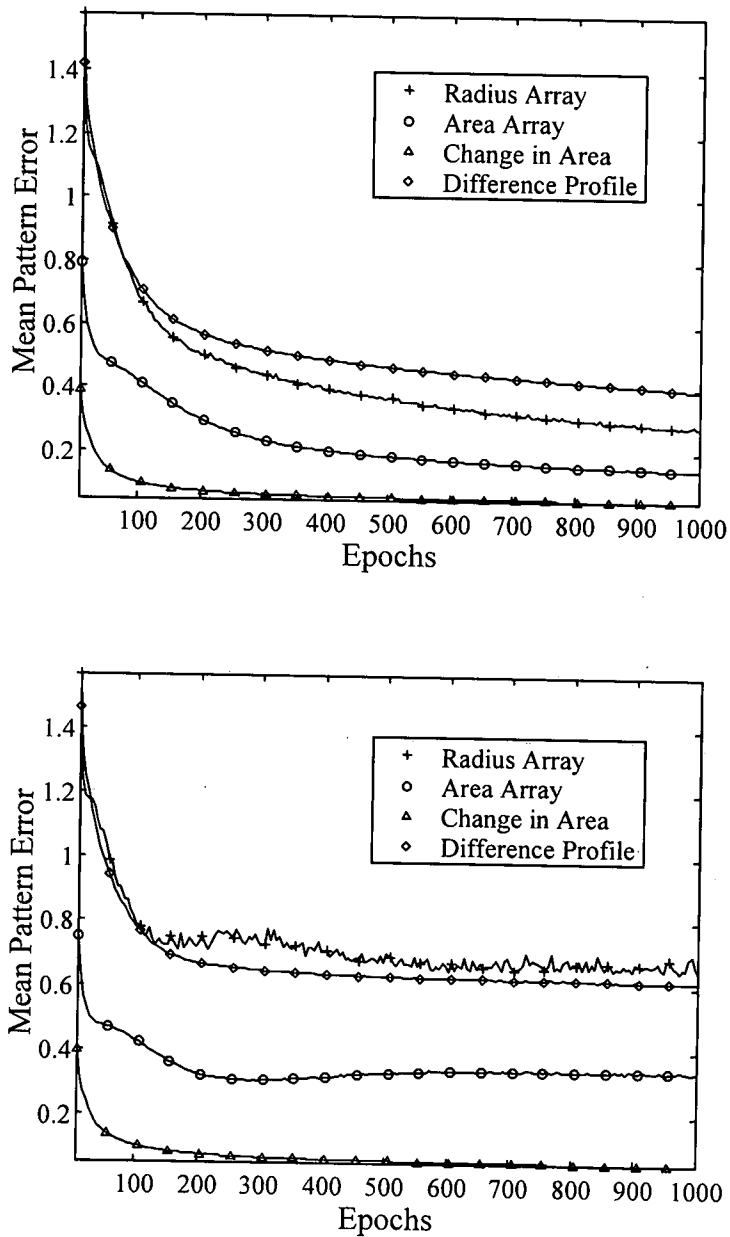


Figure 6.22 Showing network effectiveness with respect to output coding and post-processing. Top, is the training set convergence curve and below the test set curve. While these plots indicate the monotonic nature of the convergence curves it should be noted that the methods of output coding means direct comparison of network performance cannot be made through comparing the networks' mean pattern errors.

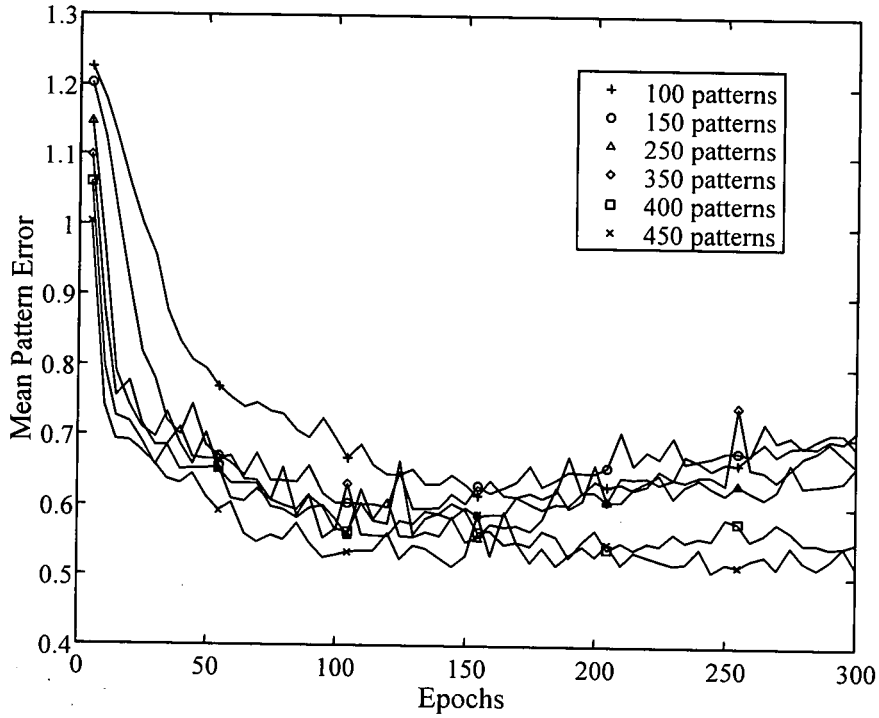


Figure 6.23 Showing the convergence curves for a network with two hidden layers each of 40 units. It is noted that for training sets of over 350 patterns no overtraining occurs. Identical test sets are used for each experiment.

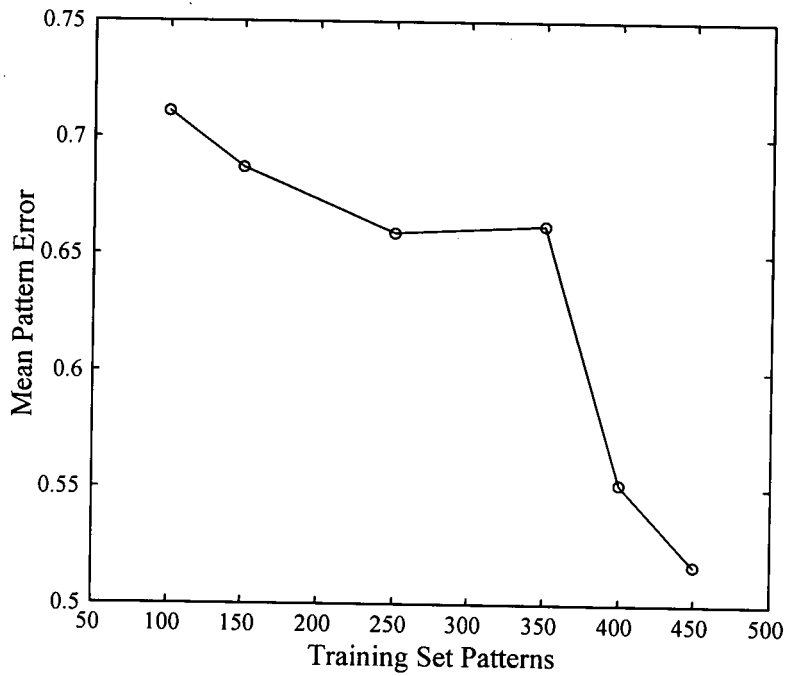


Figure 6.24 The Mean Pattern Error after 300 epochs as a function of training set size. Of particular note is the drop in error when the set size is over 350 c.f. Figure 6.23.

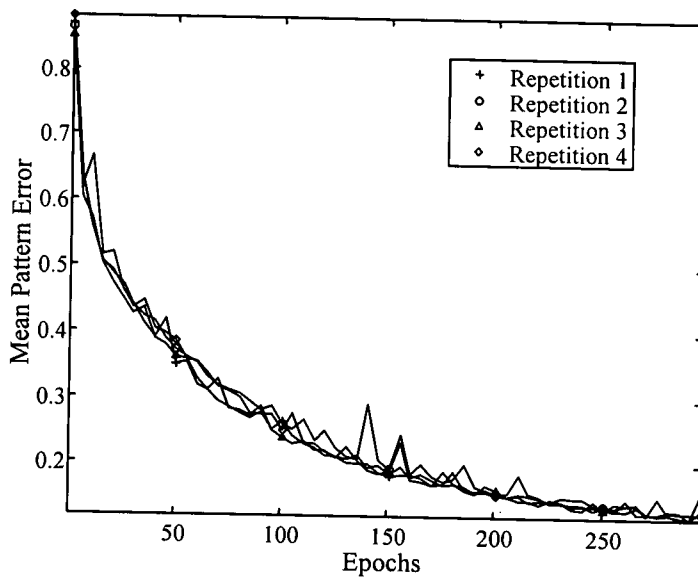


Figure 6.25 Shows the repeatability of training set learning.

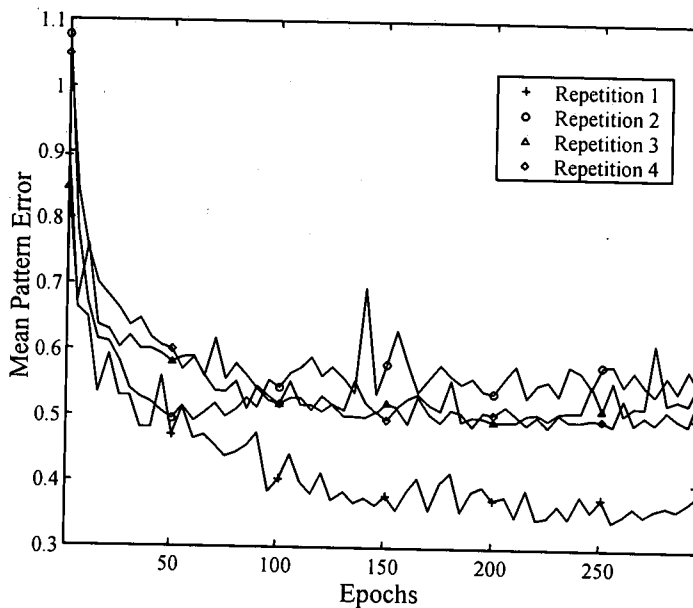


Figure 6.26 Shows how the smaller size of the test set leads to statistical and, therefore, network measure, aberrations. When these test set results are visually inspected the same strengths and weaknesses in network effectiveness are observed e.g. smaller faults are more difficult to detect (see Figure 6.33 and subsequent figures). However, the occasional test set will contain a statistically unrepresentative pattern distribution which causes measurement aberrations such that observed in repetition 1. In all parametric investigations, therefore, the same test and training sets are used in order that like be compared with like.

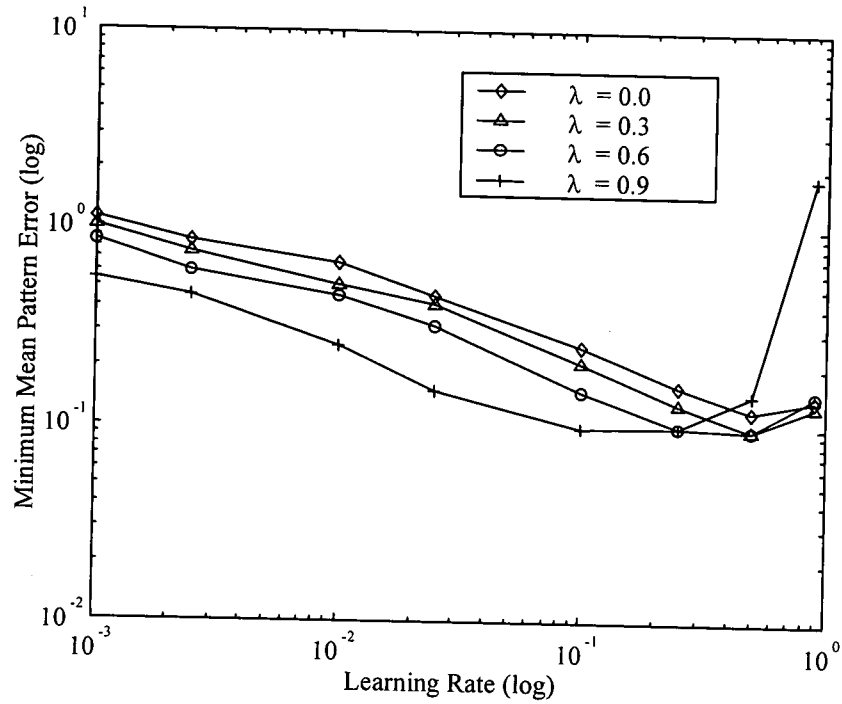


Figure 6.27 Indicates the optimum training set performance of a single layer network with respect to the training parameters momentum (λ) and learning rate (α).

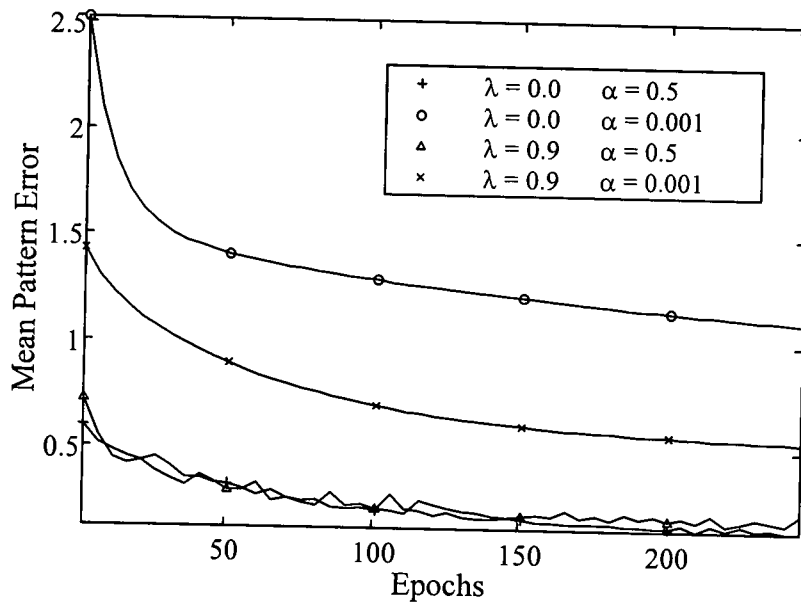


Figure 6.28 Shows how an increased learning rate results in a noisier training set convergence curve.

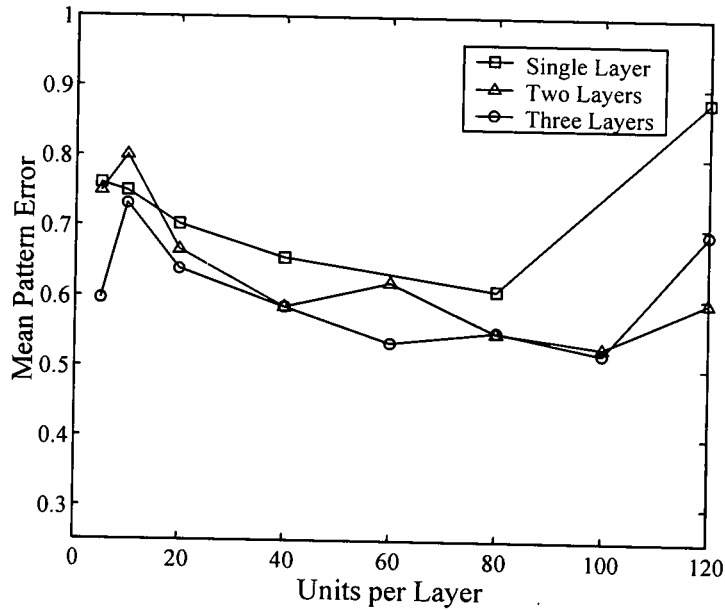


Figure 6.29 A graph showing test set mean pattern error with respect to the number of hidden units in each network layer. Note, due to the non-monotonic nature of the convergence curve (see Figure 6.30, below) the value taken is the mean error value for the final 25 epochs of training.

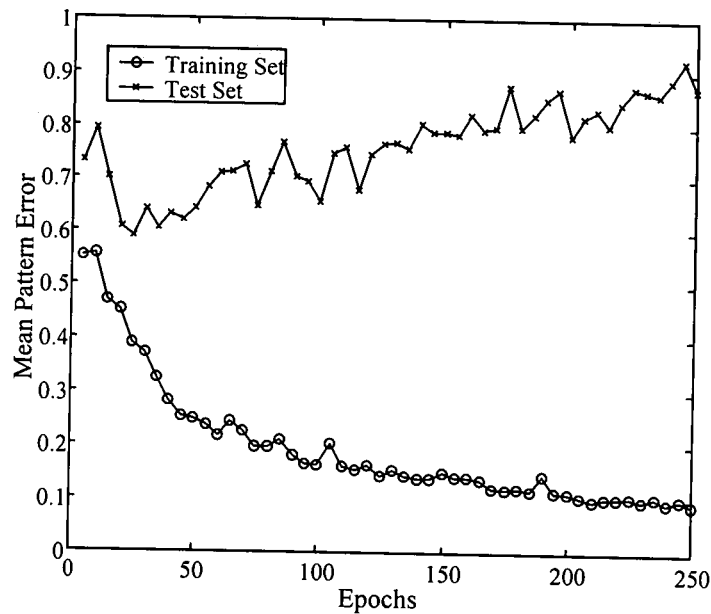


Figure 6.30 An example of overtraining in a 160 unit system with one hidden layer where, although the training pattern error decreases with learning, the test set mean pattern error increases. This is due to the network learning the patterns in the training set rather than the functional mapping i.e no generalisation occurs.

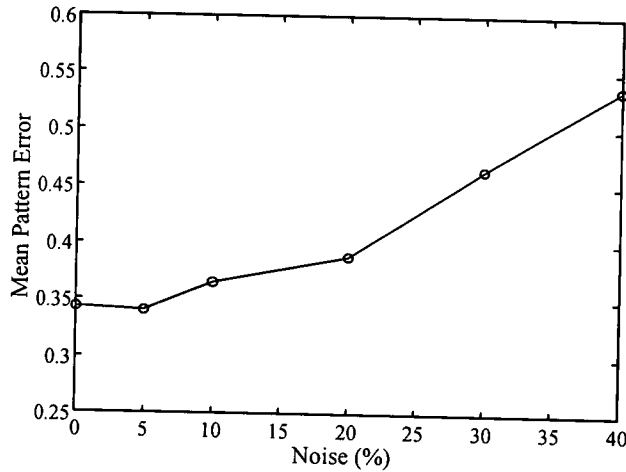


Figure 6.31 Shows how the mean pattern error for the network test set increases as more uncorrelated noise is added during training.

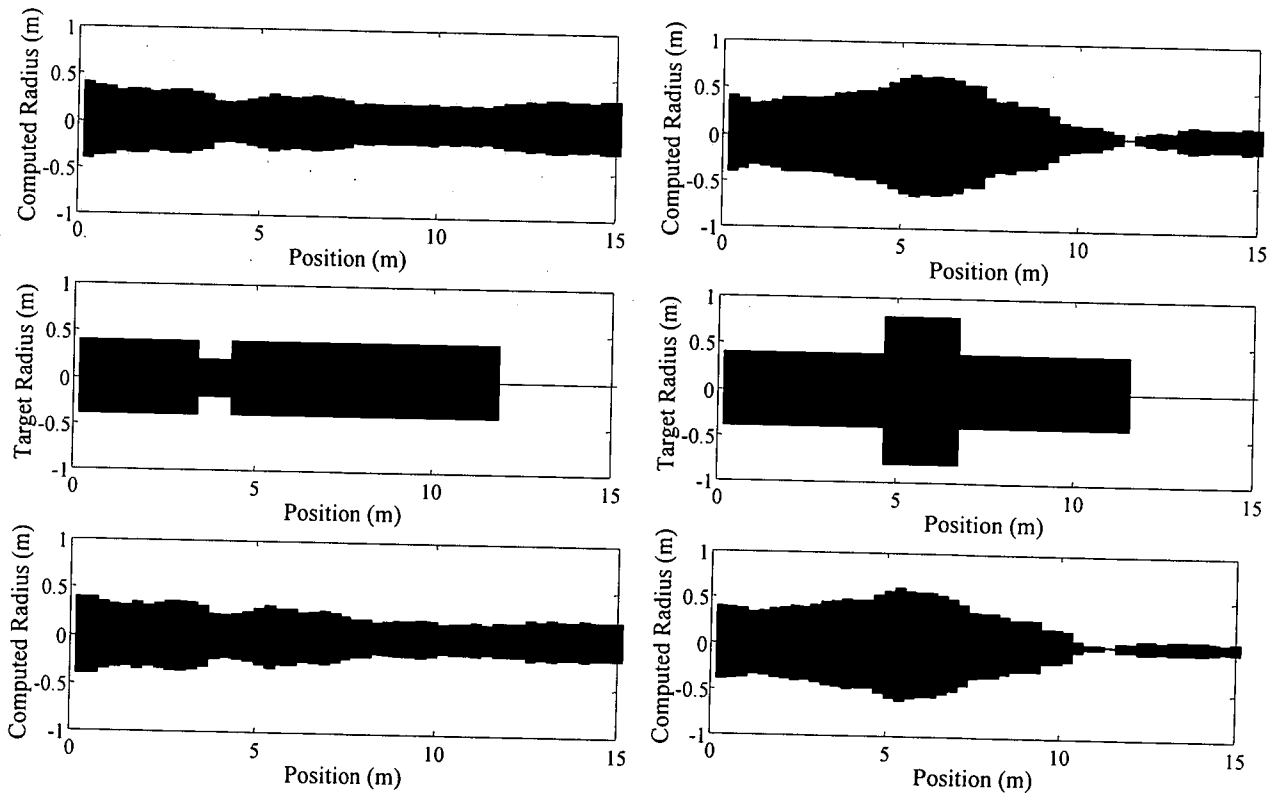


Figure 6.32 Two examples of interpretation of field test results for a pile with a neck, left, and a pile with a bulb, right. The top two profiles are the required profiles and those calculated by a system with the injection of 35% uncorrelated noise and beneath the same profiles from a network trained without noise. There is no observable improvement in network performance obtained through the use of noise.

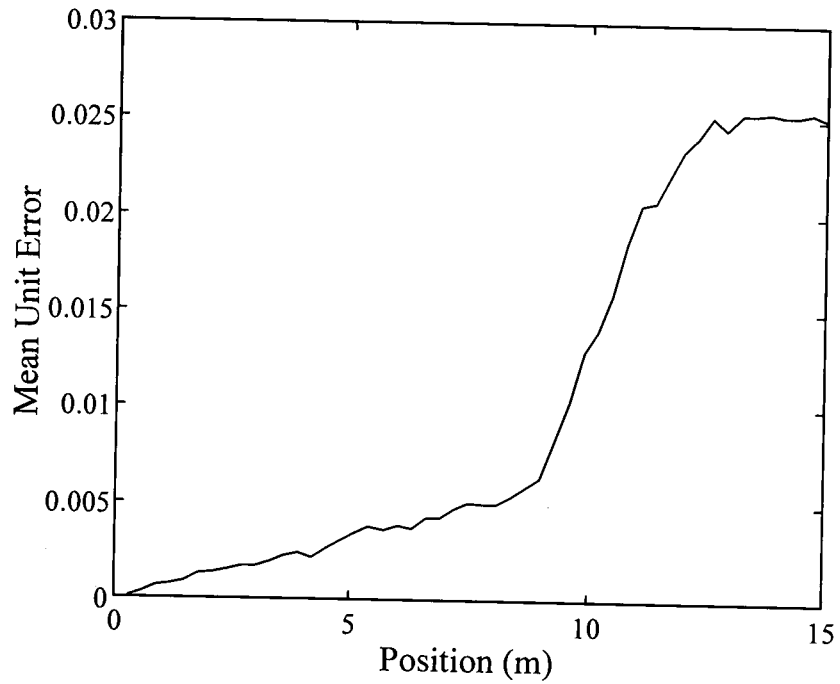


Figure 6.33 Showing the the error in calculated pile radius with respect to position. Note this error measure does not take into account the masking of faults by others further up the pile.

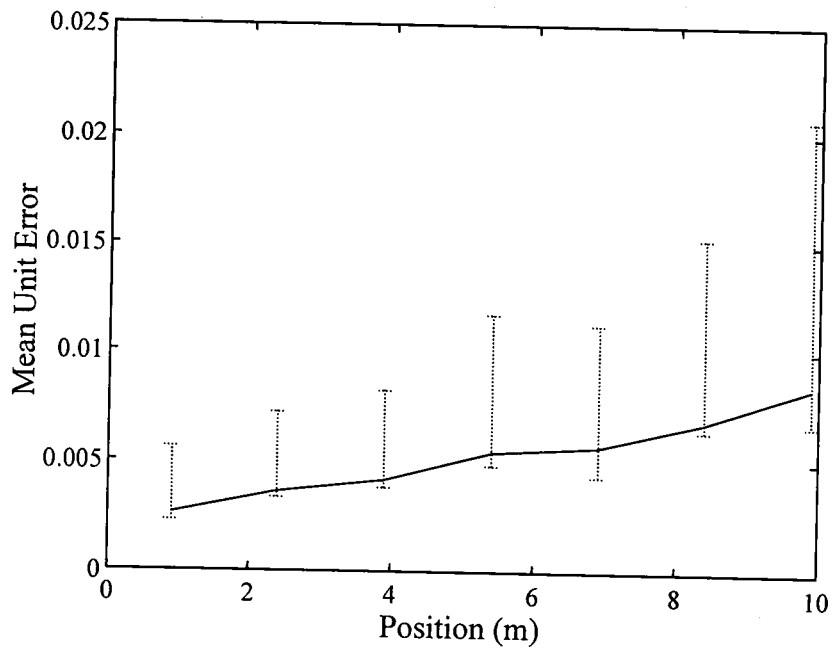


Figure 6.34 Showing the error in calculated change in radius for a single change in section along the pile length with respect to that changes position. The error bars have been calculated by the median quartile method.

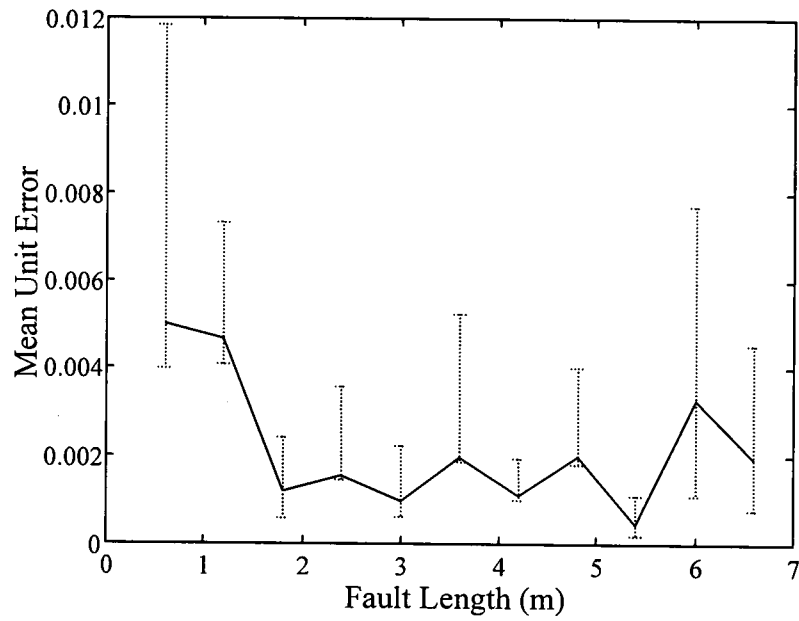


Figure 6.35 Showing the error in calculated change in radius for a single change in section with respect to the fault length. Of note is the comparative increase in errors for faults with an axial length of less than one metre.

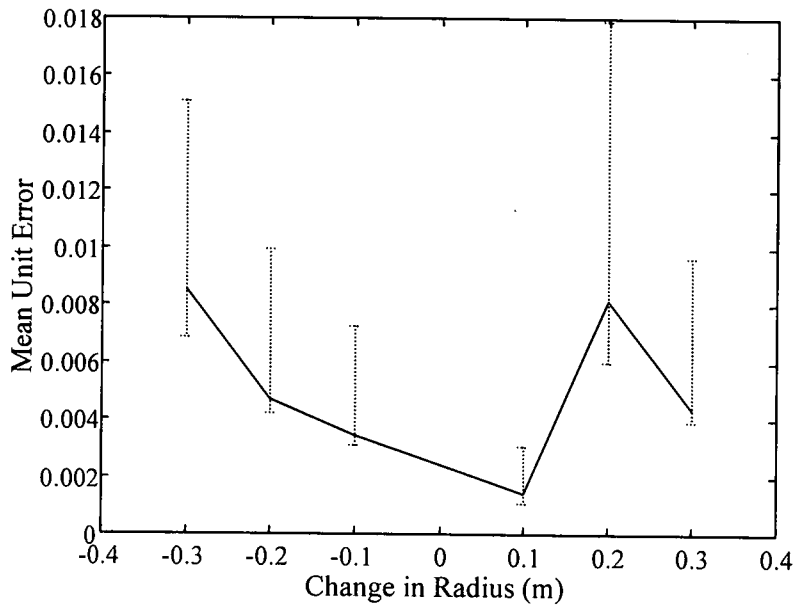


Figure 6.36 Showing the error in calculated change in radius for a single change in section along the pile length with respect to the size of radial change.

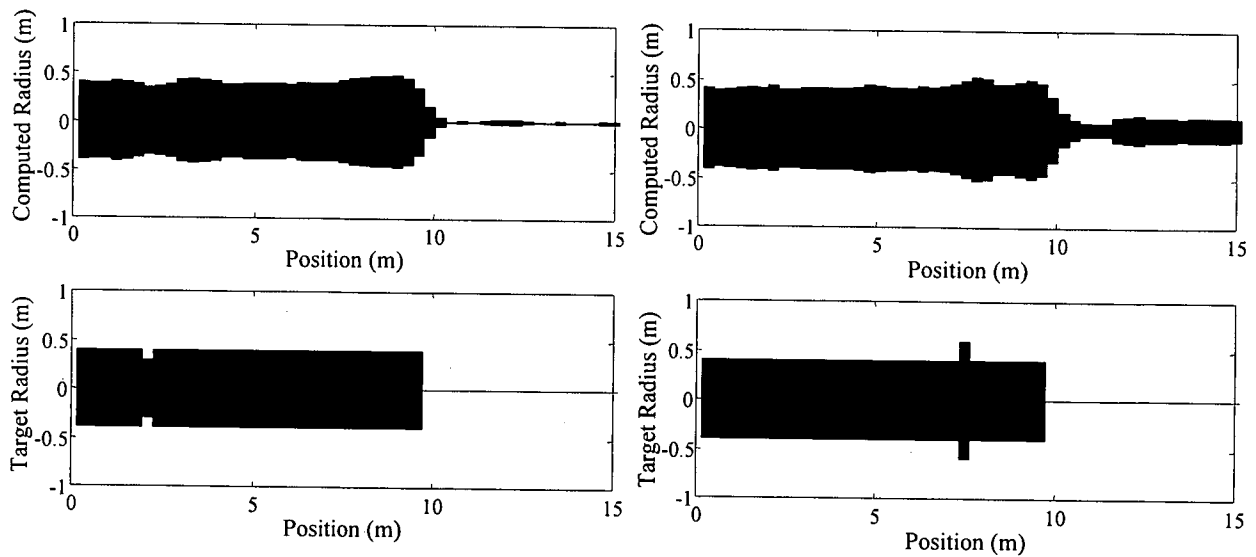


Figure 6.37 Showing how the computed pile profiles, top, for piles with faults of short axial length are less ably distinguished by the neural network.

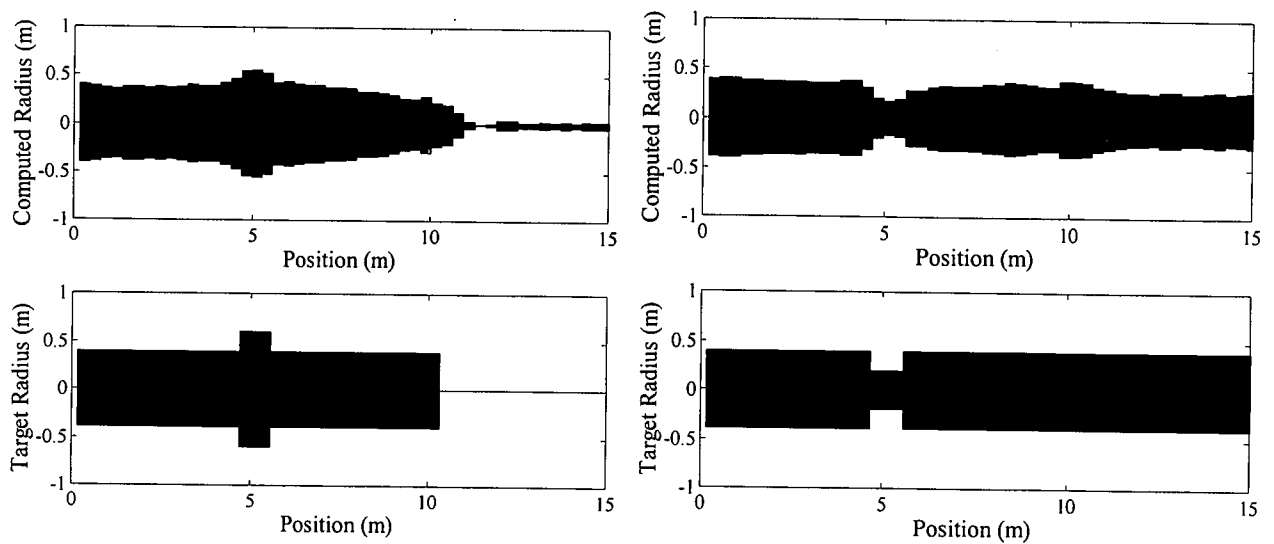


Figure 6.38 The successful identification of a neck and bulb by the MLP network, top. Beneath is the required pile profile - note the toe for the pile with necking (right) is not detectable, hence there is no observable end to the pile.

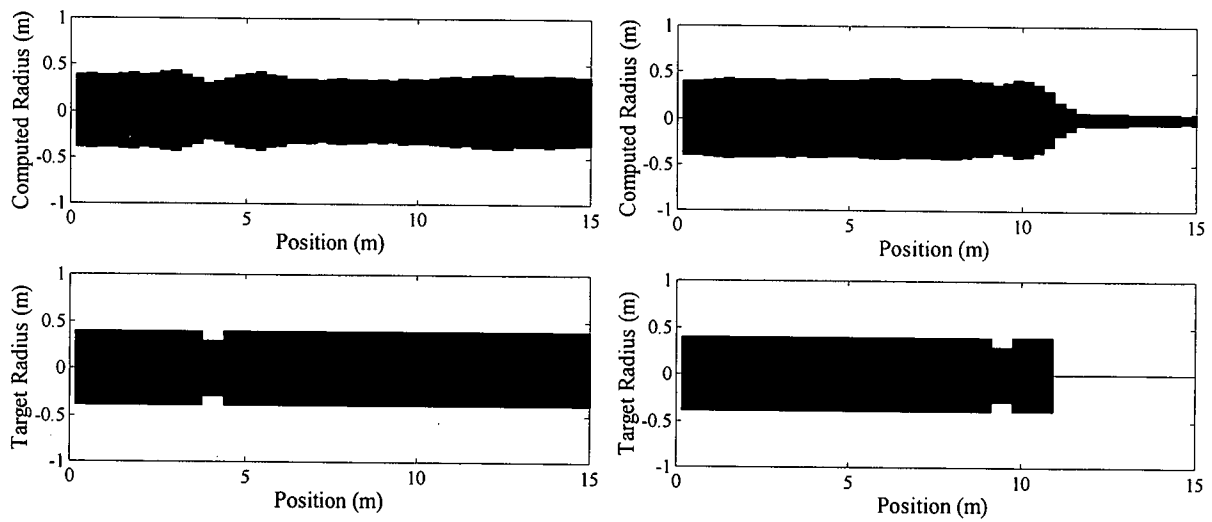


Figure 6.39 Indicates how identical faults towards the pile toe are less ably detected than those nearer the pile head.

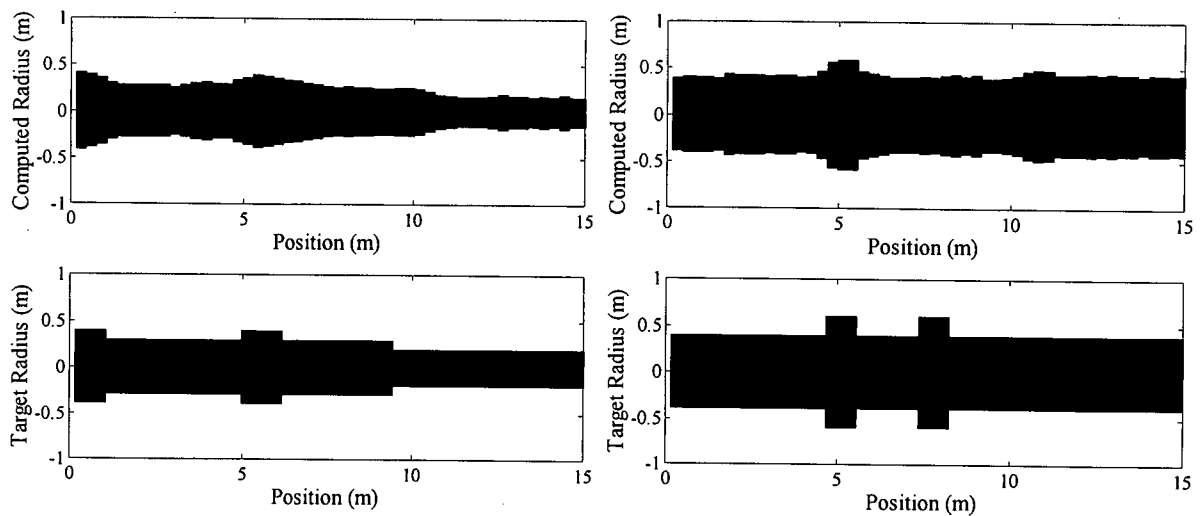


Figure 6.40 Shows how a loss in section within 1m of the pile head has been correctly diagnosed by the network (left) and gives an example of a later fault being shielded by a fault nearer the pile head (right).

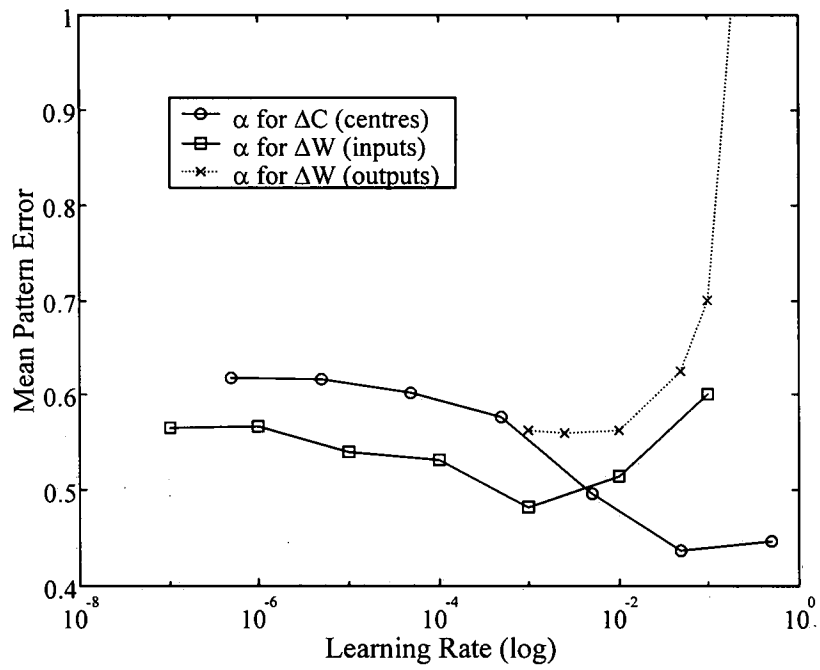


Figure 6.41 Shows the results of a parametric study on the learning rate parameters for a 50 unit Radial Basis Neural Network.

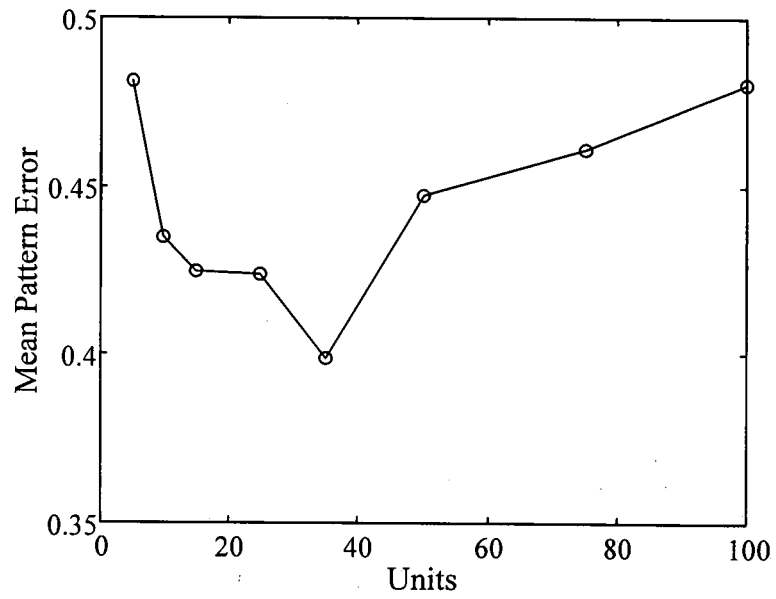


Figure 6.42 Indicates network effectiveness with respect to the number of units in the hidden layers. Overtraining was evident in systems containing over 80 units.

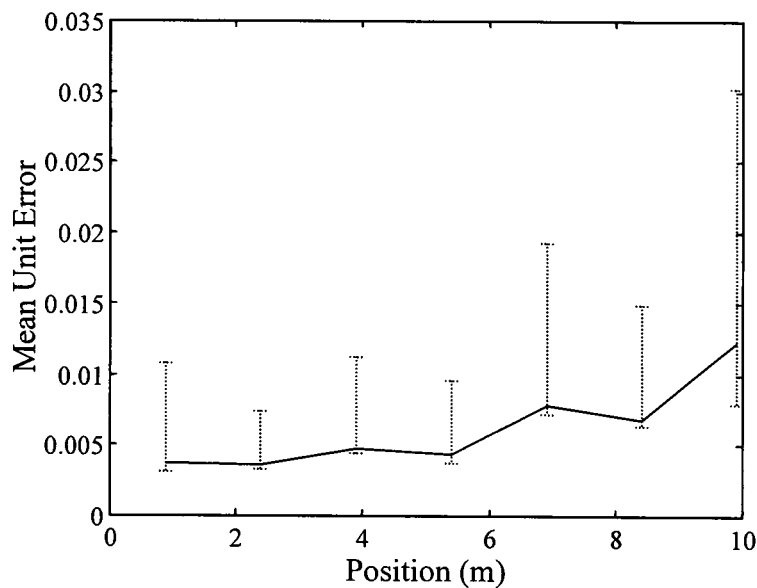


Figure 6.43 Showing the error in calculated change in radius at the *first* change in section along the pile length with respect to that changes position. As in the multi layered perceptron case the associated error increases for fault positions towards the pile toe. C.f. Figure 6.34.

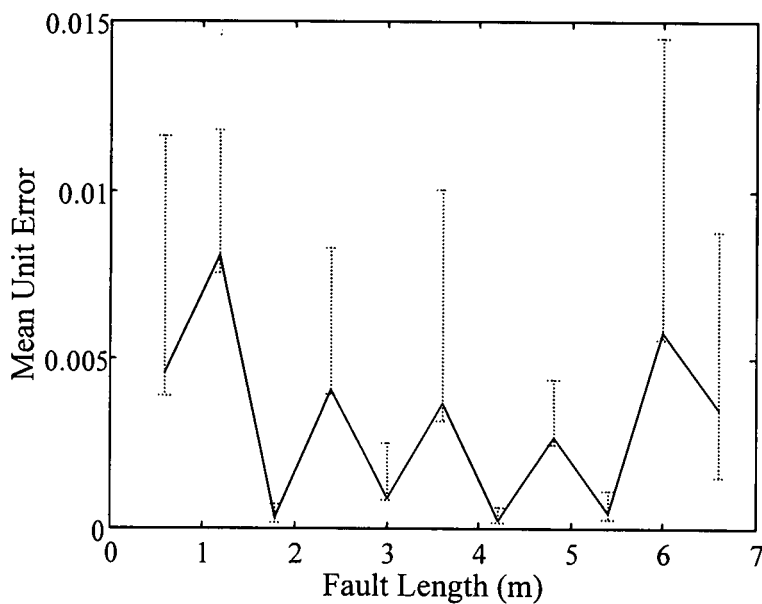


Figure 6.44 Showing the error in calculated change in radius at the *first* change in section with respect to the fault length. Of note is the comparative increase in errors for faults with an axial length of less than 1m and of 6m or over. These results are similar to those obtained for the MLP network of Figure 6.35.

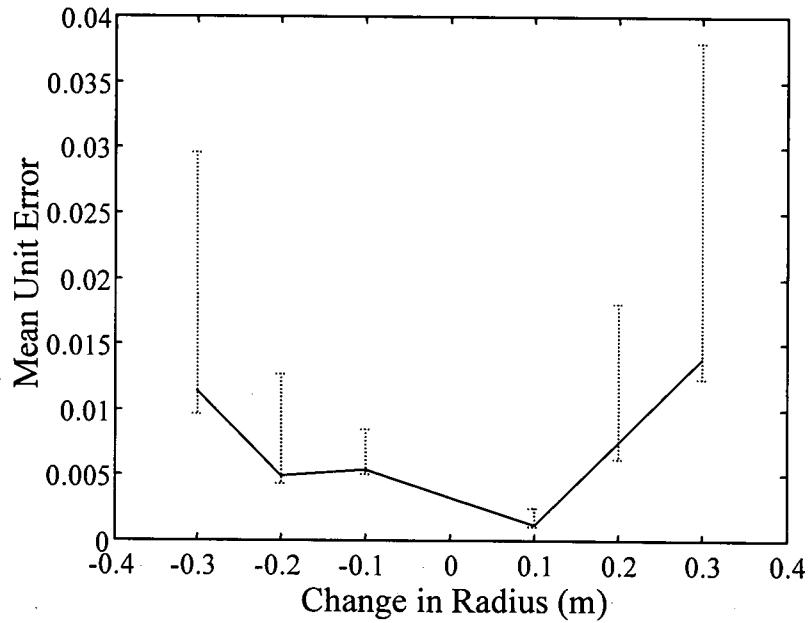


Figure 6.45 Showing the error in calculated change in radius at the *first* change in section along the pile length with respect to the size of radial change.

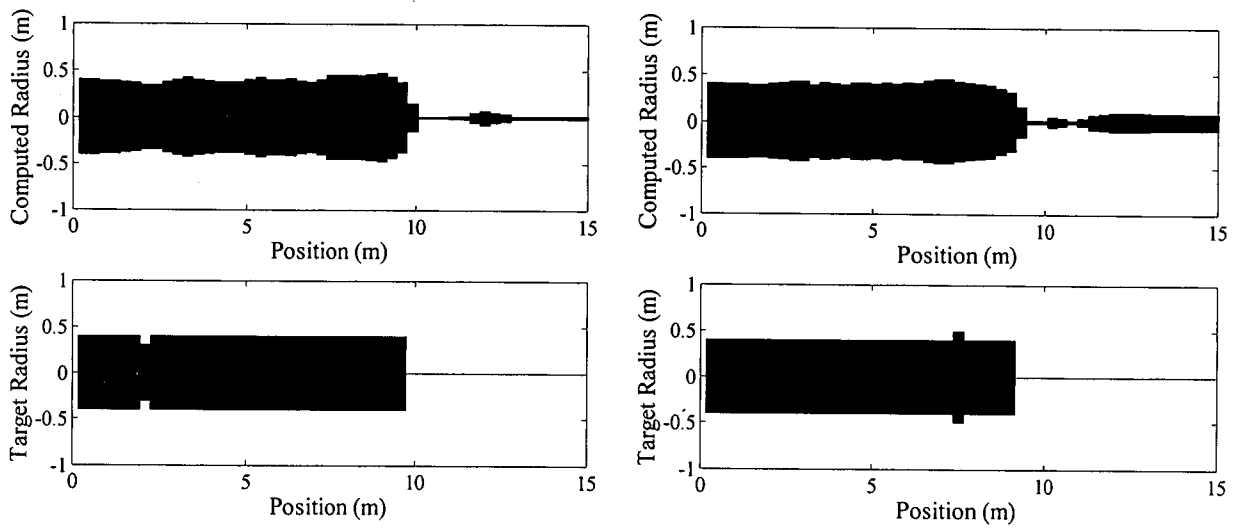


Figure 6.46 Giving examples of the network's inability to diagnose piles with faults of small (0.3m) axial length

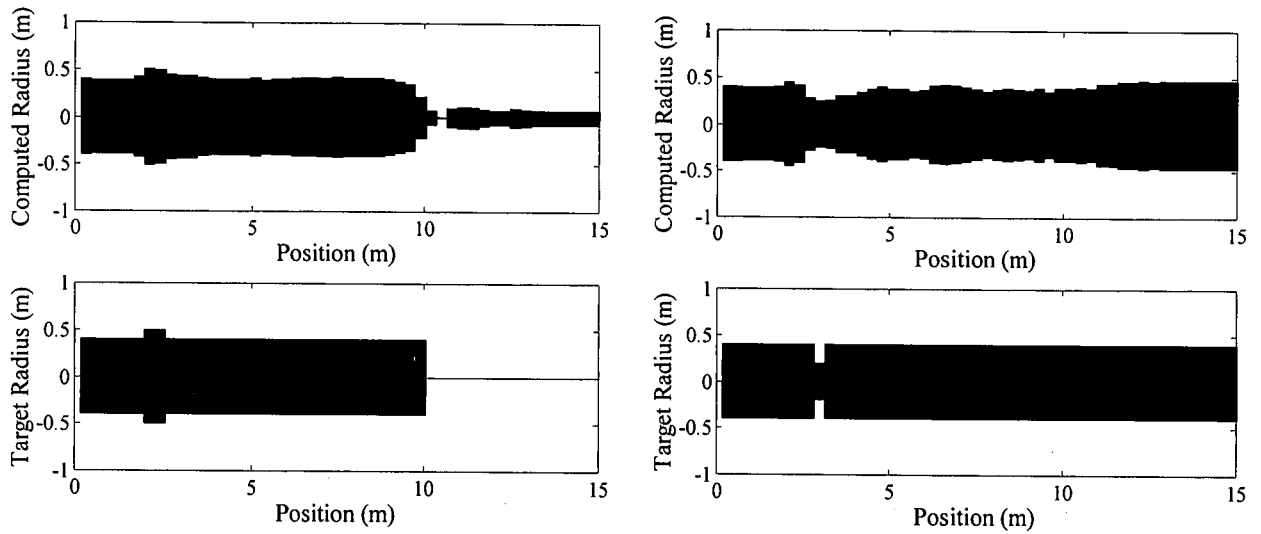


Figure 6.47 Examples of the Radial Basis Neural Network's improved ability in diagnosing faults of larger axial length (left) and degree of change in section (right) than those of Figure 6.46.

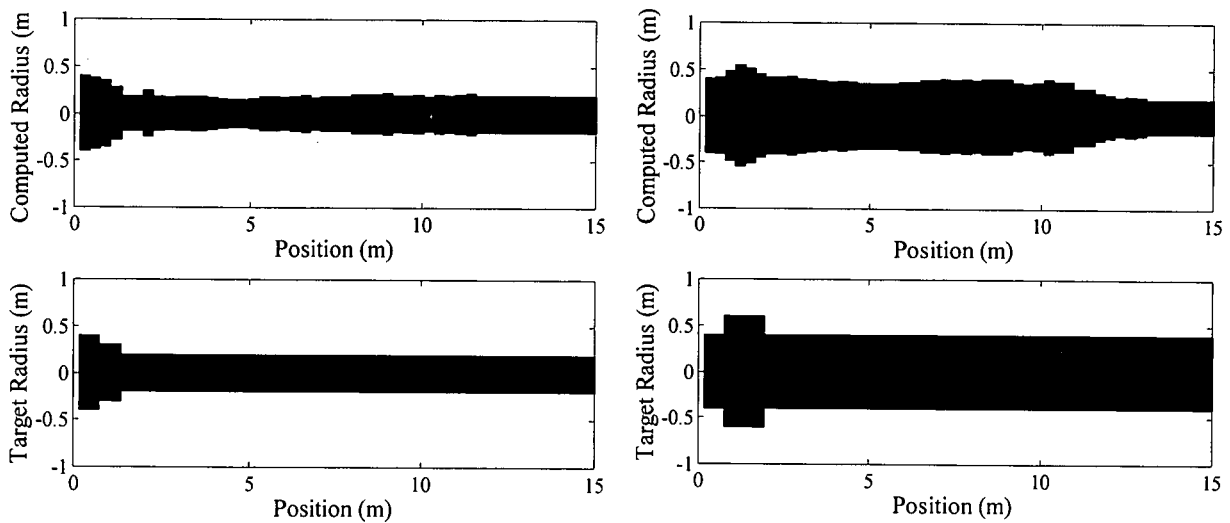


Figure 6.48 Examples of the Radial Basis Neural Networks ability in diagnosing faults at the pile head.

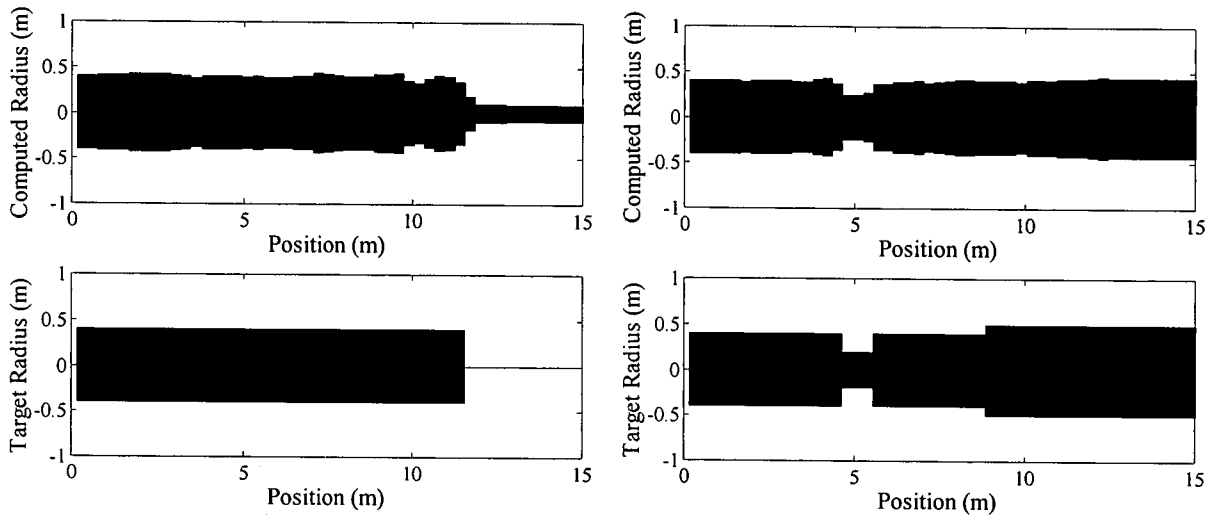


Figure 6.49 Example of the network's diagnosis of a faultless pile, left, indicates the network's ability to correctly identify the pile's length. Right and below, Figure 6.50, shows the shielding of the lower part of the pile by other faults, positioned nearer the pile head.

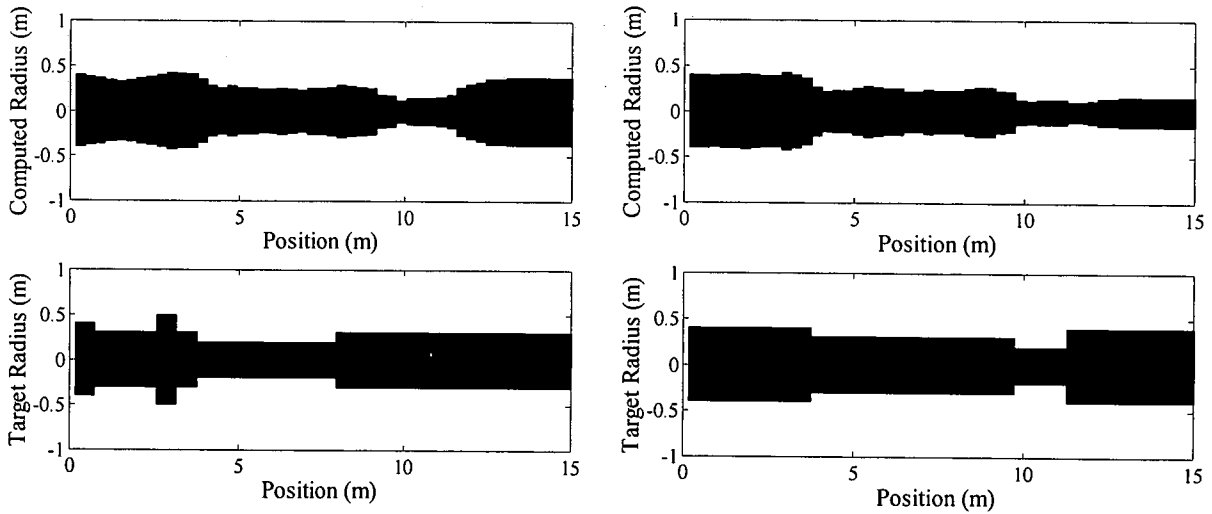


Figure 6.50 Further examples of the shielding of the lower part of the pile leading to incorrectly derived profiles. (see also Figure 6.49, above)

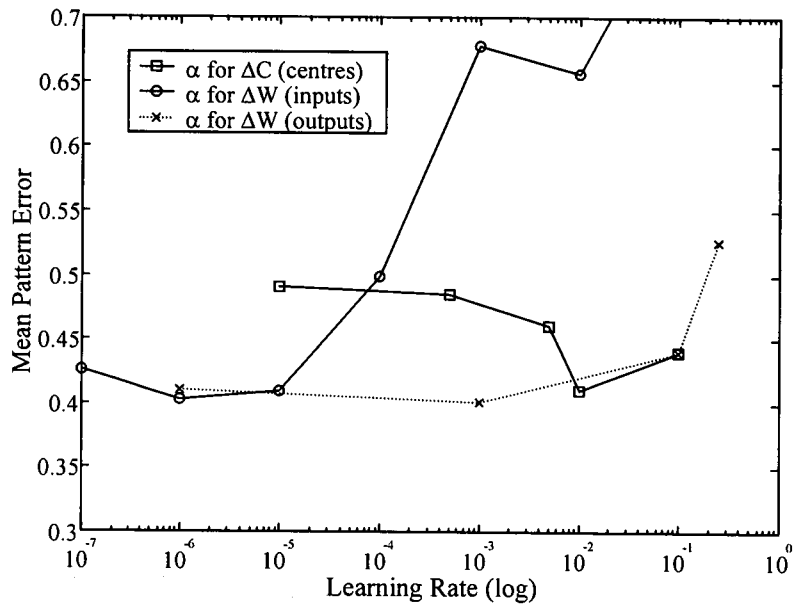


Figure 6.51 Shows the results of a parametric study on the learning rate parameters for a 50 unit Wavelet Basis Neural Network.

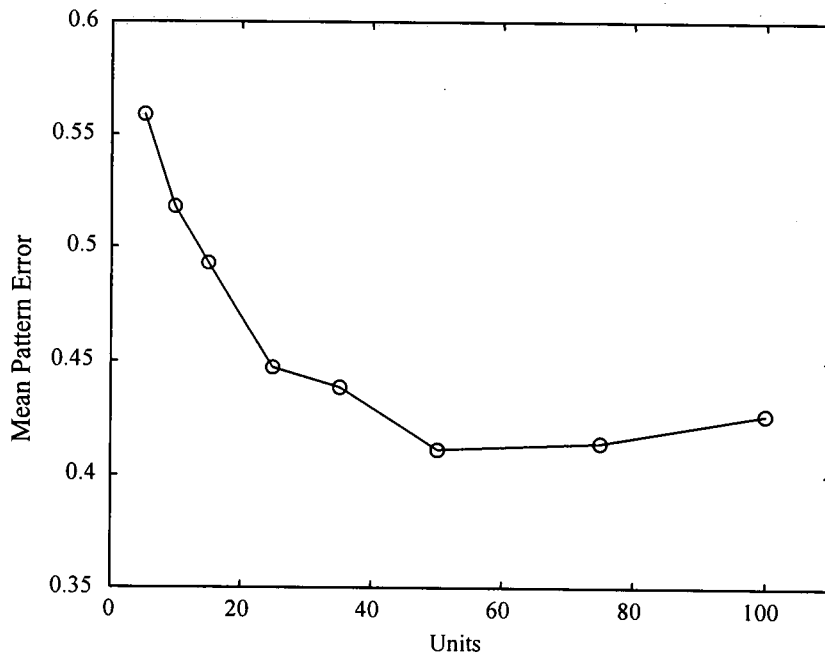


Figure 6.52 Indicates network effectiveness with respect to the number of units in the hidden layers.

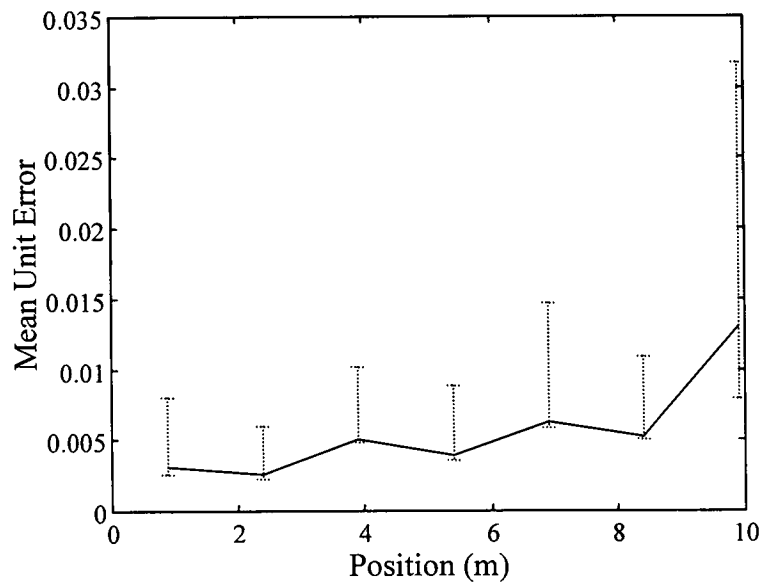


Figure 6.53 Showing the error in calculated change in radius at the *first* change in section along the pile length with respect to that changes position. As in the multi layered perceptron and RBNN cases the associated error increases for fault positions towards the pile toe. C.f. Figures 6.34 and 6.43.

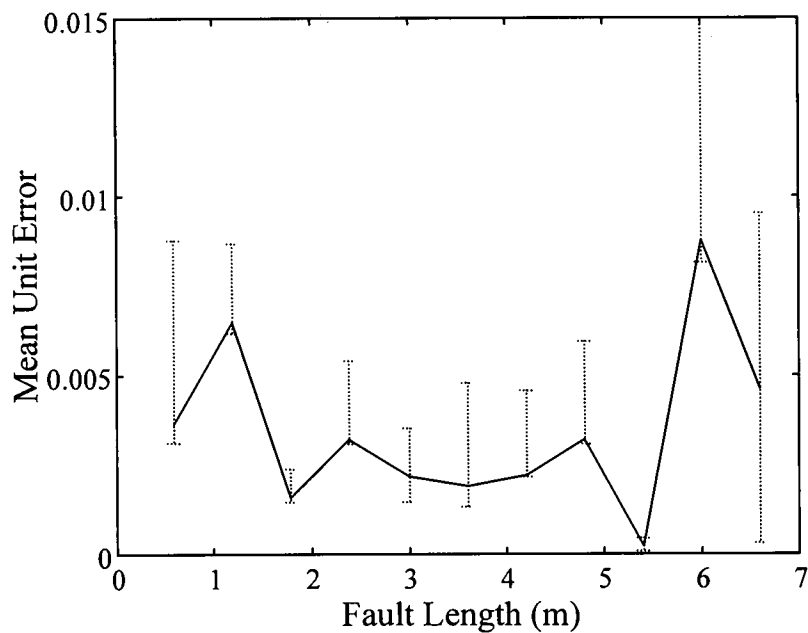


Figure 6.54 Showing the error in calculated change in radius at the *first* change in section with respect to the fault length. Of note is the comparative increase in errors for faults with an axial length of less than 1m and of 6m and over. These results are similar to those obtained for the MLP network of Figure 6.35 and very similar for that of the RBNN of Figure 6.44.

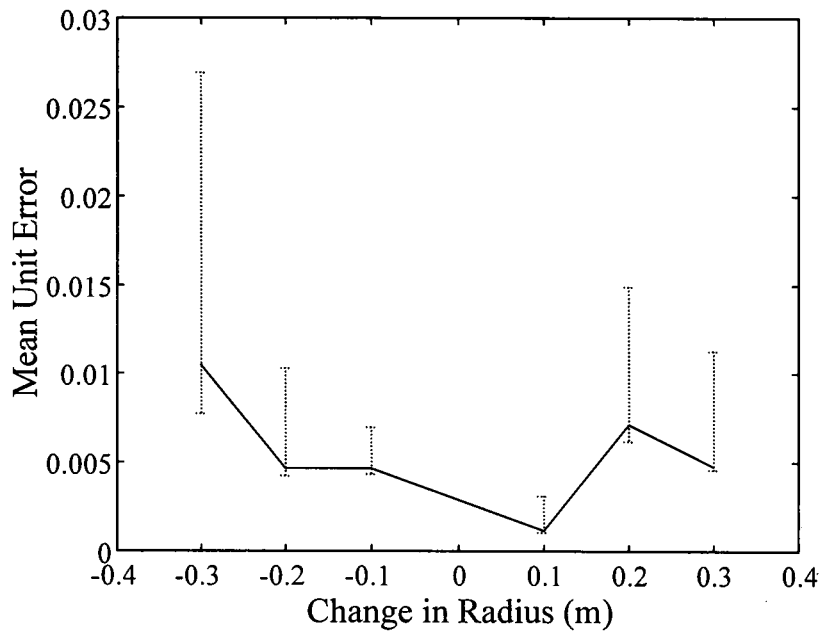


Figure 6.55 Showing the error in calculated change in radius at the *first* change in section along the pile length with respect to the size of radial change.

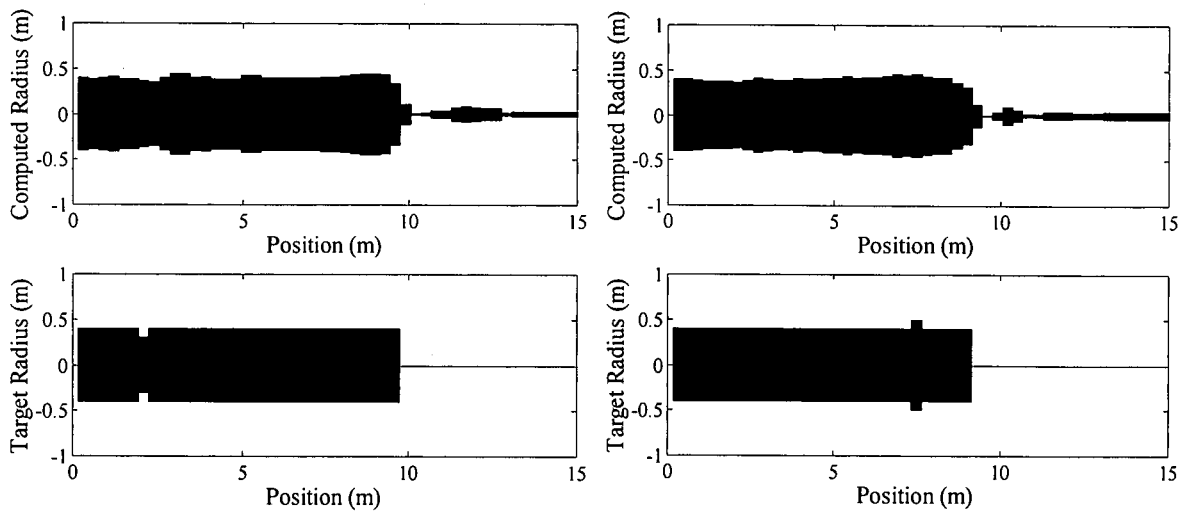


Figure 6.56 Giving examples of the network's inability to diagnose piles with faults of small (0.3m) axial length

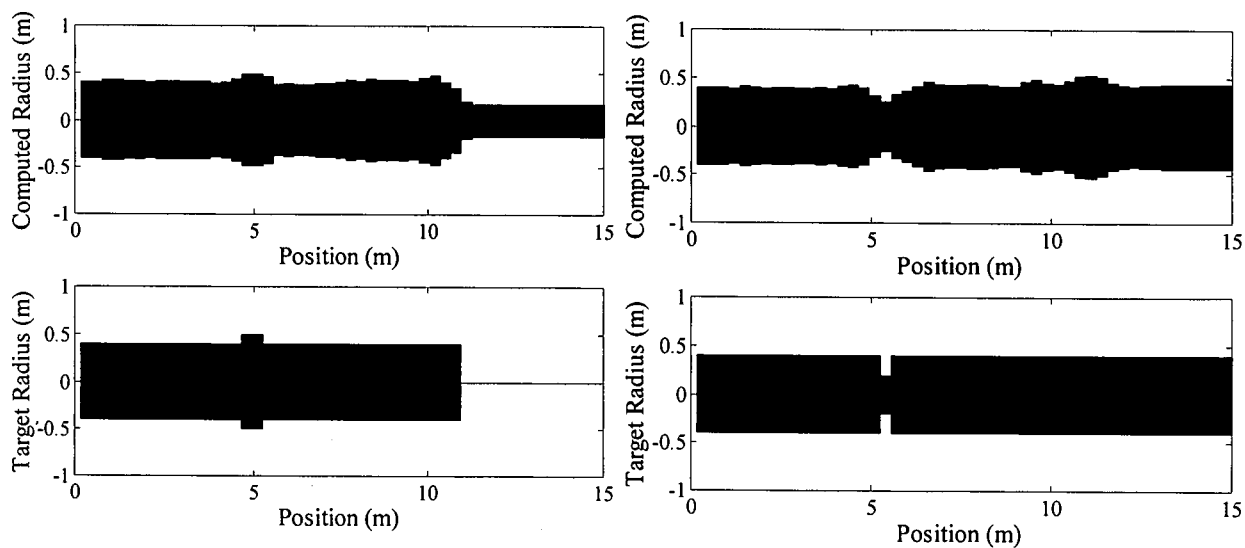


Figure 6.57 Examples of the Wavelet Basis Neural Network's improved ability in diagnosing faults of larger axial length (left) and degree of change in section (right) than those of Figure 6.56.

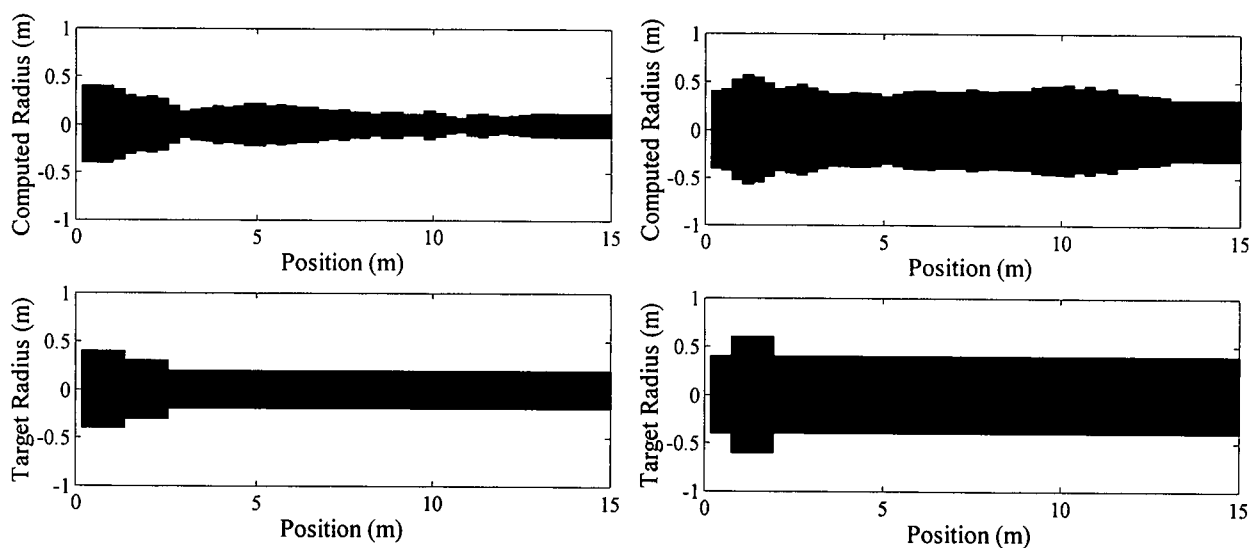


Figure 6.58 Examples of the Wavelet Basis Neural Network's ability in diagnosing faults at the pile head.

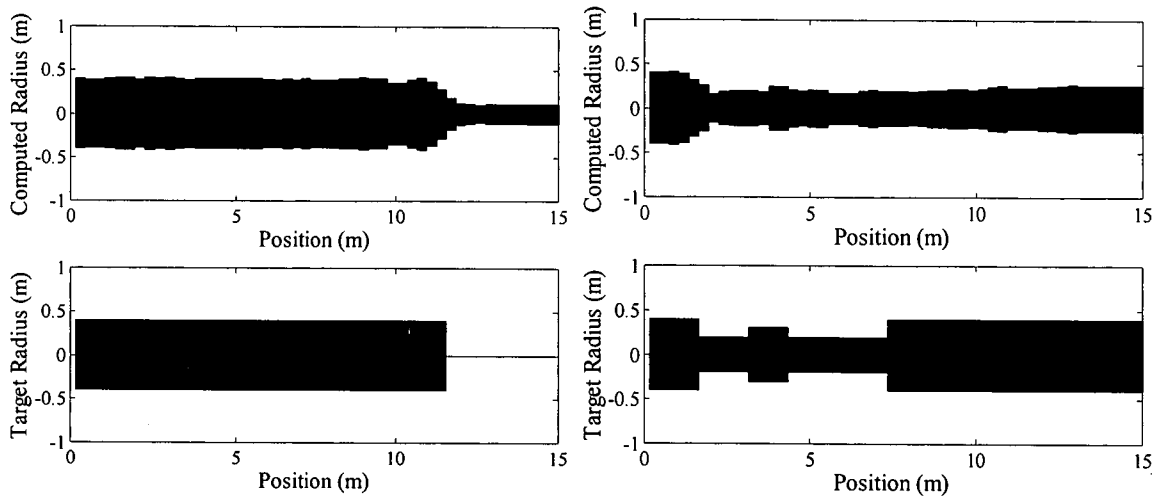


Figure 6.59 Example of the network's diagnosis of a faultless pile, left, indicates the networks ability to correctly identify the pile's length. Right and below, Figure 6.60, shows shielding of the lower part of the pile by other faults, positioned nearer the pile head.

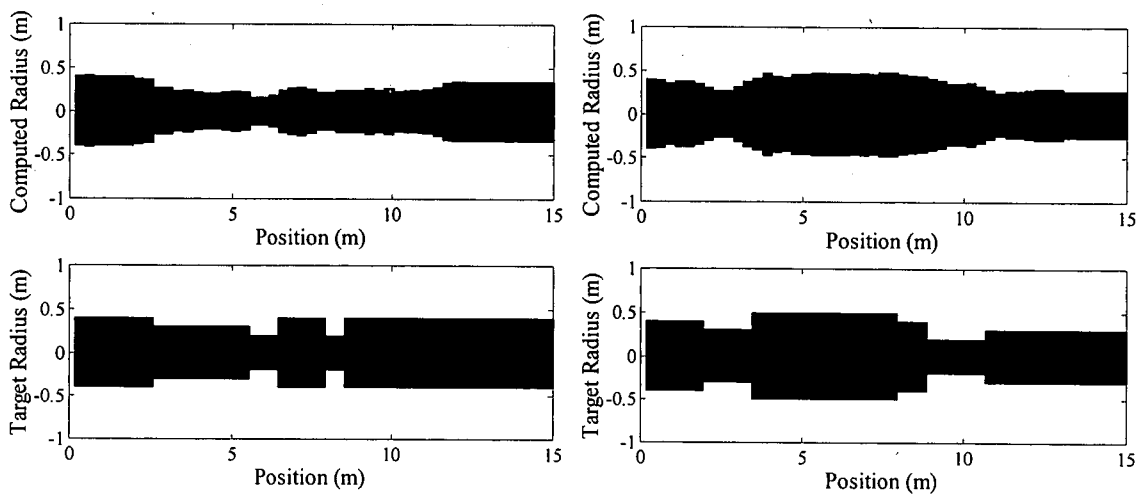


Figure 6.60 Further examples of the shielding of the lower part of the pile leading to incorrectly derived profiles. (see also Figure 6.59, above)

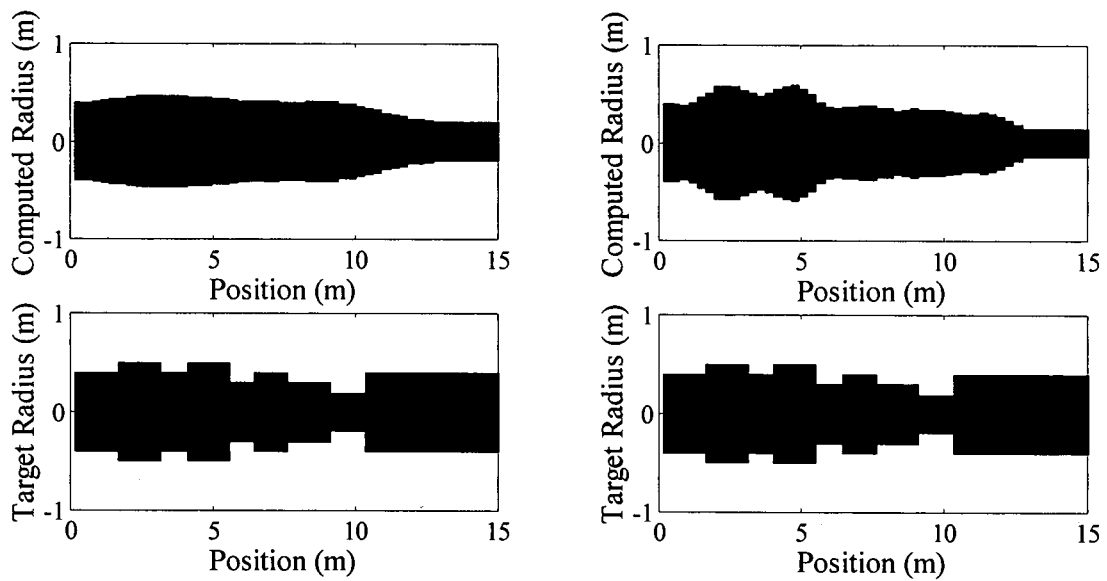


Figure 6.61 showing an example of the smoothed results obtained from the RBNN network with 5 hidden units (left) compared to those from the 50 unit network (right).

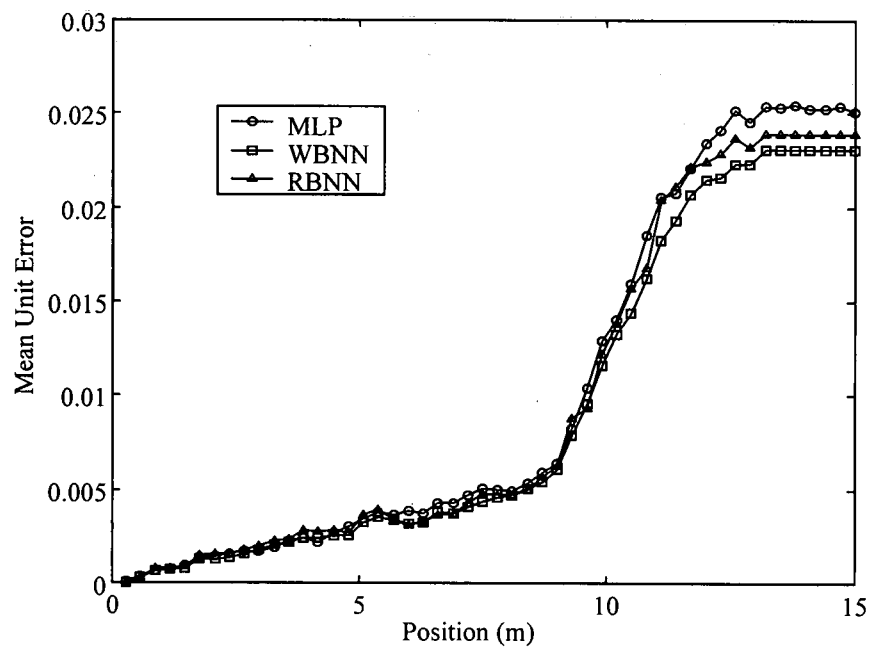


Figure 6.62 Showing that, for piles with arbitrary profiles, i.e. not just piles with a single fault, the performances of networks are almost identical until the pile toe. The difference between networks' measured performance is thus shown to be caused by their relative abilities in diagnosing the profile beyond the pile toe.

7. System Field Testing

7.1 INTRODUCTION

In this chapter the neural system described in Chapter 6 is applied to field data from three sites. These sites are: Testal Ltd's base near Kirkintilloch, the EPSRC pile test site at Blyth and the EPSRC soft clay test site at Bothkennar. Their geographical locations are illustrated in Figure 7.1. The main purpose of this work was to identify the strengths and weaknesses of the system in the field. Essentially the robustness of the system with respect to deviations in material properties due to inhomogeneity and uncertainty was tested.

At the Testal site the hardware described in Chapter 5 is validated by comparison to results from commonly used commercial equipment on uninstalled piles by an independent testing engineer: Mr Richard Nicholson of Testal Ltd. The neural system is then used to identify the length of an installed driven concrete pile having been trained on FEA data.

The results from the Blyth test site have been kindly supplied by Testconsult Ltd of Warrington. The FEA model described in Chapter 4 is used to train a neural system which is applied to 16 cast *in situ* concrete piles with known defects.

The author tested 9 piles from the Liverpool University test area at the Bothkennar test site, each with different design dimensions. A neural system was then used to estimate these piles' length and radius from the test results. A brief investigation on the effects

on network performance with respect to the amount of pile head exposed was also carried out.

The results of these experiments suggest that the neural system can identify major defects in installed piles and can be applied to driven piles and piles of a non-circular section. However, they also show how the system is highly dependant upon the accurate modelling of the installed piles in the FEA training data. Specifically, errors in prevailing soil conditions and pile head dynamic stiffness produce errors in the calculated pile profile, see Section 7.3.

For the Blyth test site data, differences in spectral mobility between the FEA training data and field test data were minimised through the use of logarithmic scaling. As described in Chapter 6, a dynamic gain was also applied to enhance small reflections from the pile toe. For the Bothkennar data, however, the soil is less stiff thereby reducing signal attenuation and so the dynamic gain was not applied. The ability to resolve differences in dynamic stiffness was necessary to distinguish between piles with different radii and so the logarithmic scaling was also withheld.

7.2 KIRKINTILLOCH SITE

The Kirkintilloch site is owned by Stent and Bardon Concrete, and used by Testal Ltd as a base for central Scotland.

7.2.1 Hardware Validation

Validation of the data acquisition system described in Chapter 5 was carried out under the supervision of an independent test engineer: Mr Richard Nicholson of Testal Ltd. Three uninstalled concrete piles with known defects were tested, see Figure 7.2. These piles were square in section (250mm×250mm). Two had design defects of a neck

(180mm×180mm) and bulb (400mm×400mm) respectively while the third was defect free as illustrated in Figure 7.3.

The hammer used for these uninstalled piles was the 'heavyweight' 11b (0.454 kg) hammer, shown in Figure 5.6, with a hard plastic tip. An example of the impact observed when the defect free pile was struck is given in Figure 7.4. As expected for this tip hardness, the rise time of the pulse was measured at about 0.75ms and the frequency spectrum drops as 1500Hz is approached, c.f. Figure 4.8.

The measured responses from the three piles tested are shown in Figures 7.5 to 7.7. Their shape is consistent with that obtained using commercial data acquisition equipment, namely: Pile Dynamics's Pile Integrity Tester (PIT) Collector, as employed by Testal Ltd. The results are summarised in Table 7.1.

As can be seen from these results the close proximity of the changes in section for the piles with faults has caused their calculated positions to be slightly closer together than that which is actually the case. This effect is discussed in Section 4.2.4.2 and is caused by the superpositioning of the two reflected pulses. The pulse propagation velocity used in these calculations is 3590ms^{-1} and is derived from the propagation time of the defect free pile.

Table 7.1 Results from Uninstalled Piles at Kirkintilloch

Pile	Change in Section	Position (m) (actual)	Computed Position (m) ($c = 3600\text{ms}^{-1}$)	Error (%)
Defect Free	Toe	10.5	10.5	0
With Bulb	Increase at start of bulb	3.0	3.1	3
	Decrease at end of bulb	4.5	4.3	4
	Toe	10.5	<i>not observed</i>	-
With Neck	Decrease at start of neck	2.5	2.8	12
	Increase at end of neck	4.0	3.7	8
	Toe	10.5	<i>not observed</i>	-

Unfortunately, these piles' supports are not axisymmetric and are positioned at arbitrary positions along the pile. This resulted in reflections and low frequency resonance of the type observed for the laboratory piles of Section 4.2.4.3. This made them inappropriate for modelling using the FEA system described previously. They cannot, therefore, be tested using the ANN system described herein. They do, however, provide evidence for the effectiveness of the data acquisition equipment developed for this study.

7.2.2 Installed Driven Pile

Also tested at this site was a short driven pile. The pile was known to have a complete loss in section at 4.2m with a measured 0.9m of the pile above ground level. The soil conditions were unknown for this case and so iterative wave matching was necessary to derive them. That is, multiple FEA runs were carried out until the generated trace matched that of the recorded trace. Notwithstanding the precedent of these techniques use in industry, it is recognised that this was not the ideal method for obtaining soil properties, but, under the circumstances, it was the only method available. The concrete material properties were derived by assuming a density of 2400kgm^{-3} and calculating the pile stiffness from the propagation velocity in the uninstalled piles. The properties used are given in Table 7.2 and the resultant trace shown in Figure 7.8 along with the recorded field test trace.

Table 7.2 Material Properties Employed for Kirkintilloch Site Modelling

Material	Depth below ground level (m)	Elastic Modulus (MNm^{-2})	Bulk Density (kgm^{-3})	Poisson's Ratio
Concrete	0 - 3.3 (+0.9 above)	30000	2400	0.2
Soil 1	0 - 0.9	50	1400	0.2
Soil 2	0.9 -	625	2000	0.4

As indicated in Table 7.2 the soil properties are typical of soft clay over stiff/very stiff clay with the soil properties being of the same orders of magnitude as those described for the Blyth (Table 4.10) and Bothkennar (Table 7.4) test sites. However, it is noted at this point that the FEA model is for a circular pile with the same cross sectional area as the square ones tested. For short piles such as this the signal attenuation caused by the difference in material properties across the pile-soil interface is minimal with respect to that caused by partial reflection at the pile toe. For longer piles where this effect is more significant it may be expected that the difference in pile profile will have an effect on the traces obtained. For a square section pile there is a greater proportional surface area making up the pile-soil interface and so the signal attenuation may be expected to be larger.

When trained on FEA traces generated for piles of varying lengths with partial or complete losses in cross-sectional area the neural network described in Chapter 6 correctly identified the length of the field tested pile, as shown in Figure 7.9. As expected the end of the pile tapers rather than coming to an abrupt end, but there is a complete loss in section at 4.2m. The effect of the modelled soil properties' contribution to this pronounced tapering will be discussed in Section 7.3.2.

7.3 BLYTH SITE

The second set of site data included in this study has been supplied by Testconsult Ltd, and comes from the EPSRC pile test site near Blyth in Northumberland, UK. The derivation of the soil and concrete properties employed in the FEA modelling has been exhaustively covered in Chapter 4 and so will not be repeated here. The reader is referred to Table 4.10 for a summary of their values. A site plan showing the piles included in this study and their location is given in Figure 7.10. The piles have a design radius of 0.375m and lengths between 11.3m and 11.7m.

7.3.1 Test Results

As indicated in Figure 7.11 the general trend of increasing profile error with depth, highlighted in Chapter 6, also occurred in the field test results from this site. As also shown in this diagram, the profile errors for some of these plots were very large (120% in some cases). This was not, however, purely a reflection of the neural systems performance; rather it was a compound error affected by: errors in the design pile profile with respect to the actual pile profile, the accuracy of the training data and the known test method limitations. This coupled with the small size of the sample set means statistical measures, of the type produced in Chapter 6, are inappropriate. Instead each of the 16 piles will be considered individually in the following sections.

One general point concerning the computed profiles presented in this section is the trend of the pile diameter to decrease with depth. This point is discussed fully in the next section, Section 7.3.2. All the velocity response traces presented in subsequent figures are shown against depth (calculated with $c = 3450\text{ms}^{-1}$) rather than time to facilitate comparisons with the pile profiles beneath them.

7.3.1.1 Piles with Necking

Shown in Figure 7.12, **Pile 1** is an 11.7m long pile with a 45% loss in diameter at 3.45m beneath the pile head extending for 0.6m. As can be seen in the computed pile profile there is a decrease in section at the expected depth A' . However, the subsequent increase is gradual and never attains the original design radius required. It is noted that the recorded test trace does not contain the pronounced trough following the first reflected peak, marked A , indicating a subsequent increase in section (c.f. Figure 4.33). This is the most likely cause of profile not returning to its original section. This would also explain the further decrease in section at approaching 8m depth, B' , where a second reflection from the fault, B is found. In all the other examples where necking occurs a trough is found to follow the first peak, as expected, and the computed profile does return to its original radius (see Figures 7.13, 7.14, 7.15). It is, therefore, suggested that

this feature is an effect of the atypical nature of the trace rather than a failure of the neural network to identify the fault correctly. Further to this it is noted that the method used in forming this fault was the insertion of a foam annulus during construction. It is quite possible that this insert has become distorted during concrete pouring causing the annulus to become compressed at its base. As such this profile may describe the actual pile profile more accurately than that of the original design drawings.

Shown in Figure 7.13, **Pile 2** is an 11.3m long pile with a 45% loss in diameter at 5.05m extending for 0.6m. Above this, at 3.65m there is a crack covering 50% of the pile area. This crack is difficult to detect due to superpositioning, as discussed in Chapter 4, and has resulted in an apparent single peak, *A*, shown on the trace. The network has interpreted this as a small loss in section at about 3.5m - *A'*. This is consistent with the data upon which it has been taught - no cracking was included in the training data and the smallest fault length the network was expected to identify is 0.3m. Subsequent to this the network has correctly identified a loss in section at around 5.5m, *B'*. As mentioned above, in this case, unlike Pile 1, a trough '*C*' follows the peak '*B*' and, hence, the network calculates a return to the original radius at *C'*.

Shown in Figure 7.14, **Pile 3** is an 11.4m long pile with 45% losses in diameter at 2.4m and 7.9m, both extending for 0.6m. The first neck, associated with reflections *A* and *B*, has been identified and can be found in the computed profile at a depth of about 3m. The minimum radius for this neck - at *A'* - is correctly identified as about 0.2m (0.21 to 2 decimal places) before returning to its design radius at *B'*. Subsequent to this the profile does decrease, but this is consistent with most other profiles and is considered a consequence of inaccurate soil modelling, see Section 7.3.2 below.

Shown in Figure 7.15, **Pile 5** is an 11.3m long pile with a 13% loss in diameter at 4.7m extending for 1.2m. The fault has been correctly identified in the computed profile. However, it appears to have been over estimated in its magnitude, the minimum computed radius being 0.19m rather than the 0.32m required i.e. the calculated neck is over double that present. This may be due to inaccurate soil modelling, but the fact that

the network has identified and positioned the fault is significant given that little indication of such an event is found on the recorded trace. Again, it is stated that the task of this test method is to identify anomalous responses for further investigation and as such this goal has been achieved.

7.3.1.2 Piles with Cracking

As stated above the neural system training set does not include piles with cracks. However, this discussion has been included as an indication of how the network performs when data upon which it has not been trained is presented.

Shown in Figure 7.16, **Pile 7** is an 11.4m long pile with a crack resulting in a 30% loss diameter at 2.2m. While in Figure 7.17, **Pile 8** is an 11.4m long pile with a crack resulting in a 16% loss in diameter at 2.9m. These have been formed by a foam and plywood insert and so the crack was designed as an open crack. As discussed in Section 2.7.7 cracks such as these are particularly difficult to detect due to the superpositioning of the two reflections from the decrease and subsequent increase in cross-section.

It is apparent when comparing the calculated profiles from these two piles that the network has interpreted reflections *A* and *B* as a small neck, *A'*, rather than a large crack. There is a loss in section reported in Figure 7.15 at about 2.5m, but none in Figure 7.16. This is consistent with known test method limitations where, as reported in Section 2.7.3, faults with an axial length of less than 100mm cannot be uniquely identified. The smaller of the two cracks cannot be resolved using this test method and, as such, it is not surprising that the ANN has failed to detect it.

7.3.1.3 Piles with Occluded Voids

As in the previous section, the system has not been trained using data that includes occluded voids. However, the loss in cross-sectional area caused by these voids

produced similar results to those produced by necking and so these traces have been included in this study.

Shown in Figure 7.18, **Pile 9** is an 11.4m long pile with an occluded void at 2.9m. This void has a 0.5m diameter and extends for 0.5m. This occluded void is the equivalent of a neck resulting in a 0.1m loss in radius (calculated from the equivalent losses in cross-sectional area). There is a drop in radius of 0.1m at 3.0m, A' , which is noticeable when comparing the profile with that of Pile 10 in Figure 7.19. However, it is not suggested that the magnitude of this calculated loss in section could be identified without *a priori* knowledge of the pile profile. That is, within the context of the presented profile it is unlikely a user would conclude a loss in section at 3m with any confidence.

Shown in Figure 7.19, **Pile 10** is an 11.3m long pile with an occluded void at 3.1m. This void has a 0.4m diameter and extends for 0.4m. This fault is not observable on the recorded trace and cannot be detected on the calculated pile profile. It is likely that the partial reflection of the propagating stress wave at the start of the foam disk has resulted in the subsequent attenuation being too great to allow the returned echo from being detected.

7.3.1.4 Pile with a 'Soft toe'

Shown in Figure 7.19, **Pile 11** is an 11.3m long pile with a soft toe. This is mimicked by a 0.3m long perforated foam disk being placed at 11m. This defect is not detectable on the recorded trace although there is some evidence for the pile length being between 11.2m and 12.8m from the TDR^{7.1}. Neither the pile toe nor the defect were detectable on the calculated pile profile .

7.3.1.5 Piles with Bulbing

The bulbs presented in these field tests have been created by under-reaming. Consequently, they have a conical leading edge as illustrated in Figures 4.40. and 4.44.

Shown in Figure 7.21, **Pile 12** is an 11.3m long pile with an open crack covering 50% of the pile sectional area at 3m and a bulb of double the pile diameter at 7.2m extending for 1.5m. The crack is not visible on the pile profile although it is noticeable that neither is any definite feature on the recorded trace. This is especially apparent when this trace is compared to that of Figure 7.13 where the reflection from a similar crack is evident as peak *A*. It is, therefore, suggested that the failure to identify this fault is reflective of the recorded test trace rather than any failure of the neural network. The increase and decrease in section of the bulb results in peaks *A* and *B* in Figure 7.21. The profile clearly shows both the position and extent of the increase in section although the subsequent decrease has not been detected.

Shown in Figure 7.22, **Pile 13** is an 11.3m long pile with a bulb of double the pile diameter at 4.0m extending for 2.4m. The bulb is correctly centred at a 5.5m depth, *A'* on the pile profile plot, and has a maximum radius of 0.71m compared to the design bulb of 0.75m. However, the smoothed nature of the profile, identified in Chapter 6, means the fault appears to extend over a larger axial length than it, in fact, does. It is also noticeable that the profile beneath the bulb is not representative of the actual profile. This is not considered particularly disappointing given that the dominant fault has been identified.

Shown in Figure 7.23, **Pile 14** is an 11.3m long pile with two bulbs of double the pile diameter at 2.2m and 6.3m, both extending for 1.5m. A first bulb is clearly evident from the computed profile. However, it appears to have a maximum radius of 0.61m as opposed to the required 0.75m and is positioned above 4.2m when it should be around 3.3m (see Figure 4.44). Clearly the nature of the bulbs, as built, means it may be closer to 0.6m rather than the design 0.75m in size. From the recorded trace it would also appear that the position of maximum radius is nearer 4.2m than the designed 3.3m. This can be estimated as the mid-point between trough '*A*' and peak '*B*' i.e. the depth was neither particularly associated with an increase in section, nor with a decrease in section - the position marked '*X*'. The second bulb and pile toe is shielded by the presence of

the first and, therefore, cannot be detected. However, again, these erroneous results include a total loss in cross-section, this time at D' which occurs at the same point as the secondary reflection from the first fault - point D on the time trace. It appears, therefore, that the presence of the secondary reflection has influenced the calculated pile profile.

Shown in Figure 7.24, **Pile 17** is an 11.3m pile with a bulb of double the pile diameter at 10m extending for 0.8m. The actual bulb shape is a wedge shape manufactured by a single under-ream. The toe reflection is not apparent in the recorded trace and is not observed in the calculated pile profile.

Shown in Figure 7.25, **Pile 18** is an 11.3m long pile with a bulb of double the pile diameter. Like the previous pile this has been formed as a wedge shape 3.8m long and gradually increasing to a radius of 0.75m over 1.3m before sharply returning to its original radius. The calculated pile profile shows a maximum pile radius of 0.59m at 4.5m depth. The gradual increase in section has produced a response lower than that expected and at a position centred on the incline. Although the network has not been trained on this gradual increase in profile it has produced a sensible response with a bulb centred at the middle of the sloping incline with a maximum radius around (5% error) the average of the incline's (0.56m). This is a good example of the neural network's generalisation abilities.

7.3.1.6 Pile with Weakened Concrete

Shown in Figure 7.26, **Pile 19** is an 11.3m pile with an area of weakened concrete at 3m down extending for a further 2m. No information concerning the composition of this concrete is given. Neither the weakened concrete area nor the pile toe are apparent in the recorded trace or the calculated pile profile. As quoted in Section 2.7.2.3 changes in concrete density must be large (of orders of magnitude) to produce a detectable reflection at the material discontinuity. It appears in this case, therefore, that the resultant reflections have not been large enough to produce detectable reflections, but

have been large enough to reduce the propagation stress wave to the extent that the reflection from the pile toe can no longer be detected.

7.3.1.7 Defect Free Pile

Shown in Figure 7.27, **Pile 24** is an 11.3m long defect free pile. Although the pile toe is visible in the recorded trace and is known to be visible in the FEA training data (see Figure 4.30) it cannot be identified in the calculated pile profile. It is likely this is due to the difference in soil stiffness along the pile shaft between the modelled, training, data and the field data. This appears to have a cumulative effect in that smaller reflections at depth are detected less reliably. Empirical evidence for this hypothesis is presented in the next section.

7.3.2 General Points

It can be seen from the traces of piles with small reflections or reflections from near the pile toe (Figures 7.16, 7.17, 7.19, 7.20, and 7.26) that for any straight, uninterrupted, shaft the ANN tends to calculate a shaft gradually tapering inwards. It is hypothesised that this is due to differences between the modelled soils and those in the field. Circumstantial evidence for this can be found in noticing that the effect is more pronounced after 4.0m depth - the point at which the modelled soil changes from stiff to stiff/very stiff clay (see Table 4.10). To test this hypothesis the damping on the trace for Pile 24 (the defect free pile) was artificially reduced. This was done by adding an exponentially increasing gain to the de-noised signal below 4m, before the hanning-like gain is applied. The gain effectively decreases the soil stiffness around the lower pile shaft and nearly doubled the amplitude of the reflection from the pile toe. As can be seen from Figure 7.28 when this changed trace is presented to the neural system the pile shaft calculated has virtually no tapering and there is a pronounced neck at about 11m - labelled *A'* - the position of the pile toe. This indicates the high dependency of the system on correctly modelled soil conditions for the identification of faults at greater depths or the pile toe. The work presented in this study represents the very limits of the

conditions under which this test is applicable as indicated by the amplitude of the returning echo from the pile toe in Figure 7.27. As such it can be considered the most testing conditions under which the network might be expected to operate.

Conversely, faults at the pile head have been more successfully identified and located. The neural network appears to have identified a small difference between the field test piles and those upon which it has been trained. As discussed in Chapter 4, the network was trained on piles with 0.4m radius - this facilitated the automatic generation of FEA meshes for piles with 25% 50% and 75% losses and corresponding increases in diameter. It was not expected that the neural network would be able to detect the 6% difference in diameter with respect to the field data given the inherent limitations of the test method. However, in all cases the calculated pile profile immediately drops from its start position of 0.4m to a value between 0.33m and 0.38m. Checking the defect free pile, where it can be reasonably assumed that there is no interference from faults near the pile head, the average pile radius over the first 2.5m is found as 0.365m - see Figure 7.29. While this ability may appear facile at first glance the fact that the neural network can identify faults with this degree of accuracy this close to the pile head in field tests as well as the FEA data of Chapter 6 would suggest a significant improvement on current test methods. As reported in Section 2.7.3, contemporary literature states that faults at the pile head cannot be identified because of the rise time associated with the input pulse. This research suggests that a fault at the pile head can be identified and quantified using an ANN system. This finding; therefore, may prove significant in many areas of impact testing analysis.

The ability of the neural system described to differentiate between piles of different design radii and length from the encoded data of the mobility scalogram was, therefore, carried out at the EPSRC's soft clay test site at Bothkennar. Here a brief study was also carried out into the effects of altering the pile head's stiffness through the excavation of surrounding soil. The results of these studies are be presented in Section 7.4, below.

7.4 BOTHKENNAR SITE

Permission was granted by the EPSRC to use the facilities at their soft clay test site at Bothkennar. The piles tested in this study were part of the University of Liverpool's test area, as identified in Figure 7.30. This site contained 15 piles positioned as shown in the plan of Figure 7.31. These piles can be divided into two groups: anchor piles and test piles. The test piles were those originally used in load test experiments and the anchor piles used as part of a reaction frame to push against the loading equipment used. Of these piles 9 were selected for this study, each representing a unique type of radius and length combination of those at the site. A summary of those piles selected can be found in Table 7.3.

Table 7.3 Summary of the Piles Included in this Study

Pile Label	Pile Type	Design Radius (m)	Design Length (m)
A01	Anchor	0.200	13
A15	Anchor	0.200	16
T02	Test	0.200	9
T03	Test	0.200	11
T07	Test	0.200	13
T09	Test	0.300	11
T10	Test	0.300	13
T11	Test	0.375	11
T12	Test	0.375	13

The soils of this site are amongst the most widely investigated in the UK. An entire issue of *Géotechnique* has been given over to papers concerned with these investigations^{7.2}. It is with some confidence, therefore, that the author has used the data published by Nash *et al.*^{7.2} and summarised in Figures 7.32 and 7.33 as a basis for the material properties used in the FEA modelling.

The primary difference between the anchor and test piles is the presence of a casing surrounding the test piles, as indicated in Figures 7.34 and 7.35. Although no documentation concerning this casing exists, Dr Edward Dickin of the department of Civil Engineering at Liverpool University has been contacted directly and confirmed its length as 1m below ground level. A parametric investigation on the FEA model confirms that, because the soils towards the head of the pile contribute little towards the overall attenuation of the signal as long as it is modelled with at least 0.6m of the head exposed and no more than 4m exposed the overall trace matches that of the 'T' piles' field test data: the dynamic stiffness is correct within 5% as is the amplitude of the echo from the pile toe. The material properties used are summarised in Table 7.4 with the first 1m of the pile modelled as being exposed.

Table 7.4 Material Properties Used in the FEA Modelling

Material	Depth (m)	Young's Modulus (MNm ⁻²)	Poisson's Ratio	Bulk Density (kgm ⁻³)
Soil 1	1.0-3.0	30	0.45	2000
Soil 2	3.0-6.9	45	0.45	1600
Soil 3	6.9-9.9	60	0.49	1700
Soil 4	9.9-12.6	75	0.49	1700
Soil 5	12.6-15.0	90	0.49	1700
Concrete	-	30000	0.22	2400

The concrete density is assumed as 2400 kgm⁻³ and the elastic modulus taken as the average of those derived from the pulse propagation velocities of the piles tested. The accelerometer was attached to the pile head using wax that was melted using a butane soldering iron with its head detached.

It should be noted at this point that, as discussed in Chapter 4, the lower stiffness of the surrounding soil, in this case, has necessitated a finer lateral mesh for the FEA

generated traces. Specifically, the inter-nodal lateral distances have been reduced from 0.1m in the above studies to 0.03m in this one. Parametric investigations indicate that no change in the reflected pulse's amplitude is observed for finer mesh divisions.

7.4.1 Test Results

As mentioned in the introduction to this chapter, because the neural network is now being required to identify piles of different dimensions the act of minimising differences in system damping is now a hindrance rather than a help. That is, in previous cases taking the logarithm of the input spectra before presenting them reduced the differences between the FEA and field test data caused by differences in prevailing soil conditions. However, in this case it is these differences that are most likely to facilitate the identification of the piles of different radii. It is also the case that reflections from the pile toes are now easily identifiable because of the reduced soil stiffness. For this study, therefore, the dynamic gain and logarithmic scaling of the input spectra are not applied.

The results from the ANN system are shown in Figures 7.36-7.42 and summarised in Table 7.5, below.

Table 7.5 A Comparison of Field Test Results and Design Pile Dimensions

Pile	Design Radius (m)	Calculated Radius (m)	Error (%)	Design Length (m)	Calculated Length (m)	Error (%)
T02	0.20	0.23	15	9.0	8.8	2
T03	0.20	0.22	10	11.0	11.1	1
T07	0.20	0.26	20	13.0	13.2	2
T09	0.30	0.35	17	11.0	10.8	2
T10	0.30	0.38	27	13.0	12.3	5
T11	0.375	0.43	15	11.0	11.4	4
T12	0.375	0.42	12	13.0	12.9	1

Given the curved nature of the pile toes in the calculated profiles a definite measure of the acoustic length of the pile is difficult. For this case the pile toe is described as the point at which the pile has lost more than half of its mean *calculated* radius. It should also be noted that because of the decimated nature of the pile profile the length cannot be given to an accuracy more than 0.3m. This having been said the calculated pile lengths fall well within the error margins associated with this test method ($\pm 10\%$, as quoted in Section 2.7.3).

The calculated radii of the tested piles are all larger than the design radii - an average of 17% larger. While some of this error is possibly due to variations in the concrete mix used, a postulate born out by the variation found in piles of the same design radii, the fact that the results are consistently high suggest a systemic error is also present. In Figure 7.43 the wavelet reflectogram (the time domain version of the spectrum presented to the ANN) for pile 'T09' is shown with FEA generated responses for its equivalent and that of a pile with a 0.35m radius. All three cases appear very similar, but the amplitude of the returning echo is clearly consistent with that of the 0.35m FEA data. As such it would appear the network has correctly identified the radius according to its experience and the error, again, is an error associated with the accurate modelling of the pile head response.

One possible reason for this over estimation of the pile radius is the apparent increase in stiffness of the pile head caused by surrounding soil. The next section, Section 7.4.3, investigates the performance of the MLP network with respect to the exposure of the pile head.

7.4.2 Effects of Exposed Pile Section

The results presented above are all for the 'T', test, piles all of which had a length of exposed shaft at the pile head. Also introduced at the start of this section were the anchor piles which did not. One of these piles 'A01' has, therefore, been tested before,

and after, 250mm and then 500mm of the shaft has been exposed. The various stages of shaft exposure are shown in the plates of Figure 7.44.

When the ANN, that has been trained on the FEA generated 'T' pile data, has the results from these tests presented to it the changes in computed radius are marked - as shown in Figure 7.44. The computed length of the pile is consistent at around 11.4m. This appears low compared to the design length of 13m, but the propagation velocity for these piles is very much larger than in the 'T' piles: an average of 3950ms^{-1} as opposed to $3507\text{ms}^{-1}(\pm 15\text{ms}^{-1})$. This increases the acoustic length of the pile to 12.8m. When the pile head is exposed to 500mm the pile radius is correct to one decimal place as 0.2m. However, for the 250mm and no excavation case the radius is computed as 0.3 and 0.4 respectively. It is apparent, therefore, that the ANN is deriving the pile radius from the dynamic stiffness of the pile head. The increase in the effective stiffness caused by the surrounding soil has then produced an overestimation of the pile radius.

It is suggested, therefore, that the overestimation of the pile radius for the 'T' piles of Section 7.4.1 is due either to the concrete stiffness being too low or the exposed section of pile being too large in the FEA training data. In either case it is another example on the network performance's dependency upon the modelled training data. However, these results provide further evidence that that a pile head profile may be estimated through mobility spectra and a neural network trained by numerically generated data.

7.5 SUMMARY AND CONCLUSIONS

The hardware developed for data acquisition has been validated by an independent test engineer and has produced test traces of the same shape as those produced by industry standard equipment. Specifically, the ratio of input pulse to reflection amplitude appears visually similar and the calculated pile lengths are the same.

The neural network system described in Chapter 6 has successfully identified a complete loss of section in a driven pile of a square sectional shape.

The neural system described in Chapter 6 has identified known faults from test traces taken from the EPSRC test site at Blyth. The performance of the system is dependent upon known test method limitations and the accuracy of the training data employed.

The network can identify faults nearer the pile head more accurately than those towards the pile toe. This is due to :

- i) Attenuation of the stress wave makes more distant faults more difficult to detect.
- ii) Inaccurate soil modelling has an additive effect on systemic errors for faults further down the pile.

The neural network can identify faults or changes in radius located within one impact pulse wavelength from the pile head. A 6% difference in pile head diameter between the FEA generated training data and data from the Blyth test site was identified and diagnosed to within 3% of its actual value.

The neural system can identify, locate and quantify necks and bulbs of greater than 50% of the pile radius, along the pile length, within the confines of known test method limitations.

The neural network gives 'sensible' results for field test data upon which it has not been trained. Specifically, small losses in section are reported when results from piles containing occluded voids and cracking are presented.

The neural network can identify changes in pile head radius in soft and stiff clay sites to an accuracy predominantly defined by the accuracy of the training data.

The derived pile lengths for all piles tested at the Bothkennar site are correct to $\pm 5\%$.

The calculated pile radii for all piles tested at the Bothkennar site are correct to within 20% of the actual radius. This error is predominantly due to errors in the modelling of the pile head where the surrounding soils' effect on the pile head's dynamic stiffness strongly influences the system's response.

REFERENCES

- (7.1) Testconsult Ltd, Blyth SERC Project, Internal Report, Testconsult Ltd, Warrington UK (1990).
- (7.2) Nash D F T, Powell J J M, and Lloyd I M, Initial Investigations of the soft clay test site at Bothkennar, Géotechnique, Vol. 42, No. 2 (1992) pp163-183.

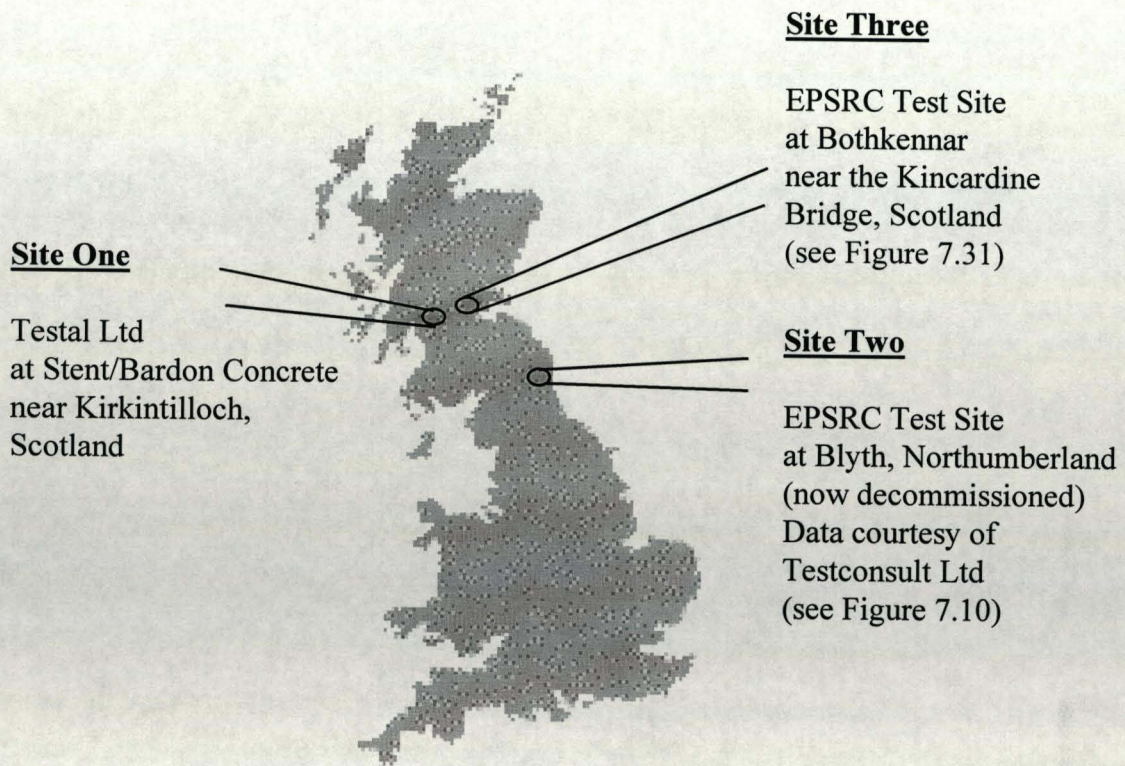


Figure 7.1 Identifies the three test sites from which data was used for the field testing of the neural system described in Chapter 6.



Figure 7.2 Testing of the three uninstalled piles (centre) with Dr Tong (Napier University, left) and Mr Nicholson (Testal Ltd, right).

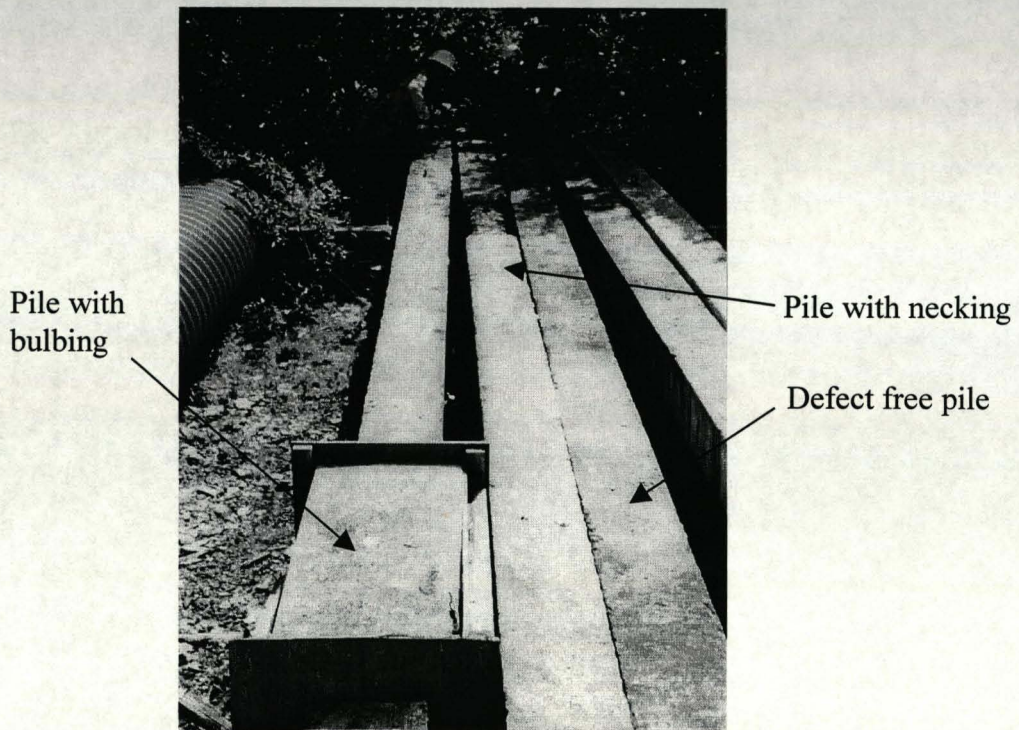


Figure 7.3 The three uninstalled piles tested, from far left: with bulbing, with necking and defect free.

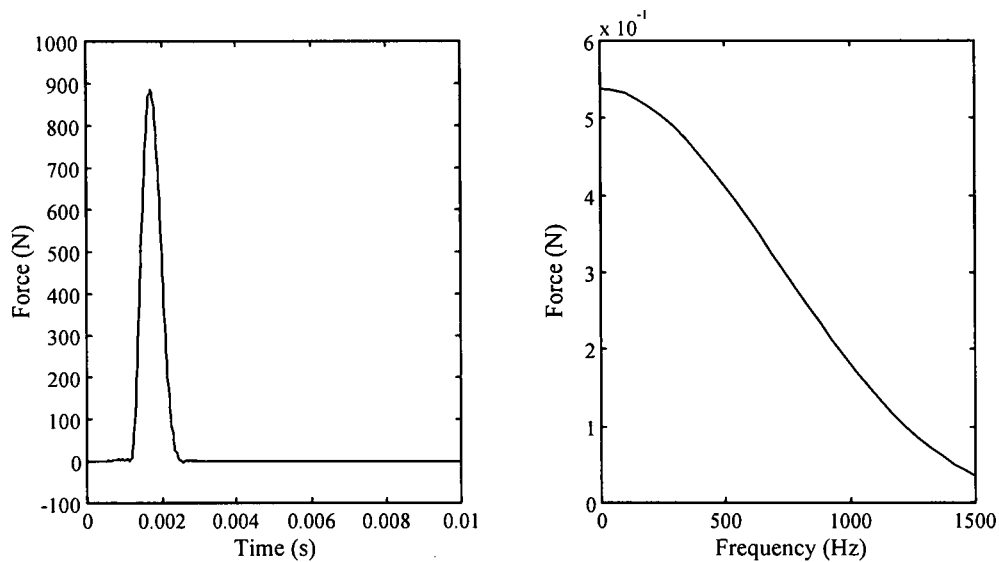


Figure 7.4 A typical impact trace obtained when striking the defect free pile. Shown both in temporal (left) and Fourier (right) domains.

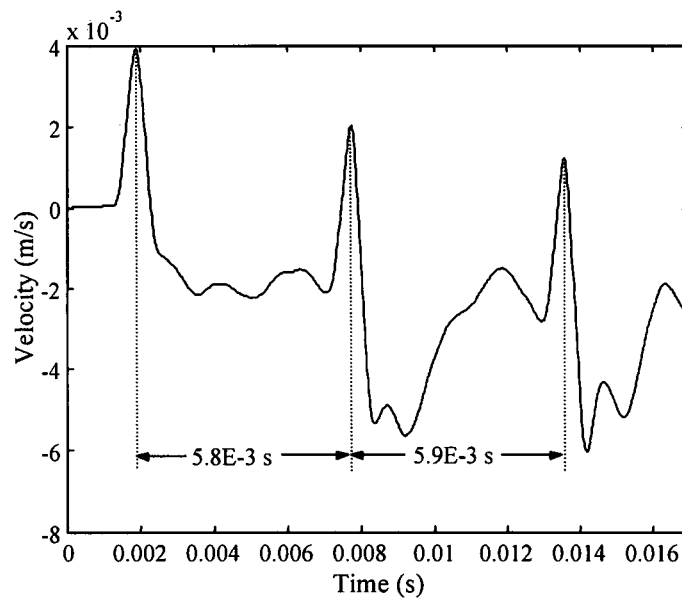


Figure 7.5 The pile head response of the defect free pile. Apart from the acoustic length being measurable and correct within known test method limitations it is noticeable that the prevailing support conditions have caused the low frequency aberrations in the trace identified in the laboratory tests of Chapter 4.

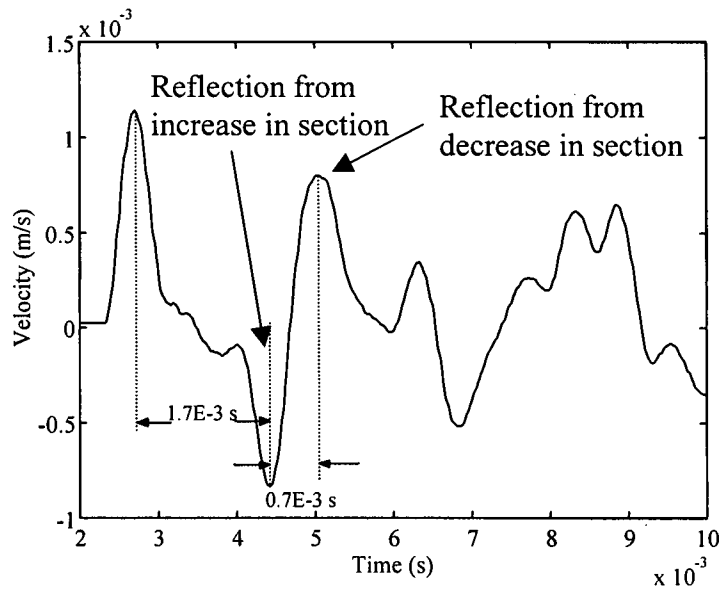


Figure 7.6 The recorded trace of the uninstalled pile with bulging. Clearly observable in this trace are the reflections from the increase and decrease in section although the pile toe has been shielded by this fault.

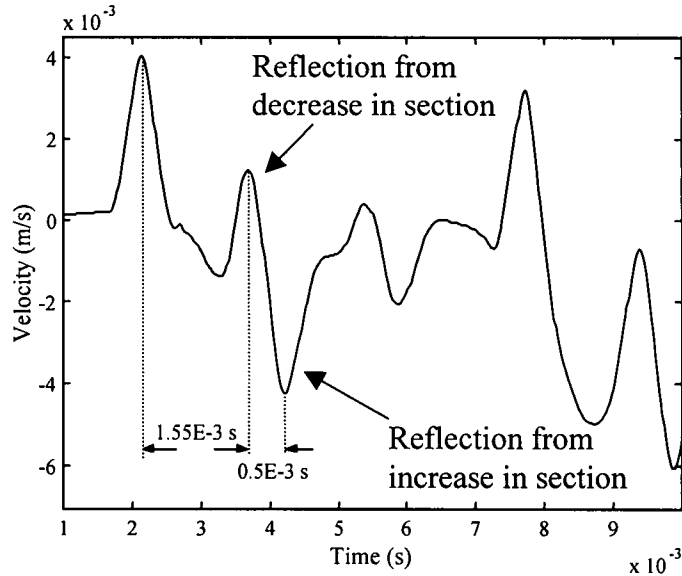


Figure 7.7 The recorded trace of the uninstalled pile with necking. As in Figure 7.6, the reflections from the decrease and increase in section are seen although, again, the pile toe cannot be resolved.

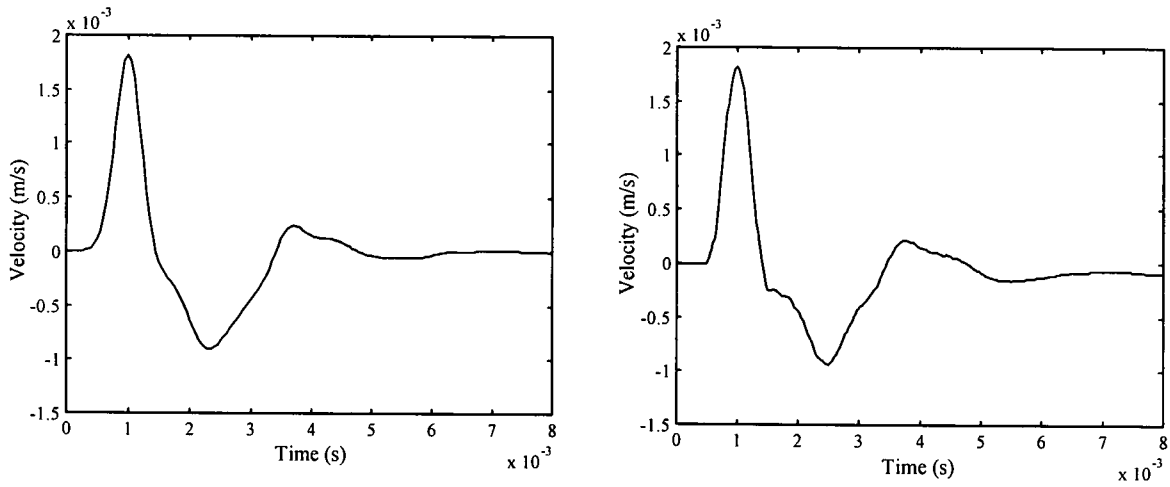


Figure 7.8 Shows the FEA generated trace for the installed foundation pile (left) and the field test data (right).

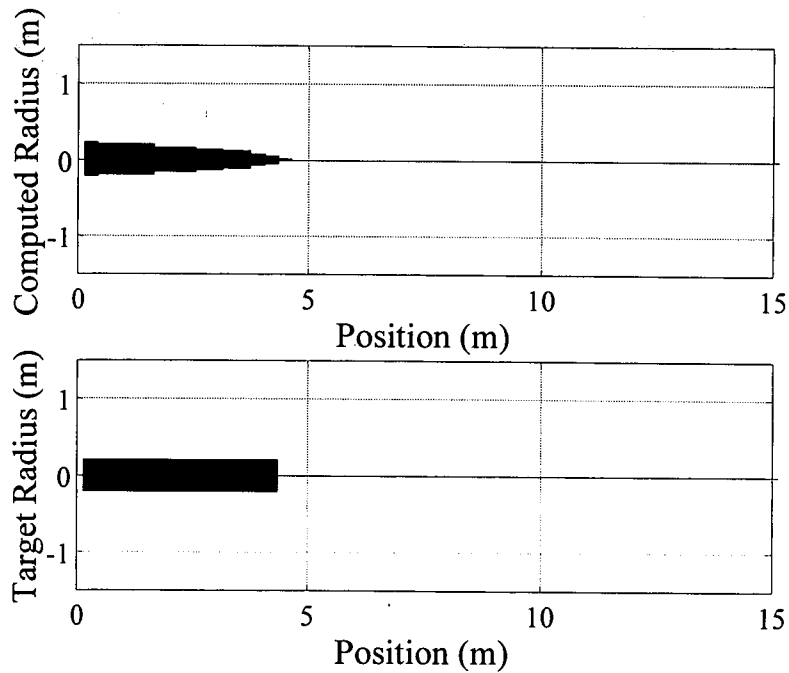
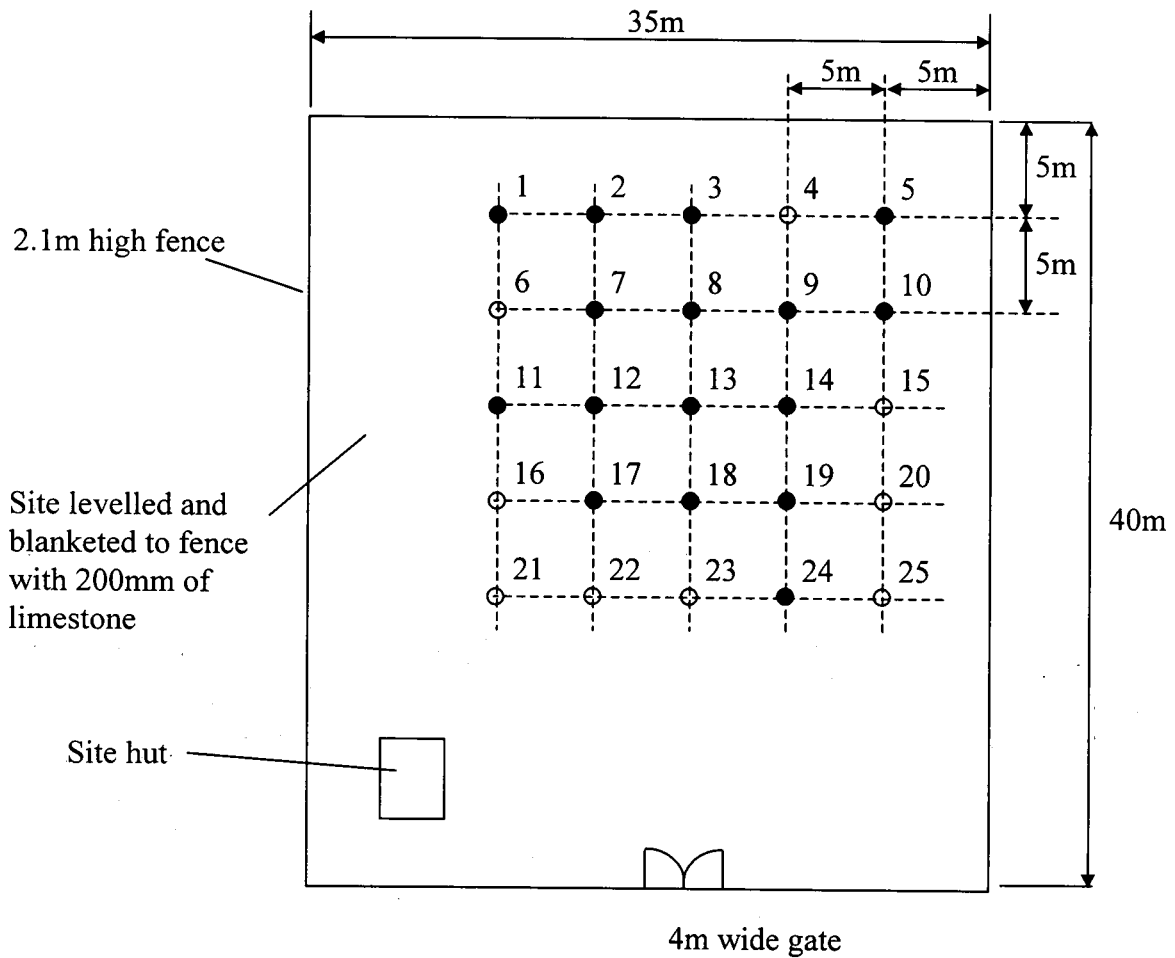


Figure 7.9 Shows the neural network's calculated pile profile (top) and the actual pile profile (beneath) for the installed concrete pile.



- Piles tested for this study.
- Piles not tested for this study

Figure 7.10 A plan view of the Blyth test site. Each pile is at least 5m from its nearest neighbour and as such group effects can be ignored. Some piles have not been included in this study. Specifically, piles 4, 6, 15, 16, 20, 21, 22, and 23 are longer than those included in this study and no reflections are observed from their toes. The data provided^{7.1} for pile 25 was incomplete and so it was also excluded from this study.

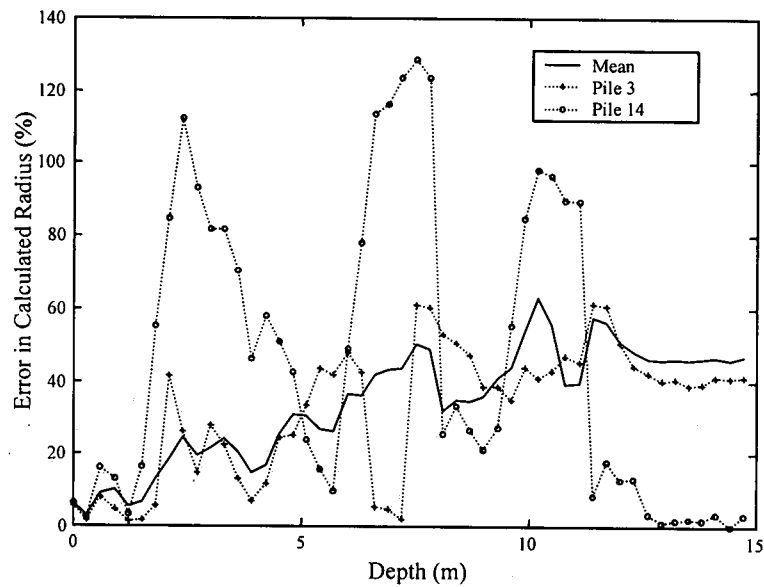


Figure 7.11 Shows the increase in calculated profile error with respect to depth. It also shows two examples where the errors appear extremely large. However, when observed in Figures 7.14 and 7.23, it is apparent that these errors are not solely reflective of the systems ability to interpret a sonic echo trace - the first major fault has been identified in both cases. In fact, they are a compound error of, the test method's limitations, the training data (modelling) accuracy, and the precision of the pile's reported dimensions with respect to its construction. For these reasons, as well as the small sample set, no statistics can be carried out as in Chapter 6. Instead each of the 16 piles are considered individually in Figures 7.12-7.27.

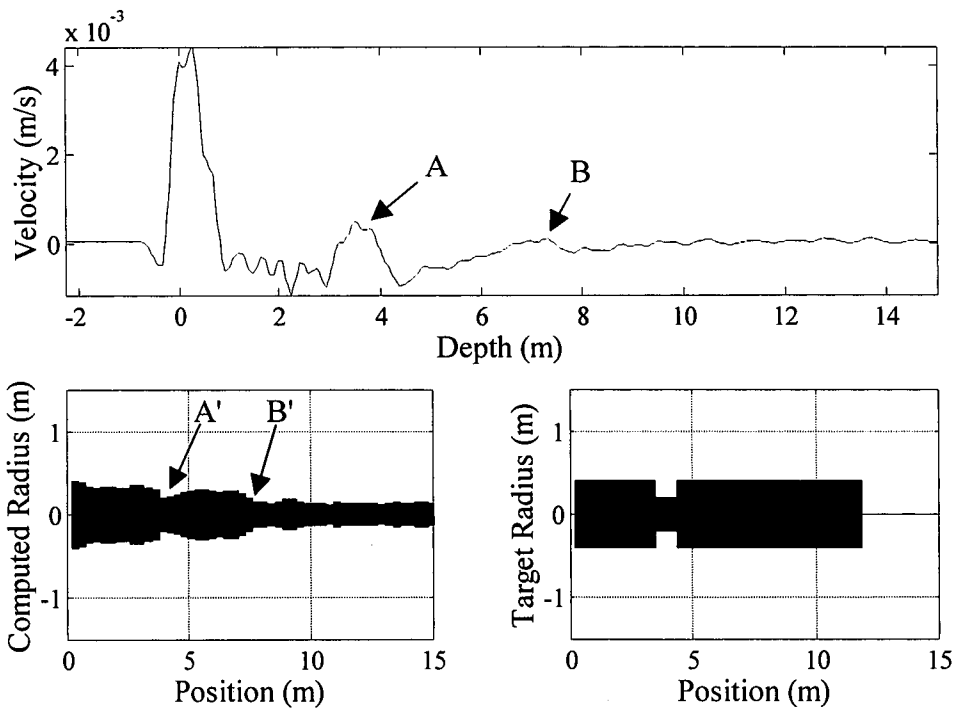


Figure 7.12 Pile 1 is an 11.7m long pile with a 45% loss in diameter at 3.45m extending for 0.6m. The loss in section, causing the positive pulse, A, in the recorded trace (top), has resulted in a loss in section on the computed diameter profile at 3.5m, A' (beneath, left).

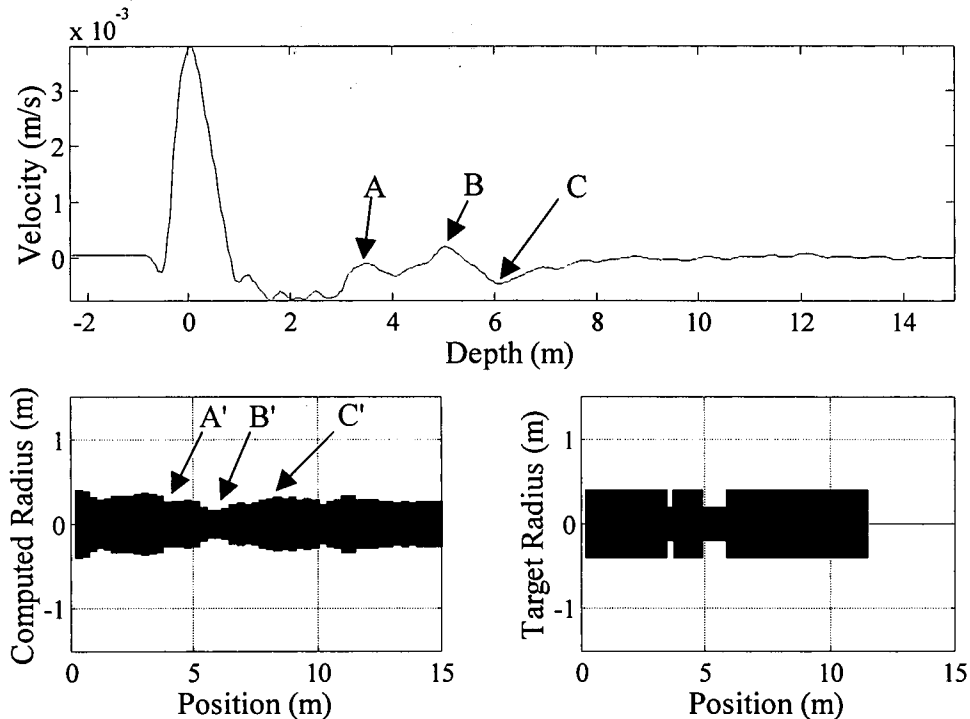


Figure 7.13 Pile 2 is an 11.3m long pile with a 45% loss in diameter at 5.05m extending for 0.6m. Above this, at 3.65m there is a crack covering 50% of the pile area. The neck detectable on the computed diameter profile, as B', at 5.5m. The crack, A', is observed as a loss in radius on the computed profile.

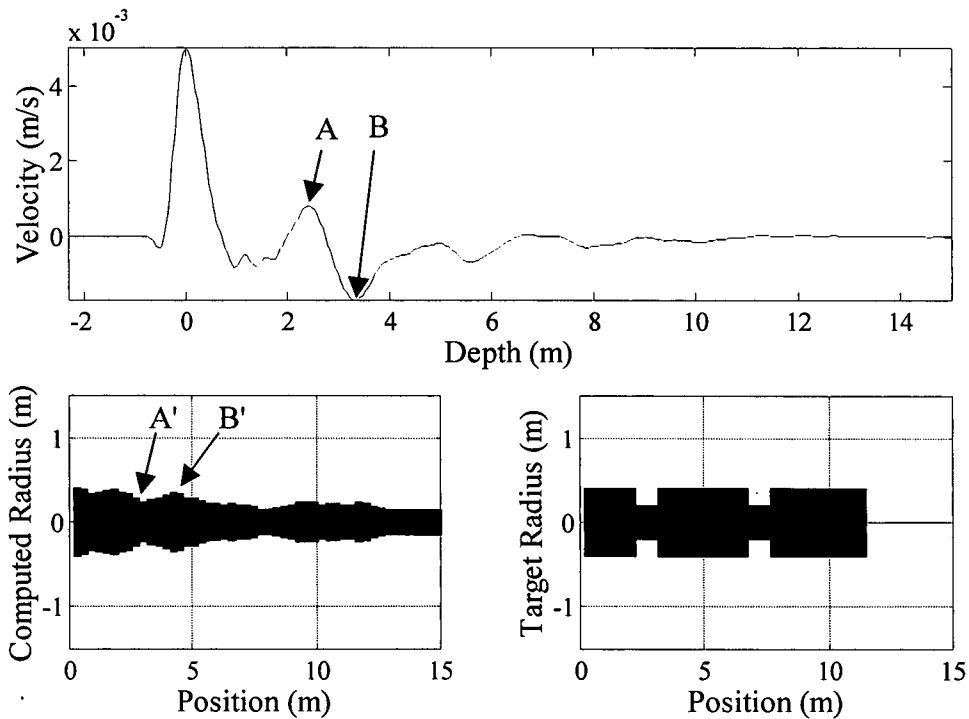


Figure 7.14 Pile 3 is an 11.4m long pile with 45% losses in diameter at 2.4m and 7.9m, both extending for 0.6m. The first loss in section is detectable on the computed profile, as A', at 3.0m before returning to its original radius at B'. The second neck is not visible on the computed profile.

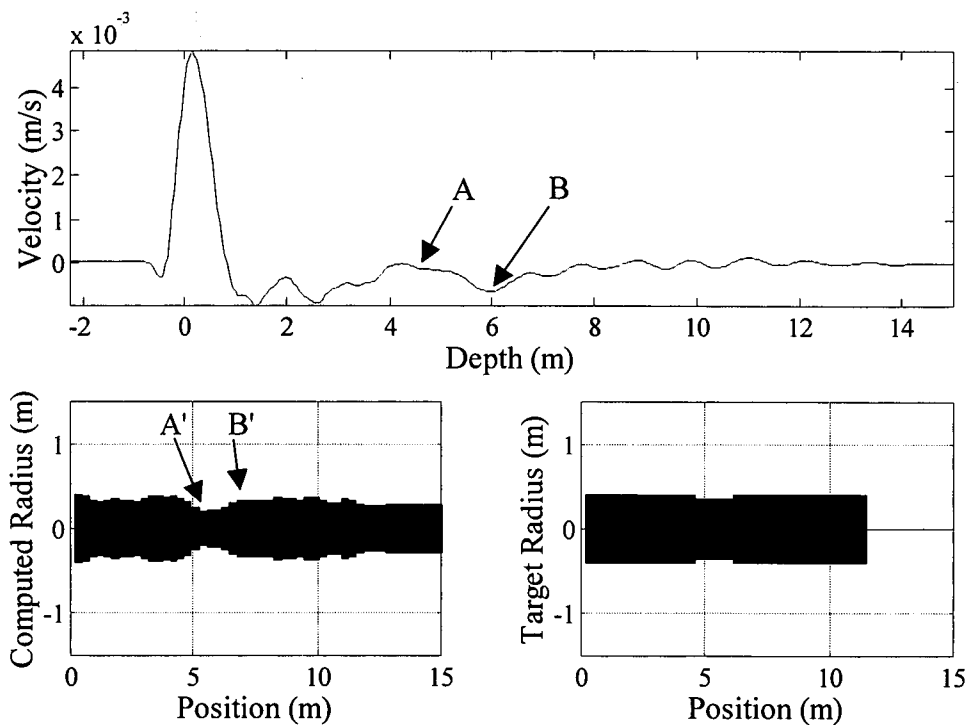


Figure 7.15 Pile 5 is an 11.3m long pile with a 13% loss in diameter at 4.7m extending for 1.2m. The loss in radius, is visible on the trace as A and on the computed profile, as A' at 5.5m. The pile profile returns to its original radius at B'.

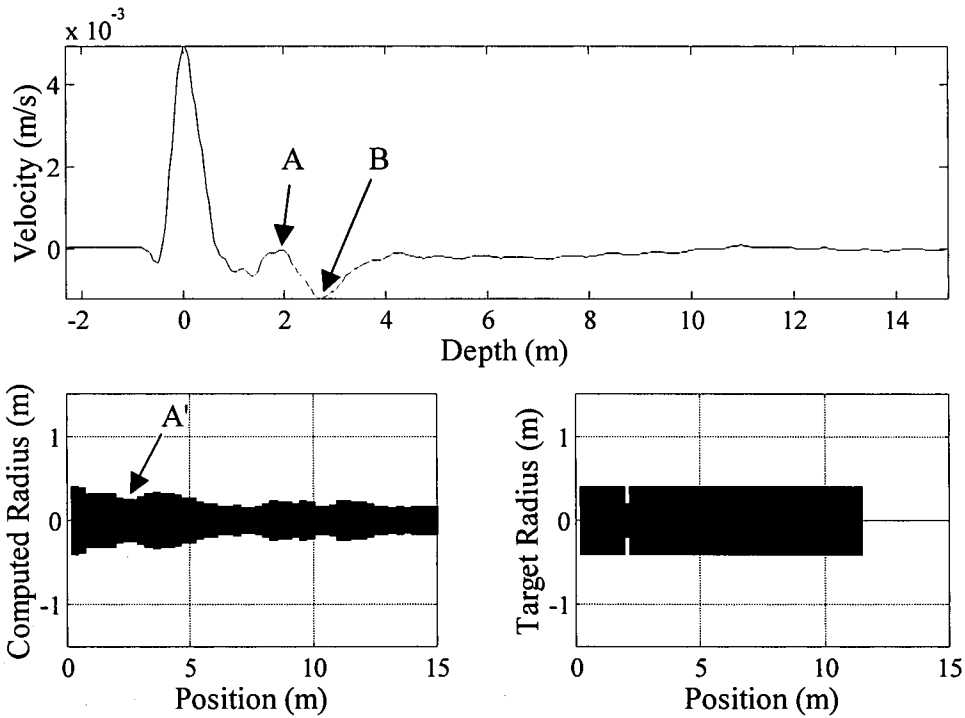


Figure 7.16 Pile 7 is an 11.4m long pile with a 50% loss sectional area at 2.2m. This crack is not visible on the computed profile although a small neck is apparent at position A'.

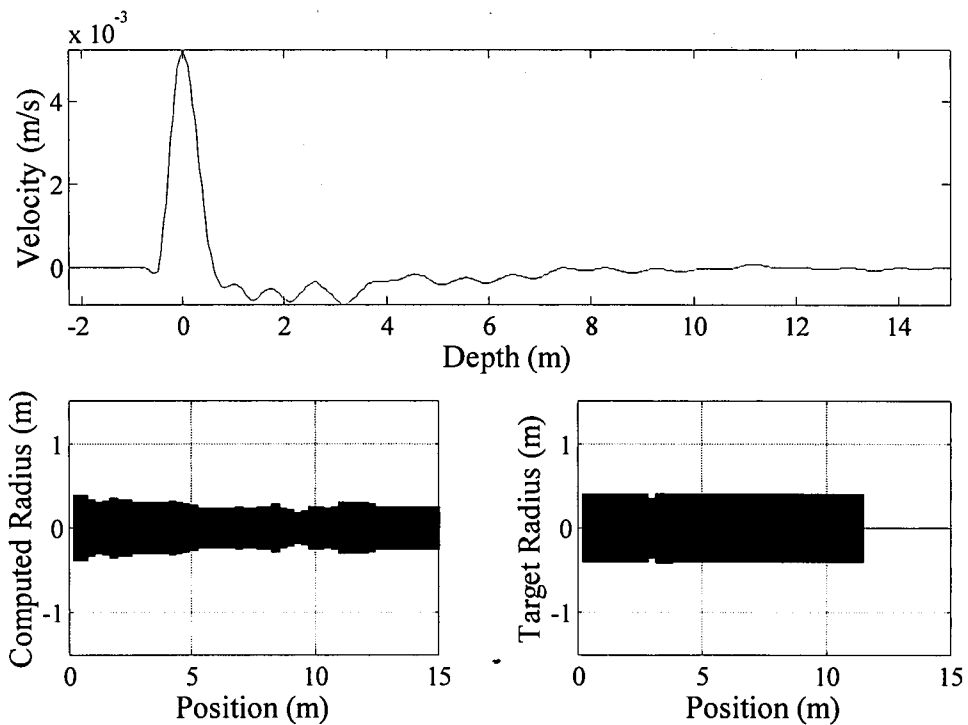


Figure 7.17 Pile 8 is an 11.4m pile with a 30% loss sectional area at 2.9m. This crack is not visible on the computed profile.

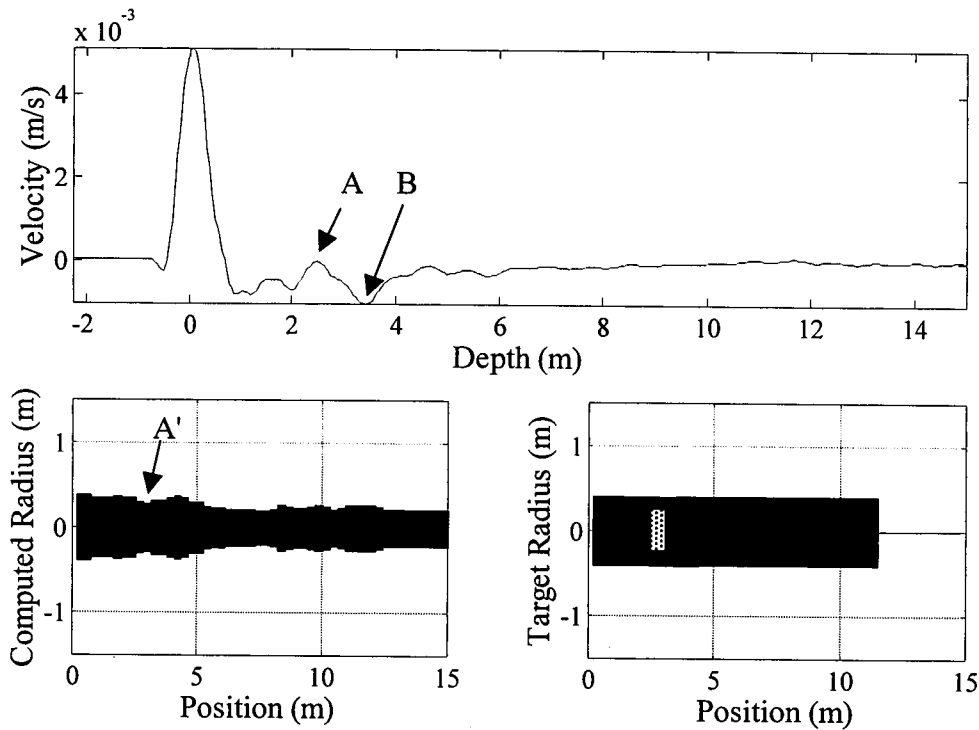


Figure 7.18 Pile 9 is an 11.4m long pile with an occluded void at 2.9m. This void has a 0.5m diameter and extends for 0.5m. This void is the equivalent of a 0.2m (25%) loss in diameter and, although visible in the recorded trace as points A and B is not conclusively visible on the computed pile profile - although there is a slight loss in radius at A' when compared to Figure 7.19, below.

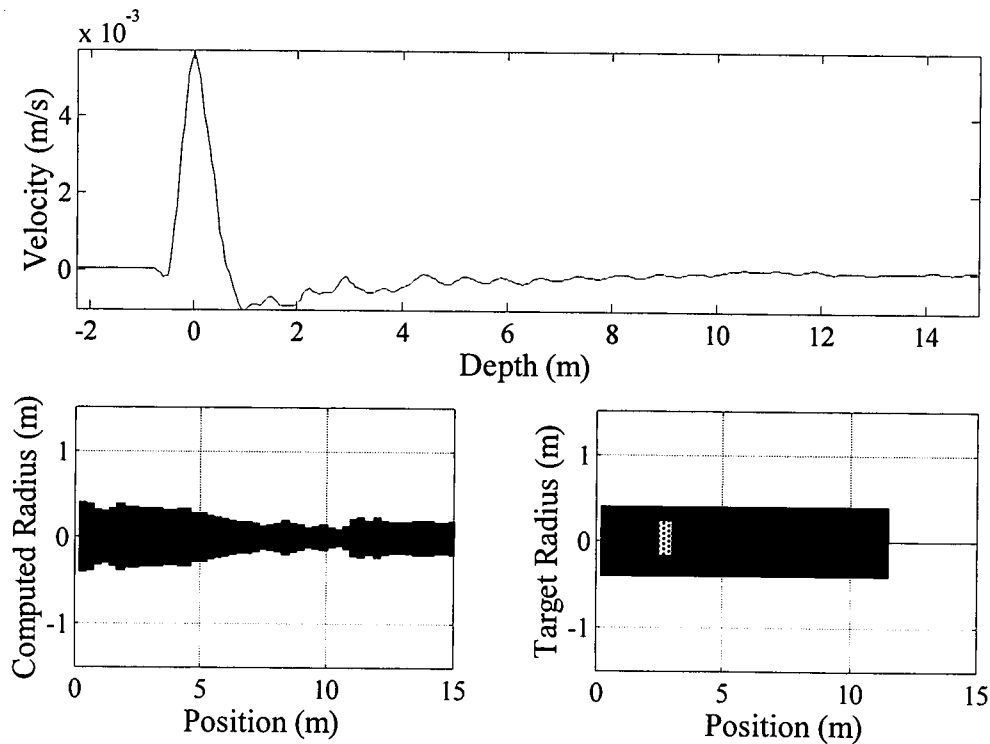


Figure 7.19 Pile 10 is an 11.3m long pile with an occluded void at 3.1m. This void has a 0.4m diameter and extends for 0.4m. This is the equivalent of a 0.12m (15%) loss in diameter. It is not visible on the computed pile profile.

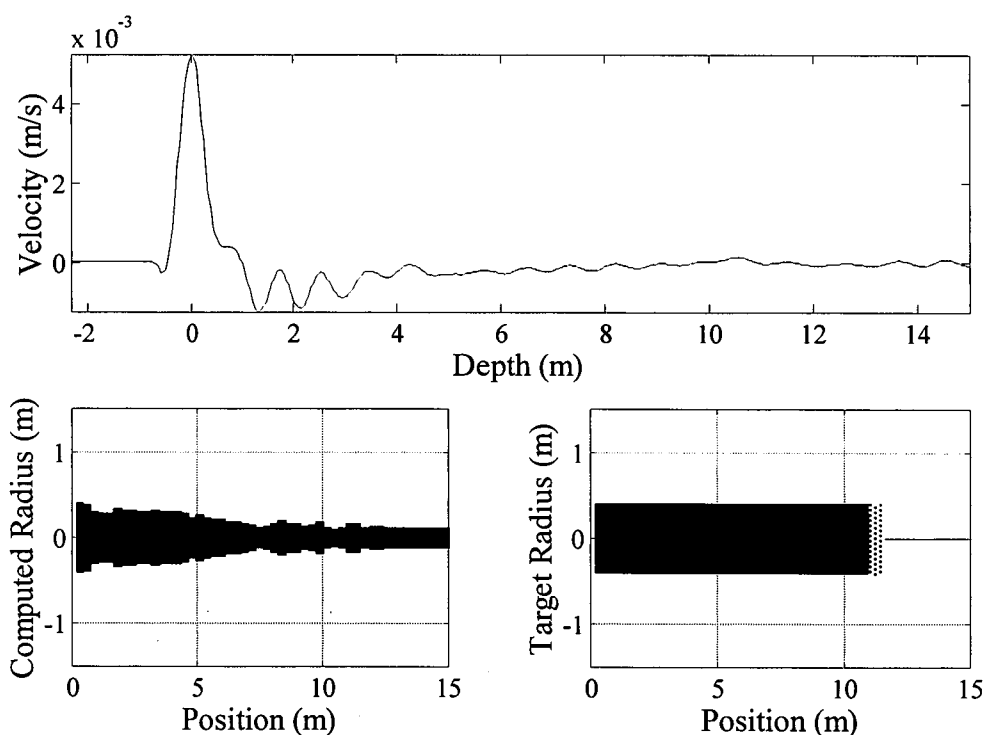


Figure 7.20 Pile 11 is an 11.3m long pile with a soft toe. This is caused by a 0.3m long perforated foam disk being placed at 11m. This defect has not been detected on the recorded trace or the pile profile.

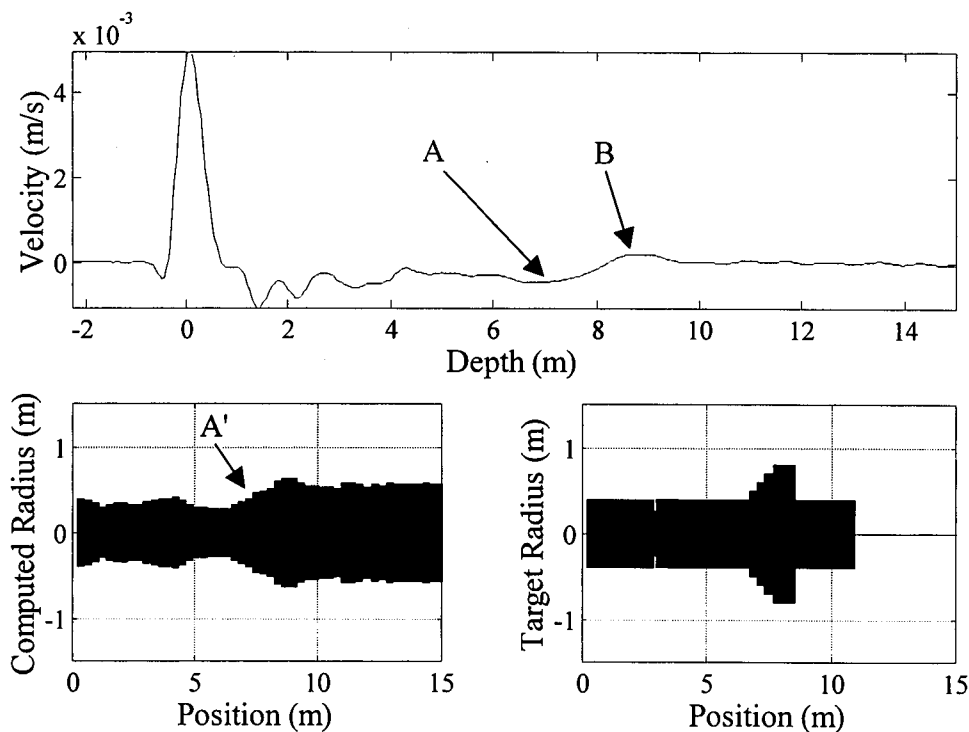


Figure 7.21 Pile 12 is an 11.3m long pile with an open crack covering 50% of the pile sectional area at 3m and a bulb of double the pile diameter at 7.2m extending for 1.5m. The crack is not visible on the computed profile although the increase in section is clearly observable at A'.

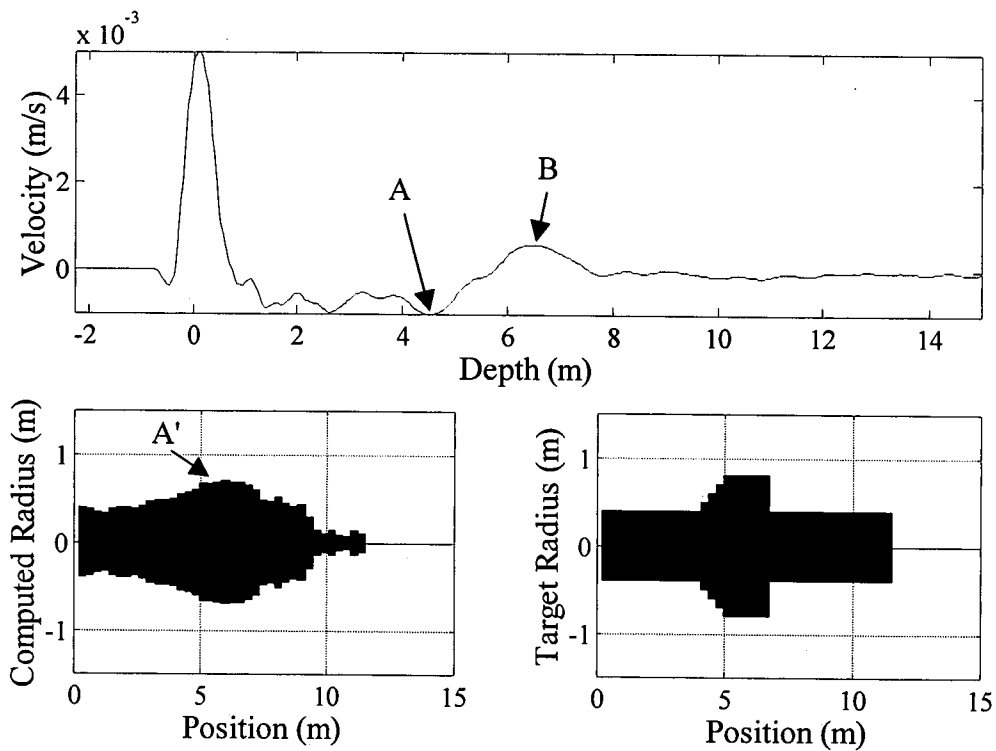


Figure 7.22 Pile 13 is an 11.3m long pile with a bulb of double the pile diameter at 4.7m extending for 1.5m. This bulb is clearly visible on the computed profile at A' although erroneous results are calculated for the shaft below it.

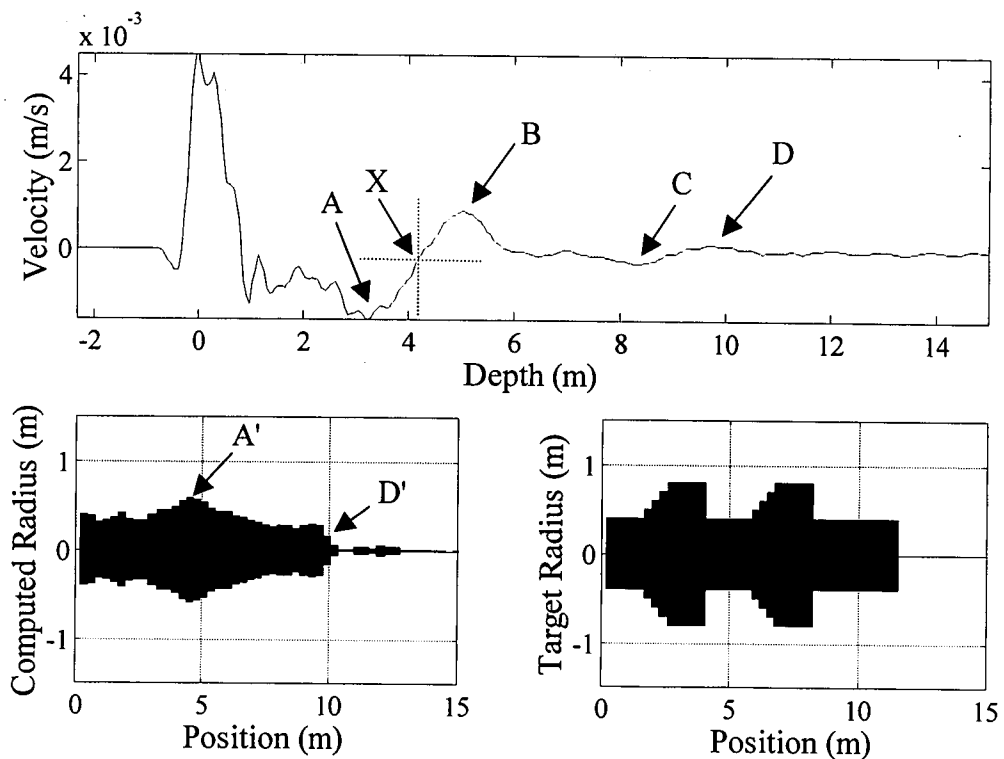


Figure 7.23 Pile 14 is an 11.3m long pile with two bulbs of double the pile diameter at 2.2m and 6.3m, both extending for 1.5m. A first bulb is visible on the computed profile at A' although erroneous results are obtained for the shaft beneath it.

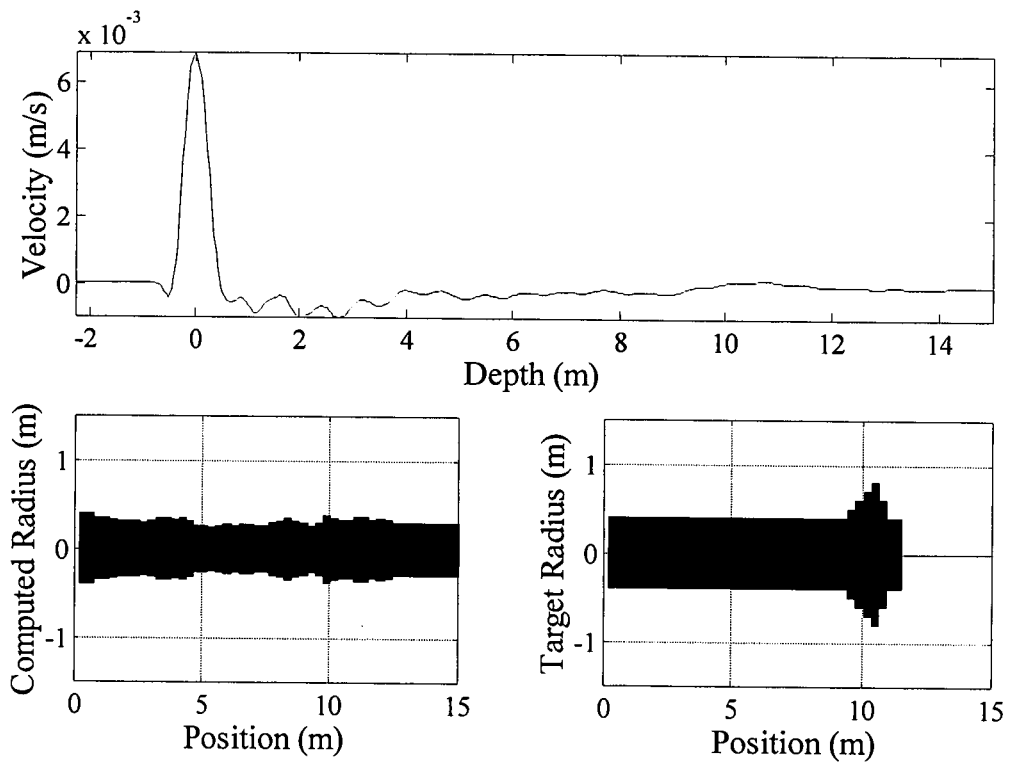


Figure 7.24 Pile 17 is an 11.3m pile with a bulb of double the pile diameter at 10m extending for 0.8m. This bulb is not visible on the computed profile.

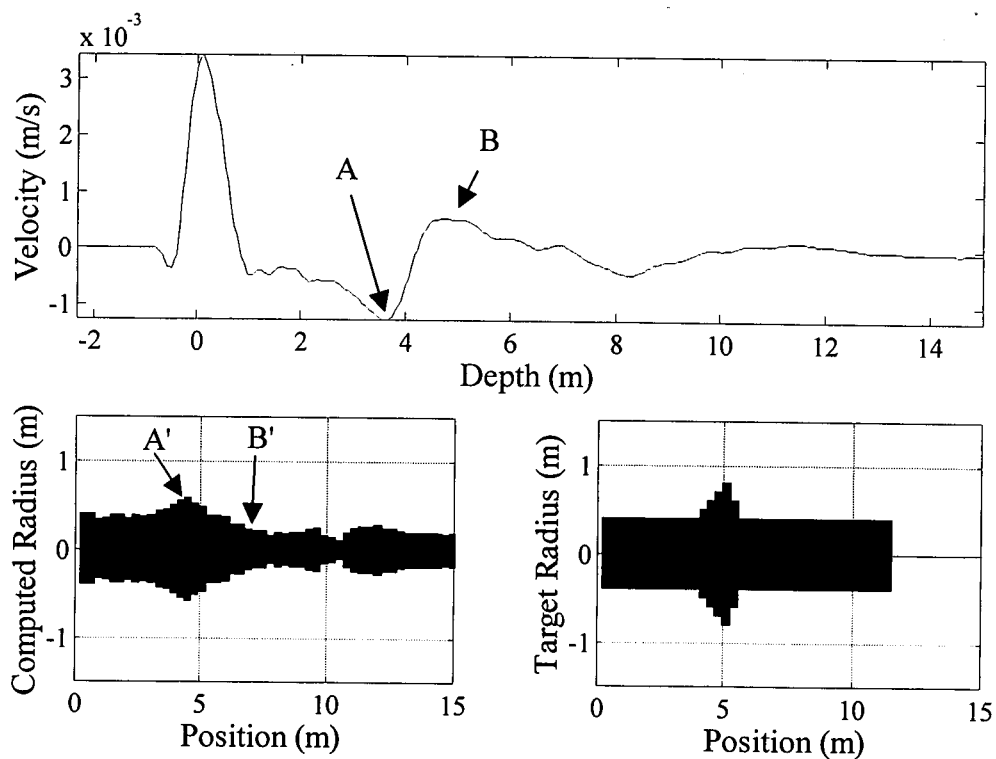


Figure 7.25 Pile 18 is an 11.3m long pile with a bulb of double the pile diameter at 4.5m extending for 0.8m. This bulb is visible on the computed profile at 4.5m, position A'.

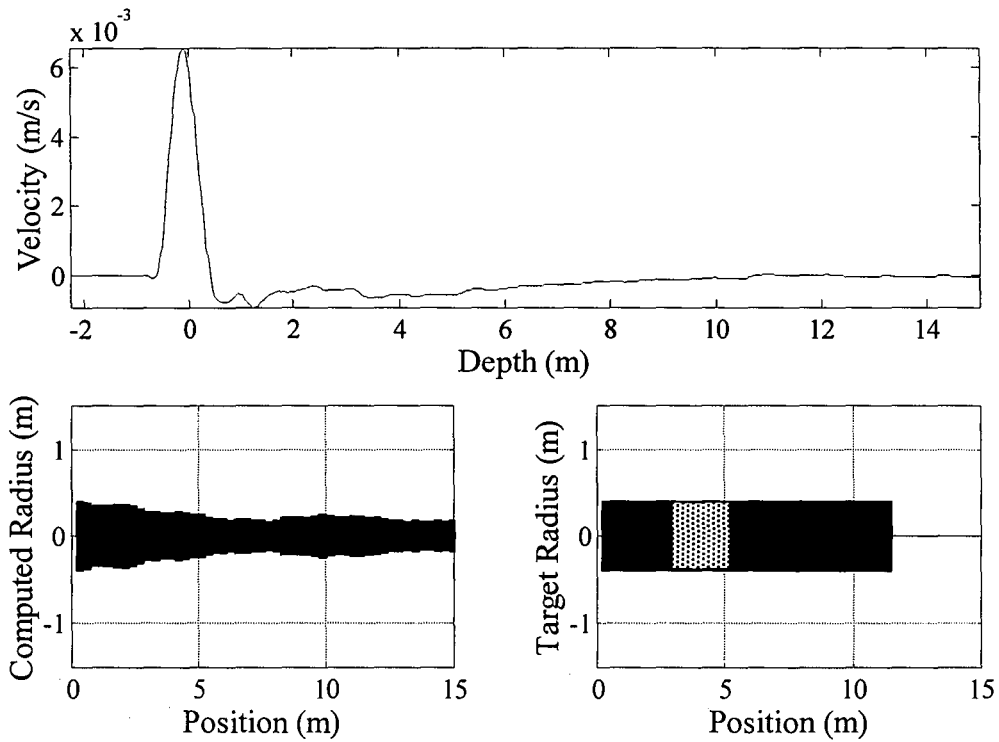


Figure 7.26 Pile 19 is an 11.3m pile with an area of weakened concrete at 3m extending for 2m. No information concerning the composition of this concrete is given and its presence is not observed in the computed pile profile.

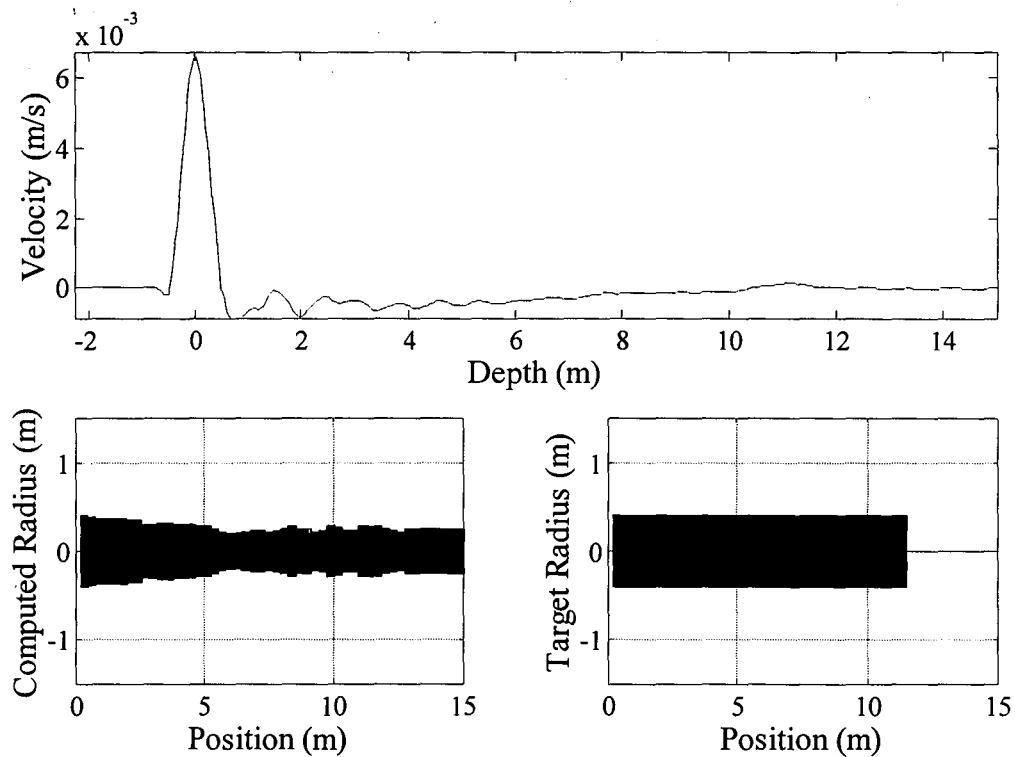


Figure 7.27 Pile 24 is an 11.3m defect free pile. The pile toe is not visible on the computed pile profile.

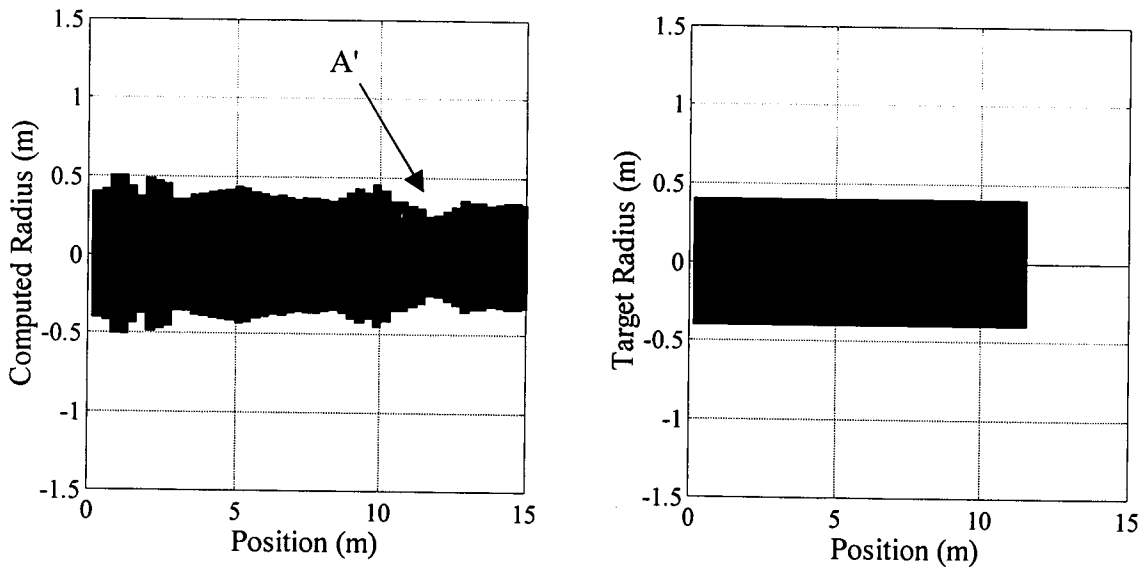


Figure 7.28 Shows the effect of artificially reducing the effects of soil damping beneath 4m for the defect free pile: Pile 24. Note how the computed pile profile, left, no longer tapers inwards as in Figure 7.27.

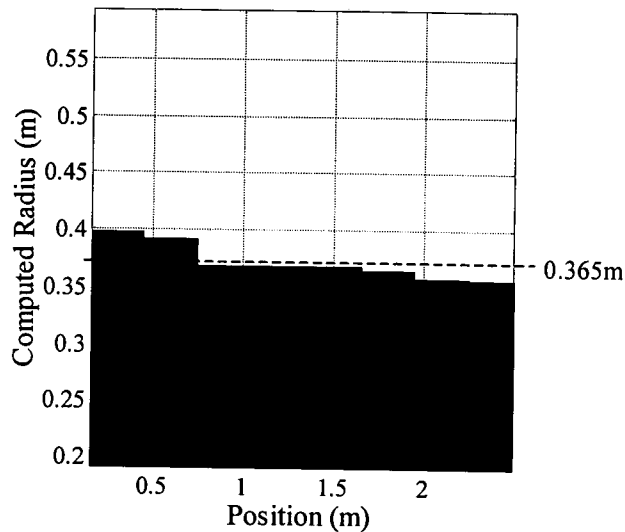


Figure 7.29 Shows the drop in computed radius from 0.400m to an average of 0.365m. This average is taken over the shaft length between 0.3 and 2.5m from the pile head for the defect free pile. The Blyth field piles have, in fact, a 0.375m radius rather than the 0.4m radius that the ANN has been trained on. The network has apparently identified this difference and derived the correct pile diameter to within a 3% margin of error.

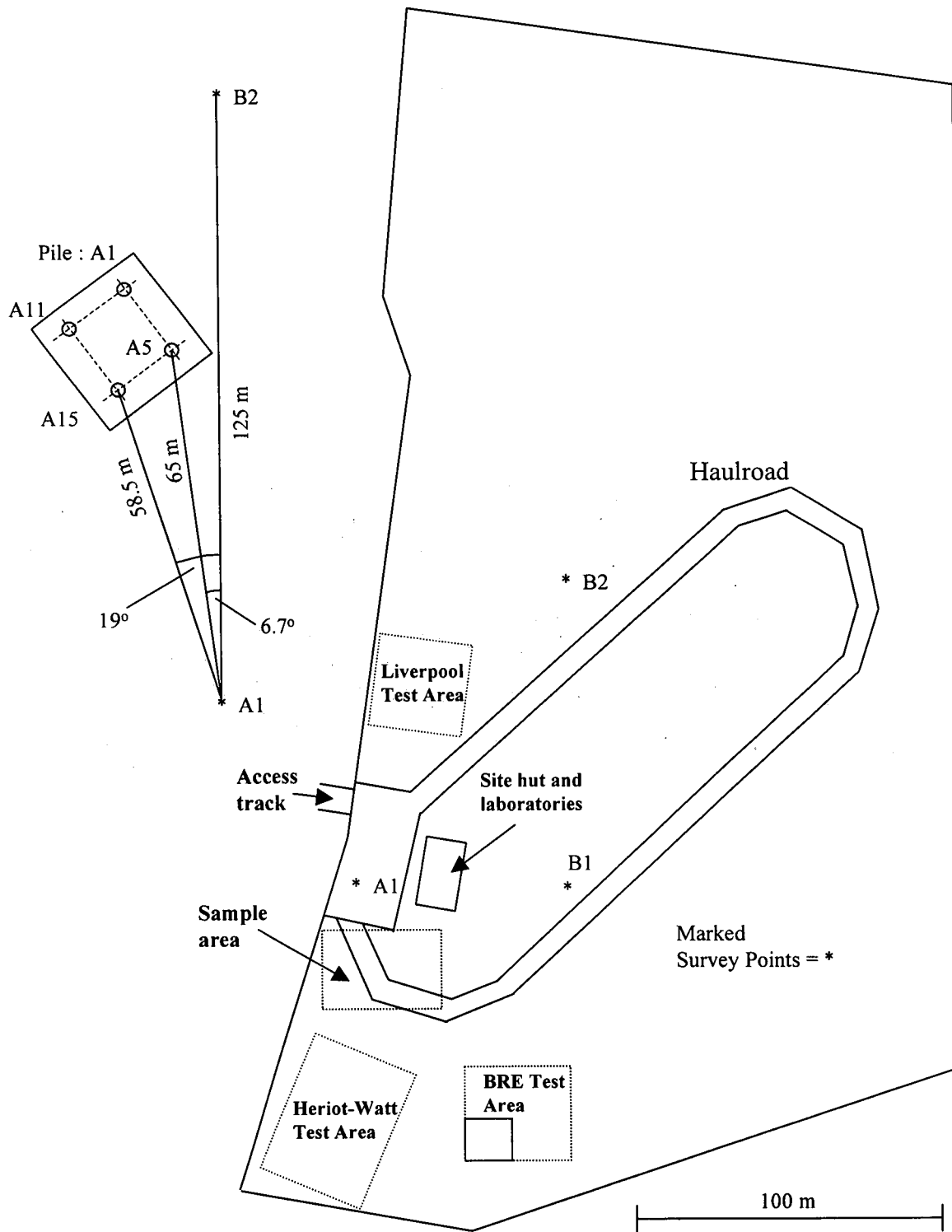


Figure 7.30 The plan for the EPSRC site at Bothkennar (see Figure 7.1). The piles included in this study are those found in the Liverpool University test area which can be located using the marked survey points and the bearings given above.

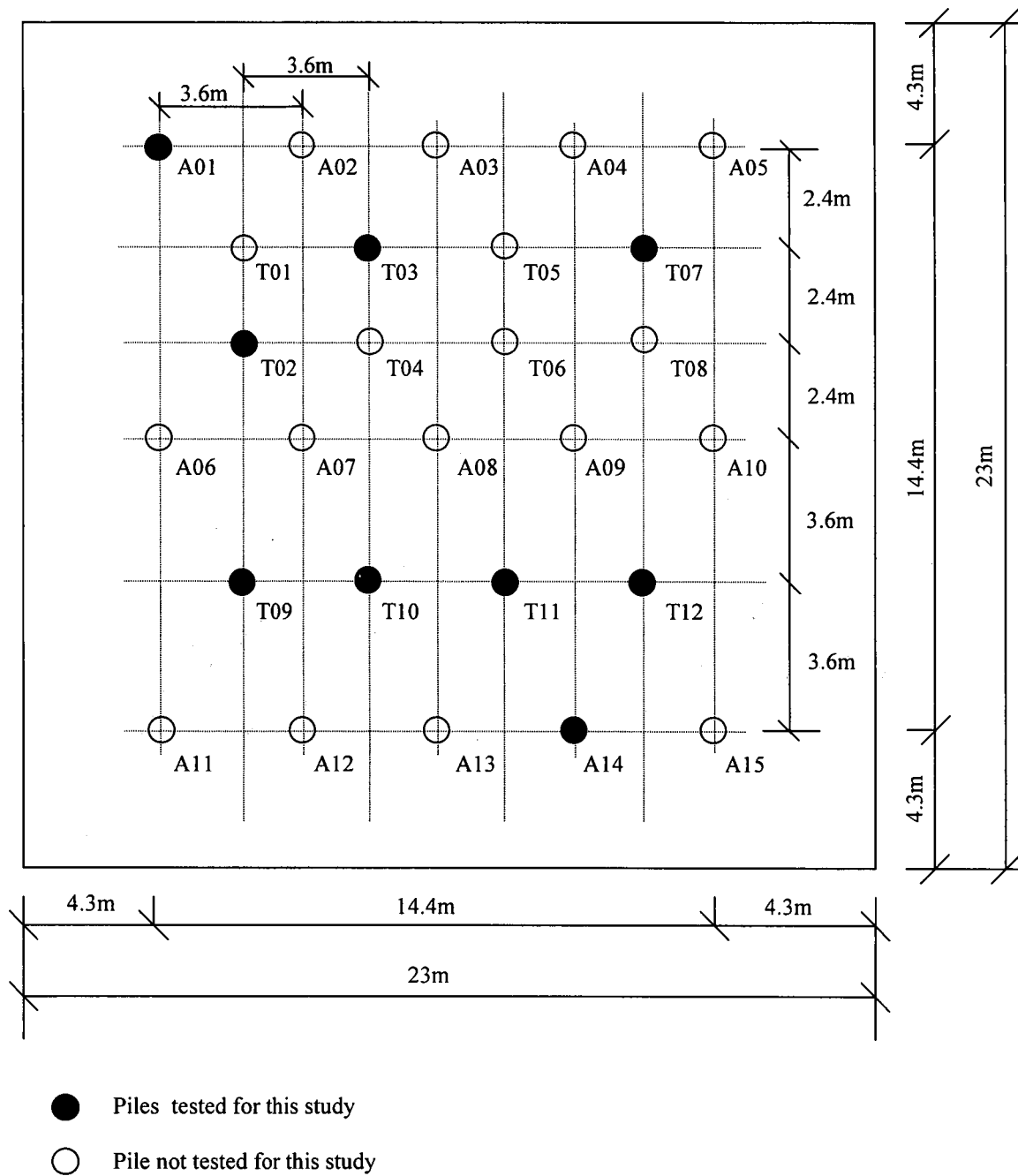


Figure 7.31 The Liverpool University test area at Bothkennar. The piles included in this study are those marked in black. These represent one of each the design dimensions present on this site thereby covering all combinations of diameter and design length.

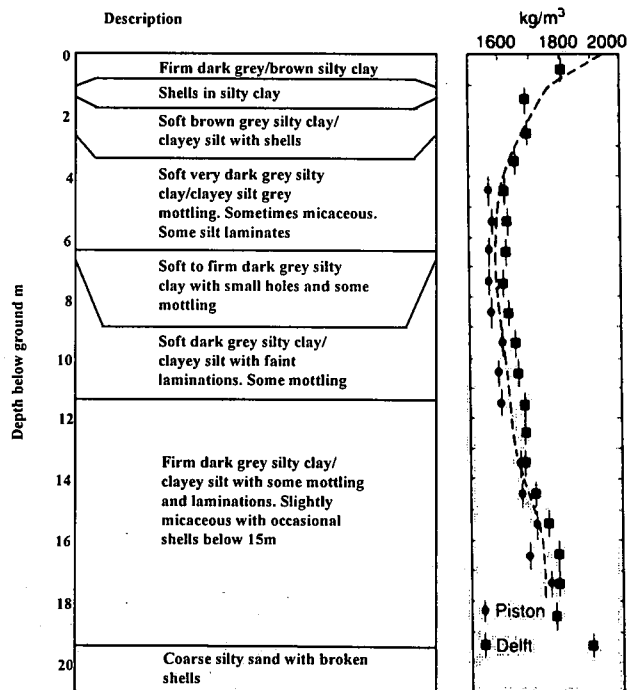


Figure 7.32 Soil constituents and bulk density with depth at Bothkennar (after Nash *et al.* ^{7.1})

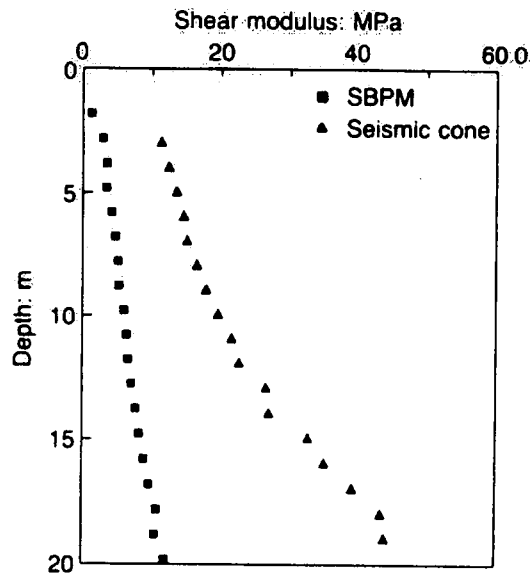


Figure 7.33 Soil shear modulus *verses* depth at Bothkennar (after Nash *et al.* ^{7.1}). The values used in this study are those associated with the seismic cone test as these were obtained using shear wave velocity measures. Thus they better represent the low strain dynamic values required for this study than those obtained by the SBPM pressure measures.

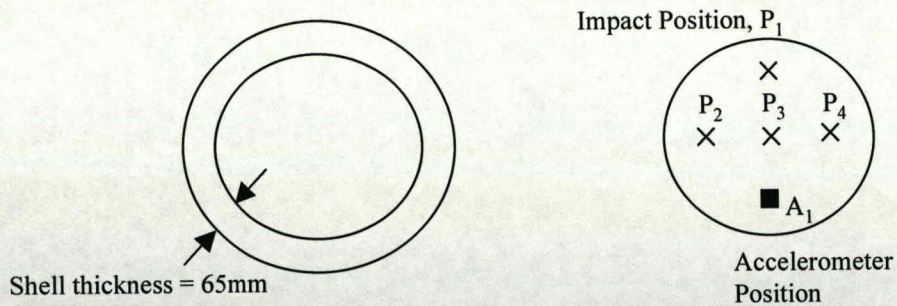


Figure 7.34 The case dimensions for the 'T' piles of this study and the impact and accelerometer positions during testing.

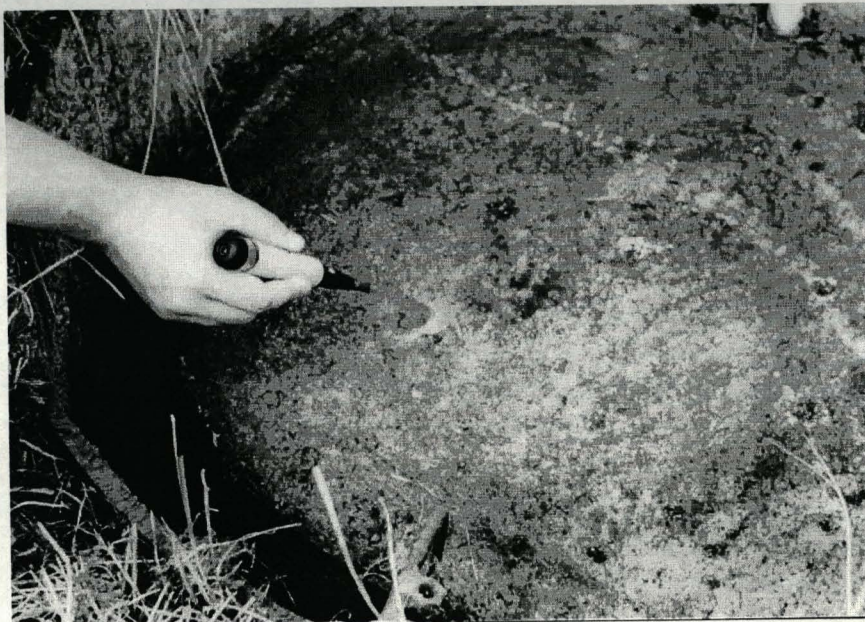


Figure 7.35 Shows the pile head of pile T12. The area of accelerometer attachment was first dried using a butane soldering iron with no head attached. The fixing wax was then melted using the same iron (shown in use, above) before the accelerometer was positioned.

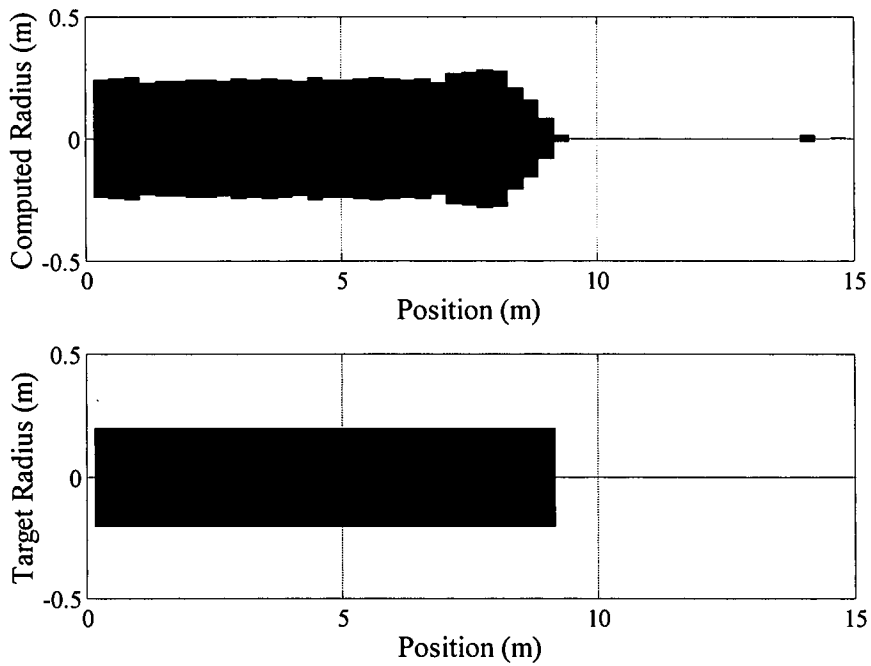


Figure 7.36 Shows the computed profile for pile T02 (top) and its actual profile (beneath). The actual radius is 0.2m while the average computed radius is 0.23m.

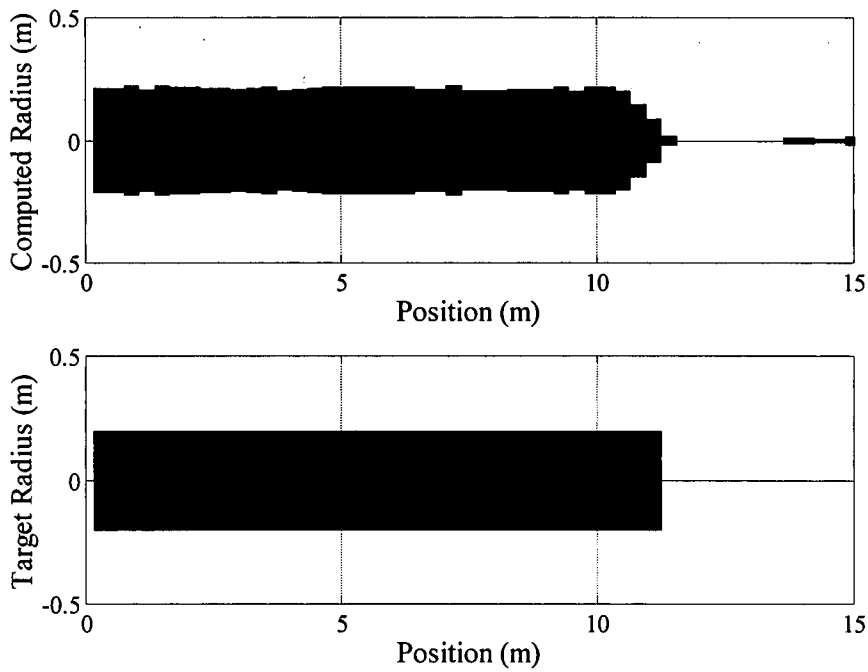


Figure 7.37 Shows the computed profile for pile T03 (top) and its actual profile (beneath). The actual radius is 0.2m while the average computed radius is 0.22m.

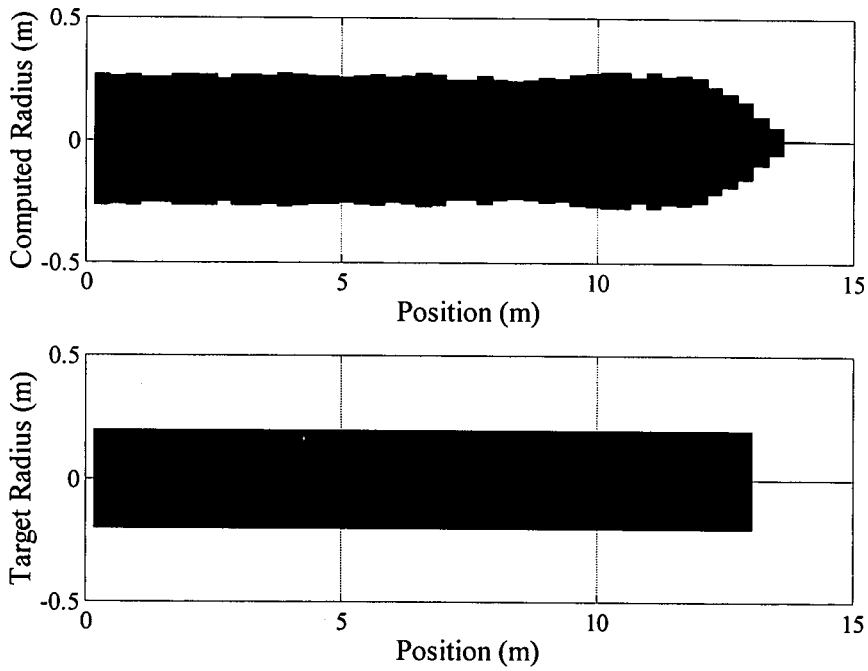


Figure 7.38 Shows the computed profile for pile T07 (top) and its actual profile (beneath). The actual radius is 0.2m while the average computed radius is 0.26m.

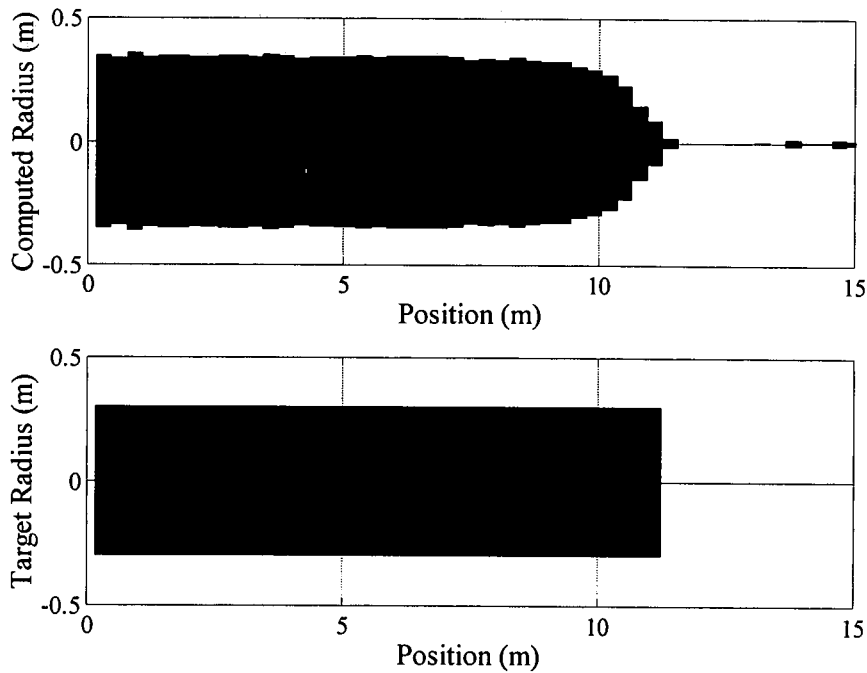


Figure 7.39 Shows the computed profile for pile T09 (top) and its actual profile (beneath). The actual radius is 0.3m while the average computed radius is 0.35m.

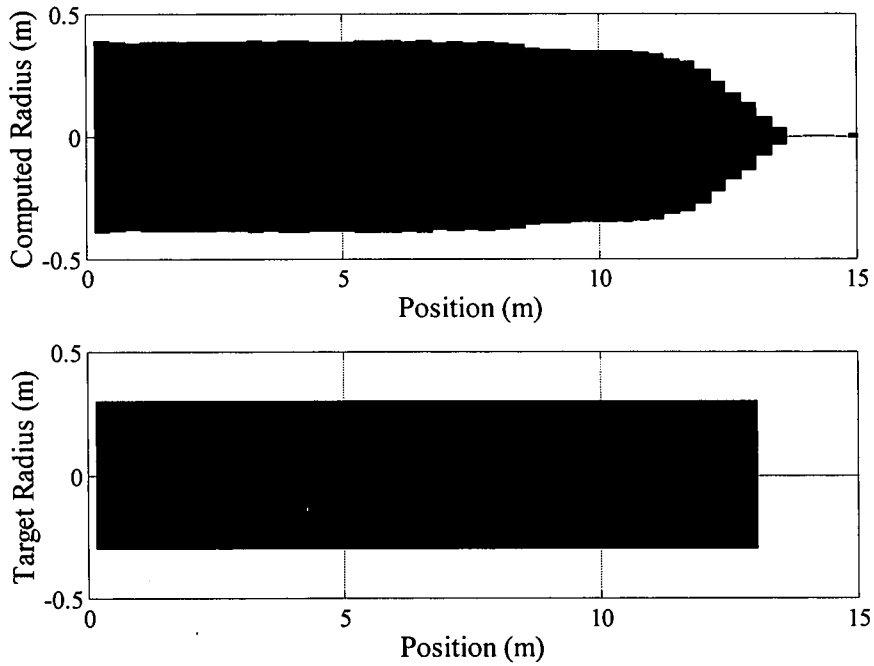


Figure 7.40 Shows the computed profile for pile T10 (top) and its actual profile (beneath). The actual radius is 0.3m while the average computed radius is 0.38m.

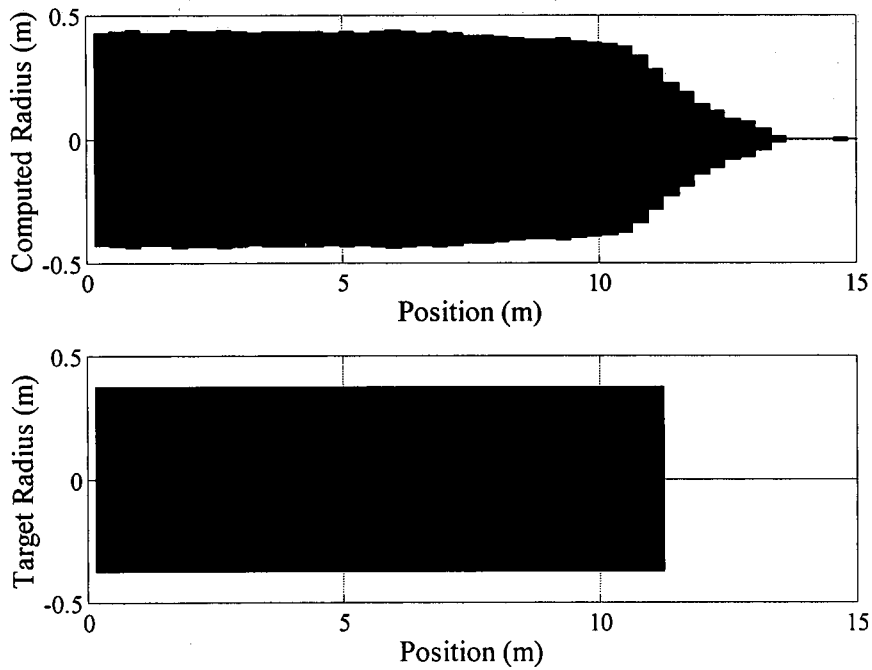


Figure 7.41 Shows the computed profile for pile T11 (top) and its actual profile (beneath). The actual radius is 0.375m while the average computed radius is 0.43m.

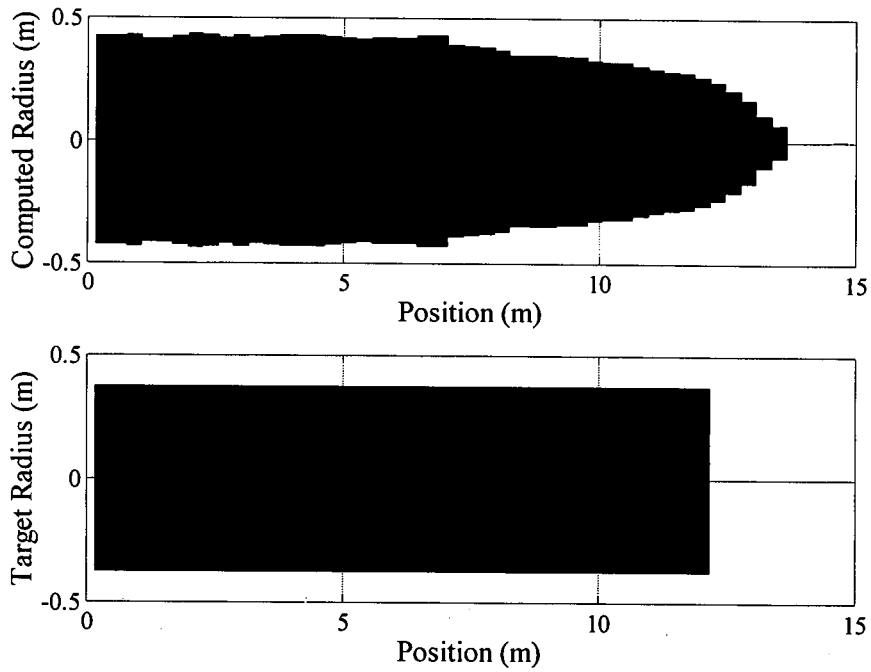


Figure 7.42 Shows the computed profile for pile T12 (top) and its actual profile (beneath). The actual radius is 0.375m while the average computed radius is 0.42m.

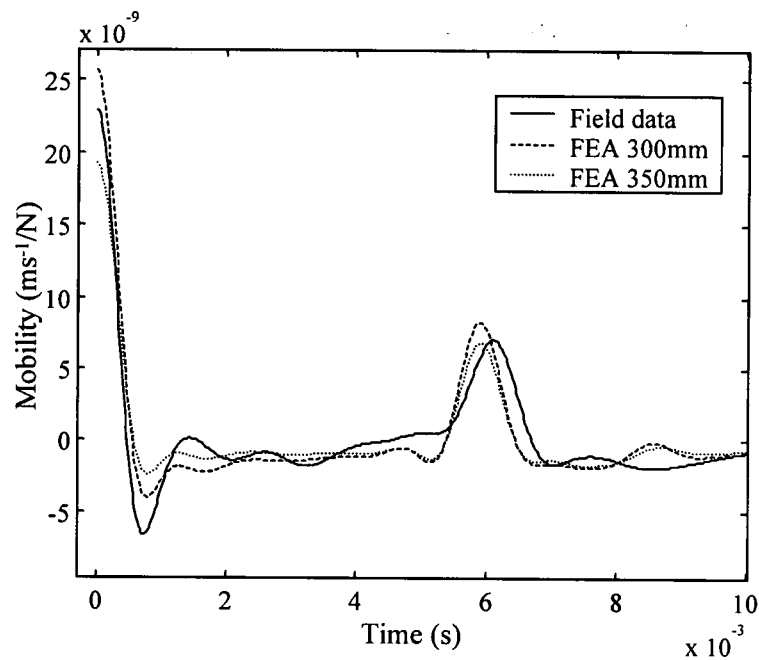


Figure 7.43 Shows how the de-noised field data for pile T09 (11m long and 300mm diameter) gives a trace closer to that of the FEA data for a 350mm diameter pile. Hence the over estimation of the pile radius shown in Figure 7.39.

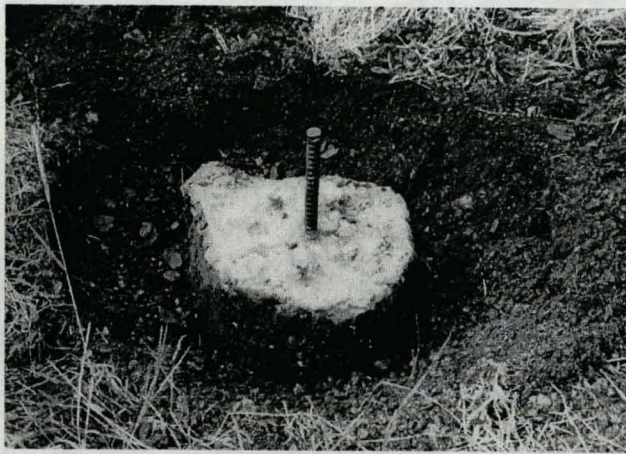


Figure 7.44 Shows plates of pile A01 excavated to 500mm (top), 250mm (middle) and with no excavation (beneath).

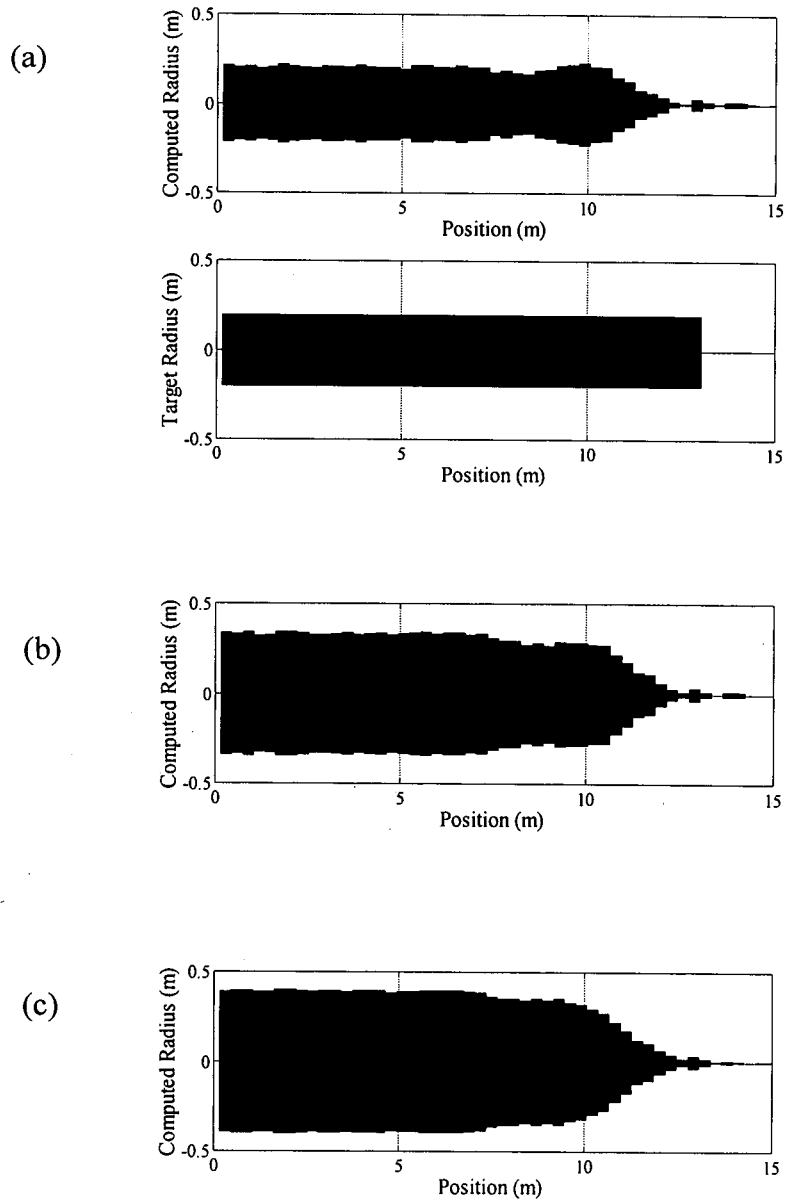


Figure 7.45 Shows the effects of excavating the pile head. When the head is excavated (as modelled in the FEA generated training data) the radius is correctly identified as 200mm (a). However, for the traces where only 250mm of the head is excavated (b) or no excavation (c) the increase in apparent pile head stiffness has resulted in an overestimate of the pile radius: 0.3m for the 250mm excavated pile and 0.4m for the results with no excavation.

8. Conclusions

The load bearing capacity and settlement characteristics of a cast *in situ* pile can only be satisfactorily deduced from static load tests. However, load testing of entire pile groups is impractical. Integrity testing is therefore employed to find piles with atypical acoustic characteristics which can then be load tested or investigated further. This enables all piles with suspected abnormalities to be included in the test set so limiting the over design necessary in the pile group.

The most widely used integrity test for small diameter cast *in situ* piles, in the UK, is the low strain integrity test.

Conventional interpretation of these tests' results requires the iterative process of wave matching which can involve a great deal of time and, therefore, expense. Recently developed deterministic methods for the automated reconstruction of the pile profile from test results suffer from the high degree of processing necessary in the wave trace methods.

The most significant achievements resulting from this research are:

- i) The development of the mobility scalogram which in the context of this research has been shown to be superior to Fourier mobility curves in the pre-processing of test data.
- ii) The use of this signal processing methodology in the development of a neural system whose strengths are the weaknesses of human experts: specifically the identification of defects within one pulse length of the pile head.

In the following section an overview of the degree to which the key objectives outlined in Chapter 1 have been achieved is given. This is followed by in-depth conclusions drawn from this study.

8.1 KEY OBJECTIVE ACHIEVEMENTS

With reference to the key research objectives outlined in Section 1.2, the overall project conclusions are as follows:

- i) Current methods employed in the integrity testing of cast *in situ* foundation piles have been reviewed and an industry survey has been completed to determine their relative popularity, perceived effectiveness, and costs. The Sonic Echo Integrity Test method has been identified as a suitable candidate for interrogation by neural networks because: it contains noisy and uncertain data, it is difficult to model the system mathematically, and the system is required to integrate different types of data (data fusion) i.e. temporal (the trace) and spatial (the environment).
- ii) An FEA model for the simulation of a pile head's response to hammer blow excitation has been presented, see Section 8.3. This generated data has been used in the supervised learning of neural systems.
- iii) A feasibility study has been completed. By limiting the problem domain to uninstalled piles containing a single fault an indication that a neural system can learn the necessary mapping such that the primary research objective can be fulfilled was obtained.
- iv) An investigation into the effects of pre- and post-processing on system performance has been completed. This included the development of a novel wavelet transform technique, *the mobility scalogram*, as well as consideration of conventional Fourier techniques. As reported in Section 6.2.4, this method of data filtering and presentation proved to give superior network performance over that of the Fourier mobility curve data ($\approx 25\%$ lower mean test pattern error).

- v) Optimum network architecture and training methods have been reported for the three networks under investigation, namely: Multilayered Perceptron (MLP) networks, Radial Basis Neural Networks (RBNN) and Wavelet Basis Neural Networks (WBNN). Specific conclusions relating to this aspect of the research can be found in Section 8.4.

- vi) The selected system, the MLP network, has been evaluated through its performance with respect to field test data - see Section 8.5.

8.2 CONCLUSIONS SPECIFIC TO MODELLING

Network training using collated field test data was impossible due to uncertainty inherent in both input and output data sets.

The finite element method was capable of generating time traces which include features associated with pile head ringdown and radial shear wave propagation within the soil. The use of implicit integration methods in this model has resulted in traces consistent with field test results. The mechanical ringdown reported in previous research and described in Chapter 4, it is suggested, is more likely to be a consequence of the numerical aberrations inherent in the explicit integration methods employed.

For plastic tipped hammers the input pulse has been shown to be better approximated through a Gaussian estimate rather than conventional half-sine pulse shapes. The frequency make-up of the resultant pulse then produces a mobility curve more in keeping with observed field test results.

The proportion of the incident pulse that is reflected and transmitted across a change in pile section is consistent with one dimensional wave theory. The presented model also has measured particle velocity attenuation consistent with that of one dimensional wave theory. The mesh density required for this correlation to hold was, however, shown to be dependent on the stiffness of the soil being modelled.

Results for this finite element model correlate well with *in situ* field test results. Calculated fault depths were consistent with theory and correspond well with field test data.

8.3 CONCLUSIONS SPECIFIC TO SYSTEM DEVELOPMENT

Commercially available data acquisition equipment is light and robust, but inflexible in its usage and prohibitively expensive for research purposes. Equipment previously employed by the University for data acquisition is bulky and complex in its usage. It is neither conducive to the rapid checking of pile groups nor the 'on-line' analysis of collected data.

A new data acquisition system has been developed for this study. All its components are ISO 9000 quality assured and have been supplied with calibration certificates.

Custom software has been developed by the author to control this hardware through a graphical user interface and import the collected data directly to Matlab™ for subsequent analysis. A suite of network simulators have also been written for the initialisation and training of Multilayered Perceptron (MLP) networks, Radial Basis Neural Networks (RBNN) and Wavelet Basis Neural Networks (WBNN).

For RBNN's, training through vector quantisation initialisation followed by back propagation learning has shown improved results over those using either one of these methods independently.

A new method for initialising WBNN's has been presented based on the vector quantisation method used for RBNN's. This is computationally quicker and less memory intensive than the modified Gram-Schmidt algorithm. No claims are made about relative performances of the two methods.

Validation of the network simulator software has been presented. For the MLP case previously published results have been satisfactorily reproduced. For the RBNN and

WBNN networks an arbitrary function containing a spike, a Gaussian and a plateau has been approximated with results consistent with those expected. That is, network performance improved as the number of hidden units was increased and improved further subsequent to back propagation training.

A new concept in sonic echo data processing has been presented: *the mobility scalogram*. De-noising using this method produces an input excitation independent trace better representative of the original signal than Fourier filtered equivalent. This method of data filtering and presentation proved to give superior network performance than that of the Fourier mobility curve data ($\approx 25\%$ lower mean test pattern error).

Parametric studies show that presenting the data as a continuous vector representation of the resultant trace gives superior error measures to those when the trace is further encoded into its predominant features. Faster learning rates have been achieved by presenting these scalars in a logarithmic form.

Superior results are obtained for an output array of 50 units where each unit represents the difference in radius over a 0.3m unit length to that which is expected rather than the pile radius at that location.

For the five hundred patterns available for this study, optimum pattern errors in an MLP network containing one hidden layer of 50 units were seen to drop by over 15% when over 400 patterns were included in the training set. Subsequent increases in the size of the training set did not provide equivalent increases in network performance. Thus, in this study, the training set consisted of 450 patterns while the test set held 50. For error analysis of network performance experiments were repeated 10 times, each time with a different test set.

For the MLP network with hyperbolic tangent hidden and output units the optimum learning rate was found to be 0.1 and the optimum momentum, 0.9. While adding a second hidden layer of units did consistently improve network performance with respect to the number of units per layer, adding a third did not. The topology of the

selected network, therefore, consisted of two hidden layers each of 40 hidden units. For both radial systems, improved results were obtained when two different learning rates were applied to the two weight layers. Optimum mean pattern errors were obtained for the Radial Basis networks of thirty five hidden units with learning parameters: $\alpha_c=5 \times 10^{-2}$, $\alpha_{wi}=1 \times 10^{-3}$, and $\alpha_{wo}=1 \times 10^{-2}$. Optimum mean pattern errors were obtained for the Wavelet Basis networks of fifty hidden units with learning parameters: $\alpha_c=1 \times 10^{-2}$, $\alpha_{wi}=1 \times 10^{-6}$, and $\alpha_{wo}=1 \times 10^{-3}$.

The MLP network was superior in identifying profiles containing a single fault, was more consistent in its selectivity and comparable with the other networks in diagnosing arbitrary pile profiles. As it is the dominant, or first, fault identification that is of primary importance in pile integrity testing it is the MLP that was, therefore, selected as the network of choice for evaluation using field test data.

8.4 CONCLUSIONS SPECIFIC TO FIELD TESTING

The neural network system described in Chapter 6 has successfully identified a complete loss of section in a driven pile of a square cross-sectional shape. Hence, this methodology need not be restricted purely to circular, cast *in situ* piles.

The neural system described in Chapter 6 has identified known faults from test traces taken from the EPSRC test site at Blyth. The performance of the system was dependent upon known test method limitations and the accuracy of the training data employed. That is, the network's performance deteriorates for smaller faults and those located nearer the pile toe.

The neural network identified faults or changes in radius located within one impact pulse wavelength from the pile head. A 6% difference in pile head diameter between the FEA generated training data and data from the Blyth test site was identified and diagnosed to within 3% of its actual value.

The neural system identified, located and quantified necks and bulbs of greater than 25% of the pile radius, along the pile length, within the confines of known test method limitations.

The neural network gave reasonable results for field test data upon which it has not been trained. Specifically, small losses in section were reported when results from piles containing occluded voids and cracking were presented.

The neural network identified changes in pile head radius in soft and stiff clay sites to an accuracy predominantly defined by the accuracy of the training data. The derived pile lengths for all piles tested at the soft clay site at Bothkennar site were correct to $\pm 5\%$. While the calculated pile radii for the piles at this site were correct to within 20% of the actual radius. This error is predominantly due to errors in the modelling of the pile head where the surrounding soils' effect on the pile head's dynamic stiffness strongly influences the system's response.

9. Recommendations for Future Research

9.1 INTRODUCTION

In this Chapter a number of suggestions are made concerning the logical continuation of the research reported in this thesis. For clarity, these suggestions have been categorised into four sections: pile response modelling, hardware, pre-processing and neural systems.

9.2 PILE RESPONSE MODELLING

With respect to the generation of the traces used for training the neural networks: it is recognised that the pattern set size of five hundred is not optimal. That is, the test set mean pattern error is still decreasing when larger training sets are applied. Using five hundred patterns also restricts the test set size such that experimental repetitions have to be carried out for error analysis to be considered valid. However, five hundred patterns represents four weeks processing time on a Pentium™ 166MHz personal computer. Even allowing for the batch processing techniques developed by the author, the mesh generation and post-processing necessitated by this technique equates to over two months work simply to provide the data needed for the execution of the presented research. Clearly this methodology would not lend itself to commercial testing.

Given that the network can analyse hundreds of traces in a matter of seconds, the rapid generation of data takes on a far greater importance if this research is to be exploited to

produce an industrially useful tool. If the time taken to produce a trace could be reduced to the order of tens of seconds rather than tens of minutes then a complete system could be trained to analyse any number of traces, automatically, overnight.

One dimensional modelling can reduce the time taken to generate a trace to less than a second. This equates to 5000 generated traces in less than an hour and a half; a trained network and its analysed results could then be expected in under four hours. However, although one dimensional modelling is widely used in industry, research suggests that its results are inferior to those obtained by finite element analysis in the modelling of *in situ* piles. The effects on network performance of this inferior modelling technique should, therefore, be quantified with a view to their use in any future applications.

Alternatively, finite element analysis may be optimised to reduce the speed of computation of a pile head response. Energy absorbing boundary conditions could be used for modelling infinite boundaries for dynamic analysis. This could potentially reduce the mesh size and, therefore, the computation time. A full parametric study of the effects of utilising such a feature would then have to be carried out.

In summary, if a method for the rapid generation of pile data could be developed then the neural network method could become a commercially useful quality assurance tool for the automated checking of integrity test data.

9.3 HARDWARE

While a considerable improvement on the data acquisition equipment previously used for impact testing research at Napier the hardware is still bulky and complicated when compared with its industrial equivalents. The cost of purchasing commercially available pile test equipment may be considered prohibitively high for the purposes of a postgraduate project, but a number of design features may be copied to improve the usability of the described hardware. Specifically, by integrating the junction box and

signal conditioning units into a single module the portability of the equipment will be improved and length of cabling reduced. This may also improve the signal to noise ratio of the recorded trace.

9.4 SIGNAL PRE-PROCESSING

A great deal of recent research has been carried out by the author, at Napier University, into the utilisation of Wavelet processing of Sonic Echo test data. This has taken the form of two successful Engineering and Physical Sciences Research Council (EPSRC) grant applications sponsored by industrial collaborators. It has culminated in a number of publications, as listed at the front of this thesis. Specifically, it has resulted in the wavelet mobility scalogram and temporal filtering techniques described herein.

Work is continuing in this field to develop more sophisticated algorithms for the interpretation of the modulus maxima plots and ridge following techniques. For example, it is known that a singularity in the analysed trace will result in scalogram coefficient values decaying exponentially from a maximum with respect to increasing scale (band pass centre frequency). It may, therefore, be possible to estimate the expected value for very high frequency components that are corrupted by white noise. The resultant de-noised trace will thus become a better estimate of the original signal through the utilisation of *a priori* knowledge of the signal under investigation and the mathematical properties of the wavelet used.

Further research into the applicability of orthonormal wavelets and discrete wavelet transforms are also being researched. Wavelets with a more compact frequency support are being considered and the effects of their lack of shift invariance quantified. If successful this could provide a basis for wavelet encoding of trace data for network input.

9.5 NEURAL SYSTEMS

Before considering possible future research concerning neural networks in this field it is worth considering the possible utilisation of the wavelet encoding strengths identified in Chapter 6. It has been shown that the salient information contained in the sonic echo trace can be encapsulated in as few as ten wavelet coefficients with their associated scale and time parameter values. It would, therefore, be reasonable to suggest that these coefficients could be used as a basis for a knowledge based system. While the complexity of the system domain would necessitate automated rule inference the coefficients do appear a more sensible primitive for the trace description than the straight line parsing used in previously reported research.

With respect to neural network types: as reported in Chapter 3 there remains a plethora of architectures and learning paradigms that may be employed for the described task. However, the promise shown by the systems developed in this thesis leads the author to believe that the feedforward networks, with their function approximation strengths, remain the most likely to be utilised in any industrial tool. The Euclidean distance measure employed by the radial network types does not, however, appear particularly suitable for this task. For example, the Mobility Curve, as discussed in Chapter 2, is highly dependent upon soil damping. Consequently piles of identical profiles in slightly different soil conditions will produce curves with the same general shape, but with consistently higher or lower values i.e. the shape will remain the same, but the curve slightly displaced. This will lead to a relatively high Euclidean separation distance between the two curves. Conversely, a third curve with completely different peak and trough positions, that happens to coincide with the first for some of its length, may give a relatively low separation distance. While it is recognised that other generally used distance measures like the Hamming distance will suffer from the same effects, there exist measures that better describe the relative curve shapes rather than simply a summation of differences between vector components considered in isolation. The application of a new rule of propagation would necessitate the derivation of a new

learning paradigm and as such would fall outside the specification of the research described herein, but may improve system performance.

As discussed in Chapter 6 it may be that improving the size of the pattern set enables the network to produce a better performance through a better description of the input space and more hidden units allowing better resolution in the output space. However, these are essentially problems associated with modelling. If these problems could be overcome then it would be feasible to extend the research contained in this thesis to produce a more flexible system capable of providing an output for any site given the prevailing soil conditions and pile design dimensions. Such a system would, however, be necessarily large and with the increased size of the required training set would take a long time to train (of the order of days, if not weeks). It is hoped the research presented in this thesis may be a step towards this ultimate goal.

APPENDIX I

**Industry Survey Questionnaire
and List of Respondents**

This Questionnaire is purely for academic research purposes. Its contents are considered to be confidential and the views of individual companies will not be disclosed or published without their express permission.

Company contact: Phone:
[Preferably the person who completes the questionnaire]

The ICE 'Specification for Piling' suggests three methods for the integrity testing of piles. Do you use:

- Sonic echo method. [Please complete section I]
- Vibrational method. [Please complete section II]
- Sonic logging (coring) [Please complete section III]

If you use none of the above, what method do you use ?

Why ?
.....
.....

I. Sonic Echo.

What type of testing do you carry-out?
[CEBTP, TNO, own method]:

Do you consider the accuracy of the testing to be limited by the hardware you presently employ? If so do you ever investigate new equipment with a view to changing to a more reliable, more automated system?

- Present system more than adequate, would stick to tried and trusted formula.
- Would change systems if it was shown to facilitate testing.

How much (very approximately) does it cost you to test a pile by this method ?

II. Vibrational Method.

Do you consider this method to be more accurate than the sonic echo method ?

- Yes
- No
- Sometimes

Why/Under what circumstances ?
.....
.....

How much (very approximately) does it cost you to test a pile by this method ?

III. Sonic Logging Method.

Do you consider this method to be more accurate than the sonic echo method ?

- Yes No Sometimes

Why/Under what circumstances ?
.....
.....

How much (very approximately) does it cost you to test a pile by this method ?

Common to all Sections:

Are you interested in fault diagnosis or is fault location adequate for the work you carry out?
e.g. if a pile had overbreak and necking which also caused areas of weakened concrete would you:

- want to know these faults & their locations?
 be satisfied with the knowledge the pile is completely unsound?

Would it be possible for me to observe some testing being carried out in the field? This would help me a great deal in appreciating the problems and principles involved in piled foundation integrity testing.

- Unfortunately, we are unable to fulfil this request.
 In principle, this could be arranged.

Thank you very much for taking the time to fill out this form. May I, again, state that this is purely for research purposes and ask that if you have any other information or literature you think may be relevant that you let me know.

Thanks Again.

Jamie Watson BSc(Hons) MSc
Dept. Civil & Transportation Engineering
Napier University
10 Colinton Road
Edinburgh.
EH10 5DT

A list of the companies that kindly replied to the questionnaire reported in Chapter 2.

British Geotechnical, Bridgenorth.

Cementation Piling and Foundations Ltd, Rickmansworth.

Central Piling Ltd, Halstead.

Colets Piling Ltd, Effingham.

Costain Civil Engineering Ltd, Erith.

Del Piling Contractors, Chesterfield.

Fugro Ltd, Hemel Hemstead.

Metropolitan Specialist Services Ltd, London.

ND Technology, Southampton.

NDT Services, Darlington.

Rock and Alluvium Ltd, Wimbledon.

Roger Bullivant, Burton on Trent.

Simplex Piling Ltd, Chingford.

Stent Foundations Ltd, Hook.

Swanthorpe Piling and Civil Engineering, Farnham.

TBV Stranger, Elstree.

Technotrade Ltd, Harpenden

Testconsult Ltd, Warrington.

Testing and Analysis Ltd (Testal), Somercotes.

Westpile Ltd, Uxbridge.

PUBLISHED PAPER(S)

NOT INCLUDED WITH THESIS